Transactions of the ASME®

Technical Editor, **LEWIS T. WHEELER (1997)**

Department of Mechanical Engineering,
University of Houston,
Houston, TX 77204-4792

APPLIED MECHANICS DIVISION

Chairman, **T. A. CRUSE**
Secretary, **A. NEEDLEMAN**
Associate Technical Editors,
R. ABEYARATNE (1997)
T. R. AKYLAS (1997)
D. M. BARNETT (1996)
R. BECKER (1998)
S. A. BERGER (1997)
I. M. DANIEL (1996)
W. J. DRUGAN (1997)
J. T. JENKINS (1996)
J. W. JU (1998)
S. KYRIAKIDES (1997)
S. LICHTER (1998)
W. K. LIU (1996)
X. MARKENSCOFF (1997)
M. ORTIZ (1998)
J. N. REDDY (1998)
W. N. SHARPE, JR. (1996)
S. W. SHAW (1997)
M. SHINOZUKA (1997)
M. TAYA (1996)

BOARD ON COMMUNICATIONS

Chairman and Vice-President
R. MATES

Members-at-Large
T. BARLOW, N. H. CHAO, A. ERDMAN, G. JOHNSON, L. KEER, E. M. PATTON, S. PATULSKI, S. ROHDE, R. SHAH, F. WHITE, J. WHITEHEAD, K. T. YANG

OFFICERS OF THE ASME
President, **D. T. KOENIG**
Executive Director, **D. L. BELDEN**
Treasurer, **R. A. BENNETT**

PUBLISHING STAFF
Managing Director, Engineering
CHARLES W. BEARDSLEY
Director, Technical Publishing
JANET M. WEINRIB
Managing Editor, Technical Publishing
CYNTHIA B. CLARK
Managing Editor, Transactions
CORNELIA MONAHAN
Production Editor
JUDITH SIERANT
Production Assistant
MARISOL ANDINO

Transactions of the ASME, Journal of Applied Mechanics (ISSN 0021-8936) is published quarterly (Mar., June, Sept., Dec.) for $210.00 per year by The American Society of Mechanical Engineers, 345 East 47th Street, New York, NY 10017.
Second class postage paid at New York, NY and additional mailing office. POSTMASTER: Send address changes to Transactions of the ASME, Journal of Applied Mechanics, c/o THE AMERICAN SOCIETY OF MECHANICAL ENGINEERS, 22 Law Drive, Box 2300, Fairfield, NJ 07007-2300.
CHANGES OF ADDRESS must be received at Society headquarters seven weeks before they are to be effective. Please send old label and new address. **PRICES:** To members, $40.00, annually: to nonmembers, $210.00. Add $30.00 for postage to countries outside the United States and Canada.

STATEMENT from By-Laws. The Society shall not be responsible for statements or opinions advanced in papers or . . . printed in its publications (B7.1, Para. 3), **COPYRIGHT © 1995** by The American Society of Mechanical Engineers. Authorization to photocopy material for internal or personal use under circumstances not falling within the fair use provisions of the Copyright Act is granted by ASME to libraries and other users registered with the Copyright Clearance Center (CCC). Transactional Reporting Service provided that the base fee of $3.00 per article is paid directly to CCC, Inc., 222 Rosewood Drive, Danvers, MA 01923. Request for special permission or bulk copying should be addressed to Reprints/Permission Department. **INDEXED** by Applied Mechanics Reviews and Engineering Information, Inc. Canadian Goods & Services Tax Registration #126148048.

Journal of Applied Mechanics

Published Quarterly by The American Society of Mechanical Engineers

VOLUME 62 • NUMBER 4 • DECEMBER 1995

TECHNICAL PAPERS

827 **Analysis of Shear Band Development in a Viscoplastic Double Slip, Single Crystal in Tension**
S. Yang and C. Rey

834 **Out-of-Plane Buckling of Fiber-Reinforced Thermoplastic Sheets Under Homogeneous Biaxial Conditions**
G. R. Christie, I. F. Collins, and D. Bhattacharyya

841 **Time Frequency Analysis of Dispersive Waves by Means of Wavelet Transform (95-WA/APM-2)**
Kikuo Kishimoto, Hirotsugu Inoue, Makoto Hamada, and Toshikazu Shibuya

847 **Distributional Concept of the Elastic-Viscoelastic Correspondence Principle**
V. Kovarik

853 **A Nonlinear Wound Roll Model Allowing for Large Deformation (95-WA/APM-4)**
R. C. Benson

860 **A Circular Inclusion With Imperfect Interface: Eshelby's Tensor and Related Problems (95-WA/APM-3)**
Zhanjun Gao

867 **Self-Excited Oscillations of Two Elastic Half-Spaces Sliding With a Constant Coefficient of Friction (95-WA/APM-6)**
G. G. Adams

873 **Propagation of Boundary Disturbances in an Axially Moving Strip in Contact With Rigid and Flexible Constraints**
W. D. Zhu and C. D. Mote, Jr.

880 **Vibration Characteristics of Simply Supported Thick Skew Plates in Three-Dimensional Setting**
K. M. Liew, K. C. Hung, and M. K. Lim

887 **Out-of-Plane Impact at the Tip of a Right-Angled Bent Cantilever Beam**
B. Wang, T. X. Yu, and S. R. Reid

893 **Three-Dimensional Frictional Rigid-Body Impact**
V. Bhatt and Jeff Koechling

899 **The Limit of Wave Propagation on the Free Surface of a Viscous Fluid**
J. P. McHugh, F. C. Bedford, and R. Leighton

903 **Intermittency Route to Chaos of a Cantilevered Pipe Conveying Fluid With a Mass Defect at the Free End**
C. Semler and M. P. Païdoussis

908 **Viscoelastic Effects in Modeling Web Handling Systems: Steady-State Analysis**
X. Guan, M. S. High, and D. A. Tree

915 **Taylor-Couette Instability With a Continuous Spectrum**
L. S. Yao and S. Ghosh Moulic

924 **On the Transformation Properties of the Nonlinear Hamel Equations**
J. G. Papastavridis

930 **Complete Solution of the Linear Magnetoelasticity and the Magnetic Fields in a Magnetized Elastic Half-Space**
Huang Ke-Fu and Wang Min-Zhong

935 **Attitude Behavior of a Variable Mass Cylinder (95-WA/APM-1)**
F. O. Eke and Song-Min Wang

941 **Boundary of the Basin of Attraction for Weakly Damped Primary Resonance**
R. Haberman and E. K. Ho

947 **The Stiffest Wire**
K. Schulgasser

952 **A Shape Design Sensitivity Approach for Two-Dimensional Mixed-Mode Fracture Analysis Under General Loading**
Tae Won Lee and I. R. Grosse

959 **Stability of Cohesive Crack Model: Part I—Energy Principles (95-WA/APM-7)**
Z. P. Bažant and Yuan-Neng Li

965 **Stability of Cohesive Crack Model: Part II—Eigenvalue Analysis of Size Effect on Strength and Ductility of Structures (95-WA/APM-8)**
Z. P. Bažant and Yuan-Neng Li

(Contents continued on Outside Back Cover)

Downloaded 04 May 2010 to 171.66.16.52. Redistribution subject to ASME license or copyright; see http://www.asme.org/terms/Terms_Use.cfm

CONTENTS (CONTINUED)

970 **Rotational Dynamics of Axisymmetric Variable Mass Systems (95-WA/APM-5)**
S.-M. Wang and F. O. Eke

975 **Optimal Design Problems in Mechanics of Growing Composite Solids, Part I: Preload Optimization**
A. D. Drozdov and A. L. Kalamkarov

983 **Optimal Design Problems in Mechanics of Growing Composite Solids, Part II: Shape Optimization**
A. D. Drozdov and A. L. Kalamkarov

989 **The Contact Problem at Delamination**
A. E. Giannakopoulos, K.-F. Nilsson, and G. Tsamasphyros

997 **Displacement and Strain Fields for a Bimetallic Strip Under Remote Tension**
J. S. Epstein, S. M. Graham, K. E. Perry, and W. G. Reuter

1005 **Analysis of Ring-Stiffened Cylindrical Shells**
Bingen Yang and Jianping Zhou

1015 **Combination Resonances of a Circular Plate With Three-Mode Interaction**
Won Kyoung Lee and Cheol Hong Kim

1023 **Elastic Moduli of Composites Reinforced by Multiphase Particles**
M. L. Dunn and H. Ledbetter

1029 **Transient Analysis of Dynamic Crack Propagation With Boundary Effect**
Chien-Ching Ma and Yi-Shyong Ing

1039 **An Energy Approach to the Plasticity of a Two-Phase Composite Containing Aligned Inclusions**
Y. P. Qiu and G. J. Weng

1074 **Symmetrical Propagation of a Central Crack in Orthotropic Material**
Y. M. Tsai

1053 **Realizability of Negative Pore Compressibility in Poroelastic Composites**
P. A. Berge and J. G. Berryman

BRIEF NOTES

Anistrophy of the Vigdergauz Microstructure
Y. Grabovsky and R. V. Kohn **1063**

Radially Inhomogeneous Sheets Under Stress
H. O. K. Kirchner **1065**

1067 Transient Thermal Stresses in a Multilayered Anisotropic Medium
Tie-Chen Chen, Horng-I Jang, and Ampere A. Tseng

ANNOUNCEMENTS AND SPECIAL NOTES

872 Third EUROMECH Solid Mechanics Conference—Announcement

892 Third International Conference on Vibration Problems—Announcement

898 19th International Congress of Theoretical and Applied Mechanics—Announcement

914 IUTAN Symposium (1988 or 1999)—Call for Proposals

1022 Change of Address Form

1052 19th International Congress of Theoretical and Applied Mechancs—Call for U.S. Papers

1070 Worldwide Mechanics Meetings List

1072 1995 Author Index

inside back cover Information for Authors

ISSN 0021-8936 JOURNAL CODE JE ISSUE CODE 9504

Downloaded 04 May 2010 to 171.66.16.52. Redistribution subject to ASME license or copyright; see http://www.asme.org/terms/Terms_Use.cfm

Analysis of Shear Band Development in a Viscoplastic Double Slip, Single Crystal in Tension

S. Yang

C. Rey

LPMTM–CNRS,
Université Paris Nord,
av. J. B. Clément,
93430 Villetaneuse, France

Using an idealized planar single crystal model undergoing symmetrical double slip in tension, the effect of rate sensitivity on shear band initiation and on shear band development is analysed. The behavior of the crystal is assumed to be rigid-viscoplastic. By analysing the kinematics and statics of shear banding, the deformation modes involving shear banding pattern are formulated. By a linearized stability analysis, the critical condition for shear band initiation is obtained. To study shear band development, the formulated constitutive equations are numerically solved, and the maximum value of the localized shear is predicted. The results show three different stages of shear band development. The first corresponds to a slow progression of shear localization in the band, the second to a rapid shear localization accompanied with an unloading of surrounding material, and the third to a resumption of deformation in the surrounding material and to a progressive saturation of the shear band. All three stages depend strongly on rate sensitivity, especially the first stage which does not exist in the rigid-plastic case. Even very small rate sensitivity can delay significantly or even preclude the shear band formation. Finally a discussion of the results illustrates how a macroscopic shear band forms and propagates.

1 Introduction

It is widely recognized that shear banding is an important deformation mechanism at large strains during metal-forming processes which limits the ductility of materials. To understand this complex mechanism, studies have been focused experimentally and theoretically on single crystals. Bifurcation analysis based on the work of Hill and Hutchinson (1975) has been applied for an idealized planar double slip, single crystal presenting a rate-independent behavior by Asaro (1979). It has been shown that the "geometrical" softening due to the lattice rotation within the shear band and the vertex "directional" softening can lead to shear band bifurcation. The comparison between the theoretical prediction and the experiments seemed qualitatively satisfying (Chang and Asaro, 1981). In order to have a good understanding of shear band formation, post-bifurcation analysis is essential. The latter has been performed using the same rate-independent single crystal model by Yang (1990), Yang and Rey (1994a, 1994b). It has been shown that in the rigid-plastic case, the shear band bifurcation is accompanied with a rigid unloading of the surrounding matrix, all the plastic deformation being localized in the band. However, at large localized shear, the shear band will saturate due to the fact that the geometrical softening decreases and tends to vanish. The saturation implies the nucleation of new shear bands in the adjacent matrix and so leads to the band thickening of the macroscopic shear band (MSB).

The present work is to complete the aforementioned study by taking into account the rate sensitivity. It deals with the effect of rate sensitivity on shear band initiation and especially on shear band development. About the effect of rate sensitivity on shear band initiation, we note that a general perturbation analysis of shear strain localization has been performed by Pan (1983). The results have shown qualitatively that the rate sensitivity has a retardation effect on shear band initiation. More recently, linearized stability analyses taking into account a constant rate sensitivity were applied to the aforementioned double slip, single crystal (Molinari, 1988a, 1988b; Balke and Estrin, 1994). It is shown that if the rate sensitivity is very small, its effect on the critical condition for shear band initiation is negligible. However, the finite element simulations performed by Peirce et al. (1983), Dève et al. (1988), Harren et al. (1988) showed that even very small rate sensitivity could delay significantly the shear band formation. This implies that the very small rate sensitivity has an important effect on shear band development. This effect will be well illustrated by a model problem in this paper.

In Section 2, we formulate the constitutive equations of shear banding. In Section 3 we perform a linearized stability analysis to determine the critical condition for shear band initiation. In Section 4 we solve numerically the constitutive equations to study the shear band development. Finally, the results are discussed in Section 5 and summarized in Section 6.

2 Formulation of Shear Banding

2.1 Constitutive Law for the Viscoplastic Single Crystal. Consider Asaro's idealized planar double slip, single crystal model as shown in Fig. 1 strained in uniaxial tension along the 2-axis. The plastic deformation is assumed to result from the crystallographic slips on the two symmetrical slip systems (1) and (2) defined by their slip directions $\mathbf{s}_i$ and their slip plane normals $\mathbf{m}_i$, where i equals 1 or 2, and represents the index of the slip systems.

The behavior of the crystals is assumed to be rigid-viscoplastic. The constitutive law for viscoplastic single crystals has been

Contributed by the Applied Mechanics Division of THE AMERICAN SOCIETY OF MECHANICAL ENGINEERS for publication in the ASME JOURNAL OF APPLIED MECHANICS.

Discussion on this paper should be addressed to the Technical Editor, Professor Lewis T. Wheeler, Department of Mechanical Engineering, University of Houston, Houston, TX 77204-4792, and will be accepted until four months after final publication of the paper itself in the ASME JOURNAL OF APPLIED MECHANICS.

Manuscript received by the ASME Applied Mechanics Division, Nov. 16, 1993; final revision, July 12, 1994. Associate Technical Editor: J. W. Rudnicki.

Copyright © 1995 by ASME

Downloaded 04 May 2010 to 171.66.16.28. Redistribution subject to ASME license or copyright; see http://www.asme.org/terms/Terms_Use.cfm

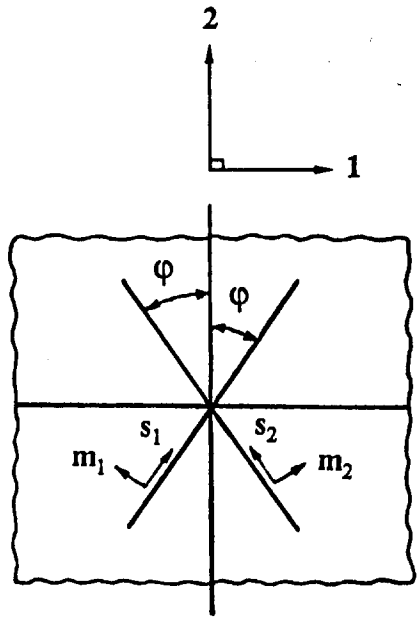


Fig. 1 The idealized planar double slip, single crystal model

established by Hutchinson (1976), Pan and Rice (1983), Peirce et al. (1983), and will be briefly recalled.

The constitutive description of the plasticity on each slip system is cast in terms of the resolved shear stress τ_i on that system and the slip rate $\dot{\gamma}_i$ on that system as

$$\dot{\gamma}_i = \dot{a}\left(\frac{\tau_i}{g_i}\right)^{1/m}, \tag{1}$$

where τ_i and $\dot{\gamma}_i$ are defined as positive value, $g_i > 0$ is the current value of the slip system hardness. In this equation, m is the rate sensitivity exponent, which is assumed to be constant in this study, $\dot{a} > 0$ is the reference shear rate. Since the strain rate is applied in the tension test, it is convenient to express Eq. (1) in the form

$$\tau_i = g_i\left(\frac{\dot{\gamma}_i}{\dot{a}}\right)^m. \tag{2}$$

From this relation, one can remark that for a rigid-plastic single crystal ($m = 0$), $\tau_i = g_i$, Eq. (2) reduces to the Schmid rule, and g_i represents the critical shear stress. As in rigid-plastic single crystals, the slip system hardness g_i evolves with the strains, and its evolution can be expressed by a latent hardening matrix (non-negative) as follows:

$$\dot{g}_i = h_{ij}\dot{\gamma}_j, \tag{3}$$

and we take h_{ij} to have elements $h_{11} = h_{22} = h$, $h_{12} = h_{21} = hq$, with $q > 0$.

2.2 Kinematic Conditions. In this paragraph, crystal kinematics involving shear banding mode will be set up. Let us assume that at one moment during tensile straining, a shear band initiates at a plane defined by the angle θ_0 inclined with respect to the tensile axis, i.e., the 2-axis (Fig. 2(a)). With increasing shear strain localization, the material is divided into two different zones, the band and the outside of the band called matrix, each zone being assumed to be homogeneous, respectively. It is evident that, with increasing straining, the lattice misorientation across the matrix/band interface, denoted by the angle α, will occur due to the localized shear λ, and that the shear band will rotate to a new angle θ as a function of the matrix strains.

Now, let us consider a volume element as shown in Fig. 2(b). For reasons of material continuity, the jump of the velocity gradient $\mathbf{L}$ across the shear band from the outside during shear banding must take the form

$$\Delta\mathbf{L} = \dot{\lambda}\mathbf{g} \otimes \mathbf{n}, \tag{4}$$

where Δ represents a jump, $\mathbf{n}$ denotes the normal to the shear band, $\mathbf{g}$ is the shear direction, $\mathbf{n}$ and $\mathbf{g}$ being orthogonal unit vectors in the current configuration and function of the angle θ. In Eq. (4), $\dot{\lambda}$ represents the localized shear rate in the shear band.

The elastic strains being neglected, one deduces that

$$\Delta\mathbf{D} = \frac{\dot{\lambda}}{2}(\mathbf{g} \otimes \mathbf{n} + \mathbf{n} \otimes \mathbf{g}) = \sum_i (\mathbf{p}_i^b\dot{\gamma}_i^b - \mathbf{p}_i^0\dot{\gamma}_i^0), \tag{5}$$

where $\mathbf{D}$ is the strain-rate tensor, the superscript 0 represents the quantity in the matrix, b in the shear band, and

$$\mathbf{p}_i = \tfrac{1}{2}(\mathbf{s}_i \otimes \mathbf{m}_i + \mathbf{m}_i \otimes \mathbf{s}_i). \tag{6}$$

In the two-dimensional case, Eq. (5) gives two useful scalar equations which allow us to obtain the following relations:

$$\begin{cases} \dot{\gamma}_1^b = \dfrac{1}{\sin 4\varphi}\,[\dot{\lambda}\sin 2(\theta + \varphi - \alpha) \\ \qquad + \dot{\gamma}_1^0 \sin 2(2\varphi - \alpha) + \dot{\gamma}_2^0 \sin 2\alpha] \\ \dot{\gamma}_2^b = \dfrac{1}{\sin 4\varphi}\,[\dot{\lambda}\sin 2(\theta - \varphi - \alpha) \\ \qquad - \dot{\gamma}_1^0 \sin 2\alpha + \dot{\gamma}_2^0 \sin 2(2\varphi + \alpha)]. \end{cases} \tag{7}$$

The jump of the lattice spin across the shear band is deduced by the difference between the jumps of the total spin and of the plastic spin as

$$\Delta\Omega^* = \frac{\dot{\lambda}}{2}(\mathbf{g} \otimes \mathbf{n} - \mathbf{n} \otimes \mathbf{g}) - \sum_i (\mathbf{w}_i^b\dot{\gamma}_i^b - \mathbf{w}_i^0\dot{\gamma}_i^0), \tag{8}$$

where Ω^* represents the lattice spin tensor and

$$\mathbf{w}_i = \tfrac{1}{2}(\mathbf{s}_i \otimes \mathbf{m}_i - \mathbf{m}_i \otimes \mathbf{s}_i). \tag{9}$$

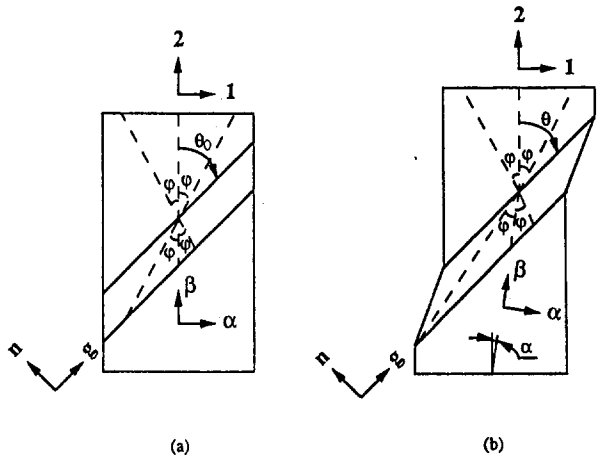


Fig. 2 (a) A shear band initiates at an angle θ_0 to the 2-axis; (b) scheme of the shear band at one moment during its development. In this figure, 1-2 is the corotational coordinate system bound to the lattice in the matrix, α–β is that in the shear band.

Downloaded 04 May 2010 to 171.66.16.28. Redistribution subject to ASME license or copyright; see http://www.asme.org/terms/Terms_Use.cfm

Using Eqs. (8), (9), and (7), we obtain

$$\dot{\alpha} = \mathbf{g}\cdot\Delta\Omega^*\cdot\mathbf{n} = \frac{\dot{\lambda}}{2}\left[1 - \frac{\cos 2(\theta-\alpha)}{\cos 2\varphi}\right] + \frac{1}{2}\left\{\left[1 - \frac{\cos 2(\varphi-\alpha)}{\cos 2\varphi}\right]\dot{\gamma}_1^0 - \left[1 - \frac{\cos 2(\varphi+\alpha)}{\cos 2\varphi}\right]\dot{\gamma}_2^0\right\}. \quad (10)$$

The spin $\dot{\theta}$ of the shear band with respect to the **2**-axis bound to the lattice in the matrix can be easily expressed in terms of the slip rates in the matrix:

$$\dot{\theta} = \dot{\gamma}_1^0 \sin^2(\theta-\varphi) - \dot{\gamma}_2^0 \sin^2(\theta+\varphi). \quad (11)$$

2.3 Static Conditions. During shear banding, the equilibrium conditions at the interface can be written as

$$\Delta\boldsymbol{\sigma}\cdot\mathbf{n} = 0, \quad (12)$$

where $\boldsymbol{\sigma}$ represents the Cauchy stress tensor. In the two-dimensional crystal model applied to an incompressible material, the component $\mathbf{n}\cdot\Delta\boldsymbol{\sigma}\cdot\mathbf{n}$ is indeterminate for a prescribed $\Delta\mathbf{D}$ (the dimension of band length is assumed to be infinite with respect to that of the band thickness), so we enforce only one nontrivial scalar equation during shear banding

$$\Delta\tau_{gn} = 0, \quad (13)$$

where τ_{gn} is the resolved shear stress on the shear band/matrix interface, i.e.,

$$\tau_{gn} = \mathbf{g}\cdot\boldsymbol{\sigma}\cdot\mathbf{n}. \quad (14)$$

Now, we shall express equilibrium Eq. (13) in terms of the slip rates in the band and in the matrix and in terms of the localized shear rate.

In two-dimensional single crystals, the resolved shear stress τ_{gn} can be expressed as a function of the current resolved shear stresses on the two slip systems as follows:

$$\tau_{gn} = \sum_i B_i\tau_i, \quad (15)$$

where B_i are factors only depending on shear band orientation with respect to the lattice axes. Expression (15) of τ_{gn} in the band is different from that in the matrix due to the lattice misorientation and due to the different strain hardening. The expressions of B_i in the band and in the matrix are given as follows:

$$\begin{cases} B_1^0 = \dfrac{\sin 2(\theta+\varphi)}{\sin 4\varphi} \\ B_2^0 = \dfrac{\sin 2(\theta-\varphi)}{\sin 4\varphi}, \end{cases} \quad (16)$$

$$\begin{cases} B_1^b = \dfrac{\sin 2(\theta+\varphi-\alpha)}{\sin 4\varphi} \\ B_2^b = \dfrac{\sin 2(\theta-\varphi-\alpha)}{\sin 4\varphi}. \end{cases} \quad (17)$$

Using relations (2) and (15) and dividing Eq. (13) by d^m, we obtain

$$\sum_i B_i^0 g_i^0 (\dot{\gamma}_i^0)^m = \sum_i B_i^b g_i^b (\dot{\gamma}_i^b)^m. \quad (18)$$

2.4 Problem Statement. We consider the uniaxial tension test along the symmetric **2**-axis (see Fig. 2). We neglect the lattice reorientation in the matrix, thus we have $\dot{\gamma}_1^0 = \dot{\gamma}_2^0$. The matrix deformation can be therefore completely determined by the stretch rate $\dot{\epsilon}^0 = \frac{1}{2}\sin 2\varphi(\dot{\gamma}_1^0 + \dot{\gamma}_2^0)$ along the **2**-axis.

The problem of shear band formation is incrementally governed by two kinematic conditions (7), one equilibrium Eq. (18) for three unknowns: $(\dot{\gamma}_1^b/\dot{\epsilon}^0)$, $(\dot{\gamma}_2^b/\dot{\epsilon}^0)$, and $(\dot{\lambda}/\dot{\epsilon}^0)$, with $\dot{\epsilon}^0 = \frac{1}{2}\sin 2\varphi(\dot{\gamma}_1^0 + \dot{\gamma}_2^0)$ and $\dot{\gamma}_1^0 = \dot{\gamma}_2^0$. The solution of these equations depends on ten state parameters: α, θ, B_1^0, B_2^0, B_1^b, B_2^b, g_1^0, g_2^0, g_1^b, and g_2^b. The lattice misorientation α and the shear band orientation θ can be at each increment updated by Eqs. (10) and (11), respectively. B_1^0 and B_2^0, B_1^b and B_2^b are function of θ and α given by (16) and (17), respectively. The increments of g_1^0, g_2^0, g_1^b and g_2^b are determined by strain-hardening law (3).

3 Linearized Stability Analysis

The homogeneous solution of the problem is $\dot{\lambda} = 0$, $\dot{\gamma}_i^b = \dot{\gamma}_i^0$, $g_i^b = g_i^0$, and $\alpha = 0$. It is evident that due to the rate sensitivity, Eq. (18) does not admit any shear band bifurcation by a jump of slip rates in the shear band from the homogeneous solution. To model shear band initiation, a linearized stability analysis is presented. The following procedure of linearized stability analysis is in fact the same as the standard one (Molinari, 1988a, 1988b; Balke and Estrin, 1994). The difference is that in the following, we try to make out the physical implication of the linearized stability analysis.

To begin with, a small shear strain $\delta\lambda$ is superposed on the homogeneous deformation field within a material band inclined at an angle θ_0 to the **2**-axis. This shear strain perturbation is accommodated by small jumps $\delta\gamma_i$ of crystallographic slip on the two slip systems inside the band, which, according to Eqs. (7), can be written as follows:

$$\begin{cases} \delta\gamma_1 = \dfrac{\sin 2(\theta_0+\varphi)}{\sin 4\varphi}\delta\lambda \\ \delta\gamma_2 = \dfrac{\sin 2(\theta_0-\varphi)}{\sin 4\varphi}\delta\lambda, \end{cases} \quad (19)$$

where δ represents a small variation in the band with respect to the corresponding quantity in the matrix. The jumps of the slip inside the band lead to a variation, in the band, of the slip system hardness which can be written from (3) as

$$\begin{cases} \delta g_1 = h(\delta\gamma_1 + q\delta\gamma_2) \\ \delta g_2 = h(q\delta\gamma_1 + \delta\gamma_2). \end{cases} \quad (20)$$

The perturbation also induces a small lattice misorientation $\delta\alpha$, which results from Eq. (10) as

$$\delta\alpha = \frac{1}{2}\left(1 - \frac{\cos 2\theta_0}{\cos 2\varphi}\right)\delta\lambda. \quad (21)$$

The lattice rotation in the band implies a variation of B_i in the band which can be written from (17) as

$$\begin{cases} \delta B_1 = -2\dfrac{\cos 2(\theta_0+\varphi)}{\sin 4\varphi}\delta\alpha \\ \delta B_2 = -2\dfrac{\cos 2(\theta_0-\varphi)}{\sin 4\varphi}\delta\alpha. \end{cases} \quad (22)$$

Let us now determine the solution of the Eqs. (7) and (18) after the perturbation. If the ratio $(\dot{\lambda}/\dot{\epsilon}^0)$ is positive, it implies that the perturbation will grow, i.e., the shear band will develop from this perturbation. On the contrary, this perturbation will decay, hence the shear band will not form.

Downloaded 04 May 2010 to 171.66.16.28. Redistribution subject to ASME license or copyright; see http://www.asme.org/terms/Terms_Use.cfm

By linearizing relations (7) we obtain

$$\begin{cases} \delta\dot{\gamma}_1 = \dfrac{1}{\sin 4\varphi}\left[\dot{\lambda}\sin 2(\theta_0+\varphi) - 2(\dot{\gamma}_1^0\cos 4\varphi - \dot{\gamma}_2^0)\delta\alpha\right] \\ \delta\dot{\gamma}_2 = \dfrac{1}{\sin 4\varphi}\left[\dot{\lambda}\sin 2(\theta_0-\varphi) - 2(\dot{\gamma}_1^0 - \dot{\gamma}_2^0\cos 4\varphi)\delta\alpha\right]. \end{cases} \tag{23}$$

After the perturbation, Eq. (18) can be written as

$$\sum_i B_i^0 g_i^0 (\dot{\gamma}_i^0)^m = \sum_i (B_i^0 + \delta B_i)(g_i^0 + \delta g_i)(\dot{\gamma}_i^0 + \delta\dot{\gamma}_i)^m. \tag{24}$$

By linearizing Eq. (24) for a constant rate sensitivity exponent m, and by taking into account (19)–(23), $\dot{\epsilon}^0 = \frac{1}{2}\sin 2\varphi(\dot{\gamma}_1^0 + \dot{\gamma}_2^0)$ and $\dot{\gamma}_1^0 = \dot{\gamma}_2^0$, we obtain

$$\frac{\dot{\lambda}}{\dot{\epsilon}^0} = -\frac{1}{ma}\left(\frac{C}{g} + mb\right)\delta\lambda, \tag{25}$$

where

$$a = \frac{1}{\sin^2 4\varphi}\left[\sin^2 2(\theta_0+\varphi) + \sin^2 2(\theta_0-\varphi)\right], \tag{26}$$

$$b = \left(\frac{\cos 2\theta_0}{\sin 2\varphi}\right)\cdot\left(1 - \frac{\cos 2\theta_0}{\cos 2\varphi}\right)\cdot tg^2 2\varphi, \tag{27}$$

$$C = \frac{1}{2}h\left\{(1+q)\left(\frac{\sin 2\theta_0}{\sin 2\varphi}\right)^2 + (1-q)\left(\frac{\cos 2\theta_0}{\cos 2\varphi}\right)^2\right\} - g\,\frac{\cos 2\theta_0}{\sin 2\varphi}\left(1 - \frac{\cos 2\theta_0}{\cos 2\varphi}\right), \tag{28}$$

and $g = g_1^0 = g_2^0$ represents the slip system hardness just before the shear band initiation. From (25) we obtain the condition for shear band initiation $(C/g + mb) \le 0$, i.e.,

$$h/g \le (h/g)_c = \frac{2\,\dfrac{\cos 2\theta_0}{\sin 2\varphi}\left(1 - \dfrac{\cos 2\theta_0}{\cos 2\varphi}\right)}{(1+q)\left(\dfrac{\sin 2\theta_0}{\sin 2\varphi}\right)^2 + (1-q)\left(\dfrac{\cos 2\theta_0}{\cos 2\varphi}\right)^2} \times (1 - mtg^2 2\varphi). \tag{29}$$

Note that in the rigid-plastic case, it reduces to the shear band bifurcation condition $C \le 0$ (Yang, 1990; Yang and Rey, 1994a; Asaro, 1979). From (29) we can see that the critical value $(h/g)_c$ for which shear band can grow. from the perturbation decreases $100\,mtg^2 2\varphi$ percent in the presence of rate sensitivity. This implies a retardation effect of rate sensitivity on shear band initiation. This result is in agreement with that of Molinari (1988a, 1988b) and Balke and Estrin (1994). From (29), one can deduce that a rate sensitivity exponent $m = ctg^2 2\varphi$ is sufficient to preclude completely the shear band initiation.

It must be indicated that in Asaro (1979), Yang (1990), and Yang and Rey (1994a), the critical value for shear band bifurcation in rate-independent single crystal is expressed in (h/σ) $[(h/\sigma)_c = (1/2)\sin 2\varphi(h/g)_c]$, where σ represents the tensile stress at the bifurcation moment. In rate-sensitive material, it is not suitable to use this ratio, because the critical value expressed in this ratio depends on applied tensile strain rate. We prefer to use the critical value in (H/σ), where H represents the tensile strain-hardening rate, i.e., the slope of the stress-strain curve. This is a macroscopic parameter (In the tension test, $(H/\sigma) = 1$ corresponds to the onset of necking.) For a constant strain-rate tensile test, one can easily deduce that $(H/\sigma)_c = [(1+q)/\sin 2\varphi](h/g)_c$. In Fig. 3, $(H/\sigma)_c$ is plotted as a function of θ_0 for different m values including the rate-independent case ($m = 0$). The curve presents a maximum value for a certain θ_0 angle. This angle corresponds potentially to the first shear band, independent of m value. But the maximum value, noted by $(H/\sigma)_c^{\max}$, decreases when the m value increases. Note that, when the ratio (H/σ) is below $(H/\sigma)_c^{\max}$, shear band can initiate from the perturbation within a range of initial angle θ_0 (see Fig. 3).

4 Shear Band Development

To understand how shear band develops, the constitutive equations governing the shear band development (see Section 2.4) are numerically solved (in the present work, the shear strain perturbation $\delta\lambda = 0.01$ is used). To study the effect of strain-hardening behavior on shear band development, the following simple strain-hardening law is used

$$dh = -khd\gamma \tag{30}$$

where k is a material constant, and $\gamma = \gamma_1 + \gamma_2$. This strain-hardening law describes a linear relation between h and g, and corresponds to the stage III of strain-hardening behavior of f.c.c. single crystals strained in tension, with k being the slope of this relation (Jasienski, 1985; Zehetbauer, 1993; Anongba et al., 1993). In addition, we take $q = 1$ in the latent hardening matrix (3). This is a reasonable value at large strains.

Let us consider such a slip geometry that $\varphi = 30$ deg and let us analyse the effect of small rate sensitivity on shear band development. The curves $(H/\sigma)_c$ versus θ_0 (Fig. 3) show that the first shear band initiates at the angle $\theta_0 \approx 37.2$ deg when the ratio (H/σ) falls to the critical value $(H/\sigma)_c^{\max}$ approximately equal to 0.268. Figure 4 shows the solution of the constitutive equations for the first shear band (which initiates at the ratio $(H/\sigma) = (H/\sigma)_c^{\max}$): matrix strain ϵ^0 versus the shear localization λ, for different values of m, where the strain-hardening parameter $k = 2.5$ is used (approximate value for copper single crystal). The effect of small rate sensitivity on shear band development is well illustrated by this figure. For very small rate sensitivity ($m = 0.001$ and 0.0015), the localized shear λ tends to be infinite. It means that the shear band will theoretically never saturate. This result is the same as predicted with the rigid-plastic model for $k = 2.5$ (Yang and Rey, 1994b). However, for m value slightly larger, the curve $\epsilon^0 - \lambda$ presents an asymptotic value when $\lambda = \lambda_{\max}$. This means that the shear band tends to saturate when the localized shear λ approaches the value $\lambda_{\max}$.

Another effect of rate sensitivity on shear band initiation can also be deduced from Fig. 4. The curves $\epsilon^0 - \lambda$ present three different stages: the important initial slope decreases slowly

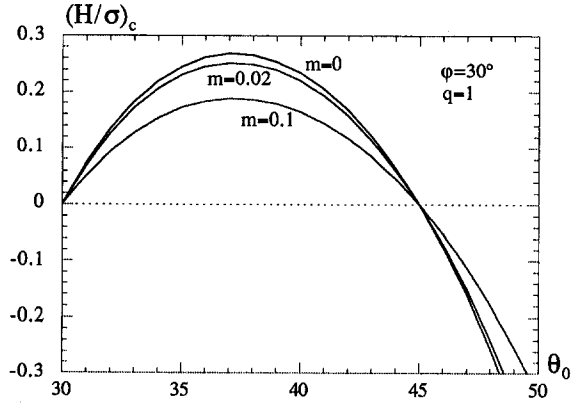


Fig. 3 The critical value $(H/\sigma)_c$ as a function of the initial angle θ_0, below which shear band can initiate from the perturbation, for different values of m

Downloaded 04 May 2010 to 171.66.16.28. Redistribution subject to ASME license or copyright; see http://www.asme.org/terms/Terms_Use.cfm

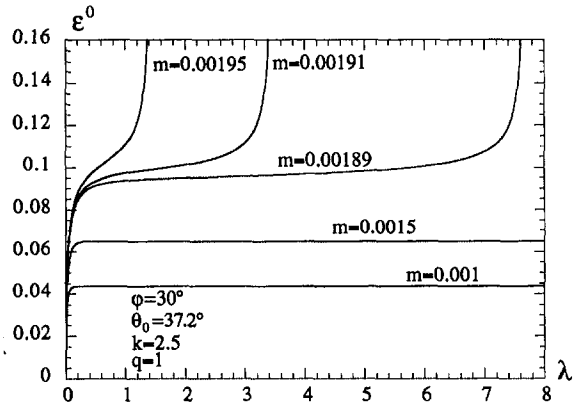


Fig. 4 The matrix strain ϵ^0 versus the localized shear λ during shear banding for different values of the rate sensitivity exponent m, the shear band initiating at the ratio $(H/\sigma) = (H/\sigma)_c^{max}$

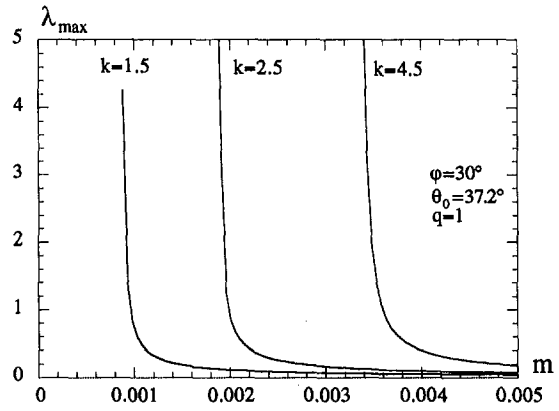


Fig. 6 Dependence of the saturation λ_{max} of the localized shear on the rate sensitivity exponent m and on the strain-hardening parameter k for the potentially first shear band

with λ, then a plateau appears and finally the slope increases sharply. The first stage corresponds to a slow progression of shear localization, the second to a rapid shear localization in shear band accompanied with an unloading of the matrix and the third to a resumption of plastic flow in the matrix and to a progressive saturation of the shear band. Recall that in the rigid-plastic case, the first stage does not exist: once the bifurcation condition is fulfilled, a rigid unloading of the matrix is accompanied with the shear localization. The first stage is therefore due to the rate sensitivity. This phenomenon implies a second retardation effect of rate sensitivity on shear band initiation. For small rate sensitivity, the first effect [$(H/\sigma)_c^{max}$ decreases when m increases] is negligible, but the second is not. The second retardation effect can be quantified by the matrix strain corresponding to the second stage. Thus we define ϵ_g^0 as the matrix tensile strain corresponding to which the slope of the curve $\epsilon^0 - \lambda$ attains to a minimum value. In Fig. 5, ϵ_g^0 is plotted as a function of the m value for different values of k, where the oscillations are due to the calculation precision (less than 0.005). From this figure, one finds that for small rate sensitivity, ϵ_g^0 increases with the m value, and the increase is more rapid when the k value is small. It must be indicated that for rate sensitivity sufficiently large, ϵ_g^0 tends to some asymptotic values. These values have not significance, because for the large rate sensitivity, the localization strain λ_{max} is too small, as can be seen in Fig. 6. This figure shows that the localized shear λ_{max} decreases sharply with increasing rate sensitivity and tends to zero if the rate sensitivity is large enough.

It is worth noting that if the m value is sufficiently small, the saturation of shear localization cannot be predicted for a large k value. This is due to the fact that a large k value corresponds to a rapid saturation of the slip system hardness in the shear band (the hardening moduli h_{ij} decrease rapidly and tend to zero). In reality, many authors have observed existence of stage IV of strain hardening which is characterized by constant strain-hardening moduli during a certain increasing strain (Jasienski, 1985; Zehetbauer, 1993; Anongba et al., 1993). If this strain-hardening property is taken into account by assuming that the stage IV begins when the ratio (h/g) reaches a critical value noted by $(h/g)_c^{IV}$, and that the stage IV holds up to rupture, the shear band saturation can be predicted. The results in Fig. 7 show that, for a k value sufficiently large and for an m value relatively small, shear band saturation depends strongly on the critical value $(h/g)_c^{IV}$.

5 Discussion

Now, let us analyse how a macroscopic shear band (MSB) forms and propagates. To begin with, it is useful to recall that a MSB is composed of numerous shear bands at slip lines scale (Yang, 1990; Yang and Rey, 1994b). They are regularly spaced. Each shear band saturates after a certain shear localization within it. The saturation of the old shear bands and nucleation of new ones in the adjacent matrix lead to the band thickening of the MSB.

In the following, as an example, we take $\varphi = 30$ deg to represent the slip geometry of the f.c.c. single crystal strained

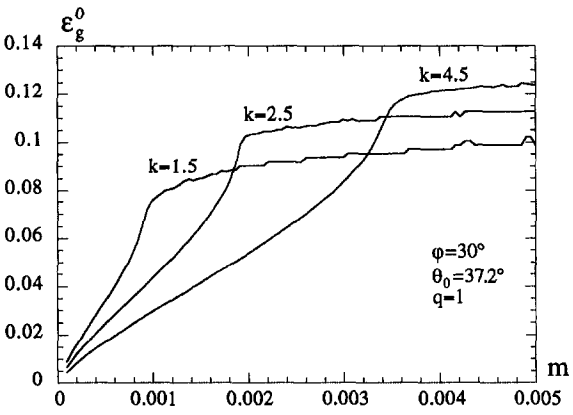


Fig. 5 The matrix strain ϵ_g^0 necessary for shear band to be well developed as a function of the rate sensitivity exponent m for different values of k

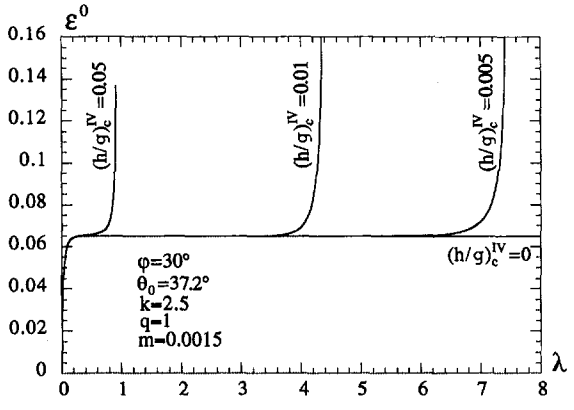


Fig. 7 The matrix strain ϵ^0 as a function of the localized shear λ during shear banding when the stage IV of strain-hardening properties is taken into account, where $(h/g)_c^{IV}$ represents the critical value for which the stage IV begins

Downloaded 04 May 2010 to 171.66.16.28. Redistribution subject to ASME license or copyright; see http://www.asme.org/terms/Terms_Use.cfm

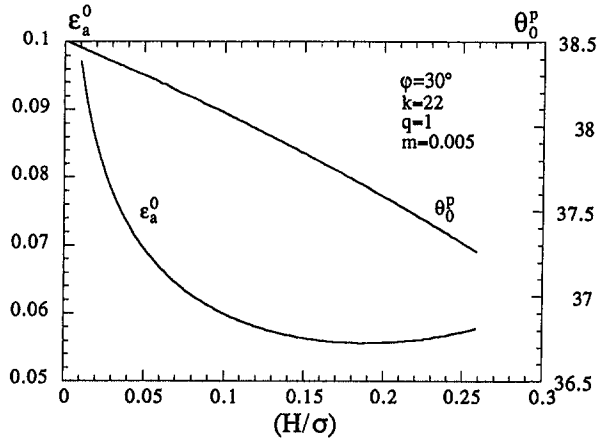


Fig. 8 The matrix strain ϵ_a^0 and the preferential initial orientation of shear band θ_0^p as a function of the ratio (H/σ) at which the shear band initiates, where ϵ_a^0 is computed from the moment when the critical condition for shear band initiation is first fulfilled $[(H/\sigma) = (H/\sigma)_c^{max}]$ to that when the shear band initiating at the given ratio of (H/σ) and at the preferential initial angle θ_0^p becomes well developed

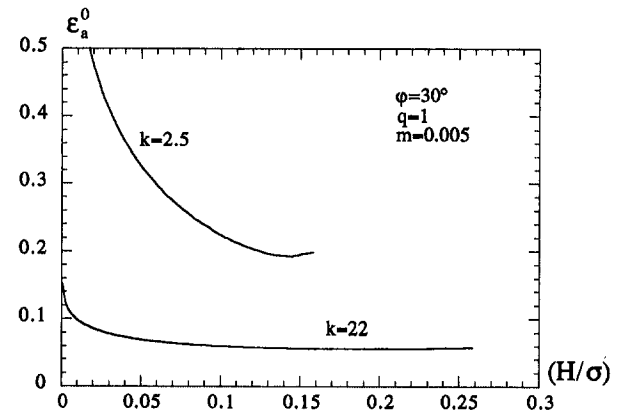


Fig. 9 The matrix strain ϵ_a^0 as a function of the ratio (H/σ) for two different values of k, where ϵ_a^0 is computed from the moment when the critical condition for shear band initiation is first fulfilled $[(H/\sigma) = (H/\sigma)_c^{max}]$ to that when the shear band initiating at the given ratio of (H/σ) and at the preferential initial angle θ_0^p becomes well developed

in tension along the [112] axis, and $m = 0.005$, which is a representative value of rate sensitivity for quasi-rate-independent material.

The condition for shear band initiation is first fulfilled at an initial angle $\theta_0 \approx 37.2$ deg when the ratio (H/σ) falls to the critical value $(H/\sigma)_c^{max}$ approximately equal to 0.268 (Fig. 3). We assume that immediately a shear band initiates with this angle. In the presence of rate sensitivity even if it is very small, development of shear strain localization in the shear band is initially slow. In other words, during the first stage of development of the shear band, the applied tensile strain is accommodated mainly by the matrix strain. As a consequence, the ratio (H/σ) in the matrix continues to decrease. When the ratio (H/σ) is below $(H/\sigma)_c^{max}$, new shear bands can initiate in the adjacent matrix within a range of initial orientation θ_0 (see Fig. 3), and the growth rate $(\dot{\lambda}/\dot{\epsilon}^0)$ of the shear localization increases (see Eqs. (25) and (28)). Within the range of the initial orientation θ_0, there is such an angle, noted by θ_0^p, corresponding to which the growth rate $(\dot{\lambda}/\dot{\epsilon}^0)$ of shear localization is the most important. One deduces that new shear band tends to initiate with this angle. This angle can be obtained by maximizing the ratio $(\dot{\lambda}/\dot{\epsilon}^0)$ in Eq. (25). In fact, it is sufficient to maximize the term $(C/g + mb)/a$. It can be shown that with decreasing ratio of (H/σ), the preferential initial angle θ_0^p of new shear bands increases and tends to a value approximately equal to 38.5 deg, independent of strain-hardening behavior. The growth rate $(\dot{\lambda}/\dot{\epsilon}^0)$ of new shear bands increases when the ratio (H/σ) decreases. One can therefore expect that some new shear bands, although they initiate later, can firstly become well developed, i.e., the second stage appears first (see Fig. 4), which corresponds to rapid shear localization with unloading of the surrounding matrix. So it is useful to define ϵ_a^0 such a matrix strain, computed from the moment when $(H/\sigma) = (H/\sigma)_c^{max}$, corresponding to which the shear band initiating at a given ratio (H/σ) below $(H/\sigma)_c^{max}$ becomes well developed. The minimum value of this quantity characterizes the retardation strain due to the rate sensitivity. The results are shown in Figs. 8 and 9.

Consider first a material constant such that $k = 22$. This is a sufficiently large k value for which shear localization λ_{max} is very important. This is also an approximate value used by Peirce et al. (1982, 1983) in the finite element simulations. Figure 8 shows the matrix strain ϵ_a^0 as a function of the ratio (H/σ) at which the shear band initiates, where the corresponding preferential initial angle θ_0^p is also plotted. It can be deduced that the first "discernible" shear band is "observed" at the strain $\epsilon_a^0 = 0.056$, which initiates at the ratio $(H/\sigma) = 0.184$ with the initial angle θ_0^p equal to 37.7 deg. In other words, the shear band formation is retarded until a strain equal to 0.056 from the moment when $(H/\sigma) = (H/\sigma)_c^{max} = 0.268$. The increasing tensile strain is then in large part concentrated in this shear band. It should be noted that during the first stage of the development of the first "observed" shear band, other shear bands initiate progressively in the adjacent matrix, and that the initial angle θ_0^p increases and tends to a value equal to 38.5 deg, because the ratio (H/σ) decreases with the matrix strain and tends to zero. Additional small matrix strain during the second stage i.e. during the large shear localization of the first "observed" shear band, especially when this shear band tends to saturate, will trigger large shear strain localization in the second, then in the third, etc. A cluster of shear bands is thus "discernible" and becomes an MSB. Old shear bands saturate consecutively. A small amount of matrix strain accompanied gives rise to nucleation of new shear bands in the adjacent matrix. As such, the MSB propagates by band thickening with a small increase of matrix strain. It can be thus deduced that new shear bands of a well-developed MSB tends to initiate at an angle of about 38.5 deg to the tensile axis.

The foregoing described propagation mechanism of MSB is the same for material with small k value. But for this type of material the retardation strain is more important, as shown by Fig. 9: for $k = 2.5$, the first "discernible" shear band initiates at the ratio $(H/\sigma) = 0.145$, and is "observed" at strain $\epsilon_a^0 = 0.192$. In addition, for this type of material the localized shear

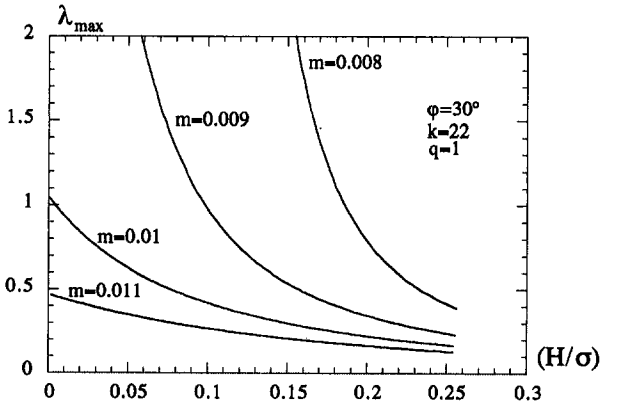


Fig. 10 The important effect of rate sensitivity on shear band saturation: the maximum value of the localized shear λ_{max} as a function of the ratio (H/σ) at which the shear band initiates, for different values of m

Downloaded 04 May 2010 to 171.66.16.28. Redistribution subject to ASME license or copyright; see http://www.asme.org/terms/Terms_Use.cfm

strain λ_{max} is relatively less important. Nevertheless, λ_{max} increases with decreasing ratio of (H/σ). This explains that the localized shear in the MSB increases with increasing straining (Yang, 1990; Yang and Rey, 1994b).

In the finite element simulations performed by Pierce et al. (1982, 1983), the slip geometry φ is taken to be 30 deg—the strain hardening properties beyond the necking corresponds to a k value approximately equal to 22. The MSBs are "observed" for rate-independent behavior ($m = 0$) at a strain interval 0.083–0.09. When the rate sensitivity $m = 0.005$ is taken into account, the MSBs are observed at strain interval 0.11–0.14. No shear band forms for $m = 0.02$. According to our model the rate sensitivity $m = 0.005$ delays shear band formation until a strain $\epsilon_a^0 = 0.056$, the localized shear λ_{max} being theoretically infinite. A rate sensitivity such as $m = 0.011$ is almost sufficient to preclude the shear band formation (Fig. 10). This is in good agreement with the finite element simulations.

6 Summary and Conclusions

By the linearized stability analysis, we have determined the condition for shear band initiation in the viscoplastic single crystal in tension. The shear band development is for the first time analyzed by solving the constitutive equations. The model shows clearly three different stages of shear band development: initiation, large shear strain localization, and saturation. By contrast to the rate-independent model (Yang, 1990; Yang and Rey, 1994a), we show that even very small rate sensitivity has an important retardation effect on shear band formation: in the rate-independent case, the second stage, i.e., the large shear strain localization begins as soon as the critical value $(H/\sigma)_c^{max}$ is reached; however, in the presence of very small rate sensitivity, although the variation of the critical value $(H/\sigma)_c^{max}$ is negligible, the second stage begins only after the first stage when (H/σ) falls sufficiently below $(H/\sigma)_c^{max}$, depending on the strain-hardening behavior (value of k). Our model also demonstrates clearly that even very small rate sensitivity must be taken into account to have a good prediction of shear band saturation, and that the shear band saturation is strongly related to the strain-hardening properties of stage III and stage IV. Finally, by taking into account the rate sensitivity, we improve the understanding of the formation and propagation mechanism of MSB (macroscopic shear band).

References

Anongba, P. N. B., Bonneville, J., and Martin, J. L., 1993, "Hardening Stages of [112] Copper Single Crystals at Intermediate and High Temperatures—I. Mechanical Behaviour," *Acta Metall. Mater.*, Vol. 41, pp. 2897–2906.

Asaro, R. J., 1979, "Geometrical Effects in The Inhomogeneous Deformation of Ductile Single Crystals," *Acta Metallurgica*, Vol. 27, pp. 445–453.

Balke, H., and Estrin, Y., 1994, "Micromechanical Modelling of Shear Banding in Single Crystals," *International Journal of Plasticity*, Vol. 10, pp. 133–147.

Chang, Y. W., and Asaro, R. J., 1981, "An Experimental Study of Shear Localization in Aluminium-Copper Single Crystals," *Acta Metallurgica*, Vol. 29, pp. 241–257.

Dève, H., Harren, S., Mccullough, C., and Asaro, R. J., 1988, "Micro and Macro Aspects of Shear Band Formation in Internally Nitrided Single Crystals of Fe-Ti-Mn Alloys," *Acta Metall.*, Vol. 36, pp. 341–365.

Harren, S. V., Dève, H. E., and Asaro, R. J., 1988, "Shear Band Formation in Plane Strain Compression," *Acta Metall.*, Vol. 36, pp. 2435–2480.

Hill, R., and Hutchinson, J. W., 1975, "Bifurcation Phenomena in The Plane Tension Test," *J. Mech. Phys. Solids*, Vol. 23, pp. 239–264.

Hutchinson, J. W., 1976, "Bounds and Self-consistent Estimates for Creep of Polycrystalline Materials," *Proc. R. Soc. Lond.*, Vol. A348, pp. 101–127.

Jasienski, 1985, "Instabilité et Localization de la Déformation dans les Monocristaux," *Matériaux et Techniques*, Août-Septembre, pp. 91–95.

Molinari, A., 1988a, "Shear Bands in a Viscoplastic Single Crystal in Tension," *C. R. Acad. Sci. Paris*, t. 306, Série II, pp. 841–846.

Molinari, A., 1988b, "Shear Band Analysis," *Solid State Phenomena*, Vol. 3 & 4, pp. 447–468.

Pan, J., 1983, "Perturbation Analysis of Shear Strain Localization in Rate Sensitive Materials," *Int. J. Solids Structures*, Vol. 19, pp. 153–164.

Pan, J., and Rice, J. R., 1983, "Rate Sensitivity of Plastic Flow and Its Implications for Yield-surface Vertices," *Int. J. Solids Structures*, Vol. 19, pp. 973–987.

Peirce, D., Asaro, R. J., and Needleman, A., 1982, "An Analysis of Nonuniform and Localized Deformation in Ductile Single Crystals," *Acta Metall.*, Vol. 30, pp. 1087–1119.

Peirce, D., Asaro, R. J., and Needleman, A., 1983, "Material Rate Dependence and Localized Deformation in Crystalline Solids," *Acta Metall.*, Vol. 31, pp. 1951–1976.

Yang, S., 1990, "Experimental and Theoretical Study of Shear Banding in Ductile Metals," Ph.D. Thesis, University of Paris XIII.

Yang, S., and Rey, C., 1994a, "Shear Band Post-bifurcation Analysis in a Planar Double Slip Single Crystal Model," *International Journal of Plasticity*, Vol. 10, pp. 279–301.

Yang, S., and Rey, C., 1994b, "Shear Band Post-bifurcation in Oriented Copper Single Crystals," *Acta Metall. Mater.*, Vol. 42, pp. 2763–2774.

Zehetbauer, M., and Seumer, V., 1993, "Cold Work Hardening in Stages IV and V of F.C.C. Metals—I. Experiments and Interpretation," *Acta Metall. Mater.*, Vol. 41, pp. 577–588.

Downloaded 04 May 2010 to 171.66.16.28. Redistribution subject to ASME license or copyright; see http://www.asme.org/terms/Terms_Use.cfm

G. R. Christie
Department of Mechanical Engineering.

I. F. Collins
Department of Engineering Science.

D. Bhattacharyya
Department of Mechanical Engineering, Mem. ASME.

School of Engineering, University of Auckland, Auckland, New Zealand

Out-of-Plane Buckling of Fiber-Reinforced Thermoplastic Sheets Under Homogeneous Biaxial Conditions

The mechanical behavior of fiber-reinforced composite thermoplastic sheets during forming processes is modelled as a viscous fluid with inextensibility and incompressibility constraints. Techniques of linear stability analysis are used to study the growth or decay of initial imperfections in plane sheets reinforced by two *families of fibers subjected to biaxial strains. This theory delimits situations when buckles can be expected to form during forming operations.*

1 Introduction

Though the use of thermoplastic sheets in component manufacturing is not uncommon, the more recent introduction of fiber reinforcement in thermoplastics has added a new dimension in their usage for load-bearing engineering products. Depending on the requirements of the final product, the nature of reinforcement can vary from continuous fiber systems to others containing some form of discontinuity in the fibers. Continuous fibers render the sheet practically inextensible in the fiber direction whereas the discontinuities provide some degree of extensibility depending on the length-to-diameter ratios of the fibers. However, the former type of sheet possesses inherently superior mechanical properties, so that as a result of the relatively recent and ready availability of continuous-fiber prepregs, new interest in the forming methodology of continuous-fiber reinforced thermoplastic sheets has been generated (Mallon et al., 1988; Smiley, 1988; Soll and Gutowski, 1988; Hou and Friedrich, 1991; Martin et al., 1992a; Bhattacharyya et al., 1993; Ó 'Brádaigh et al., 1993).

Unidirectional fiber-reinforced thermoplastic prepimpregnated sheets are commonly consolidated into laminates with the required fiber architecture. While thermoforming bidirectional laminates it has often been observed that they behave like inextensible nets (Martin et al., 1992b), deforming in a "trellis-like" manner. This type of behavior is even more closely associated with deformations of thermoplastics reinforced by fiber cloth, and has frequently been assumed in analyses of the draping of composite fabrics over nonplanar surfaces (Pipkin, 1984; Van West et al., 1991).

The formation of out-of-plane buckles is a commonly occurring defect encountered in sheet forming experiments carried out at elevated temperatures on these materials (Ó 'Brádaigh, 1991; Martin et al., 1992b). The constraints imposed by the inextensible fibers severely limit the range of possible *in-plane* deformations that the sheet can undergo. It is hence not surprising that the sheets are frequently forced to deform out of their own plane. Further to ruining the appearance of the formed part, these buckles can cause a significant reduction in the compressive strength of the composite, frequently rendering the product unacceptable.

The occurrence of these buckles is due to the slight fiber misalignments and irregularities that are always present in the composite material. In theoretical mechanics a well accepted method for investigating the possible growth of such initial imperfections is to use linear stability analysis. Small perturbations are superimposed on the fiber orientation and on to the steady-state values of the other main variables influencing the flow. These perturbations, commonly assumed to be sinusoidal in form, have an exponential variation with time, and the object of the analysis is to investigate whether or not the growth rate of these perturbations is positive, signifying that they will grow into macroscopic defects. Analyses of this type have been carried out previously in the field of fiber-reinforced thermoforming by Hull et al. (1991 and 1992) who analysed the stability of shear flows of *unidirectional* composites.

In this paper, a linear stability analysis has been used to determine the conditions that lead to instability during the homogeneous "trellis flow" of a *bidirectional* composite sheet, Fig. 1. In a trellis flow the two families of fiber shear relative to each other but there is no relative slip at the nodes. The assumption of a homogeneous deformation enables us to determine a local instability criterion which is generally applicable to a wide variety of manufacturing processes. The matrix material is also assumed to behave as an isotropic, incompressible fluid constrained by two families of inextensible fibers. As in the work by Hull et al. (1991), it is assumed that the fibers are embedded in the matrix and convect with it, so that no matrix percolation can take place. It will be shown that such an approach leads to a relatively simple instability criterion, which can be used as a first approximation in more complicated flow processes.

2 Governing Equations

In this paper we will use the general continuum mechanics models developed by Spencer, Rogers, and co-workers for idealized inextensible fiber-reinforced materials. Accounts of the general theory can be found in references (Spencer, 1972; Spencer, 1984; Hull et al., 1994). The current directions of the two families of fibers are defined by the unit vectors **a** and **b** as shown in Fig. 1 together with the coordinate system used to formulate the governing equations throughout this analysis. The x_1 and x_2-axes are the bisectors of the angles between the two fiber direction vectors and x_3 is normal to the unperturbed sheet. Hence, $\mathbf{a} = (\cos\phi, \sin\phi, 0)$ and $\mathbf{b} = (\cos\phi, -\sin\phi, 0)$ which by reason of being unit vectors, satisfy

Contributed by the Applied Mechanics Division of THE AMERICAN SOCIETY OF MECHANICAL ENGINEERS for publication in the ASME JOURNAL OF APPLIED MECHANICS.

Discussion on this paper should be addressed to the Technical Editor, Professor Lewis T. Wheeler, Department of Mechanical Engineering, University of Houston, Houston, TX 77204-4792, and will be accepted until four months after final publication of the paper itself in the ASME JOURNAL OF APPLIED MECHANICS.

Manuscript received by the ASME Applied Mechanics Division, Mar. 2, 1994; final revision, June 10, 1994. Associate Technical Editor: I. M. Daniel.

Copyright © 1995 by ASME

Downloaded 04 May 2010 to 171.66.16.28. Redistribution subject to ASME license or copyright; see http://www.asme.org/terms/Terms_Use.cfm

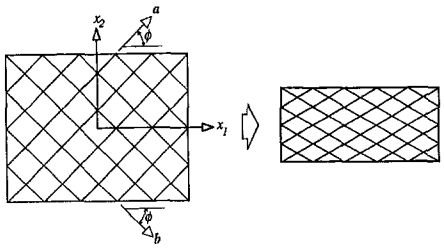


Fig. 1 Homogeneous, trellis-like deformation of an inextensible net. Notations describe the undeformed configuration.

$$a_i a_i = 1, \quad \text{and} \quad b_i b_i = 1, \tag{1}$$

where repeated indices denote summation from 1 to 3. The first kinematic constraint on the material is that of incompressibility, so that

$$\partial u_i / \partial x_i = 0 \tag{2}$$

where u_i are the velocity components. It is further assumed that the two families of fibers are inextensible so that

$$a_i a_j D_{ij} = 0 \quad \text{and} \quad b_i b_j D_{ij} = 0 \tag{3}$$

where the rate of deformation tensor D_{ij}, is defined by

$$D_{ij} = \frac{1}{2}\left(\frac{\partial u_i}{\partial x_j} + \frac{\partial u_j}{\partial x_i}\right). \tag{4}$$

Since the fibers are assumed to convect with the flowing fluid, the same element of fluid remains beside the same length of fiber. As shown by Spencer (1972) this can be expressed by

$$\dot{a} \equiv \frac{\partial a_i}{\partial t} + u_j \frac{\partial a_i}{\partial x_j} = a_j \frac{\partial u_i}{\partial x_j} \quad \text{and}$$

$$\dot{b} \equiv \frac{\partial b_i}{\partial t} + u_j \frac{\partial b_i}{\partial x_j} = b_j \frac{\partial u_i}{\partial x_j} \tag{5}$$

where the superposed $\dot{}$ denotes the material derivative D/Dt. Spencer also shows that Eq. (3) can be derived from (1) and (5) and so that these equations are not independent. The stress state in such a constrained material is the sum of reaction stresses for each of the kinematic constraints, and the deviatoric or extra stress which is related to the deformation by the constitutive equation, i.e.,

$$T_{ij} = R_{ij} + S_{ij} \tag{6}$$

where the reaction stress and the extra stress are

$$R_{ij} = T_a a_i a_j + T_b b_i b_j - p\delta_{ij} \tag{7}$$

$$S_{ij} = 2\mu D_{ij}. \tag{8}$$

The first two terms in (7) are the reaction stresses to the kinematic constraints of inextensibility in the two fiber directions, comprising two tensions T_a and T_b, while the third term is the hydrostatic pressure arising from the incompressibility constraint. As in a normal Newtonian fluid, the extra stress is assumed to be proportional to the rate of deformation tensor, D_{ij} with μ denoting the shear viscosity.

The simple form of Eq. (8) is not the most general that can be proposed for a constrained isotropic material. Rogers (1989 and 1991) presents a number of constitutive equations for the simpler case of *unidirectional* reinforced liquids which involve *two* shear viscosities, along and transverse to the fiber direction. By analogy with the analysis of a bidirectional linear elastic composite sheet analysed by Spencer (1972), one would require *five* such viscosities. However, even in the simpler uniaxial case, the values of the two viscosities are difficult to determine experimentally and researchers do not yet agree on the relative values of the two shear viscosities (Hull et al., 1992). Hence, in this first attempt at modeling the bidirectional problem the simplest model based upon Eq. (8) has been used.

The system of governing equations are closed by the three equations of motion:

$$\frac{\partial T_{ij}}{\partial x_j} = \rho\left(\frac{\partial u_i}{\partial t} + u_j \frac{\partial u_i}{\partial x_j}\right) \tag{9}$$

for $i = 1, 2, 3$ and where ρ is the density of the composite.

3 Background Homogeneous Solution

For a given fiber angle the current homogeneous deformation is defined if just one of the normal terms in the rate of deformation tensor is specified, D_1, say the extension rate in the x_1-direction, Fig. 1. Since the fibers are inextensible the directions, inclined at angles $\pm\,\phi$ to the x_1-axis, are zero extension rate directions, it follows, e.g., from Mohr's circle, that

$$D_2 = -D_1 \cot^2 \phi. \tag{10}$$

From the incompressibility condition, Eq. (2), the rate of deformation normal to the sheet is found to be

$$D_3 = -D_1(1 - \cot^2 \phi). \tag{11}$$

Note that only one of the $D_i s$ may be kept constant with time in any deformation of this type, since the fiber angle ϕ also changes with time. The material rate of change of ϕ can be calculated from

$$D(\cos 2\phi)/Dt = a_i b_i D_{ij} \tag{12}$$

which reduces to

$$\dot{\phi} = -D_1 \cot \phi = D_2 \tan \phi = -D_3(\tan (2\phi)/2). \tag{13}$$

The extra stress is found simply from the rate of deformation tensor using Eq. (8). The reaction stresses are found in terms of the fiber tensions T_a and T_b and the hydrostatic pressure p using Eq. (7):

$$R_{11} = (T_a + T_b)\cos^2 \phi, \quad R_{33} = -p$$

$$R_{22} = (T_a + T_b)\sin^2 \phi,$$

$$R_{12} = (T_a - T_b)\sin \phi \cos \phi. \tag{14}$$

Since the composite is assumed to be a thin sheet with free surfaces on each face, the stress state is one of plane stress, which implies that $T_{33} = 0$ and $p = S_{33}$. The in-plane total stress components are hence

$$T_{11} = (T_a + T_b)\cos^2 \phi + 2\mu D_1(2 - \cot^2 \phi)$$

$$T_{22} = (T_a + T_b)\sin^2 \phi + 2\mu D_1(1 - 2\cot^2 \phi)$$

$$T_{12} = (T_a - T_b)\sin \phi \cos \phi. \tag{15}$$

The background state is thus determined by four parameters, which can be chosen to be ϕ, D_1, T_a, and T_b or, equivalently, ϕ, T_{11}, T_{22}, and T_{12} as convenient.

The inverses of the relations (15) are

$$D_1 = (T_{11}\sin^2 \phi - T_{22}\cos^2 \phi)/\mu B$$

$$T_a = +T_{12}/\sin 2\phi + (T_{22}(2 - \cot^2 \phi) - T_{11}(1 - 2\cot^2 \phi))/2B$$

$$T_b = -T_{12}/\sin 2\phi + (T_{22}(2 - \cot^2 \phi) - T_{11}(1 - 2\cot^2 \phi))/2B \tag{16}$$

where

$$B = 4(\cot^2 \phi \cos^2 \phi - \cos 2\phi).$$

Downloaded 04 May 2010 to 171.66.16.28. Redistribution subject to ASME license or copyright; see http://www.asme.org/terms/Terms_Use.cfm

Spencer (1972) made the important observation that during such biaxial deformations of bidirectionally reinforced materials, only a *limited* contraction in the through-thickness direction can occur. The material is at its thinnest when the two families of fibers are mutually orthogonal ($\phi = \pi/4$) and any in plane trellis-like deformation that shifts the fiber directions away from this state will make the material thicker. This can be seen directly from Eqs. (10)–(13).

4 Stability Analysis of Out-of-Plane Buckling

Two types of instabilities are observed during the forming of thermoplastic composites. The first, in-plane *wrinkling*, appears as fiber waviness *in the plane of a ply*. In thermoforming experiments carried out at the University of Auckland with both single and double curvature moulds, this phenomenon has been observed principally on inner surface plies. Hence, it appears that in-plane wrinkling is a function of the deformation and stresses within the individual, unidirectional plies. By contrast, out-of-plane *buckling* is a phenomenon that occurs through the entire thickness of the laminate, and it is thus realistic to model the growth of these buckles with the continuum model used here.

The governing equations for the perturbed flows, which are introduced below, allow for the possibility of both modes of instability occurring. However, it will be shown that if the growing instability has an *in-plane* component, then it must be growing along one of two possible directions for a given composite with two distinct families of fibers. On the other hand, pure *out-of-plane* buckling has been observed at many angles to the fiber orientations, and most notably in the hemispherical dome forming experiments of O'Bradaigh et al. (1993) and Martin et al. (1992) where buckles occur along the bisectors of the angles between the two fiber directions.

We begin by assuming that the fibers embedded in the matrix have been perturbed from their nominally straight state. If the through thickness position of a fiber is defined by its height h from the center line, then when it buckles

$$h(x_1, x_2, t) = h^0(t) + \epsilon h'(x_1, x_2, t) + 0(\epsilon^2) \quad (17)$$

where h^0 is the unperturbed height, h' is the perturbation with a spatial variation which we will assume is sinusoidal, and ϵ is the dimensionless perturbation parameter. All terms of order ϵ^2 and higher will be ignored. Since in the background homogeneous deformation the velocity of the matrix in the thickness direction varies linearly with x_3, the amplitude of such a fiber perturbation will change as the fiber convects with the matrix even if the background deformation state of the sheet is unchanged. The material derivative of the height is

$$\dot{h} = \dot{h}^0(t) + \epsilon \dot{h}'(x_1, x_2, t) + \ldots \quad (18)$$

which, by continuity, must be equal to the 3-component of the velocity evaluated at h. In the background deformation this is

$$u_3^0(h) = D_3^0 h = D_3^0 h^0(t) + \epsilon D_3^0 h'(x_1, x_2, t) \ldots \quad (19)$$

where D_3^0 denotes the unperturbed, through thickness, strain rate, so that the total velocity component is

$$u_3 = D_3^0 h^0 + \epsilon(D_3^0 h' + u_3') + \ldots \quad (20)$$

and thus equating first-order terms in Eqs. (18) and (20):

$$\dot{h}' = D_3^0 h' + u_3'. \quad (21)$$

Thus as a result of the background deformation alone h' grows at a rate of D_3^0 so that the *additional convected growth rate G* will be defined to be such that

$$\dot{h}' = (D_3^0 + G)h' \quad (22)$$

and therefore

$$Gh' = u_3'. \quad (23)$$

The system will be deemed unstable when $G > 0$, so that the amplitude of the perturbed fiber is growing relative to the background homogeneous deformation.

The perturbed height is assumed to vary sinusoidally with x_1 and x_2, so that at the generic instant ($t = 0$) it has the variation

$$h'(x_1, x_2, 0) = h^* \exp iK(x_1 \cos\theta + x_2 \sin\theta) \quad (24)$$

where h^* is the initial amplitude, K is the wave number (i.e., the number of waves per unit length) so that $\lambda = 2\pi/K$ is the wavelength, whilst the ridges of the buckles, on which h' is constant, make an angle $\pi/2 + \theta$ with the x_1-direction. The θ-direction, which is perpendicular to the ridges, will be referred to as the buckle direction.

Even in the absence of a perturbed velocity field the wavelength and direction of these buckles will change as a result of the background deformation. Hence for $t > 0$, the perturbed height will be written in the form

$$h'(x_1, x_2, t) = h^* \exp((D_3^0 + G)t) \times (\exp iK(x_1 \cos(\theta)e^{-D_1^0 t} + x_2 \sin(\theta)e^{-D_2^0 t}) \quad (25)$$

which reduces to Eq. (24) when $t = 0$, and as can be readily verified, Eq. (22) is recovered upon use of the following expression for the material derivative applied to the background state:

$$\dot{h}' = \frac{\partial h'}{\partial t} + u_1^0 \frac{\partial h'}{\partial x_1} + u_2^0 \frac{\partial h'}{\partial x_2}. \quad (26)$$

A constructive proof of Eq. (25), based on the concept of characteristic curves, is given in the Appendix.

If the variables in the governing equations of Section 2 are perturbed in the same way as h in Eq. (17), the linearized form of the governing equations can be obtained by equating terms of order ϵ. For example, expanding Eq. (1) gives

$$a_i a_i = (a_i^0 + \epsilon a_i')(a_i^0 + \epsilon a_i') = a_i^0 a_i^0 + 2\epsilon a_i^0 a_i' + 0(\epsilon^2).$$

Since the left-hand side and the first term on the right side are both equal to unity, it follows that to order ϵ,

$$a_i^0 a_i' = 0. \quad (27)$$

The perturbation in the fiber direction is hence seen to be *orthogonal* to the original fiber direction, so that the perturbation vector can be written

$$a' = (-\alpha \sin\phi, \alpha \cos\phi, \gamma) \quad (28)$$

for some values α and γ. Similarly, the perturbation in the second fiber direction can be written

$$b' = (\beta \sin\phi, \beta \cos\phi, \delta). \quad (29)$$

Note that the perturbations to the fiber directions are not themselves unit vectors.

The incompressibility condition (2) implies that

$$\frac{\partial u_1'}{\partial x_1} + \frac{\partial u_2'}{\partial x_2} + \frac{\partial u_3'}{\partial x_3} = 0 \quad (30)$$

and from substitution into Eq. (5) the perturbed fiber convection equations are

$$\frac{\partial a_1'}{\partial t} + u_j^0 \frac{\partial a_1'}{\partial x_j} = a_1' D_1^0 + a_1^0 \frac{\partial u_1'}{\partial x_1} + a_2^0 \frac{\partial u_1'}{\partial x_2} \quad (31)$$

$$\frac{\partial a_2'}{\partial t} + u_j^0 \frac{\partial a_2'}{\partial x_j} = a_2' D_2^0 + a_1^0 \frac{\partial u_2'}{\partial x_1} + a_2^0 \frac{\partial u_2'}{\partial x_2} \quad (32)$$

Downloaded 04 May 2010 to 171.66.16.28. Redistribution subject to ASME license or copyright; see http://www.asme.org/terms/Terms_Use.cfm

$$\frac{\partial a_3'}{\partial t} + u_j^0 \frac{\partial a_3'}{\partial x_j} = a_3' D_3^0 + a_1^0 \frac{\partial u_3'}{\partial x_1} + a_2^0 \frac{\partial u_3'}{\partial x_2}. \quad (33)$$

The corresponding linearized convection equations for the perturbation of the second family of fibers can be found by replacing a with b in the above expressions.

The reason why the coupling between the in-plane wrinkling and out-of-plane buckling can be neglected will now be explained. The in-plane components of the perturbation to the fiber direction vector are assumed to have the same form as h' in Eq. (25), with amplitudes α^* and γ^*, except that the *total* growth rate G_T will be used in place of $D_3^0 + G$. Substitution of these forms into the first two perturbed convection Eqs. (31) and (32) yields

$$-\alpha^* \sin \varphi(G_T - D_1^0) - u_1^* iK \cos(\varphi - \theta) = 0 \quad (34)$$

$$\alpha^* \cos \varphi(G_T - D_2^0) - u_2^* iK \cos(\varphi - \theta) = 0 \quad (35)$$

and similarly for the second family of fibers:

$$\beta^* \sin \varphi(G_T - D_1^0) - u_1^* iK \cos(\varphi + \theta) = 0 \quad (36)$$

$$\beta^* \cos \varphi(G_T - D_2^0) - u_2^* iK \cos(\varphi + \theta) = 0. \quad (37)$$

Comparing the above relations yields *both* the equations,

$$\beta^* = \pm\alpha^* \frac{\cos(\varphi + \theta)}{\cos(\varphi - \theta)} \quad (38)$$

It is therefore clear that if in-plane wrinkling occurs, either

$$\beta^* = 0 \quad \text{and} \quad \cos(\varphi + \theta) = 0 \quad (\text{i.e., } \theta = \pi/2 - \varphi) \quad (39)$$

or alternatively,

$$\alpha^* = 0 \quad \text{and} \quad \cos(\varphi - \theta) = 0 \quad (\text{i.e., } \theta = \pi/2 + \varphi). \quad (40)$$

Thus, the direction of the in-plane wrinkle must be orthogonal to either of the two families of fibers. Physically this means that geometrical compatibility requires one family of fibers to undergo differential displacements in the *direction* of the fibers and so fibers of this family do not wrinkle.

Since for the principal case of interest, pure out-of-plane buckling, there is no such angle restriction, the in-plane components of the perturbation to the fiber direction vector are set to zero in the linearized governing equations. The first two linearized convection Eqs. (31) and (32) then reduce to

$$a_1^0 \frac{\partial u_1'}{\partial x_1} + a_2^0 \frac{\partial u_1'}{\partial x_2} = 0 \quad (41)$$

$$a_1^0 \frac{\partial u_2'}{\partial x_1} + a_2^0 \frac{\partial u_2'}{\partial x_2} = 0 \quad (42)$$

and similarly for the second family of fibers,

$$b_1^0 \frac{\partial u_1'}{\partial x_1} + b_2^0 \frac{\partial u_1'}{\partial x_2} = 0 \quad (43)$$

$$b_1^0 \frac{\partial u_2'}{\partial x_1} + b_2^0 \frac{\partial u_2'}{\partial x_2} = 0. \quad (44)$$

It follows that all the differential terms in the above expressions are zero so that u_1' and u_2' can only depend on the through thickness variable x_3. The linearized incompressibility condition (30) hence reduces to

$$\frac{\partial u_3'}{\partial x_3} = 0 \quad (45)$$

so that u_3' depends only on x_1 and x_2, and the perturbed deformation field is one of antiplane strain. In addition, it will be assumed that the initial out-of-plane perturbation to the fiber direction does not depend on x_3. Thus, u_3', γ, and δ are related to x_1 and x_2 in the same way that h' is in Eq. (25) and their initial amplitudes, u_3^*, γ^*, and δ^* will be constant through the thickness. Substituting these perturbed forms into the third convection Eq. (33) gives

$$\gamma^* G - u_3^* iK \cos(\varphi - \theta) = 0 \quad (46)$$

and similarly for the b-direction,

$$\delta^* G - u_3^* iK \cos(\varphi + \theta) = 0. \quad (47)$$

Although different in initial appearance, Eqs. (46) and (47) are equivalent to Eq. (23). Here, instead of relating the perturbed velocity to the amplitude of the perturbation, the velocity is related to the out-of-plane components of the perturbed fiber direction vectors, which, to first order, can be interpreted as the angle of inclination of the buckled fiber. The oscillation of this angle is out of phase with the amplitude by 90 deg, hence the presence of i in the above expressions. Comparing Eqs. (46) and (47) yields the relation between the two angles of inclination of

$$\delta^* = \gamma^* \cos(\varphi + \theta)/\cos(\varphi - \theta), \quad (48)$$

which can also be found simply from geometry.

The first-order perturbations to the stress components are now found by substituting perturbed variables of the form in Eq. (17) into the constitutive Eq. (6) to (8), and only retaining terms of order ϵ:

$$T_{11}' = T_a' a_1 a_1 + T_b' b_1 b_1 - p',$$

$$T_{22}' = T_a' a_2 a_2 + T_b' b_2 b_2 - p', \quad T_{12}' = T_a' a_1 a_2 + T_b' b_1 b_2$$

$$T_{13}' = T_a a_1 a_3' + T_b b_1 b_3' + \mu(\partial u_1'/\partial x_3 + \partial u_3'/\partial x_1),$$

$$T_{33}' = -p', \quad \text{and}$$

$$T_{23}' = T_a a_2 a_3' + T_b b_2 b_3' + \mu(\partial u_2'/\partial x_3) + \partial u_3'/\partial x_2). \quad (49)$$

The first-order perturbed form of the equations of motion (9) is

$$\partial T_{ij}'/\partial x_j = \rho(\partial u_i'/\partial t + u_j' \partial u_i/\partial x_j + u_j^0 \partial u_i'/\partial x_j) \quad (50)$$

which upon substitution of (49) gives the three equations:

$$\frac{\partial T_a'}{\partial x_1} a_1 a_1 + \frac{\partial T_b'}{\partial x_1} b_1 b_1 - \frac{\partial p'}{\partial x_1} + \frac{\partial T_a'}{\partial x_2} a_1 a_2 + \frac{\partial T_b'}{\partial x_2} b_1 b_2 + \mu \frac{\partial^2 u}{\partial x_3^2} = \rho\left(\frac{\partial u'}{\partial t} + u_1' D_1^0 + u_3^0 \frac{\partial u_1'}{\partial x_3}\right) \quad (51)$$

$$\frac{\partial T_a'}{\partial x_1} a_1 a_2 + \frac{\partial T_b'}{\partial x_1} b_1 b_2 + \frac{\partial T_a'}{\partial x_2} a_2 a_2 + \frac{\partial T_b'}{\partial x_2} b_2 b_2 - \frac{\partial p'}{\partial x_2} + \mu \frac{\partial^2 u_2'}{\partial x_3^2} = \rho\left(\frac{\partial u_2'}{\partial t} + u_2' D_2^0 + u_3^0 \frac{\partial u_2'}{\partial x_3}\right) \quad (52)$$

$$T_a a_1 \frac{\partial a_3'}{\partial x_1} + T_b b_1 \frac{\partial b_3'}{\partial x_1} + \mu \frac{\partial^2 u_3'}{\partial x_1^2} + T_a a_2 \frac{\partial a_3'}{\partial x_2} + T_b b_2 \frac{\partial b_3'}{\partial x_2} + \mu \frac{\partial^2 u_3'}{\partial x_2^2} - \frac{\partial p'}{\partial x_3} = \rho\left(\frac{\partial u_3'}{\partial t} + u_3' D_3^0 + u_1^0 \frac{\partial u_3'}{\partial x_1} + u_2^0 \frac{\partial u_3'}{\partial x_2}\right). \quad (53)$$

The third linearized equation of motion (53) has only one variable, the perturbed pressure, in common with Eqs. (51) and (52). By comparison with the other variables in Eq. (53) it can be deduced that $\partial p'/\partial x_3$ is independent of x_3 and hence constant through the thickness; its value is determined by the stress boundary conditions on the top and bottom surfaces.

Downloaded 04 May 2010 to 171.66.16.28. Redistribution subject to ASME license or copyright; see http://www.asme.org/terms/Terms_Use.cfm

Since the surface tractions are zero, the stress tensor referred to a local coordinate system, with the 3-axis normal to the surface, takes the form

$$T_{ij}^s = \begin{pmatrix} T_{11}^s & T_{12}^s & 0 \\ T_{12}^s & T_{22}^s & 0 \\ 0 & 0 & 0 \end{pmatrix} \tag{54}$$

where the superscript s stands for the local surface coordinate system. This tensor can be transformed into the original reference frame using the tensor transformation relation:

$$T = Q^T T^s Q, \tag{55}$$

where the transformation matrix Q is defined as

$$Q = \begin{bmatrix} \cos\omega\cos\theta & \cos\omega\sin\theta & \sin\omega \\ -\sin\theta & \cos\theta & 0 \\ -\sin\omega\cos\theta & -\sin\omega\sin\theta & \cos\omega \end{bmatrix} \tag{56}$$

where ω is the slope of the buckled surface, which is of order ϵ. The rows of Q are the basis vectors of the surface coordinate system given as component triples relative to the original reference frame. If this transformation is performed, it is found that

$$T_{33} = T_{11}^s \sin^2\omega \tag{57}$$

which is zero to first order in ϵ. Hence from the background solution and the expression for T_{33}' in Eq. (49) it is seen that on the top surface, $p' = 0$. Also, as the same relations hold on the bottom surface, p' is also zero there. Since the perturbed pressure gradient through the thickness has already been shown to be constant, p' must therefore be zero everywhere.

The zero *shear* traction components on the surface put no restriction on the deformation since the boundary fibers, being inextensible, are capable of sustaining *infinite* direct stresses, and as a result the shear stresses can be discontinuous at the free surface. This is a very common feature of solutions to boundary value problems involving inextensible fibers (Spencer, 1972, 1984; Hull et al., 1994). It follows that any in-plane movement, defined by u_1' and u_2', is governed by the equations of motion (51) and (52), and is *decoupled* from the out-of-plane buckling deformation.

Equation (53) can now be solved for G by substituting in the perturbed forms given by Eq. (25), and relating γ^* and δ^* to u_3^* by Eqs. (46) and (47). If u_3^* is eliminated, then after a little manipulation it is found that

$$G = -(\mu K^2/2\rho + D_3) \pm \sqrt{(\mu K^2/2\rho + D_3)^2 - K^2 T_\theta/\rho} \tag{58}$$

where

$$T_\theta = T_a \cos^2(\phi - \theta) + T_b \cos^2(\phi + \theta) \tag{59}$$

is the sum of the tensions in the fibers resolved in the buckle direction. As can be formally verified by letting $\rho \to 0$ in Eq. (58), when inertia is neglected in the equations of motion, the growth rate is given simply by

$$G = -T_\theta/\mu. \tag{60}$$

Since the system is unstable if the convected growth rate is positive, it can be seen from both Eqs. (58) and (60) that the system becomes unstable when the fiber tensions resolved in the direction of the buckle become negative. Note that Eqs. (16) can be used to express the growth rate in terms of the applied stress state.

Closer inspection of Eq. (58) shows that G can also become positive if

$$D_3 < -\mu K^2/2\rho, \tag{61}$$

which corresponds to rapid thinning of the sheet.

In the following section the influence of the wavelength on the growth rate through Eq. (58) will be systematically investigated.

5 Analysis and Discussion of Results

In the above analysis it was assumed that the perturbations have a sinusoidal shape with an arbitrary wavelength. In reality, the slight fiber misalignments present in composite sheets are of arbitrary shape. This does not nullify the analysis because any arbitrary shape and distribution can be expressed, using a Fourier analysis, as a sum of sinusoidal terms. In effect, the composite laminate is thought of as containing perturbations of all wavelengths at the same time and that the wavelengths with the *highest growth rates* will dominate as the buckles grow. This is the standard procedure in viscous buckling analyses (Biot, 1964). Some manufacturing processes for preimpregnated tape may favor the production of certain fiber-misalignment wavelengths. However, for this study it is assumed that all wavelengths occur with equal likelihood.

To analyze the influence of the wavelength on the growth rate, a nondimensional growth rate will be defined by dividing Eq. (58) by the *modulus* of the through-thickness strain rate, $|D_3|$. The cases when D_3 is positive and negative need to be considered separately, but in either case Eq. (58) can be written in the form:

$$G/|D_3| = -\text{sgn}(D_3)(\kappa + 1) + \sqrt{(\kappa + 1)^2 - 2\kappa\tau} \tag{62}$$

where

$$\kappa = \mu K^2/2\rho D_3 \tag{63}$$

will be referred to as the nondimensional wave number factor. It is, in fact, essentially the reciprocal of the Reynolds number, which uses the wavelength as the length scale, as is commonly employed in wave problems (Kinsman, 1965). The second dimensionless parameter involves the fiber tension factor:

$$\tau = T_\theta/\mu D_3. \tag{64}$$

In Fig. 2 the nondimensional growth rate, as given by Eq. (62), is plotted against the nondimensional wave number factor for a few values of the nondimensional fiber tension factor. It can be seen from Fig. 2(a) that when D_3 is positive (so that the fibers are rotating away from the ±45 deg configuration) the growth rate is only positive when τ, and hence T_θ, is negative. It is also apparent that in the unstable regions the growth rate is greatest for very high wave numbers. Since the wave number is the reciprocal of the wavelength, this indicates that buckles with very small wavelengths are the most likely to develop.

On the other hand when D_3 is negative (i.e., the fibers are moving towards ±45 deg), κ is necessarily strictly negative, the growth rate will be positive when τ is also positive as shown in Fig. 2(b). Again this requires the resolved fiber tension T_θ to be negative. However, the predictions of the critical wavelengths is more complex. When τ is greater than 2, the predictions match those for the case where D_3 is positive so that buckles with very small wavelengths are favoured to develop. However, in the region where τ is less than 2, the reverse is true—the smaller wave numbers and thus the very high wavelengths have the highest growth rates. This means that wavelengths of the order of the size of the part itself will grow and dominate the small wavelengths, which effectively means that out-of-plane buckling will not be observed.

In some of the cases above, buckles with very small wavelengths were predicted to grow. However, thermoforming experiments with fiber-reinforced thermoplastics have tended to produce buckles with wavelengths in the range of 20-40 mm (Mallon et al., 1988; Smiley, 1988). There are a succession of reasons to explain this behavior. First, from Figs. 2(a) and (b) it can be seen that the curves become very flat and the growth

Downloaded 04 May 2010 to 171.66.16.28. Redistribution subject to ASME license or copyright; see http://www.asme.org/terms/Terms_Use.cfm

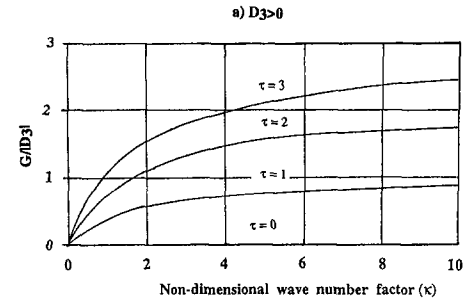


Fig. 2(*a*)

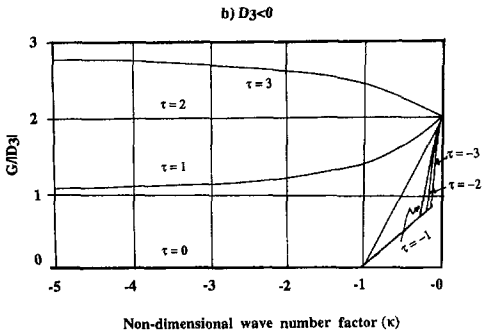


Fig. 2(*b*)

Fig. 2 Variation of nondimensional growth rate with dimensionless wave number κ when sheet is (*a*) thickening ($D_3 > 0$), and (*b*) thinning ($D_3 < 0$)

rates becomes asymptotic to $-\text{sgn}\,(D_3)\tau$ as the modulus of the nondimensional wave number factor tends to infinity. (This corresponds to the zero Reynolds number, creeping flow, limit.) Thus, infinitesimal wavelengths have only slightly higher growth rates than the wavelengths that are actually observed. The second point is that, as mentioned above, the prepregs are likely to have some inherent distribution of wavelengths, and in this distribution the wavelengths of order 20-40 mm are well represented. The third factor, which is not independent from the last, is that the fibers themselves have some inherent bending stiffness which restricts the growth of buckles with extremely small wavelengths. The continuum model used here could well be modified to take account of this extra stiffness. However, this is probably unnecessary as the effect of the fiber bending stiffness is likely to have already played its part in producing the inherent distribution of wavelengths in the original prepregs. It should be pointed out that in the regions of Fig. 2(*b*) where $\tau < 2$, the very small wave numbers and thus high wavelengths have sharply higher growth rates, and thus the argument used above does not apply.

It is further to be noted that Fig. 2(*b*) also predicts unstable behavior for *negative* τ values (i.e., *positive* resolved fiber tensions) with small wave numbers such that $|\kappa| < 1$. This corresponds to the rapid thinning of the sheet as noted above with reference to inequality (63).

The principal result of this work, that is, the dependence of the convected growth rate of the buckles on the fiber tensions resolved in the buckle direction, is similar to the results of Hull et al. (1991 and 1992), who found that the stability of shear flows of unidirectional plies depends on the sign of the fiber tension. The bidirectional situation is somewhat more complicated, because it is possible for the tensions in each of two families of fibers to be both positive, both negative, or opposite in sign. From Eq. (59) we infer that a buckle can be expected to form in the direction θ in which the resolved tension is the most negative. This, of course, will be one of the principal directions of the reaction stress field R_{ij} defined in Eq. (7). We hence predict that buckling will occur when the corresponding principal stress relating to the combined fiber tension field is compressive. In a real thermoformed part the out-of-plane buckles will more likely occur as "bubbles," i.e., the buckles will have finite wavelengths in two mutually orthogonal directions.

The ultimate goal of this research is to find ways to eliminate out-of-plane buckling. One remote possibility could be to attempt to alter the distribution of wavelengths in pre-impregnated tape, to overwhelmingly favor larger wavelengths. A more direct method would be to alter either the blank geometry or method of forming to reduce the compression in the fibers, so that the growth rates of the fiber misalignments become negative. Many reports in the literature describe successful methods for reducing buckling, which undoubtedly do so by reducing these negative tensions. Mallon et al. (1988) demonstrated the benefits of reducing the size of the unformed areas of the blank, while Martin et al. (1992b) have shown that changing the blank geometry can lead to a similar reduction in buckling. It has also been shown that the use of stiffer diaphragms and slower forming speeds during thermoforming reduce or eliminate buckling. The latter point is not surprising since the stresses in a viscous fluid are proportional to the forming speed, and thus the overall stresses, compressive or otherwise, are reduced.

The final discussion topic concerns the validity of both the continuum model and the homogeneous deformations studied here for the analysis of the actual deformations that take place during thermoforming. To the first point it must be said that the model does not take into account the true anisotropic, viscoelastic behavior of the matrix. The model used here is a first approximation, treating the matrix as a purely viscous fluid it is more appropriate in the high temperature (or alternatively low forming speed) region of the processing windows of fiber-reinforced thermoplastics. Despite this it is encouraging to see that the stability criterion is principally governed by the reaction tensions, which would still be present in a more complicated continuum model involving inextensible fibers. Finally, such idealized trellis-like homogeneous deformations are only an approximation to the situations encountered during a real thermoforming operation. In general the deformation will be inhomogeneous and, in addition, other flow mechanisms can occur, notably matrix percolation and interply slip. Nevertheless the results presented here can be usefully applied as a first approximation to understanding the conditions that cause out-of-plane buckles to develop.

6 Conclusions

In this paper the out-of-plane buckling stability of homogeneous inextensible-net-like deformations of molten thermoplastics reinforced by two families of fibers have been analyzed. The result is a stability criterion which relates the growth rate of out-of-plane buckles to the stress conditions inside the laminate. This condition states principally that when the tensions in the two families of fibers resolved in some direction are negative, any fiber misalignments present in the composite are expected to grow. Also, the direction along which the resolved tension is most negative is where the buckle is most likely to form. This is vindicated by the formation of buckles away from the fibers during dome forming as has been shown by Martin et al. (1992a, b). However, it must be noted that for fiber-reinforced sheets, the buckling phenomenon is dominated by the state of *stress* in a region. Because of the presence of reaction stresses it is difficult to obtain a full quantitative knowledge of the stress state from the measured strain distribution. Hence, in contrast to sheet metal forming, the construction of a *forming limit diagram* based on stretching and drawing strains (Hosford and Caddell, 1983) is not possible for these composite sheets.

The stability criterion has been analyzed further to determine whether certain wavelengths are preferred to develop, using the logic that the wavelength with the highest growth rate will out

Downloaded 04 May 2010 to 171.66.16.28. Redistribution subject to ASME license or copyright; see http://www.asme.org/terms/Terms_Use.cfm

grow and dominate all others. In the majority of cases, notably the case where the laminate is thickening in the deformation, very small wavelengths were found to have the highest growth rates. The bending stiffness of the fibers and the inherent wavelength distribution in actual laminates were neglected in this analysis but are thought to be the reasons why experimentally observed wavelengths are of finite size. In the cases where the laminate was thinning and the rate of thinning was not too great, a different behavior was noted. Here, misalignments with very high wavelengths have sharply higher growth rates, and thus wavelengths as large as the part being formed are expected to dominate, so that effectively out-of-plane buckling is not observed.

Despite the many assumptions and simplifications used in this analysis, it is felt that the results can be of practical use in finding ways to eliminate the buckling phenomenon. The importance of the blank shape, of fiber misalignment in the original prepreg, of keeping the laminate in tension during thermoforming have all been clearly demonstrated and some of the experimental findings of other researchers have been explained.

References

Bhattacharyya, D., Burt, C. R., and Martin, T. A., 1993, "Forming of Fibre Reinforced Thermoplastic Sheets," *Advanced Composites '93,* T. Chandra and A. K. Dhingra, eds., Minerals, Metals and Materials Society, Warrendale, PA, pp. 875–882.

Biot, M. A., 1964, "Theory of Viscous Buckling of Multilayered Fluids Undergoing Finite Strain," *Physics of Fluids,* Vol. 7, pp. 855–859.

Hosford, W. F., and Caddell, R. M., 1983, *Metal Forming: Mechanics and Metallurgy,* Prentice-Hall, Englewood Cliffs, NJ, pp. 294–309.

Hou, M., and Friedrich, K., 1991, "Stamp Forming of Carbon Fibre/Polypropelene Composites," *Composites Manufacturing,* Vol. 2, No. 1, pp. 3–9.

Hull, B. D., Rogers, T. G., and Spencer, A. J. M., 1991, "Theory of Fibre Buckling and Wrinkling in Shear Flows of Fibre-Reinforced Composites," *Composites Manufacturing,* Vol. 2, No. 3-4, pp. 185–191.

Hull, B. D., Rogers, T. G., and Spencer, A. J. M., 1992, "A Linear Stability Analysis of Flows Transversely Isotropic Non-Newtonian Fluids," *J. Non-Newtonian Fluid Mech.,* Vol. 43, pp. 325–349.

Hull, B. D., Rogers, T. G., and Spencer, A. J. M., 1994, "Theoretical Analysis of Forming Flows of Continuous Fibre Resin Systems," *Flow Phenomena in Polymeric Composites,* S. G. Advani, ed., Elsevier Science Publishers, Amsterdam, The Netherlands, pp. 203–256.

Kinsman, B., 1965, *Wind Waves,* Prentice-Hall, Englewood Cliffs, NJ, pp. 498.

Mallon, P. J., Ó 'Brádaigh, C. M., and Pipes, R. B., 1988, "Polymeric Diaphragm Forming of Continuous Fiber Reinforced Thermoplastics," *Composites,* Vol. 19, pp. 33–47.

Martin, T. A., Bhattacharyya, D., and Pipes, R. B., 1992a, "Computer Aided Grid Strain Analysis in Fibre Reinforced Thermoplastic Sheet Forming," *Computer Aided Design in Composite Material Technology III,* S. G. Advani et al., eds., Computational Publications-Elsevier Applied Science, London, pp. 143–162.

Martin, T. A., Bhattacharyya, D., and Pipes, R. B., 1992b, "Deformation Characteristics and Formability of Fibre-Reinforced Thermoplastic Sheets," *Composites Manufacturing,* Vol. 3, No. 3, pp. 165–172.

Ó'Brádaigh, C. M., 1991, "Analysis and Experiments in Diaphragm Forming of Continuous Fibre Reinforced Thermoplastics," PhD thesis, University of Delaware, DE.

Ó 'Brádaigh, C. M., McGuiness, G. B., and Pipes, R. B., 1993, "Numerical Analysis of Stress and Deformation in Composite Materials Sheet Forming: Central Indentation of a Circular Sheet," *Composites Manufacturing,* Vol. 4, No. 2, pp. 67–83.

Pipkin, A. C., 1984, "Equilibrium of Tchebychev Nets," *Arch. Rat. Mech. Anal.,* Vol. 85, pp. 81–97.

Rogers, T. G., 1989, "Rheological Characterisation of Anisotropic Materials," *Composites,* Vol. 20, No. 1, pp. 21–27.

Rogers, T. G., 1991, "Shear Characterisation and Inelastic Torsion of Fibre-Reinforced Materials," *Inelastic Deformation of Composite Materials,* George J. Dvorak, ed., Springer-Verlag, New York, pp. 653–674.

Smiley, A. J., 1988, "Diaphragm Forming of Carbon Fibre Reinforced Thermoplastic Composite Materials," PhD thesis, University of Delaware, DE.

Soll, W., and Gutowski, T. N., 1988, "Forming of Thermoplastic Composite Parts," *SAMPE Journal,* Vol. 24, No. 3, pp. 15–19.

Spencer, A. J. M., 1972, *Deformations of Fibre-Reinforced Materials,* Clarendon Press, Oxford, UK.

Spencer, A. J. M., 1984, "Constitutive Theory for Strogly Anisotropic Solids," *Continuum Theory of the Mechanics of Fibre-Reinforced Composites,* A. J. M. Spencer, ed., CISM No. 282, Springer-Verlag, New York, pp. 1–72.

Van West, B. P., Pipes, R. B., Keefe, M., and Advani, S. G., 1991, "The Draping of Bidirectional Fabric over Three-Dimensional Surface," *Composites Manufacturing,* Vol. 2, No. 1, pp. 10–22.

APPENDIX

Derivation of Eq. (25)

In Eq. (22) the convective growth rate G was defined by

$$\dot{h}' = (D_3^0 + G)h', \tag{A.1}$$

while from Eq. (26),

$$\dot{h}' = \frac{\partial h'}{\partial t} + u_1^0 \frac{\partial h'}{\partial x_1} + u_2^0 \frac{\partial h'}{\partial x_2} = (D_3^0 + G)h'. \tag{A.2}$$

Comparison with the standard expression for a differential identity

$$dh' = \frac{\partial h'}{\partial t}\, dt + \frac{\partial h'}{\partial x_1}\, dx_1 + \frac{\partial h'}{\partial x_2}\, dx_2 \tag{A.3}$$

gives

$$\frac{dt}{1} = \frac{dx_1}{u_1^0} = \frac{dx_2}{u_2^0} = \frac{dh'}{(D_3^0 + G)h'}. \tag{A.4}$$

But these zeroth-order velocity components are given by $u_1^0 = D_1^0 x_1$ and $u_2^0 = D_2^0 x_2$, so that

$$\frac{dt}{1} = \frac{dx_1}{D_1^0 x_1} = \frac{dx_2}{D_2^0 x_2} = \frac{dh'}{(D_3^0 + G)h'}, \tag{A.5}$$

which upon integration yields the equations $x_1 = x_1^0 e^{+D_1^0 t}$ and $x_2 = x_2^0 e^{+D_2^0 t}$, of the characteristic lines in (x_1, x_2, t) space, while integration of the last equation in (A5) shows that $h' e^{-(D_3^0+G)t}$ is constant on each such characteristic line. Therefore,

$$\begin{aligned} h'(x_1, x_2, t)e^{-(D_3^0+G)t} &= h'(x_1^0, x_2^0, 0) \\ &= h'(x_1 e^{-D_1^0 t}, x_2 e^{-D_2^0 t}, 0) \end{aligned}$$

so that finally

$$h'(x_1, x_2, t) = e^{(D_3^0+G)t} h'(x_1 e^{-D_1^0 t}, x_2 e^{-D_2^0 t}, 0), \tag{A.6}$$

which leads directly to Eq. (25).

Downloaded 04 May 2010 to 171.66.16.28. Redistribution subject to ASME license or copyright; see http://www.asme.org/terms/Terms_Use.cfm

Kikuo Kishimoto
Professor,
Mem. ASME.

Hirotsugu Inoue
Research Associate.

Makoto Hamada[1]
Former Graduate Student.

Toshikazu Shibuya
Professor.

Department of Mechanical and Intelligent Systems Engineering,
Tokyo Institute of Technology,
2-12-1, O-okayama,
Meguro-ku, Tokyo 152, Japan

Time Frequency Analysis of Dispersive Waves by Means of Wavelet Transform

A new approach is presented for investigating the dispersive character of structural waves. The wavelet transform is applied to the time-frequency analysis of dispersive waves. The flexural wave induced in a beam by lateral impact is considered. It is shown that the wavelet transform using the Gabor wavelet effectively decomposes the strain response into its time-frequency components. In addition, the peaks of the time-frequency distribution indicate the arrival times of waves. By utilizing this fact, the dispersion relation of the group velocity can be accurately identified for a wide range of frequencies.

1 Introduction

The analysis of wave propagation in structures is a fundamental issue related to a wide range of engineering problems, such as analysis of impact response of structures, characterization of structure-borne noises, and ultrasonic identification of material properties. Since structural waves are often dispersive, evaluation of their dispersive characters is essential to understanding the wave propagation phenomena. For the experimental identification of the dispersive character, the time-frequency analysis of wave data may be one of the most sophisticated because it enables to extract the time variation of each frequency component of the data.

There are many methods for the time-frequency analysis of signals. As mentioned by Flandrin et al. (1991), these methods are related each other and each of them has both advantages and disadvantages over others. Among these methods, the Short-Time Fourier Transform (STFT) and the Wigner-Ville Distribution (WVD) have been widely applied to engineering problems. Hodges et al. (1985) applied the STFT to the time-frequency analysis of waves in strings, beams and shells. Wahl and Bolton (1993) proposed the use of the WVD to the analysis of dispersive waves in structures. However, to the authors knowledge, there have been no other studies on the time-frequency analysis of dispersive waves.

During the last decade, a new mathematical technique for the time-frequency analysis, called the Wavelet Transform (WT), has been extensively developed (e.g., Chui, 1992; Daubechies, 1992). The WT has some features different from those of the STFT or WVD (Rioul and Vetterli, 1991; Hlawatsch and Boudreaux-Bartels, 1992). Recently, applications of the WT are actively studied in a variety of fields of engineering science. As for vibration problems of structures, Newland (1993a; 1993b) contributed basic and pioneering works. Several practical applications are also found in the defect detection of mechanical components or machine tools (Li and Ma, 1992; Tansel et al., 1992; Pandit et al., 1993; Tansel et al., 1993). However, applications to the analysis of dispersive waves have not been considered yet very much. It seems interesting to examine the applicability of the WT to the time-frequency analysis of dispersive waves. The authors (Hamada et al., 1992; Inoue et al., 1993) attempted to apply the WT to the time-frequency analysis of dispersive waves and found that it is also an effective technique as the STFT and WVD.[2]

In this paper, we advance our consideration about the use of the WT to the time-frequency analysis of dispersive waves in structures. First, the WT theory is outlined and the analyzing wavelet adopted in this study is explained. The next section illustrates some features of the WT through the time-frequency analysis of a simple signal. After that, the wavelet analysis of dispersive waves are discussed in terms of mathematical expressions. Finally, the flexural wave in a beam is analyzed as a typical example of dispersive waves. A method is shown to identify the dispersion relation of the group velocity by using information extracted from wave data by the WT.

2 The Wavelet Transform

The continuous wavelet transform of a function $f(t)$ is defined by (e.g., Chui, 1992)

$$(\mathcal{W}f)(a, b) = \frac{1}{\sqrt{a}} \int_{-\infty}^{\infty} f(t) \overline{\psi\left(\frac{t-b}{a}\right)} dt, \qquad (1)$$

where $a > 0$ and the overline indicates the complex conjugate. By the Parseval identity, Eq. (1) can be rearranged as

$$(\mathcal{W}f)(a, b) = \frac{\sqrt{a}}{2\pi} \int_{-\infty}^{\infty} \hat{f}(\omega) e^{ib\omega} \overline{\hat{\psi}(a\omega)} d\omega, \qquad (2)$$

where $\hat{f}(\omega)$ indicates the Fourier transform of $f(t)$ defined by

[1] Presently at Communication and Switching Laboratories, NTT Corporation, 3-9-11, Midori-cho, Musasino-shi, Tokyo 180, Japan.

Contributed by the Applied Mechanics Division of THE AMERICAN SOCIETY OF MECHANICAL ENGINEERS for presentation at the International Mechanical Engineering Congress and Exhibition, the Winter Annual Meeting of the ASME, San Francisco, CA, Nov. 12-17, 1995.

Discussion on this paper should be addressed to the Technical Editor, Professor Lewis T. Wheeler, Department of Mechanical Engineering, University of Houston, Houston, TX 77204-4792, and will be accepted until four months after final publication of the paper itself in the ASME JOURNAL OF APPLIED MECHANICS.

Manuscript received by the ASME Applied Mechanics Division, Mar. 31, 1994; final revision, Mar. 10, 1995. Associate Technical Editor: P. D. Spanos.

Paper No. 95-WA/APM-2.

[2] During the review process of this paper, Newland (1994) also published a paper indicating that the WT is an effective tool for the time-frequency analysis of dispersive waves.

Copyright © 1995 by ASME

Downloaded 04 May 2010 to 171.66.16.28. Redistribution subject to ASME license or copyright; see http://www.asme.org/terms/Terms_Use.cfm

$$\hat{f}(\omega) = \int_{-\infty}^{\infty} f(t) e^{-i\omega t} dt. \tag{3}$$

The function $\psi(t)$ is termed as the analyzing wavelet and satisfies the admissibility condition:

$$\int_{-\infty}^{\infty} \frac{|\hat{\psi}(\omega)|^2}{|\omega|} d\omega < \infty. \tag{4}$$

In practice, the analyzing wavelet is chosen such that $\psi(t)$ and its Fourier transform $\hat{\psi}(\omega)$ satisfy

$$\int_{-\infty}^{\infty} |t\psi(t)|^2 dt < \infty \tag{5}$$

and

$$\int_{-\infty}^{\infty} |\omega\hat{\psi}(\omega)|^2 d\omega < \infty, \tag{6}$$

respectively (Chui, 1992). Then the analyzing wavelet may be considered as a window function both in the time and frequency domain. Let us assume that the time window $\psi(t)$ is centered at $t = 0$ and the frequency window $\hat{\psi}(\omega)$ at $\omega = \omega_0$. The function $\psi((t - b)/a)$ is then localized around $t = b$ and its Fourier transform $[a \exp(-ib\omega)\hat{\psi}(a\omega)]$ around $\omega = \omega_0/a$. It is understood from Eqs. (1) and (2) that the WT $(\mathcal{W}f)(a, b)$ corresponds to the time-frequency component of $f(t)$ in the vicinity of $t = b$ and $\omega = \omega_0/a$. If the parameters a and b are changed independently, the distribution of each time-frequency component is obtained on the b-a-plane, that is, on the time-frequency plane. Thus the WT enables the time-frequency analysis.

According to the sampling theorem, a sufficiently wide time window is required to appropriately characterize low frequency signals. Conversely, to successfully detect the position of high-frequency components on the time axis, a sufficiently narrow time window is required. The WT automatically satisfies these requirements since the width of the time window $\psi((t - b)/a)$ is proportional to the parameter a, that is, inversely proportional to the frequency. This character of the WT is beneficial to the analysis of structural waves usually composed of a wide range of frequency components. In the case of STFT, in contrast, the width of the window is fixed regardless of frequency (e.g., Rioul and Vetterli, 1991). As pointed out by Hodges et al. (1985), when using the STFT, one have to adjust the resolution so as to give the best view of the aspect of the behavior one wants to bring out. From this point of view, the WT possesses a more favorable character than the STFT.

The WT has another feature that should be noted. All methods of time-frequency analysis are suffered from existence of cross terms which appear between two signal components. The cross term does not reflect the true time-frequency distribution and, consequently, might cause misunderstanding of wave propagation phenomena. However, the nature of the cross term depends on the method of time-frequency analysis. According to Kadambe and Boudreaux-Bartels (1992), the cross term of the WT occurs at the intersection of two components, which is similar to that of the STFT, while the cross term of the WVD appears at the mid-time and mid-frequency of two components. If there are two independent pulses propagating in a structure, the cross term of the WT may occur only when these pulses meet at the observation location of the structure whereas that of the WVD always occurs between these pulses. Such a cross term of the WVD is undesirable since it seems like an another pulse propagating between two pulses. This is the reason why Wahl and Bolton (1993) required the smoothing of the WVD. Therefore, from this viewpoint, the WT is advantageous over the WVD for the analysis of wave propagation phenomena in structures.

In this study, the Gabor function is adopted as the analyzing wavelet because it provides smaller area of time-frequency window than any other functions according to the uncertainty principle (e.g., Chui, 1992). The Gabor function is expressed as (Sato, 1991)

$$\psi_g(t) = \frac{1}{\sqrt[4]{\pi}} \sqrt{\frac{\omega_0}{\gamma}} \exp\left[-\frac{(\omega_0/\gamma)^2}{2} t^2 + i\omega_0 t \right] \tag{7}$$

and its Fourier transform is

$$\hat{\psi}_g(\omega) = \frac{\sqrt{2\pi}}{\sqrt[4]{\pi}} \sqrt{\frac{\gamma}{\omega_0}} \exp\left[-\frac{(\gamma/\omega_0)^2}{2} (\omega - \omega_0)^2 \right], \tag{8}$$

where ω_0 and γ are positive constants. Figures 1(a) and (b) show the Gabor function and its Fourier transform, respectively. The Gabor function is a complex-valued sinusoidal function windowed by a Gaussian function centered at the origin and its Fourier transform is a Gaussian function centered at $\omega = \omega_0$. Although the Gabor function does not satisfy the admissibility condition (4) in the strict sense, it approximately satisfies the condition if γ is sufficiently large (Goupillaud et al., 1984). In this study, we set $\gamma = \pi\sqrt{2/\ln 2} \approx 5.336$. In addition, if Eq. (7) is substituted into Eq. (1), it is understood that the WT using the Gabor wavelet is equivalent to the Fourier transform with a Gaussian window. Therefore, the squared magnitude of the WT using the Gabor wavelet corresponds to the energy spectrum. In this study, we set $\omega_0 = 2\pi$ such that the value of a is equal to the period of vibration.

3 Time-Frequency Analysis of a Sinusoidal Pulse

In this section, an example is shown to illustrate the time-frequency analysis by means of the WT. The WT was computed for the following function:

$$f(t) = \begin{cases} \sin 20\pi(t - 0.45) & \text{at} \quad 0.45 \le t \le 0.55, \\ 0 \quad \text{otherwise.} \end{cases} \tag{9}$$

In this study, the integral in Eq. (1) is evaluated numerically according to the trapezoidal rule with sufficiently small interval

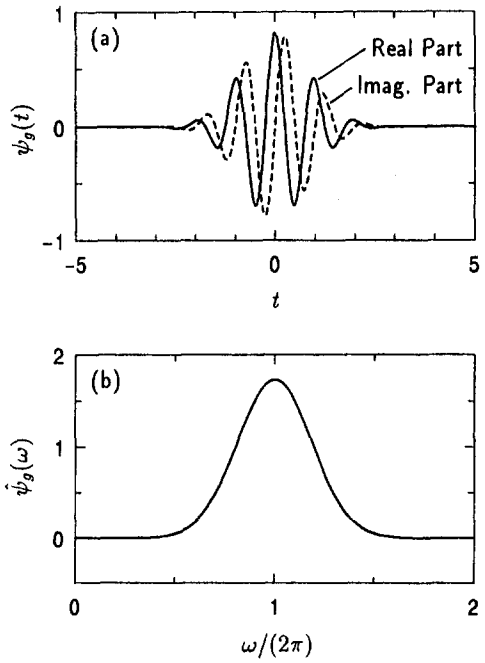


Fig. 1 (a) The Gabor function; (b) its Fourier transform when $\gamma = \pi\sqrt{2/\ln 2}$ and $\omega_0 = 2\pi$

Downloaded 04 May 2010 to 171.66.16.28. Redistribution subject to ASME license or copyright; see http://www.asme.org/terms/Terms_Use.cfm

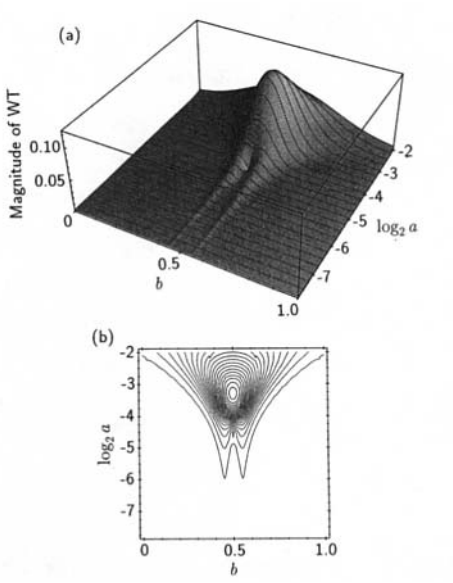


Fig. 2 The WT of the sinusoidal pulse: (*a*) time-frequency distribution of the magnitude; (*b*) its contour plot

Δt. The range of integration is truncated as $b - 4a \le t \le b + 4a$ because the Gabor function is negligibly small outside this range. The parameters a and b are discretized as follows:

$$a = 2^{m/4}, \tag{10}$$

$$b = n\Delta t, \tag{11}$$

where m and n are integers.

Figure 2 shows the time-frequency distribution of the magnitude of WT. The maximum is located at $\log_2 a = -3.25$ and $b = 0.5$. The value $\log_2 a = -3.25$ is the nearest to $\log_2 a = -3.32$, which corresponds to the angular frequency 20π, among all values of a where the WTs are computed. The time $b = 0.5$ coincides with the center of the pulse. For large values of a, namely, in the lower frequency range, single peak is located at $b = 0.5$. On the other hand, for small values of a, two peaks are found at $b = 0.45$ and $b = 0.55$, which represents the concentration of high-frequency components due to the truncation of the sinusoid. The overall representation of such a wide range of time-frequency components is owing to the flexible nature of the window function of the WT. These results indicate that the WT using the Gabor wavelet provides an appropriate time-frequency representation of a signal.

4 Time-Frequency Analysis of Wave Propagation

In this section, the application of the WT to the time-frequency analysis of wave propagation is discussed mathematically. Let us consider two harmonic waves of unit amplitude and different frequency ω_1 and ω_2 propagating in the x-direction, given by

$$u(x, t) = e^{-i(k_1 x - \omega_1 t)} + e^{-i(k_2 x - \omega_2 t)}, \tag{12}$$

where k_1 and k_2 are wave numbers. Equation (12) can be rearranged as

$$u(x, t) = 2\cos(\Delta k x - \Delta\omega t)e^{-i(k_c x - \omega_c t)}, \tag{13}$$

where

$$k_c = (k_1 + k_2)/2, \quad \omega_c = (\omega_1 + \omega_2)/2 \tag{14}$$

and

$$\Delta k = (k_1 - k_2)/2, \quad \Delta\omega = (\omega_1 - \omega_2)/2. \tag{15}$$

If $\Delta\omega$ is sufficiently small such that $\omega_1 \simeq \omega_2$, the phase velocity c_p and the group velocity c_g at the frequency ω_c can be respectively defined as

$$c_p = \omega_c/k_c, \quad c_g = \Delta\omega/\Delta k. \tag{16}$$

The WT of $u(x, t)$ is given by

$$(\mathcal{W}u)(x, a, b) = \sqrt{a}[e^{-i(k_1 x - \omega_1 b)}\overline{\hat{\psi}(a\omega_1)} + e^{-i(k_2 x - \omega_2 b)}\overline{\hat{\psi}(a\omega_2)}]. \tag{17}$$

Taking the magnitude of the WT, we obtain

$$|(\mathcal{W}u)(x, a, b)| = \sqrt{a}\{[\hat{\psi}(a\omega_1)]^2 + [\hat{\psi}(a\omega_2)]^2 + 2\hat{\psi}(a\omega_1)\hat{\psi}(a\omega_2)\cos(2\Delta k x - 2\Delta\omega b)\}^{1/2}, \tag{18}$$

where it is assumed that $\hat{\psi}(\omega)$ is a real function. Now let us consider the following two cases: (a) $\Delta\omega$ is sufficiently small and (b) $\Delta\omega$ is sufficiently large.

(a) The Case of Sufficiently Small $\Delta\omega$: In this case, $u(x, t)$ may be considered as a wave with phase velocity c_p and group velocity c_g as shown in Eq. (13). If $\Delta\omega$ is sufficiently small such that $\hat{\psi}(a\omega_1) \simeq \hat{\psi}(a\omega_2) \simeq \hat{\psi}(a\omega_c)$, we obtain

$$|(\mathcal{W}u)(x, a, b)| \simeq \sqrt{2a}|\hat{\psi}(a\omega_c)|[1 + \cos(2\Delta k x - 2\Delta\omega b)]^{1/2}. \tag{19}$$

If the Gabor wavelet is used, the function $\hat{\psi}_g(a\omega_c)$ has its maximum at $a = \omega_0/\omega_c$. Consequently, for fixed x, the magnitude of the WT reveals a peak at $a = \omega_0/\omega_c$ and $b = (\Delta k/\Delta\omega)x = x/c_g$ on the time-frequency plane. Therefore, the peak of the magnitude of the WT corresponds to the propagation of a wave with group velocity c_g at frequency ω_c.

(b) The Case of Sufficiently Large $\Delta\omega$: In this case, there observed a stationary vibration composed of two harmonics with frequencies ω_1 and ω_2. If the Gabor wavelet is used, the function $\hat{\psi}_g(a\omega)$ is localized around $\omega = \omega_0/a$. If $\Delta\omega$ is sufficiently large such that $\hat{\psi}_g(a\omega_1)\hat{\psi}_g(a\omega_2) \simeq 0$, we obtain

$$|(\mathcal{W}u)(x, a, b)| \simeq \sqrt{a}\{[\hat{\psi}_g(a\omega_1)]^2 + [\hat{\psi}_g(a\omega_2)]^2\}^{1/2}. \tag{20}$$

It follows that the magnitude of the WT reveals two peaks at $a = \omega_0/\omega_1$ and $a = \omega_0/\omega_2$ regardless of b. Therefore, two frequency components are represented as two separated peaks on the time-frequency plane.

5 Time-Frequency Analysis of Flexural Waves in Beams

In this section, several results of the time-frequency analysis of dispersive waves in structures are shown. As a typical example of dispersive waves, the flexural wave in a beam of uniform cross section was considered. A comparable problem was treated by Hodges et al. (1985) using the STFT, and Wahl and Bolton (1993) using the WVD. Figure 3 shows the model: a simply supported beam with a rectangular cross section sub-

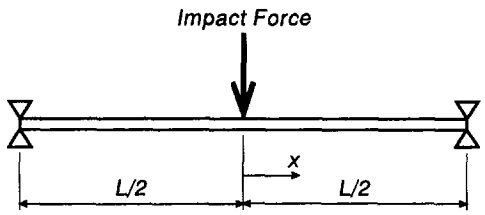


Fig. 3 A simply supported beam subjected to impact at the center of the span

Downloaded 04 May 2010 to 171.66.16.28. Redistribution subject to ASME license or copyright; see http://www.asme.org/terms/Terms_Use.cfm

Table 1 The dimensions and material constants of the beam

Width	$B = 20$ mm
Height	$H = 10$ mm
Span	$L = 2$ m
Cross sectional area	$A = 2 \times 10^{-4}$ m^2
Moment of inertia	$I = 1.667 \times 10^{-9}$ m^4
Young's modulus	$E = 206$ GPa
Mass density	$\rho = 7.86 \times 10^3$ kg/m^3

jected to an impact force at the center of the span. The dimensions and material constants of the beam are shown in Table 1.

The bending strain at the distance x from the impact site was computed according to the Bernoulli-Euler theory for simplicity. The equation of motion is given by

$$\frac{\partial^4 w}{\partial x^4} + \frac{1}{c_b^2}\frac{\partial^2 w}{\partial t^2} = \frac{q(x,t)}{EI}, \tag{21}$$

where w is the deflection, $q(x, t)$ the external force per unit length, and $c_b^2 = EI/(\rho A)$. Two kinds of impact force history were assumed:

$$F_1(t) = \begin{cases} 0 & \text{at} \quad t < 0, \\ F_0 & \text{at} \quad t \geq 0, \end{cases} \tag{22}$$

$$F_2(t) = \begin{cases} F_0 & \text{at} \quad 0 \leq t \leq t_0, \\ 0 & \text{otherwise}, \end{cases} \tag{23}$$

where $F_0 = 1$ kN and $t_0 = 0.1$ ms. The bending strain of the beam can be obtained by solving Eq. (21) under appropriate boundary conditions. If the beam is subjected to the impact force $F_1(t)$, the strains at $x = 0$ and 400 mm are obtained as shown in Figs. 4(a) and (b), respectively. The strain history changes with the distance x due to the dispersive nature of the flexural wave.

Figures 5 and 6 show the magnitude of the WT of the strain shown in Figs. 4(a) and (b), respectively. At the impact site

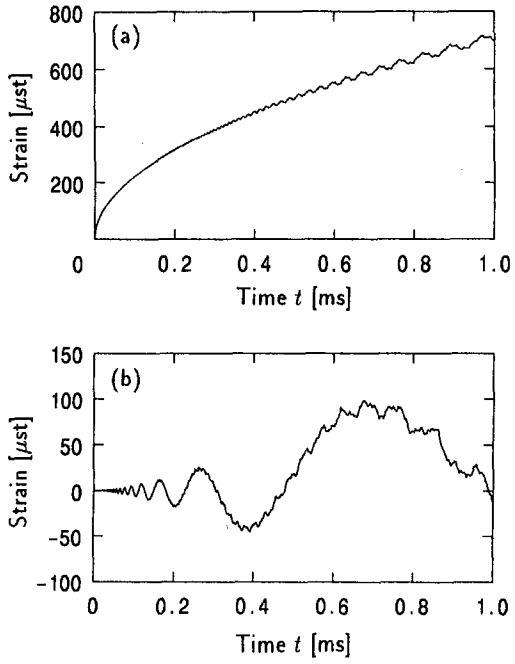


Fig. 4 The bending strain at (a) $x = 0$ and (b) $x = 400$ mm when the beam is subjected to the impact force $F_1(t)$

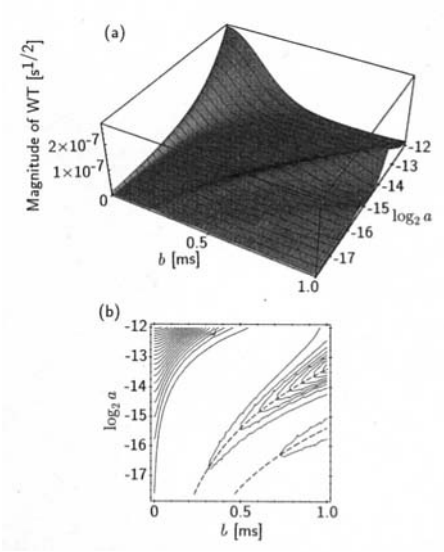


Fig. 5 The WT of the bending strain at $x = 0$ when the beam is subjected to the impact force $F_1(t)$: (a) time-frequency distribution of the magnitude; (b) its contour plot

$x = 0$, there appear three peaks in the time-frequency distribution. The first peak lies on the line $b = 0$, which corresponds to the beginning of the strain response. The second peak passes through the point $\log_2 a = -16$ and $b = 0.4$ ms and shifts later as a increases, that is, as the frequency decreases. The third passes through the point $\log_2 a = -16$ and $b = 0.8$ ms. As derived in the previous section, the peak of the magnitude of the WT corresponds to the wave propagation with the group velocity. The group velocity c_g of the flexural wave is given by (e.g., Kolsky, 1953)

$$c_g = 2\sqrt{c_b \omega} = 2\sqrt{c_b \omega_0 / a}. \tag{24}$$

The period for the flexural wave to make a round trip from the impact site to the end of the beam is given by L/c_g. The broken curves drawn in the contour plot of Fig. 5 are $b = L/c_g$ and $b = 2L/c_g$. It is clear that the second peak represents the wave reflected once at the end and that the third represents the wave reflected twice.

At the point $x = 400$ mm, there appear more peaks in the time-frequency distribution as shown in Fig. 6. The broken

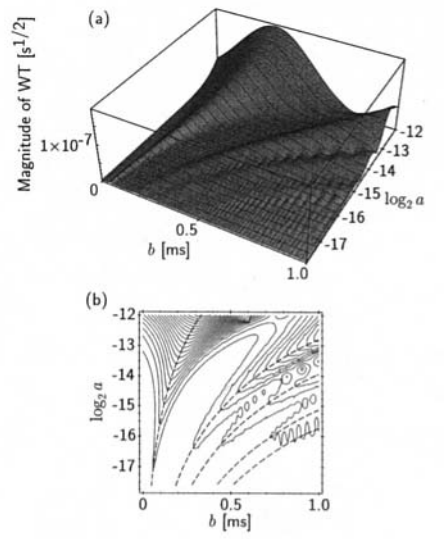


Fig. 6 The WT of the bending strain at $x = 400$ mm when the beam is subjected to the impact force $F_1(t)$: (a) time-frequency distribution of the magnitude; (b) its contour plot

Downloaded 04 May 2010 to 171.66.16.28. Redistribution subject to ASME license or copyright; see http://www.asme.org/terms/Terms_Use.cfm

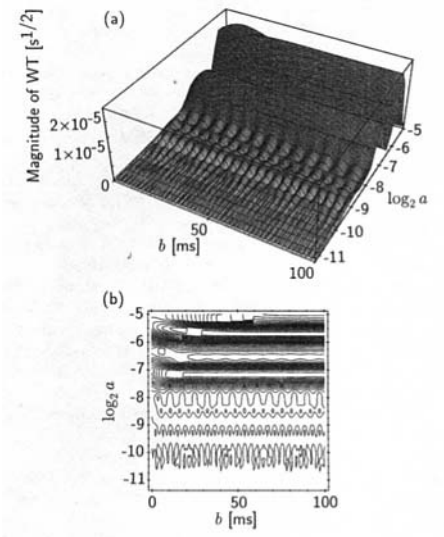


Fig. 7 The WT of the bending strain at $x = 400$ mm when the beam is subjected to the impact force $F_1(t)$ for large values of a and b: (a) time-frequency distribution of the magnitude; (b) its contour plot

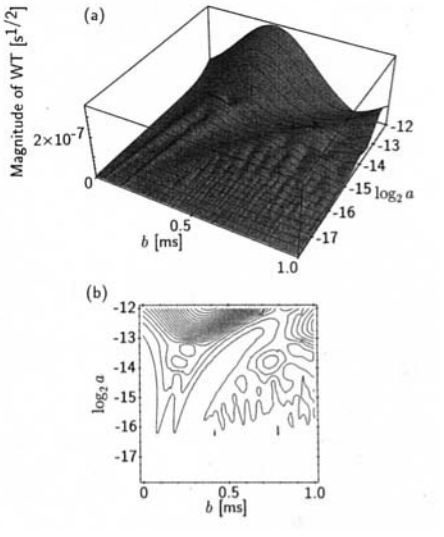


Fig. 9 The WT of the bending strain at $x = 400$ mm when the beam is subjected to the impact force $F_2(t)$: (a) time-frequency distribution of the magnitude; (b) its contour plot

curves in the contour plot indicate the arrival times of the flexural wave again. It is understood that the first peak represents the wave arrived directly from the impact site. In this case, the wave reflected at one end, $x = L/2$, arrives earlier than that reflected at the other end, $x = -L/2$, by $2x/c_g$. Although cross terms appear between closely spaced pulses, namely, the reflected pulses, the peaks are clearly distinguishable before the pulses are reflected twice. From Figs. 5 and 6, it is understood that the time-frequency distribution by the WT correctly figures the wave propagation phenomena.

Figure 7 shows the magnitude of the WT of the strain at $x = 400$ mm for large values of a and b. There appear two main peaks in the time-frequency distribution; one lies on the line $\log_2 a = -5.7$ and the other on the line $\log_2 a = -7.2$. As mentioned in the previous section, these peaks represent stationary vibrations of the beam. The natural frequencies of a simply supported beam are given by (e.g., Graff, 1975)

$$f_j = \frac{j^2 \pi c_b}{2L^2}, \quad j = 1, 2, 3, \ldots. \tag{25}$$

In this case, only symmetric modes ($j = 1, 3, 5, \ldots$) are excited since the beam is struck at the center of the span. The natural frequencies $f_3 = 52.2$ Hz and $f_5 = 145$ Hz correspond to $\log_2 a = -5.7$ and $\log_2 a = -7.2$, respectively, which are coincide well with the locations of the peaks. Peaks corresponding to the natural frequencies higher than f_5 are obscured by the cross terms and, therefore, care must be taken against them to determine the higher natural frequencies by using the WT.

Figures 8 and 9 show the magnitude of the WT of the strain at $x = 0$ and $x = 400$ mm, respectively, in the case that the beam is subjected to the impact force $F_2(t)$. In these figures, there appear patterns different from those in Figs. 5 and 6. At the impact site $x = 0$, the first peak is at $b = 0.05$ ms in the range $\log_2 a > -13$, while it splits into two peaks at $b = 0$ and $b = 0.1$ ms in the range $\log_2 a < -14$. The time $b = 0.05$ corresponds to the center of the force history $F_2(t)$. On the other hand, the time $b = 0$ and $b = 0.1$ ms correspond to the rising and settling of the force history $F_2(t)$. This tendency is same as that found in Fig. 2. It is interesting that the transition from one peak to two peaks occurs at about $\log_2 a = -13.25$, which corresponds to 10 kHz and is comparable to reciprocal of the duration of the impact force $F_2(t)$.

Figure 10 shows the locations of the first peak for each value of a, where the open circles indicate the peaks in Fig. 8 while the solid ones indicate those in Fig. 9. If strains are measured at any two points of a beam, a similar plot may be obtained by computing the WT of measured strains. According to such a plot, the traveling time of flexural waves between these two points can be obtained for each value of a. Since the distance between two measuring points is given, the group velocity can be identified at each value of a, namely, at each frequency.

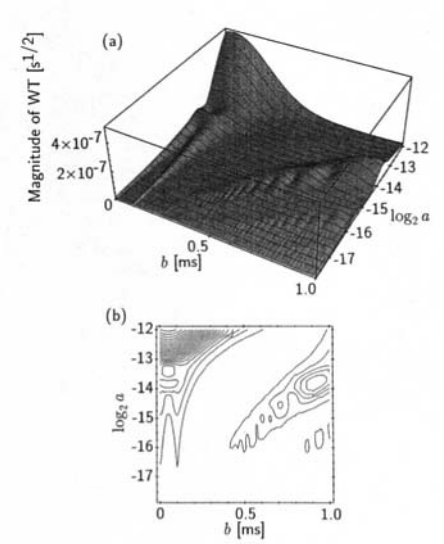


Fig. 8 The WT of the bending strain at $x = 0$ when the beam is subjected to the impact force $F_2(t)$: (a) time-frequency distribution of the magnitude; (b) its contour plot

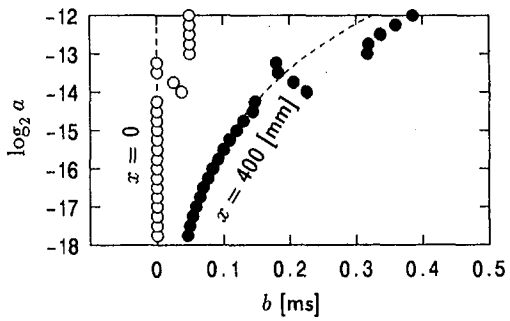


Fig. 10 The location of the first peaks in Figs. 8 and 9

Downloaded 04 May 2010 to 171.66.16.28. Redistribution subject to ASME license or copyright; see http://www.asme.org/terms/Terms_Use.cfm

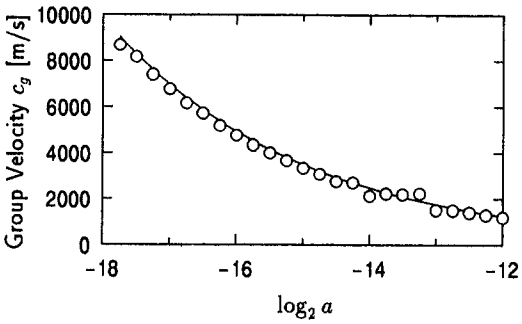


Fig. 11 The dispersion relation of the group velocity identified from the data in Fig. 10

Figure 11 shows the group velocity obtained from the data shown in Fig. 10. The solid curve indicates theoretical group velocity given by Eq. (24). The group velocity obtained by the WT coincides well with the theoretical value.

6 Conclusions

In this paper, the applicability of the WT to the time-frequency analysis of dispersive waves in structures has been examined. It has been found that the WT with the Gabor wavelet is an effective tool for analyzing the wave propagation phenomena in structures. Since the WT provides an appropriate resolution for a wide range of frequency, it can be applied not only to transient phenomena but also to stationary phenomena. The dispersion relation of the group velocity can be accurately evaluated by the information extracted by using the WT.

References

Chui, C. K., 1992, *An Introduction to Wavelets,* Academic Press, San Diego, CA.

Daubechies, I., 1992, *Ten Lectures on Wavelets,* SIAM, Philadelphia, PA.

Flandrin, P., Vidalie, B., and Rioul, O., 1991, "Fourier and Wavelet Spectrograms Seen as Smoothed Wigner-Ville Distributions," *Wavelets and Applications,* Y. Mayer, ed., Masson/Springer-Verlag, Paris/Berlin, pp. 93–103.

Goupillaud, P., Grossmann, A., and Morlet, J., 1994, "Cycle-Octave and Related Transforms in Seismic Signal Analysis," *Geoexploration,* Vol. 23, pp. 85–102.

Graff, K. F., 1975, *Wave Motion in Elastic Solids,* Dover, New York.

Hamada, M., Inoue, H., Kishimoto, K., Shibuya, T., and Koizumi, T., 1992, "An Inverse Analysis of Impact Problem by Means of Wavelet Transformation," *Proceedings of the 1992 Annual Meeting of JSME/MMD,* pp. 503–504 (in Japanese).

Hlawatsch, F., and Boudreaux-Bartels, G. F., 1992, "Linear and Quadratic Time-Frequency Signal Representations," *IEEE Signal Processing Magazine,* Vol. 9, No. 2, pp. 21–67.

Hodges, C. H., Power, J., and Woodhouse, J., 1985, "The Use of the Sonogram in Structural Acoustics and an Application to the Vibrations of Cylindrical Shells," *Journal of Sound and Vibration,* Vol. 101, No. 2, pp. 203–218.

Inoue, H., Hamada, M., Kishimoto, K., Shibuya, T., and Koizumi, T., 1993, "Application of the Wavelet Transform to Dispersive Stress Wave," *Proceedings of the 70th JSME Spring Annual Meeting,* Vol. 1, pp. 261–263 (in Japanese).

Kadambe, S., and Boudreaux-Bartelts, G. F., 1992, "A Comparison of the Existence of 'Cross Terms' in the Wigner Distribution and the Squared Magnitude of the Wavelet Transform and the Short Time Fourier Transform," *IEEE Transactions of Signal Processing,* Vol. 40, pp. 2498–2517.

Kolsky, H., 1953, *Stress Waves in Solids,* Dover, New York.

Li, C. J., and Ma, J., 1992, "Bearing Localized Defect Detection through Wavelet Decomposition of Vibrations," *Sensors and Signal Processing for Manufacturing,* ASME, PED-Vol. 55, pp. 187–195.

Newland, D. E., 1993a, *Random Vibrations, Spectral and Wavelet Analysis,* 3rd. ed., Longman/John Wiley and Sons, Harlow/New York.

Newland, D. E., 1993b, "Harmonic Wavelet Analysis," *Proceedings of the Royal Society of London,* Vol. A443, pp. 203–225.

Newland, D. E., 1994, "Wavelet Theory and Applications," *Proceedings of the Third International Congress on Air- and Structure-Borne Sound and Vibrations,* pp. 695–713.

Pandit, S. M., Joshi, G. A., and Paul, D., 1993, "Bearing Defect Detection Using DDS and Wavelet Methods," *Symposium on Mechatronics,* ASME, DSC-Vol. 50/PED-Vol. 63, pp. 285–293.

Rioul, O., and Vetterli, M., 1991, "Wavelets and Signal Processing," *IEEE Signal Processing Magazine,* Vol. 8, No. 4, pp. 14–38.

Sato, M., 1991, "Mathematical Foundation of Wavelets," *Journal of Acoustical Society of Japan,* Vol. 47, No. 6, pp. 405–423 (in Japanese).

Tansel, I. N., Mekdeci, C., Rodriguez, O., and Uragun, B., 1992, "Monitoring Microdrilling Operations with Wavelets," *Quality Assurance through Integration of Manufacturing Processes and Systems,* ASME, PED-Vol. 56, pp. 151–163.

Tansel, I. N., Mekdeci, C., and McLaughlin, C., 1993, "Detection of Tool Failure in End Milling with Wavelet Transformations and Neural Networks (WT-NN)," *Manufacturing Science and Engineering,* ASME, PED-Vol. 64, pp. 369–374.

Wahl, T. J., and Bolton, J. S., 1993, "The Application of the Wigner Distribution to the Identification of Structure-Borne Noise Components," *Journal of Sound and Vibration,* Vol. 163, No. 1, pp. 101–122.

Downloaded 04 May 2010 to 171.66.16.28. Redistribution subject to ASME license or copyright; see http://www.asme.org/terms/Terms_Use.cfm

Distributional Concept of the Elastic-Viscoelastic Correspondence Principle

V. Kovarik
Department of Composite Materials and Structures,
Klokner Institute of Czech Technical University,
166 08 Prague, Czech Republic

Distribution concept of physical variables in viscoelasticity theory enables to represent the stress-strain relations in the form of convolution equations, that is algebraic equations in the convolution algebra of right-sided distributions. These equations can be handled in much the same way that one handles matrix equations. Distributional correspondence principle is formulated as a transition process from the algebra of numbers (elastic solution) to the convolution algebra of distributions (viscoelastic solution). Corresponding elements and operations, respectively, in both algebras are established. Applications to a wide class of problems of the plate and shell theory are shown.

1 Introduction

Elasticity or viscoelasticity, being a property of the material, enters into the formulation of a problem through the constitutive (stress-strain) equations. In the linear theory of elasticity, these equations are always represented by the generalized Hooke's law. No similar unequivocal statement can be made in the linear theory of viscoelasticity. Several theories have been established employing different forms of constitutive relations. Dominating position has the so-called time-invariant hereditary theory which is frequently termed the linear theory of viscoelasticity, the mathematical theory of viscoelasticity a.s.o. (Christensen, 1971; Findley et al., 1976; Flügge, 1975). This theory finds application to a fairly wide range of structural materials. In general, there are two alternative forms to represent the constitutive equations of the time-invariant hereditary theory: the differential operator form and the integral representation. The first of them has been widely used for analysis since the mathematical processes required are rather simple. Mathematical tools for this representation are those from the differential equations theory. On the other hand, there are many reasons speaking in the favor of the integral representation:

- the ability to describe the time dependence more generally,
- the flexibility of representation of the actually measured viscoelastic material properties,
- the possibility of acceptable description of the behavior of ageing materials, and
- easy incorporation of temperature effects etc.

Unfortunately, it sometimes leads to difficult mathematics in stress analysis. The mathematical means required are those from the integral equation theory.

In the present discussion, the integral representation will be generalized with the aid of the Schwartz distribution theory. As a result, constitutive equations will be transformed to convolution equations which can be manipulated in much the same way that one manipulates matrix equations. Mathematical tools required for such an approach are given in Appendix A.

Contributed by the Applied Mechanics Division of THE AMERICAN SOCIETY OF MECHANICAL ENGINEERS for publication in the ASME JOURNAL OF APPLIED MECHANICS.

Discussion on this paper should be addressed to the Technical Editor, Professor Lewis T. Wheeler, Department of Mechanical Engineering, University of Houston, Houston, TX 77204-4792, and will be accepted until four months after final publication of the paper itself in the ASME JOURNAL OF APPLIED MECHANICS.

Manuscript received by the ASME Applied Mechanics Division, May 16, 1994; final revision, Aug. 5, 1994. Associate Technical Editor: G. J. Dvorak.

2 Correspondence Principle as Transition Process

Time-invariant hereditary theory renders a very effective tool for viscoelastic analysis represented by the so-called correspondence principle. This principle enables to utilize known elastic solutions for establishing the viscoelastic ones.

Inspecting the corresponding systems of elastic and viscoelastic equations (Appendix B), it is seen that

- the elastic equations represent algebraic equations in the algebra of "numbers" $\mathcal{A}$,
- the viscoelastic equations similarly are algebraic equations in the convolution algebra $\mathcal{A}'$, that is in the space $\mathcal{D}'_R$.

Thus, our consideration as the time-dependence concerns are focused on the algebra $\mathcal{A}$ when solving an elastic problem, and on the algebra $\mathcal{A}'$ when solving a viscoelastic one. Consequently, the transition from the elastic to the viscoelastic range may be interpreted as the transition from the algebra $\mathcal{A}$ to the algebra $\mathcal{A}'$.

Comparing the pairs of corresponding constitutive equations (the elastic and viscoelastic ones), it is seen that the unknowns involved are the same—the stress and/or the strain components σ_{ij}, ϵ_{ij}, the coefficients differ. They are represented by the elastic moduli—G the shear modulus, B the bulk modulus, and E the Young's modulus—and/or corresponding compliances

$$G, \quad B, \quad E$$
$$1/G, \quad 1/B, \quad 1/E \tag{2.1}$$

in the algebra $\mathcal{A}$, and by the distributional derivatives of the corresponding relaxation and/or creep functions

$$R_S^{[1]}, \quad R_O^{[1]}, \quad R_1^{[1]}$$
$$D_S^{[1]}, \quad D_O^{[1]}, \quad D_1^{[1]} \tag{2.2}$$

in the algebra $\mathcal{A}'$. Further, it is observed that the dot product in $\mathcal{A}$ corresponds to the convolution in $\mathcal{A}'$, and that the unit elements are 1 in $\mathcal{A}$, and $\delta(t)$ in $\mathcal{A}'$, respectively. It should be noted that the quantities (2.2) are called viscoelastic equivalents to the equally located elastic constants (2.1); e.g., $R_S^{[1]}$ is the viscoelastic equivalent to G, etc.

Having the results of the elastic boundary value problem at one's disposal, the transition from the elastic (algebra $\mathcal{A}$) to the viscoelastic range (algebra $\mathcal{A}'$) can be performed according to the distributional correspondence principle: Solutions of quasi-static elastic problems can be converted to solutions of corresponding (conjugate) viscoelastic problems, by simply replacing elements and operations in $\mathcal{A}$ (i.e., elastic constants,

Copyright © 1995 by ASME

Downloaded 04 May 2010 to 171.66.16.28. Redistribution subject to ASME license or copyright; see http://www.asme.org/terms/Terms_Use.cfm

multiplication) by corresponding elements and operations in $\mathcal{A}'$ (viscoelastic material characteristics, convolution), their reciprocals by corresponding inverse elements in $\mathcal{A}'$, and the additive unit 1 by the unit element $\delta(t)$.

The limitation of this approach lies in the boundary conditions. The subdivision of the boundary into the part on which boundary tractions are prescribed and the part on which displacements are prescribed must be independent of time.

The power of the distribution concept of the correspondence principle rests in large part on the facts that the use of the Laplace transformation is reduced to the calculation of some inverse elements in $\mathcal{A}'$ and that often the transform inversion is not as complex as in applying the classical principle.

3 Viscoelastic Equivalents

Fundamental viscoelastic equivalents have been found in the preceding section, namely

$$E \simeq R_1^{[1]}, \quad G \simeq R_S^{[1]}, \quad B \simeq R_O^{[1]}$$
$$1/E \simeq D_1^{[1]}, \quad 1/G \simeq D_S^{[1]}, \quad 1/B \simeq D_O^{[1]}. \tag{3.1}$$

Any of the right-hand side quantities in (3.1) represents a distribution in $\mathcal{D}_R'$ (this space constitutes the convolution algebra $\mathcal{A}'$) of the form

$$F(t) = f(t)h(t) \tag{3.2}$$

so that the distributional derivative $F^{[1]}$ reads

$$F^{[1]} = f(0^+)\delta(t) + f^{(1)}(t)h(t). \tag{3.3}$$

Further, it should be kept in mind that the distributions $R_j^{[1]}$ and $D_j^{[1]}$ in (3.1) are mutually inverse elements in $\mathcal{A}'$

$$R_j^{[1]} * D_j^{[1]} = \delta(t), \quad (j = 1, S, O). \tag{3.4}$$

If use is made of the well-known relations between elasticity constants, new viscoelastic equivalents can be established. Denoting

$$K^{[1]} = R_1^{[1]} * D_S^{[1]}, \tag{3.5}$$

one can, for example, write

$$\mu = \tfrac{1}{2}EG^{-1} - 1 \simeq \tfrac{1}{2}R_1^{[1]} * D_S^{[1]} - \delta(t) = \tfrac{1}{2}K^{[1]} - \delta(t)$$
$$1 + \mu = \tfrac{1}{2}EG^{-1} \simeq \tfrac{1}{2}K^{[1]}$$
$$1 - \mu = 2 - \tfrac{1}{2}EG^{-1} \simeq 2\delta(t) - \tfrac{1}{2}K^{[1]}$$
$$1 - \mu^2 = (1 + \mu)(1 - \mu) \simeq \tfrac{1}{2}K^{[1]} * (2\delta(t) - \tfrac{1}{2}K^{[1]})$$
$$= K^{[1]} * [\delta(t) - \tfrac{1}{4}K^{[1]}], \tag{3.6}$$

where μ stands for the Poisson's ratio.

In a more complex case of a reciprocal we have, e.g.,

$$(1 - \mu^2)^{-1} \simeq (K^{[1]})^{*-1} * (\delta - \tfrac{1}{4}K^{[1]})^{*-1} \tag{3.7}$$

where

$$(K^{[1]})^{*-1} = (R_1^{[1]} * D_S^{[1]})^{*-1} = D_1^{[1]} * R_S^{[1]} \tag{3.8}$$

and also

$$\left(\delta - \frac{1}{4}K^{[1]}\right)^{*-1} = \mathcal{L}^{-1}\left\{\frac{1}{1 - \frac{1}{4}p\hat{K}}\right\}$$
$$= \mathcal{L}^{-1}\left\{\frac{1}{1 - \frac{1}{4}p^3\hat{R}_1\hat{D}_S}\right\}. \tag{3.9}$$

With respect to (3.4)–(3.8), it holds that

$$E(1 - \mu^2)^{-1} \simeq R_1^{[1]} * D_1^{[1]} * R_S^{[1]} * J$$
$$= \delta * R_S^{[1]} * J = R_S^{[1]} * J. \tag{3.10}$$

The symbol $J(t)$ has been adopted for the inverse element (3.9) in order to simplify the writing

$$J(t) = (\delta - \tfrac{1}{4}K^{[1]})^{*-1}. \tag{3.11}$$

Some problems occur when trying to establish the viscoelastic equivalent to the expression

$$(1 - \mu^2)^{\beta} \simeq N^{[1]} \tag{3.12}$$

for any β. Especially, viscoelastic equivalents can hardly be found if

$$-1 < \beta < 0, \quad 0 < \beta < 1 \tag{3.13}$$

which proves to be a frequent case in stress analysis. Then, it is possible to proceed in the following manner. First, the left-hand side member of (3.12) is expanded in binomic series

$$(1 - \mu^2)^{\beta} = 1 - \binom{\beta}{1}\mu^2 + \binom{\beta}{2}\mu^4 - \binom{\beta}{3}\mu^6 + \ldots \tag{3.14}$$

where

$$\binom{\beta}{k} = \frac{\beta(\beta - 1)(\beta - 2)\ldots(\beta - k + 1)}{k!}. \tag{3.15}$$

Denoting

$$\binom{\beta}{j} = c_j \tag{3.16}$$

and keeping in mind that

$$c_0 = \binom{\beta}{0} = 1, \quad c_1 = \binom{\beta}{1} = \beta,$$
$$c_2 = \binom{\beta}{2} = \tfrac{1}{2}\beta(\beta - 1), \tag{3.17}$$

Eq. (3.14) may be rewritten to read

$$(1 - \mu^2)^{\beta} = \sum_{j=0}^{\infty} (-1)^j c_j \mu^{2j}$$
$$= 1 - \beta\mu^2 + \tfrac{1}{2}\beta(\beta - 1)\mu^4 + \ldots. \tag{3.18}$$

With respect to the weight of individual terms in (3.18), this series can often be reduced to only two members

$$(1 - \mu^2)^{\beta} \doteq 1 - \beta\mu^2 = 1 - \beta + \beta(1 - \mu^2). \tag{3.19}$$

Consequently,

$$N^{[1]} = (1 - \beta)\delta(t) + \beta K^{[1]} * [\delta(t) - \tfrac{1}{4}K^{[1]}]. \tag{3.20}$$

If there are any doubts about the rôle of the third term in (3.18), it is possible to take this term into consideration and to write

$$(1 - \mu^2)^{\beta} \doteq 1 - c_1\mu^2 + c_2\mu^4 = 1 - c_1 + c_2$$
$$+ (c_1 - 2c_2)(1 - \mu^2) + c_2(1 - \mu^2)^2. \tag{3.21}$$

In this case, we have

$$N^{[1]} = (1 - c_1 + c_2)\delta(t) + (c_1 - 2c_2)K^{[1]} * [\delta(t) - \tfrac{1}{4}K^{[1]}]$$
$$+ c_2 K^{[1]} * K^{[1]} * [\delta(t) - \tfrac{1}{4}K^{[1]}] * [\delta(t) - \tfrac{1}{4}K^{[1]}] \tag{3.22}$$

instead of (3.20).

Downloaded 04 May 2010 to 171.66.16.28. Redistribution subject to ASME license or copyright; see http://www.asme.org/terms/Terms_Use.cfm

4 Applications

Before applying the correspondence principle it is useful to recall some experience.

In one-dimensional (as the space coordinates concerns) quasi-static problems of the elasticity theory closed-form solutions are preferred to infinite series solutions. For conjugate elastic solutions, i.e., the bases for transition processes to the viscoelastic range, similar preference can hardly be recommended. The exception is the case of zero roots of the corresponding characteristic equation resulting in polynomial forms of general solutions. In the case of different roots, no matter whether real or complex, fundamental systems consist of either hyperbolic or trigonometric functions. These functions have elastic constants in their arguments. Because of this fact the application of the correspondence principle is rather problematic. The distributional correspondence principle is inapplicable. In applications of the classical one based on the Laplace transformation some problems arise in inverse transformation. Those problems must be solved either by means of the residue theorem of the complex variable function theory or with the aid of approximate inversion (Schapery, 1974). For that reason series form solutions, found, for example, by means of variational methods, are to be preferred.

In two-dimensional problems, the Kantorovich variational method cannot be recommended for analogical reasons. Similarly, the Lévy's solution of plates is not a very good basis for the transition process to the viscoelastic range.

As an illustration, the solution of a circular isotropic plate with built-in contour under uniform loading will now be shown. Conjugate elastic solution to that problem can be found in many textbooks (e.g., Timoshenko and Woinowsky-Krieger, 1959). With some changes in the notation, necessary to avoid the conflict with symbols introduced in the foregoing sections, this solution—i.e., the deflection u, and the bending moments M_ϱ (radial direction) and M_Φ (circumferential direction)—can be expressed in the form

$$u = \frac{q}{64H(E,\mu)}(a^2-\varrho^2)^2$$

$$M_\varrho = \frac{q}{16}[(a^2-\varrho^2)(1+\mu)-2\varrho^2]$$

$$M_\phi = \frac{q}{16}[(a^2-\varrho^2)(1+\mu)-2\mu\varrho^2] \tag{4.1}$$

where

$$H(E,\mu) = \frac{Ec^3}{12(1-\mu^2)} \tag{4.2}$$

and a, c denote the radius and the thickness of the plate, ϱ is the radial polar coordinate, and q means the intensity of the transverse loading.

First, the expression (4.1) for the deflection u will be rewritten with respect to Eq. (4.2) to read

$$u = \frac{3(a^2-\varrho^2)^2}{16c^3}\, q\, \frac{1-\mu^2}{E}. \tag{4.3}$$

Next, the element q in $\mathcal{A}$ will be replaced by the right-sided distribution

$$Q(t) = q(t)h(t) \tag{4.4}$$

in $\mathcal{A}'$. With the aid of Eqs. (3.1), (3.6) also the viscoelastic equivalent to the last elastic quantity in Eq. (4.3) can be established

$$\frac{1-\mu^2}{E} \simeq D_1^{[1]} * K^{[1]} * \left[\delta(t) - \frac{1}{4}K^{[1]}\right]. \tag{4.5}$$

Also, the correspondence relation $1 \simeq \delta(t)$ finds its application. The remaining quantities in Eq. (4.3) are "numerical" coefficients in the algebra $\mathcal{A}'$ and require no transformation. Viscoelastic equivalents for elastic constants in the expressions for bending moments are found in Eqs. (3.6).

Now, the distributional correspondence principle is easily applied to get

$$U(t) = \frac{3(a^2-\varrho^2)^2}{16c^3}\, Q * D_1^{[1]} * K^{[1]} * \left[\delta(t) - \frac{1}{4}K^{[1]}\right]$$

$$M_\varrho(t) = \tfrac{1}{16}[\tfrac{1}{2}(a^2-\varrho^2)K^{[1]} - 2\varrho^2\delta(t)] * Q$$

$$M_\phi(t) = \tfrac{1}{16}\{\tfrac{1}{2}(a^2-\varrho^2)K^{[1]} - 2\varrho^2[\tfrac{1}{2}K^{[1]} - \delta(t)]\} * Q. \tag{4.6}$$

For a stationary loading

$$q(t) = q_c = \text{const.}, \tag{4.7}$$

the above expressions convert to

$$U(t) = \frac{3(a^2-\varrho^2)^2}{16c^3}\, q_c D_1 * K^{[1]} * \left[\delta(t) - \frac{1}{4}K^{[1]}\right]$$

$$M_\varrho(t) = \tfrac{1}{16}[\tfrac{1}{2}(a^2-\varrho^2)K - 2\varrho^2 h(t)]q_c$$

$$M_\phi(t) = \tfrac{1}{16}\{\tfrac{1}{2}(a^2-\varrho^2)K - 2\varrho^2[\tfrac{1}{2}K - h(t)]\}q_c. \tag{4.8}$$

In this conversion use has been made of Eqs. (A.7), (A.10), and (A.11).

Second illustration pertains to a wide class of solutions of plate and shell problems. It can be shown that many elastic solutions of important plate and/or shell problems can be expressed in a rather general form

$$V = f(\text{geom})\psi(E,\mu)q(x,t) \tag{4.9}$$

where $f(\text{geom})$ denotes a quantity depending on geometrical characteristics of the structure considered and on numerical coefficients only. Further

$$\psi(E,\mu) = E\psi(\mu) + E^{-1}\psi^*(\mu) \tag{4.10}$$

and also

$$\psi(\mu) = \sum_{j=1}^{5} a_j\varphi_j(\mu), \quad \psi^*(\mu) = \sum_{j=1}^{5} b_j\varphi_j(\mu). \tag{4.11}$$

In the above equations the following notation has been introduced:

$$\varphi_1(\mu) = 1, \quad \varphi_2(\mu) = 1+\mu = \tfrac{1}{2}EG^{-1} \tag{4.12}$$

$$\varphi_3(\mu) = (1+\mu)^{-1} = 2GE^{-1}, \quad \varphi_4(\mu) = 1-\mu^2$$

$$\varphi_5(\mu) = (1-\mu^2)^\beta, \quad -1 \le \beta \le 1. \tag{4.13}$$

The symbol $q(x,t)$ stands for the input (loading, temperature), a_j, b_j ($j = 1, 2, 3, 4, 5$) are time-independent quantities (often constants). Instead of $\varphi_5(\mu)$ according to Eq. (4.13), the approximate expression

$$\varphi_5(\mu) \doteq 1 - \beta\mu^2 = (1-\beta)\psi_1(\mu) + \beta\psi_4(\mu) \tag{4.14}$$

can often be employed to better advantage.

Viscoelastic equivalents to (4.12), (4.14) read

$$\Phi_1^{[1]}(R,D) = \delta(t), \quad \Phi_2^{[1]}(R,D) = \tfrac{1}{2}K^{[1]} = \tfrac{1}{2}R_1^{[1]} * D_S^{[1]}$$

$$\Phi_3^{[1]}(R,D) = 2D_1^{[1]} * R_S^{[1]},$$

$$\Phi_4^{[1]}(R,D) = \tfrac{1}{2}K^{[1]} * (2\delta - \tfrac{1}{2}K^{[1]})$$

$$\Phi_5^{[1]}(R,D) \doteq (1-\beta)\delta(t) + \tfrac{1}{2}\beta K^{[1]} * (2\delta - \tfrac{1}{2}K^{[1]}). \tag{4.15}$$

Downloaded 04 May 2010 to 171.66.16.28. Redistribution subject to ASME license or copyright; see http://www.asme.org/terms/Terms_Use.cfm

Next, the equivalent $\Phi^{[1]}(R, D)$ to $\psi(E, \mu)$, Eq. (4.10), can be expressed in the form

$$\Phi^{[1]}(R, D) = \sum_{j=1}^{5} (a_j R_1^{[1]} + b_j D_1^{[1]}) * \Phi_j^{[1]} \qquad (4.16)$$

in connection with Eqs. (4.15). Finally, application of the correspondence principle to the conjugate solution (4.9) results in

$$V(t) = f(\text{geom})\Phi^{[1]}(R, D) * Q(x, t). \qquad (4.17)$$

For a stationary input

$$Q(x, t) = q(x)h(t), \qquad (4.18)$$

the relation (4.17) reduces to

$$V(t) = f(\text{geom})\Phi(R, D)q(x). \qquad (4.19)$$

It is easily seen that the foregoing illustration example is involved in the more general case considered in conclusion.

Acknowledgment

This work has been supported by Grant Agency Czech Republic grant No. 103/93/1046.

References

Christensen, R. M., 1971, *Theory of Viscoelasticity,* Academic Press, New York.

Doetsch, G., 1967, *Anleitung zum praktischen Gebrauch der Laplace-Transformation und der z-Transformation,* R. Oldenbourg, Munich.

Findley, W. N., Lai, J. S., and Onaran, K., 1976, *Creep and Relaxation of Nonlinear Viscoelastic Materials,* North-Holland Publishing Company, Amsterdam, pp. 15–130.

Flügge, W., 1975, *Viscoelasticity,* Springer-Verlag, Berlin.

Korn, G. A., and Korn, T. M., 1968, *Mathematical Handbook,* McGraw-Hill, New York.

Kovařík, V., 1989, *Stresses in Layered Shells of Revolution,* Academia, Prague; Elsevier, Amsterdam, pp. 269–368.

Kovařík, V., 1988, "Distributional Concept of Constitutive Equations for Viscoelastic Anisotropic Bodies," *Stavebnícky časopis,* Vol. 36, pp. 779–793.

Schapery, R. A., 1974, "Viscoelastic Behavior and Analysis of Composite Materials," *Composite Materials,* Vol. 2, G. P. Sendeckyj, ed., Academic Press, New York, pp. 86–165.

Timoshenko, S., and Woinowsky-Krieger, S., 1959, *Theory of Plates and Shells,* McGraw-Hill, New York, pp. 54–56.

Zemanian, A. H., 1965, *Distribution Theory and Transform Analysis,* McGraw-Hill, New York.

APPENDIX A

Schwartz Theory of Distributions

The objective of this Appendix is to list some definitions and operations of the Schwartz theory of distributions used throughout this paper. The attention will be restricted to the case of one-dimensional independent real variable t. For more details see Zemanian (1965), cf. also Doetsch (1967), and Korn and Korn (1968).

A *distribution* is defined as a continuous linear functional on a certain space $\mathcal{D}$ of testing functions. The space of all such distributions is denoted by $\mathcal{D}'$. $\mathcal{D}'$ is the *dual* (*conjugate*) space of $\mathcal{D}$.

Testing functions are infinitely differentiable functions which are zero outside some finite interval called *the support.*

Denoting a functional by the symbol F, we designate the number that F assigns to a particular testing function ϕ by $\langle F, \phi \rangle$.

Let $f(t)$ be a locally (Lebesgue) integrable function, then a distribution can be defined through the convergent integral

$$\langle F, \phi \rangle = \langle f(t), \phi(t) \rangle = \int_{-\infty}^{\infty} f(t)\phi(t)dt. \qquad (A.1)$$

In this case *a regular distribution* is spoken of. All distributions that are not regular are called *singular distributions.*

Alternative notations F and $F(t)$ are employed for distributions. Generally, the notation $F(t)$ is merely a convenient symbolism displaying the variable t that occurs in testing functions.

The equivalence class of functions $f(t)$ includes functions differing only on a set of measure zero.

The one-to-one relation exists between an equivalence class of functions and the corresponding regular distribution $F(t)$ generated by this class.

Definitions.

Shifting of a Distribution:

$$\langle F(t - \tau), \phi(t) \rangle = \langle F(t), \phi(t + \tau) \rangle. \qquad (A.2)$$

Differentiation of a Distribution:

$$\langle F^{[n]}(t), \phi(t) \rangle = \langle F(t), (-1)^n \phi^{(n)}(t) \rangle \qquad (A.3)$$

$n = 1, 2, 3, \ldots$ (infinite differentiability) and

$$\phi^{(n)} = \frac{d^n \phi}{dt^n}.$$

The space of distributions $\mathcal{D}'_R$ having their supports bounded on the left is called the space of *right-sided distributions,* $\mathcal{D}'_R \subset \mathcal{D}'$ (proper subspace). The space of distributions with bounded supports is denoted by $\mathcal{E}'$, $\mathcal{E}' \subset \mathcal{D}'_R$ (proper subspace).

The *Heaviside function* $h(t)$ is a regular distribution in $\mathcal{D}'_R$ generated by the locally integrable function

$$h(t) = \begin{cases} 0 & \text{for } t < 0 \\ 1 & \text{for } t \geqq 0. \end{cases} \qquad (A.4)$$

The so-called *Dirac function* $\delta(t)$ (better *Dirac functional, D. distribution, D. measure*) is a singular distribution in $\mathcal{E}'$ defined by the relation

$$\langle \delta(t - \tau), \phi(t) \rangle = \phi(\tau). \qquad (A.5)$$

Relation between the Dirac measure and the Heaviside function: Eq. (A.5) for $\tau = 0$ reads

$$\langle \delta(t), \phi(t) \rangle = \phi(0). \qquad (A.6)$$

Equations (A.1), (A.3) for $F = f = h$, $n = 1$ yield

$$\langle h^{[1]}(t), \phi(t) \rangle = -\langle h, \phi^{(1)} \rangle = -\int_0^{\infty} \phi^{(1)}(t)dt = \phi(0).$$

Comparing this result with Eq. (A.6), it is seen that

$$\delta(t) = h^{[1]}(t). \qquad (A.7)$$

Definitions.

The Convolution $C(t)$ of Two Right-Sided Distributions $A(t)$, $B(t)$:

$$C(t) = \langle A * B, \phi \rangle = \langle A(t), \langle B(\tau), \phi(t + \tau) \rangle \rangle$$
$$= \langle B(\tau), \langle A(t), \Phi(t + \tau) \rangle \rangle = \langle B * A, \Phi \rangle$$
$$C \in \mathcal{D}'_R. \qquad (A.8)$$

Shifting of a Convolution:

$$C(t - a) = A(t - a) * B(t) = A(t) * B(t - a). \qquad (A.9)$$

Differentiation of a Convolution:

$$C^{[m]} = A^{[j]} * B^{[k]}, \quad j + k = m. \qquad (A.10)$$

Substituting $A(t) = \delta(t)$ in Eq. (A.8) and taking Eq. (A.5) into account, we have

$$\langle \delta * B, \phi \rangle = \langle B(\tau), \langle \delta(t), \Phi(t + \tau) \rangle \rangle$$
$$= \langle B(\tau), \Phi(\tau) \rangle = \langle B, \phi \rangle.$$

Downloaded 04 May 2010 to 171.66.16.28. Redistribution subject to ASME license or copyright; see http://www.asme.org/terms/Terms_Use.cfm

Comparing the first and the last expression, it is seen that

$$\delta * B = B. \tag{A.11}$$

Thus, the Dirac measure is *the unit element* for convolution.

In the case of regular distributions $A(t), B(t)$ definition (A.8) converts to the classical definition of a convolution of functions

$$C(t) = A*B = \int_0^t A(\tau)B(t-\tau)d\tau$$

$$= \int_0^t A(t-\tau)B(\tau)d\tau = B*A. \tag{A.12}$$

Convolving the first distributional derivative of a right-sided distribution $F(t)$ with the Heaviside function $h(t)$, we have if respect is taken of Eqs. (A.10), (A.11), (A.7)

$$F^{[1]}*h = F*h^{[1]} = F*\delta = F. \tag{A.13}$$

In this manner "the primary" distribution is arrived at.

Definitions. A space $\mathcal{A}'$ of distributions is said to be *a convolution algebra* if it is a linear space which is closed under convolution, and if convolution is associative for any three distributions in $\mathcal{A}'$.

An inverse A^{*-1} of A in $\mathcal{A}'$ is any element in $\mathcal{A}'$ such that

$$A^{*-1}*A = \delta. \tag{A.14}$$

A convolution equation:

$$A*U = B \tag{A.15}$$

where A, B are known distributions in $\mathcal{A}'$, and U is unknown (it is also expected to be in $\mathcal{A}'$), has a unique solution in $\mathcal{A}'$ for every B in $\mathcal{A}'$ if A possesses an inverse A^{*-1} in $\mathcal{A}'$. Then, this solution reads

$$U = A^{*-1}*B. \tag{A.16}$$

The space $\mathcal{D}'_R$ of all right-sided distributions is a commutative convolution algebra having a unit element $\delta(t)$ which does not contain divisors of zero. The last property being the consequence of *the Titchmarsh theorem.* It should further be noted that Eq. (A.14) is usually solved (that is the inverse element calculated) by means of the Laplace transform.

Definitions. *The space of Laplace transformable distributions* is denoted by $\mathcal{D}'_0$. This space is a proper subspace of $\mathcal{D}'_R$.

For a distribution $F(t)$ in $\mathcal{D}'_0$, *the Laplace transform* is defined as

$$\hat{F}(p) = \mathcal{L}\{F(t)\} = \langle e^{-at}F(t), \lambda(t)e^{-(p-a)t}\rangle \tag{A.17}$$

where $\lambda(t)$ is any infinitely smooth function with support bouded on the left, which equals one over the neighborhood of the support of $F(t)$. For regular distributions this definition reduces to

$$\hat{F}(p) = \langle F(t), e^{-pt}\rangle = \int_0^\infty f(t)e^{-pt}dt. \tag{A.18}$$

Laplace transforms of some distributions (Doetsch, 1967):

$$\mathcal{L}\{\delta(t)\} = 1, \quad \mathcal{L}\{h(t)\} = 1/p$$

$$\mathcal{L}\{t^n h(t)\} = \Gamma(n+1)p^{-(n+1)}, \quad \mathcal{L}\{e^{at}h(t)\} = (p-a)^{-1}$$

$$\mathcal{L}\{F^{[n]}(t)\} = p^n\hat{F}(p), \quad \mathcal{L}\{A*B\} = \hat{A}\cdot\hat{B}$$

$$\mathcal{L}\{A^{*-1}\} = 1/\mathcal{L}\{A\} \tag{A.19}$$

where $\Gamma(n+1)$ denotes the gamma function.

Many of the physical variables in the viscoelasticity theory can generally be thought of as right-sided distributions of the form

$$F = f(t)h(t) \tag{A.20}$$

where $f(t)$ denotes a smooth function defined over the entire real axis $\mathcal{R}^1$. Distributional derivatives of such distributions can be calculated according to the formula

$$F^{[n]} = \sum_{j=1}^{n} f^{(n-j)}(0^+)\delta^{[j-1]}(t) + [f^{(n)}(t)] \tag{A.21}$$

where the brackets round the last right-hand side member denote that this member has to be taken into account only for $t > 0$.

Very often distributional convolutions are required of first distributional derivatives of two right-sided distributions (A.20). According to the formula (A.21) the derivatives are calculated

$$A^{[1]} = a(0^+)\delta(t) + [a^{(1)}(t)]$$

$$B^{[1]} = b(0^+)\delta(t) + [b^{(1)}(t)]. \tag{A.22}$$

Convolving these expressions, we successively get

$$C = A^{[1]}*B^{[1]}$$

$$= \{a(0^+)\delta(t) + [a^{(1)}(t)]\}*\{b(0^+)\delta(t) + [b^{(1)}]\}$$

$$= a(0^+)b(0^+)\delta*\delta + a(0^+)\delta*[b^{(1)}(t)]$$

$$+ b(0^+)\delta*[a^{(1)}(t)] + [a^{(1)}(t)]*[b^{(1)}(t)]$$

$$= a(0^+)b(0^+)\delta(t) + a(0^+)[b^{(1)}(t)]$$

$$+ b(0^+)[a^{(1)}(t)] + [a^{(1)}(t)]*[b^{(1)}(t)]. \tag{A.23}$$

The last right-hand side member in Eq. (A.23) is the classical convolution of functions (A.12)

$$[a^{(1)}(t)]*[b^{(1)}(t)] = \int_0^t a^{(1)}(t-\tau)b^{(1)}(\tau)d\tau. \tag{A.24}$$

APPENDIX B

Constitutive Equations

Decomposition of the strain tensor

$$\epsilon_{ij} = e_{ij} + \epsilon_0\delta_{ij}, \tag{B.1}$$

where e_{ij} is the strain deviator,

$$\epsilon_0 = \tfrac{1}{3}\epsilon_{ii}, \tag{B.2}$$

and δ_{ij} denotes the Kronecker tensor.

Decomposition of the stress tensor

$$\sigma_{ij} = s_{ij} + \sigma_0\delta_{ij} \tag{B.3}$$

where s_{ij} is the stress deviator, and

$$\sigma_0 = \tfrac{1}{3}\sigma_{ii} \tag{B.4}$$

is the mean normal stress.

Constitutive (stress-strain) equations of an elastic body

$$s_{ij} = 2Ge_{ij}, \quad \sigma_0 = 3B\epsilon_0 \tag{B.5}$$

$$e_{ij} = \frac{1}{2}\frac{1}{G}s_{ij}, \quad \epsilon_0 = \frac{1}{3}\frac{1}{B}\sigma_0 \tag{B.6}$$

where G, B are the shear and bulk moduli, respectively.

Integral form of the constitutive equations of the time-invariant hereditary theory in the classical concept:

$$s_{ij}(t) = 2r_S(0^+)e_{ij}(t) + 2r_S^{(1)}*e_{ij}$$

$$\sigma_0(t) = 3r_0(0^+)\epsilon_0(t) + 3r_0^{(1)}*\epsilon_0 \tag{B.7}$$

Downloaded 04 May 2010 to 171.66.16.28. Redistribution subject to ASME license or copyright; see http://www.asme.org/terms/Terms_Use.cfm

and

$$e_{ij}(t) = \tfrac{1}{2}d_S(0^+)s_{ij}(t) + \tfrac{1}{2}d_S^{(1)} * s_{ij}$$
$$\epsilon_0(t) = \tfrac{1}{3}d_0(0^+)\sigma_0(t) + \tfrac{1}{3}d_0^{(1)} * \sigma_0. \qquad \text{(B.8)}$$

The symbols $r_S(t)$, $r_0(t)$ stand for shear and volume relaxation functions. Similarly, $d_S(t)$, $d_0(t)$ denote shear and volume creep functions; the asterisks mean classical convolutions of functions (A.12).

In the distribution concept, the above equations can be given a very concise form. First, it is observed that the relaxation and creep functions, $r(t)$ and $d(t)$, generate right-sided regular distributions of the type (A.20)

$$R(t) = r(t)h(t), \quad D(t) = d(t)h(t) \qquad \text{(B.9)}$$

whose first derivatives are calculated according to Eq. (A.21) to give

$$R^{[1]} = r(0^+)\delta(t) + [r^{(1)}],$$
$$D^{[1]} = d(0^+)\delta(t) + [d^{(1)}]. \qquad \text{(B.10)}$$

It should be noted that in Eqs. (B.9), (B.10) proper indices have been dropped in order to simplify the writing. The same holds true for the following part. Moreover, Eqs. (B.7) will be involved into one more general relation

$$\sigma(t) = k[r(0^+)\epsilon(t) + r^{(1)} * \epsilon] \qquad \text{(B.11)}$$

and the equation

$$\epsilon(t) = \frac{1}{k}[d(0^+)\sigma(t) + d^{(1)} * \sigma] \qquad \text{(B.12)}$$

will be considered instead of Eqs. (B.8). In these equations k denotes a constant ($k = 1, 2, 3$) depending on the particular state of stress and strain considered (cf. Eqs. (B.7), (B.8) and also the following Eqs. (B.17)–(B.19)).

Next, the use is made of Eq. (A.11) and the convolution is taken in the distribution concept to obtain

$$\sigma(t) = k\{r(0^+)\delta * \epsilon + [r^{(1)}] * \epsilon\} = k\{r(0^+)\delta(t) + [r^{(1)}]\} * \epsilon$$
$$\epsilon(t) = \qquad\qquad = \frac{1}{k}\{d(0^+)\delta(t) + [d^{(1)}]\} * \sigma.$$

Taking Eqs. (B.10) into account the above relations can be given their final forms:

$$\sigma(t) = kR^{[1]} * \epsilon, \quad \epsilon(t) = \frac{1}{k}D^{[1]} * \sigma. \qquad \text{(B.13)}$$

Equations (B.13) are typical convolution equations (A.15). Convolving these equations with each other, we have

$$\sigma * \epsilon = kR^{[1]} * \epsilon * \frac{1}{k}D^{[1]} * \sigma = R^{[1]} * D^{[1]} * \sigma * \epsilon.$$

Application of the Titchmarsh theorem to the above equation results in the relation between the relaxation function and the corresponding creep function (cf. Definition (A.14))

$$R^{[1]} * D^{[1]} = \delta(t). \qquad \text{(B.14)}$$

In addition, Eq. (A.10) enables to rewrite Eqs. (B.13) immediately into their alternative forms

$$\sigma(t) = kR^{[1]} * \epsilon = kR * \epsilon^{[1]} \qquad \text{(B.15)}$$

$$\epsilon(t) = \frac{1}{k}D^{[1]} * \sigma = \frac{1}{k}D * \sigma^{[1]}. \qquad \text{(B.16)}$$

Dissimilarly to the classical concept no integration by parts is required in this transition.

Inserting $k = 2$, $\sigma = s_{ij}$, $\epsilon = e_{ij}$ as well as the lower index S with R, D, the full-form constitutive equations for simple shearing are received:

$$s_{ij}(t) = 2R_S^{[1]} * e_{ij} = 2R_S * e_{ij}^{[1]}$$
$$e_{ij}(t) = \tfrac{1}{2}D_S^{[1]} * s_{ij} = \tfrac{1}{2}D_S * s_{ij}^{[1]}. \qquad \text{(B.17)}$$

For $k = 3$, $\sigma = \sigma_0$, $\epsilon = \epsilon_0$ and the lower indices 0 with R, D constitutive equations for isotropic states of stress and strain result:

$$\sigma_0(t) = 3R_0^{[1]} * \epsilon_0 = 3R_0 * \epsilon_0^{[1]}$$
$$\epsilon_0(t) = \tfrac{1}{3}D_0^{[1]} * \sigma_0 = \tfrac{1}{3}D_0 * \sigma_0^{[1]}. \qquad \text{(B.18)}$$

It can be easily shown that for $k = 1$, $\sigma = \sigma_{11}$, $\epsilon = \epsilon_{11}$ and the lower indices 1, constitutive equations for simple tension in the x_1 direction are established

$$\sigma_{11}(t) = R_1^{[1]} * \epsilon_{11} = R_1 * \epsilon_{11}^{[1]}$$
$$\epsilon_{11}(t) = D_1^{[1]} * \sigma_{11} = D_1 * \sigma_{11}^{[1]} \qquad \text{(B.19)}$$

corresponding to the elastic case

$$\sigma_{11} = E\epsilon_{11}, \quad \epsilon_{11} = \frac{1}{E}\sigma_{11}. \qquad \text{(B.20)}$$

For more details and applications see Kovařík (1988), (1989).

Downloaded 04 May 2010 to 171.66.16.28. Redistribution subject to ASME license or copyright; see http://www.asme.org/terms/Terms_Use.cfm

A Nonlinear Wound Roll Model Allowing for Large Deformation

R. C. Benson[1]
Mechanics of Flexible Structures Project,
Department of Mechanical Engineering,
University of Rochester,
Rochester, NY 14627
Mem. ASME.

A new model is developed for predicting the internal loads in a wound roll. The principal contribution is the ability to account for large deformation. This is important for applications that require tightly packed rolls with large interlayer pressure and web compression. A nonlinear, orthotropic, plane-strain, pseudoelastic constitutive law is used. Arguments are made as to why the "material symmetry condition" does not apply to the wound roll. An efficient numerical solution scheme is developed, and a good correlation is achieved with interlayer pressure measurements available in the literature.

Introduction

Winding a flexible web into a compact roll is a common process for such materials as paper, cloth and magnetic tape, and an analysis of the internal stresses that develop is important for a number of design reasons. For example, one wants to develop sufficient interlayer pressure so that the frictional contact prevents slipping. The pressure should not be so large, however, that damage is done to a coating, or that the core of the roll is cracked. One may face a situation where a roll is repeatedly wound and unwound, as in a videotape, or wound once for use many years later, as in the archival storage of data on magnetic tape. Design trends in magnetic and optical recording are to ever-increasing data storage density, and a tightly wound roll of thin tape is one of the most efficient ways of achieving a high three-dimensional density. This makes it desirable to extend the wound roll simulation capability to larger interlayer pressures and web compression—the topic of this paper.

The internal loads of a wound roll are complicated by the accumulative way in which the roll is formed. The modeling device that has been used in the past, and again here, is to assume that the roll is formed by a succession of tensioned hoops being shrink-fit onto the underlying roll. This leads to the curious fact that if each lap was allowed to shrink to its tensionless circumference, an incompatible geometry would be produced. Of course, actual wound rolls never wholly exist in a stress-free state. The lap-by-lap construction mandates a need to know the *history* of the loading.

There is an extensive literature devoted to the wound roll problem, and only a few selected papers will be discussed here. The earliest models were based upon the assumption that the wound roll could be treated as a linear, plane-strain, orthotropic, pseudoelastic medium with a much lower stiffness in the radial direction than in the circumferential direction. The pseudoelastic assumption remains a way of approximating highly complicated *inelastic* behavior occurring between compressing laps, such as fiber crushing. Altman (1968) produced a linear model that was popular because it produced answers in the form of easily computed integrals. Tramposch (1965, 1967), in a pair of papers, examined issues of stress relaxation using a linear viscoelastic model. Yagoda (1980) recognized the importance of even minute compressibility at the core in affecting the wound roll stresses, and incorporated the effect in his model.

A more recent series of papers is important for introducing nonlinearity to the interlayer stress/strain law. Pfeiffer's experiments (1979) on stack compression led to the, now widely used, "Pfeiffer model" which exhibits an exponential growth in compressive stress due to increasing compressive strain. Hakiel's nonlinear analysis (1987) marks an important transition in wound roll modeling. Because it can be efficiently solved numerically, and because its correlation with experiments is significantly better than linear models, the "Hakiel model" has become the building block for most all other models in use today. Willett and Poesch (1988) independently arrived at a nonlinear model with features similar to the Hakiel model.

A number of very recent papers have focused on the consequences of different winding conditions. Good, Pfeiffer, and Giachetto (1992) took note of the fact that the outer lap tension immediately relaxes slightly from the "winding tension" and that this has important consequences for the interlayer pressures that develop. Two papers by Good and Wu (1993) and Good, Wu, and Fikes (1994) provide experimental and modeling studies of the effect of a "nip roller" on wound roll composition. Cole and Hakiel (1992) study "widthwise" variation in a wound roll that enters through imperfections at the outer lap. Zabaras et al. (1994) have a novel, hypoelastic approach to the wound roll problem. They introduce time as a parameter, and treat the problem as one of elastic loading and growth. They achieve high correlation with the Hakiel model.

The objective of the present analysis is to extend the modeling capability to account for finite displacements, and this will require a departure from previous modeling approaches. That is because the radial location of material particles becomes an unknown of the problem. Thus, we cannot use the roll radius, as other analysts have, as the independent coordinate of the roll. Instead, we will base our analysis on the lap number, which always marks the same material location, no matter how much deformation occurs. The radius in the deformed configuration, becomes the key *dependent* variable of the problem, and from it we can compute lap thickness changes, interlayer pressure, and lap tension.

We will find it convenient to work with stretch ratios rather than conventional strain measures, and this will lead to a variation in the Pfeiffer constitutive model. "Poisson effects" will be assumed to be zero, which is common in wound roll analyses. Perhaps more importantly, an argument will be made to show that the "material symmetry condition" of past analyses should not be applied to rolls that have a significant component of

[1] Currently Professor and Head, Department of Mechanical Engineering, Pennsylvania State University, 136 Reber Building, University Park, PA 16802.

Contributed by the Applied Mechanics Division of THE AMERICAN SOCIETY OF MECHANICAL ENGINEERS for presentation at the International Mechanical Engineering Congress and Exhibition, the Winter Annual Meeting of the ASME, San Francisco, CA, Nov. 12-17, 1995.

Discussion on this paper should be addressed to the Technical Editor, Professor Lewis T. Wheeler, Department of Mechanical Engineering, University of Houston, Houston, TX 77204-4792, and will be accepted until four months after final publication of the paper itself in the ASME JOURNAL OF APPLIED MECHANICS.

Manuscript received by the ASME Applied Mechanics Division, Sept. 29, 1994; final revision, Apr. 18, 1995. Associate Technical Editor: R. Abeyaratne.

Paper No. 95-WA/APM-4.

Copyright © 1995 by ASME

Downloaded 04 May 2010 to 171.66.16.28. Redistribution subject to ASME license or copyright; see http://www.asme.org/terms/Terms_Use.cfm

inelastic deformation, despite their being modeled with a pseudoelastic constitutive law.

Because of the nature of the incremental loading, it will prove effective to solve the problem through a lap-by-lap linearization of the nonlinear governing equations. Like models of the past, this will usually require the single solution of a tridiagonal matrix system for each added lap. Because of its wide-spread adoption, a detailed comparison will be made with the Hakiel model. The present model will be seen to predict a more compact geometry, essentially the same lap tensions, and reduced interlayer pressures. Because of the valuable interlayer pressure measurements that they present, and their treatment of "tension loss" the Good, Pfeiffer, and Giachetto (1992) paper will be discussed in detail and comparison will be made to one of their experiments.

Equations of Equilibrium

Figure 1 shows the loads on a segment of the ith lap. The interlayer pressure is P, measured positive in compression. The circumferential stress resultant is T, measured positive in tension. This is the resultant value through the lap thickness, so the units will be force per unit width of the lap. The radius of curvature and the thickness of the lap are r and h, respectively. Note that the lap number, i, is being used to locate material points in the roll, rather than the radius r. That is because we wish to solve for the radius as a dependent variable of the loading. The lap index, i, is a convected coordinate that will have the same value at a given material location no matter how much deformation occurs in the roll. It is a helpful convention (but not a necessary one) to let integer values of i mark the centers of laps, and half-integers mark the interfaces.

Balancing radial loads on the free body diagram of Fig. 1 leads to the following equation of equilibrium

$$r\frac{dP}{di} + hP + T = \frac{d}{di}(rP) + T = 0. \tag{1}$$

In this equation we have employed an equation of compatibility

$$\frac{dr}{di} = h. \tag{2}$$

Equations (1) and (2) require two boundary conditions. At the core, $i = \frac{1}{2}$, we will assume that there is a linear proportionality, E_c, between the radial stress and strain

$$P(\tfrac{1}{2}) = (E_c/a)[a - r(\tfrac{1}{2})]. \tag{3}$$

Here, a is the radius of the core before any laps have been wound on. If a total of I laps have been wound onto the roll, then at the outer surface, $i = I + \frac{1}{2}$, the pressure should be zero

$$P(I + \tfrac{1}{2}) = 0. \tag{4}$$

EQUILIBRIUM OF LOADS

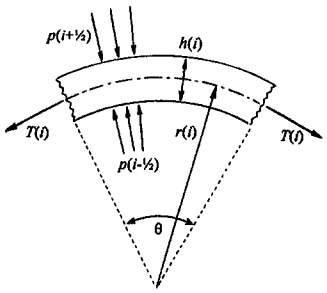


Fig. 1

LOAD VERSUS DEFORMATION

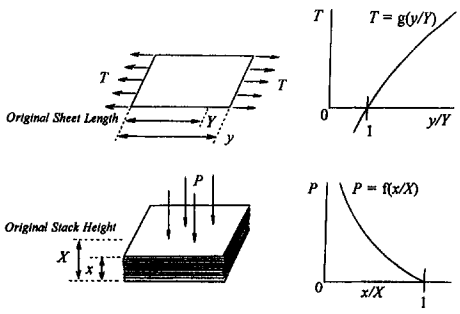


Fig. 2

Constitutive Behavior

Figure 2 schematically shows the two load-versus-deflection relationships that need to be specified. In the plane of the web we need to know the relationship between the stretch ratio, y/Y, and the tension, T,

$$T = g(y/Y). \tag{5}$$

Here, Y is the unstretched length of the sheet, y is the stretched length, and g is an experimentally determined function. Because of the orthotropy of many webs, the experiment should obviously be performed in the direction that will become the circumferential direction in the wound roll. For a great many applications the relationship will be linear

$$T = E\bar{h}[(y/Y) - 1] \tag{6}$$

where E is the elastic "Young's modulus" and $\bar{h}$ is the original thickness of the sheet.

As made clear by Hakiel (1987) and Willett and Poesch (1988), it is important to employ a nonlinear relationship between interlayer pressure and stack compression. Again referring to Fig. 2, we let X denote the original stack height, and x denote the deformed stack height under pressure P. A pressure/stretch relationship f is then experimentally determined,

$$P = f(x/X). \tag{7}$$

Equation (7) represents a pseudoelastic approximation to a highly complicated deformation that includes such inelastic phenomena as fiber crushing. It can, nevertheless, be an effective approximation if one takes care to use it only for loading. A new functional relationship would have to be determined for unloading, or if loading rates changed substantially. More information on hysteresis effects may be found in Olivé (1994).

Hakiel (1987), Willett and Poesch (1988) and others have found it convenient to employ a general power law for curve-fitting the stress/strain experimental data. Pfeiffer's model (1979) is also popular as it requires the definition of only two material constants, K_1 and K_2, and yet has sufficient versatility in fitting the stress/strain data for many stack materials. The Pfeiffer constitutive model is of the form

$$P = K_1[e^{K_2\epsilon_{\text{lin}}} - 1] = K_1[e^{K_2(1-x/X)} - 1] \tag{8}$$

where $\epsilon_{\text{lin}} = (1 - x/X)$ is the linear, compressive strain. Because the present paper has an emphasis on large interlayer deformation we prefer to use the nonlinear "log-strain" definition, $\epsilon_{\text{nonlin}} = \ln(X/x)$, that arises when increments of deformation are scaled to the *deformed* length of the object rather than the undeformed length of the object. When Eq. (8) is modified to use the log-strain expression, the Pfeiffer constitutive equation takes on an especially simple form

$$P = \alpha[e^{\beta\epsilon_{\text{nonlin}}} - 1] = \alpha[(x/X)^{-\beta} - 1]. \tag{9}$$

Downloaded 04 May 2010 to 171.66.16.28. Redistribution subject to ASME license or copyright; see http://www.asme.org/terms/Terms_Use.cfm

Here we have also made the replacements, $K_1 \rightarrow \alpha$ and $K_2 \rightarrow \beta$ to emphasize the fact that the two constants in the Pfeiffer model will be somewhat different depending on whether the pressure is curve-fit to the linear strain or to the nonlinear log strain. When deformations are small then ϵ_{lin} and ϵ_{nonlin} become nearly the same, and the two Eqs. (8) and (9) become nearly the same.

Later in this paper we will wish to make comparison to the Hakiel (1987) model which requires a specification for the compressive "tangent modulus" as a function of the interlayer pressure

$$E_{\text{tan}} = \frac{dP}{d\epsilon_{\text{lin}}} = \alpha\beta\left(1 + \frac{P}{\alpha}\right)^{(\beta+1)/\beta}. \tag{10}$$

Substituting $x/X = (1 - \epsilon_{\text{lin}})$ into Eq. (9), and following through on the algebra allows us to express E_{tan} in terms of the α and β coefficients, as done in Eq. (10).

It will be noted in this analysis that the in-plane and interlayer constitutive laws have not been coupled to each other. In other words, it has been assumed that there is no "Poisson effect." Many of the past analysts have measured or assumed *very* small values for the Poisson coefficients. For example, Good, Pfeiffer, and Giachetto (1992) state; ". . . winding models seem to be almost completely insensitive to the value of Poisson's ratio. Changing Poisson's ratio from 0.01 to 0.10 may affect the radial stress profile by less than 1 percent depending on the material." Others, like Hakiel (1987) carry a Poisson effect in their models, but use a value of zero in their numerical examples. Further clouding the question about Poisson effects is the fact that a number of recent authors have observed a conflict between the experimentally measured material constants, and the "material symmetry condition." Willett and Poesch (1988) provide the most detailed description. In the next section we provide what is hoped to be a clarifying analysis.

Observation on Poisson's Ratios and the Material Symmetry Condition

The equations in this section follow the notation established in Hakiel (1987). For an orthotropic elastic body in a plane-strain state of deformation, it is assumed that there exists a "complementary energy density function" (Shames and Dym, 1985), $u^*(\sigma_r, \sigma_t)$, that can be differentiated with respect to the stresses, σ_r and σ_t, to give the strains ϵ_r and ϵ_t in the principal frame

$$\epsilon_r = \frac{\partial u^*}{\partial \sigma_r} = \frac{\sigma_r}{E_r} - \frac{\nu_{rt}\sigma_t}{E_t}, \quad \epsilon_t = \frac{\partial u^*}{\partial \sigma_t} = \frac{\sigma_t}{E_t} - \frac{\nu_{tr}\sigma_t}{E_r}. \tag{11}$$

Here, the subscripts r and t correspond to the "radial" and "tangential" directions as they would appear in a wound roll. The radial elastic modulus, E_r, and Poisson's ratio, ν_{tr}, are expected to vary with the radial stress, σ_r, but not with the tangential stress, σ_t. The tangential elastic modulus, E_t, and Poisson's ratio, ν_{rt}, are expected to be constants, with no functional dependence on either σ_r or σ_t.

We may differentiate the first equation of (11) by σ_t, the second by σ_r, and then equate the mixed derivatives of u^* to get the material symmetry condition

$$-\frac{\nu_{rt}}{E_t} = -\frac{d}{d\sigma_r}\left(\frac{\nu_{tr}\sigma_r}{E_r}\right). \tag{12}$$

Noting that the left-hand side is presumed to be a constant with respect to σ_r, Eq. (12) may be easily integrated to give the material symmetry condition in its familiar form

$$\frac{\nu_{rt}}{E_t} = \frac{\nu_{tr}}{E_r}. \tag{13}$$

Equation (13) is a mathematical consequence of having assumed the existence of the complementary energy function, u^*. This is questionable, as it presumes that the roll is deforming *elastically,* with no energy dissipation and no dependence on the loading path. For example, Zabaras et al. (1994) and Olivé (1994) both report hysteresis in stacks that are loaded and then unloaded. The problem does not arise with the stress-versus-strain portions of Eq. (11). These may be accepted as a useful pseudoelastic approximation to a complicated, inelastic loading. The problem arises from the *further* assumption that these equations were derivable from an elastic potential, u^*. If this function does not exist, then there is no conclusion to be drawn from its nonexistent mixed derivatives.

In the nonlinear analyses stemming from the Hakiel (1987) and Willett and Poesch (1988) analyses, only the material symmetry condition requires this higher level of assumption. The basic nature and utility of these models would not be diminished if the material symmetry condition was discarded. Indeed, it would eliminate a problem that has been raised from the beginning by analysts who have been unable to reconcile discrepancies with their experimental measurements. For many other analysts, the question has been rendered moot by the assumption that both Poisson's ratios are effectively zero.

Accumulation Effect

Like other analysts it will be assumed here that the roll is built through a succession of new hoops being shrink-fit onto the underlying roll. A new lap enters with tension $\bar{T}$, thickness $\bar{h}$, and centerline radius $\bar{r}$. If this new lap becomes the Ith lap, then the radius of application is assumed to be

$$\bar{r}(I) = r(I-1) + \bar{h} \tag{14}$$

where $r(I-1)$ was the radius to the centerline of the outermost lap prior to the new lap being added. It is a known value.

This newly applied hoop of material, being under tension, would like to contract to a new "relaxation radius," R, for which the tension would vanish. By inverting Eq. (5) we may calculate this relaxation radius

$$\bar{T} = g(\bar{r}/R) \quad \Rightarrow \quad R = \bar{r}/g^{-1}(\bar{T}). \tag{15}$$

Here, for axisymmetric deformation, r/R is the stretch ratio in the hoop direction for the added lap. The relaxation radius for a given lap will not change as new laps are added, thus at any time we may compute the tension through the formula

$$T = g(r/R). \tag{16}$$

The interlayer pressure is similarly found through Eq. (7)

$$P = f(h/\bar{h}) \tag{17}$$

Here, the ratio of the deformed lap thickness, h, to the undeformed thickness, $\bar{h}$, becomes the stretch ratio in the radial direction.

If we utilize the linear Eq. (6) for the hoop tension, and the modified Pfeiffer law of equation (9) for the interlayer pressure, then Eqs. (15b), (16), and (17) become, respectively,

$$R = \bar{r}\left(1 + \frac{\bar{T}}{E\bar{h}}\right)^{-1}, \quad T = E\bar{h}\left(\frac{r}{R} - 1\right),$$
$$P = \alpha\left[\left(\frac{h}{\bar{h}}\right)^{-\beta} - 1\right]. \tag{18}$$

Quasi-linearization

The Eqs. (1)-(4) and (14)-(17) form a complete set that can be used to compute the loads and deformation of a wound roll. It is a nonlinear system because of the constitutive laws and because deformations are allowed to be large. The wound roll, however, is built lap-by-lap through an accumulation of

Downloaded 04 May 2010 to 171.66.16.28. Redistribution subject to ASME license or copyright; see http://www.asme.org/terms/Terms_Use.cfm

relatively small loads. Thus, it is useful to linearize the system for small perturbations from a known but unequilibrated state, and then to iterate until equilibrium is achieved. Let

$$r = r^* + \epsilon \tag{19}$$

where r is the desired radius that puts a lap into equilibrium, r^* is what is currently the best estimate to r, and ϵ is the difference between the two.[2] Then, from Eq. (2), the perturbation on lap thickness would be

$$h = \frac{dr^*}{di} + \frac{d\epsilon}{di} = h^* + \frac{d\epsilon}{di}. \tag{20}$$

From Eq. (16) we can linearize the hoop tension

$$T = g[(r^* + \epsilon)/R]$$

$$\approx g(r^*/R) + \frac{g'(r^*/R)}{R}\epsilon \equiv g^* + \frac{g'^*}{R}\epsilon \tag{21}$$

where a prime represents the derivative of the function with respect to its stretch ratio argument, and an asterisk represents an evaluation of the function at the previously computed r^*. Similarly, with Eq. (20), we can linearize the pressure function of Eq. (17),

$$P = f\left[\left(h^* + \frac{d\epsilon}{di}\right)\Big/\bar{h}\right]$$

$$\approx f(h^*/\bar{h}) + \frac{f'(h^*/\bar{h})}{\bar{h}}\frac{d\epsilon}{di} \equiv f^* + \frac{f'^*}{\bar{h}}\frac{d\epsilon}{di}. \tag{22}$$

The equilibrium Eq. (1) also requires a value for

$$\frac{dP}{di} = \frac{f'^*}{\bar{h}}\frac{dh^*}{di} + \frac{f''^*}{\bar{h}^2}\frac{dh^*}{di}\frac{d\epsilon}{di} + \frac{f'^*}{\bar{h}}\frac{d^2\epsilon}{di^2} \tag{23}$$

which is achieved after some algebra, and following the style of Eqs. (21) and (22).

When Eqs. (19)-(23) are substituted back into Eq. (1) we obtain a linearized differential equation of equilibrium of the form

$$A_i\frac{d^2\epsilon}{di^2} + B_i\frac{d\epsilon}{di} + C_i\epsilon = D_i \tag{24}$$

where A_i, B_i, C_i, and D_i are known functions of the lap index, i, and are given by

$$A_i = \frac{f'^*}{\bar{h}}r^* \quad B_i = \frac{f''^*}{\bar{h}^2}\frac{dh^*}{di}r^* + \frac{f'^*}{\bar{h}}h^* + f^*$$

$$C_i = \frac{f'^*}{\bar{h}}\frac{dh^*}{di} + \frac{g'^*}{R}$$

$$D_i = -\frac{f'^*}{\bar{h}}\frac{dh^*}{di}r^* - f^*h^* - g^*. \tag{25}$$

In a similar fashion we can use Eqs. (19), (20), and (22) to linearize the boundary conditions of Eqs. (3) and (4). At the "inside" boundary, $i = \frac{1}{2}$, we get

$$B_{\text{in}}\left(\frac{d\epsilon}{di}\right)_{1/2} + \epsilon_{1/2} = D_{\text{in}} \text{ with } B_{\text{in}} = \frac{a(f'^*)_{1/2}}{\bar{h}E_c}$$

$$\text{and} \quad D_{\text{in}} = a - \left(r^* + \frac{af^*}{E_c}\right)_{1/2} \tag{26}$$

and, at the "outside" boundary, $i = I + \frac{1}{2}$, we get

[2] The perturbation on radius, ϵ, should not be confused with the strain measures used elsewhere: ϵ_{lin}, ϵ_{nonlin}, ϵ_r, ϵ_t.

Table 1 Numerical Solution Algorithm

1 **Add a lap:** Let $I_{(\text{new})} = I_{(\text{old})} + 1$. The outermost variables are guessed to be: $r_I = r_{I-1} + \bar{h}$, $h_I = \bar{h}$, $T_I = \bar{T}$, $P_I = 0$.

2 **Compute the relaxation radius** of the added lap, R_I, by Eq. (15). (An example constitutive function, g^{-1}, is given in Eq. (18*a*).)

3 **Convergence loop:** Assign current values to the "old" variables: $r \to r^*$, $h \to h^*$, $T \to T^*$, $P \to P^*$.

4 **Establish the linear perturbation system** using Eqs. (25)-(27). (Example constitutive functions, f and g, are given in Eqs. (18*b*, *c*)).

5 **Solve the numerical problem** using Eqs. (28)-(30).

6 **Update values** for r, h, T, P, and dP/di using Eqs. (19)-(23). (Under- or over-relaxation is possible with $\epsilon \to \gamma\epsilon$, and $0 < \gamma < 2$.)

7 **Check for convergence:** If $\epsilon \ll r$ for all i then return to Step 1, otherwise, return to Step 3.

$$B_{\text{out}}\left(\frac{d\epsilon}{di}\right)_{I+1/2} = D_{\text{out}} \text{ with } B_{\text{out}} = \frac{(f'^*)_{I+1/2}}{\bar{h}}$$

$$\text{and} \quad D_{\text{out}} = -f^*_{I+1/2}. \tag{27}$$

Numerical Solution

Equations (24)-(27) can be readily solved through numerical finite difference equations. For interior laps, $2 \le i \le I - 1$, we discretize Eq. (24) as follows:

$$A_i(\epsilon_{i+1} - 2\epsilon_i + \epsilon_{i-1}) + \tfrac{1}{2}B_i(\epsilon_{i+1} - \epsilon_{i-1}) + C_i = D_i. \tag{28}$$

For the innermost lap, $i = 1$, we use a discretization and extrapolation that allows us to evaluate the boundary condition at lap centerlines rather than at lap interfaces

$$(\tfrac{3}{2} - B_{\text{in}})\epsilon_1 - (\tfrac{1}{2} - B_{\text{in}})\epsilon_2 = D_{\text{in}} \tag{29}$$

Similarly, at the outermost lap, $i = I$, we obtain

$$B_{\text{out}}\epsilon_I - B_{\text{out}}\epsilon_{I-1} = D_{\text{out}}. \tag{30}$$

Equations (28)-(30) form a tridiagonal matrix system that is easily inverted. It should be updated and inverted however many times is required to drive the epsilon vector to a desirably small value; that is to achieve $\epsilon \ll r$ for all laps. One might also use an under or over-relaxation by replacing ϵ with a scaled substitute $\gamma\epsilon$ in Eqs. (19)-(23). A "relaxation coefficient" in the range $0 < \gamma < 1$ restrains iterations that may be overshooting the desired answer, and enhances numerical stability. A value in the range $1 < \gamma < 2$ speeds a slowly converging series, but risks a loss of numerical stability. See Golub and Van Loan (1985) for details. The basic numerical algorithm is summarized in Table 1.

General Results

The model and solution scheme will be tested on a system for which the winding tension is a constant, and the constitutive behavior follows Eq. (18). Specifications are given in Case 1 of Table 2. The web material constants, E, α, and β, are based on a curve fit to experiments performed on paper sheets by Olivé (1994). This example has been deliberately designed to produce unusually large pressure and lap compression in order to exhibit the range of the new model.

Figure 3 shows the lap thickness plotted against the radius in the wound roll for 250, 500, 750, and 1000 laps. It will be seen that significant compression occurs in the roll, with steep

Downloaded 04 May 2010 to 171.66.16.28. Redistribution subject to ASME license or copyright; see http://www.asme.org/terms/Terms_Use.cfm

Table 2 Example Specifications

	Case 1	Case 2
Core radius, a	25.0 mm	38.1 mm
Elastic modulus of the core, E_c	6.0 GPa	12.4 GPa
Web thickness, $\bar{h}$	0.076 mm	0.089 mm
Constant winding tension, $\bar{T}$	1.23 kN/m	0.46 kN/m
Elastic modulus in the hoop direction, E	3.12 GPa	4.13 GPa
Interlayer compression modulus, α	47.9 kPa	1.10 kPa
Interlayer "springiness," β	26.3	45.0

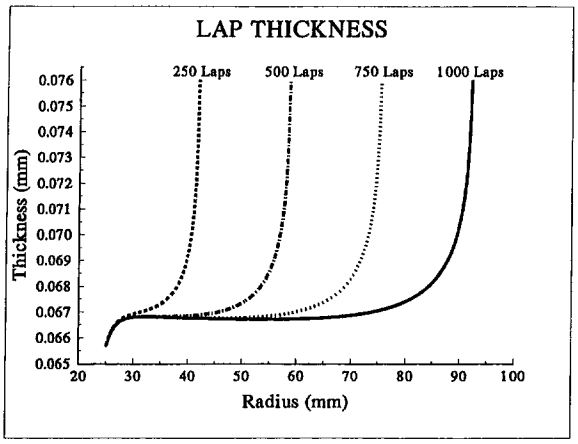


Fig. 3

gradients at the inner and outer boundaries. At the outer surface, the lap thickness has the nominal value of 76.0 μm which is consistent with the stress free boundary condition there. A short distance in from the outer surface, say about 15 mm, the laps have a roughly constant thickness of about 66.7 μm. Near the core, the web compresses to its minimum thickness of 65.7 μm. This is a significant amount of deformation. The stretch ratio, nonlinear strain, and linear strain are, respectively,

$$\frac{h}{\bar{h}} = \frac{65.7\ \mu\text{m}}{76.0\ \mu\text{m}} = 0.864, \quad \epsilon_{\text{nonlin}} = -\ln(0.864) = 0.146,$$

$$\epsilon_{\text{lin}} = 1.000 - 0.864 = 0.136. \tag{31}$$

A second measure of the lap compression is the 92.2 mm radius of the outermost lap. If, as in previous wound roll models, we were to ignore the lap compression in computing the radial growth, we would have computed an outer lap radius of 101 mm. This is about a 9 percent difference in the predicted roll diameter. Alternatively, with a web thickness of about 66.7 μm in the near-constant zone, by the present model we could wind on about 132 additional laps before the outer radius reached 101 mm. This is a 13 percent increase in the amount of material predicted to be in the roll.

Figure 4 shows the lap tension for 250, 500, 750, and 1000 laps. As is commonly observed there are steep gradients near the core and outer surface, and over much of the roll the laps are in compression. In the near-constant zone the tension is about -0.1 kN/m. At no point does the tension equal the winding tension of 1.23 kN/m. That is because every added lap has been shrink-fit onto a compressible foundation, including the core. Figure 5 shows the interlayer pressure for 250, 500, 750, and 1000 laps. Once again, there are steep gradients at the

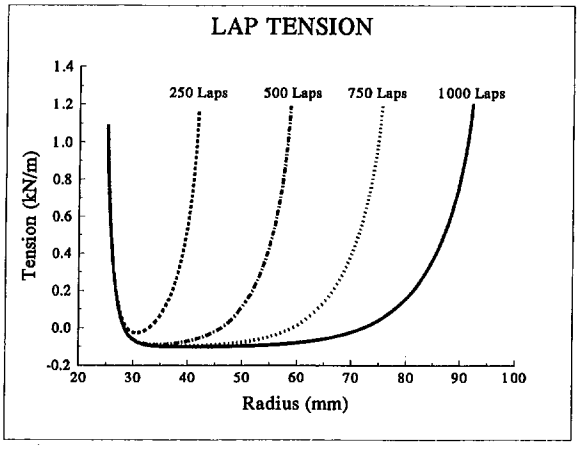


Fig. 4

boundaries and a near-constant zone through much of the interior. The peak pressure at the core, of about 2.20 MPa, is established very quickly, and then holds to that value as additional laps are added. In the near-constant zone the pressure is roughly 1.4 MPa. A local minimum in the pressure occurs around the $r = 30$ mm location.

The convergence speed of the solution scheme was tested on this example geometry. The results of Figs. 3-5 were reproduced using one, three, and five interations for $\epsilon(i)$. Recall the algorithm of Table 1. No discernable difference could be detected when the respective graphs were overlaid (even for very fine line widths). This is a welcome result. It suggests that, as long as convergence is achieved without need of under-relaxation, one may maximize computational speed by using a single quasilinear interation for $\epsilon(i)$. Not all systems will be so accommodating, however. Later in this paper we will discuss numerical results for Case 2 of Table 2. That model has an interlayer compression that is at first very soft, and then greatly stiffens. The strong nonlinearity made it necessary to use an under-relaxation scheme to avoid numerical instability caused by overshooting the desired answer during the quasilinear updating. A relaxation factor of $\gamma = \frac{1}{4}$ restored stability. Five iterations brought results to within 5 percent of the fully converged solution. Nine iterations brought results to within 1 percent. The interlayer pressure was the most slowing converging variable.

Comparison to the Hakiel Model

Figure 6 is a comparison to the Hakiel model (1987). The Hakiel model uses the compatibility equation to solve for the

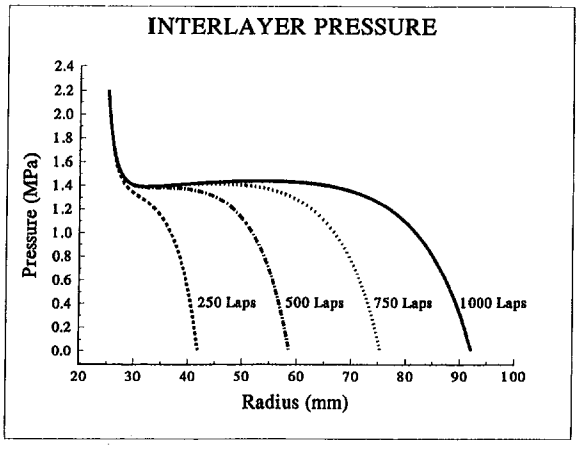


Fig. 5

Downloaded 04 May 2010 to 171.66.16.28. Redistribution subject to ASME license or copyright; see http://www.asme.org/terms/Terms_Use.cfm

interlayer pressure as a function of radius, $P(r)$. It assumes small displacements, but allows for nonlinearity in the interlayer stress/strain law. Because of the small displacement assumption, the roll radius may be used as the independent variable of the problem. The present model differs, principally, in that deformations will no longer be assumed to be small. Thus the roll radius becomes the key *dependent* variable of the problem, and solution is achieved by finding the functional relationship, $r(i)$, that produces a radial load balance.

In making comparison to the Hakiel model, we have used the tangent modulus expansion of Eq. (10), and the othotropic Poisson ratios have both been set to zero. A 1000-lap simulation of the Hakiel model was run, which could be compared to the 1000-lap tension and pressure results of Figs. 4 and 5, respectively. A more informative comparison is achieved, however, when the two models are run to the same outer lap radius. That occurred for the present model at 1132 laps. This immediately points out the principal difference between the two models. In a 101-mm radius roll the Hakiel model predicts that there will be 396 meters of material wound into the roll. The present model predicts that there will be 449 meters of material. The difference is obviously due to the present model's accounting for web compressibility.

Turning to the two tension graphs of Fig. 6 we see excellent agreement. In terms of predicting the amount of circumferential compression in the near-constant zone, both models yield essentially the same values. It is hard to discern in the figure, but the Hakiel models predicts slightly higher tension at the outer lap (and elsewhere). That is because the Hakiel model assumes that the outermost lap tension is equal to the winding tension. The present model allows all lap tensions, including the outermost one, to diminish as the roll compresses. Thus, there is a slight, 2.5 percent reduction in outer lap tension (1.20 kN/m versus 1.23 kN/m) when the lap is shrink-fit on to the underlying roll.

There is a more pronounced difference between the pressure predictions of the two models. The present model gives lower values. The reason is due to the "hard to discern" tension reduction in the outer lap. Although for the present example the difference in outer lap tension is only 2.5 percent, as lap after lap is wound on, the accumulated effect on the interlayer pressure is quite substantial. From a design standpoint, the most important location is at the core where the peak pressure occurs. The present model predicts a core pressure of 2.17 MPa. The Hakiel model predicts 2.74 MPa. This is about a 26 percent difference.

Comparison to Good, Pfeiffer, and Giachetto Experiments

The investigation of lower-than-expected pressures is not new. Good, Pfeiffer, and Giachetto (1992) recount in detail the events that led them to reconcile the problem that "pressures which were measured in centerwound rolls were often half that predicted by the roll models." To rectify the problem, they track outer lap displacements as the roll is built, which they then extrapolate to predict the displacement for the next added lap. The predicted displacement, which will be negative, is then used to compute a "hoop stress" reduction in the outer lap. This results in an interlayer pressure reduction similar to what is seen in Fig. 6.

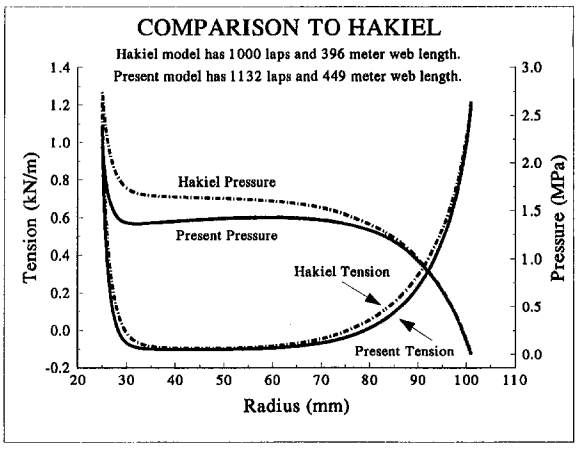


Fig. 6

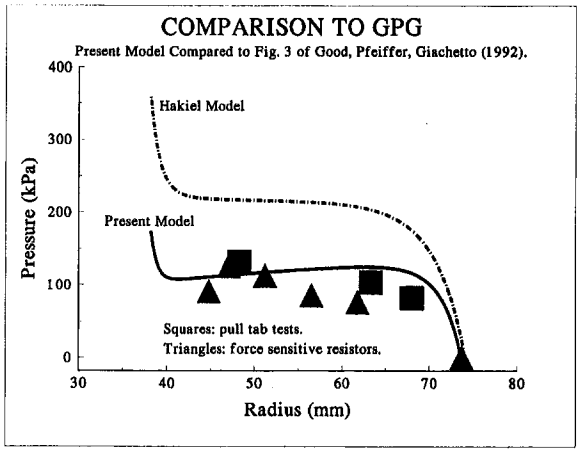


Fig. 7

The "GPG" and present models differ in the way that loads and deflection influence each other. The GPG model employs two distinct "subroutines" that run *sequentially* to each other: (1) a standard Hakiel model for stresses, and (2) a calculation of radial strains and displacements. Subroutine (1) is input to subroutine (2) for a given sized roll, while subroutine (2) is input to subroutine (1) following the addition of the next lap. The present algorithm has full coupling, thus the calculations for loads and displacements may be thought to be running in *parallel* to each other.

Comparison of the two models may also be made in the context of numerical stability. Good, Pfeiffer, and Giachetto (1992) report instances of "sawtooth" instability following the extrapolated assignment of negative tension to the outer lap boundary condition. The present model avoids this problem through its fully coupled construction, and because of its treatment of the outer boundary condition. The present model uses the zero pressure condition of Eq. (4) which is unambiguously known. Numerical instability can, nevertheless, be introduced to the present model through the quasilinearization. This is easily eliminated by under-relaxation, but carries the numerical cost of having to perform additional iterations on the "epsilon" vector.

The Good, Pfeiffer, and Giachetto (1992) paper is also valuable for its presentation of interlayer pressure measurements. It was desired to make a comparison of the present model to one of their figures. We chose the case that exhibited the greatest discrepancy between the data and existing models.[3] It was Fig. 3 of the GPG paper, which corresponds to the specifications of Case 2 in Table 2 in the present paper. The one specification not readily available from the GPG paper is the number of laps in the tested roll. As their experimental data shows the pressure falling to zero near $r = 74$ mm, the computer simulation was run until the outer radius reached this value. That occurred for 443 laps. Results for the interlayer pressure are shown in Fig.

[3] A number of other figures containing data plus the GPG model predictions were also of interest, but were nondimensionalized in a way that prevented reconstruction of a full set of system specifications.

Downloaded 04 May 2010 to 171.66.16.28. Redistribution subject to ASME license or copyright; see http://www.asme.org/terms/Terms_Use.cfm

7. The experimental data is taken from the GPG Fig. 3.[4] Our graph for the "Hakiel Model" also coincided with theirs. The match of the "Present Model" to the data is quite good considering the difficulty of making interlayer pressure measurements, and the fact that earlier models were predicting pressures that were roughly twice what the experiments showed. It suggests that the large deflection capabilities of the present model are important features for simulating conditions in actual wound rolls.

Summary

A new nonlinear model has been presented for computing internal loads in a wound roll. The model extends upon previous work by being able to simulate conditions over a greater range of interlayer pressure and web compression. This attribute mandates a different formulation that treats the radial location of a material point as a dependent rather than an independent variable of the problem. The numerical solution scheme is built upon a quasi linearization of the governing equations, and requires the solution of a tridiagonal matrix equation for each added lap. Comparison to experimental data in the literature was good. A variation in the Pfeiffer constitutive model has been suggested, and an argument for the elimination of the material symmetry condition for a pseudoelastic medium has been presented.

Acknowledgments

Support received from the Eastman Kodak Company for the Mechanics of Flexible Structures Project (MFSP) at the University of Rochester is very gratefully acknowledged. The author has benefitted greatly from the help of his MFSP colleagues, especially Kevin Cole, John LaFleche, Sinan Müftü, and Ken Stack.

[4] The size of the symbols in Fig. 7 was made to match the size of the symbols in the original Fig. 3 of Good, Pfeiffer, and Giachetto (1992).

References

Altman, H. C., 1968, "Formulas for Computing the Stresses in Center-Wound Rolls," *Journal of the Technical Association of the Paper and Pulp Industry (TAPPI)*, Vol. 51, No. 4, pp. 176–179.

Cole, K. A., and Hakiel, Z., 1992, "A Nonlinear Wound Roll Model Accounting for Widthwise Web Thickness Nonuniformities," *Proceedings of the Web Handling Symposium*, ASME Applied Mechanics Division, AMD-Vol. 149, pp. 13–24.

Golub, G. H., and Van Loan, C. F., 1985, *Matrix Computations*, Johns Hopkins University Press, Baltimore, MD.

Good, J. K., Pfeiffer, J. D., and Giachetto, R. M., 1992, "Losses in Wound-On Tension in the Centerwinding of Wound Rolls," *Proceedings of the Web Handling Symposium*, ASME Applied Mechanics Division, AMD-Vol. 149, pp. 1–12.

Good, J. K., and Wu, Z., 1993, "The Mechanism of Nip-Induced Tension in Wound Rolls," ASME JOURNAL OF APPLIED MECHANICS, Vol. 60, pp. 942–947.

Good, J. K., Wu, Z., and Fikes, M. W. R., 1994, "The Internal Stresses in Wound Rolls With the Presence of a Nip Roller," ASME JOURNAL OF APPLIED MECHANICS, Vol. 61, pp. 182–185.

Hakiel, Z., 1987, "Nonlinear Model for Wound Roll Stresses," *Journal of the Technical Association of the Paper and Pulp Industry (TAPPI)*, Vol. 70, No. 5, pp. 113–117.

Olivé, G. A., 1994, "A Study of Wound Rolls During Winding and Unwinding," M.S. Thesis, Department of Mechanical Engineering, University of Rochester, Rochester, NY.

Pfeiffer, J. D., 1979, "Prediction of Roll Defects from Roll Structure Formulas," *Journal of the Technical Association of the Paper and Pulp Industry (TAPPI)*, Vol. 62, No. 10, pp. 83–88.

Shames, I. H., and Dym, C. L., 1985, *Energy and Finite Element Methods in Structural Mechanics*, Hemisphere, New York.

Tramposch, H., 1965, "Relaxation of Internal Forces in a Wound Reel of Magnetic Tape," ASME JOURNAL OF APPLIED MECHANICS, Vol. 32, pp. 865–873.

Tramposch, H., 1967, "Anisotropic Relaxation of Internal Forces in a Wound Reel of Magnetic Tape," ASME JOURNAL OF APPLIED MECHANICS, Vol. 34, pp. 888–894.

Willett, M. S., and Poesch, W. L., 1988, "Determining the Stress Distributions in Wound Reels of Magnetic Tape Using a Nonlinear Finite-Difference Approach," ASME JOURNAL OF APPLIED MECHANICS, Vol. 55, pp. 365–371.

Yagoda, H. P., 1980, "Resolution of a Core Problem in Wound Rolls," ASME JOURNAL OF APPLIED MECHANICS, Vol. 47, pp. 847–854.

Zabaras, N., Liu, S., Koppuzha, J., and Donaldson, E., 1994, "A Hypoelastic Model for Computing the Stresses in Center-Wound Rolls of Magnetic Tape," ASME JOURNAL OF APPLIED MECHANICS, Vol. 61, pp. 290–295.

Downloaded 04 May 2010 to 171.66.16.28. Redistribution subject to ASME license or copyright; see http://www.asme.org/terms/Terms_Use.cfm

A Circular Inclusion With Imperfect Interface: Eshelby's Tensor and Related Problems

Zhanjun Gao
Department of Mechanical and Aeronautical Engineering, Clarkson University, Potsdam, NY 13699

Eshelby's tensor for an ellipsoidal inclusion with perfect bonding at interface has proven to have a far-reaching influence on the subsequent development of micromechanics of solids. However, the condition of perfect interface is often inadequate in describing the physical nature of the interface for many materials in various loading situations. In this paper, Airy stress functions are used to derive Eshelby's tensor for a circular inclusion with imperfect interface. The interface is modeled as a spring layer with vanishing thickness. The normal and tangential displacement discontinuities at the interface are proportional to the normal and shear stresses at the interface. Unlike the case of the perfectly bonded inclusion, the Eshelby's tensor is, in general, not constant for an inclusion with the spring layer interface. The normal stresses are dependent on the shear eigenstrain. A closed-form solution for a circular inclusion with imperfect interface under general two-dimensional eigenstrain and uniform tension is obtained. The possible normal displacement overlapping at the interface is discussed. The conditions for nonoverlapping are established.

Introduction

An inclusion is defined in this paper as a subdomain Ω (in domain, D) where an eigenstrain (stress-free transformation strain, misfit strain, nonelastic strain) ϵ_{ij}^* is prescribed. The elastic moduli in Ω (inclusion) may or may not be different from those in D-Ω (matrix). For an ellipsoidal inclusion in an infinite domain with perfect bonding at the interface, Eshelby (1957) has provided a closed-form solution of the stress and strain in terms of Eshelby's tensor. In recent years, the well-known solution of Eshelby (1957) has been applied to various fields of micromechanics of solids such as average stiffness analysis (Jasiuk, Chen, and Thorpe, 1992), nondilute stresses under a quasi-static loading (Mori and Tanaka, 1973), creep deformation (Wang and Weng, 1992), and fatigue life modeling (Reifsnider and Gao, 1992). Luo and Weng (1989) have obtained the Eshelby's tensor in a three-phase cylindrically concentric solid.

The condition of perfect bonding at the inclusion/matrix interface is often inadequate in describing the physical nature and mechanical behavior of the interface. Inclusions in high-strength steel, for instance, are easily debonded by a fatigue loading. Grain boundary sliding in polycrystals and granular media can be observed even at room temperature (Mura and Furuhashi, 1984). Interface failure is primarily responsible for the stiffness reduction of certain metal and polymer matrix composites under a static or cyclic loading (Gao, 1993).

In related studies the interface is modeled as a spring layer with vanishing thickness by Lene and Leguillon (1982), Aboudi (1987), Achenbach and Zhu (1989), Hashin (1990), and Jasiuk, Chen, and Thorpe (1992), among others. The jumps in displacement across the interface are allowed and these jumps are proportional to the conjugate tractions transmitted across the interface. This model allows one to represent intermediate states between perfect bonding and complete debonding. The problem is significantly simplified by eliminating the displacement jump in the normal direction along the interface. Such an inclusion is called a sliding inclusion (Mura and Furahashi, 1984), and various solutions to stress fields and moduli of sliding inclusions are available in the literature (e.g., Kouris and Mura, 1989; Shibata et al., 1992; Jun and Jasiuk, 1993). For an inclusion with the general spring layer interface (tangential as well as normal displacement jumps), Hashin (1991, 1992) has derived a closed-form solution under a pure shear loading. With exceptions of this and other simple cases, the inclusion problems with imperfect interface require a numerical approach such as boundary element method (Achenbach and Zhu, 1989), or infinite series expansion (Kouris and Mura, 1989). The Eshelby's tensors have been derived for sliding inclusion by Shibata et al. (1992). As a limiting situation where the compliance of the spring layer is much smaller than that of the matrix material, Qu (1993) has derived an explicit first-order expression of the Eshelby's tensor. To the author's knowledge, for a circular inclusion with the general spring layer interface (tangential as well as normal displacement jumps) no closed-form solution is available in the literature for the Eshelby's tensor.

The objective of the paper is to develop closed-form solutions of circular inclusion problems with a general spring layer interface condition. A representation of the Eshelby's tensor will be derived. A closed-form solution for the imperfectly bonded circular inclusion with eigenstrain and unidirectional tension at infinity will also be obtained. From this solution, the inclusion problem with a general two-dimensional loading can be superimposed. The conditions for which the spring layer constants must satisfy to avoid normal displacement overlapping will also be discussed.

The Problem and the Interface Conditions

A schematic view of the circular inclusion problem is shown in Fig. 1. The cross section, Ω, of the inclusion is circular with a radius, a. The materials are assumed to be isotropic with μ^i and κ^i, μ^m, and κ^m as the material properties of inclusion and matrix. Throughout this paper the superscripts i and m denote

Contributed by the Applied Mechanics Division of THE AMERICAN SOCIETY OF MECHANICAL ENGINEERS for presentation at the International Mechanical Engineering Congress and Exhibition, the Winter Annual Meeting of the ASME, San Francisco, CA, Nov. 12-17, 1995.

Discussion on this paper should be addressed to the Technical Editor, Professor Lewis T. Wheeler, Department of Mechanical Engineering, University of Houston, Houston, TX 77204-4792, and will be accepted until four months after final publication of the paper itself in the ASME JOURNAL OF APPLIED MECHANICS.

Manuscript received by the ASME Applied Mechanics Division, Sept. 7, 1994; final revision, Mar. 15, 1995. Associate Technical Editor: D. M. Barnett.

Paper No. 95-WA/APM-3.

Copyright © 1995 by ASME

Downloaded 04 May 2010 to 171.66.16.28. Redistribution subject to ASME license or copyright; see http://www.asme.org/terms/Terms_Use.cfm

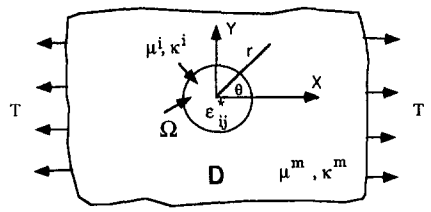


Fig. 1

quantities related to inclusion and matrix, respectively. Herein, μ is the Lame's constant; $\kappa = (3 - \nu)/(1 + \nu)$ for plane stress and $\kappa = 3 - 4\nu$ for plane strain, where ν is the Poisson's ratio. The eigenstrains, ϵ_{ij}^* $(i = 1, 2; j = 1, 2)$ are constant in Ω and zero in D-Ω. The applied load at infinity is $\sigma_{xx} = T$.

The mechanical behavior of the interface is modeled by a spring layer with vanishing thickness. With respect to the polar coordinates in Fig. 1, the relations between the relevant stresses and displacements at the interface, $r = a$, are written as

$$\sigma_{rr}^i(a, \theta) = \sigma_{rr}^m(a, \theta), \quad (1)$$

$$\sigma_{r\theta}^i(a, \theta) = \sigma_{r\theta}^m(a, \theta), \quad (2)$$

$$\sigma_{rr}^i(a, \theta) = \frac{n\mu^m}{a}\{u_r^m(a, \theta) - u_r^i(a, \theta) - u_r^*(a, \theta)\}, \quad (3)$$

$$\sigma_{r\theta}^i(a, \theta) = \frac{k\mu^m}{a}\{u_\theta^m(a, \theta) - u_\theta^i(a, \theta) - u_\theta^*(a, \theta)\}, \quad (4)$$

where k and n are (dimensionless) sliding and debonding parameters, and

$$\begin{aligned} u_r^*(a, \theta) &= u_r^*(r, \theta)|_{r=a} \\ &= r\{\epsilon_{11}^* \operatorname{Cos}^2\theta + \epsilon_{22}^* \operatorname{Sin}^2\theta + \epsilon_{12}^* \operatorname{Sin} 2\theta\}|_{r=a} \\ &= a\{\epsilon_{11}^* \operatorname{Cos}^2\theta + \epsilon_{22}^* \operatorname{Sin}^2\theta + \epsilon_{12}^* \operatorname{Sin} 2\theta\}, \\ u_\theta^*(a, \theta) &= u_\theta^*(r, \theta)|_{r=a} \\ &= r\left\{\frac{\epsilon_{22}^* - \epsilon_{11}^*}{2} \operatorname{Sin} 2\theta + \epsilon_{12}^* \operatorname{Cos} 2\theta\right\}\Big|_{r=a} \\ &= a\left\{\frac{\epsilon_{22}^* - \epsilon_{11}^*}{2} \operatorname{Sin} 2\theta + \epsilon_{12}^* \operatorname{Cos} 2\theta\right\}. \end{aligned}$$

Here $u_r^*(r, \theta)$ and $u_\theta^*(r, \theta)$ are radial and tangential displacements of the inclusion due to uniform eigenstrains, ϵ_{11}^*, ϵ_{22}^*, and ϵ_{12}^*, in the inclusion when the matrix material is removed, and a is the radius of the circular inclusion. The intermediate state between perfect bonding and complete debonding can be represented by varying the sliding and debonding parameters, k and n. The condition (3) needs to be used with caution because of possible overlapping of materials (Achenbach and Zhu, 1989). This issue will be discussed in some details later.

Eigenstrain Problem

The eigenstrain problem with zero applied load at infinity, i.e., $T = 0$, is considered first. The Airy stress functions for matrix and inclusion are

$$\phi^m = A^* a^2 \operatorname{Log} r + B^* a^2 \operatorname{Cos} 2\theta + C^* a^4 \frac{\operatorname{Cos} 2\theta}{r^2} + B_1^* a^2 \operatorname{Sin} 2\theta + C_1^* a^4 \frac{\operatorname{Sin} 2\theta}{r^2}, \quad (5)$$

$$\phi^i = D^* r^2 + E^* r^2 \operatorname{Cos} 2\theta + \frac{F^*}{a^2} r^4 \operatorname{Cos} 2\theta + E_1^* r^2 \operatorname{Sin} 2\theta + \frac{F_1^*}{a^2} r^4 \operatorname{Sin} 2\theta, \quad (6)$$

where $A^*, B^*, C^*, D^*, E^*, F^*, B_1^*, C_1^*, E_1^*, F_1^*$ are unknown constants to be determined from the interface conditions (1)–(4). The displacements and stresses for the biharmonic functions appeared in Eqs. (5) and (6) are given in the Appendix using the results of Dundurs and Mura (1964). Let $\tilde{\epsilon}_{11} = \mu^m \epsilon_{11}^*$, $\tilde{\epsilon}_{22} = \mu^m \epsilon_{22}^*$, $\tilde{\epsilon}_{12} = \mu^m \epsilon_{12}^*$ and $t = \mu^m/\mu^i$. One finds from the interface conditions (1)–(4)

$$\begin{aligned} A^* - 2D^* &= 0 \\ -4B^* - 6C^* + 2E^* &= 0 \\ -6C_1^* - 4B_1^* + 2E_1^* &= 0 \\ 2B^* + 6C^* + 2E^* + 6F^* &= 0 \\ 6C_1^* + 2B_1^* + 2E_1^* + 6F_1^* &= 0 \\ \frac{4D^*}{n} &= -A^* - t(\kappa^i - 1)D^* - (\tilde{\epsilon}_{11} + \tilde{\epsilon}_{22}) \\ \frac{-4E^*}{n} &= (\kappa^m + 1)B^* + 2C^* \\ &\quad + t[2E^* + (3 - \kappa^i)F^*] - (\tilde{\epsilon}_{11} - \tilde{\epsilon}_{22}) \\ \frac{-4E_1^*}{n} &= 2C_1^* + (\kappa^m + 1)B_1^* \\ &\quad - t[-2E_1^* - (3 - \kappa^i)F_1^*] - 2\tilde{\epsilon}_{12} \\ \frac{4E^* + 12F^*}{k} &= -(\kappa^m - 1)B^* + 2C^* + (\tilde{\epsilon}_{11} - \tilde{\epsilon}_{22}) \\ &\quad - t[2E^* + (3 + \kappa^i)F^*] \\ -\frac{4E_1^* + 12F_1^*}{k} &= (\kappa^m - 1)B_1^* - 2C_1^* - 2\tilde{\epsilon}_{12} \\ &\quad - t[-2E_1^* - (3 + \kappa^i)F_1^*]. \end{aligned} \quad (7)$$

Equation (7) is solved using a symbolic computation package, MAPLE (Heck, 1993), and the results are

$$\begin{aligned} A^* &= -2\frac{n(\tilde{\epsilon}_{11} + \tilde{\epsilon}_{22})}{tk\kappa^i n - tn + 4 + 2n}, \\ B^* &= \frac{tk\kappa^i n + kn + 3k + 3n}{I}(\tilde{\epsilon}_{11} - \tilde{\epsilon}_{22}), \\ C^* &= -\frac{tk\kappa^i n + kn + 4k + 2n}{2I}(\tilde{\epsilon}_{11} - \tilde{\epsilon}_{22}), \quad D^* = \frac{A^*}{2}, \\ E^* &= \frac{n(tk\kappa^i + k + 6)}{2I}(\tilde{\epsilon}_{11} - \tilde{\epsilon}_{22}), \\ F^* &= \frac{k - n}{I}(\tilde{\epsilon}_{11} - \tilde{\epsilon}_{22}), \\ B_1^* &= 2\frac{tk\kappa^i n + kn + 3k + 3n}{I}\tilde{\epsilon}_{12}, \\ C_1^* &= -\frac{tk\kappa^i n + kn + 4k + 2n}{I}\tilde{\epsilon}_{12}, \\ E_1^* &= \frac{n(tk\kappa^i + k + 6)}{I}\tilde{\epsilon}_{12}, \quad F_1^* = 2\frac{k - n}{I}\tilde{\epsilon}_{12}, \end{aligned} \quad (8)$$

where $I = 3k\kappa^m + 3n\kappa^m + 12 + 3tn + 3tk + tk\kappa^i + tn\kappa^i + k + n + t^2nk\kappa^i + tkn + k\kappa^m tn\kappa^i + k\kappa^m n$.

Downloaded 04 May 2010 to 171.66.16.28. Redistribution subject to ASME license or copyright; see http://www.asme.org/terms/Terms_Use.cfm

The stresses in the inclusion in polar and Cartesian coordinate systems are

$$\sigma^i_{rr} = 2D^* - 2E^* \operatorname{Cos} 2\theta - 2E_1^* \operatorname{Sin} 2\theta,$$

$$\sigma^i_{\theta\theta} = 2D^* + \left[2E^* + 12\left(\frac{r}{a}\right)^2 F^*\right] \operatorname{Cos} 2\theta + \left[2E_1^* + 12\left(\frac{r}{a}\right)^2 F_1^*\right] \operatorname{Sin} 2\theta,$$

$$\sigma^i_{r\theta} = \left[2E^* + 6\left(\frac{r}{a}\right)^2 F^*\right] \operatorname{Sin} 2\theta - \left[2E_1^* + 6\left(\frac{r}{a}\right)^2 F_1^*\right] \operatorname{Cos} 2\theta, \quad (9)$$

and

$$\sigma^i_{xx} = 2\left[D^* - E^* - 3\left(\frac{r}{a}\right)^2 F^*\right] + 6\left(\frac{r}{a}\right)^2 F^* \operatorname{Cos} 2\theta + 6\left(\frac{r}{a}\right)^2 F_1^* \operatorname{Sin} 2\theta,$$

$$\sigma^i_{yy} = 2\left[D^* + E^* + 3\left(\frac{r}{a}\right)^2 F^*\right] + 6\left(\frac{r}{a}\right)^2 F^* \operatorname{Cos} 2\theta + 6\left(\frac{r}{a}\right)^2 F_1^* \operatorname{Sin} 2\theta,$$

$$\sigma^i_{xy} = -2\left[E_1^* + 3\left(\frac{r}{a}\right)^2 F_1^*\right].$$

The total strains in the inclusion are obtained from Hooke's law as

$$\epsilon^i_{11} = \epsilon^i_{xx} = \frac{1}{2\mu^i}\left\{(\kappa^i - 1)D^* - 2E^* - 6\left(\frac{r}{a}\right)^2 F^* + 3\left(\frac{r}{a}\right)^2 (\kappa^i - 1)F^* \operatorname{Cos} 2\theta + 3\left(\frac{r}{a}\right)^2 (\kappa^i - 1)F_1^* \operatorname{Sin} 2\theta\right\} + \epsilon^*_{11},$$

$$\epsilon^i_{22} = \epsilon^i_{yy} = \frac{1}{2\mu^i}\left\{\left[(\kappa^i - 1)D^* + 2E^* + 6\left(\frac{r}{a}\right)^2 F^*\right] + 3\left(\frac{r}{a}\right)^2 (\kappa^i - 1)F^* \operatorname{Cos} 2\theta + 3\left(\frac{r}{a}\right)^2 (\kappa^i - 1)F_1^* \operatorname{Sin} 2\theta\right\} + \epsilon^*_{22},$$

$$\epsilon^i_{12} = \epsilon^i_{xy} = -\frac{1}{\mu^i}\left\{E_1^* + 3\left(\frac{r}{a}\right)^2 F_1^*\right\} + \epsilon^*_{12}. \quad (10)$$

The Eshelby's S-tensor is defined by the relation

$$\epsilon^i_{kl} = S_{klrs}\epsilon^*_{rs}, \quad (11)$$

where ϵ^i_{kl} is the total strain of the inclusion. Therefore,

$$S_{klrs} = \frac{\partial \epsilon^i_{kl}}{\partial \epsilon^*_{rs}} \quad \text{for} \quad r = s, \quad (12)$$

and

$$S_{klrs} = \frac{1}{2}\frac{\partial \epsilon^i_{kl}}{\partial \epsilon^*_{rs}} \quad \text{for} \quad r \neq s. \quad (13)$$

Using Eqs. (8), (10), (12), and (13), and noting that $\tilde{\epsilon}_{ij} = \mu^m \epsilon^*_{ij}$, the Eshelby's S-tensor for the inclusion problem is then found as

$$S_{1111} = \frac{1 - \kappa^i}{2(t\kappa^i n - tn + 4 + 2n)} nt - \frac{nt(t\kappa^i k + k + 6) + 6(k - n)t\left(\frac{r}{a}\right)^2}{2I} + 3(n - k)(1 - \kappa^i)t\left(\frac{r}{a}\right)^2 \frac{\operatorname{Cos} 2\theta}{2I} + 1,$$

$$S_{2222} = \frac{1 - \kappa^i}{2(t\kappa^i n - tn + 4 + 2n)} nt - \frac{nt(t\kappa^i k + k + 6) + 6(k - n)t\left(\frac{r}{a}\right)^2}{2I} - 3(n - k)(1 - \kappa^i)t\left(\frac{r}{a}\right)^2 \frac{\operatorname{Cos} 2\theta}{2I} + 1,$$

$$S_{1122} = \frac{1 - \kappa^i}{2(t\kappa^i n - tn + 4 + 2n)} nt + \frac{nt(t\kappa^i k + k + 6) + 6(k - n)t\left(\frac{r}{a}\right)^2}{2I} - 3(n - k)(1 - \kappa^i)t\left(\frac{r}{a}\right)^2 \frac{\operatorname{Cos} 2\theta}{2I},$$

$$S_{2211} = \frac{1 - \kappa^i}{2(t\kappa^i n - tn + 4 + 2n)} nt + \frac{nt(t\kappa^i k + k + 6) + 6(k - n)t\left(\frac{r}{a}\right)^2}{2I} + 3(n - k)(1 - \kappa^i)t\left(\frac{r}{a}\right)^2 \frac{\operatorname{Cos} 2\theta}{2I},$$

$$S_{1212} = \frac{-nt(tk\kappa^i + k + 6) + 6t(n - k)\left(\frac{r}{a}\right)^2}{2I} + \frac{1}{2},$$

$$S_{2212} = S_{1112} = -3\left(\frac{r}{a}\right)^2 \frac{t(n - k)(\kappa^i - 1)}{2I} (\operatorname{Sin} 2\theta),$$

$$S_{1211} = S_{1222} = 0. \quad (14)$$

It should be mentioned that although the inclusion is circular, and both the inclusion and matrix are isotropic, the local anisotropy is introduced by the spring layer interface. As a result, S_{1111} is not equal to S_{2222}, S_{1122} is different from S_{2211}. Furthermore, S_{2212} and S_{1112} are nonzero, indicating that the normal stresses, σ^i_{11} and σ^i_{22}, are dependent of shear eigenstrain, ϵ^*_{12}. For a perfectly bonded inclusion, the normal stresses are independent of shear eigenstrain components even for a general three-dimensional ellipsoidal inclusion (Eshelby, 1957). Unlike the perfectly bonded inclusion, the Eshelby's S-tensor is, in general, not constant for an inclusion with the spring layer interface.

It is easily seen from Eq. (14) that the necessary and sufficient condition for the Eshelby's tensor to be constant is that the sliding and debonding parameters are equal, i.e., $k = n$. In

Downloaded 04 May 2010 to 171.66.16.28. Redistribution subject to ASME license or copyright; see http://www.asme.org/terms/Terms_Use.cfm

this case all terms in Eq. (14) related to Cos 2θ and r vanish, and Eq. (14) becomes

$$S_{1111} = S_{2222} = \frac{1-\kappa^i}{2(t\kappa^i n - tn + 4 + 2n)} nt - \frac{nt(t\kappa^i k + k + 6)}{2I} + 1,$$

$$S_{1122} = S_{2211} = \frac{1-\kappa^i}{2(t\kappa^i n - tn + 4 + 2n)} nt + \frac{nt(t\kappa^i k + k + 6)}{2I},$$

$$S_{1212} = \frac{-nt(tk\kappa^i + k + 6)}{2I} + \frac{1}{2},$$

$$S_{2212} = S_{1112} = S_{1211} = S_{1222} = 0. \quad (15)$$

Local anisotropy disappears, and normal stresses do not depends on shear strain components.

For a perfectly bonded interface, the sliding and debonding parameters, k and n, approach infinity. Equation (15) is reduced to

$$S_{1111} = S_{2222} = \frac{\kappa^m(t\kappa^i - t + 4) + 2t}{2(\kappa^m + t)(t\kappa^i - t + 2)},$$

$$S_{1122} = S_{2211} = \frac{2 + \kappa^m(1-\kappa^i)}{(\kappa^m + t)(t\kappa^i - t + 2)} t,$$

$$S_{1212} = \frac{\kappa^m}{2(\kappa^m + t)},$$

$$S_{2212} = S_{1112} = S_{1211} = S_{1222} = 0. \quad (16)$$

For a homogenous inclusion, $t = 1$, $\kappa^m = \kappa^i$, Eq. (16) yields

$$S_{1111} = S_{2222} = \frac{2 + \kappa^m}{2(1 + \kappa^m)}, \quad S_{1122} = S_{2211} = \frac{2 - \kappa^m}{2(1 + \kappa^m)},$$

$$S_{1212} = \frac{\kappa^m}{2(1 + \kappa^m)},$$

$$S_{2212} = S_{1112} = S_{1211} = S_{1222} = 0, \quad (17)$$

which are the same as the results of Eshelby (Mura, 1987, p. 68).

Uniform Tension

The solution under a uniform tension, $\sigma_{xx} = T$ at the infinity is considered next. The eigenstrain vanishes in this case. The Airy stress functions are

$$\phi^i = \frac{T}{4}\left\{r^2 - r^2 \operatorname{Cos} 2\theta + Aa^2 \operatorname{Log} r + Ba^2 \operatorname{Cos} 2\theta + Ca^4 \frac{\operatorname{Cos} 2\theta}{r^2}\right\}, \quad (18)$$

$$\phi^m = \frac{T}{4}\left\{Dr^2 + Er^2 \operatorname{Cos} 2\theta + \frac{F}{a^2} r^4 \operatorname{Cos} 2\theta\right\}. \quad (19)$$

When the interface conditions (1)–(4) are applied, one obtains

$$2 + A - 2D = 0$$

$$2 - 4B - 6C + 2E = 0$$

$$2 + 2B + 6C + 2E + 6F = 0$$

$$\frac{4D}{n} = (\kappa^m - 1) - A - t(\kappa^i - 1)D$$

$$\frac{-4E}{n} = 2 + (\kappa^m + 1)B + 2C + t[2E + (3 - \kappa^i)F]$$

$$\frac{4E + 12F}{k} = -2 - (\kappa^m - 1)B + 2C - t[2E + (3 + \kappa^i)F]. \quad (20)$$

The solution of Eq. (20) is

$$A = 2\frac{-4 - n - tn\kappa^i + tn + \kappa^m n}{t\kappa^i n - tn + 4 + 2n},$$

$$B = 2\frac{-ktn\kappa^i + tkn - kn + t^2 kn\kappa^i}{I} + 2\frac{tk\kappa^i - 2k + 3tk + 3tn + 12 + tn\kappa^i - 2n}{I},$$

$$C = -\frac{-k\kappa^m + \kappa^m n - ktn\kappa^i + tkn - kn + t^2 kn\kappa^i}{I} - \frac{tk\kappa^i - 3k + 3tk + 3tn + 12 + tn\kappa^i - n}{I},$$

$$D = \frac{n(\kappa^m + 1)}{t\kappa^i n - tn + 4 + 2n},$$

$$E = -n(\kappa^m + 1)\frac{6 + k + tk\kappa^i}{I},$$

$$F = 2(\kappa^m + 1)\frac{n - k}{I}. \quad (21)$$

The solutions for pure shear at the infinity, as well as for the general in plane loading can be obtained by using the results of Eqs. (18) and (19) and the principle of superposition.

Uniform Tension With Eigenstrain

The Airy stress functions for nonzero applied load, T, and eigenstrain, ϵ_{ij}^*, are obtained by superimposing the stress functions for the eigenstrain problem, Eqs. (5) and (6), and for uniform tension problem, Eqs. (18) and (19). Therefore,

$$\phi^m = \frac{T}{4}\left\{r^2 - r^2 \operatorname{Cos} 2\theta + Aa^2 \operatorname{Log} r + Ba^2 \operatorname{Cos} 2\theta + Ca^4 \frac{\operatorname{Cos} 2\theta}{r^2}\right\} + A^* a^2 \operatorname{Log} r + B^* a^2 \operatorname{Cos} 2\theta + C^* a^4 \frac{\operatorname{Cos} 2\theta}{r^2} + B_1^* a^2 \operatorname{Sin} 2\theta + C_1^* a^4 \frac{\operatorname{Sin} 2\theta}{r^2}, \quad (22)$$

$$\phi^i = \frac{T}{4}\left\{Dr^2 + Er^2 \operatorname{Cos} 2\theta + \frac{F}{a^2} r^4 \operatorname{Cos} 2\theta\right\} + D^* r^2 + E^* r^2 \operatorname{Cos} 2\theta + \frac{F^*}{a^2} r^4 \operatorname{Cos} 2\theta + E_1^* r^2 \operatorname{Sin} 2\theta + \frac{F_1^*}{a^2} r^4 \operatorname{Sin} 2\theta. \quad (23)$$

The constants, A^*, B^*, C^*, D^*, E^*, F^*, B_1^*, C_1^*, E_1^*, and F_1^* are shown in Eq. (8), while the constants, A, B, C, D, E, and F are given in Eq. (21).

Downloaded 04 May 2010 to 171.66.16.28. Redistribution subject to ASME license or copyright; see http://www.asme.org/terms/Terms_Use.cfm

Displacement Overlapping

The use of interface conditions (1)-(4) may cause an unrealistic radial overlapping of the two materials at the interface (Achenbach and Zhu, 1989). In this section, the condition that determines displacement overlapping is discussed.

The radial displacements for the inclusion problem with eigenstrain and tensile load are obtained using Eqs. (22) and (23) and the Appendix as

$$u_r^m(r,\theta) = \frac{1}{2\mu^m}\frac{T}{4} r\Bigg\{(\kappa^m - 1) - \left(\frac{a}{r}\right)^2 A + \left[2 + (\kappa^m + 1)\left(\frac{a}{r}\right)^2 B + 2\left(\frac{a}{r}\right)^4 C\right]\cos 2\theta\Bigg\} + \frac{1}{2\mu^m} r\Bigg\{-\left(\frac{a}{r}\right)^2 A^* + \left[(\kappa^m + 1)\left(\frac{a}{r}\right)^2 B^* + 2\left(\frac{a}{r}\right)^4 C^*\right]\cos 2\theta + \left[(\kappa^m + 1)\left(\frac{a}{r}\right)^2 B_1^* + 2\left(\frac{a}{r}\right)^4 C_1^*\right]\sin 2\theta\Bigg\}, \quad (24)$$

$$u_r^i(r,\theta) = \frac{1}{2\mu^i}\frac{T}{4} r\Bigg\{(\kappa^m - 1)D - \left[2E + (3 - \kappa^i)\left(\frac{a}{r}\right)^2 F\right]\cos 2\theta\Bigg\} + \frac{1}{2\mu^i} r\Bigg\{(\kappa^m - 1)D^* - \left[2E^* + (3 - \kappa^i)\left(\frac{a}{r}\right)^2 F^*\right] \times \cos 2\theta - \left[2E_1^* + (3 - \kappa^i)\left(\frac{a}{r}\right)^2 F_1^*\right]\sin 2\theta\Bigg\}. \quad (25)$$

The condition that insures no overlapping is that the normal displacement jump at the interface is larger than or equal to zero, i.e.,

$$[u_r(a,\theta)] \overset{df}{=} u_r^m(a,\theta) - u_r^i(a,\theta) - u_r^*(a,\theta)$$

$$= \frac{a}{2\mu^m}\Bigg\{\frac{T}{4}\{(\kappa^m - 1) - A + [2 + (\kappa^m + 1)B + 2C] \times \cos 2\theta\} + \{-A^* + [(\kappa^m + 1)B^* + 2C^*]\cos 2\theta + [(\kappa^m + 1)B_1^* + 2C_1^*]\sin 2\theta\} - t\frac{T}{4}\{(\kappa^m - 1)D - [2E + (3 - \kappa^i)F]\cos 2\theta\} - t\{(\kappa^m - 1)D^* - [2E^* + (3 - \kappa^i)F^*]\cos 2\theta - [2E_1^* + (3 - \kappa^i)F_1^*]\sin 2\theta\} - 2\mu^m \times \{\epsilon_{11}^*\cos^2\theta + \epsilon_{22}^*\sin^2\theta + \epsilon_{12}^*\sin 2\theta\}\Bigg\} \geq 0. \quad (26)$$

The quantity, $[u_r(a,\theta)]$, defined above denotes the radial displacement jump at the interface.

Uniform Tension Problem. For uniform tension problem (no eigenstrain), $A^* = B^* = C^* = D^* = E^* = F^* = B_1^* = C_1^* = E_1^* = F_1^* = 0$. The displacement jump is reduced to, using (21) and (26)

$$[u_r(a,\theta)] = \frac{aT}{8\mu^m}\{(\kappa^m - 1) - A + [2 + (\kappa^m + 1)B + 2C]\cos 2\theta - t\{(\kappa^m - 1)D - [2E + (3 - \kappa^i)F]\cos 2\theta\}\}$$

$$= \frac{aT}{2\mu^m}(\kappa^m + 1)\left\{\frac{1}{t\kappa^i n - tn + 4 + 2n} + \frac{k + 6 + tk\kappa^i}{I}\cos 2\theta\right\}. \quad (27)$$

Note that $1/(t\kappa^i n - tn + 4 + 2n)$ and $(k + 6 + tk\kappa^i)/I$ are positive. Therefore,

$[u_r(a,\theta)] \geq 0$ if and only if

$$\Delta = \frac{1}{t\kappa^i n - tn + 4 + 2n} - \frac{k + 6 + tk\kappa^i}{I} \geq 0. \quad (28)$$

Any combination of inclusion, matrix properties and sliding, debonding parameters, k and n, satisfying the inequality (28) guarantees that no overlapping occurs. On the other hand, if the inequality (28) is violated, overlapping occurs at certain portion of the interface.

Several limit situations are considered next.

(i) Pure Sliding: limit $\Delta = 0$. No overlapping occurs for any material properties and sliding parameter k. The pure sliding interface condition involves continuity of tractions and of normal displacement, and discontinuity in tangential displacement across the interface. The sliding inclusion problem has been discussed by several researchers, Mura and Furuhashi (1984), Kouris and Mura (1989), Jasiuk, Chen, and Thorpe (1992), among others.

(ii) Fully Debonding: limit $\Delta = -1/4$. Overlapping occurs for any material properties under unidirectional tension.

(iii) Equal Sliding and Debonding Parameters:

$$\lim_{k\to n}\Delta = \frac{n[t(2 - \kappa^i) - (2 - \kappa^m)] - 2}{(tn + n\kappa^m + 2)(4 + 2n + tn\kappa^i - tn)}.$$

When n is sufficient large, $\Delta \geq 0$ if and only if $t(2 - \kappa^i) - (2 - \kappa^m) \geq 0$. Here $t = \mu^m/\mu^i$.

(iv) Rigid Inclusion:

$$\lim_{t\to 0}\Delta = \frac{3\kappa^m n + \kappa^m nk - 12 - 11n + 3k\kappa^m - 3k - 2nk}{2(2 + n)(3\kappa^m n + 12 + n + nk\kappa^m + 3k\kappa^m + k)}.$$

The surface $\Delta = 0$ in the three-dimensional space (κ^m, n, k) is shown in Fig. 2. The surface defines the critical state of variables for which the normal displacement jump is zero. For variable values above the surface, overlapping will not occur, while for variable values below the surface, overlapping will occur. The physically meaningful ranges for the variables κ^m, n, and k are

$$0 \leq k \leq \infty, \quad 0 \leq n \leq \infty,$$

$1 \leq \kappa^m \leq 3$ for plane strain, $1.67 \leq \kappa^m \leq 2$ for plane stress.

(v) Small Normal Compliance and Large Tangential Compliance ($n \ll 1$, $k \gg 1$):

$$\lim_{k\to\infty, n\to 0}\Delta = \frac{3}{4}\frac{(\kappa^m - 1) - t(\kappa^i - 1)}{3\kappa^m + 3t + t\kappa^i + 1}.$$

A three-dimensional surface similar to Fig. 2 can be constructed for the above equation.

Eigenstrain Problem. For eigenstrain problem the normal displacement jump is written as, using the inequality (26),

$$[u_r(a,\theta)] = \frac{a}{2\mu^m}\{-A^* + [(\kappa^m + 1)B^* + 2C^*]\cos 2\theta + [(\kappa^m + 1)B_1^* + 2C_1^*]\sin 2\theta - t\{(\kappa^m - 1)D^*$$

Downloaded 04 May 2010 to 171.66.16.28. Redistribution subject to ASME license or copyright; see http://www.asme.org/terms/Terms_Use.cfm

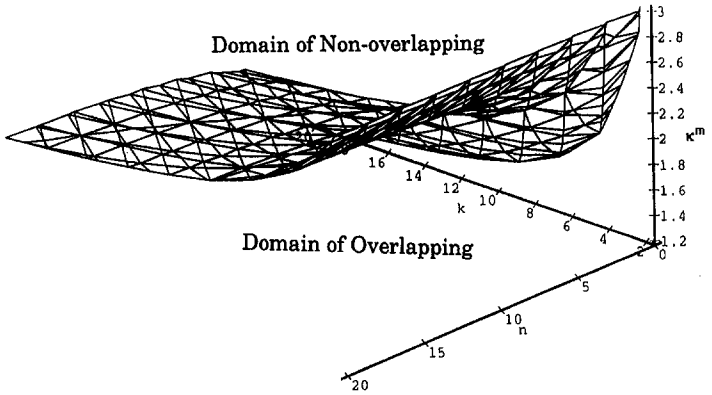


Fig. 2

$$- [2E^* + (3 - \kappa^i)F^*] \operatorname{Cos} 2\theta$$

$$- [2E_1^* + (3 - \kappa^i)F_1^*] \operatorname{Sin} 2\theta\}$$

$$- 2\mu^m\{\epsilon_{11}^* \operatorname{Cos}^2\theta + \epsilon_{22}^* \operatorname{Sin}^2\theta + \epsilon_{12}^* \operatorname{Sin} 2\theta\}\}.$$

When ϵ_{12}^* is zero, one has, from Eq. (8),

$$[u_r(a, \theta)] = \frac{a}{2\mu^m}\left\{-4\frac{\epsilon_{11}^* + \epsilon_{22}^*}{t\kappa^i n - tn + 4 + 2n} + 2(\epsilon_{22}^* - \epsilon_{11}^*)\frac{k + 6 + tk\kappa^i}{I}\operatorname{Cos} 2\theta\right\}.$$

Therefore,

$$[u_r(a, \theta)] \geq 0 \quad \text{if and only if} \quad -4\frac{\epsilon_{11}^* + \epsilon_{22}^*}{t\kappa^i n - tn + 4 + 2n} + 2(\epsilon_{22}^* - \epsilon_{11}^*)\frac{k + 6 + tk\kappa^i}{I} \geq 0, \quad (29)$$

and

$$-4\frac{\epsilon_{11}^* + \epsilon_{22}^*}{t\kappa^i n - tn + 4 + 2n} - 2(\epsilon_{22}^* - \epsilon_{11}^*)\frac{k + 6 + tk\kappa^i}{I} \geq 0. \quad (30)$$

Discussions similar to that of the inequality (28) for the uniform tension problem can be carried out for the inequalities (29) and (30) for the eigenstrain problem.

It should be emphasized that the condition for nonoverlapping depends very much on the combined effects of eigenstrain and loading. For the inclusion problem with eigenstrain and unidirectional loading, the general nonoverlapping condition is given by the inequality (26). Since the solution of the inclusion problem under a general plane loading can be obtained from Eqs. (24) and (25) and principle of superposition. The nonoverlapping condition for the inclusion problem under a general plane loading can be obtained easily.

Conclusion

Eshelby's tensor for a circular inclusion with general spring layer interface is derived. It has been shown that unlike the perfectly bonded inclusion, the local anisotropy is introduced by the imperfect interface represented by the spring layer. As a result, S_{1111} is not equal to S_{2222}, S_{1122} is different from S_{2211}. Furthermore, S_{2212} and S_{1112} are nonzero, indicating that the normal stresses are dependent of shear eigenstrain. The Eshelby's S-tensor is, in general, not constant for an inclusion with the spring layer interface. The necessary and sufficient condition for the Eshelby's tensor to be constant, and the local anisotropy to disappear is that the sliding and debonding parameters are equal, i.e., $k = n$.

A closed-form solution for the circular inclusion problem with general two-dimensional eigenstrain and uniform tension is also obtained. From this solution, the solution for an inclusion problem with eigenstrain and general two-dimensional applied load can be constructed. Finally, the possible normal displacement overlapping at the interface is discussed. The conditions for nonoverlapping are established.

The Eshelby's tensor for a perfectly bonded inclusion has proven to be instrumental for different micromechanical analyses of materials. The Eshelby's tensor developed in this paper may play a similar role for an inclusion which has an imperfect bonding. One application is metal matrix composite under a transverse loading at high temperatures. Representing the imperfect fiber/matrix interface and nonelastic strain of the matrix has proved to be critical in determining the mechanical response of the material (Gao and Zhao, 1995).

References

Aboudi, J., 1987, "Damage in Composites Modeling of Imperfect Bonding," *Composite Science and Technology,* Vol. 28, pp. 103–128.

Achenbach, J. D., and Zhu, H., 1989, "Effect of Interfacial Zone on Mechanical Behavior and Failure of Fiber-Reinforced Composites," *Journal of the Mechanics and Physics of Solids,* Vol. 37, pp. 381–393.

Dundurs, J., and Mura, T., 1964, "Interaction Between an Edge Dislocation and a Circular Inclusion," *Journal of the Mechanics and Physics of Solids,* Vol. 12, pp. 177–189.

Eshelby, J. D., 1957, "The Determination of the Elastic Field of an Ellipsoidal Inclusion, and Related Problems," *Proceedings of the Royal Society,* Vol. A241, pp. 376–396.

Gao, Z., 1993, "Center Notched Metal Matrix Composite With Interphase," *Engineering Fracture Mechanics,* Vol. 44, pp. 663–679.

Gao, Z., and Zhao, H., 1995, "Life Predictions of Metal Matrix Composite Laminates Under Isothermal and Nonisothermal Fatigue," *Journal of Composite Materials,* Vol. 29, No. 9, pp. 1142–1168.

Hashin, Z., 1990, "Thermoelastic Properties of Fiber Composite with Imperfect Interface," *Mechanics of Materials,* Vol. 8, pp. 333–348.

Hashin, Z., 1991, "Thermoelastic Properties of Particulate Composites With Imperfect Interface," *Journal of the Mechanics and Physics of Solids,* Vol. 39, pp. 745–762.

Heck, A., 1993, *Introduction to Maple,* Springer-Verlag, New York.

Jasiuk, I., Chen, J., and Thorpe, M. F., 1992, "Elastic Moduli of Composites With Rigid Sliding Inclusions," *Journal of the Mechanics and Physics of Solids,* Vol. 40, pp. 373–391.

Jun, S., and Jasiuk, I., 1993, "Elastic Moduli of Two-Dimensional Composites With Sliding Inclusions—A Comparison of Effective Medium Theories," *International Journal of Solids and Structures,* Vol. 30, pp. 2501–2523.

Kouris, D., and Mura, T., 1989, "The Elastic Field of a Hemispherical Inhomogeneity at the Free Surface of an Elastic Half Space," *Journal of the Mechanics and Physics of Solids,* Vol. 37, pp. 365–379.

Lene, F., and Leguillon, D., 1982, "Homogenized Constitutive Law for a Partially Cohesive Composite Material," *International Journal of Solids and Structures,* Vol. 18, pp. 443–458.

Lou, H. A., and Weng, G. J., 1989, "On Eshelby's *S*-Tensor in a Three-Phase Cylindrically Concentric Solid, and the Elastic Moduli of Fiber-Reinforced Composites," *Mechanics of Materials,* Vol. 8, pp. 77–88.

Downloaded 04 May 2010 to 171.66.16.28. Redistribution subject to ASME license or copyright; see http://www.asme.org/terms/Terms_Use.cfm

Mori, T., and Tanaka, K., 1973, "Average Stress in Matrix and Average Elastic Energy of Materials With Misfitting Inclusions," *Acta Metallurgica,* Vol. 21, pp. 571–574.

Mura, T., 1987, *Micromechanics of Defects in Solids,* 2nd ed., Martinus Nijhoff, Dordrecht, The Netherlands.

Mura, T., and Furuhashi, R., 1984, "The Elastic Inclusion With a Sliding Interface," ASME JOURNAL OF APPLIED MECHANICS, Vol. 51, pp. 308–310.

Qu, J., 1993, "Eshelby Tensor for an Elastic Inclusion With Slightly Weakened Interface," ASME JOURNAL OF APPLIED MECHANICS, Vol. 60, pp. 1048–1050.

Reifsnider, K. L., and Gao, Z., 1992, "A Micromechanics Model for Composites Under Fatigue Loading," *International Journal of Fatigue,* Vol. 13, pp. 149–156.

Shibada, S., Jasiuk, I., Mori, T., and Mura, T., 1990, "Successive Iteration Method Applied to Composites Containing Sliding Inclusions: Effective Modulus and Anelasticity," *Mechanics of Materials,* Vol. 9, pp. 229–243.

Wang, Y. M., and Weng, G. J., 1992, "Transient Creep Strain of a Fiber-Reinforced Metal-Matrix Composite Under Transverse Loading," ASME *Journal of Engineering Materials and Technology,* Vol. 114, pp. 237–244.

APPENDIX

Stress and Displacement Components for Biharmonic function, ϕ (after Dundurs and Mura, 1964)

ϕ	σ_{rr}	$\sigma_{r\theta}$	$\sigma_{\theta\theta}$	$2\mu u_r$	$2\mu u_\theta$
r^2	2	0	2	$(\kappa-1)\, r$	0
Log r	$1/r^2$	0	$-1/r^2$	$-1/r$	0
$\cos 2\theta$	$-4\cos 2\theta/r^2$	$-2\sin 2\theta/r^2$	0	$(\kappa+1)\cos 2\theta/r$	$-(\kappa-1)\sin 2\theta/r$
$\sin 2\theta$	$-4\sin 2\theta/r^2$	$2\cos 2\theta/r^2$	0	$(\kappa+1)\sin 2\theta/r$	$(\kappa-1)\cos 2\theta/r$
$r^2\cos 2\theta$	$-2\cos 2\theta$	$2\sin 2\theta$	$2\cos 2\theta$	$-2r\cos 2\theta$	$2r\sin 2\theta$
$r^2\sin 2\theta$	$-2\sin 2\theta$	$-2\cos 2\theta$	$2\sin 2\theta$	$-2r\sin 2\theta$	$-2r\cos 2\theta$
$r^4\cos 2\theta$	0	$6r^2\sin 2\theta$	$12\, r^2\cos 2\theta$	$(\kappa-3)\, r^3\cos 2\theta$	$(\kappa+3)\, r^3\sin 2\theta$
$r^4\sin 2\theta$	0	$-6r^2\cos 2\theta$	$12\, r^2\sin 2\theta$	$(\kappa-3)\, r^3\sin 2\theta$	$-(\kappa+3)\, r^3\cos 2\theta$
$\cos 2\theta/r^2$	$-6\cos 2\theta/r^4$	$-6\sin 2\theta/r^4$	$6\cos 2\theta/r^4$	$2\cos 2\theta/r^3$	$2\sin 2\theta/r^3$
$\sin 2\theta/r^2$	$-6\sin 2\theta/r^4$	$6\cos 2\theta/r^4$	$6\sin 2\theta/r^4$	$2\sin 2\theta/r^3$	$-2\cos 2\theta/r^3$

Downloaded 04 May 2010 to 171.66.16.28. Redistribution subject to ASME license or copyright; see http://www.asme.org/terms/Terms_Use.cfm

Self-Excited Oscillations of Two Elastic Half-Spaces Sliding With a Constant Coefficient of Friction

G. G. Adams
Professor,
Department of Mechanical Engineering,
Northeastern University,
Boston, MA 02155
Fellow ASME

Two flat isotropic elastic half-spaces, of different material properties, are pressed together and slide against each other with a constant *coefficient of friction. Although a nominally steady-state solution exists, an analysis of the dynamic problem demonstrates that the steady solution can be dynamically unstable. Eigenvalues with positive real parts give rise to self-excited motion which occurs for a wide range of material pairs, coefficients of friction, and sliding velocities (including very low speeds). These self-excited oscillations are generally confined to the region near the interface and can lead either to regions of loss of contact or to areas of stick slip. The mechanism responsible for the instability is essentially one of destabilization of interfacial (slip) waves. It is expected that these vibrations might play an important role in the behavior of sliding members with dry friction.*

Introduction

When two surfaces slide upon each other, their relative motion is resisted by a frictional force. The ratio of the tangential force to the normal force is called the coefficient of kinetic friction. However, the mechanics of contact and friction is actually quite complex. Ibrahim (1994a) reviewed the experimental and theoretical results which relate the dependence of friction upon time of contact, sliding velocity, normal load, and temperature. Nonuniform sliding, in the form of stick-slip motion or tangential oscillations, can be attributed to any of three causes—the difference between the coefficients of static and kinetic friction, a decrease in the coefficient of kinetic friction with increased sliding velocity, or variations in the friction coefficient along the contacting surfaces. Such nonuniform motion is particularly undesirable in machine tool and robotic applications. The review article by Ibrahim (1994b) pertains to the dynamics and modeling of frictional sliding in various industrial applications. Tworzydlo, Becker, and Oden (1994) discuss numerical modeling of friction-induced vibrations and dynamic instabilities. The role of friction in automatic control systems is reviewed by Armstrong-Hélouvry, Dupont, and Canudas de Wit (1994).

Tolstoi (1967) investigated the effect of the normal degree-of-freedom of sliding surfaces. His experiments indicated the existence of natural normal microvibrations which strongly affects the magnitude of the frictional force as well as the stability of sliding. During sliding the nonuniformities in the tangential motion are accompanied by synchronous nonuniformities in the normal motion. Furthermore, both the negative slope of the friction-velocity curve and the friction-induced self-excited oscillations disappear when motion in the normal direction is suppressed. However, damping of the tangential vibrations does not affect the negative slope of the friction-velocity curve. The mechanism responsible for the coupling between normal and tangential motion relies on two effects—the friction force decreases with increased separation of the rough surfaces, and increased sliding velocities lead to greater separations. The experimental work of Soom and Kim (1983a, b) measured the oscillations in the normal and tangential contact forces during sliding. These contact vibrations are induced by surface irregularities which move into the contact region. Although the friction force fluctuations are in phase with the normal force variations, their ratio is greater than the measured kinetic coefficient of friction. It was also conjectured that an important contribution to the effectiveness of a lubricant, in boundary lubrication, is its role in reducing dynamic loading. Soom and Chen (1986) performed a numerical simulation, the results of which were in good agreement with the measurements of Soom and Kim (1983a).

Oden and Martins (1985) and Martins, Oden, and Simões (1990) investigated dynamic friction phenomena and included extensive reviews of previous works. They present a nonlinear contact law based upon the deformation of a rough surface. No distinction is made between static and kinetic friction coefficients; nor is it assumed that the friction coefficient decreases with increasing sliding speed. Variational principles are established and applied in order to develop numerical methods. The sliding of a rigid block is modeled as a three-degree-of-freedom system. Stick-slip motion is shown to occur as a consequence of a dynamic instability involving the coupling between normal and tangential motions. Tworzydlo and Becker (1991) applied a numerical method to the model of Oden and Martins and show that sliding can initiate at a lower value of the friction force than a purely static analysis would indicate. The influence of angular motions was also incorporated into the analysis of rough planar sliding of a block by Hess and Soom (1992), although a detailed stability analysis was beyond the scope of that work. Additional results were obtained by Hess and Soom (1993) for a sliding block in which only angular motion is allowed.

Rayleigh waves can propagate along the free surface of a semi-infinite elastic body. These waves have amplitudes which decay exponentially with distance from the free surface. Waves which are similar in nature to Rayleigh waves can travel along

Contributed by the Applied Mechanics Division of THE AMERICAN SOCIETY OF MECHANICAL ENGINEERS for presentation at the International Mechanical Engineering Congress and Exhibition, the Winter Annual Meeting of the ASME, San Francisco, CA, Nov. 12-17, 1995.

Discussion on this paper should be addressed to the Technical Editor, Professor Lewis T. Wheeler, Department of Mechanical Engineering, University of Houston, Houston, TX 77204-4792, and will be accepted until four months after final publication of the paper itself in the ASME JOURNAL OF APPLIED MECHANICS.

Manuscript received by the ASME Applied Mechanics Division, Jan. 9, 1995; final revision, May 1, 1995. Associate Technical Editor: D. M. Barnett.

Paper No. 95-WA/APM-6.

Copyright © 1995 by ASME

Downloaded 04 May 2010 to 171.66.16.28. Redistribution subject to ASME license or copyright; see http://www.asme.org/terms/Terms_Use.cfm

the interface of two contacting elastic bodies. Such waves were investigated by Stoneley (1924) for bonded contact and are known as Stoneley waves. Stoneley waves exist only if the shear wave speeds of the two materials do not differ greatly. Achenbach and Epstein (1967) and Murty (1975) investigated interface waves in unbonded frictionless contacts in which separation does not occur. These "smooth contact Stoneley waves" (also known as slip waves) differ from those for bonded contact and occur for a wider range of material combinations. Slip waves with interface separation were found by Comninou and Dundurs (1977). Such waves are inherently nonlinear due to the existence of both contact and separation regions whose locations are a priori unknown. Barnett, Gavazza, and Lothe (1988) investigated slip waves in the sliding of anisotropic elastic half-spaces. A second slip wave was discovered; its existence is due strictly to anisotropy. Wang and Lothe (1993) investigated the second slip wave using a different method.

It is the purpose of the present investigation to demonstrate that the steady sliding of two elastic half-spaces is dynamically unstable. This result does not depend upon nonuniformities in the coefficient of sliding friction nor does it rely upon a nonlinear contact law. The instability mechanism is essentially one of slip wave destabilization. The analysis presented is for two perfectly flat isotropic elastic half-spaces sliding with a *constant* coefficient of friction. Steady-state sliding is shown to give rise to a dynamic instability in the form of self-excited motion. These self-excited oscillations are generally confined to a region near the sliding interface and can eventually lead to either partial loss of contact or to regions of stick-slip motion.

Problem Description

Consider two perfectly flat elastic half-spaces sliding with respect to each other (Fig. 1) with velocity $\hat{v}_0$ and coefficient of sliding friction f. The plane-strain equations of motion for a linear isotropic elastic solid are

$$(\lambda + \mu)\hat{u}_{j,jk} + \mu\hat{u}_{k,jj} = \rho\ddot{\hat{u}}_k, \quad (k = 1, 2) \tag{1}$$

where $\hat{u}_k = \hat{u}_k(\hat{x}_1, \hat{x}_2, \hat{t})$ are the components of displacement in the $\hat{x}_k$ directions, $\hat{t}$ is time, μ is the shear modulus, λ is the Lamé's constant, and ρ is the mass density. In (1) the summation convention has been used and

$$\hat{u}_{k,j} \equiv \frac{\partial \hat{u}_k}{\partial \hat{x}_j}, \quad \dot{\hat{u}}_k \equiv \frac{\partial \hat{u}_k}{\partial \hat{t}}.$$

Equation (1) pertains to the lower body whereas the corresponding quantities for the upper body are denoted with a prime ($'$). Now (1) is transformed into a dimensionless coordinate system moving to the right with constant speed $\hat{v}$ ($\hat{v}$ is not necessarily equal to $\hat{v}_0$), which yields

$$(\beta^2 - v^2)u_{1,11} + u_{1,22} + (\beta^2 - 1)u_{2,21} = \ddot{u}_1 - 2v\dot{u}_{1,1}$$
$$\beta^2 u_{2,22} + (1 - v^2)u_{2,11} + (\beta^2 - 1)u_{1,12} = \ddot{u}_2 - 2v\dot{u}_{2,1} \tag{2}$$

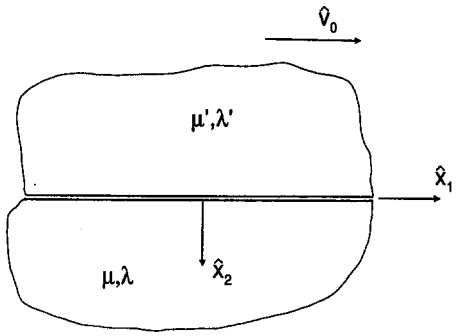


Fig. 1 Two sliding isotropic elastic half-spaces

where

$$x_1 = (\hat{x}_1 - \hat{v}\hat{t})/l, \quad x_2 = \hat{x}_2/l, \quad t = \hat{t}c_2/l$$
$$u_k(x_1, x_2, t) = \hat{u}_k(\hat{x}_1, \hat{x}_2, \hat{t})/l, \quad (k = 1, 2)$$
$$\beta = c_1/c_2 = \sqrt{\frac{2(1-\nu)}{(1-2\nu)}}, \quad c_1 = \sqrt{\frac{\lambda + 2\mu}{\rho}}, \quad c_2 = \sqrt{\frac{\mu}{\rho}}$$
$$v = \hat{v}/c_2, \quad u_{k,j} = \frac{\partial u_k}{\partial x_j}, \quad \dot{u}_k = \frac{\partial u_k}{\partial t}$$

and ν is Poisson's ratio. It is noted that the characteristic length (l) has yet to be chosen. Finally the dimensionless stresses and the stress-displacement laws are defined by

$$\tau_{jk}(x_1, x_2, t) = \hat{\tau}_{jk}(\hat{x}_1, \hat{x}_2, \hat{t})/\mu = u_{k,j} + u_{j,k} + (\beta^2 - 2)(u_{1,1} + u_{2,2})\delta_{jk}, \quad (j, k = 1, 2). \tag{3}$$

The solution of (2) is decomposed into two parts, i.e.,

$$u_k(x_1, x_2, t) = u_k^*(x_1, x_2) + \text{Real}\{\bar{u}_k(x_1, x_2, t)\}$$
$$\bar{u}_k(x_1, x_2, t) = U_k(x_2)e^{2\pi i x_1 + \Lambda t}, \quad (k = 1, 2). \tag{4}$$

The nominally steady-state solution (u_k^*) is for a moving surface load distribution which is invariant in time and space. The corresponding dimensionless stresses are

$$\tau_{12}^* = -fp^*, \quad \tau_{22}^* = -p^*. \tag{5}$$

The second term ($\bar{u}_k$) is the unsteady part, the stability of which will be investigated here. It is noted that Λ and $U_k(x_2)$ appearing in (4) are in general complex and the unsteady solution represents a spatially periodic propagating motion. Furthermore, if the real part of Λ does not vanish, the unsteady solution possesses a time-varying *amplitude* of oscillation. Note that the characteristic length (l) has been taken to be the dimensioned wavelength. The displacements (4) are substituted into (2) and give

$$U_{1,22} + Q_1 U_1 + 2\pi i(\beta^2 - 1)U_{2,2} = 0$$
$$\beta^2 U_{2,22} + Q_2 U_2 + 2\pi i(\beta^2 - 1)U_{1,2} = 0 \tag{6}$$

where

$$Q_1 = 4\pi i v\Lambda - \Lambda^2 - 4\pi^2(\beta^2 - v^2),$$
$$Q_2 = 4\pi i v\Lambda - \Lambda^2 - 4\pi^2(1 - v^2).$$

In arriving at (6) the steady-state solution has been subtracted out.

The solution of (6) is written as

$$U_1(x_2) = Ae^{sx_2}, \quad U_2(x_2) = Be^{sx_2} \tag{7}$$

which, upon substitution into (6), leads to the homogeneous equations

$$(s^2 + Q_1)A + 2\pi i(\beta^2 - 1)sB = 0$$
$$2\pi i(\beta^2 - 1)sA + (\beta^2 s^2 + Q_2)B = 0. \tag{8}$$

Nontrivial solutions of (8) requires the vanishing of the determinant, i.e.,

$$\beta^2 s^4 + [Q_1\beta^2 + Q_2 + 4\pi^2(\beta^2 - 1)^2]s^2 + Q_1 Q_2 = 0 \tag{9}$$

which is the characteristic equation and is quadratic in s^2. The four roots of (9) are denoted by $\pm s_1$, $\pm s_2$. The condition that the stresses vanish at infinity leads to the proper selection of the signs of s_1, s_2, i.e.,

$$\text{Real}\{s_1\} < 0, \quad \text{Real}\{s_2\} < 0 \tag{10}$$

Downloaded 04 May 2010 to 171.66.16.28. Redistribution subject to ASME license or copyright; see http://www.asme.org/terms/Terms_Use.cfm

for the lower half-space. Furthermore, (8) gives

$$B_k = \alpha_k A_k, \quad \alpha_k = -\frac{s_k^2 + Q_1}{2\pi i(\beta^2 - 1)s_k}, \quad (k = 1, 2) \quad (11)$$

and thus

$$U_1(x_2) = A_1 e^{s_1 x_2} + A_2 e^{s_2 x_2},$$
$$U_2(x_2) = \alpha_1 A_1 e^{s_1 x_2} + \alpha_2 A_2 e^{s_2 x_2}. \quad (12)$$

For sliding friction the shear stress is proportional to the normal stress at the boundary of the half-space, i.e.,

$$\bar{\tau}_{12}(x_1, 0, t) = f\bar{\tau}_{22}(x_1, 0, t). \quad (13)$$

From (3), (4), (12), (13),

$$A_2 = \theta A_1,$$
$$\theta = -\frac{s_1 + 2\pi i\alpha_1 - f[2\pi i(\beta^2 - 2) + \beta^2 s_1\alpha_1]}{s_2 + 2\pi i\alpha_2 - f[2\pi i(\beta^2 - 2) + \beta^2 s_2\alpha_2]}. \quad (14)$$

A similar procedure is used for the upper half-space in which $\lambda, \mu, \beta, \rho, v, \Lambda, t, s_k, A_k, B_k, \alpha_k, \theta$ are replaced by $\lambda', \mu', \beta', \rho', v', \Lambda', t', s_k', A_k', B_k', \alpha_k', \theta'$, respectively. Furthermore,

$$v - v'\kappa = v_0, \quad \text{Real}\{s_1'\} > 0, \quad \text{Real}\{s_2'\} > 0,$$
$$\Lambda' = \Lambda/\kappa, \quad \kappa = \frac{c_2'}{c_2}, \quad \Lambda' t' = \Lambda t. \quad (15)$$

It is noted that although u_k' is a function of (x_1, x_2, t'), the solution for u_k' will be expressed as a function of (x_1, x_2, t) by using $(15)_6$.

Finally, the normal displacements and normal stresses on the two half-spaces are continuous across their common boundary, i.e.,

$$\bar{u}_2(x_1, 0, t) = \bar{u}_2'(x_1, 0, t),$$
$$\bar{\tau}_{22}(x_1, 0, t) = (\mu'/\mu)\bar{\tau}_{22}'(x_1, 0, t), \quad (16)$$

which yields

$$(\mu'/\mu)(\alpha_1 + \theta\alpha_2)\{2\pi i[(\beta')^2 - 2] + (\beta')^2(s_1'\alpha_1' + s_2'\alpha_2'\theta') + 2\pi i\theta'[(\beta')^2 - 2]\} - (\alpha_1' + \theta'\alpha_2')[2\pi i(\beta^2 - 2) + \beta^2(s_1\alpha_1 + s_2\alpha_2\theta) + 2\pi i\theta(\beta^2 - 2)] = 0 \quad (17)$$

and

$$A_1' = A_1(\alpha_1 + \alpha_2\theta)/(\alpha_1' + \alpha_2'\theta') \quad (18)$$

For given sliding velocity, coefficient of friction, and material properties, all of the terms in (17) can be determined for a chosen value of Λ. Thus (17) represents one complex nonlinear equation with one complex unknown (Λ) and can be solved by standard methods.

With Λ known, the dimensionless contact pressure (p) and the dimensionless slip velocity (v_S) at the surface can be found according to

$$p = p^* - Ce^{2\pi i x_1 + \Lambda t},$$
$$C = [2\pi i(\beta^2 - 2)(1 + \theta) + \beta^2(s_1\alpha_1 + s_2\alpha_2\theta)]A_1 \quad (19)$$

$$v_S = v_0 + \dot{u}_1'(x_1, 0, t) - \dot{u}_1(x_1, 0, t)$$
$$= v_0 + D'e^{2\pi i x_1 + \Lambda t} - De^{2\pi i x_1 + \Lambda t}$$
$$D' = \Lambda(1 + \dot{\theta}')A_1', \quad D = \Lambda(1 + \theta)A_1. \quad (20)$$

Finally, the solutions obtained as described above are subject to the inequality constraints that the contact pressure and the slip velocity both be non-negative, i.e.,

$$p \geq 0, \quad v_S \geq 0, \quad -\infty < x_1 < \infty. \quad (21)$$

Results and Discussion

Results are obtained using the method described in the previous section. An initial guess is used for Λ based upon the result for zero friction and zero velocity. A solution of (17) is obtained by iteration using complex root-finder software (IMSL, 1989). Then either the friction coefficient or velocity is increased and the result from the previous solution is used as an initial guess. In all of the calculations, the value $v = 0$ is used along with $v' = -v_0/\kappa$, which means that the solution obtained is in a reference frame fixed to the lower body. Also, the Poisson's ratios of the two materials were chosen as $\nu = \nu' = 0.25$. Furthermore, without loss of generality, the upper body is taken to have a shear wave speed less than or equal to that of the lower body, i.e., $c_2' \leq c_2$. The damping ratio ζ is defined by

$$\zeta = -\Lambda^R/|\Lambda^I|, \quad \Lambda^R = \text{Real}\{\Lambda\}, \quad \Lambda^I = \text{Imag}\{\Lambda\} \quad (22)$$

in analogy to a *lightly* damped one-degree-of-freedom system. Thus positive damping ($\zeta > 0$) corresponds to stable motion ($\Lambda^R < 0$), whereas negative damping ($\zeta < 0$) represents unstable (self-excited) motion ($\Lambda^R > 0$). Results, for various material pairs, are shown for the negative of the damping ratio ($-\zeta$) versus friction coefficient (f) in Figs. 2-3, and versus the dimensionless sliding speed (v_0) in Fig. 4. Only results for negative values of damping (unstable motion) are given. In Figs. 2-3 the sliding velocity is very small compared to the shear wave speed and thus $v_0 = 0$ in the equations leading to (17). However, v_0 is not neglected in determining the slip velocity through (20).

First consider the case in which *identical* materials slide at very low velocities ($v_0 \approx 0$). This configuration allows for two Rayleigh waves of equal amplitude and equal wavelength but with 180 deg phase difference to propagate in the same direction without interaction. Thus $\zeta = 0$ for all values of the friction coefficient. For very low sliding velocities and *different* material pairs, the results for $f = 0$ give Stoneley waves for smooth contact (Achenbach and Epstein, 1967). The results in Fig. 2 are all for cases in which the material mismatch is small enough that such slip waves exist. As f is increased from zero, the value of $-\zeta$ is also seen to increase from zero. The same trend is true for the material pairs shown in Fig. 3 which correspond to larger mismatches in materials. For these cases smooth contact Stoneley waves do not exist for $f = 0$, but analogous waves appear at finite values of the friction coefficient. For all of the cases in which $v_0 \approx 0$, if a given value of Λ is a solution then $-\Lambda$ is also a solution. Since the imaginary parts of these two

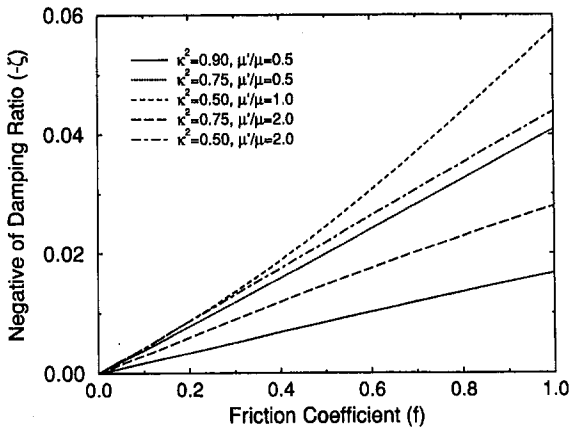


Fig. 2 Negative of damping ratio ($-\zeta$) versus friction coefficient (f) for slow sliding speeds ($v_0 \approx 0$) and for various material combinations

Downloaded 04 May 2010 to 171.66.16.28. Redistribution subject to ASME license or copyright; see http://www.asme.org/terms/Terms_Use.cfm

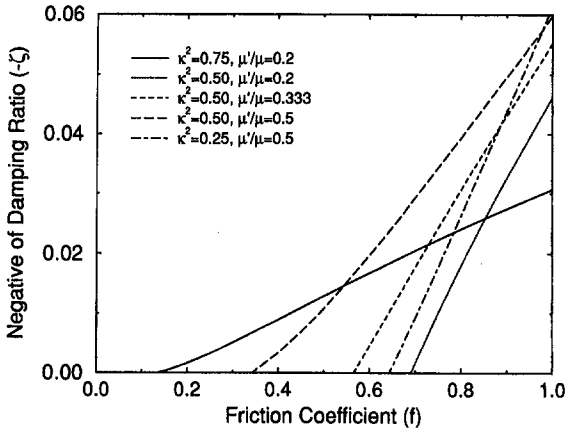


Fig. 3 Negative of damping ratio ($-\zeta$) versus friction coefficient (f) for slow sliding speeds ($v_0 \approx 0$) and for various material combinations

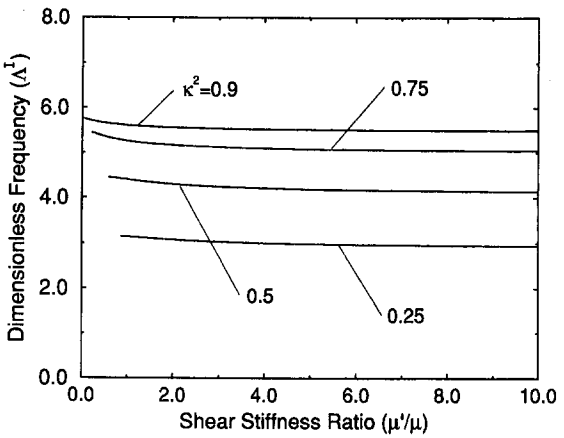


Fig. 5 Dimensionless frequency (Λ^I) versus shear stiffness ratio (μ'/μ) for $f = 0$, $v_0 = 0$, and for various shear wave-speed ratios (κ)

solutions have opposite signs, the "$-\Lambda$" solution moves in the opposite direction as the "Λ" solution. Also these motions have the reverse stability properties since their real parts are of different signs. It is noted that the solutions in Figs. 2-4 are all for negative values of Λ^I which correspond to waves traveling to the right. Thus only waves travelling in the same direction as sliding are destabilized. In Fig. 4 is shown $-\zeta$ versus dimensionless sliding speed (v_0) for $f = 0.2$, and for various material combinations. Note that the value of negative damping decreases with increasing speed and eventually reaches zero. From Fig. 2 and Fig. 4 the material pairs with the lower κ are more susceptible to dynamic instabilities than are the higher κ cases. Although that trend is not apparent in Fig. 3, it does hold after the curves cross at high values of the friction coefficient.

The question remains as to what the physical mechanism is which is responsible for the self-excited motion described above. The energy dissipated (due to friction) per unit surface area over one period of oscillation is given by

$$\mathcal{E} = \int_0^{2\pi/|\Lambda^I|} f \,\text{Real}\,\{p\}\,\text{Real}\,\{v_S\}\,dt. \qquad (23)$$

Now consider the difference between the phase of the variable parts of v_S and of p ((19)-(20)). The results showed that for small friction this phase difference is approximately 0 deg and 180 deg for left and right-traveling waves, respectively. Thus for small friction, $\mathcal{E}$ will be somewhat less than $\mu p^* v_0$ for a right-traveling wave and hence the energy dissipated at the interface will be less than the work done in moving the bodies. This extra energy is the contributor to the self-excited motion which continues to grow with time. For a left-traveling wave $\mathcal{E} > \mu p^* v_0$, and the energy dissipated at the interface will be greater than the work done in moving the bodies, forcing the left-traveling wave to decay. For larger values of friction the same general trends are true. Clearly for zero friction, $\mathcal{E}$ vanishes.

Although not shown, the imaginary parts of the eigenvalues do not change by more than three percent along any curve in Figs. 2-3. In Fig. 5 is shown Λ^I versus μ'/μ for various values of κ^2 and for $v_0 = 0$ and $f = 0$. For fixed values of κ^2 there is little change in frequency with stiffness ratio. However, the frequency does vary significantly with the shear wave speed ratio. It is noted that the nature of these waves is such that motion is usually confined to the region near the interface. An exception occurs for a value of friction close to that for which a curve in Fig. 3 first has an eigenvalue with a positive real part. In those cases the decay of the "interfacial" wave with depth becomes vanishingly small. Such cases also occur in Fig. 5 in the region where a curve starts at a finite value of the stiffness ratio (μ'/μ). Note that the appropriate characteristic length is the dimensioned wavelength l. Furthermore, the dimensionless propagation velocity is equal to $|\Lambda^I|/2\pi$ and can thus be found from Fig. 5 for $v_0 = 0$. As the sliding speed ($\hat{v}_0$) increases, a speed is reached at which $\hat{v}_0$ is equal to the difference in the Rayleigh wave speeds of the two half-spaces. At this point ($\zeta = 0$, in Fig. 4) Rayleigh waves of equal magnitude

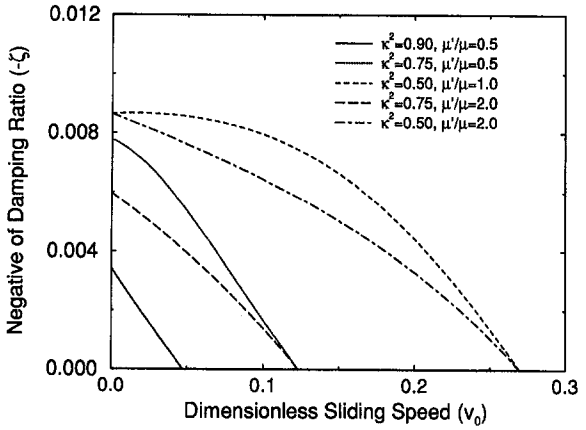


Fig. 4 Negative of damping ratio ($-\zeta$) versus dimensionless sliding speed (v_0) for $f = 0.2$ and for various material combinations

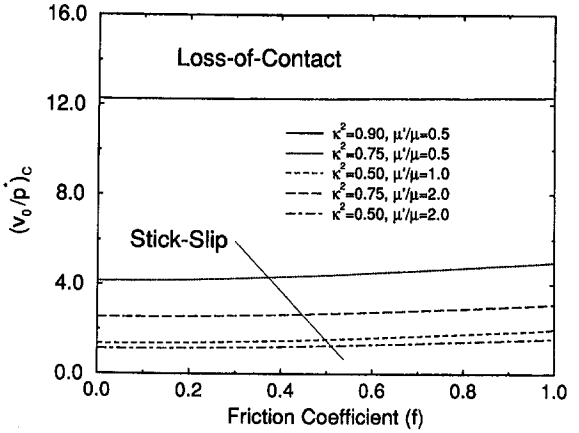


Fig. 6 Critical value of the ratio of the dimensionless sliding speed to the dimensionless average contact pressure $(v_0/p^*)_c$ versus friction coefficient (f) for slow sliding speeds ($v_0 \approx 0$) and for various material combinations

Downloaded 04 May 2010 to 171.66.16.28. Redistribution subject to ASME license or copyright; see http://www.asme.org/terms/Terms_Use.cfm

and equal wavelength but with a 180 deg phase difference can propagate in the same direction without interaction. Thus as v_0 increases from 0 to the value corresponding to $\zeta = 0$, the propagation velocity changes from the value obtained from Fig. 5 to the Rayleigh wave speed. Note from Fig. 4 that any pair of curves with the same value of κ cross the $\zeta = 0$ axis at the same point.

For cases in which the dynamic instability exists, the amplitude of the motion continues to increase until either of the inequalities (21) cease to hold. Regions of loss of contact initiate when the contact pressure becomes zero, whereas areas of stick-slip commence when the slip velocity vanishes. From (19)-(21) the critical value of v_0/p^* is defined as

$$\left(\frac{v_0}{p^*}\right)_c = \frac{|D - D'|}{|C|} \tag{24}$$

and

$$\left(\frac{v_0}{p^*}\right) > \left(\frac{v_0}{p^*}\right)_c \Rightarrow \text{loss of contact occurs first}$$

$$\left(\frac{v_0}{p^*}\right) < \left(\frac{v_0}{p^*}\right)_c \Rightarrow \text{stick slip occurs first.} \tag{25}$$

Results are shown in Figs. 6-8 for the critical value of (v_0/p^*) for the same three cases used in Figs. 2-4, respectively. If the actual value of (v_0/p^*) is greater than the critical value the instability leads to loss-of-contact, whereas if the value of (v_0/p^*) is less than the critical value the result will be stick-slip. It is emphasized that the analysis presented here pertains only until the *onset* of either stick-slip or loss-of-contact. The results in Figs. 6-8 all indicate that the greater the mismatch in shear wave speed, the more prone the material pair is to loss of contact rather than to stick-slip.

Conclusions

The dry frictional sliding of two flat isotropic half-spaces with a constant coefficient of friction has been investigated. Several conclusions can be made based strictly on the model presented here. Self-excited oscillations exist for a wide range of material combinations, friction coefficients, and sliding speeds (including very low speeds). The magnitude of these dynamic instabilities tends to increase with the extent of mismatch in the shear wave speeds of the two materials. These self-excited vibrations are usually restricted to the region close to the sliding interface. Their existence is due to destabilization of interface waves which travel in the same direction as sliding. These dynamic instabilities can eventually give rise either to partial separation or to regions of stick-slip. The greater the mismatch in shear wave speeds, the less likely is stick-slip as opposed to loss-of-contact. Furthermore, for a given material pair, high contact pressure and slow sliding speeds make stick-slip more apt to occur.

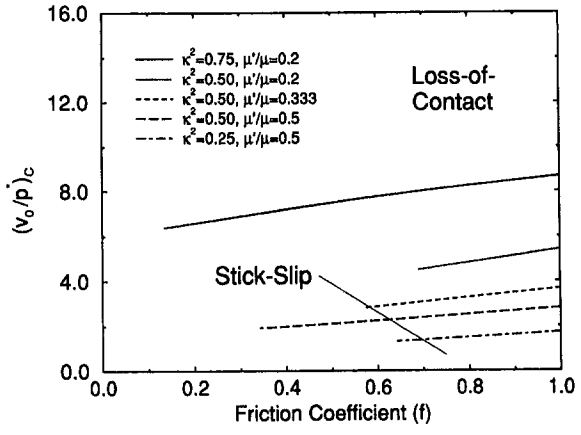


Fig. 7 Critical value of the ratio of the dimensionless sliding speed to the dimensionless average contact pressure $(v_0/p^*)_c$ versus friction coefficient (f) for slow sliding speeds ($v_0 \approx 0$) and for various material combinations

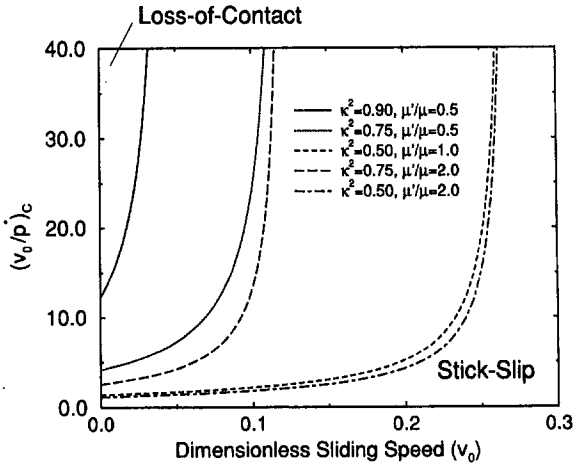


Fig. 8 Critical value of the ratio of the dimensionless sliding speed to the dimensionless average contact pressure $(v_0/p^*)_c$ versus dimensionless sliding speed (v_0) for f = 0.2 and for various material combinations

It is emphasized that the model presented in this work is greatly idealized. Many effects have been omitted which, no doubt, play an important role in dry sliding. These effects include those of surface layers, surface roughness, plastic deformation, determination of the friction force from the real contact area, loss-of-contact and impact damping, stick-slip motion, and thermal expansion. Nonetheless it is hoped that the results obtained in this investigation will help to shed some light on the process of dry frictional sliding.

References

Achenbach, J. D., and Epstein, H. I., 1967, "Dynamic Interaction of a Layer and a Half-Space," *ASCE Journal of the Engineering Mechanics Division,* Vol. EM5, pp. 27–42.

Armstrong-Hélouvry, B., Dupont, P., and Canudas de Wit, C., 1994, "Friction in Servo Machines: Analysis and Control Methods," ASME *Applied Mechanics Reviews,* Vol. 47, pp. 275–305.

Barnett, D. M., Gavazza, S. D., and Lothe, J., 1988, "Slip Waves Along the Interface Between Two Anisotropic Elastic Half-Spaces in Sliding Contact," *Proceedings of the Royal Society of London,* Vol. A415, pp. 389–419.

Comninou, M., and Dundurs, J., 1977, "Elastic Interface Waves Involving Separation," ASME JOURNAL OF APPLIED MECHANICS, Vol. 44, pp. 222–226.

Hess, D. P., and Soom, A., 1992, "Normal and Angular Motions at Rough Planar Contacts During Sliding With Friction," ASME *Journal of Tribology,* Vol. 114, pp. 567–578.

Hess, D. P., and Soom, A., 1993, "The Effects of Relative Angular Motions on Friction at Rough Planar Contacts," ASME *Journal of Tribology,* Vol. 115, pp. 96–101.

Ibrahim, R. A., 1994a, "Friction-Induced Vibration, Chatter, Squeal, and Chaos, Part I: Mechanics of Contact and Friction," ASME *Applied Mechanics Reviews,* Vol. 47, pp. 209–226.

Ibrahim, R. A., 1994b, "Friction-Induced Vibration, Chatter, Squeal, and Chaos, Part II: Dynamics and Modeling," ASME *Applied Mechanics Reviews,* Vol. 47, pp. 227–253.

IMSL, 1989, *IMSL Math/Library,* (subroutine DZANLY), IMSL, Houston, TX.

Martins, J. A. C., Oden, J. T., and Simões, F. M. F., 1990, "A Study of Static and Kinetic Friction," *International Journal of Engineering Science,* Vol. 28, pp. 29–92.

Murty, G. S., 1975, "Wave Propagation at an Unbonded Interface Between Two Elastic Half-Spaces," *Journal of the Acoustical Society of America,* Vol. 58, pp. 1094–1095.

Oden, J. T., and Martins, J. A. C., 1985, "Models and Computational Methods for Dynamic Friction Phenomena," *Computer Methods in Applied Mechanics and Engineering,* Vol. 52, pp. 527–634.

Soom, A., and Kim, C., 1983a, "Interactions Between Dynamic Normal and

Downloaded 04 May 2010 to 171.66.16.28. Redistribution subject to ASME license or copyright; see http://www.asme.org/terms/Terms_Use.cfm

Frictional Forces During Unlubricated Sliding," ASME *Journal of Lubrication Technology,* Vol. 105, pp. 221–229.

Soom, A., and Kim, C., 1983b, "Roughness-Induced Dynamic Loading at Dry and Boundary-Lubricated Sliding Contacts," ASME *Journal of Lubrication Technology,* Vol. 105, pp. 514–517.

Soom, A., and Chen, J. W., 1986, "Simulation of Random Surface Roughness-Induced Contact Vibrations at Hertzian Contacts During Steady Sliding," ASME *Journal of Tribology,* Vol. 108, pp. 123–127.

Stoneley, R., 1924, "Elastic Waves at the Surface of Separation of Two Solids," *Proceedings of the Royal Society of London,* Vol. A106, pp. 416–428.

Tolstoi, D. M., 1967, "Significance of the Normal Degree of Freedom and Natural Normal Vibrations in Contact Friction," *Wear,* Vol. 10, pp. 199–213.

Tworzydlo, W. W., and Becker, E., 1991, "Influence of Forced Vibrations on the Static Coefficient of Friction—Numerical Modeling," *Wear,* Vol. 143, pp. 175–196.

Tworzydlo, W. W., Becker, E. B., and Oden, J. T., 1994, "Numerical Modeling of Friction-Induced Vibrations and Dynamic Instabilities," ASME *Applied Mechanics Reviews,* Vol. 47, pp. 255–274.

Wang, L., and Lothe, J., 1993, "Existence of Second Slip Waves in Anisotropic Elastic Media," *Wave Motion,* Vol. 18, pp. 79–99.

Downloaded 04 May 2010 to 171.66.16.28. Redistribution subject to ASME license or copyright; see http://www.asme.org/terms/Terms_Use.cfm

Propagation of Boundary Disturbances in an Axially Moving Strip in Contact With Rigid and Flexible Constraints[1]

W. D. Zhu
Research Assistant.
Assoc. Mem. ASME,

C. D. Mote, Jr.
FANUC Chair in Mechanical Systems and Vice Chancellor,
Fellow ASME.

Department of Mechanical Engineering,
University of California at Berkeley,
Berkeley, CA 94720

The exact expression describing the contact force between an axially moving flexible strip and a one-sided constraint is derived using the Green's function formulation. Discontinuity of the initial velocity at a boundary of the strip due to a disturbance, causes discontinuity in the contact force history at any constraint that is not modeled by a single spring element. The discontinuities in the contact force occur at the instants when those propagating wavefronts in the strip with nonvanishing slope interact with the constraint. A model of a magnetic tape-recording head system is analyzed. Tape-head contact loss is predicted, depending on the amplitude and frequency of a disturbance, the head location, and the preload of the tape against the head.

1 Introduction

The axially moving strip models high-speed magnetic tapes, bandsaws, belt drives, and paper sheets during processing. The model is often subject to a stationary, one-sided constraint, such as a read/write head in magnetic tape drives or a guide bearing in bandsaws. The natural frequencies and modes of vibration of a traveling string, guided by an elastically supported eyelet, are calculated approximately by Schajer (1984), and exactly by Perkins and Mote (1986) and Perkins (1990). The eigenvalue inclusion principle for an axially moving string, under several pointwise, nondissipative constraints is presented by Yang (1992) through a transfer function formulation.

The steady forced response of a constrained axially moving strip subjected to a harmonic end excitation can easily be determined (Sack, 1954; Perkins, 1990). The transient response to arbitrary boundary disturbances, external forces and initial conditions is an unsolved, but important problem. For example, in design of magnetic tape drives, prediction of operating conditions ensuring tape and head contact for all "reasonable" disturbances is a transient problem. In control of axially moving strip vibration, a control action at one point affects response at times dependent on the different, and finite, propagation speeds upstream and downstream of the point of control.

In this work, the transient response of an axially moving strip under a one-sided, rigid or flexible, constraint to arbitrary external forces and boundary disturbances is investigated. The strip is modeled as an axially moving string, and the constraint is either a rigid, pointwise stop or a spring-mass-dashpot. The contact force between the string and the constraint is composed of a static preload component existing at equilibrium and a dynamic component. The equation governing the dynamic contact force component is derived using the Green's function for a fixed-fixed, traveling string. It is found that for a disturbance causing discontinuous initial velocity at one boundary of the string, the dynamic contact force at the constraint is discontinuous for all modeled constraints other than a single spring element. A physical interpretation of the discontinuity is provided in the Appendix. These discontinuities occur at the instants when propagating wavefronts with nonvanishing slope contact the constraint. Numerical results for the contact force history and the disturbance propagation are presented for a model representing a magnetic tape-recording head system.

2 Equations of Motion

An axially moving string of mass per unit length ρ, traveling at a subcritical speed V between supports separated by L, is shown schematically in Figs. 1(a, b). At $V = 0$, the special case for a stationary string results. A discrete constraint, contacting the string at a distance D ($0 < D < L$) from the left end, is rigid in Fig. 1(a) and flexible in Fig. 1(b) with mass M, stiffness K, and damping constant C. The contact force is $R(T)$. The string is subjected to gravitational force ρg, distributed external force $F(X, T)$ and boundary disturbance $E(T)$ at the left, upstream, end. By replacing V by $-V$, the following analysis applies to a boundary disturbance at the downstream end. The transverse displacements of the string and the mass M, relative to the horizontal X-axis, are $U(X, T)$ and $Z(T)$, respectively. The displacement of the point of contact between the string and the rigid constraint, $U(D, T)$, is specified by H.

Application of the model is limited by the following conditions. The string transverse displacement $U(X, T)$ is small and planar. The contact between the string and the constraint is frictionless. The initial tension P in the string is sufficiently large that changes in tension under the transverse displacement $U(X, T)$ are negligible.

Introduce the following dimensionless variables:

$$x = X/L \quad u = U/L \quad z = Z/L \quad e = E/L \quad d = D/L$$

$$h = H/L \quad t = T(P/\rho L^2)^{1/2} \quad m = M/\rho L \quad k = KL/P$$

$$c = C/(P\rho)^{1/2} \quad v = V(\rho/P)^{1/2} \quad w = \rho gL/P$$

$$f = FL/P \quad r = R/P. \tag{1}$$

The equation governing transverse motion of the traveling string is

[1] The authors would like to thank the National Science Foundation and the authors' industrial sponsors for their support and interest in this work.

Contributed by the Applied Mechanics Division of THE AMERICAN SOCIETY OF MECHANICAL ENGINEERS for publication in the ASME JOURNAL OF APPLIED MECHANICS.

Discussion on this paper should be addressed to the Technical Editor, Professor Lewis T. Wheeler, Department of Mechanical Engineering, University of Houston, Houston, TX 77204-4792, and will be accepted until four months after final publication of the paper itself in the ASME JOURNAL OF APPLIED MECHANICS.

Manuscript received by the ASME Applied Mechanics Division, Nov. 19, 1993; final revision, June 6, 1994. Associate Technical Editor: J. N. Reddy.

Copyright © 1995 by ASME

Downloaded 04 May 2010 to 171.66.16.28. Redistribution subject to ASME license or copyright; see http://www.asme.org/terms/Terms_Use.cfm

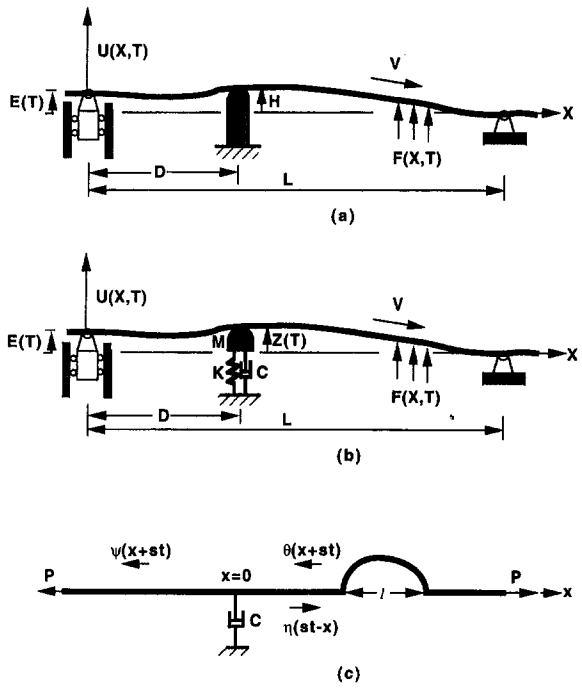


Fig. 1 Schematic of a constrained translating string under distributed force $F(X, T)$ and boundary disturbance $E(T)$ at $x = 0$: (a) rigid constraint, (b) flexible constraint. (c) is the schematic of a propagating pulse in an infinite, stationary string with an attached damper at the origin.

$$u_{tt}(x, t) + 2vu_{xt}(x, t) + (v^2 - 1)u_{xx}(x, t) = r(t)\delta(x - d) + f(x, t) - w \quad (2)$$

with the boundary and initial conditions given by

$$u(0, t) = e(t) \quad u(1, t) = 0, \quad 0 \le t \le t_f \quad (3)$$

$$u(x, 0) = a(x) \quad u_t(x, 0) = 0, \quad 0 < x < 1 \quad (4)$$

where $a(x)$ is the initial displacement of the string and t_f is an arbitrarily specified final time ($0 < t_f < \infty$). Continuity of the initial displacement of the string at the left end $x = 0$, i.e., $e(0) = a(0^+)$, limits the analysis to continuous displacement $u(x, t)$. The initial velocity of the string at $x = 0$, however, may be discontinuous, i.e., $\dot{e}(0) \neq 0$, the consequence of which is shown in the sequel. The equation of motion and initial conditions for the flexible constraint in contact with the string are

$$-r(t) + k[z_0 + z^* - z(t)] - c\dot{z}(t) - mw = m\ddot{z}(t) \quad (5)$$

$$z(0) = a(d) \quad \dot{z}(0) = 0 \quad (6)$$

where z^* is the equilibrium displacement of the constraint mass m to be determined, and z_0 is the compression of the linear spring k at equilibrium. The contact conditions are

$$u(d, t) = h \quad \text{for a rigid constraint;}$$

$$u(d, t) = z(t) \quad \text{for a flexible constraint.} \quad (7)$$

At equilibrium, the string displacement $u^*(x)$ and the static preload r^* are derived from the static counterparts of (2), (3), (5), and (7):

$$(v^2 - 1)u^*_{xx}(x) = r^*\delta(x - d) + f^*(x) - w \quad (8)$$

$$u^*(0) = e(0) \quad u^*(1) = 0 \quad (9)$$

where

$$r^* = kz_0 - mw \quad z^* = u^*(d) \quad \text{for a flexible constraint;}$$

$$u^*(d) = h \quad \text{for a rigid constraint,} \quad (10)$$

and $f^*(x)$ is the static part of $f(x, t)$. The equilibrium solution for $f^*(x) = 0$ and $e(0) = 0$ is

$$u^*(x) = \begin{cases} wx^2/2(1 - v^2) + Ax, & 0 < x < d \\ w(1 - x)^2/2(1 - v^2) + B(1 - x), & d < x < 1 \end{cases} \quad (11)$$

where $A = h/d - wd/2(1 - v^2)$, $B = h/(1 - d) - w(1 - d)/2(1 - v^2)$ for the rigid constraint and $A = -w/2(1 - v^2) + (1 - d)(kz_0 - mw)/(1 - v^2)$, $B = d(kz_0 - mw - w/2d)/(1 - v^2)$ for the flexible constraint. In addition, $r^* = w/2 + (1 - v^2)h/d(1 - d)$ for the rigid constraint; r^* is given in (10) and $z^* = d(1 - d)(kz_0 - mw - w/2)/(1 - v^2)$ for the flexible constraint.

Substitution of $u(x, t) = u^*(x) + \tilde{u}(x, t)$, $z(t) = z^* + \tilde{z}(t)$, $r(t) = r^* + \tilde{r}(t)$, and $f(x, t) = f^*(x) + \tilde{f}(x, t)$ into (2)–(6), and use of (8)–(9), yield the equations describing small amplitude motion of the string and the flexible constraint around the system equilibrium

$$\tilde{u}_{tt}(x, t) + 2v\tilde{u}_{xt}(x, t) + (v^2 - 1)\tilde{u}_{xx}(x, t) = \tilde{r}(t)\delta(x - d) + \tilde{f}(x, t) \quad (12)$$

$$\tilde{u}(0, t) = e(t) - e(0) \quad \tilde{u}(1, t) = 0, \quad 0 \le t \le t_f \quad (13)$$

$$\tilde{u}(x, 0) = a(x) - u^*(x) \quad \tilde{u}_t(x, 0) = 0, \quad 0 < x < 1 \quad (14)$$

$$\tilde{r}(t) = -k\tilde{z}(t) - c\dot{\tilde{z}}(t) - m\ddot{\tilde{z}}(t) \quad (15)$$

$$\tilde{z}(0) = a(d) - u^*(d) \quad \dot{\tilde{z}}(0) = 0. \quad (16)$$

The equation of motion for a flexible massless constraint around the equilibrium is given by (15) when $m = 0$. The contact conditions (7) become

$$\tilde{u}(d, t) = 0 \quad \text{for a rigid constraint;}$$

$$\tilde{u}(d, t) = \tilde{z}(t) \quad \text{for a flexible constraint} \quad (17)$$

3 Method of Analysis

The transient wave propagation problem in (12)–(17) is studied, without loss of generality, for a string initially at rest in its equilibrium configuration: i.e., $a(x) = u^*(x)$. Equations (12)–(14) are solved by first applying the transformation $\tilde{u}(x, t) = \hat{u}(x, t) + (1 - x)[e(t) - e(0)]$ to render the boundary condition (13) homogeneous for the new variable $\hat{u}(x, t)$. $\hat{u}(x, t)$ is then determined from the transformed equations of (12)–(14) in terms of the Green's function for a fixed-fixed traveling string (Wickert and Mote, 1990). The final expression for $\tilde{u}(x, t)$ is

$$\tilde{u}(x, t) = (1 - x)[e(t) - e(0)] + \int_0^t \int_0^1 [\tilde{f}(\xi, \tau) - (1 - \xi)\ddot{e}(\tau) + 2v\dot{e}(\tau)] \times g(x, \xi; t - \tau)d\xi d\tau + \int_0^t \tilde{r}(\tau)g(x, d; t - \tau) \times d\tau - \dot{e}(0)\int_0^1 (1 - \xi)g(x, \xi; t)d\xi \quad (18)$$

where the Green's function is piecewise continuous and given by (Wickert and Mote, 1991)

$$g(x, \xi; t - \tau) = \sum_{n=1}^{\infty} \frac{2}{n\pi} \sin [n\pi(1 - v^2)(t - \tau) + n\pi v(x - \xi)] \sin n\pi x \sin n\pi\xi \quad (19a)$$

Downloaded 04 May 2010 to 171.66.16.28. Redistribution subject to ASME license or copyright; see http://www.asme.org/terms/Terms_Use.cfm

$$= \phi[(1-v^2)(t-\tau) - (1-v)(x-\xi)] + \phi[(1-v^2)(t-\tau) + (1+v)(x-\xi)] - \phi[(1-v^2)(t-\tau) - (1-v)x - (1+v)\xi] - \phi[(1-v^2)(t-\tau) + (1+v)x + (1-v)\xi] \quad (19b)$$

$$\phi(s) = \sum_{n=-\infty}^{\infty} [H(s-2n) - H(s-2(n+1))](2n+1-s)/4 \quad (19c)$$

and $g(x, \xi; 0) = 0$, $g_t(x, \xi; 0) = \delta(x-\xi)$. The time derivative of g is represented by an infinite series of delta functions (Zhu and Mote, 1994)

$$g_t(x, \xi; t-\tau) = \frac{1-v^2}{2} \times \sum_{n=-\infty}^{\infty} \{\delta[(1-v^2)(t-\tau) - (1-v)(x-\xi) - 2n] + \delta[(1-v^2)(t-\tau) + (1+v)(x-\xi) - 2n] - \delta[(1-v^2)(t-\tau) - (1-v)x - (1+v)\xi - 2n] - \delta[(1-v^2)(t-\tau) + (1+v)x + (1-v)\xi - 2n]\}. \quad (20)$$

The solution to (15) and (16) for $m \neq 0$ and $0 \leq \zeta < 1$, is

$$\tilde{z}(t) = -\frac{1}{m\omega\sqrt{1-\zeta^2}} \times \int_0^t e^{-\zeta\omega(t-\tau)} \sin[\omega\sqrt{1-\zeta^2}(t-\tau)]\tilde{r}(\tau)d\tau \quad (21)$$

where $\omega = \sqrt{k/m}$ and $\zeta = c/2\sqrt{km}$. $\tilde{z}(t)$ for the critically damped ($\zeta = 1$) and overdamped ($\zeta > 1$) models can be obtained. These expressions and (18) are substituted into the contact condition for a flexible constraint in (17) to yield a Volterra integral equation of the first kind describing the dynamic contact force $\tilde{r}(t)$ between the string and a flexible constraint with nonvanishing mass m

$$\int_0^t [g(d, d; t-\tau) + \kappa_1(t, \tau)]\tilde{r}(\tau)d\tau = -p_1(t) \quad (22)$$

where

$$\kappa_1(t, \tau) = \begin{cases} \dfrac{1}{m\omega\sqrt{1-\zeta^2}} e^{-\zeta\omega(t-\tau)} \times \sin[\omega\sqrt{1-\zeta^2}(t-\tau)], & 0 \leq \zeta < 1 \\ \dfrac{1}{m} e^{-\omega(t-\tau)}(t-\tau), & \zeta = 1 \\ \dfrac{1}{m\omega\sqrt{\zeta^2-1}} e^{-\zeta\omega(t-\tau)} \times \sinh[\omega\sqrt{\zeta^2-1}(t-\tau)], & \zeta > 1 \end{cases} \quad (23)$$

$$p_1(t) = (1-d)[e(t) - e(0)] + \int_0^t \int_0^1 [\tilde{f}(\xi, \tau) - (1-\xi)\ddot{e}(\tau) + 2v\dot{e}(\tau)] \times g(d, \xi; t-\tau)d\xi d\tau - \dot{e}(0) \times \int_0^1 (1-\xi)g(d, \xi; t)d\xi. \quad (24)$$

The discontinuous $g(d, d; t-\tau)$ in the kernel of (22) can produce noise in its numerical solution. Because $p_1(t)$ is continuous, (22) can be differentiated distributionally to eliminate the discontinuity in the kernel. Integration by use of (20) gives

$$\int_0^t g_t(d, d; t-\tau)\tilde{r}(\tau)d\tau = \frac{1}{2}\tilde{r}(t) + \sum_{j=1}^{N} \tilde{r}\left(t - \frac{2j}{1-v^2}\right)H\left(t - \frac{2j}{1-v^2}\right) - \frac{1}{2}\sum_{j=1}^{N+1} \tilde{r}\left(t - \frac{2d}{1-v^2} - \frac{2(j-1)}{1-v^2}\right) \times H\left(t - \frac{2d}{1-v^2} - \frac{2(j-1)}{1-v^2}\right) - \frac{1}{2}\sum_{j=1}^{N+1} \tilde{r}\left(t + \frac{2d}{1-v^2} - \frac{2j}{1-v^2}\right) \times H\left(t + \frac{2d}{1-v^2} - \frac{2j}{1-v^2}\right) \equiv \mathbf{D}[\tilde{r}] \quad (25)$$

where $N = \text{Int}[(1-v^2)t_f/2]$ and $\mathbf{D}$ is defined as the *delay operator*. Distributional differentiation of (22) using (25) and $g(d, d; 0) = 0$ yields the delay-integral equation

$$\int_0^t \kappa(t, \tau)\tilde{r}(\tau)d\tau + \mathbf{D}[\tilde{r}] = -p(t) \quad (26)$$

where $\kappa(t, \tau) = d\kappa_1(t, \tau)/dt$ and

$$p(t) = dp_1/dt = (1-d)\dot{e}(t) + \int_0^t \int_0^1 [\tilde{f}(\xi, \tau) - (1-\xi)\ddot{e}(\tau) + 2v\dot{e}(\tau)] \times g_t(d, \xi; t-\tau)d\xi d\tau - \dot{e}(0)I_1(t) \quad (27)$$

where $I_1(t) = \int_0^1 (1-\xi)g_t(d, \xi; t)d\xi$ is shown to be discontinuous in the sequel. The double integral in (27), denoted by $I_2(t)$, is continuous, if $\tilde{f}(x, t)$ is piecewise continuous and $e(t)$ is continuously differentiable. Hence $p(t)$ is discontinuous only when $\dot{e}(0) \neq 0$. By (25) and (26), discontinuity of $p(t)$ and nonvanishing initial value $\tilde{r}(0)$ can cause discontinuity in $\tilde{r}(t)$. Here, the initial value is $\tilde{r}(0) = -2p(0) = 0$ by (26) and (27), as $I_1(0) = 1 - d$ recalling $g_t(d, \xi; 0) = \delta(\xi - d)$. Consequently, $\tilde{r}(t)$ is discontinuous if and only if $\dot{e}(0) \neq 0$, as the discontinuities of the Heaviside functions in $\mathbf{D}[\tilde{r}]$ vanish because $\tilde{r}(0) = 0$.

The Volterra integral equation of the first kind, governing the dynamic contact force $\tilde{r}(t)$ between the string and a rigid constraint, is derived from (17) and (18):

$$\int_0^t g(d, d; t-\tau)\tilde{r}(\tau)d\tau = -p_1(t) \quad (28)$$

where $p_1(t)$ is given by (24). Distributional differentiation of (28), using (25), yields the delay equation describing $\tilde{r}(t)$

$$\mathbf{D}[\tilde{r}] = -p(t) \quad (29)$$

where $p(t)$ is given by (27).

For a flexible, massless constraint, (17) and (18) are substituted into (15) with vanishing m to derive a Volterra integral equation of the second kind governing $\tilde{r}(t)$:

$$\int_0^t [kg(d, d; t-\tau) + cg_t(d, d; t-\tau)]\tilde{r}(\tau)d\tau + \tilde{r}(t) + p_2(t) = 0 \quad (30)$$

Downloaded 04 May 2010 to 171.66.16.28. Redistribution subject to ASME license or copyright; see http://www.asme.org/terms/Terms_Use.cfm

where

$$p_2(t) = \int_0^t \int_0^1 [\tilde{f}(\xi, \tau) - (1 - \xi)\ddot{e}(\tau) + 2v\dot{e}(\tau)] \times (k + c\partial/\partial t)g(d, \xi; t - \tau)d\xi d\tau - k\dot{e}(0) \int_0^1 (1 - \xi)g(d, \xi; t)d\xi - c\dot{e}(0)I_1(t) + (1 - d)[k(e(t) - e(0)) + c\dot{e}(t)]. \quad (31)$$

Use of (25) reduces (30) to the delay-integral equation

$$\int_0^t kg(d, d; t - \tau)\tilde{r}(\tau)d\tau + c\mathbf{D}[\tilde{r}] + \tilde{r}(t) + p_2(t) = 0 \quad (32)$$

with the initial value $\tilde{r}(0) = 0$ by (32) and (31). $p_2(t)$ is discontinuous if and only if $c\dot{e}(0) \neq 0$. Hence by (32), $\tilde{r}(t)$ is discontinuous if and only if $c\dot{e}(0) \neq 0$. Unlike (22) and (28), distributional differentiation of (32) for nonvanishing $c\dot{e}(0)$ can not be used to eliminate the discontinuity in the kernel, for the singular delta functions arise from the discontinuities in $\tilde{r}(t)$ and $p_2(t)$. The delta function terms resulting from the Heaviside functions in $\mathbf{D}[\tilde{r}]$ after differentiation, for example, $\tilde{r}[t - 2j/(1 - v^2)]\delta[t - 2j/(1 - v^2)]$, all vanish because $\tilde{r}(0) = 0$.

The strategy devised for $c\dot{e}(0) \neq 0$ is to first compute the discontinuities of $\tilde{r}(t)$ from the discontinuities of $I_1(t)$ in $p_2(t)$. By the calculus of generalized functions (Hoskins, 1979),

$$I_1(t) = \frac{1 + v}{2}\left(\sum_{l_1 \le i \le r_1}{}' \text{coef}_1(i) \times \left[1 + (1 + v)t - d - \frac{2i}{1 - v}\right] - \sum_{l_4 \le i \le r_4} \text{coef}_4(i) \times \left[1 + (1 + v)t + \frac{1 + v}{1 - v}d - \frac{2i}{1 - v}\right]\right) + \frac{1 - v}{2}\left(\sum_{l_2 \le i \le r_2} \text{coef}_2(i) \times \left[1 - (1 - v)t - d + \frac{2i}{1 + v}\right] - \sum_{l_3 \le i \le r_3} \text{coef}_3(i) \times \left[1 - (1 - v)t + \frac{1 - v}{1 + v}d + \frac{2i}{1 + v}\right]\right) \quad (33)$$

where

$$l_1 = (1 - v)[(1 + v)t - d]/2$$
$$r_1 = (1 - v)[1 + (1 + v)t - d]/2$$
$$l_2 = (1 + v)[(1 - v)t + d - 1]/2$$
$$r_2 = (1 + v)[(1 - v)t + d]/2$$
$$l_3 = -(1 - v)d/2 + (1 - v^2)t/2 - (1 + v)/2$$
$$r_3 = -(1 - v)d/2 + (1 - v^2)t/2$$
$$l_4 = (1 - v^2)t/2 + (1 + v)d/2$$
$$r_4 = (1 - v)/2 + (1 - v^2)t/2 + (1 + v)d/2$$

$$\text{coef}_m(i) = \begin{cases} 1, & \text{if } i \text{ is the integer in the region } (l_m, r_m) \\ 0.5, & \text{if the integer } i = l_m \text{ or } i = r_m \\ 0, & \text{if the integer } i \text{ is not in the region } [l_m, r_m] \end{cases} \quad (m = 1, 2, 3, 4).$$

The discontinuities of $I_1(t)$ in $0 \le t \le t_f$ occur at $t_+^{(j)} = 2(j - 1)/(1 - v^2) + d/(1 + v)$ for $j = 1, 2, \ldots, N_+$ and $t_-^{(j)} = 2j/(1 - v^2) - d/(1 - v)$ for $j = 1, 2, \ldots, N_-$, where $N_+ = 1 + \text{Int}[(1 - v^2)t_f/2 - (1 - v)d/2]$ and $N_- = \text{Int}[(1 - v^2)t_f/2 + (1 + v)d/2]$. As shown in Fig. 2, $t_+^{(j)}$ and $t_-^{(j)}$ are the instants when propagating wavefronts of the main transmitted wave component in the string interact with the constraint at $x = d$ in $0 \le t \le t_f$. The discontinuity of I_1 at $t_+^{(j)}$, due to the discontinuities in the first and fourth summations in (33), is calculated explicitly to be -1. Likewise, the discontinuity of I_1 at $t_-^{(j)}$ due to the second and third summations in (33) is $+1$. Hence, the discontinuity of $\tilde{r}(t)$ directly due to the discontinuity of $p_2(t)$ at $t_+^{(j)}$ is obtained from (32)

$$\tilde{r}[(t_+^{(j)})^+] - \tilde{r}[(t_+^{(j)})^-] = -2/(c + 2) \quad (p_2[(t_+^{(j)})^+] - p_2[(t_+^{(j)})^-]) = -2c/(c + 2) \quad \dot{e}(0). \quad (34)$$

The discontinuity of $\tilde{r}(t)$ directly due to the discontinuity of $p_2(t)$ at $t_-^{(j)}$ is similarly obtained:

$$\tilde{r}[(t_-^{(j)})^+] - \tilde{r}[(t_-^{(j)})^-] = 2c/(c + 2) \quad \dot{e}(0). \quad (35)$$

These discontinuities in (34) and (35) are independent of the transport speed v and vanish when $c\dot{e}(0) = 0$. In particular, the first discontinuity of $\tilde{r}(t)$ at $t_+^{(1)} = d/(1 + v)$, given by (34), agrees with that given in the Appendix when a propagating pulse in a stationary string approaches an attached spring/damper.

Distributional differentiation of (32) is then performed, dropping the delta function terms associated with the discontinuities in $\tilde{r}(t)$ and $p_2(t)$ at $t_+^{(j)}$ and $t_-^{(j)}$. The resulting delay-differential equation

$$k\mathbf{D}[\tilde{r}] + \left(1 + \frac{c}{2}\right)\frac{d}{dt}\tilde{r}(t) + c\left[\sum_{j=1}^{N} \frac{d}{dt}\tilde{r}\left(t - \frac{2j}{1 - v^2}\right)H\left(t - \frac{2j}{1 - v^2}\right)\right.$$

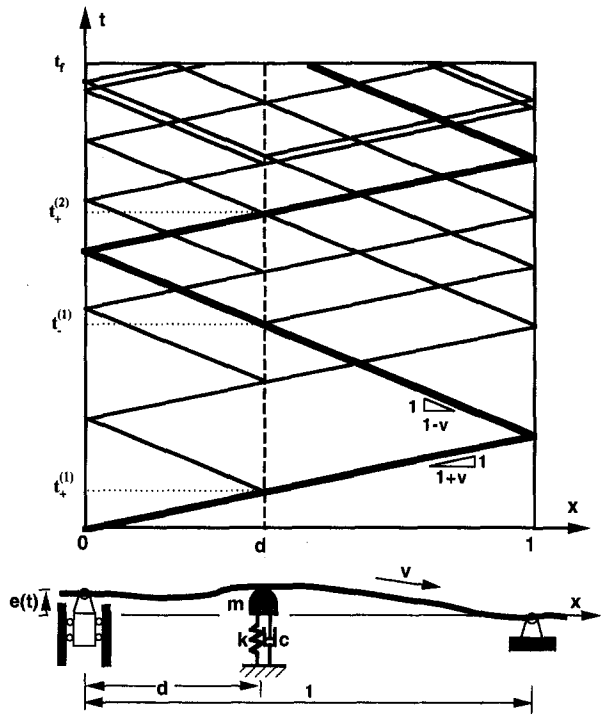


Fig. 2 Multiple wave scattering at a flexible constraint in the translating string. Intersections of the characteristic lines with the dashed line $x = d$ are the instants when propagating wavefronts in the string interact with the constraint. The heavy line is the main transmitted wave component.

Downloaded 04 May 2010 to 171.66.16.28. Redistribution subject to ASME license or copyright; see http://www.asme.org/terms/Terms_Use.cfm

$$-\frac{1}{2}\sum_{j=1}^{N+1}\frac{d}{dt}\tilde{r}\left(t-\frac{2d}{1-v^2}-\frac{2(j-1)}{1-v^2}\right)$$
$$\times H\left(t-\frac{2d}{1-v^2}-\frac{2(j-1)}{1-v^2}\right)$$
$$-\frac{1}{2}\sum_{j=1}^{N+1}\frac{d}{dt}\tilde{r}\left(t+\frac{2d}{1-v^2}-\frac{2j}{1-v^2}\right)$$
$$\times H\left(t+\frac{2d}{1-v^2}-\frac{2j}{1-v^2}\right)\Bigg]+q(t)=0 \quad (36)$$

is valid at all $t \in [0, t_f]$, except at the $t_+^{(j)}$ and $t_-^{(j)}$ when $c\dot{e}(0) \neq 0$ where discontinuity in $\tilde{r}$ at those instants is supplied by (34) and (35). Here d/dt is the distributional derivative without regard to discontinuities at $t_+^{(j)}$ and $t_-^{(j)}$ (Stakgold, 1979) and

$$q(t) = dp_2/dt = (1-d)[k\dot{e}(t) + c\ddot{e}(t)]$$
$$- \dot{e}(0)(k + c\, d/dt)I_1(t) + (k + c\, d/dt)I_2(t) \quad (37)$$

where $I_2(t)$ is the continuous double integral in (27). $dI_1(t)/dt$ is the distributional derivative of the discontinuous $I_1(t)$, upon ignoring the delta functions at $t_+^{(j)}$ and $t_-^{(j)}$, given by

$$\frac{dI_1(t)}{dt} = \frac{(1+v)^2}{2}\Big(\sum_{l_1\le i\le r_1}\text{coef}_1(i) - \sum_{l_4\le i\le r_4}\text{coef}_4(i)\Big)$$
$$-\frac{(1-v)^2}{2}\Big(\sum_{l_2\le i\le r_2}\text{coef}_2(i) - \sum_{l_3\le i\le r_3}\text{coef}_3(i)\Big). \quad (38)$$

4 Numerical Solution

The delay equation (29), delay-integral equation (26), and delay-differential equation (36) along with discontinuity in $\tilde{r}$ supplied by (34) and (35) when $c\dot{e}(0) \neq 0$, are solved numerically for $\tilde{r}(t)$. The temporal domain $[0, t_f]$ is divided into n_p equal subintervals of width $\Delta t = t_f/n_p$.

The double integral $I_2(t)$ in $p(t)$ can be evaluated either by series summation for the Green's function (19a) or by the delta function series (20) for $g_t(x, \xi; t-\tau)$ using the numerical algorithm developed in Zhu and Mote (1994). $dI_2(t)/dt$ in $q(t)$ is then evaluated by finite difference. The discontinuous $I_1(t)$ in $p(t)$ is computed by (33) to avoid the Gibb's phenomenon that occurs at the discontinuities of $I_1(t)$ when the truncated series of (19a) represents the Green's function. The distributional derivative of $I_1(t)$, $dI_1(t)/dt$ in $q(t)$, neglecting the delta functions at $t_+^{(j)}$ and $t_-^{(j)}$, is computed by (38); the series expansion (19a) is divergent for $dI_1(t)/dt$ and cannot be used.

The delay terms in $\mathbf{D}[\tilde{r}]$ are represented by linear interpolation. The integral in (26) is replaced by trapezoidal integration (Linz, 1985) and $d\tilde{r}(t)/dt$ in (36) is replaced by a backward finite difference operator. The derivatives of the delay terms in (36) are evaluated by linear interpolation and then by backward finite differences. With the forcing terms $p(t)$ and $q(t)$ computed, the discretized delay-difference equations for (26), (29), and (36) are solved recursively for $\tilde{r}(t)$ from the initial value $\tilde{r}(0) = 0$. For $c\dot{e}(0) \neq 0$, the discontinuities of $\tilde{r}(t)$, given by (34) and (35), are accounted for at $t_+^{(j)}$ and $t_-^{(j)}$ in the recursive solution of the discretized representation of (36). Prediction of a negative contact force $r(t) = r^* + \tilde{r}(t)$ signals contact loss between the string and the constraint.

The string displacement $\tilde{u}(x, t)$ at time t is determined by (18), once $\tilde{r}(t)$ is known. The double integral is calculated by using the Green's function series (19a). $I_3(x) = \int_0^1 (1-\xi)g(x, \xi; t)d\xi$ for given t and v can be integrated in closed form using (19b) and (19c). For example, for $v = 1/2$ and at $t = 1$, $I_3(x)$ equals: $-2x^2/9 + x/3$ for $0 \le x \le 1/2$, $-20x^2/9 + 7x/3 - 1/2$ for $1/2 \le x \le 5/6$, and $-2x^2/9 + x - 7/9$ for $5/6 \le x \le 1$. Because exact integration of $I_3(x)$ requires considerable effort for different t and v, $I_3(x)$ is computed by the series expansion (19a). With the spatial domain divided into 500 equal intervals and 200 terms retained in (19a) for the above example, the maximum relative error of the series solution over the spatial domain is 0.73 percent. $I_4(x, t) = \int_0^t \tilde{r}(\tau)g(x, d; t-\tau)d\tau$ is obtained by integrating $dI_4(x, t)/dt$, which is computed by the generalized function approach similar to (33) with linear interpolation used for $\tilde{r}(t)$. I_4 can also be computed by the series expansion (19a).

5 Result and Discussion

The results are presented for a model of a magnetic tape-head system typical of those used in data storage technology. The tape of thickness 28 μm, width 12.7 mm and density 1.4 g/cm^3, under tension $P = 0.5$ N, is modeled as an axially moving string of mass per unit length $\rho = 0.49784$ g/m. The tape travels at a speed $V = 2$ m/s ($v = 0.0631$) between two reels separated by $L = 200$ mm. The dimensionless tape weight $w = \rho gL/P$ is 1.9515 10^{-3}. For a rigid head at $d = 0.25$ or 0.75 with the head penetration $h = 0.015$ (3 mm), the preload $r^* = 0.08066$ (0.04033 N). For a rigid head at $d = 0.5$ with the same penetration 3 mm, the preload is 0.03075 N. For a flexible head, the preload r^* is chosen to be that for the rigid head with $z_0 = (mw + r^*)/k$ by (10) for comparison purposes. Two types of boundary disturbances due to the reel eccentricity at the upstream end are used: $e_1(t) = e_0 \sin \Omega t$ and $e_2(t) = e_0(1 - \cos \Omega t)$ with $e_0 = 7.5\ 10^{-3}$ (1.5 mm) and $\Omega = 4$. Initially the tape is at rest in equilibrium given by (11) and $f(x, t) = 0$. The transient response is calculated for $t_f = 8$.

The solid line in Fig. 3(a) shows the dimensional contact force history $R(T) = R^* + \tilde{R}(T)$ between the tape and a rigid head located at $d = 0.25$ under boundary disturbance $e_1(t)$. The preload is $R^* = 0.04033$ N before the disturbance reaches, and is reflected by, the rigid head at $t_+^{(1)} = d/(1+v) = 0.2352$ (1.48 ms) when a negative jump in $R(T)$ $-2\dot{e}_1(0) = -0.06$ (-0.03 N) occurs. This jump is predicted by (29). The jump in $R(T)$ is also -0.03 N at subsequent instants $t_r^{(n)} = d/(1+$

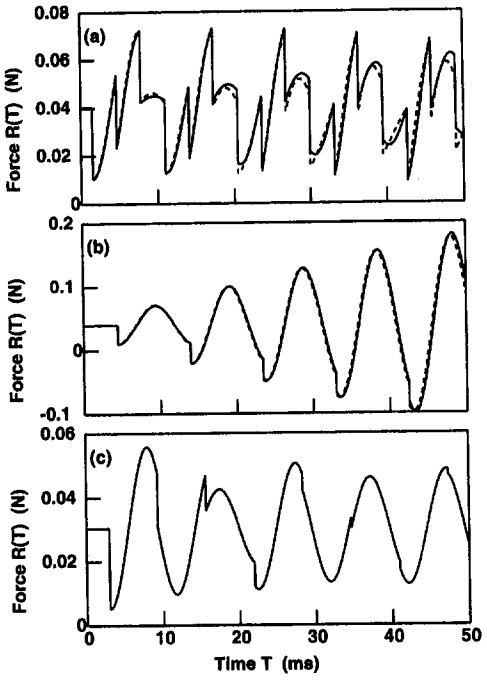


Fig. 3 Contact force history under disturbance $e_1(t)$, in which discontinuity exists because $\dot{e}_1(0) \neq 0$: (a) rigid (——) and flexible (– – –, $k = m = 10$, $\zeta = 0.05$) heads at $d = 0.25$, $n_p = 4000$; (b) rigid (——) and flexible (– – –, $k = m = 10$, $\zeta = 0.05$) heads at $d = 0.75$, $n_p = 4000$; (c) flexible massless head at $d = 0.5$, $k = c = 10$, $n_p = 3100$.

Downloaded 04 May 2010 to 171.66.16.28. Redistribution subject to ASME license or copyright; see http://www.asme.org/terms/Terms_Use.cfm

$v) + 2dn/(1 - v^2) = 0.73716$ (4.65 ms), 1.23916 (7.82 ms), 1.74116 (10.99 ms), etc. ($n = 1, 2, 3, \ldots, 15$) when the reflected wave interacts with the rigid head. The dashed line in Fig. 3(a) represents the contact force with $k = m = 10$ and $\zeta = 0.05$. The spring compression at equilibrium is $Z_0 = 2.0034$ mm. Unlike the rigid head case, waves are transmitted across the flexible head. However, transmitted waves introduce no additional discontinuity in the contact force because the slope of the tape at a transmitted wavefront is zero. Vanishing slope at a transmitted wavefront occurs when $m \neq 0$. The contact force history for this relatively stiff head suspension resembles that for a rigid head. For a soft suspension, $k = m = 1$, with the preload R^* and other parameters unaltered, which is not shown here, a contact loss is signaled at $T = 10.98$ ms by a negative R. Also for a smaller head penetration, say $h = 0.01$ (2 mm), and with other parameters unchanged, the loss of contact occurs at $T = 1.48$ ms when the disturbance reaches the head.

The solid and dashed lines in Fig. 3(b) show the contact forces for the head positioned at $d = 0.75$ and other parameters unchanged. Again $R(T)$ has negative jumps of -0.03 N at the instants $t_r^{(n)} = d/(1 + v) + 2dn/(1 - v^2) = 0.7055$ (4.45 ms), 2.2115 (13.96 ms), 3.7174 (23.46 ms), etc. ($n = 0, 1, 2, 3, 4$), for both rigid and flexible heads. Discontinuity of $R(T)$ vanishes at the instant a transmitted wavefront interacts with the flexible head (e.g., $t_-^{(1)} = 1.2075$ (7.62 ms)) because the slope of the transmitted wavefront is zero. Although the natural frequencies of the coupled tape-flexible head system are identical for symmetric head locations, like $d = 0.25$ and $d = 0.75$, the transient responses are different. While contact loss does not occur in Fig. 3(a) when $d = 0.25$, loss occurs when $d = 0.75$ at $T = 13.98$ ms for both rigid and flexible heads, as shown in Fig. 3(b). Therefore, the force prediction by this model is not valid for $T > 13.98$ ms in Fig. 3(b). The initially growing contact force history suggests that a small eccentricity e_0 can lead to tape-head contact loss. In fact contact loss will always occur in this case for a disturbance with amplitude $e_0 > 1.535\ 10^{-3}$ (0.307 mm). For example, for $e_0 = 2.5\ 10^{-3}$ (0.5 mm) and other parameters unchanged, contact loss occurs at $T = 42.58$ ms and at 42.51 ms for the rigid and flexible head models, respectively. For the flexible head with $e_0 = 2.5\ 10^{-3}$ (not presented here), the sinusoidal contact force at the steady state is always positive. Therefore operating conditions ensuring tape-head contact at steady state do not prevent contact loss in the transient.

Under the same disturbance $e_1(t)$, the contact force between the tape and a flexible massless head with $k = c = 10$, which represents an air bearing model, is shown in Fig. 3(c). The head is positioned at $d = 0.5$, the preload is $R^* = 0.03705$ and $Z_0 = 1.613$ mm. The slope at a transmitted wavefront through the flexible massless head does not vanish, and consequently discontinuity in R occurs at the instant a transmitted wavefront interacts with the head. The head is located at the midspan, $d = 0.5$, so all instants of wave-head interaction are at $t_+^{(j)}$ and $t_-^{(j)}$. The first discontinuity in R at $t_+^{(1)} = 0.4704$ (2.968 ms) is $-2c\dot{e}_1(0)/(c + 2) = -0.05$ (-0.025 N), as predicted by (34). The discontinuity in $R(T)$ at later instants is not that given by (34) or (35). The wave-head interactions that occur at the same time from earlier reflected and transmitted waves, as predicted by the delay terms in (36), sum with the discontinuity due to the main transmitted wave component given by (34) or (35). The discontinuity in $R(T)$ decreases in amplitude with time and vanishes eventually. The contact force approaches to the sinusoidal response at the steady state because of the presence of damping c. While the velocity $\dot{z}(t)$ is continuous by (21) for the case of nonvanishing head mass m, it is discontinuous here for the flexible massless head when $c \neq 0$, as predicted by (15), because $\bar{r}(t)$ is discontinuous.

Figures 4(a-c) show the contact forces under disturbance $e_2(t)$ with all other parameters equal to those in Figs. 3(a-c).

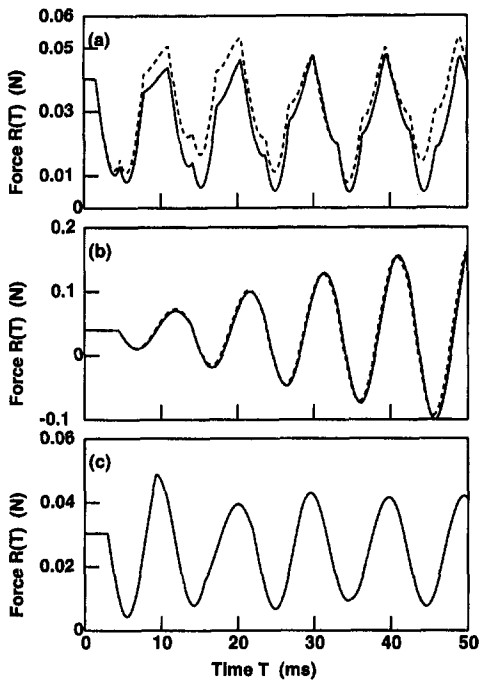


Fig. 4 Contact force history under disturbance $e_2(t)$, in which discontinuity is absent because $e_2(0) = \dot{e}_2(0) = 0$: (a) rigid (——) and flexible (– – –, $k = m = 10$, $\zeta = 0.05$) heads at $d = 0.25$, $n_p = 2000$; (b) rigid (——) and flexible (– – –, $k = m = 10$, $\zeta = 0.05$) heads at $d = 0.75$, $n_p = 2000$; (c) flexible massless head at $d = 0.5$, $k = c = 10$, $n_p = 3100$.

The trend and amplitude ranges of the contact force histories in Fig. 4 are generally similar to those in Fig. 3, except discontinuity in $R(T)$ vanishes in Fig. 4 because $\dot{e}_2(0) = 0$. Contact losses occur at $T = 15.35$ ms and $T = 15.42$ ms in Fig. 4(b) for the rigid and flexible heads, respectively.

Figures 5(a-e) show the propagation of the disturbance $e_1(t)$ from the left end of the tape for the case in Fig. 3(a). The displacement $\tilde{U}(X, T)$, relative to the parabolic static equilibrium $U^*(X)$ given by (11), is calculated from (18) at each instant, once the contact force history is known. In the tape modeled as a string, waves (solid lines) are not transmitted through a rigid head, and accordingly are confined in the upstream section ($X < 50$ mm) of the tape. Waves are transmitted through the flexible head however, as shown by the dashed lines. It is seen in Fig. 5(b) that the slope of the transmitted wavefront ($X = 134.76$ mm) through the flexible head with nonzero mass vanishes.

6 Conclusion

1 The dynamic contact force $\bar{r}(t)$ is governed by the delay Eq. (29) for a rigid constraint, by the delay-integral equation (26) for a linear, flexible constraint with nonvanishing mass, and by the delay-differential Eq. (36) along with (34) and (35) when $c\dot{e}(0) \neq 0$ for a linear, flexible massless constraint.

2 Disturbance causing discontinuity in initial velocity at a boundary of a string, such as $\dot{e}(0) \neq 0$ in this study, introduces discontinuity in the forcing term $p(t)$ in (26) and (29), and $p_2(t)$ in (32). Consequently discontinuity in the contact force $r(t)$ between the string and a constraint results when the constraint is other than a single spring element. In addition, $\dot{e}(0) \neq 0$ produces discontinuity in the velocity $\dot{z}(t)$ for a flexible massless constraint with nonvanishing damping c.

3 For a rigid or flexible ($m \neq 0$) constraint, discontinuity in $r(t)$, which occurs only at $t_r^{(n)} = d/(1 + v) + 2dn/(1 - v^2)$ ($n = 0, 1, 2, \ldots,$ Int $[(1 - v^2)t_f/2d - (1 - v)/2]$), equals $-2\dot{e}(0)$. Waves transmitted through a flexible constraint with

Downloaded 04 May 2010 to 171.66.16.28. Redistribution subject to ASME license or copyright; see http://www.asme.org/terms/Terms_Use.cfm

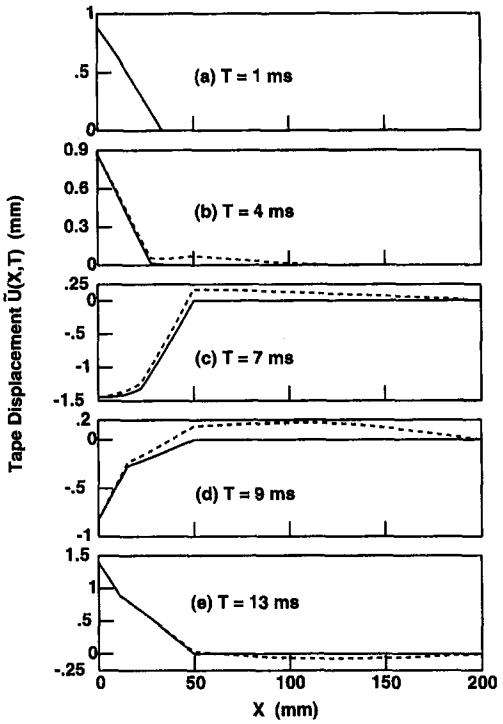


Fig. 5 Propagation of boundary disturbance $e_1(t)$ in the tape in contact with a rigid (——) or flexible (– – –, $k = m = 10$, $\zeta = 0.05$) head at $d = 0.25$. The tape displacement $\tilde{U}(X, T)$ is relative to its equilibrium. The spatial domain is divided into 500 equal intervals.

nonzero mass introduce no additional discontinuity in $r(t)$ because the slope of the string at the wavefronts vanishes.

4 For a flexible massless constraint, a transmitted wave can cause discontinuity in the contact force because the slope at its wavefront may not vanish. The first discontinuity in $r(t)$ occurring at $t_+^{(1)}$ equals $-2c\dot{e}(0)/(c+2)$. Discontinuities in $r(t)$ at later times decrease in amplitude with time and eventually vanish. All discontinuities occur when the propagating wavefronts in the string interact with the constraint, and they are implicitly accounted for in the analysis.

5 Besides boundary disturbances, nonzero initial values of the dynamic contact force $\tilde{r}(0)$, such as those resulting from the inequality $\dot{z}(0) \neq u_t(d, 0)$, can also cause discontinuity in the contact force. For example, when a recording head starts to load the tape with an initial transverse velocity, the contact force can be discontinuous even in the absence of boundary disturbances.

6 Large amplitude, high-frequency disturbances can cause contact loss between the string and constraint. Increased preload r^* and suspension stiffness can usually eliminate contact loss. Proper selection of the constraint location is important too, because there exist constraint locations that result in contact loss even for disturbances of small amplitude.

References

Hoskins, R. F., 1979, *Generalised Functions,* Ellis Horwood Limited, Chichester, U.K.

Linz, P., 1985, *Analytical and Numerical Methods for Volterra Equations,* SIAM, Philadelphia, PA.

Perkins, N. C., 1990, "Linear Dynamics of a Translating String on an Elastic Foundation," ASME *Journal of Vibration and Acoustics,* Vol. 112, pp. 2–7.

Perkins, N. C., and Mote, C. D., Jr., 1986, "Comments on Curve Veering in Eigenvalue Problems," *Journal of Sound and Vibration,* Vol. 106, No. 3, pp. 451–463.

Sack, R. A., 1954, "Transverse Oscillations in Travelling Strings," *British Journal of Applied Physics,* Vol. 5, pp. 224–226.

Schajer, G. S., 1984, "The Vibration of a Rotating Circular String Subject to a Fixed Elastic Restraint," *Journal of Sound and Vibration,* Vol. 92, No. 1, pp. 11–19.

Stakgold, I., 1979, *Green's Functions and Boundary Value Problems,* John Wiley and Sons, New York.

Wickert, J. A., and Mote, C. D., Jr., 1990, "Classical Vibration Analysis of Axially Moving Continua," ASME JOURNAL OF APPLIED MECHANICS, Vol. 57, No. 3, pp. 738–744.

Wickert, J. A., and Mote, C. D., Jr., 1991, "Traveling Load Response of an Axially-Moving String," *Journal of Sound and Vibration,* Vol. 149, No. 2, pp. 267–284.

Yang, B., 1992, "Eigenvalue Inclusion Principles for Distributed Gyroscopic Systems," ASME JOURNAL OF APPLIED MECHANICS, Vol. 59, pp. 650–656.

Zhu, W. D., and Mote, C. D., Jr., 1994, "Free and Forced Response of an Axially Moving String Transporting a Damped Linear Oscillator," *Journal of Sound and Vibration,* Vol. 177, No. 5, pp. 591–610.

APPENDIX

Consider a pulse of length l propagating towards a damper attached at the origin $x = 0$ in an infinite, taut string of mass/length ρ and tension P, as shown in Fig. 1(*c*). The pulse is initially at $x \in [a, a + l]$ with its shape described by $\Theta(x - a)(a \leq x \leq a + l, a > 0)$. Assume $\Theta(0) = \Theta(l) = 0$ to ensure continuous displacement of the string. The incident wave is

$$\theta(x + st) = [H(x + st - a) - H(x + st - a - l)]\Theta(x + st - a) \quad \text{(A1)}$$

where $s = \sqrt{P/\rho}$ is the wave speed in the string. The transmitted and reflected waves from the damper with damping constant C are denoted by $\psi(st + x)$ and $\eta\ (st - x)$, respectively. The boundary conditions at $x = 0$ are

$$\psi(st) = \theta(st) + \eta(st)$$
$$P[\theta'(st) - \eta'(st) - \psi'(st)] = sC\psi'(st) \quad \text{(A2)}$$

where the "prime" denotes differentiation with respect to the argument. Solution to (A2) by use of the initial conditions $\psi(0) = \theta(0) = 0$ yields

$$\psi(st) = 2P\theta(st)/(2P + sC)$$
$$\eta(st) = -sC\theta(st)/(2P + sC). \quad \text{(A3)}$$

By (A3) and (A1), the damping force at $x = 0$ is

$$\begin{aligned} F_d &= -Cs\psi'(st) \\ &= -\frac{2CsP}{2P + Cs}\{[\delta(st - a) - \delta(st - a - l)]\Theta(st - a) \\ &\quad + [H(st - a) - H(st - a - l)]\Theta'(st - a)\} \\ &= -2CsP/(2P + Cs) \\ &\quad \times [H(st - a) - H(st - a - l)]\Theta'(st - a) \end{aligned} \quad \text{(A4)}$$

where the delta function terms vanish because $\Theta(0) = \Theta(l) = 0$. The discontinuities of the damping force at $t = a/s$ and $t = (a + l)/s$ obtained from (A4) are $-2CsP/(2P + Cs)\Theta'(0)$ and $2CsP/(2P + Cs)\Theta'(l)$, respectively. The discontinuity of the dimensionless damping force F_d/P when the pulse reaches the damper is $-2c/(c + 2)\Theta'(0)$, where $c = C/(P\rho)^{1/2}$. This discontinuity is equivalent to (34) because the slope at the wavefront $\Theta'(0)$ is equivalent to $\dot{e}(0)$.

Likewise, the discontinuities in the spring force, when the pulse reaches and leaves an attached spring, vanish because $\Theta(0) = \Theta(l) = 0$. This agrees with the prediction from (32).

Downloaded 04 May 2010 to 171.66.16.28. Redistribution subject to ASME license or copyright; see http://www.asme.org/terms/Terms_Use.cfm

Vibration Characteristics of Simply Supported Thick Skew Plates in Three-Dimensional Setting

K. M. Liew
Senior Lecturer,
Mem. ASME.

K. C. Hung
Teaching Assistant.

M. K. Lim
Associate Professor.

School of Mechanical and Production Engineering,
Nanyang Technological University,
Nnyang Avenue,
Singapore 639798

A procedure is presented for determining the three-dimensional elasticity solutions for free vibration analysis of simply supported thick skew plates. The exact expressions of strain and kinetic energies are derived from linear, small-strain, three-dimensional elasticity theory. To allow the treatment of soft *and* hard *simple support conditions, sets of three-dimensional spatial displacement functions are expressed in terms of unit normals to the edges. By virtue of the three-dimensional elasticity theory, the present method does not require a special treatment for stress singularity at the obtuse corners. This method is also demonstrated to be free from shear locking phenomena. The significant difference in the vibration response of skew plates with* soft *and* hard *simple support conditions is highlighted. The influence of skew angle on the eigenvalues of thick skew plate is discussed in the context of the three-dimensional elasticity solutions.*

1 Introduction

Several analytical solutions to free vibration of thick elastic rectangular plates have been reported in recent years. Approaches based on three-dimensional elasticity theory such as the power series methods (Fromme and Leissa, 1970; Hutchinson and Zillmer, 1983), the exact method (Srinivas et al., 1970), and the Ritz method (Leissa and Zhang, 1983) have been proposed for solutions. It was demonstrated in these works that models constructed on the basis of three-dimensional elasticity theory is imperative in obtaining a full vibration spectrum of thick plates.

Gorman (1991) emphasised on the importance of free vibration of skew plates and noted the lack of research in this area. Similarly, frequency results for thick skew plates are also very scarce despite their significance applications in many branches of engineering. Solution methods developed for the analysis of thick plates in skew domain are more involved and need to address two important issues: (1) the consideration of strong singularity occurring at the obtuse vertex; and (2) the incremental effects of transverse shear deformation and rotary inertia. The presence of strong localized stress singularity at the obtuse vertex of plates in skew domain often causes numerical difficulties in the solution process. Whereas the negligence of shear deformation and rotary inertia effects in the solutions based on the classical thin plate theory often leads to erroneous results. Despite the apparent difficulties, numerous researchers have attempted the problems using different approaches. A comprehensive review on these approaches can be found in the work of Liew et al. (1993). Most of these approaches have successfully accounted for the shear deformation and rotary inertia effects by using Mindlin's plate theory. No particular attention, however, was drawn to the treatment of stress singularity associated with the obtuse vertex of skew plate.

Contributed by the Applied Mechanics Division of THE AMERICAN SOCIETY OF MECHANICAL ENGINEERS for publication in the ASME JOURNAL OF APPLIED MECHANICS.

Discussion on this paper should be addressed to the Technical Editor, Professor Lewis T. Wheeler, Department of Mechanical Engineering, University of Houston, Houston, TX 77204-4792, and will be accepted until four months after final publication of the paper itself in the ASME JOURNAL OF APPLIED MECHANICS.

Manuscript received by the ASME Applied Mechanics Division, Oct. 12, 1993; final revision, July 11, 1994. Associate Technical Editor: F. Y. M. Wan.

In this paper, solutions to the title problem are obtained from the three-dimensional elasticity theory. This formulation has inherently accounted for the effects of shear deformation and in-plane (rotary) inertia which have been demonstrated for rectangular plates (Liew et al., 1994, 1995). In addition, this three-dimensional formulation will be proven to work for plates of high skewness without suffering the stress singularities. The present work focuses on the application of this method to the vibration analysis of homogeneous, isotropic elastic thick plates in skew domain with simply supported edges and stress free boundaries at the top and bottom surfaces. Two types of simple support conditions have been considered, namely: *hard* and *soft* simple supports. The definition correlates directly to the extents of kinematic constraints being imposed at the edges. The paradox of hard and soft simple supports in plate problems has been addressed by Babuška and Pitkäranta (1990) and Babuška and Li (1992). However, their treatments are limited to rectangular plate problems.

By virtue of its exact derivation from the three-dimensional elasticity theory, the proposed method is capable of providing a full vibration spectrum including both the symmetric and antisymmetric thickness modes. The symmetric thickness modes, in particular, are absence in the reported solutions based on the classical thin plate theory (Durvasula, 1968) and the Mindlin plate theory (Liew et al., 1993). The present work contains the detailed three-dimensional contour plots and deformed geometries for some selected cases. Hitherto, comprehensive vibration mode shapes for thick skew plates have not been reported elsewhere.

2 Theoretical Formulation

2.1 Basic Geometry Definitions and Notations. Figure 1 shows a thick, homogeneous, isotropic skew plate of uniform thickness, h. The plate dimensions are described by the oblique length, a, width, b, and its skewness indicated by an angle, θ with respect to the horizontal axis. A right-handed Cartesian coordinate system (x_1, x_2, x_3) is defined with its origin located at the geometric center. The reference plane containing x_1 and x_2 lies symmetrically amidst the top and bottom surfaces. At a general point, the spatial displacement is resolved into the in-plane (u_1, u_2) and out-of-plane (u_3) components. The in-plane

Copyright © 1995 by ASME

Downloaded 04 May 2010 to 171.66.16.28. Redistribution subject to ASME license or copyright; see http://www.asme.org/terms/Terms_Use.cfm

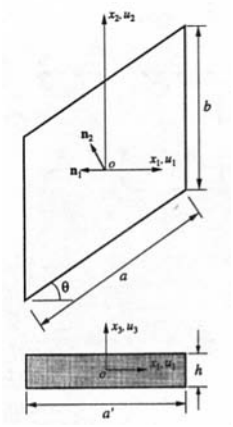


Fig. 1 Geometry and dimensions of thick skew plate

components are redefined in terms of unit normals ($\mathbf{n}_1$, $\mathbf{n}_2$) with respect to the edges.

In the present analysis, the ratios, a/b and h/a are defined as the aspect and thickness ratios, respectively. The square ($a/b = 1.0$ and $\theta = 0$ deg), rectangular ($a/b \neq 1.0$ and $\theta = 0$ deg) and rhombic ($a/b = 1.0$ and $\theta \neq 0$ deg) plates may be treated as special cases of the skew plate having specific aspect ratios and skew angles.

2.2 Derivation of the Energy Functional. Denoting the displacement vectors and strain tensors by $\epsilon_{\alpha\beta}$ ($\alpha, \beta = 1, 2, 3$), the strain energy can be expressed as

$$V = \frac{1}{2}\iiint_{\mathrm{v}} [\Delta\{(1-\nu)A_1 + 2\nu A_2 + (1-2\nu)A_3\}]d\mathrm{v} \quad (1)$$

in which v is the total volume of the plate and

$$A_1 = \epsilon_{11}^2 + \epsilon_{22}^2 + \epsilon_{33}^2 \quad (2a)$$

$$A_2 = \epsilon_{11}\epsilon_{22} + \epsilon_{11}\epsilon_{33} + \epsilon_{22}\epsilon_{33} \quad (2b)$$

$$A_3 = \epsilon_{12}^2 + \epsilon_{13}^2 + \epsilon_{23}^2 \quad (2c)$$

$$\Delta = \frac{E}{(1+\nu)(1-2\nu)} \quad (2d)$$

The Young's modulus and Poisson's ratios are denoted by E and ν, respectively.

The linear strain components at a general point can be defined in terms of spatial displacement vectors u_α ($\alpha = 1, 2, 3$) as:

$$\epsilon_{\alpha\beta} = \frac{1}{2}\left[\frac{\partial u_\alpha}{\partial x_\beta} + \frac{\partial u_\beta}{\partial x_\alpha}\right]; \quad \alpha, \beta = 1, 2, 3. \quad (3)$$

Introducing Eq. (3) into the strain energy expression and expanding yields

$$V = \frac{1}{2}\iiint_{\mathrm{v}} [\lambda'(\sum_{\alpha=1}^{3} u_{\alpha,\alpha})^2 + 2G(\sum_{\alpha=1}^{3} u_{\alpha,\alpha}^2) + G\{(u_{1,2} + u_{2,1})^2 + (u_{2,3} + u_{3,2})^2 + (u_{1,3} + u_{3,1})^2\}]d\mathrm{v} \quad (4)$$

where $(\ )_{,\alpha} = \partial(\ )/\partial x_\alpha$ and the Lamé constants, λ' and G (shear modulus), are defined as

$$\lambda' = \frac{\nu E}{\{(1+\nu)(1-2\nu)\}} \quad (5a)$$

$$G = \frac{E}{2(1+\nu)}. \quad (5b)$$

The total energy functional of a vibrating plate consists of maximum strain and kinetic energies

$$\Pi = V_{\max} - T_{\max}. \quad (6)$$

The maximum strain energy, $V_{\max}$, is obtained by introducing the displacement amplitude functions, U_α to replace u_α, in Eq. (4). The maximum kinetic energy is given by

$$T_{\max} = \frac{\rho\omega^2}{2}\iiint_{\mathrm{v}} (\sum_{\alpha=1}^{3} U_\alpha^2)d\mathrm{v}. \quad (7)$$

The parameters ρ and ω are the mass per unit volume and angular frequency of vibration, respectively.

The boundary conditions of plates are uniquely characterised by the choice of U_α which are the displacement amplitude functions.

2.3 Soft and Hard Simply Supported Conditions. In the present study, we confine ourselves to the analysis of thick skew plates subjected to simply supported boundary conditions. In a three-dimensional setting, there exists two types of simple supports, namely: (a) the *hard* simple support condition and (b) the *soft* simple support condition.

For the *soft* simple support, the essential and natural boundary conditions are

$$u_3 = 0, \quad \sigma_{nt} = 0 \quad \text{and} \quad \sigma_{nn} = 0 \quad (8)$$

in which t and n are the tangent and normal to the edges. However, the *hard* simple support requires both the out-of-plane and tangential displacements at the edges restraint, i.e.,

$$u_3 = 0, \quad u_t = 0 \quad \text{and} \quad \sigma_{nn} = 0. \quad (9)$$

To allow the treatment of plates with both support conditions, we introduce the unit normal vectors, $\mathbf{n}_1$ and $\mathbf{n}_2$. The in-plane spatial displacement components, u_1 and u_2 are related to the unit normals as follows:

$$u_1 = -(\mathbf{n}_1 + \mathbf{n}_2 \sin\theta) \quad (10a)$$

and

$$u_2 = \mathbf{n}_2 \cos\theta. \quad (10b)$$

Introducing Eqs. (10a) and (10b) to (6) and rearranging gives an alternate form of the total energy functional defined in terms of the displacement amplitude functions φ_1, φ_2, and U_3 of the corresponding spatial quantities, $\mathbf{n}_1$, $\mathbf{n}_2$ and u_3:

$$\Pi' = \frac{1}{2}\iiint_{\mathrm{v}} [\lambda'\{-(\varphi_{1,1} + \varphi_{2,1}\sin\theta) + (\varphi_{2,2}\cos\theta) + U_{3,3}\}^2 + 2G\{(\varphi_{1,1} + \varphi_{2,1}\sin\theta)^2 + (\varphi_{2,2}\cos\theta)^2 + U_{3,3}^2\} + G\{(\varphi_{1,2} + \varphi_{2,2}\sin\theta + \varphi_{2,1}\cos\theta)^2 + (\varphi_{2,3}\cos\theta + U_{3,2})^2 + (\varphi_{1,3} + \varphi_{2,3}\sin\theta + U_{3,1})^2\}]d\mathrm{v} - \frac{\rho\omega^2}{2}\iiint_{\mathrm{v}} (\varphi_1^2 + 2\varphi_1\varphi_2\sin\theta + \varphi_2^2 + U_3^2)d\mathrm{v}. \quad (11)$$

Depending on the type of simple support conditions, the displacement functions, $\mathbf{n}_1$, $\mathbf{n}_2$, and u_3 take on different forms. For the *hard* simple support condition, it is expedient to choose $\mathbf{n}_1$, $\mathbf{n}_2$, and u_3 that satisfy the boundary requirements of

$$u_t = \mathbf{n}_2 \cos\theta = 0 \text{ and } u_3 = 0 \text{ at the straight edges} \quad (12a)$$

and

$$u_t = \pm(\mathbf{n}_1 + \mathbf{n}_2 \sin\theta) = 0 \text{ and } u_3 = 0 \text{ at the oblique edges.} \quad (12b)$$

Downloaded 04 May 2010 to 171.66.16.28. Redistribution subject to ASME license or copyright; see http://www.asme.org/terms/Terms_Use.cfm

Table 1 Convergence of frequency parameters, $(\omega a^2/\pi^2)\sqrt{\rho h/D}$, for thick skew plates with *hard* and *soft* simple supports ($a/b = 1.0$, $\theta = 60$ deg and $\nu = 0.3$)

No. of terms	Antisymmetric thickness mode						Symmetric thickness mode					
$p \times q$	1	2	3	4	5	6	1	2	3	4	5	6
(a) *Hard support*												
10×5	4.9743	7.0003	9.0207	10.982	11.433	13.387	3.4502	4.0711	6.5295	7.4515	7.7059	9.7400
10×6	4.9742	7.0003	9.0206	10.982	11.433	13.387	3.4502	4.0711	6.5294	7.4515	7.7059	9.7400
11×5	4.9280	6.9996	8.9793	10.944	11.425	12.957	3.4479	4.0708	6.5268	7.4505	7.7059	9.7372
12×5	4.9263	6.9979	8.9776	10.876	11.386	12.878	3.3561	4.0708	6.4222	7.4505	7.7048	9.6257
(b) *Soft support*												
10×5	4.5038	6.7458	8.7330	10.747	11.065	13.633	1.6205	2.5493	3.8854	4.0507	5.0931	6.4836
10×6	4.5037	6.7458	8.7329	10.747	11.064	13.632	1.6204	2.5493	3.8854	4.0507	5.0930	6.4835
11×5	4.4926	6.7368	8.6212	10.547	11.028	12.498	1.6202	2.5495	3.8842	4.0500	5.0914	6.4838
12×5	4.4916	6.7360	8.6152	10.514	11.021	12.364	1.6200	2.5493	3.8836	4.0498	5.0904	6.4835

For the *soft* simple support condition, it needs to satisfy the only constraint of $u_3 = 0$ at all edges.

The present analysis uses sets of uniquely defined one and two-dimensional polynomials to form the respective displacement amplitude functions for $\mathbf{n}_1$, $\mathbf{n}_2$, and u_3.

3 Method of Solution

3.1 Admissible Displacement Functions. The sets of one and two-dimensional polynomial based displacement amplitude functions have the following forms:

$$\varphi_1 = \sum_{m=1}^{M}\sum_{n=1}^{N} C^1_{mn}\,{}^1\phi_m(x_1, x_2)\,{}^1\psi_n(x_3), \tag{13a}$$

$$\varphi_2 = \sum_{m=1}^{M}\sum_{n=1}^{N} C^2_{mn}\,{}^2\phi_m(x_1, x_2)\,{}^2\psi_n(x_3), \tag{13b}$$

and

$$U_3 = \sum_{m=1}^{M}\sum_{n=1}^{N} C^3_{mn}\,{}^3\phi_m(x_1, x_2)\,{}^3\psi_n(x_3), \tag{13c}$$

where N is the number of terms used in the one-dimensional polynomial approximation across the thickness and M is the number of terms used in the two-dimensional polynomial approximation of the plate surface variations.

The set of one-dimensional thickness functions, ${}^\alpha\psi_n(x_3)$, are orthogonally generated in a recursive manner. These polynomials have been used in the authors' earlier work (Liew et al., 1994). The basic functions, ${}^\alpha\psi_1(x_3)$ are chosen according to symmetry classes of vibration in the thickness direction. For symmetric thickness modes, in which the in-plane displacements (φ_1, φ_2) are each even function of the one-dimensional polynomials, the basic functions, ${}^\alpha\psi_1(x_3)$, take on the following form:

$${}^1\psi_1(x_3) = 1.0; \quad {}^2\psi_1(x_3) = 1.0 \tag{14a}$$

$${}^3\psi_1(x_3) = x_3. \tag{14b}$$

For antisymmetric thickness modes, the in-plane displacements are odd functions of the one-dimensional polynomials, the basic functions, ${}^\alpha\psi_1(x_3)$, are defined as

$${}^1\psi_1(x_3) = x_3; \quad {}^2\psi_1(x_3) = x_3 \tag{15a}$$

$${}^3\psi_1(x_3) = 1.0. \tag{15b}$$

These sets of thickness variation functions satisfy the stress-free requirement at the top and bottom surfaces of the plate at each symmetry class.

The generation of the sets of two-dimensional surface functions, ${}^\alpha\phi_m(x_1, x_2)$, on the other hand, has been detailed in the authors' earlier work (Hung et al., 1995). The basic surface functions that satisfy the *soft* simple support condition are

$${}^1\phi_1(x_1, x_2) = 1.0 \tag{16a}$$

$${}^2\phi_1(x_1, x_2) = 1.0 \tag{16b}$$

Table 2 Comparison of frequency parameters, $(\omega a^2/\pi^2)\sqrt{\rho h/D}$, for thin and moderately thick skew plates with $a/b = 1.0$ and $\nu = 0.3$ (antisymmetric thickness modes)

h/a	θ (degree)	Source of results	Mode sequence number					
			1	2	3	4	5	6
0.01	0	Liew and Lam (1990)	2.0000	5.0000	5.0000	8.0000	-	-
		Liew *et al.* (1993)	2.0000	5.0000	5.0000	7.9999	9.9999	9.9999
		Present (*hard*)	1.9993	4.9956	4.9956	7.9888	9.9826	9.9826
		Present (*soft*)	1.9958	4.9897	4.9897	7.9770	9.9771	9.9771
	15	Durvasula (1968)	2.115	4.884	5.688	8.015	10.54	11.04
		Liew and Lam (1990)	2.11	4.88	5.69	8.01	-	-
		Liew *et al* (1993)	2.1147	4.8842	5.6856	8.0090	10.537	11.034
		Present (*hard*)	2.1147	4.8800	5.6814	7.9987	10.518	11.016
		Present (*soft*)	2.1103	4.8747	5.6726	7.9877	10.512	11.007
	45	Durvasula (1968)	3.523	6.724	10.18	10.87	14.30	17.10
		Liew and Lam (1990)	3.54	6.73	10.22	10.92	-	-
		Liew *et al* (1993)	3.5800	6.7153	10.176	10.975	14.266	17.052
		Present (*hard*)	3.6320	6.7076	10.175	11.052	14.232	17.012
		Present (*soft*)	3.5407	6.6992	10.135	10.879	14.227	16.999
0.10	0	Liew *et al.* (1993)	1.9311	4.6050	4.6050	7.0642	8.6055	8.6055
		Srinivas *et al.* (1970)	1.9342	4.6222	4.6222	7.1030	8.6618	8.6618
		Present (*hard*)	1.9342	4.6222	4.6222	7.1030	8.6617	8.6617
		Present (*soft*)	1.8591	4.5159	4.5159	6.8658	8.5563	8.5563
	15	Liew *et al.* (1993)	2.0379	4.5061	5.1842	7.0713	9.0077	9.3749
		Present (*hard*)	2.0420	4.5226	5.2068	7.1108	9.0690	9.4432
		Present (*soft*)	1.9584	4.4235	5.0765	6.8940	8.9563	9.3109
	45	Liew *et al.* (1993)	3.3548	6.0344	8.7332	9.3043	11.677	13.549
		Present (*hard*)	3.4126	6.0633	8.8037	9.4352	11.777	13.681
		Present (*soft*)	3.1692	5.9162	8.5193	9.0734	11.461	13.483

Downloaded 04 May 2010 to 171.66.16.28. Redistribution subject to ASME license or copyright; see http://www.asme.org/terms/Terms_Use.cfm

$$^3\phi_1(x_1, x_2) = (x_1 + a'/2)(x_1 - a'/2) \times (\Theta x_1 - x_2 + b/2)(\Theta x_1 - x_2 - b/2). \quad (16c)$$

For the *hard* simple support condition defined in Eq. (12*a, b*), the corresponding basic functions are

$$^1\phi_1(x_1, x_2) = (x_2 + a'/2)(x_2 - a'/2) \quad (17a)$$

$$^2\phi_1(x_1, x_2) = 1.0 \quad (17b)$$

$$^3\phi_1(x_1, x_2) = (x_1 + a'/2)(x_1 - a'/2) \times (\Theta x_1 - x_2 + b/2)(\Theta x_1 - x_2 - b/2) \quad (17c)$$

where $a' = a \cos\theta$, $\Theta = \tan\theta$ and θ is the skew angle.

3.2 Derivation of Governing Eigenvalue Equation. Substituting the displacement amplitude functions defined in the preceding sections into the energy functional of Eq. (11) and minimizing with respect to the unknown coefficients

$$\frac{\partial \Pi'}{\partial C^{\alpha}_{mn}} = 0; \quad \alpha = 1, 2 \text{ or } 3 \quad (18)$$

yields the linear eigenvalue equation for obtaining the vibration frequencies and mode shapes of the thick skew plate

$$(\mathbf{K} - \Omega^2\mathbf{M})\{\mathbf{C}\} = \{\mathbf{0}\} \quad (19)$$

where $\{\mathbf{C}\} = \{\mathbf{C}^1\mathbf{C}^2\mathbf{C}^3\}^T$ is the eigenvector. The generalized stiffness matrix $\mathbf{K}$ is expressed in the form

$$\mathbf{K} = \begin{bmatrix} \mathbf{K}^{11} & \mathbf{K}^{12} & \mathbf{K}^{13} \\ & \mathbf{K}^{22} & \mathbf{K}^{23} \\ \text{Sym} & & \mathbf{K}^{33} \end{bmatrix} \quad (20a)$$

and the consistent mass matrix $\mathbf{M}$ is given by

$$\mathbf{M} = \begin{bmatrix} \mathbf{M}^{11} & \mathbf{M}^{12} & \mathbf{M}^{13} \\ & \mathbf{M}^{22} & \mathbf{M}^{23} \\ \text{Sym} & & \mathbf{M}^{33} \end{bmatrix}. \quad (20b)$$

The explicit expressions of the respective elements, $\mathbf{k}^{\alpha\beta}$ and $\mathbf{m}^{\alpha\beta}$; $\alpha, \beta = 1, 2, 3$ may be written as

Table 3(*a*) Frequency parameters, $(\omega a^2/\pi^2)\sqrt{\rho h/D}$, for thick skew plates with $a/b = 1.0$, $h/a = 0.2$ and $\nu = 0.3$ (antisymmetric thickness modes)

θ (degree)	Source of results	Mode sequence number 1	2	3	4	5	6
0	Liew *et al.* (1993)	1.7661	3.8580	3.8580	5.5737	6.5820	6.5820
	Srinivas *et al.* (1970)	1.7757	3.8991	3.8991	5.6527	-	-
	Present (*hard*)	1.7758	3.8991	3.8991	5.6524	6.6868	6.6868
	Present (*soft*)	1.6668	3.7758	3.7758	5.4185	6.5775	6.5775
15	Liew *et al.* (1993)	1.8560	3.7856	4.2763	5.5784	6.8385	7.0702
	Present (*hard*)	1.8672	3.8253	4.3263	5.6576	6.9503	7.1897
	Present (*soft*)	1.7517	3.7035	4.1917	5.4406	6.8346	7.0843
45	Liew *et al.* (1993)	2.9129	4.8736	6.6622	7.0148	8.4831	9.5878
	Present (*hard*)	2.9689	4.9358	6.7751	7.1612	8.6438	9.7850
	Present (*soft*)	2.7468	4.7643	6.5226	6.9304	8.3779	9.6057

Table 3(*b*) Frequency parameters, $(\omega a^2/\pi^2)\sqrt{\rho h/D}$, for thick skew plates with $a/b = 1.0$, $h/a = 0.2$, and $\nu = 0.3$ (symmetric thickness modes)

θ (degree)	Source of results	Mode sequence number 1	2	3	4	5	6
0	Srinivas *et al.* (1970)	-	-	4.6128	-	-	7.2936
	Present (*hard*)	3.2617	3.2617	4.6128	6.5234	6.5234	7.2934
	Present (*soft*)	4.0750	4.3601	4.3601	4.6128	5.2877	6.0394
15	Present (*hard*)	2.9779	3.6879	4.5237	6.6777	6.7679	6.8312
	Present (*soft*)	3.6307	4.0692	4.6988	5.0462	5.2544	6.2306
45	Present (*hard*)	2.9138	4.1879	5.4677	6.2148	7.6300	8.4487
	Present (*soft*)	2.3182	3.4950	4.0496	5.1028	6.3188	6.4853

$$\mathbf{k}^{11}_{mn} = \left[\lambda' E^{1100}_{mi} + G\left\{2E^{1100}_{mi} + \left(\frac{a'}{b}\right)^2 E^{0011}_{mi}\right\}\right] F^{00}_{nj} + G\left(\frac{a'}{h}\right)^2 E^{0000}_{mi} F^{11} \quad (21a)$$

$$\mathbf{k}^{12}_{mn} = \left[\lambda'\left\{E^{1100}_{mi}\mathbf{s} - \left(\frac{a'}{b}\right)E^{1001}_{mi}\mathbf{c}\right\} + G\left\{\left(\frac{a'}{b}\right)^2 E^{0011}_{mi}\mathbf{s} + 2E^{1100}_{mi}\mathbf{s} - \left(\frac{a'}{b}\right)E^{0110}_{mi}\mathbf{c}\right\}\right] F^{00}_{nj} + G\left(\frac{a'}{h}\right)^2 E^{0000}_{mi} F^{11}_{nj}\mathbf{s} \quad (21b)$$

$$\mathbf{k}^{13}_{mn} = -\lambda'\left(\frac{a'}{h}\right)E^{1000}_{mi}F^{01}_{nj} - G\left(\frac{a'}{h}\right)E^{0100}_{mi}F^{10}_{nj} \quad (21c)$$

$$\mathbf{k}^{22}_{mn} = \lambda'\left[E^{1100}_{mi}\mathbf{s}^2 - \left(\frac{a'}{b}\right)(E^{1001}_{mi} + E^{0110}_{mi})\mathbf{sc} + \left(\frac{a'}{b}\right)^2 E^{0011}_{mi}\mathbf{c}^2\right] F^{00}_{nj} + G\left[\left\{E^{1100}_{mi}(2\mathbf{s}^2 + \mathbf{c}^2) + \left(\frac{a'}{b}\right)^2 E^{0011}_{mi}(2\mathbf{s}^2 + c^2) - \left(\frac{a'}{b}\right)(E^{0110}_{mi} + E^{1001}_{mi})\mathbf{sc}\right\} F^{00}_{nj} + \left(\frac{a'}{h}\right)^2 (E^{0000}_{mi}\mathbf{s}^2 + E^{0000}_{mi}\mathbf{c}^2)F^{11}_{nj}\right] \quad (21d)$$

$$\mathbf{k}^{23}_{mn} = \lambda'\left[\left(\frac{a'^2}{bh}\right)E^{0010}_{mi}\mathbf{c} - \left(\frac{a'}{h}\right)E^{1000}_{mi}\mathbf{s}\right]F^{01}_{nj} + G\left[\left(\frac{a'^2}{bh}\right)E^{0001}_{mi}\mathbf{c} - \left(\frac{a'}{h}\right)E^{0100}_{mi}\mathbf{s}\right]F^{10}_{nj} \quad (21e)$$

$$\mathbf{k}^{33}_{mi} = \left\{\left(\frac{a'}{h}\right)^2(\lambda' + 2G)E^{0000}_{mi}F^{11}_{nj}\right\} + G\left\{\left(\frac{a'}{b}\right)^2 E^{0011}_{mi} + E^{1100}_{mi}\right\}F^{00}_{nj} \quad (21f)$$

and

$$\mathbf{m}^{11}_{mn} = E^{0000}_{mi}F^{00}_{nj}; \quad \mathbf{m}^{22}_{mn} = E^{0000}_{mi}F^{00}_{nj}; \quad \mathbf{m}^{33}_{mn} = E^{0000}_{mi}F^{00}_{nj} \quad (21g, h, i)$$

$$\mathbf{m}^{12}_{mn} = E^{0000}_{mi}F^{00}_{nj}\mathbf{s}; \quad \mathbf{m}^{13}_{mn} = \mathbf{m}^{23}_{mn} = 0 \quad (21j, k)$$

where

$$\mathbf{s} = \sin\theta; \quad \mathbf{c} = \cos\theta \quad (22a, b)$$

$$(E^{defg}_{mi})^{\alpha\beta} = \int_{-0.5}^{0.5}\int_{-0.5}^{0.5}\left[\left\{\frac{\partial^{d+e\,\alpha}\phi_m}{\partial\bar{x}_1^d\partial\bar{x}_2^e}\right\}\left\{\frac{\partial^{f+g\,\beta}\phi_l}{\partial\bar{x}_1^f\partial\bar{x}_2^g}\right\}\right]d\bar{x}_1\,d\bar{x}_2 \quad (23a)$$

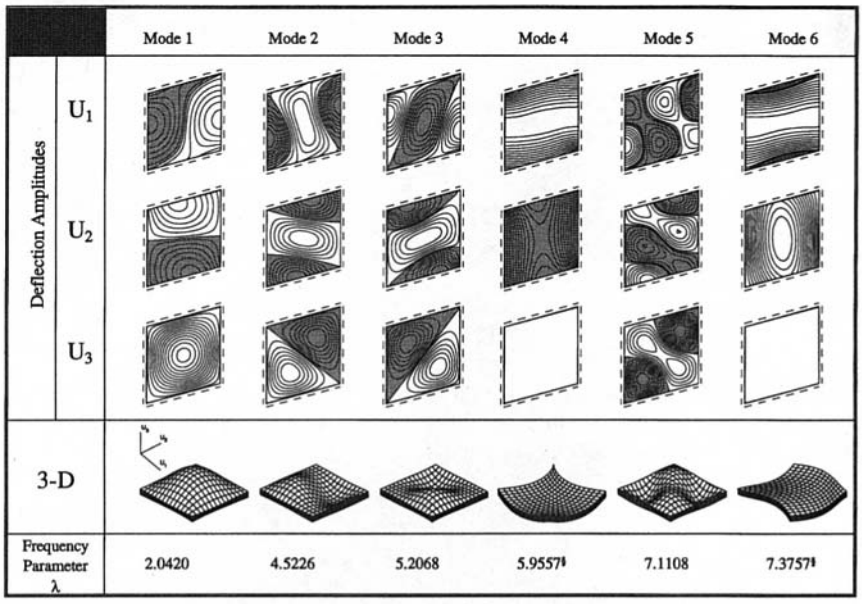
$$(F^{rs}_{nj})^{\alpha\beta} = \int_{-0.5}^{0.5}\left[\left\{\frac{\partial^{r\,\alpha}\psi_n}{\partial\bar{x}_3^r}\right\}\left\{\frac{\partial^{s\,\beta}\psi_j}{\partial\bar{x}_3^s}\right\}\right]d\bar{x}_3 \quad (23b)$$

where $\alpha, \beta = 1, 2$ or 3; and the variables $\bar{x}_1$, $\bar{x}_2$, and $\bar{x}_3$ in the above integrations are the normalized coordinates given by

$$\bar{x}_1 = \frac{x_1}{a'}; \quad \bar{x}_2 = \frac{x_2}{b} \quad \text{and} \quad \bar{x}_3 = \frac{x_3}{h}. \quad (24)$$

Finally, by solving the eigenvalue equation of Eq. (19), it yields the eigenvectors and the corresponding eigenvalues

Downloaded 04 May 2010 to 171.66.16.28. Redistribution subject to ASME license or copyright; see http://www.asme.org/terms/Terms_Use.cfm



‡Symmetric thickness modes (surface parallel motion).

Fig. 2 Three-dimensional mode shapes for *hard* simply supported moderately thick ($h/a = 0.1$) skew plate with $a/b = 1.0$, $\theta = 15$ deg and $\nu = 0.3$

$$\Omega = \omega a' \sqrt{\rho / E}. \tag{25}$$

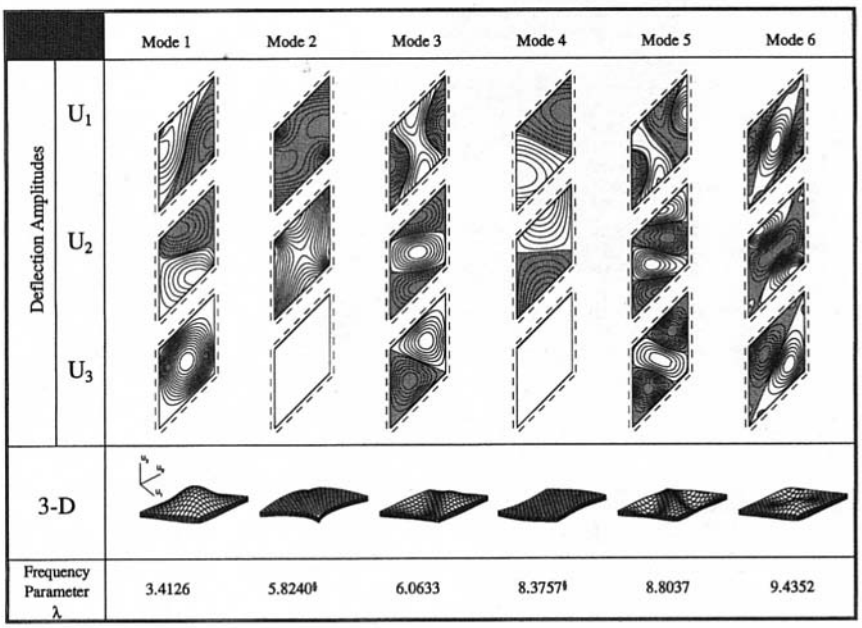
4 Results and Discussion

The eigenvalues computed are transformed into a nondimensionalized form:

$$\lambda = (\omega a^2 / \pi^2) \sqrt{\rho h / D}, \tag{26}$$

which can be used later for the comparison purpose.

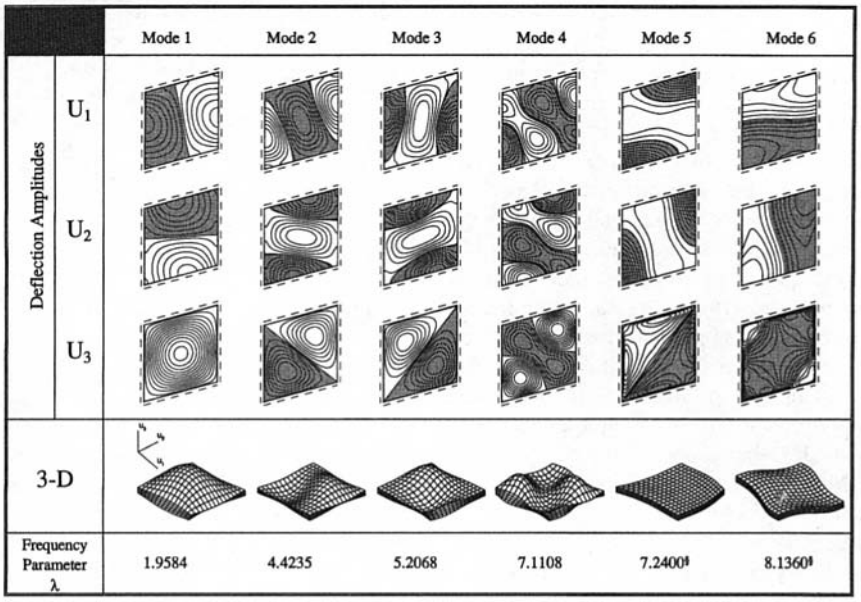
4.1 Convergence Studies. To assess the efficiency and accuracy of the method, convergence studies have been performed. The convergence pattern of the frequency parameters for thick skew plates with both *hard* and *soft* simple support conditions of thickness ratio, $h/a = 0.2$ and skew angle, $\theta = 60$ deg is shown in Table 1. The degree of polynomial, p, for the surface functions ${}^{\alpha}\phi(x_1, x_2)$ and the number of terms, q, for the thickness functions ${}^{\alpha}\psi(x_3)$ are varied in different steps to demonstrate the relative effects on the overall convergence of the frequency parameters. Equal number of terms are assumed for both in-plane (φ_1, φ_2) and out-of-plane (U_3) dis-



‡Symmetric thickness modes (surface parallel motion).

Fig. 3 Three-dimensional mode shapes for *hard* simply supported moderately thick ($h/a = 0.1$) skew plate with $a/b = 1.0$, $\theta = 45$ deg and $\nu = 0.3$

Downloaded 04 May 2010 to 171.66.16.28. Redistribution subject to ASME license or copyright; see http://www.asme.org/terms/Terms_Use.cfm



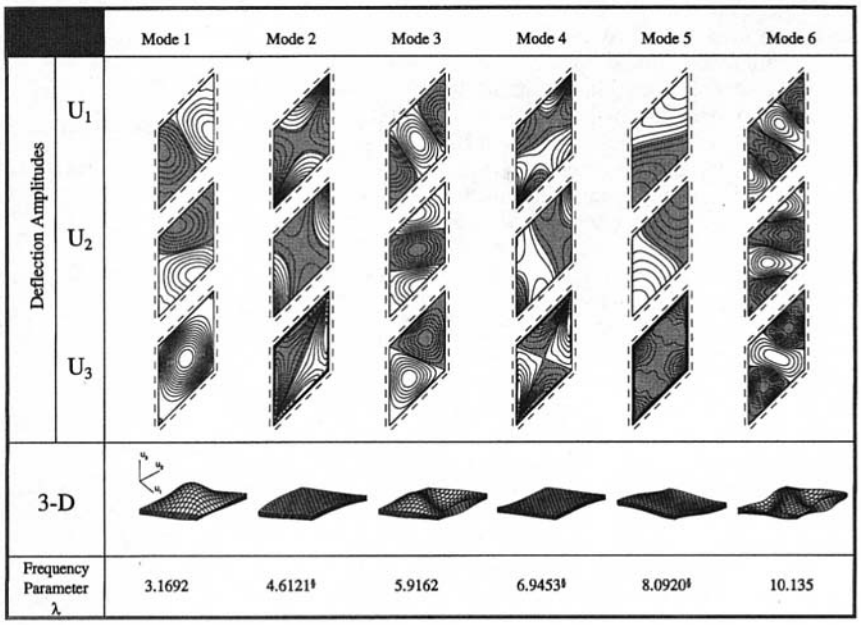
§Symmetric thickness modes (surface parallel motion).

Fig. 4 Three-dimensional mode shapes for *soft* simply supported moderately thick ($h/a = 0.1$) skew plate with $a/b = 1.0$, $\theta = 15$ deg and $\nu = 0.3$

placement functions. It is observed that both types of simple support conditions required as much terms for converged solutions. From the convergence tests conducted, it is decided that 12×5 terms (surface function of polynomial degree, $p = 12$ and thickness function of polynomial terms, $q = 5$) are used for subsequent calculations.

4.2 Comparison Studies. For thin skew plates, the computed results were compared in Table 2 with the frequency data of Durvasula (1968) and Liew and Lam (1990). All researchers adopted the classical thin plate theory in their formulations. It is observed that the present three-dimensional solutions for plates with *hard* and *soft* simple support conditions compared well with the literature. The frequency parameters for plates with *soft* simple support conditions are slightly lower in values. It can be deduced that as the thickness dimension of the plate degenerates further, the difference between the *hard* and *soft* simply supported models becomes negligible. The effect of shear locking phenomena which often jeopardises the shear deformable Mindlin/Reissner finite elements does not lead to numerical difficulty in the present analysis with degenerated thickness dimension.

For moderately thick plates ($h/a = 0.1$), the frequency solutions for antisymmetric thickness modes computed based on the three-dimensional elasticity theory are compared in Table 2 with the existing shear deformable plate solutions. For the spe-



§Symmetric thickness modes (surface parallel motion).

Fig. 5 Three-dimensional mode shapes for *soft* simply supported moderately thick ($h/a = 0.1$) skew plate with $a/b = 1.0$, $\theta = 45$ deg and $\nu = 0.3$

Downloaded 04 May 2010 to 171.66.16.28. Redistribution subject to ASME license or copyright; see http://www.asme.org/terms/Terms_Use.cfm

cial case of a square plate ($\theta = 0$ deg), the comparison is made with the Ritz solutions based on the Mindlin plate theory reported by Liew et al. (1993). The exact three-dimensional elasticity analytical solutions of Srinivas et al. (1970) are also included. It is observed that the present three-dimensional elasticity solutions for plates with *hard* simple support correspond very well with the exact analytical solutions of Srinivas et al. (1970). Slight discrepancy, however, is found between the Mindlin solutions and the three-dimensional elasticity results. The Mindlin plate theory tends to give a lower frequency values. Significant differences are observed between the solutions for plates with *hard* and *soft* simple supports at this thickness dimension. Judging from the results in Table 2, it is obvious that the kinematics constraints imposed in Mindlin's theory is closer to the *hard* simple support conditions in the three-dimensional setting. At other skew angles, the computed frequency results are compared with the Mindlin solutions by Liew et al. (1993) who assumed a constant shear correction factor of $\kappa = \frac{5}{6}$ for plates having arbitrary degrees of skewness. Similar frequency trends with respect to the skew angle are observed in both approaches.

The discrepancies between the solutions from the refined theory and the three-dimensional elasticity approach widen as the plate thickness increases beyond the ratio of $h/a = 0.1$ are demonstrated in Tables 3(a) for the antisymmetric thickness modes. It is attributed to the fact that as the thickness dimension increases, the thickness variation becomes parabolic instead of linear as it is assumed in the first-order shear deformable plate theory. The symmetric thickness modes (which are significant in thicker plates) computed from the three-dimensional elasticity approach, are also included in Table 3(b). By virtue of the exact three-dimensional elasticity expressions being used in the formulation, the present method is capable of predicting a full vibration spectrum which includes both the antisymmetric and symmetric thickness modes. The solution based on Mindlin's theory, however, fails to identify these symmetric thickness modes. These modes are found to be dominating in the lower vibration spectrum of thick skew plates. The physical appearance of symmetric and antisymmetric thickness modes of vibration can be read directly from the vibration mode shapes in the following section.

4.3 Three-Dimensional Vibration Frequencies and Mode Shapes. A set of vibration mode shapes for moderately thick ($h/b = 0.1$), *hard* simple support skew plates with skew angle $\theta = 15$ deg and 45 deg is depicted in Figs. 2 and 3, respectively. The normalized in-plane deflections in U_1 and U_2 and the out-of-plane deflection in U_3 are presented in shaded contour plots. The corresponding frequency parameters for the three-dimensional deformed mode shapes are given below each plot. These diagrams express vividly the vibratory motion of the moderately thick skew plate at each normal mode. At $\theta = 15$ deg it is noticed that the first three modes which correspond to antisymmetric thickness modes, exhibit predominant transverse bending motion. Pure surface parallel modes (which correspond to symmetric thickness modes) are found in the fourth and sixth modes of vibration. At a higher skew angle of $\theta = 45$ deg, the surface parallel symmetric thickness modes occur much earlier at the second and fourth vibration sequences. Predominant transverse bending motions are observed in the first, third, fifth, and sixth modes of vibration.

The vibration mode shapes for the *soft* simply supported skew plate of $\theta = 15$ deg as shown in Fig. 4 exhibit very similar vibration patterns to that shown in Fig. 2. Except in this case, strong surface parallel motions occur much later at the fifth and sixth modes of vibration. The number of symmetric thickness modes (which correspond to surface parallel motion) and antisymmetric thickness modes (which correspond to bending motion) are well distributed for the *soft* simply supported skew plate with $\theta = 45$ deg as shown in Fig. 5. These mode shapes demonstrate that the surface parallel symmetric thickness modes are significant in the vibration of thick skew plates. They become dominant in the lower vibration spectrum as the skew angle and thickness of plate increase.

5 Conclusions

An approximate procedure for three-dimensional elasticity solutions to free vibration of simply supported thick skew plates has been presented. The solution procedure was developed on the basis of a linear, small-strain, three-dimensional elasticity theory which is capable of overcoming several inherent numerical difficulties in the modelling of thick skew plates, such as, strong singularity at the obtuse corners of a highly skewed plate and the shear locking effect in the analysis of plates with degenerated thickness. The validity of the technique has been demonstrated through direct comparison with the existing data. The convergence test conducted further testifies to the efficiency and numerical stability of the method. To provide better insight into the vibration phenomena of thick skew plates, the method was used to compute both the eigenvalues and vibration mode shapes of moderately thick skew plates having *hard* and *soft* simple support conditions. It was demonstrated through the numerical examples that formulation based on three-dimensional elasticity theory is capable of extracting the full vibration spectrum of thick elastic plates in skew domain.

References

Babuška, I., and Li, L., 1992, "The Problem of Plate Modelling: Theoretical and Computational Results," *Computer Methods in Applied Mechanics and Engineering,* Vol. 100, pp. 249–273.

Babuška, I., and Pitkäranta, J., 1990, "The Plate Paradox for Hard and Soft Simple Support," *SIAM Journal of Math. Anal.,* Vol. 21, pp. 551–576.

Chihara, T. S., 1978, *An Introduction to Orthogonal Polynomials,* Gordon and Breach, New York.

Durvasula, S., 1968, "Natural Frequencies and Modes of Skew Membranes," *Journal of the Acoustical Society of America,* Vol. 44, pp. 1636–1646.

Fromme, J. A., and Leissa, A. W., 1970, "Free Vibration of the Rectangular Parallelepipeds," *Journal of the Acoustical Society of America,* Vol. 48, pp. 290–298.

Gorman, D. J., 1991, "Accurate Analytical Type Solutions for the Free Vibration of Simply Supported Parallelogram Plates," ASME JOURNAL OF APPLIED MECHANICS, Vol. 58, pp. 203–208.

Hung, K. C., Liew, K. M., and Lim, M. K., 1994, "Three-Dimensional Elasticity Solutions to Vibration of Cantilevered Skewed Trapezoids," AIAA Journal, Vol. 32, pp. 2080–2089.

Hutchinson, J. R., and Zillmer, S. D., 1983, "Vibration of a Free Rectangular Parallelepiped," ASME JOURNAL OF APPLIED MECHANICS, Vol. 50, pp. 123–130.

Leissa, A. W., and Zhang, Z. D., 1983, "On the Three-Dimensional Vibrations of the Cantilevered Rectangular Parallelepiped," *Journal of the Acoustical Society of America,* Vol. 73, pp. 2013–2021.

Liew, K. M., Hung, K. C., and Lim, M. K., 1994, "Three-Dimensional Vibration of Rectangular Plates: Variance of Simple Support Conditions and Influence of In-Plane Inertia," *International Journal of Solids and Structures,* Vol. 31, pp. 3233–3247.

Liew, K. M., Hung, K. C., and Lim, M. K., 1995, "Three-Dimensional Vibration of Rectangular Plates: Effects of Thickness and Edge Constraints," *Journal of Sound and Vibration,* Vol. 182, pp. 709–727.

Liew, K. M., and Lam, K. Y., 1990, "Application of Two-Dimensional Orthogonal Plate Function to Flexural Vibration of Skew Plates," *Journal of Sound and Vibration,* Vol. 139, pp. 241–252.

Liew, K. M., Xiang, Y., Wang, C. M., and Kitiporchai, S., 1993, "Vibration of Thick Skew Plate Based on Mindlin Shear Deformation Plate Theory," *Journal of Sound and Vibration,* Vol. 168, pp. 39–69.

Srinivas, S., Rao, C. V., and Rao, A. K., 1970, "An Exact Analysis for Vibration of Simply Supported Homogeneous and Laminated Thick Rectangular Plates," *Journal of Sound and Vibration,* Vol. 12, pp. 187–199.

Downloaded 04 May 2010 to 171.66.16.28. Redistribution subject to ASME license or copyright; see http://www.asme.org/terms/Terms_Use.cfm

B. Wang
School of Mechanical and Production Engineering, Nanyang Technological University, Singapore 2263
Mem. ASME

T. X. Yu
Mem. ASME.

S. R. Reid
Fellow ASME.

Department of Mechanical Engineering, UMIST, P.O. Box 88, Sackville Street, Manchester, M60 1QD, U.K.

Out-of-Plane Impact at the Tip of a Right-Angled Bent Cantilever Beam

The present paper provides an analysis of the response of a right-angled bent cantilever beam subjected to an out-of-plane impulsive load (i.e., suddenly imposed velocity) applied to concentrated mass at its tip. If T_0 *and* M_0 *are the fully plastic torque and bending moment, respectively, of the cross section, it is shown that for the case* $T_0/M_0 < 1$*, a double hinge mechanism is required, with a pure bending hinge in the first segment of the beam and a combined bending-torsion hinge in the second segment. The history of deformation is described following impartation of the load.*

1 Introduction

Recently, solutions have been achieved for a bent cantilever subjected to an out-of-plane *force pulse,* i.e., a dynamic constant force of finite duration applied at its tip (Hua et al., 1988; Reid et al., 1994a, 1994b). These problems were solved in an effort to understand the dynamic failure mechanisms of components, such as pipes during pipe-whip in a high pressure piping system. They involve a generalization of plastic hinges, which were first introduced in dynamic problems by Lee and Symonds (1952), to situations in which combined bending and torsion occurs. It was shown by Wang (1991) that for a right-angled bent cantilever with $T_0/M_0 < 1$ subjected to a pulse loading, a double-hinge mechanism is required with a pure bending hinge in the first segment of the beam and a combined bending and torsion one in the second segment. After the force is removed, both hinges travel towards the bend and the pure bending one becomes inactive, then the bending-torsion hinge travels to the beam root. Finally the beam ceases to move after a rotation about the root.

Martin (1964) examined the out-of-plane *impulsive loading* (impact by a moving mass) of a right-angled bent cantilever with $T_0/M_0 = 1$. It was shown that a pure bending hinge forms at the tip and moves towards the corner. It then crosses the corner and becomes a pure torsion hinge and finally arrives at the beam root. The response was almost identical to that of an equivalent straight beam solved by Parkes (1955) which is governed by a single hinge mechanism. Martin's work was a special case. For most cross sections used in practice, the fully plastic torque T_0 is smaller than the fully plastic bending moment M_0. For example, for circular cross section or circular tubular cross section, $T_0/M_0 = \pi/2\alpha$, where $\alpha = 2$ or $\sqrt{3}$ when the Tresca or von Mises yield criterion is applied, respectively. Thus $T_0/M_0 = 0.785$ or 0.907, respectively. In the case of a square cross section, $T_0/M_0 = 4/3\alpha$, i.e., $T_0/M_0 = 0.770$ if von Mises yield criterion is adopted. More details on this ratio can be found in Table 6.2 (p. 234) of the book by Stronge and Yu (1993). The present paper provides an analysis of the response of a right-angled bent cantilever beam with $T_0/M_0 < 1$ subjected to an out-of-plane impact. A double-hinge mechanism is developed with a pure bending hinge in the first segment of the beam and a combined bending-torsion hinge in the second segment. Both hinges travel along the beam segments and show three different transient phases. The influence of the magnitude of the tip mass and the energy dissipated in the beam are also discussed.

2 Theoretical Model

Consider a right-angled bent cantilever struck by a rigid mass G at its tip moving with a speed of V_0, as shown in Fig. 1. If the impact duration is very short and the rigid mass adheres to the beam after the impact, the loading pulse may be idealized as impulsive. The beam segment lengths, mass per unit length, and the fully dynamic plastic bending moment and torque are denoted by L_1, L_2, μ, M_0, and T_0, respectively.

Assuming that the beam is rigid, perfectly plastic with a uniform cross section and the deflection is small, the response of the beam can be described by a double-hinge mechanism. A pure bending hinge initially forms at tip A and a combined bending-torsion hinge forms in the second segment of the beam. This is due to the fact that when an initial hinge forms at tip A where the beam is struck, a single hinge mode would leave segment CB under a pure torsion state with a torque equal to M_0. For beams with $M_0 > T_0$, this is inadmissible. Therefore as well as a pure bending hinge in AC, a combined bending-torsion hinge is required in CB. Both hinges will move along the beam segments. There is no stationary hinge in this case.

Figure 2 shows the free-body diagram of the bent cantilever under a double-hinge mechanism. Using $\dot{\vartheta}_1$, $\dot{\vartheta}_2$, and $\dot{\varphi}_2$ to denote the relative angular velocities due to bending and torsion at the plastic hinges, and if x_1 and x_2 are the positions of hinges H_1 and H_2 measured from A and C, respectively, the governing equations for segment H_1CH_2 are,

$$\mu \frac{(L_1 - x_1)^2}{2} \dot{\varphi}_2 - \mu(L_1 - x_1)x_2\ddot{\vartheta}_2 - \mu(L_1 - x_1)\dot{x}_2\dot{\vartheta}_2 - \mu \frac{x_2^2}{2} \ddot{\vartheta}_2 - \mu x_2\dot{x}_2\dot{\vartheta}_2 = 0, \quad (1)$$

$$M_0 - T_2 = \mu \frac{(L_1 - x_1)^3}{3} \dot{\varphi}_2 - \mu \frac{(L_1 - x_1)^2}{2} x_2\ddot{\vartheta}_2 - \mu \frac{(L_1 - x_1)^2}{2} \dot{x}_2\dot{\vartheta}_2, \quad (2)$$

Contributed by the Applied Mechanics Division of THE AMERICAN SOCIETY OF MECHANICAL ENGINEERS for publication in the ASME JOURNAL OF APPLIED MECHANICS.

Discussion on this paper should be addressed to the Technical Editor, Professor Lewis T. Wheeler, Department of Mechanical Engineering, University of Houston, Houston, TX 77204-4792, and will be accepted until four months after final publication of the paper itself in the ASME JOURNAL OF APPLIED MECHANICS.

Manuscript received by the ASME Applied Mechanics Division, Dec. 20, 1993; final revision, June 28, 1994. Associate Technical Editor: F. Y. M. Wan.

Copyright © 1995 by ASME

Downloaded 04 May 2010 to 171.66.16.28. Redistribution subject to ASME license or copyright; see http://www.asme.org/terms/Terms_Use.cfm

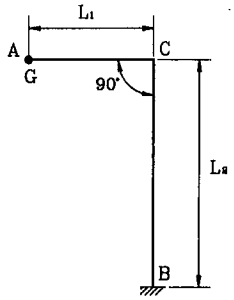


Fig. 1 A right-angled bent cantilever. Impact at *A* into the plane of the figure.

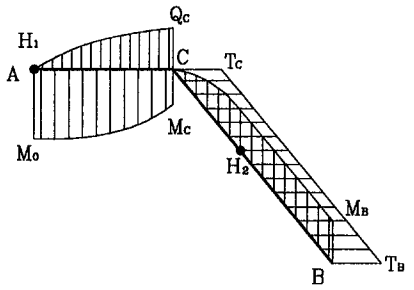


Fig. 3 Distributions of bending moment, torque, and shear force along beam segments at the beginning of the response

and

$$M_2 = \frac{\mu}{6} x_2^3 \ddot{\vartheta}_2 + \frac{\mu}{2} x_2^2 \dot{x}_2 \dot{\vartheta}_2. \tag{3}$$

In this formulation, the rotary inertia of elements of the bent cantilever with respect to the centroidal axis is neglected, and consequently the torque remains constant along each straight segment of the cantilever beam. This approximation is similar to that used in analyzing the dynamic behavior of straight beams where the rotary inertia of a beam element with respect to the neutral axis is usually ignored.

For segment AH_1, we have

$$G(L_1\ddot{\varphi}_2 - x_2\ddot{\vartheta}_2 - \dot{x}_2\dot{\vartheta}_2 + \dot{x}_1 + \dot{\vartheta}_1 + x_1\dot{\vartheta}_1) + \mu\left(\left(L_1 - \frac{x_1}{2}\right)x_1\ddot{\varphi}_2 - x_1x_2\ddot{\vartheta}_2 - x_1\dot{x}_2\dot{\vartheta}_2 + \frac{x_1^2}{2}\ddot{\vartheta}_1 + x_1\dot{x}_1\dot{\vartheta}_1\right) = 0, \tag{4}$$

and

$$\mu x_1^2\left[\left(\frac{L_1}{2} - \frac{x_1}{3}\right)\ddot{\varphi}_2 - \frac{x_2}{2}\ddot{\vartheta}_2 - \frac{1}{2}\dot{x}_2\dot{\vartheta}_2 + \frac{x_1}{6}\ddot{\vartheta}_1 + \frac{1}{2}\dot{x}_1\dot{\vartheta}_1\right] = M_0. \tag{5}$$

The yield condition at hinge H_2 is

$$\left(\frac{M_2}{M_0}\right)^2 + \left(\frac{T_2}{T_0}\right)^2 = 1 \tag{6}$$

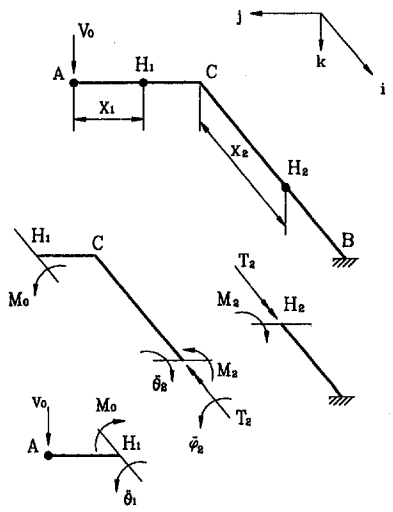


Fig. 2 The free-body diagram for a double-hinge mechanism

and the associated flow rule gives

$$\dot{\varphi}_2 = \left(\frac{M_0}{T_0}\right)^2 \frac{T_2}{M_2}\dot{\vartheta}_2. \tag{7}$$

2.1 Initial Hinge Configuration. If τ is the time after impact, clearly at $\tau = 0$, we have $x_1 = 0$, $\dot{\vartheta}_2 = \dot{\varphi}_2 = 0$ and $V_0 = x_1\dot{\vartheta}_1$. Assuming that after a very short interval of time $\tau_0(=0^+)$, x_1, $\dot{\vartheta}_2$ and $\dot{\varphi}_2$ are all small quantities, Eq. (1) can be rewritten to first order as

$$\frac{L_1^2}{2}\ddot{\varphi}_2 - L_1x_2\ddot{\vartheta}_2 - L_1\dot{x}_2\dot{\vartheta}_2 - \frac{x_2^2}{2}\ddot{\vartheta}_2 - x_2\dot{x}_2\dot{\vartheta}_2 = 0$$

or

$$\frac{d}{d\tau}\left(\frac{L_1^2}{2}\dot{\varphi}_2 - L_1x_2\dot{\vartheta}_2 - \frac{x_2^2}{2}\dot{\vartheta}_2\right) = 0.$$

Thus

$$\frac{L_1^2}{2}\dot{\varphi}_2 - L_1x_2\dot{\vartheta}_2 - \frac{x_2^2}{2}\dot{\vartheta}_2 = A.$$

Since $\dot{\varphi}_2$ and $\dot{\vartheta}_2$ are zero initially, we have $A = 0$. Hence

$$\dot{\varphi}_2 = \frac{2L_1 + x_2}{L_1^2}x_2\dot{\vartheta}_2. \tag{8}$$

Similarly, from Eqs. (2), (3), and (5), we have

$$\frac{L_1^3}{3}\dot{\varphi}_2 - \frac{L_1^2}{2}x_2\dot{\vartheta}_2 = \frac{(M_0 - T_2)\tau_0}{\mu}, \tag{9}$$

$$\frac{x_2^3}{6}\dot{\vartheta}_2 = \frac{M_2\tau_0}{\mu} \quad \text{or} \quad M_2 = \frac{\mu}{6\tau_0}x_2^3\dot{\vartheta}_2 \tag{10}$$

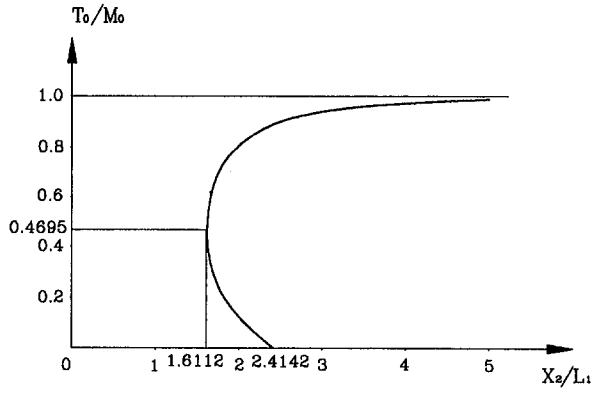


Fig. 4 Initial position of H_2 in CB relative to the length of AC versus ratio T_0/M_0. Beam parameters are listed in Table 1.

Downloaded 04 May 2010 to 171.66.16.28. Redistribution subject to ASME license or copyright; see http://www.asme.org/terms/Terms_Use.cfm

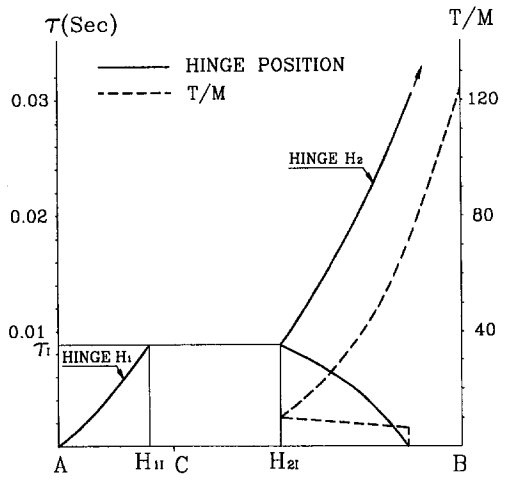


Fig. 5 Hinge position at various time and the ratio T_2/M_2 against hinge position. Beam parameters are listed in Table 1.

and

$$\frac{x_1^3}{6}\dot{\vartheta}_1 = \frac{M_0\tau_0}{\mu}. \tag{11}$$

With $V_0 = x_1\dot{\vartheta}_1$, Eq. (11) gives

$$x_1 = \sqrt{\frac{6M_0\tau_0}{\mu V_0}}. \tag{12}$$

Substituting Eq. (8) into (9) produces

$$T_2 = M_0 - \frac{\mu}{6\tau_0} L_1(L_1 + 2x_2)x_1\dot{\vartheta}_2. \tag{13}$$

With Eqs. (10) and (13), the yield condition and flow rule become

$$\left(\frac{\frac{\mu}{6}x_2^3\dot{\vartheta}_2}{M_0\tau_0}\right)^2 + \left(\frac{M_0\tau_0 - \frac{\mu}{6}L_1(L_1 + 2x_2)x_2\dot{\vartheta}_2}{T_0\tau_0}\right)^2 = 1 \tag{14}$$

and

$$\frac{(2L_1 + x_2)x_2}{L_1^2} = \left(\frac{M_0}{T_0}\right)^2 \frac{M_0\tau_0 - \frac{\mu}{6}L_1(L_1 + 2x_2)x_2\dot{\vartheta}_2}{\frac{\mu}{6}x_2^3\dot{\vartheta}_2}. \tag{15}$$

Equation (15) gives

$$\dot{\vartheta}_2 = \frac{6M_0\tau_0}{\mu x_2\left(\frac{(2L_1 + x_2)x_2^3}{L_1^2}\left(\frac{T_0}{M_0}\right)^2 + L_1(L_1 + 2x_2)\right)} \tag{16}$$

and the yield condition can be rewritten as

$$\left(\frac{x_2^2}{\frac{(2L_1 + x_2)x_2^3}{L_1^2}\left(\frac{T_0}{M_0}\right)^2 + L_1(L_1 + 2x_2)}\right)^2 + \left(1 - \frac{L_1(L_1 + 2x_2)}{\frac{(2L_1 + x_2)x_2^3}{L_1^2}\left(\frac{M_0}{T_0}\right)^2 + L_1(L_1 + 2x_2)}\right)^2 = \left(\frac{T_0}{M_0}\right)^2. \tag{17}$$

Equation (17) gives the initial position of the bending-torsion hinge H_2 in CB measured from bend C. It is noted that the position, x_2, is only dependent on the ratio of T_0/M_0 and the length of AC, L_1. The impulsive velocity V_0 and the rest of beam parameters have no influence. This differs from the pulse loading case (Reid, Wang, and Hua, 1994b) where the pulse magnitude plays an important role in deciding the initial hinge positions. The bending moment and torque distributions in the beam at $\tau = 0$ are shown in Fig. 3.

Table 1 Response under a light striker, $G = 0.1$ kg

V_0 (m/s)	E (Nm)	x_{1f} (m)	E_1 (%)	ϑ_1 (rad)	ϑ_2 (rad)	φ_2 (rad)	δ_A (m)
100	500	0.79	95.9	1.51	0.003	0.07	0.29
150	1125	0.80	95.4	3.39	0.006	0.19	0.62
200	2000	0.80	95.1	6.01	0.011	0.36	1.07

Note: Structural parameters are $M_0 = 316$ Nm, $T_0/M_0 = 0.9$, $\mu = 2.662$ kg/m, $L_1 = 1$ m, $L_2 = 2.5$ m. E is the total energy provided to the system, x_{1f} is the limiting position of H_1 in AC where it becomes inactive at the end of Phase I, E_1 is the energy absorbed by H_1 expressed as a percentage of the total input energy, ϑ_1 is the final rotation at H_1, ϑ_2, and φ_2 are the final rotations at H_2 due to bending and torsion, respectively, and δ_A is the final deflection at tip A.

Figure 4 shows the ratio of the initial position of H_2 to the length of AC versus T_0/M_0. There is a limiting position in CB where hinge H_2 may appear. Calculations show that the limiting position is $1.61L_1$ at $T_0/M_0 = 0.47$. This indicates that the hinge cannot form initially at a position in CB less than a distance of 1.61 times the length of AC from the bend C, whatever the value of the impulsive velocity and the beam parameters.

When the length of CB is shorter than this limiting distance for a particular value of T_0/M_0, H_2 will form at the end of CB, i.e., the root B. Let $x_2 = L_2$ and $\dot{x}_2 = 0$, Eqs. (1) to (3) become

$$\frac{(L_1 - x_1)^2}{2}\ddot{\varphi}_2 - (L_1 - x_1)L_2\ddot{\vartheta}_2 - \frac{L_2^2}{2}\dot{\vartheta}_2 = -Q_B, \tag{18}$$

$$M_0 - T_2 = \frac{\mu}{3}(L_1 - x_1)^3\ddot{\varphi}_2 - \frac{\mu}{2}(L_1 - x_1)^2L_2\ddot{\vartheta}_2 \tag{19}$$

and

$$M_2 = \frac{\mu}{6}L_2^3\ddot{\vartheta}_2. \tag{20}$$

Note that the left side of Eq. (1) is replaced by $-Q_B$, representing the shear force at the root. The rest of the Eqs. (4) to (7) remain unchanged.

It is noted that at $T_0/M_0 = 1$, Eq. (17) implies $x_2 \to \infty$. This indicates a single-hinge mechanism, with only a pure bending hinge H_1 in AC and no hinge in CB. This results in the same solution as that given by Martin (1964). When $T_0/M_0 = 0$, or $M_0 \gg T_0$, we have $\ddot{\vartheta}_2 = 0$, the second hinge will be a pure torsion one and be formed at the bend C and CB undergoes a pure torsion mode.

2.2 Transient Response. The complete response of the beam can be divided into three phases. After the impact, both hinges H_1 and H_2 move towards C. H_1 then becomes inactive before reaching C. In Phase II, hinge H_2 reverses its direction and travels towards root B. Finally, in Phase III, the whole

Table 2 Response under a heavy striker, $G = 2.0$ kg

V_0 (m/s)	E (Nm)	x_{1f} (m)	E_1 (%)	ϑ_1 (rad)	ϑ_2 (rad)	φ_2 (rad)	δ_A (m)
5	25	0.76	35.3	0.03	0.001	0.06	0.07
10	100	0.76	36.3	0.12	0.002	0.22	0.27
15	225	0.75	36.7	0.26	0.005	0.50	0.59

Note: see Table 1.

Downloaded 04 May 2010 to 171.66.16.28. Redistribution subject to ASME license or copyright; see http://www.asme.org/terms/Terms_Use.cfm

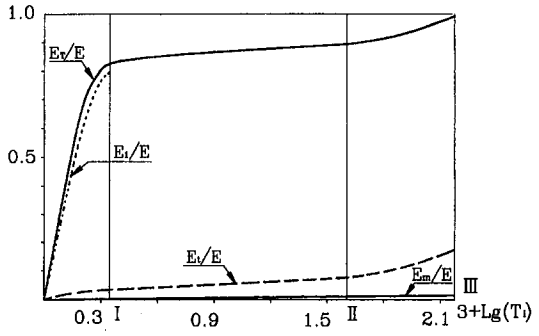


Fig. 6 Ratio of energies dissipated to the total input energy E with respect to time, G = 0.3 kg and V_0 = 10 m/s. E_T is the total energy ratio dissipated; E_1 the energy dissipated at H_1; E_t and E_m the energies dissipated at H_2 due to torsion and bending; I, II, and III pertain to phase I, II, and III, respectively. Beam parameters are M_0 = 316 Nm, T_0/M_0 = 0.9, μ = 2.662 kg/m, L_1 = 1 m and L_2 = 2.5 m.

beam rotates about B as a rigid body until all the remaining kinetic energy is dissipated.

Phase I. The governing Eqs. (1) to (5) can be adapted for numerical solution of Phase I.

$$\dot{x}_2 = \frac{3}{\dot{\vartheta}_2(L_1 - x_1 + x_2)} \times \left(\frac{M_2}{\mu x_2^2}(L_1 - x_1 + x_2) - \frac{M_0 - T_2}{\mu(L_1 - x_1)}\right), \quad (22)$$

$$\ddot{\vartheta}_2 = \frac{6M_2 - 3\mu x_2^2 \dot{x}_2 \dot{\vartheta}_2}{\mu x_2^3}, \quad (23)$$

$$\ddot{\varphi}_2 = \frac{3(M_0 - T_2)}{\mu(L_1 - x_1)^3} + \frac{3x_2\ddot{\vartheta}_2}{2(L_1 - x_1)} + \frac{3\dot{x}_2\dot{\vartheta}_2}{2(L_1 - x_1)}, \quad (24)$$

$$\ddot{\vartheta}_1 = -\ddot{\varphi}_2 - \frac{12M_0(G + \mu x_1)}{\mu x_1^3(4G + \mu x_1)}, \quad (25)$$

$$\dot{x}_1 = \frac{1}{\dot{\vartheta}_1}\left(\frac{2M_0}{\mu x_1^2} - \left(L_1 - \frac{2}{3}\right)\ddot{\varphi}_2 + x_2\ddot{\vartheta}_2 + \dot{x}_2\dot{\vartheta}_2\frac{1}{3}x_1\ddot{\vartheta}_1\right). \quad (26)$$

Let $T_2/T_0 = \sin\sigma$ and $M_2/M_0 = \cos\sigma$, the yield condition (6) is satisfied automatically. From the flow rule, we have

$$\sigma = \tan^{-1}\left(\frac{T_0\dot{\varphi}_2}{M_0\dot{\vartheta}_2}\right). \quad (27)$$

Given the value of τ_0, say $\tau_0 = 10^{-6}$ sec, the initial values of x_1, $\dot{\vartheta}_1$, $\dot{\vartheta}_2$, $\dot{\varphi}_2$, M_2, and T_2 can all be calculated. A fourth-order Runge-Kutta approach may be employed to solve the above equations. At the end of each time step, σ (i.e., M_2 and T_2) is updated.

This phase finishes when the angular velocity of H_1 becomes zero, i.e., $\dot{\vartheta}_1 = 0$. The energy dissipated during Phase I is $M_0\vartheta_{1I}$ by H_1 and $\int_0^{\tau_I}(M_2\dot{\vartheta}_2 + T_2\dot{\varphi}_2)d\tau$ by H_2, where τ_I denotes the time at the end of Phase I.

Phase II. When hinge H_1 becomes inactive, the combined bending-torsion hinge H_2 remains as the only plastic hinge in the system. The governing equations of this phase are given as follows. Derivation of these equations are similar to those in Phase I.

$$G(L_1\ddot{\varphi}_2 + x_2\ddot{\vartheta}_2 + \dot{x}_2\dot{\vartheta}_2) + \mu\left(L_1 + \frac{1}{2}x_2\right)x_2\ddot{\vartheta}_2 + \frac{\mu}{2}L_1^2\ddot{\varphi}_2 + \mu(L_1 + x_2)\dot{x}_2\dot{\vartheta}_2 = 0, \quad (28)$$

$$G(L_1\ddot{\varphi}_2 + x_2\ddot{\vartheta}_2 + \dot{x}_2\dot{\vartheta}_2)L_1 + \frac{\mu}{3}L_1^3\ddot{\varphi}_2 + \frac{\mu}{2}L_1^2x_2\ddot{\vartheta}_2 + \frac{\mu}{2}L_1^2\dot{x}_2\dot{\vartheta}_2 = -T_2, \quad (29)$$

$$\frac{\mu}{6}x_2^3\ddot{\vartheta}_2 + \frac{\mu}{2}x_2^2\dot{x}_2\dot{\vartheta}_2 = M_2. \quad (30)$$

The yield condition and flow rule remain the same as those in Phase I.

The above equations can be rewritten into a form suitable for numerical solutions,

$$\dot{x}_2 = \frac{T_2\left(G + \frac{\mu}{2}L_1\right) - \mu\left(G\left(\frac{L_1}{3} + \frac{x_2}{2}\right) + \frac{\mu}{6}\left(\frac{L_1}{2} + x_2\right)L_1\right)x_2\ddot{\vartheta}_2}{\mu\left(G\left(\frac{L_1}{3} + x_2\right) + \frac{\mu}{3}\left(\frac{L_1}{4} + x_2\right)L_1\right)}, \quad (31)$$

$$\ddot{\vartheta}_2 = \frac{6M_2 - 3\mu x_2^2\dot{x}_2\dot{\vartheta}_2}{\mu x_2^3}, \quad (32)$$

$$\ddot{\varphi}_2 = -\frac{G + \mu\left(L_1 + \frac{x_2}{2}\right)}{\left(G + \frac{\mu}{2}L_1\right)L_1}x_2\ddot{\vartheta}_2 - \frac{G + \mu(L_1 + x_2)}{\left(G + \frac{\mu}{2}L_1\right)L_1}\dot{x}_2\dot{\vartheta}_2. \quad (33)$$

The solution procedure is similar to that in the previous phase. Initial values of all the variables are obtained from the end of Phase I. Note that in the above equations for Phase II, the positive direction of $\dot{\vartheta}_2$ is defined as being opposite to that in Phase I.

When hinge H_2 reaches root B, the motion of the whole cantilever becomes a rigid-body rotation about the root.

Phase III. With subscript "B" denoting the variables at B, the equations of motion of ACB can be expressed as follows:

$$G(L_1\ddot{\varphi}_B + L_2\ddot{\vartheta}_B) + \mu\left(L_1 + \frac{1}{2}L_2\right)L_2\ddot{\vartheta}_B + \frac{\mu}{2}L_1^2\ddot{\varphi}_B = -Q_B, \quad (34)$$

$$G(L_1\ddot{\varphi}_B + L_2\ddot{\vartheta}_B)L_1 + \frac{\mu}{2}L_1^2L_2\ddot{\vartheta}_B + \frac{\mu}{3}L_1^3\ddot{\varphi}_B = -T_B, \quad (35)$$

$$G(L_1\ddot{\varphi}_B + L_2\ddot{\vartheta}_B)L_2 + \mu\left(L_1 + \frac{1}{3}L_2\right)L_2^2\ddot{\vartheta}_B + \frac{\mu}{2}L_1L_2^2\ddot{\varphi}_B = -M_B. \quad (36)$$

The flow rule and yield condition at B are

$$\dot{\varphi}_B = \left(\frac{M_0}{T_0}\right)^2\frac{T_B}{M_B}\dot{\vartheta}_B, \quad (37)$$

$$\left(\frac{M_B}{M_0}\right)^2 + \left(\frac{T_B}{T_0}\right)^2 = 1. \quad (38)$$

The above equations can be rearranged and solved numerically by a standard Runge-Kutta method.

Downloaded 04 May 2010 to 171.66.16.28. Redistribution subject to ASME license or copyright; see http://www.asme.org/terms/Terms_Use.cfm

$$\ddot{\vartheta}_B = \frac{M_0 \cos\sigma_B\left(G + \frac{\mu}{3}L_1\right)L_1 - T_0 \sin\sigma_B\left(G + \frac{\mu}{2}L_2\right)L_2}{\left(\left(G + \frac{\mu}{2}L_1\right)\left(G + \frac{\mu}{2}L_2\right) - \left[G + \mu\left(L_1 + \frac{1}{3}L_2\right)\right]\left(G + \frac{\mu}{3}L_1\right)\right)L_2^2 L_1}, \quad (39)$$

$$\ddot{\varphi}_B = \frac{T_0 \sin\sigma_B\left[G + \mu(L_1 + \frac{\mu}{3}L_2)\right]L_2 - M_0 \cos\sigma_B\left(G + \frac{\mu}{2}L_1\right)L_1}{\left(\left(G + \frac{\mu}{2}L_1\right)\left(G + \frac{\mu}{2}L_2\right) - \left[G + \mu\left(L_1 + \frac{1}{3}L_2\right)\right]\left(G + \frac{\mu}{3}L_1\right)\right)L_1^2 L_2}, \quad (40)$$

$$\sigma_B = \tan^{-1}\left(\frac{T_0\dot{\varphi}_B}{M_0\dot{\vartheta}_B}\right). \quad (41)$$

When $\dot{\vartheta}_B = \dot{\varphi}_B = 0$, the whole beam ceases to move.

3 Numerical Solutions

Numerical solutions have been carried out for all three phases of the response for different values of impulsive loading. The energy balance has been examined at the end of each phase by checking that the total energy supplied to the cantilever is equal to the sum of kinetic energy and the energy dissipated in the plastic hinges during the response. Checks were also made to verify that the yield conditions were not violated in each segment and during each phase of the response. In the calculation the structural parameters of the beam were taken as $M_0 = 316$ Nm, $T_0/M_0 = 0.9$, $\mu = 2.662$ kg/m, $L_1 = 1$ m and $L_2 = 2.5$ m.

Figure 5 shows the variations of hinge positions and values of T_2/M_2 at H_2 for a typical case with $V_0 = 100$ m/s and $G = 0.1$ kg. It shows that immediately after the impact, both hinges move towards the bend, and hinge H_1 becomes inactive before it reaches there, then H_2 moves backwards and arrives at B. The value of T_2/M_2 increases while H_2 travels towards the root B, indicating that torsion becomes more and more dominant in the later stages of the response.

Calculations show that the responses under a light striker and a heavy striker differ significantly from each other. Under a light striker, as shown in Table 1 where $G = 0.1$ kg, more than 90 percent of the input energy is dissipated at H_1 in Phase I, indicating a severe local bending deformation over the beam portion close to the tip. The rest of the beam bears little deformation.

Table 2 gives the results under a heavy and slow striker where $G = 2$ kg. In contrast with the light striker case, most of the energy is dissipated in Phase III at the root hinge, i.e., the main response is a root rotation.

The above results are consistent with Parkes' findings (1955) where the value of $G/2\mu L$ controls the response mode of a straight beam under a transverse impact by a striker. Tables 1 and 2 also show that striking velocity has little influence on both the response mode and the limiting position of H_1 in AC where the pure bending hinge becomes inactive. In both cases, it is shown that the root rotation phase is almost a pure torsion one, this agrees well with the observation of some full-scale pipe whip tests carried out by Reid (1992) which have shown that the rotation at the root due to torsion (about the longitudinal axis of the second segment) is far more severe than that due to bending, indicating that for a heavy striker case, the main deformation is a torsional one.

Figure 6 shows how the energy dissipation occurs as a function of time for $G = 0.3$ kg and $V_0 = 10$ m/s. As G is relatively light, most of the input energy is dissipated in AC during Phase I.

4 Discussion and Conclusions

The response of a bent cantilever with a bend angle equal to $\pi/2$ subjected to an out-of-plane impact has been analyzed. A double-hinge mechanism has been introduced and a complete solution for the problem has been achieved.

Checks have been made to verify that the yield condition is not violated in each segment of the beam and during each of the response phases examined herein.

A related problem is that of an out-of-plane pulse loading of a bent cantilever. Wang (1991) demonstrated that for beams with $T_0/M_0 < 1$, a similar double-hinge mechanism is required with a pure bending hinge in the first segment of the beam and a combined bending-torsion hinge in the second segment. There are four response phases, viz. a stationary hinge phase during the application of the pulse; a traveling hinge phase with H_1 and H_2 moving towards C; a phase when H_2 travels towards B and, finally, root rotation. One of the main differences between a pulse loading case and an impulsive loading one lies in the initial hinge positions. In a pulse loading case the hinge positions are mainly determined by the magnitude of the dynamic force while in the present problem the details of the loading have no influence at all. The impulsive case also has different response modes depending on the mass of the striker. With a light projectile, the deformation is mainly local bending in the beam portion close to the striking point. For a heavy slow striker, the response is mainly torsional rotation about the beam root. This differs from pulse loading in which about one third of the total energy is dissipated during the application of the pulse (Phase I) whatever the magnitude of the force.

The two problems also show some similarities. Both the pulse loading (when the magnitude is sufficiently high) and impulsive loading cases require a double-hinge mechanism. Traveling hinge phases are also similar with the two hinges first moving towards the bend, then H_1 becoming inactive while H_2 travels to the root. Hinge velocities are not constant. In both cases, while H_2 runs towards B, the value of T_2/M_2 increases rapidly, indicating that torsion becomes the dominant response mode eventually. In both problems the motion concludes with rigid rotation about the root.

The work presented in this paper provides a complete small deflection analysis for rigid, perfectly plastic cantilevers with a right-angled bend subjected to an out-of-plane impulsive loading. The analysis covers the whole range of magnitudes of applied loading and beam geometries with $T_0/M_0 < 1$.

References

Hua, Y. L., Yu, T. X., and Reid, S. R., 1988, "Double-hinge modes in the dynamic response of plastic cantilever beams subjected to step loading," *International Journal of Impact Engineering*, Vol. 7, pp. 401–413.

Downloaded 04 May 2010 to 171.66.16.28. Redistribution subject to ASME license or copyright; see http://www.asme.org/terms/Terms_Use.cfm

Lee, E. H., and Symonds, P. S., 1952, "Large Deformation of Beams Under Transverse Impact," ASME JOURNAL OF APPLIED MECHANICS, Vol. 19, pp. 308–314.

Martin, J. B., 1964, "The plastic deformation of a bent cantilever," Division of Engineering, Brown University, Report N87 GP 1115/15.

Parkes, E. W., 1955, "The permanent deformation of a cantilever struck transversely at its tip," *Proc. Roy. Soc.*, London, Vol. A228, pp. 462–476.

Reid, S. R., 1992, "Pipe motions during pipe whip," Report to National Nuclear Corporation under order No. 30227, University of Manchester Institute of Science and Technology (UMIST).

Reid, S. R., Wang, B., and Yu, T. X., 1994a, "Yield mechanisms of a bent cantilever beam subjected to a suddenly applied constant out-of-plane force," *International Journal of Impact Engineering,* Vol. 16, pp. 49–73.

Reid, S. R., Wang, B., and Hua, Y. L., 1994b, "Triple plastic hinge mechanism for a bent cantilever beam subjected to an out-of-plane tip force pulse of finite duration," *International Journal of Impact Engineering,* Vol. 16, pp. 75–93.

Stronge, W. J., and Yu, T. X., 1993, *Dynamic Models of Structural Plasticity,* Springer-Verlag, London.

Wang, B., 1991, "Response of two-dimensional piping systems during pipe whip," Ph.D. Thesis, University of Manchester (UMIST).

Downloaded 04 May 2010 to 171.66.16.28. Redistribution subject to ASME license or copyright; see http://www.asme.org/terms/Terms_Use.cfm

Three-Dimensional Frictional Rigid-Body Impact

V. Bhatt

Jeff Koechling

Sibley School of Mechanical and Aerospace Engineering, Cornell University, Ithaca, NY 14853-7501

We present an analysis of the rigid-body model for frictional three-dimensional impacts, which was originally studied by Routh. Using Coulomb's law for friction, a set of differential equations describing the progress and outcome of the impact process for general bodies can be obtained. The differential equations induce a flow in the tangent velocity space for which the trajectories cannot be solved for in a closed form, and a numerical integration scheme is required. At the point of sticking, the numerical problem becomes ill-conditioned and we have to analyze the flow at the singularity to determine the rest of the process. A local analysis at the point of sticking provides enough information about the global nature of the flow to let us enumerate all the possible dynamic scenarios for the sliding behavior during impact. The friction coefficient, and the mass parameters at the point of contact, determine the particular sliding behavior that would occur for a given problem. Once the initial conditions are specified, the possible outcome of the impact can then be easily determined.

1 Introduction

The general formulation of the rigid-body impact with finite friction was first suggested by Routh (1877), who developed a geometrical representation in the impulse space for planar impact, and solved it using simple algebraic equations. Routh noticed that depending on the mass parameters and the initial velocity, the contact point could slide continuously, slide followed by pure rolling, or slide followed by sliding in the reverse direction. Wang and Mason (1992) extended Routh's graphical technique and used it to model impact of bodies constrained to move in a plane.

Whittaker (1904) used a different approach by considering planar impact as a finite time process for which the contact conditions remain unchanged during impact. Kane (1985) pointed out an inconsistency in Whittaker's model by showing that if the direction of slip reversed during impact, it could result in an energy increase. By allowing for a changing contact condition as in Routh's work, Keller (1986) noted that some inconsistencies in Whittaker's model could be avoided. Although allowing for changing contact conditions removed the problem of energy increase during impact, Stronge (1990) showed the inconsistency that for purely elastic impacts, there could still be finite energy dissipation in the normal mode. To avoid it, he suggested an energetically consistent definition for the coefficient of restitution.

Brach (1991) suggested a purely algebraic formulation which requires that the parametric relationship of the ratio of the normal to the tangential impulse be obtained experimentally or by using energy constraints.

Routh (1877) developed the equations of motion for frictional impacts in three dimensions, and found that apart from special cases there was no closed-form solution, and that the direction of sliding changes continuously except for a finite number of invariant directions.

More recently, Stronge (1993) studied the swerve behavior for the specific case of impact of a spherical pendulum against a rough half-space using the general equations for three-dimensional collisions.

Batlle and Condomines (1991) presented a detailed study of frictional collisions in multibody systems. They looked at the hodographs of the sliding velocity and present conditions on the friction coefficient that determines reachability of the point of sticking. We follow a different approach than their work and get similar conditions on reachability that depend on both the friction coefficient and the mass parameters. In addition to this we are also able to predict the qualitative behavior of the solution to the equations of motion.

We use the three-dimensional rigid-body model with friction, and get a classification of all the possible sliding behaviors during impact for any general body. Since the direction of sliding depends on the net accumulated impulse at that instant, the impact process is described by a set of differential equations. The solution to these differential equations, referred to as a "flow" in the velocity space, defines the progress of the impact.

The differential equations for planar impacts reduce to an algebraic form, and can be easily solved. For three-dimensional impacts, there is no closed-form solution, and numerical integration is required. Although the equations require a numerical solution, using ideas from dynamical systems theory, qualitative properties of the sliding behavior can be obtained, and the system parameters linked to the behavior of the solution.

A singularity in the flow occurs at the point of sticking, where the direction of sliding is not defined. For Coulomb's model of friction, the frictional impulse increment becomes ill-defined, and any numerical scheme breaks down in the neighborhood of this point. We unfold the singularity in the velocity space and get analytical results which can be used to guide the numerical integration as the point of sticking is reached, making the integration of the equations defining the impact process more robust.

The analysis is also used to classify all the possible flow patterns for the sliding velocity. Given the initial contact velocity, the mass parameters and the contact interface material properties, we can analytically predict the qualitative behavior of the impact. Determination of the qualitative behavior a priori leads to a better understanding of the process and gives an analytical tool to explore the sensitivity to initial conditions that certain configurations and initial conditions might cause. Some preliminary results from this paper have been reported in Bhatt and Koechling (1993).

Contributed by the Applied Mechanics Division of THE AMERICAN SOCIETY OF MECHANICAL ENGINEERS for publication in the ASME JOURNAL OF APPLIED MECHANICS.

Discussion on this paper should be addressed to the Technical Editor, Professor Lewis T. Wheeler, Department of Mechanical Engineering, University of Houston, Houston, TX 77204-4792, and will be accepted until four months after final publication of the paper itself in the ASME JOURNAL OF APPLIED MECHANICS.

Manuscript received by the ASME Applied Mechanics Division, Nov. 17, 1993; final revision, May 17, 1994. Associate Technical Editor: E. J. Haug, Jr.

Copyright © 1995 by ASME

Downloaded 04 May 2010 to 171.66.16.28. Redistribution subject to ASME license or copyright; see http://www.asme.org/terms/Terms_Use.cfm

2 Problem Formulation

The assumptions used for rigid-body impact are that the impulsive forces are infinitely larger than the gravitational, centrifugal, or Coriolis forces. The effect of finite forces is negligible over the infinitesimal time duration of impact. There is ideal point contact, with no impulsive moments, and restitution occurs only in the direction normal to the impacting surfaces.

Equation of Motion. We choose the coordinate system shown in Fig. 1, where the z-axis is normal to the contact interface, and the x and y-axes form the tangent sliding plane. The equations of motion during impact can be put in the form of the following impulse-momentum change relation, which is essentially the same set of equations as developed by Routh (1877).

$$\begin{aligned} v_x &= v_{x0} + a_{11}P_x + a_{12}P_y + a_{13}P_z \\ v_y &= v_{y0} + a_{21}P_x + a_{22}P_y + a_{23}P_z \\ v_z &= v_{z0} + a_{31}P_x + a_{32}P_y + a_{33}P_z \end{aligned} \tag{1}$$

where v_x, v_y, v_z is the relative velocity of the impacting surfaces, and P_x, P_y, P_z the net accumulated impulse. The coefficients a_{ij} refer to the elements of the inverse mass matrix at the point of contact, which being symmetric implies that $a_{ij} = a_{ji}$. The subscript $_0$ refers to the initial value of the contact velocity.

Friction. We use isotropic Coulomb friction, with the coefficient of friction μ. The differential of the tangential impulse bears the same ratio to the differential of the normal impulse as the tangential force to the normal force:

$$\frac{dP_x}{dP_z} = \frac{dF_x}{dF_z} = -\frac{\mu v_x}{\sqrt{v_x^2 + v_y^2}} \quad \frac{dP_y}{dP_z} = \frac{dF_y}{dF_z} = -\frac{\mu v_y}{\sqrt{v_x^2 + v_y^2}} \tag{2}$$

Restitution. The internal dissipation during impact is modeled by a coefficient of restitution, e, which measures the relative "elasticity" of the body. The particular choice of the coefficient of restitution does not affect the sliding behavior and is used to provide just the termination condition for the impact.

Equation (2), and the impulse-momentum change equations when differentiated with respect to P_z, give us five differential equations defining the rates of change of P_x, P_y, v_x, v_y, v_z. We can integrate the equations to solve for these variables. The model of restitution provides only the limits of integration for P_z, and therefore only the "duration" of the impact process, or equivalently, the length of the flow trajectory, will depend on the particular choice of the restitution model.

3 The Tangent Velocity Space

Direction of the sliding velocity determines the accumulation of tangential impulses, and is thus critical to the evolution of impact. There is a singularity at the point of sticking, which affects the sliding velocity, and therefore its analysis provides useful insights into the impact process.

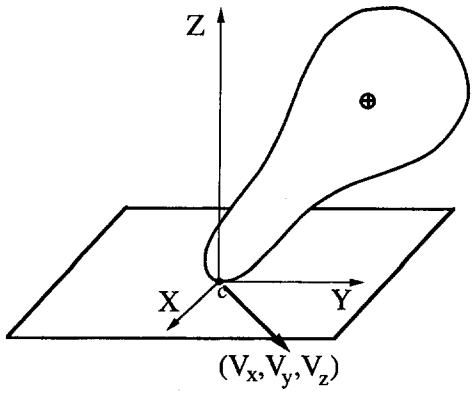


Fig. 1 Coordinate system for the rigid body

3.1 Defining the Flow. Impact is assumed to be instantaneous, and therefore we cannot talk in terms of time rates of change. Since the normal impulse increases monotonically, and remains finite as the impact progresses, we can use it as the "time-like" quantity in terms of which the progress of impact can be expressed.

Differentiating Eq. (1) with respect to P_z and substituting for the impulse rates from Eq. (2), we get the following equations defining the flow for the sliding velocity:

$$\frac{dv_x}{dP_z} = -\frac{\mu a_{11} v_x}{\sqrt{v_x^2 + v_y^2}} - \frac{\mu a_{12} v_y}{\sqrt{v_x^2 + v_y^2}} + a_{13} \tag{3}$$

$$\frac{dv_y}{dP_z} = -\frac{\mu a_{21} v_x}{\sqrt{v_x^2 + v_y^2}} - \frac{\mu a_{22} v_y}{\sqrt{v_x^2 + v_y^2}} + a_{23}. \tag{4}$$

Equations (3)-(4) cannot be solved in a closed form and have to be numerically integrated. The numerical scheme is well behaved as long as the contact point slides. The contact point sticks at $v_x = v_y = 0$, and Eqs. (3)-(4) become ill-defined, leading to numerical instabilities. In this regime, we have to use analytical studies to guide the numerical integration.

We use the "stretching," $d\tau = (\mu/\sqrt{v_x^2 + v_y^2})dP_z$, to define the following modified flow, for which the flow is no longer ill-defined at $v_x = v_y = 0$.

$$\frac{dv_x}{d\tau} = -a_{11}v_x - a_{12}v_y + \frac{a_{13}}{\mu}\sqrt{v_x^2 + v_y^2} \tag{5}$$

$$\frac{dv_y}{d\tau} = -a_{21}v_x - a_{22}v_y + \frac{a_{23}}{\mu}\sqrt{v_x^2 + v_y^2} \tag{6}$$

The change from P_z to τ as the variable along the flow, essentially has the effect of rescaling the normal impulse in a way that pushes the degeneracy at the point of sticking to infinity. In terms of τ it takes in finite accumulation before the degeneracy is reached, and therefore these equations are valid only up to the point where sticking occurs.

3.2 Analyzing the Flow. Flow in the neighborhood of the fixed point of Eqs. (5)-(6) at $v_x = v_y = 0$, can be studied using "blow-up transformations" (Guckenheimer and Holmes, 1983). Changing the equations from Cartesian (v_x, v_y), to polar coordinates (v_r, v_θ),

$$\frac{dv_r}{d\tau} = v_r(-a_{11}\cos^2 v_\theta - (a_{12} + a_{21})\cos v_\theta \sin v_\theta - a_{22}\sin^2 v_\theta + \frac{a_{13}}{\mu}\cos v_\theta + \frac{a_{23}}{\mu}\sin v_\theta) \equiv f \tag{7}$$

$$\frac{dv_\theta}{d\tau} = -a_{21}\cos^2 v_\theta + a_{12}\sin^2 v_\theta + (a_{11} - a_{22})\cos v_\theta \sin v_\theta + \frac{a_{23}}{\mu}\cos v_\theta - \frac{a_{13}}{\mu}\sin v_\theta \equiv g, \tag{8}$$

for which the fixed points are

$$\bar{v}_r = 0, \quad -a_{21}\cos^2 \bar{v}_\theta + a_{12}\sin^2 \bar{v}_\theta + (a_{11} - a_{22})\cos \bar{v}_\theta \sin \bar{v}_\theta + \frac{a_{23}}{\mu}\cos \bar{v}_\theta - \frac{a_{13}}{\mu}\sin \bar{v}_\theta = 0.$$

Their stability can be determined if the determinant and the trace of the linearized system about the fixed points $(\bar{v}_r, \bar{v}_\theta)$ are known. If $c = \cos \bar{v}_\theta$, $s = \sin \bar{v}_\theta$,

Downloaded 04 May 2010 to 171.66.16.28. Redistribution subject to ASME license or copyright; see http://www.asme.org/terms/Terms_Use.cfm

$$\text{Det} = \left.\frac{\partial f}{\partial v_r}\right|_{(\bar{v}_r,\bar{v}_\theta)} \left.\frac{\partial g}{\partial v_\theta}\right|_{(\bar{v}_r,\bar{v}_\theta)} \tag{9}$$

$$\text{Trace} = -a_{11}s^2 + (a_{12} + a_{21})cs - a_{22}c^2 \tag{10}$$

Stability of the Fixed Points.

Lemma 1 *The trace of the linearized flow at the fixed points is always negative.*

The trace, Tr, at the fixed points is given by Eq. (10). The inverse mass matrix has the properties that $a_{11}, a_{22} > 0$, $a_{21} = a_{12}$ and $a_{12}^2 < a_{11}a_{22}$. For the trace to change sign, $Tr = 0$ should have a real solution, which from Eq. (10) requires that $4a_{12}^2 \geq 4a_{11}a_{22}$. However, by the properties of the mass matrix, we know that this is not true. Therefore, the trace never crosses zero for any v_θ. Since $Tr = -a_{22} < 0$ at $s = 0$, the trace is always negative.

Lemma 2 *$Tr^2 \geq 4D$, where Tr is the trace and D the determinant of the linearized flow at the fixed points.*

Using the expressions for the determinant and the trace from Eqs. (9)–(10), after some symbolic manipulations we get

$$Tr^2 - 4D = \left(a_{22}(2s^2 - c^2) + a_{11}(2c^2 - s^2) + 6a_{12}cs - 2\frac{a_{23}}{\mu}s - 2\frac{a_{13}}{\mu}c\right)^2.$$

Since the expression is always ≥ 0, we get $Tr^2 \geq 4D$.

Theorem 1 *The fixed points of the flow given by (7)–(8) can only be either saddle points or node sinks.*

If D is negative, the fixed point is a saddle point (Guckenheimer and Holmes, 1983).

From Lemma 1 we know that the trace is always negative, and Lemma 2 gives that $Tr^2 > 4D$. Therefore, if D is positive, the fixed point is a node sink.

Invariant Directions. Flow in the v_θ direction is independent of v_r, and the invariant directions ($\tilde{v}_\theta$) can be obtained by setting $g = 0$. Any flow that starts on the invariant direction, remains restricted to it for all time. The $\tilde{v}_\theta$ also correspond to the $\bar{v}_\theta$ values for the fixed points.

If we set $\cos\tilde{v}_\theta = 1/\sqrt{1+\alpha^2}$, $\sin\tilde{v}_\theta = \alpha/\sqrt{1+\alpha^2}$ and use $a_{21} = a_{12}$ in the expression $g = 0$ in Eq. (8), we get the following quartic in $\alpha = \tan\tilde{v}_\theta$:

$$\left(\frac{a_{13}^2}{\mu^2} - a_{12}^2\right)\alpha^4 + \left(2a_{12}(a_{22} - a_{11}) - 2\frac{a_{13}a_{23}}{\mu^2}\right)\alpha^3 + \left(\frac{a_{23}^2 + a_{13}^2}{\mu^2} + 2a_{12}^2 - (a_{11} - a_{22})^2\right)\alpha^2 + \left(-2a_{12}(a_{22} - a_{11}) - 2\frac{a_{13}a_{23}}{\mu^2}\right)\alpha + \left(\frac{a_{23}^2}{\mu^2} - a_{12}^2\right) = 0 \tag{11}$$

$$\text{sign}\left(\frac{a_{12}(1-\alpha^2) - (a_{11} - a_{22})\alpha}{a_{23} - a_{13}\alpha}\right) = \text{sign}(\cos\tilde{v}_\theta).$$

The real roots for α correspond to the invariant directions. Figure 2 shows the flow for some representative parameter values in the v_r–v_θ space. The invariant directions are marked by the thick horizontal lines.

Flow Change Directions. Along the flow change directions, $\hat{v}_\theta$, the radial component of the flow changes from being directed inwards to being directed outward. The direction is constant because the sign of $dv_r/d\tau$, given by Eq. (7), is independent of v_r.

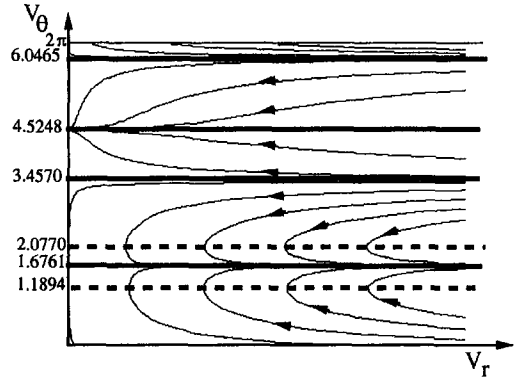


Fig. 2 Flow in the v_r–v_θ plane. The mass parameters used are $a_{11} = 0.8$, $a_{12} = a_{21} = 0$, $a_{22} = 0.05$, $a_{13}/\mu = -0.1$, $a_{23}/\mu = 0.2$. The $\tilde{v}_\theta$, given by Eq. (11), are marked by the solid horizontal lines. $\hat{v}_\theta$ from Eq. (12), are marked by the thick dashed lines.

If we set $\cos\hat{v}_\theta = 1/\sqrt{1+\beta^2}$, $\sin\hat{v}_\theta = \beta/\sqrt{1+\beta^2}$ in $f = 0$ from Eq. (7), we get the following quartic for the flow change directions:

$$\left(\frac{a_{23}^2}{\mu^2} - a_{22}^2\right)\beta^4 + \left(2\frac{a_{13}a_{23}}{\mu^2} - 4a_{12}a_{22}\right)\beta^3 + \left(\frac{a_{13}^2 + a_{23}^2}{\mu^2} - 4a_{12}^2 - 2a_{11}a_{22}\right)\beta^2 + \left(2\frac{a_{13}a_{23}}{\mu^2} - 4a_{12}a_{11}\right)\beta + \left(\frac{a_{13}^2}{\mu^2} - a_{11}^2\right) = 0 \tag{12}$$

$$\text{sign}\left(\frac{a_{11} + 2a_{12}\beta + a_{22}\beta^2}{a_{13} + a_{23}\beta}\right) = \text{sign}(\cos\hat{v}_\theta).$$

For the case shown in Fig. 2, there are only two flow change directions, marked by the thick dashed horizontal lines.

3.3 Possible Flow Patterns. The global behavior of the flow in the velocity space can be determined by counting the number of the invariant directions ($\tilde{v}_\theta$), and the sign of flow along them. Finer details regarding the local maxima or minima of the flow are determined by the number of flow change directions ($\hat{v}_\theta$). Since $\tilde{v}_\theta$ and $\hat{v}_\theta$ are the real roots of quartics, they are finite in number and so we can easily enumerate all the possibilities, which are illustrated in Fig. 3.

Lemma 3 *Between any pair of fixed points of the flow that are node sinks, there has to be a fixed point that is a saddle.*

If there are two node sinks contiguous along the v_θ-axis, the direction of flow on the line at $v_r = 0$ connecting these points cannot be defined, because the flow on $v_r = 0$ has to be locally directed into both. This is only possible if there is another fixed point of either the saddle or a node source type that lies between these two. By Theorem 1, we know that no node sources exist for the flow, and therefore, there has to be a saddle point between any two node sinks.

Four Invariant Directions (4 Real $\tilde{v}_\theta$).

- *Four saddles, zero nodes (2 outward flow; 4 real $\hat{v}_\theta$; Case 0 a).* The four flow change directions given by Eq. (12) are distributed one each between the invariant directions. The point of sticking is unstable and is not reached for any initial velocity. The contact point will keep on sliding throughout the impact process in this case and the tangential velocity will tend towards one of the directions (depending on the initial velocity) on which the flow is directed outward.
- *Three saddles, one node (1 outward flow; 4, 2 real $\hat{v}_\theta$; Case 1 a, b).* The node sink forms the stable, constant approach direction to the point of sticking. Of the three saddle points,

Downloaded 04 May 2010 to 171.66.16.28. Redistribution subject to ASME license or copyright; see http://www.asme.org/terms/Terms_Use.cfm

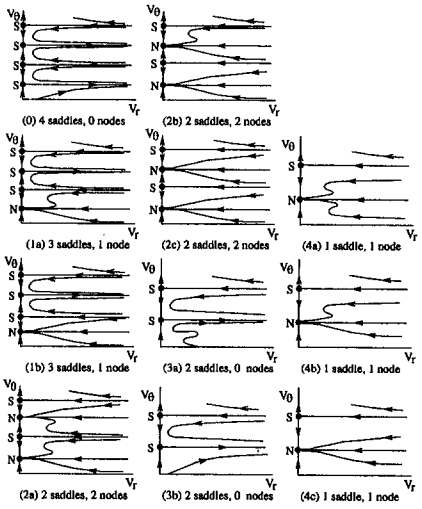


Fig. 3 The possible flow patterns for the sliding velocity. The horizontal lines represent the invariant directions and the sign of flow along them.

the one in the middle forms the unstable direction which takes the flow away from the fixed point. The two other saddle points form the separatrices that partition the initial conditions according to whether they approach the point of sticking along the node sink or move away from it along the unstable saddle direction.

- *Two saddles, two nodes (No outward flow; 4, 2, 0 real $\hat{v}_\theta$; Case 2 a, b, c).* The two saddles partition the velocity space into two regions. The node sinks lie one each in these regions and the flow always approaches the point of sticking along one of the stable node direction depending on which region the initial conditions started in.

Two Invariant Directions (2 Real $\hat{v}_\theta$).

- *Two saddles, zero nodes (1 outward flow; 4, 2 real $\hat{v}_\theta$; Case 3 a, b).* One of the saddles acts as the separatrix and the other as the unstable direction to which all the flow tends and goes away from the point of sticking. The point of sticking can never be reached and the contact point will always keep on sliding.
- *One saddle, one node (no outward flow; 4, 2, 0 real $\hat{v}_\theta$; Case 4 a, b, c).* The saddle acts as the separatrix and for all initial conditions, the flow approaches the point of sticking along the stable node sink direction.

Zero Invariant Directions (0 Real $\tilde{v}_\theta$). It can be analytically shown that this case cannot occur at all.

Just by counting the number of $\tilde{v}_\theta$ and the sign of flow along them, and the number of $\hat{v}_\theta$, we can determine which of the preceding flow patterns a given problem corresponds to. The number of $\tilde{v}_\theta$ and $\hat{v}_\theta$ depends on the real roots of the corresponding quartics, whose coefficients are functions of the mass parameters at the impact point.

In addition to providing information about the possible flow patterns, the analysis can be used to guide the numerical integration through the instability at the point of sticking. By identifying the flow pattern corresponding to the impact configuration, given the initial conditions, we can analytically determine the invariant direction along which the flow would approach the point of sticking.

4 Motion Subsequent to Sticking

The analysis in the tangent velocity space is valid only until the point of sticking is reached. To determine the motion subsequent to sticking, we have to determine whether the contact point remains stuck or sliding resumes along some direction. The same questions have to be answered if the contact point initially has no relative tangential velocity.

If the line of sticking lies inside the local friction cone, friction will always be enough to resist any resumption of sliding and the contact point will remain stuck. Otherwise, sliding will resume and we have to determine the direction along which this happens.

4.1 Point Remains Stuck. The line of sticking is defined by the intersection of the planes, $v_x = 0$ and $v_y = 0$,

$$\left(\frac{(a_{13}a_{22} - a_{12}a_{23})P_z + a_{22}v_{x0} - a_{12}v_{y0}}{(a_{12}a_{21} - a_{11}a_{22})}, \right.$$

$$\left. - \frac{(a_{13}a_{21} - a_{11}a_{23})P_z + a_{21}v_{x0} - a_{11}v_{y0}}{(a_{12}a_{21} - a_{11}a_{22})}, P_z \right).$$

If the angle of the line of sticking from the P_z-axis is less than the angle of the friction cone at that point, friction will always be enough to prevent the contact point from sliding. In terms of the mass parameters, the body sticks if

$$\frac{(a_{23}a_{12} - a_{13}a_{22})^2 + (a_{21}a_{13} - a_{23}a_{11})^2}{(a_{11}a_{22} - a_{12}a_{21})^2} < \mu^2.$$

In this case, pure rolling motion follows sticking and the impact proceeds along the line of sticking in the impulse space.

4.2 Resumption of Sliding. If the line of sticking lies outside the local friction cone, then a tangential impulse larger than that obtainable from the frictional interaction is required to maintain sticking. In that case, sliding will resume in a direction which has to be found analytically. We consider the problem of resumption of sliding in the impulse space by setting $v_{x0} = v_{y0} = 0$ in Eqs. (1) and (2):

$$\frac{dP_y}{dP_x} = \frac{v_y}{v_x} = \frac{a_{21}P_x + a_{22}P_y + a_{23}P_z}{a_{11}P_x + a_{12}P_y + a_{13}P_z}.$$

For a differential step ΔP_z out of the point of sticking, at the incipience of motion the friction constraint for sliding is given by $\mu\Delta P_z = \sqrt{\Delta P_x^2 + \Delta P_y^2}$. To get the invariant direction along which sliding resumes, substitute $\Delta P_y = \gamma \Delta P_x$, where $\tan^{-1}\gamma$ would give the invariant direction. This gives the following equation in γ which can be put in the quartic form:

$$\left(\frac{a_{13}^2}{\mu^2} - a_{12}^2\right)\gamma^4 + \left(2a_{12}(a_{22} - a_{11}) - 2\frac{a_{13}a_{23}}{\mu^2}\right)\gamma^3$$

$$+ \left(\frac{a_{23}^2 + a_{13}^2}{\mu^2} + 2a_{12}^2 - (a_{11} - a_{22})^2\right)\gamma^2$$

$$+ \left(-2a_{12}(a_{22} - a_{11}) - 2\frac{a_{13}a_{23}}{\mu^2}\right)\gamma$$

$$+ \left(\frac{a_{23}^2}{\mu^2} - a_{12}^2\right) = 0 \quad (13)$$

$$\text{sign}\left(-\frac{a_{12}(1 - \gamma^2) - (a_{11} - a_{22})\gamma}{a_{23} - a_{13}\gamma}\right)$$

$$= \text{sign}\,(\cos\,(\tan^{-1}\gamma)).$$

The quartic equation in γ is the same as that for the invariant directions, α, in the velocity space except for the change in sign. This leads to the interesting result that although the friction relation between ΔP_z and ΔP_x, ΔP_y is valid only instantly, the fact that sliding resumes along a direction in the impulse space (which exactly opposes the motion along the invariant direction in the velocity space) makes the flow proceed along the invariant direction even for finite changes in P_x, P_y. The motion of the point of contact will remain on this invariant direction until the impact process terminates. This indirectly implies that the

Downloaded 04 May 2010 to 171.66.16.28. Redistribution subject to ASME license or copyright; see http://www.asme.org/terms/Terms_Use.cfm

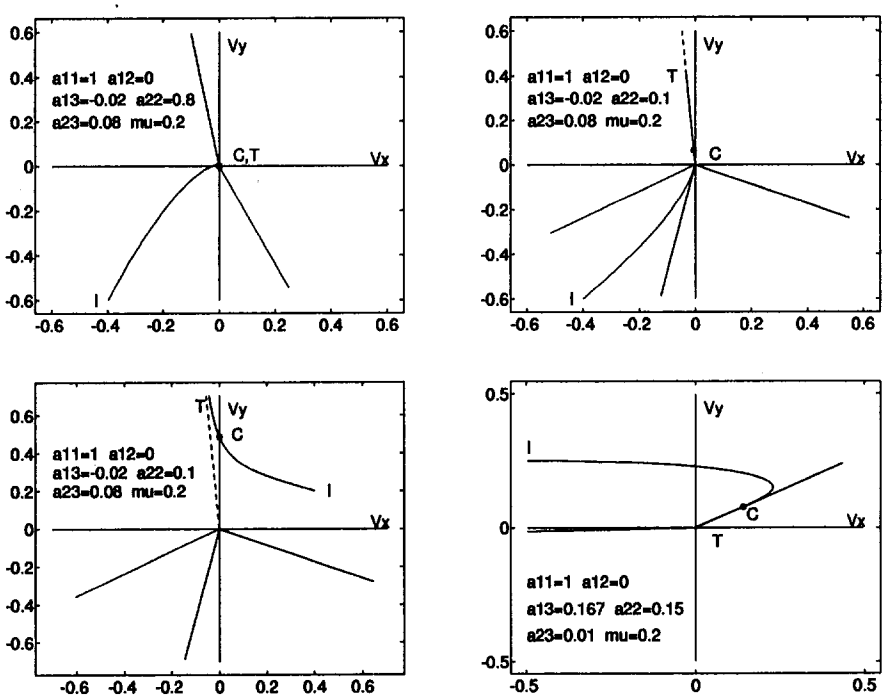


Fig. 4 Examples showing the evolution of the impact for different choices of mass parameters. The invariant directions along which the flow approaches the point of sticking are shown by solid lines and the those along which the flow leaves by the dashed lines. Impact starts at "*I*" and ends at "*T*." The point of maximum compression is marked by a "*C*."

flow will remain on the surface of the local friction cone centered at the point in the impulse space where the line of sticking was reached.

There are four possible solutions for the direction of resumption of sliding motion. Since the motion in the velocity space is also constrained to lie on the same invariant direction, sliding will resume only along a direction that takes the flow in the velocity space away from the point of sticking.

Sliding remains constrained to the invariant direction until the termination of impact, giving a closed-form solution for the flow when sliding resumes after the point of sticking is reached.

5 Examples

Figure 4 shows some example of the evolution of impact in the velocity space to illustrate some of the cases for flow behavior. On the top left hand is the case where there are two invariant directions with one being a saddle and the other a node sink (Case 4c). Since the slope of the line of sticking in the impulse space lies within the friction cone, once the point of sticking is reached, the contact point will keep sticking till the impact terminates.

The top right and bottom left figures are for the same mass parameters but different initial velocities (Case 1b). Of the four invariant directions, three are saddle points and one a node sink. Depending on the initial conditions, the point of sticking may or may not be reached. The bottom right plot illustrates the case when there are local maxima and minima for the flow (Case 4a).

6 Discussion and Summary

Using analytical techniques, we were able to characterized the behavior of the contact point during three-dimensional impact of a rigid body with finite friction. Questions about the qualitative nature of the flow and its behavior in the vicinity of the ill-defined point of sticking can be answered using the results presented. A characterization of all the possible behavior of the contact point is obtained by simply solving for the roots of two quartic equations, that depend only on the mass parameters at the point of contact.

For a general rigid body, we can get the mass parameters and solve for the invariant directions and the flow change directions in the velocity space. Then using the ideas discussed in Section 3.3, we can identify the separatrices and the stable and unstable directions for the flow. The separatrices partition the velocity space into regions from which the flow tends to the eigendirections. Given an initial velocity, this information is enough to determine if the contact point approaches sticking or recedes from it along some eigendirection.

Since the flow patterns depend only on the mass parameters, a natural extension would be to partition the parameter space into regions where different sliding behavior might exist. We are working on such a classification at the present.

Apart from its use as a model for three-dimensional impacts with finite friction, the article suggests that a local analysis using "blow-up transforms" might be useful in simulations where due to some singularity, numerical integration becomes unstable. This is frequently encountered in simulations of incipient motion or cessation of motion problems for systems with Coulomb friction.

Acknowledgments

We thank Andy Ruina for the various discussions from which this work has benefited. We also thank Bruce Donald for discussions about a robust root finder for quartics which was an important part of the numerical simulations. Thanks are also due to Yu Wang for pointing out the work of Batlle and Condomines (1991) to us.

References

Batlle, J. A., and Condomines, A. B., 1991, "Rough collisions in multibody systems," *Mech. Mach. Theory,* Vol. 26, No. 6, pp. 565–577.

Bhatt, V., and Koechling, J. C., 1993, "Modeling three-dimensional frictional rigid body impact: Dealing with degenerate singularities," *Proceedings of the*

Downloaded 04 May 2010 to 171.66.16.28. Redistribution subject to ASME license or copyright; see http://www.asme.org/terms/Terms_Use.cfm

IASTED International Conference on Modeling and Simulation, M. H. Hamza, ed., May, pp. 5–8.

Brach, R. M., 1991, *Mechanical Impact Dynamics: Rigid Body Collisions,* John Wiley and Sons, New York.

Guckenheimer, J., and Holmes, P., 1983, *Nonlinear Oscillations, Dynamical Systems, and Bifurcations of Vector Fields,* Springer-Verlag, New York.

Kane, T. R., and Levinson, D. A., 1985, *Dynamics: Theory and Applications,* McGraw-Hill, New York.

Keller, J. B., 1986, "Impact With Friction," ASME JOURNAL OF APPLIED MECHANICS, Vol. 53, pp. 1–4.

Routh, E. J., 1877, *An Elementary Treatise on the Dynamics of a System of Rigid Bodies,* 3rd ed., MacMillan, London.

Stronge, W. J., 1990, "Rigid Body Collisions with Friction," *Proceedings of the Royal Society of London,* Vol. A431, pp. 168–181.

Stronge, W. J., "Swerve During Impact of Rough Rigid Bodies," ASME JOURNAL OF APPLIED MECHANICS, to appear.

Whittaker, E. T., 1904, *A Treatise on the Analytical Dynamics of Particles and Rigid Bodies,* Cambridge University Press, Cambridge, MA.

Wang, Y., and Mason, M. T., 1992, Two-Dimensional Rigid Body Collisions With Friction," ASME JOURNAL OF APPLIED MECHANICS, Vol. 59, pp. 635–642.

Downloaded 04 May 2010 to 171.66.16.28. Redistribution subject to ASME license or copyright; see http://www.asme.org/terms/Terms_Use.cfm

J. P. McHugh
Assoc. Mem. ASME.

F. C. Bedford

Department of Mechanical Engineering,
University of New Hampshire,
Durham, NH 03824

R. Leighton
Laboratory for Advanced Space Sensing,
Naval Research Laboratory,
Washington, DC 20375

The Limit of Wave Propagation on the Free Surface of a Viscous Fluid

1 Introduction

The exact solution to the linear problem of small amplitude waves on a viscous fluid was considered long ago by Basset (1888). The algebraic expression whose roots are the complex wave speeds is too complicated to evaluate analytically. By considering only high Reynolds number waves, Bassett was able to solve for an approximate dispersion relation. The approximate result shows that the waves at high Reynolds number propagate with the same wavespeed as the irrotational waves, but have a decay rate which depends on the Reynolds number and wave number. Further work on analytic expressions for very large and very small Reynolds numbers is reviewed in Wehausen and Laitone (1960), including some results with a finite bottom.

The roots of the characteristic equation are evaluated below numerically for arbitrary Reynolds numbers. Waves which propagate both upstream and downstream are found for large Reynolds numbers and small wave numbers, similar to the well-known dispersion relation for linear surface waves. However, above a critical wave number for a fixed Reynolds number, the upstream and downstream propagating solutions merge into one solution. There are no propagating solutions to the system for wave numbers above this critical value of wave number. Similarly, for a fixed wave number there is a Reynolds number below which there are no propagating solutions.

Beyond the critical values, the waves decay without propagating. There are two solutions for the decay rate in this region for a given value of wave number and Reynolds number. Similar behavior has been previously found in two-layer flow, Chandrasekhar (1955), and surface waves with infinite depth, Wehausen and Laitone (1960).

A third solution exists for certain wave numbers at small values of Reynolds number. The third solution is a decaying nonpropagating wave, and is an isolated solution which exists only for one or two wave numbers, depending on the Reynolds number.

2 Governing Equations The flow is assumed to be incompressible and two dimensional. The governing equations are the Navier-Stokes equations. Small amplitude waves on the surface of a viscous fluid are considered, hence the Navier-Stokes equations are linearized to get the Stokes equations:

$$\frac{\partial u_i}{\partial t} = -\frac{\partial p}{\partial x_i} + \frac{1}{\mathrm{Re}}\nabla^2 u_i, \tag{1}$$

where u_i are the velocity components, p is the dynamic pressure, Re is the Reynolds number,

$$\mathrm{Re} = \frac{\sqrt{gd^3}}{\nu}, \tag{2}$$

d is the depth of the layer, ν is the kinematic viscosity, and g is the gravitational constant. The continuity equation is

$$\frac{\partial u_j}{\partial x_j} = 0. \tag{3}$$

Employing the streamfunction reduces Eqs. (1) and (3) to

$$\frac{\partial}{\partial t}(\nabla^2\psi) = \frac{1}{\mathrm{Re}}\nabla^4\psi. \tag{4}$$

The solution to (4) is assumed to have the form

$$\psi = \phi(y)e^{i(kx-\omega t)}. \tag{5}$$

Substituting (5) into (4) results in

$$\phi'''' - 2k^2\phi'' + k^4\phi = i\omega\,\mathrm{Re}(k^2\phi - \phi''), \tag{6}$$

which is the familiar Orr-Sommerfeld equation with zero mean-flow. A detailed derivation can be found in Yih (1977). The upper boundary is a free surface for which the linearized boundary conditions are

$$p - \eta - \frac{2}{\mathrm{Re}}\frac{\partial v}{\partial y} + S\frac{\partial^2\eta}{\partial x^2} = 0, \tag{7}$$

$$\frac{\partial u}{\partial y} + \frac{\partial v}{\partial x} = 0, \tag{8}$$

$$\frac{\partial \eta}{\partial t} - v = 0, \tag{9}$$

where η is the elevation of the free surface above its mean value, S is the inverse of the Weber number,

$$S = \frac{T}{\rho g d^2}, \tag{10}$$

and T denotes the surface tension. Equation (7) is the zero normal stress condition, (8) is the zero shear stress condition, and (9) is the kinematic condition.

Contributed by the Applied Mechanics Division of THE AMERICAN SOCIETY OF MECHANICAL ENGINEERS for publication in the ASME JOURNAL OF APPLIED MECHANICS.

Discussion on this paper should be addressed to the Technical Editor, Professor Lewis T. Wheeler, Department of Mechanical Engineering, University of Houston, Houston, TX 77204-4792, and will be accepted until four months after final publication of the paper itself in the ASME JOURNAL OF APPLIED MECHANICS.

Manuscript received by the ASME Applied Mechanics Division, July 13, 1992; final revision, Apr. 5, 1994. Associate Technical Editor: S. A. Berger.

Copyright © 1995 by ASME

Downloaded 04 May 2010 to 171.66.16.28. Redistribution subject to ASME license or copyright; see http://www.asme.org/terms/Terms_Use.cfm

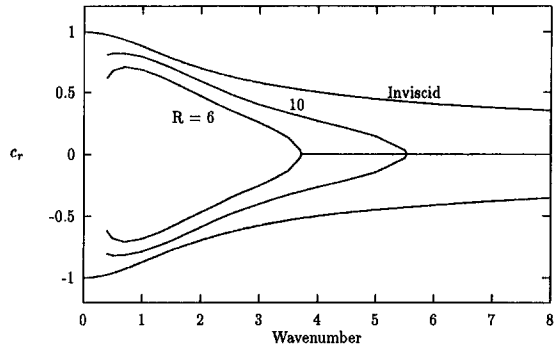


Fig. 1 Wave speed versus wave number for Re = 6.0, 10.0, inviscid flow

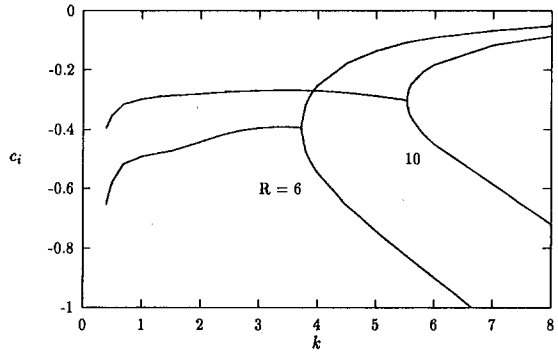


Fig. 2 Damping rate versus wave number for Re = 6.0 and 10.0

The lower boundary is a solid wall with the conditions

$$u = v = 0 \tag{11}$$

on $y = -1$.

The pressure is eliminated from (7) using the streamwise component of (1) and η is eliminated using (9). Then the boundary conditions are reduced as before to obtain

$$\frac{-i\omega}{\mathrm{Re}}(\phi''' - 3k^2\phi') + \omega^2\phi' - k^2(1 + Sk^2)\phi = 0, \tag{12}$$

$$\phi'' + k^2\phi = 0, \tag{13}$$

$$\phi' = \phi = 0, \tag{14}$$

where (12) and (13) hold on $y = 0$, and (14) holds on $y = -1$.

The solution to (6) is $\phi = Ce^{my}$. Equation (6) becomes

$$(i\omega)(k^2 - m^2) - \frac{1}{\mathrm{Re}}(k^4 - 2k^2m^2 + m^4) = 0, \tag{15}$$

which has the four distinct roots

$$m = \pm k, \pm\sqrt{k^2 - i\omega\,\mathrm{Re}}. \tag{16}$$

Since the roots to the characteristic equation are distinct, the general solution to Eq. (6) is

$$\phi(y) = C_1\cosh(ky) + C_2\sinh(ky) + C_3\cosh(my) + C_4\sinh(my). \tag{17}$$

Applying the boundary conditions gives four linearly independent expressions for the constants C_1 through C_4. In matrix form this is

$$\begin{bmatrix} -k^2(1+Sk^2) & A_1 & -k^2(1+Sk^2) & A_2 \\ 2k^2 & 0 & (k^2+m^2) & 0 \\ -\tanh(k) & 1 & -\frac{m}{k}A_3 & \frac{m}{k}A_4 \\ 1 & -\tanh(k) & A_4 & -A_3 \end{bmatrix} \begin{bmatrix} C_1 \\ C_2 \\ C_3 \\ C_4 \end{bmatrix} = \begin{bmatrix} 0 \\ 0 \\ 0 \\ 0 \end{bmatrix} \tag{18}$$

where A_1, A_2, A_3, and A_4 are defined by

$$A_1 = k\left(\frac{3k^2\omega}{\mathrm{Re}} - \omega^2\right) - \frac{i\omega k^3}{\mathrm{Re}},$$

$$A_2 = m\left(\frac{3k^2\omega}{\mathrm{Re}} - \omega^2\right) - \frac{i\omega m^3}{\mathrm{Re}},$$

$$A_3 = \frac{\sinh(m)}{\cosh(k)},$$

$$A_4 = \frac{\cosh(m)}{\cosh(k)}.$$

The determinant of the matrix in (18) is set to zero to determine the complex wavespeed.

3 Results

Basset (1888) obtained (18), but was unable to evaluate it exactly. Bassett discarded some terms in the determinant and found the following approximation:

$$c = \pm\sqrt{\frac{\tanh(k)}{k}} - i\frac{2k}{\mathrm{Re}}, \tag{19}$$

which is accurate only for high Reynolds numbers and moderate wave numbers. The real part of (19) is the wave speed, and is identical to the speed of a wave traveling on an inviscid fluid with infinite depth (Lamb, 1932). The imaginary part of (19) is negative, indicating that the waves always decay with time.

The complex wavespeed, c, has been determined in this paper for the complete determinant in (18) using a numerical technique for finding the roots of an analytic expression (Delves and Lyness, 1967). The root-finding method first calculates the number of zeros of a given analytic complex function inside a closed contour using

$$s_0 = \frac{1}{2\pi i}\int_C \frac{f'(z)}{f(z)}\,dz, \tag{20}$$

where s_0 is the number of roots inside the contour and $f(z)$ is the given function, which in this case is the determinant in (18). The integral in (20) is performed numerically using the trapezoidal rule to obtain an approximation for s_0. If s_0 is large,

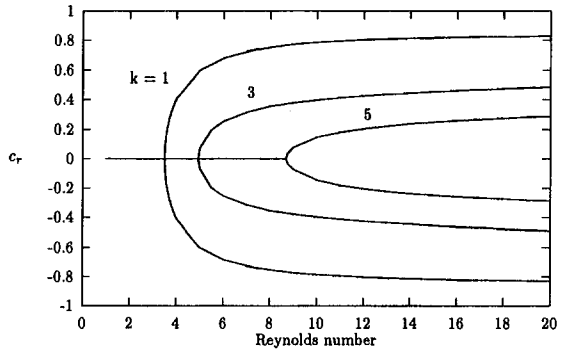


Fig. 3 Wave speed versus Reynolds number for k = 1, 3, and 5

Downloaded 04 May 2010 to 171.66.16.28. Redistribution subject to ASME license or copyright; see http://www.asme.org/terms/Terms_Use.cfm

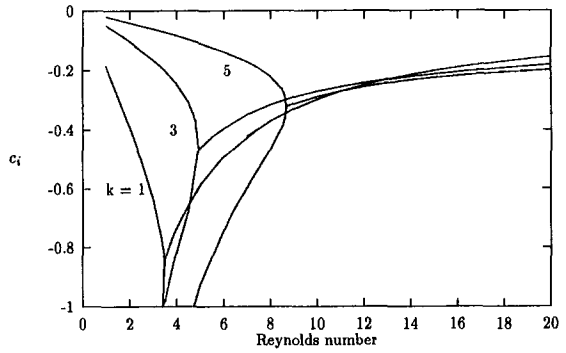


Fig. 4 Damping rate versus Reynolds number for k = 1, 3, and 5

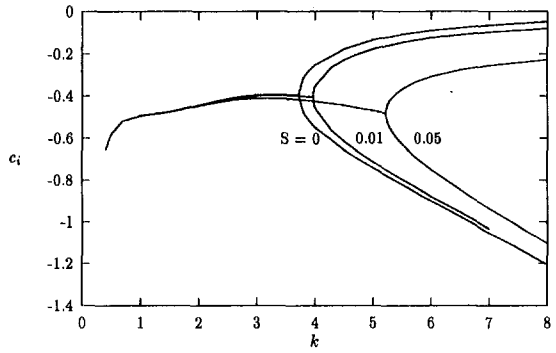


Fig. 6 Damping rate versus wave number for S = 0, 0.01, and 0.05

the domain is segmented until each subregion contains a small number of roots. The location of the roots are then found using

$$s_N = \frac{1}{2\pi i}\int_C z^N \frac{f'(z)}{f(z)}\,dz = \sum_{i=1}^{m} z_i^N. \qquad (21)$$

The integral in (21) is evaluated numerically for $N = 1, 2, \ldots, s_0$, which gives a low-order polynomial with the same zeros as the original function. The roots of the polynomial are easily found using Lehmer's method (Lehmer, 1961). A final iteration using Newton's method is used to improve the accuracy of the method. The details are given in Delves and Lyness (1967).

The results for wave speed, c_r, from the numerical evaluation of the determinant in (18) are given in Fig. 1 for several Reynolds numbers. Also shown in Fig. 1 is the dispersion relation for an inviscid flow. Figure 1 shows that the viscous case has an upstream and downstream propagating wave, analogous to the inviscid case, but only for small wave number. For large wave numbers, which are short waves, the wavespeed for the upstream and downstream propagating waves merge at the zero value. Waves beyond this critical value do not propagate, but merely decay. Waves with wave numbers less than the critical value propagate and decay.

The damping rate, c_i, is shown in Fig. 2 for the waves which correspond to Fig. 1. Figure 2 shows that all the values of c_i are negative, which indicates a stable flow, as expected. Also evident in Fig. 2 is the critical value of wavenumber, above which there is no propagation. It is seen in Fig. 2 that there are still two solutions beyond the critical wave number, both of which are nonpropagating decaying waves.

Figures 3 and 4 show the real and imaginary part of the wavespeed versus Reynolds number for several wave numbers. It is seen that there is also a critical Reynolds number where the upstream and downstream propagating waves merge. Reynolds numbers below the critical value do not propagate, but merely decay. As the Reynolds number approaches zero, one damping rate approaches zero while the other appears to approach negative infinity. Thus one long wave solution decays very slowly, while the other decays very rapidly. The results for high Reynolds number agree quite accurately with the approximate form of Bassett (1888).

The critical point between propagating and nonpropagating waves has been noted before for the infinite depth case, Wehausen and Laitone (1960). The finite depth case is also discussed, but no results are given since an analytical result was too difficult to obtain. Similar results are also presented in Chandrasekhar (1955) for waves on the interface of two infinite viscous layers.

The infinite depth case discussed in Wehausen and Laitone (1961) produces a relatively simple fourth-order characteristic equation for the complex wavespeed, which may then be solved exactly. The characteristic equation for the finite depth case would be found by expanding the determinant in (18). The wavespeed would appear to a high power in this equation, indicating that there may be many solutions for the wavespeed. However, wavespeed also appears in the argument of the hyperbolic tangent function. Since the hyperbolic tangent function is not a polynomial, then there is not necessarily many roots to the characteristic equation. In the numerical work, only three roots have been found for any set of parameters. Two of these roots correspond to the upstream and downstream propagating waves, and the third root is the isolated root discussed in the next section.

The effect of surface tension is shown in Figs. 5 and 6, which give the real and imaginary values of the wavespeed versus wave number for several surface tensions. Figure 5 shows that increasing surface tension from zero has little effect for long waves, but does have a significant effect for shorter waves. The dispersion curve in Fig. 5 is very similar to the zero surface tension limit, except the nonzero surface tension case shows that the critical value of wave number has moved to a larger value.

4 A Nonoscillatory Damped Solution

The determinant in (18) has two roots which provide a valid solution to the differential system given by (17), for a given

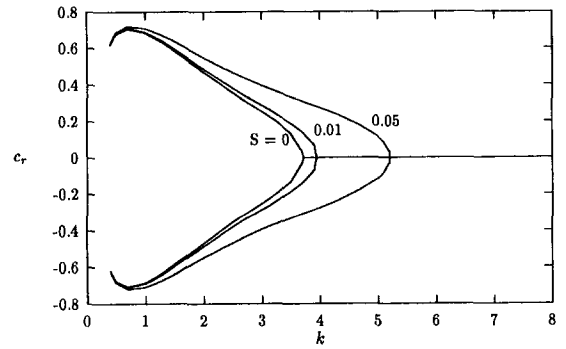


Fig. 5 Wave speed versus wave number for S = 0, 0.01, and 0.05

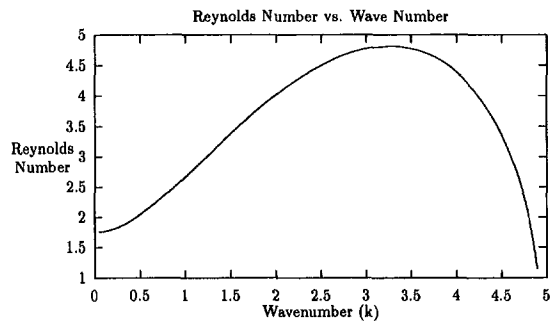


Fig. 7 Reynolds number versus wave number for the isolated solution

Downloaded 04 May 2010 to 171.66.16.28. Redistribution subject to ASME license or copyright; see http://www.asme.org/terms/Terms_Use.cfm

set of parameters, k, Re, and S. The two roots are the upstream and downstream propagating waves. There is one other root of (18), namely, choosing $\omega\ \mathrm{Re} = -ik^2$ makes the determinant in (18) zero regardless of the values of k, Re, and S. When $\omega\ \mathrm{Re} = -ik^2$, (16) requires $m = 0$ and hence the last column in (18) becomes zero. However, this other root is not generally a legitimate solution of the differential system. When m is zero, two of the expressions in (17) are the same and the solution is incomplete.

An alternate solution must be found by setting $\omega\ \mathrm{Re} = -ik^2$ in (6) to get

$$\phi'''' - k^2\phi'' = 0. \tag{22}$$

The solution to (22) is

$$\phi(y) = C_1 \cosh(ky) + C_2 \sinh(ky) + C_3 y + C_4. \tag{23}$$

Applying the boundary conditions as before gives

$$\begin{bmatrix} A_5 & -k^3 & -2k^2 & A_5 \\ 2 & 0 & 0 & 1 \\ \cosh(k) & -\sinh(k) & -1 & 1 \\ -k\sinh(k) & k\cosh(k) & 1 & 0 \end{bmatrix} \begin{bmatrix} C_1 \\ C_2 \\ C_3 \\ C_4 \end{bmatrix} = \begin{bmatrix} 0 \\ 0 \\ 0 \\ 0 \end{bmatrix} \tag{24}$$

where

$$A_5 = \mathrm{Re}^2(1 + Sk^2). \tag{25}$$

Setting the determinant of the matrix in (24) to zero and rearranging gives

$$\mathrm{Re}^2 = \frac{(4 - 5\cosh k + k\sinh k)k^3}{(\sinh k - k\cosh k)(Sk^2 + 1)}. \tag{26}$$

Equation (26) gives the value of the Reynolds number for a given wave number where the solution exists, as shown in Fig. 7. Therefore, the solutions given by (23) are isolated solutions which exist for only one or two wave numbers for a given Reynolds number. These solutions are free surface disturbances which do not oscillate or propagate, but merely decay. The solution (23) is clearly distinct from the solutions of discussed in the previous section.

The waves given by the solution (23) have zero real part, and hence have no oscillation. There are no solutions which have the damping ratio $\omega = -ik^2/\mathrm{Re}$ and propagate at the same time. However, in direct simulations of the Navier-Stokes system with a free surface, standing waves have been found which oscillate and decay with a damping rate remarkably close to $\omega = -ik^2/\mathrm{Re}$ (Bedford et al., 1994). The standing waves in the direct simulation appear to be spurious, although the solutions given by (23) are true solutions.

Acknowledgment

Support for this work from the Office of Naval Research is much appreciated. Thanks to Prof. James Duncan for suggesting the root-finding method and providing the root-finding software.

References

Basset, A. B., 1888, *A Treatise on Hydrodynamics,* Cambridge University Press, Cambridge, U.K.

Bedford, F. C., McHugh, J. P., and Leighton, R. I., 1994, "Direct numerical simulation of waves on a viscous fluid," to be submitted.

Chandrasekhar, S., 1955, "The character of the equilibrium of an incomressible heavy viscous fluid of variable density," *Proc. Cambridge Phil. Soc.,* Vol. 51, pp. 162–178.

Delves, L. M., and Lyness, J. M., 1967, "A numerical method for locating the zeros of an analytic function," *Mathematics of Computation,* Vol. 21, pp. 543–560.

Lamb, H., 1932, *Hydrodynamics,* Macmillan, New York.

Lehmer, D. H., 1961, "A machine method for solving polynomial equations," *J. Assoc. Compt. Mach.,* Vol. 8, pp. 151–162.

Wehausen, J. V., and Laitone, E. V., 1960, *Encyclopedia of Physics,* Vol. 9, Springer-Verlag, New York.

Yih, C. S., 1977, *Fluid Mechanics,* West River Press.

Downloaded 04 May 2010 to 171.66.16.28. Redistribution subject to ASME license or copyright; see http://www.asme.org/terms/Terms_Use.cfm

Intermittency Route to Chaos of a Cantilevered Pipe Conveying Fluid With a Mass Defect at the Free End

C. Semler

M. P. Païdoussis
Fellow ASME.

Department of Mechanical Engineering,
McGill University,
817 Sherbrooke Street West,
Montréal, Québec, H3A 2K6, Canada

The nonlinear equations for planar motions of a vertical cantilevered pipe conveying fluid are modified to take into account a small lumped mass added at the free end. The resultant equations contain nonlinear inertial terms; by discretizing the system first and inverting the inertia matrix, these terms are transferred into other matrices. In this paper, the dynamics of the system is examined when the added mass is negative (a mass defect*), by means of numerical computations and by the software package AUTO. The system loses stability by a Hopf bifurcation, and the resultant limit cycle undergoes pitchfork and period-doubling bifurcations. Subsequently, as shown by the computation of Floquet multipliers, a* type I intermittency *route to chaos is followed—as illustrated further by a Lorenz return map, revealing the well-known normal form for this type of bifurcation. The period between "turbulent bursts" of nonperiodic oscillations is computed numerically, as well as Lyapunov exponents. Remarkable qualitative agreement, in both cases, is obtained with analytical results.*

1 Introduction

Ever since the early work on the dynamics of pipes conveying fluid, e.g., by Housner (1952) and Benjamin (1961), well over 200 papers have been published on the subject. Indeed, as recently discussed in an extensive review of the topic (Païdoussis and Li, 1993), this system has now become a new paradigm in dynamics, on a par with the classical problems of a column subjected to axial loading and a rotating shaft. This is especially so for the inherently nonconservative system of a cantilevered pipe conveying fluid (Benjamin, 1961; Gregory and Païdoussis, 1966; Herrmann and Nemat-Nasser, 1967).

More recently, increased effort has been devoted to the study of the nonlinear dynamics of the cantilevered system (e.g., Bajaj et al., 1980; Rousselet and Herrmann, 1981; Bajaj and Sethna, 1991; Li and Païdoussis, 1994), as well as on chaotic dynamics in variants of the basic system (Tang and Dowell, 1988; Païdoussis and Moon, 1988; Païdoussis et al., 1991, 1992). Païdoussis and Moon (1988) studied theoretically and experimentally the planar dynamics of a cantilevered pipe conveying fluid and interacting with motion-limiting restraints. They showed that, after the Hopf bifurcation, which arises in all cantilevered pipes at sufficiently high flow velocity, the resulting limit cycle undergoes a cascade of period-doubling bifurcations, leading to chaos. Fractal dimension calculations (Païdoussis et al., 1992) showed definitively that the essential dynamics may indeed be captured by a two-degree-of-freedom ($N = 2$) discrete model (as heuristically done in the earlier study), but that $N = 4$ or 5 may be necessary for adequate quantitative prediction. This was found to be the case, and agreement with experiment to within 5-10 percent was obtained for the Hopf and first period-doubling bifurcations and the onset of chaos (Païdoussis et al., 1991). This was later confirmed by Païdoussis and Semler (1993), in which, in contrast to previous studies, the full nonlinear form of the equation of motion was utilized, and through which one can also predict the experimentally observed "sticking" of the pipe to the restraints at very high flow velocities.

Chaos was never found in the case of planar motions of the *plain* autonomous cantilevered system, i.e., without lateral restraints (Païdoussis and co-workers) or magnets (Tang and Dowell, 1988). The same was concluded by Copeland and Moon (1992) for *three-dimensional* motions of the system, who nevertheless found that chaotic motions are indeed possible, provided that a mass is attached to the free end of the cantilevered pipe.

The present study was initiated to investigate the *planar* version of Copeland and Moon's system. The nonlinear equation of motion of the system is first modified to account for the presence of a lumped end-mass. Then, the dynamics of the system is studied for the case of a mass defect at the free end, which is the same as the addition of a negative end-mass. There is no particular engineering application for the system, although it is obvious that a pipe with a reduction in the outer diameter over a segment near the free end is easily physically possible (as much as an addition of a lumped mass would be); nevertheless the justification for the study—as in the case for most if not all of what has already been done on the dynamics of pipes conveying fluid (Païdoussis and Li, 1993; Païdoussis, 1993)—owes more to fundamental interest in its dynamical behavior than to practical applications.

2 The Analytical Model

The system under consideration (Fig. 1) is the same as that considered by Copeland and Moon (1992). The equations of motion without the end-mass have been derived by Semler et al. (1994), and are similar to those derived earlier by Lundgren et al. (1979); they are here modified to take into account the presence of the end-mass, modeled as a lumped point-mass, $\mathcal{M}$, at $x = L$.

2.1 Contribution of the End-Mass to the Equation of Motion. The addition of a lumped end-mass to an otherwise uniform vertical pipe conveying fluid makes inertial and gravitational contributions to the equation of motion. In the context of a Lagrangian derivation of the equations, these contributions will be derived here as additional components in the kinetic and potential energies of the system.

Contributed by the Applied Mechanics Division of THE AMERICAN SOCIETY OF MECHANICAL ENGINEERS for publication in the ASME JOURNAL OF APPLIED MECHANICS.

Discussion on this paper should be addressed to the Technical Editor, Professor Lewis T. Wheeler, Department of Mechanical Engineering, University of Houston, Houston, TX 77204-4792, and will be accepted until four months after final publication of the paper itself in the ASME JOURNAL OF APPLIED MECHANICS.

Manuscript received by the ASME Applied Mechanics Division, July 19, 1993; final revision, Oct. 31, 1994. Associate Technical Editor: T. R. Akylas.

Copyright © 1995 by ASME

Downloaded 04 May 2010 to 171.66.16.28. Redistribution subject to ASME license or copyright; see http://www.asme.org/terms/Terms_Use.cfm

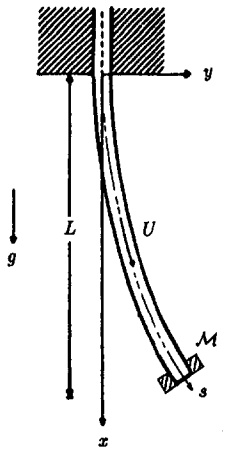


Fig. 1 Schematic of the system

The variation of the kinetic energy component associated with the lumped end-mass is

$$\delta \int_{t_1}^{t_2} T_{\mathcal{M}} dt = \delta \int_{t_1}^{t_2} \tfrac{1}{2}\mathcal{M} v_L^2 dt = -\int_{t_1}^{t_2} \mathcal{M}(\ddot{x}_L \delta x_L + \ddot{y}_L \delta y_L) dt = A + B, \quad (1)$$

in which the dot stands for $\partial(\ )/\partial t$. Introducing the Dirac delta function (of dimension L^{-1}), the B term may be written as

$$B = -\int_{t_1}^{t_2} \int_0^L \mathcal{M}\ddot{y}\delta(s - L)\delta y ds dt. \quad (2)$$

To compute the A term in (1), the inextensibility condition and its variational form (Semler et al., 1992) is used, namely,

$$x'^2 + y'^2 = 1,$$

$$\delta x = -(y' + \tfrac{1}{2}y'^3)\delta y + \int_0^s (y'' + \tfrac{3}{2}y'^2 y'')\delta y ds, \quad (3)$$

where $(\ )' = \partial(\ )/\partial s$, with the aid of which

$$A = -\int_{t_1}^{t_2} \mathcal{M}\ddot{x}_L \delta x_L dt = \int_{t_1}^{t_2} \mathcal{M} \int_0^L (\dot{y}'^2 + y'\ddot{y}')\, du \times \left\{ -y'_L \delta y_L + \int_0^L y'' \delta y du \right\} dt. \quad (4)$$

Using again the delta function, A becomes

$$A = \mathcal{M} \int_{t_1}^{t_2} \int_0^L \left[-y'\delta(s - L) \int_0^s (\dot{y}'^2 + y'\ddot{y}')du + y'' \int_0^L (\dot{y}'^2 + y'\ddot{y}')du \right] \delta y ds dt. \quad (5)$$

This can be transformed into

$$\int_0^L \left[-y' \mathcal{M}\delta(s - L) \int_0^s (\dot{y}'^2 + y'\ddot{y}')du + y'' \int_s^L \mathcal{M}\delta(u - L) \int_0^u (\dot{y}'^2 + y'\ddot{y}')dv du \right] \delta y ds; \quad (6)$$

which depends on the fact that $y''(L) = 0$. This equation is now of similar form to the equation for the inertial terms in the equation of motion, and hence may directly be incorporated in it.

For the gravitational term, one needs to compute

$$\delta \int_{t_1}^{t_2} \mathcal{G} dt = \delta \int_{t_1}^{t_2} \mathcal{M} g x_L dt = \int_{t_1}^{t_2} \mathcal{M} g \delta x_L dt, \quad (7)$$

which, after use of (3), becomes equal to

$$\int_{t_1}^{t_2} \mathcal{M} g \int_0^L [-(y' + \tfrac{1}{2}y'^3)\delta y \delta(s - L)] ds dt + \int_{t_1}^{t_2} \mathcal{M} g \int_0^L (y'' + \tfrac{3}{2}y'^2 y'')\delta y ds dt. \quad (8)$$

Consequently, incorporating Eqs. (2), (6), and (8), the complete equation of motion for the cantilevered pipe with an end-mass, containing steady flow ($\dot{U} = 0$), becomes

$$\begin{aligned}
&[m + M + \mathcal{M}\delta(s - L)]\ddot{y} + 2MU\dot{y}'(1 + y'^2) \\
&+ [m + M + \mathcal{M}\delta(s - L)]gy'(1 + \tfrac{1}{2}y'^2) \\
&+ y''\Big[MU^2(1 + y'^2) - (1 + \tfrac{3}{2}y'^2) \int_s^L (m + M \\
&+ \mathcal{M}\delta(u - L))g du \Big] + EI[y''''(1 + y'^2) \\
&+ 4y'y''y''' + y''^3] - y''\Big[\int_s^L \Big([m + M \\
&+ \mathcal{M}\delta(u - L)] \int_0^u (\dot{y}'^2 + y'\ddot{y}')dv \Big) du \\
&+ \int_s^L (2MU\dot{y}'\dot{y}' + MU^2 y'y'')du \Big] \\
&+ y'[m + M + \mathcal{M}\delta(s - L)] \\
&\times \int_0^s (\dot{y}'^2 + y'\ddot{y}')du = 0, \quad (9)
\end{aligned}$$

correct to $\mathcal{O}(\epsilon^3)$ for lateral displacements of the pipe, y, of $\mathcal{O}(\epsilon)$. In this equation, m is the mass of the pipe per unit length, EI its flexural rigidity, and L its length; M is the mass of the fluid per unit length, flowing in the pipe with mean velocity U. The contribution of the terms due to the end-mass was also determined independently by using the Newtonian approach (force balance method), confirming that (9) is indeed correct. This equation of motion is essentially very similar to that derived by Copeland (1992), with some differences: (i) the inextensibility condition has been used to obtain a single equation, instead of one each for the axial and the lateral components of motion; (ii) only one equation is needed since *planar* motion is considered; (iii) the effect of the lumped mass $\mathcal{M}$ is incorporated in the equation itself, rather than in the boundary conditions (Hill and Swanson, 1970).

Comparing Eq. (9) to that without the end-mass, it is seen that by the judicious utilization of the Dirac delta function, $m + M$, representing the mass per unit length of the pipe and the contained flow, is replaced by

$$m + M \rightarrow m + M + \mathcal{M}\delta(s - L). \quad (10)$$

Equation (9) contains nonlinear inertial terms that cannot be removed from the partial differential equation, because of the presence of the delta function $\delta(s - L)$. Therefore, they will be removed from the discretized ordinary differential equation (o.d.e.), obtained by Galerkin's technique.

To simplify the analysis, the equation of motion is first put in nondimensional form. The same nondimensional quantities as before (Païdoussis, 1970) are used, plus a nondimensional end-mass parameter Γ, namely

$$\xi = \frac{s}{L}, \quad \eta = \frac{y}{L}, \quad \tau = \left(\frac{EI}{m + M}\right)^{1/2} \frac{t}{L^2},$$

$$\Gamma = \frac{\mathcal{M}}{(m + M)L}, \quad u = \left(\frac{M}{EI}\right)^{1/2} UL,$$

$$\gamma = \frac{m + M}{EI} L^3 g, \quad \beta = \frac{M}{m + M}. \quad (11)$$

Downloaded 04 May 2010 to 171.66.16.28. Redistribution subject to ASME license or copyright; see http://www.asme.org/terms/Terms_Use.cfm

In physical terms, u is the nondimensional fluid velocity, γ represents the relative measure of gravity to flexural forces, and β is the ratio of the fluid mass to the total mass per unit length. The resulting nondimensional equation of motion may be written in the compact form

$$\ddot{\eta}(1 + \Gamma\delta(\xi - 1)) + 2u\sqrt{\beta}\dot{\eta}' + \eta''\left[u^2 - \gamma\int_\xi^1 (1 + \Gamma\delta(\xi - 1))d\xi\right] + \gamma[1 + \Gamma\delta(\xi - 1)]\eta' + \eta'''' + N(\eta) = 0, \quad (12)$$

where

$$N(\eta) = 2u\sqrt{\beta}\dot{\eta}'\eta'^2 + \eta''\left[u^2 - \tfrac{3}{2}\int_\xi^1 \gamma[1 + \Gamma\delta(\xi - 1)d\xi]\right]\eta'^2 + \tfrac{1}{2}\gamma[1 + \Gamma\delta(\xi - 1)]\eta'^3 + \eta''''\eta'^2 + 4\eta'\eta''\eta''' + \eta''^3 + \eta'[1 + \Gamma\delta(\xi - 1)]\int_0^\xi (\dot{\eta}'^2 + \eta'\ddot{\eta}')d\xi - \eta''\left[\int_\xi^1 [1 + \Gamma\delta(\xi - 1)]\int_0^\xi (\dot{\eta}'^2 + \eta'\ddot{\eta}')d\xi d\xi + \int_\xi^1 (2u\sqrt{\beta}\,\eta'\dot{\eta}' + u^2\eta'\eta'')d\xi\right]. \quad (13)$$

The system is now discretized by expressing $\eta(\xi, \tau) = \sum_{r=1}^{N} \phi_r(\xi) \times q_r(\tau)$, in which the cantilever beam eigenfunctions $\phi_r(\xi)$ are used as a suitable set of base functions, and $q_r(\tau)$ represent the corresponding generalized coordinates. This leads to

$$[\delta_{ij} + \Gamma\phi_i(1)\phi_j(1) + \gamma_{ilkj}q_kq_l]\ddot{q}_j + c_{ij}\dot{q}_j + k_{ij}q_j + \alpha_{ijkl}q_jq_kq_l + \beta_{ijkl}q_jq_k\dot{q}_l + \gamma_{ijkl}q_j\dot{q}_k\dot{q}_l = 0; \quad (14)$$

δ_{ij} is the Kronecker delta, c_{ij} and k_{ij} are elements of the damping and stiffness matrices, and α_{ijkl}, β_{ijkl}, and γ_{ijkl} are coefficients, computed numerically, involving the integrals of the eigenfunctions $\phi_i(\xi)$; note the inversion of the indices (j, l) for the nonlinear inertial term and the fact that the indices implicitly follow the summation convention. The inertia matrix can be inverted by assuming q_r small—as will be explained later—so that Eq. (14) may be converted into a second-order o.d.e. of more standard form, and then put into first-order form,

$$\dot{y} = [A]y + f(y), \quad (15)$$

where f is a third-order polynomial function, $[A]$ is a $2N \times 2N$ matrix, and $\{y\} = \{q, \dot{q}\}'$. In the rest of the paper, $N = 4$ is used as an appropriate approximation.

2.2 Method of Solution. Solutions of Eq. (15) are obtained principally by a fourth-order Runge-Kutta integration algorithm, with a time step size of 0.001, and different initial conditions representing a pipe with no initial velocity, $y_{i+N}(0) = 0$. From the numerical integration of (15), time traces and the corresponding power spectra, phase plane plots, and bifurcation diagrams can easily be constructed and Lyapunov exponents calculated. However, in order to find also unstable limit cycles, AUTO (Doedel, 1981) was used. Indeed, AUTO can deal with o.d.e.s of the type of (15) and with computing both stable and unstable limit cycles, as well as determining how they lose or gain stability; see also Seydel (1988), for a good introduction on the subject. The results obtained may be presented in the form of bifurcation diagrams, where the maximum values of any generalized coordinate, or the period of oscillation, can be displayed as functions of one parameter (usually the flow velocity u).

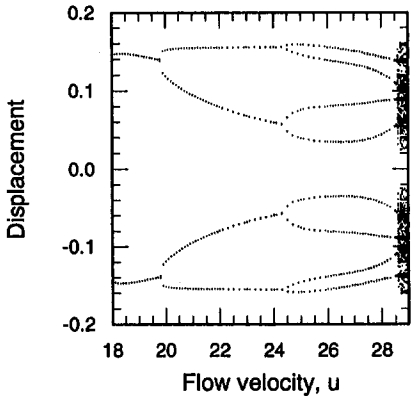


Fig. 2 Bifurcation diagram for the free-end displacement versus dimensionless flow velocity after the Hopf bifurcation, $\Gamma = -0.3$

2.3 Physical Parameters. In order to simplify the analysis, most of the parameters are kept constant, with values equal to those in the experiments of Païdoussis and Moon (1988): $\gamma = 26.75$ and $\beta = 0.216$. Also, the dissipative forces are modeled via a viscous damping idealization with the individual modal logarithmic decrements, δ_j, corresponding to the experimentally measured values (Païdoussis et al., 1991): $\delta_1 = 0.028$, $\delta_2 = 0.081$, $\delta_3 = 0.144$; with $\delta_4 = 0.200$ linearly extrapolated. The nondimensional flow velocity u and end-mass Γ are the main parameters to be varied.

Although interesting dynamics is obtained with $\Gamma > 0$, it is not nearly as remarkable as in the case of $\Gamma < 0$; hence, only results for $\Gamma < 0$ will be discussed in this paper. Physically, a negative Γ represents a small mass defect over a small segment of the free end of the pipe to be modelled as a negative mass. Denoting the external and internal radii of the pipe by r_0 and $r_i = \alpha' r_0$, and considering the external radius of the pipe reduced to αr_0 over a segment of length L', then the end-mass defect is given by $\mathcal{M} = mL'(1 - \alpha^2)/(1 - \alpha'^2)$. For example, for $\beta = 0.15$, $\alpha' = 0.5$, $\alpha = 0.55$, and $L'/L = 0.12$, one obtains $|\Gamma| = 0.093$.

3 Analysis

Assuming Γ to be sufficiently small (of the same order as q_kq_l), the inversion of the inertia matrix is simply

$$[\delta_{ij} + \Gamma\phi_i(1)\phi_j(1) + \gamma_{ilkj}q_kq_l]^{-1} \sim \delta_{ij} - \Gamma\phi_i(1)\phi_j(1) - \gamma_{ilkj}q_kq_l, \quad (16)$$

so that (14) can easily be recast in its first-order form. Moreover, as $\Gamma \sim \mathcal{O}(q_kq_l)$, the nonlinear inertial terms due to Γ may be neglected in the analysis. Approximation (16) suggests that $\Gamma \ll 1$. For computational convenience, the results shown in the sequel correspond to the case $\Gamma = -0.3$, but qualitatively similar results were obtained for more physically realistic values of Γ (e.g., $\Gamma = -0.085$).

The equations of motion in their first-order form are integrated numerically with the fourth-order Runge-Kutta scheme. For $\Gamma = 0$, after the Hopf bifurcation at $u = u_H = 8.7$, the system performs limit-cycle motion. For $\Gamma = -0.3$, however, the situation is more complex and interesting, as seen in Fig. 2; in this case, $u_H = 7.07$. At $u = 19.82$, the limit cycle becomes unstable: a new periodic orbit is created through a pitchfork bifurcation, which breaks the symmetry of the system. At $u = 24.37$, the system undergoes a period-doubling bifurcation. However, instead of developing the usual period-doubling cascade, an interesting phenomenon occurs: at $u = 28.56$, this

Downloaded 04 May 2010 to 171.66.16.28. Redistribution subject to ASME license or copyright; see http://www.asme.org/terms/Terms_Use.cfm

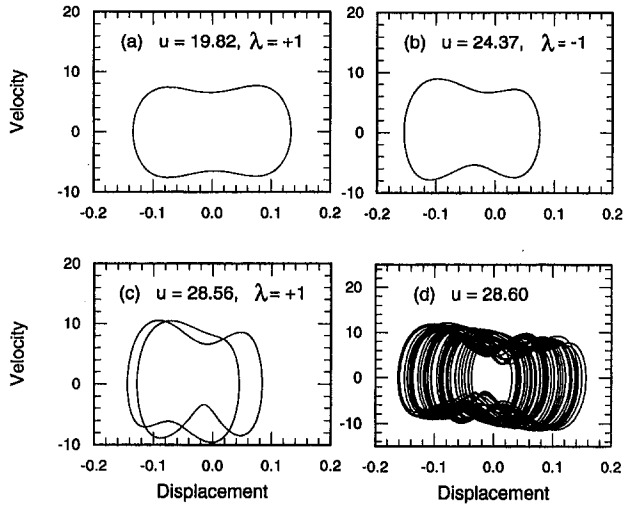


Fig. 3 Phase portraits representing (*a*) the symmetric limit cycle before the pitchfork instability (λ = +1), (*b*) the asymmetric limit cycle before period-doubling (λ = −1), (*c*) the period-two motion before intermittency (λ = +1), (*d*) chaotic oscillations; Γ = −0.3

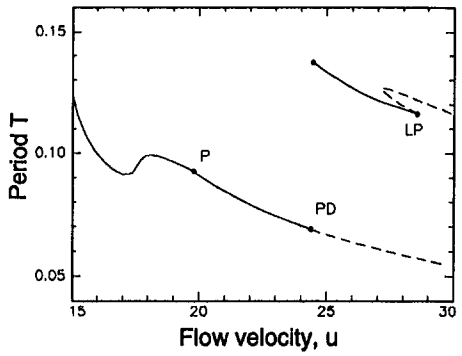


Fig. 5 Bifurcation diagram obtained by AUTO showing the period of oscillation as a function of the dimensionless flow velocity, u. Dotted lines represent unstable limit cycles and full lines stable ones. The letters P and PD refer to pitchfork and period-doubling bifurcations, and LP to limit point.

newly generated steady-state undergoes another bifurcation which leads the system to chaos.

In order to understand what kind of bifurcation takes place, it is of interest to compute the Floquet multipliers (Hartman, 1964) in the neighborhood of the different points of instability. Indeed, the multipliers are a mathematical representation of the type of instability that occurs for a periodic orbit, while the trajectory on the phase plane is a more geometrical picture of the dynamics (Fig. 3). As expected (Guckenheimer and Holmes, 1983), $\lambda = +1$ for $u = 19.82$, and $\lambda = -1$ at $u = 24.37$. The major finding is that one of the multipliers crosses the unit circle at $\lambda = +1$ for $u = 28.56$, which is characteristic of a *"type I" intermittency* route to chaos (Bergé et al., 1984). This route to chaos is also evident in the bifurcation diagram of Fig. 2, since no transition is found between the period-2 orbit at $u = 28.56$ of Fig. 3(c) and the chaotic-looking trajectory at $u = 28.60$ of Fig. 3(d), even when the step size in u is greatly refined. A Poincaré map (not shown), representing the displacement versus velocity of the pipe end when the velocity of the pipe at $x = 0.2$ is zero, gives additional proof that the signal never repeats itself, even over a very long period of time.

Finally, the transition to intermittency is definitely established by Fig. 4, which is a different type of map: for each cycle, the first-mode component $q_1(\tau)$ is tracked, and it is saved when it reaches its maximum (i.e., when $q_5 = 0$ in our eight-dimensional system). It is then possible to compute the map $q_1(n+1) = f(q_1(n))$, for a very long period of time (~8200 cycles). On the map obtained—also called a Lorenz map or a return map—four curves, almost tangent to the 45 deg "identity line" are obviously present, showing the presence of four "channels." The resulting behavior is nearly of period-2; thus, the system visits two steady-states, but the dynamics is interspersed with bursts of aperiodic behavior. As u is increased, the nearly periodic intervals become shorter on the average, while aperiodic motion becomes predominant. This is characteristic of intermittency (Bergé et al., 1984). The structure of the map itself is also of importance, demonstrating, once again, the existence of order in chaos.

Bergé et al. (1984) have studied type I intermittency in detail, by constructing a "generic form" representing a function f on a Poincaré map, which describes the dynamics of the problem

$$y_{n+1} = f(y_n) = y_n + \mu + \alpha y_n^2. \tag{17}$$

If $\mu \equiv u - u_{\text{int}} < 0$ (u_{int} represents the flow velocity at which intermittency occurs), Eq. (17) has two fixed points: one stable, the other unstable. When $\mu > 0$, these fixed points disappear: the system defined by (17) undergoes a saddle-node bifurcation at $\mu = 0$.

The bifurcation diagram shown in Fig. 5 has been obtained by using AUTO; it is a plot of the period of oscillation T as a function of u. The pitchfork bifurcation is indicated by P and the period-doubling bifurcation, clearly detected by the jump in the period of oscillation, by PD. Of more interest is what happens in the neighborhood of the limit point—or turning point—LP; the same qualitative behavior as that given by (17) is observed: for $u < u_{\text{int}} = 28.56$, one stable and one unstable limit cycles coexist, and for $u > u_{\text{int}}$, they have both disappeared, indicating the occur-

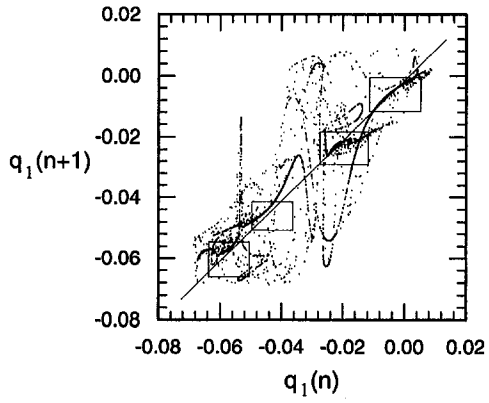


Fig. 4 One-dimensional return map of successive maxima of the q_1 coordinate, demonstrating the existence of four channels in the neighborhood of the identity line $y = x$; $u = 28.6$, $\Gamma = -0.3$, $20 \le \tau \le 1000$

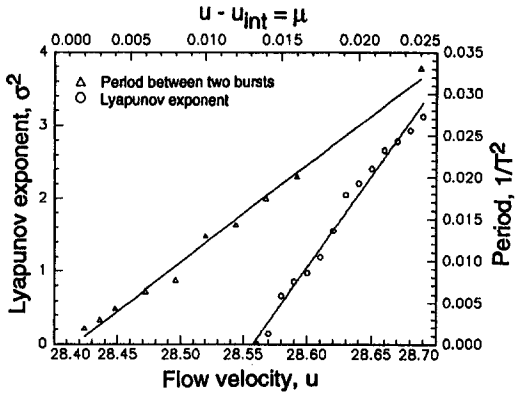


Fig. 6 Lyapunov exponent σ, squared, as a function of the flow velocity u, and the period between two bursts as a function of $\mu = u - u_{\text{int}}$

Downloaded 04 May 2010 to 171.66.16.28. Redistribution subject to ASME license or copyright; see http://www.asme.org/terms/Terms_Use.cfm

rence of a saddle-node bifurcation at $u = u_{int}$. Therefore, the dynamics given by (17) is the same as in the eight-dimensional system. Moreover, the difference equation can be approximated by a differential equation, and it can be shown that the Lyapunov exponent varies like $\mu^{1/2} = \sqrt{u - u_{int}}$, while the period between bursts is given by $T \sim 1/\sqrt{u - u_{int}}$ (Manneville and Pomeau, 1980). This is nicely demonstrated in Fig. 6, obtained by numerically integrating the equation of motion: the maximum Lyapunov exponent has been computed (the procedure for calculating this exponent may be found in Moon (1992), for example), and the period between two bursts can also be found, for several values of u. Qualitative agreement between the generic form and the complete equations is excellent.

It was also attempted to obtain *quantitative* agreement between the period obtained for the normal form (17) and the period computed numerically, without success. Three reasons for this may be put forward: (i) the period found from (17) represents the longest duration between two bursts due to the randomness in the reinjection process (Manneville and Pomeau, 1980), while only a few periods were tracked from the direct numerical integration, (ii) the normal form predicts a distribution of periods between bursts, and not a unique period (Bergé et al., 1984); the normal form describes only the local dynamics, whereas one also needs global information about how the orbits are reinjected into the channels to obtain a quantitative agreement; and (iii) it is believed that equation (17) is only a "trace" of the normal form. Indeed, as can be seen from Fig. 4, the coefficient α (introduced in (17) and representing the curvature of the parabola) for the four curves is not the same. This is due to the fact that the q_1 direction used to compute the return map is not the center manifold before the onset of intermittency. Therefore, the Poincaré section used is not perpendicular to the centre manifold, so that the trace obtained on Fig. 4 represents a projection of the normal form rather than the normal form itself. Finding this centre manifold is not an obvious task—especially for an eight-dimensional system—and it would be a challenging task to solve the problem of a more simple "analytical" set of equations. This, however, is beyond the scope of this paper.

4 Conclusions

The results presented confirm, for planar motions also, Copeland and Moon's (1992) finding for three-dimensional motions that for $\Gamma = 0$ no chaotic motion occurs—indeed, no major qualitative change in the dynamics beyond the Hopf bifurcation. If $\Gamma < 0$ (end-mass defect), however, it is the principal finding of this paper that chaotic oscillations do become possible, even for planar motions. Furthermore, it is shown that the route to chaos is via type I intermittency (Bergé et al., 1984). (For $\Gamma > 0$, the dynamical behavior (not discussed in this paper) is entirely different.) This route to chaos was illustrated for $\Gamma = -0.3$, but the same results were also obtained for $\beta = 0.15$ and $\Gamma = -0.085$ that can be achieved easily in experiments. Nevertheless, the velocities for which chaotic oscillations are then found are much higher, $u \sim 60$.

In order to examine the robustness of the dynamics obtained, all *nonlinear* terms associated with Γ were neglected, as it has been assumed that $\Gamma = \mathcal{O}(q_k q_l)$; these terms are due to gravity, and hence may easily be put to zero by taking $\gamma = 0$. No qualitative change in the dynamics was observed, namely the route to chaos via intermittency was still the same. It is believed that post-Hopf-bifurcation dynamics is mostly influenced by the nonlinear inertial term γ_{ilkj}, which appears directly in the transformation of α_{ijkl} and β_{ijkl} in Eq. (14).

Acknowledgments

The authors express their appreciation to the Natural Sciences and Engineering Research Council of Canada, Le Fonds FCAR of Québec and Hydro Québec for supporting this research, and the referees for their useful comments.

References

Bajaj, A. K., and Sethna, P. R., 1991, "Effect of Symmetry-Breaking Perturbations on Flow-Induced Oscillations in Tubes," *Journal of Fluids and Structures*, Vol. 5, pp. 651–679.

Bajaj, A. K., Sethna, P. R., and Lundgren, T. S., 1980, "Hopf Bifurcation Phenomena in Tubes Carrying a Fluid," *SIAM Journal of Applied Mathematics*, Vol. 39, pp. 213–230.

Benjamin, T. B., 1961, "Dynamics of a System of Articulated Pipes Conveying Fluid. I. Theory; II. Experiments," *Proceedings of the Royal Society London*, Vol. A261, pp. 457–486, 487–499.

Bergé, P., Pomeau, Y., and Vidal, C., 1984, *Order within Chaos*, John Wiley and Sons, New York.

Copeland, G. S., 1992, "Flow-Induced Vibration and Chaotic Motion of a Slender Tube Conveying Fluid," Ph.D. Thesis, Cornell University, Ithaca, NY.

Copeland, G. S., and Moon, F. C., 1992, "Chaotic Flow-Induced Vibration of a Flexible Tube with End Mass," *Journal of Fluids and Structures*, Vol. 6, pp. 705–718.

Doedel, E., 1981, "AUTO: A Program for the Automatic Bifurcation Analysis of Autonomous Systems," *Congressus Numerantium*, Vol. 30, pp. 265–284.

Gregory, R. W., and Païdoussis, M. P., 1966, "Unstable Oscillation of Tubular Cantilevers Conveying Fluid. I. Theory; II. Experiments," *Proceedings of the Royal Society London*, Vol. A293, pp. 512–527, 528–542.

Guckenheimer, J., and Holmes, P. J., 1983, *Nonlinear Oscillations, Dynamical Systems and Bifurcations of Vector Fields*, Springer-Verlag, New York.

Hartman, P., 1964, *Ordinary Differential Equations*, John Wiley and Sons, New York.

Herrmann, G., and Nemat-Nasser, S., 1967, "Instability Modes of Cantilevered Bars Induced by Fluid Flow through Attached Pipes," *International Journal of Solids and Structures*, Vol. 3, pp. 39–52.

Hill, J. L., and Swanson, C. P., 1970, "Effects of Lumped Masses on the Stability of Fluid Conveying Tubes," ASME JOURNAL OF APPLIED MECHANICS, Vol. 37, pp. 494–497.

Housner, G. W., 1952, "Bending Vibrations of a Pipe Line Containing Flowing Fluid," ASME JOURNAL OF APPLIED MECHANICS, Vol. 19, pp. 205–208.

Li, G. X., and Païdoussis, M. P., 1993, "Stability, Double Degeneracy and Chaos in Cantilevered Pipes Conveying Fluid," *International Journal of Non-Linear Mechanics*, Vol. 29, pp. 83–107.

Lundgren, T. S., Sethna, P. R., and Bajaj, A. K., 1979, "Stability Boundaries for Flow-Induced Motions of Tubes with an Inclined Terminal Nozzle," *Journal of Sound and Vibration*, Vol. 64, pp. 553–571.

Manneville, P., and Pomeau, Y., 1980, "Different Ways to Turbulence in Dissipative Dynamical Systems," *Physica 1D*, Vol. 1, pp. 219–226.

Moon, F. C., 1992, *Chaotic and Fractal Dynamics: an Introduction for Applied Scientists and Engineers*, John Wiley and Sons, New York.

Païdoussis, M. P., 1970, "Dynamics of Tubular Cantilevers Conveying Fluid," *Journal of Mechanical Engineering Science*, Vol. 12, pp. 85–103.

Païdoussis, M. P., 1993, "Calvin Rice Lecture: Some Curiosity-Driven Research in Fluid-Structure Interactions and Its Current Applications," ASME *Journal of Pressure Vessel Technology*, Vol. 115, pp. 2–14.

Païdoussis, M. P., Cusumano, J. P., and Copeland, G. S., 1992, "Low-Dimensional Chaos in a Flexible Tube Conveying Fluid," ASME JOURNAL OF APPLIED MECHANICS, Vol. 59, pp. 196–205.

Païdoussis, M. P., and Li, G. X., 1993, "Pipes Conveying Fluid: A Model Dynamical Problem," *Journal of Fluids and Structures*, Vol. 7, pp. 137–204.

Païdoussis, M. P., Li, G. X., and Rand, R. H., 1991, "Chaotic Motions of a Constrained Pipe Conveying Fluid: Comparison between Simulation, Analysis and Experiment," ASME JOURNAL OF APPLIED MECHANICS, Vol. 58, pp. 559–565.

Païdoussis, M. P., and Moon, F. C., 1988, "Nonlinear and Chaotic Fluidelastic Vibrations of a Flexible Pipe Conveying Fluid," *Journal of Fluids and Structures*, Vol. 2, pp. 567–591.

Païdoussis, M. P., and Semler, C., 1993, "Nonlinear and Chaotic Oscillations of a Constrained Cantilevered Pipe Conveying Fluid: a Full Nonlinear Analysis," *Nonlinear Dynamics*, Vol. 4, pp. 655–670.

Rousselet, J., and Herrmann, G., 1981, "Dynamic Behavior of Continuous Cantilevered Pipes Conveying Fliud near Critical Velocities," ASME JOURNAL OF APPLIED MECHANICS, Vol. 48, pp. 945–947.

Semler, C., Li, G. X., and Païdoussis, M. P., 1994, "The Nonlinear Equations of Motion of a Pipe Conveying a Fluid," *Journal of Sound and Vibration*, Vol. 169, pp. 577–599.

Seydel, R., 1988, *From Equilibrium to Chaos: Practical Bifurcation and Stability Analysis*, Elsevier, New York.

Tang, D. M., and Dowell, E. H., 1988, "Chaotic Oscillations of a Cantilevered Pipe Conveying Fluid," *Journal of Fluids and Structures*, Vol. 2, pp. 263–283.

Downloaded 04 May 2010 to 171.66.16.28. Redistribution subject to ASME license or copyright; see http://www.asme.org/terms/Terms_Use.cfm

Viscoelastic Effects in Modeling Web Handling Systems: Steady-State Analysis

X. Guan

M. S. High

D. A. Tree[1]

School of Chemical Engineering,
Oklahoma State University,
423 Engineering North
Stillwater, OK 74078

The effect of viscoelasticity in web handling systems is examined by introducing a viscoelastic equation of state into a model for tension control. Case studies and generalized results for a single open-span system and a double open-span system are presented to compare the results of the viscoelastic model to a model based on a purely elastic equation of state. The results show only small differences in the tension behavior for the single-span system. However, large differences in the magnitude and reversal of the sign of the tension in the second span of a two-span system are seen for even small degrees of viscoelasticity in the web material. The results clearly demonstrate that viscoelasticity must be considered in modeling multispan web handling systems.

1 Introduction

Modeling of systems which rapidly convey thin flexible materials (webs) is extremely important to a wide range of industries, including polymer processing, paper manufacturing, printing, and wrapping, since a reliable model is essential for the design, analysis, and control of a system before or after construction. Among the modeling concerns tension control is paramount, since improper tension in the web line may cause web failure or product damage resulting in downtime or unacceptable product quality.

The tension in the web line is a function of the operating conditions, the system configuration, and the web material response. The economics of the web handling industries require the web to move as rapidly as possible with velocities that may reach 160 km/hr. Web handling configurations typically consist of very complex combinations of different types of rolls, rollers, and open spans. Web materials, especially polymer films at higher temperatures and wet paper, will behave viscoelastically under tension; meaning that the material response is dependent on present as well as past rheological events, and that only partial recovery of any deformation can be expected.

Shin (1991) has given an extensive review of the efforts to simulate and control web handling systems beginning with the work of Campbell (1958) to model some simple systems and apply control methods. With only a few exceptions (Akatsuka, 1990), modeling efforts in web handling have relied exclusively on purely elastic models.

The work of Shin (1991) and Reid and Lin (1993) is of particular note since these investigators have been very successful in addressing the issues of system configuration and operating conditions. Shin developed models for seven "primitive elements" which correspond to the most common components of web handling systems. The primitive elements can be assembled into any desired configuration to simulate even the most complex web handling operation. Shin also developed techniques to assemble the corresponding model equations into a set of system equations which can be solved with standard techniques. Reid and Lin expanded Shin's work to simulate tension control in multispan systems during startup.

Incorporation of the viscoelastic properties of the web significantly complicates the modeling. However, a realistic model, which must include the viscoelastic properties of the web, will allow for more accurate and confident control of a web handling system which is extremely important for industries in which profit margins are small and very sensitive to even small increases in productivity.

Viscoelastic models have been widely and successfully used to model many operations which subject a material to an extensional deformation. Examples include fiber spinning (Spearot and Metzner, 1972), thin film casting (Alaie and Papanastasiou, 1991), and paper making (Hauptmann and Cutshall, 1977). In these examples the material under consideration is subjected to extensional deformations; analogous to the deformations experienced by materials in web handling operations. Particular note should be made of the work of Fisher and Denn (1976) who used the White-Metzner equation, in a manner similar to the treatment given below for multispan operations, to model the fiber spinning process.

The applications of viscoelasticity cited above can be described as single-span operations. Therefore, only the total draw ratio was allowed to contribute to the material response. However, in a multispan web handling system, the interaction of tensions in different spans must also be considered; thus the draw ratio only partially contributes to the viscoelastic deformation.

This paper merges and extends the previous work in multispan simulation with the viscoelastic modeling of single-span operations to predict the tension of thin, flexible materials in web handling systems. The interaction of tension across spans is also considered. The viscoelastic behavior is simulated by the White-Metzner equation.

2 Model Development

A representative web handling system and a cartesian coordinate system are shown in Fig. 1. The system consists of pairs of rollers and open spans. In actual practice the rollers may be driven, idle, dance, winding, or unwinding and need not occur in pairs; however, each represents a means of applying forces to the web. The web moves in the positive z-direction and is considered continuous. The width of the web (y-direction) is considered to be orders of magnitude greater than the thickness (x-direction).

[1] To whom all correspondence should be addressed.

Contributed by the Applied Mechanics Division of THE AMERICAN SOCIETY OF MECHANICAL ENGINEERS for publication in the ASME JOURNAL OF APPLIED MECHANICS.

Discussion on this paper should be addressed to the Technical Editor, Professor Lewis T. Wheeler, Department of Mechanical Engineering, University of Houston, Houston, TX 77204-4792, and will be accepted until four months after final publication of the paper itself in the ASME JOURNAL OF APPLIED MECHANICS.

Manuscript received by the ASME Applied Mechanics Division, Jan. 5, 1994; final revision, July 18, 1994. Associate Technical Editor: I. M. Daniel.

Copyright © 1995 by ASME

Downloaded 04 May 2010 to 171.66.16.28. Redistribution subject to ASME license or copyright; see http://www.asme.org/terms/Terms_Use.cfm

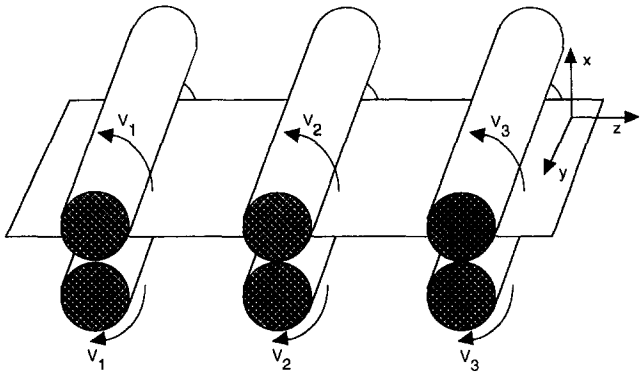


Fig. 1 Schematic drawing of a typical web handling system showing the coordinate system

Figure 1 suggests that a material element experiences three distinct time scales while traversing a web handling system: the contact time with the rollers, t_{roller}; the time required to traverse an open span, t_{span}; and the time required to traverse the entire system, t_{system}. For a typical operation,

$$t_{\text{system}} > t_{\text{span}} \gg t_{\text{roller}}. \tag{1}$$

The typical time required to transverse a span may be within a few orders of magnitude or less of the characteristic relaxation time of the materials. Hence, viscoelastic effects can be significant in the open spans. However, the contact time with the rollers is generally much smaller than the material relaxation time.

The large difference in time scales simplifies the modeling since a material element passing through the system can be envisioned to experience a series of viscoelastic deformations (open spans) separated by purely elastic step changes (rollers). Therefore, the change in the stress, σ_{zz}, during the roller contact can be found from Hooke's law

$$\Delta\sigma_{zz} = E\Delta\epsilon_z \tag{2}$$

where E is Young's modulus and $\Delta\epsilon_z$ is the change in strain in the z-direction.

In order to develop the model of viscoelastic material behavior in a free span, a control element was considered as depicted in Fig. 2. Deformation of the web results in incline angles, α and β. The following assumptions were made during the derivation of the model:

1 the system is at steady state;
2 inertial, gravitational, and air traction forces are negligible;
3 no shearing deformations;
4 incline angles are very small;
5 constant density and temperature, no heat effects;
6 the isotropic pressure, p, is given by (Han, 1976):

$$-p = \tfrac{1}{3}(\sigma_{xx} + \sigma_{yy} + \sigma_{zz}) \tag{3}$$

where σ_{ij} $(i, j = x, y, z)$ are total stresses; and
7 stresses and v_z are functions of z only.

Industrially significant cases do exist in which the roller contact time, heat effects, and air traction are important. However, these problems are beyond the scope of this paper and will be considered in subsequent studies as will transient conditions.

The deviatoric stresses, τ_{ij} $(i, j = x, y, z)$, are defined by

$$\sigma_{ij} = \tau_{ij} - p\delta_{ij} \tag{4}$$

where δ_{ij} is the unit tensor.

The governing equations for the free span were derived from the conservation of mass, the force balance, and the rheological equation of state. Consideration of assumption 5 allows the conservation of mass to be expressed as

$$\frac{\partial(Av_z)}{\partial z} = 0 \tag{5}$$

where v_z is the web velocity in the z-direction.

The force balance follows from assumption 2:

$$F = (\tau_{zz} - \tau_{xx})A \tag{6}$$

where A and F represent the cross-sectional area and tension, respectively. The force balance could have been written in terms of τ_{yy} instead of τ_{xx}. However, the choice is arbitrary since the resulting governing equation is the same in either case.

The momentum equation can be derived by taking the derivative of the force balance with respect to z

$$\frac{\partial F}{\partial z} = \frac{\partial(\tau_{zz} - \tau_{xx})}{\partial z}A + (\tau_{zz} - \tau_{xx})\frac{\partial A}{\partial z} = 0 \tag{7}$$

expanding and substituting the mass conservation equation, and changing the partial derivatives to total derivatives (assumption 7):

$$\frac{d}{dz}(\tau_{zz} - \tau_{xx}) = \frac{\tau_{zz} - \tau_{xx}}{v_z}\frac{dv_z}{dz}. \tag{8}$$

The final element of the model is the White-Metzner rheological equation of state (Bird et al., 1987)

$$\boldsymbol{\tau} + \frac{\eta(\dot{\gamma})}{G}\boldsymbol{\tau}_{(1)} = \eta(\dot{\gamma})\boldsymbol{\gamma}_{(1)}. \tag{9}$$

In Eq. (9), $\boldsymbol{\tau}$ is the deviatoric stress tensor; $\boldsymbol{\gamma}_{(1)}$ is the rate of strain tensor; η is the viscosity function, which is a function of the second invariant of the rate of strain tensor; G is the elastic modulus; and $\boldsymbol{\tau}_{(1)}$ is the contravariant convected time derivative of the stress tensor defined as

$$\boldsymbol{\tau}_{(1)} = \frac{D\boldsymbol{\tau}}{Dt} - \{\boldsymbol{\tau}\cdot\nabla\mathbf{v}\}^T - \{\boldsymbol{\tau}\cdot\nabla\mathbf{v}\} \tag{10}$$

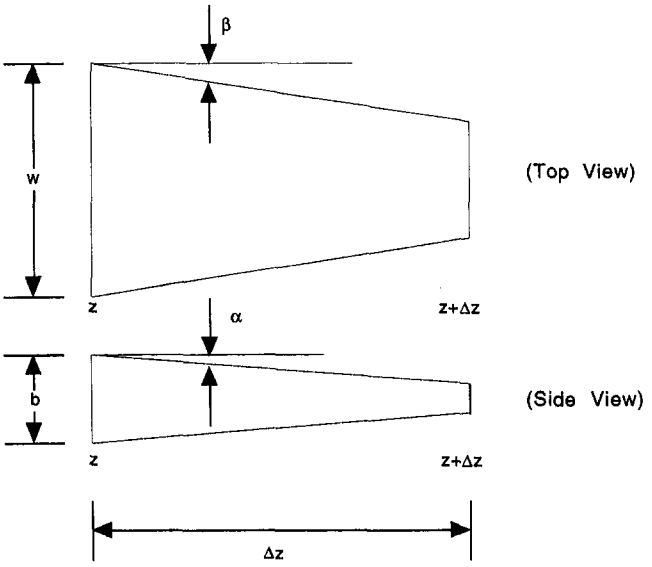


Fig. 2 A material control volume showing the incline angles

Downloaded 04 May 2010 to 171.66.16.28. Redistribution subject to ASME license or copyright; see http://www.asme.org/terms/Terms_Use.cfm

where

$$\frac{D\boldsymbol{\tau}}{Dt} = \frac{\partial \boldsymbol{\tau}}{\partial t} + \{\mathbf{v}\cdot\nabla\boldsymbol{\tau}\}, \tag{11}$$

and nabla denotes the gradient operator. The second invariant of the rate of strain tensor is defined as

$$\dot{\gamma} = \sqrt{\tfrac{1}{2}\boldsymbol{\gamma}_{(1)}:\boldsymbol{\gamma}_{(1)}}. \tag{12}$$

In a shear free deformation (assumption 3),

$$\dot{\gamma} = \sqrt{\frac{1}{2}\left[\left(2\frac{\partial v_x}{\partial x}\right)^2 + \left(2\frac{\partial v_y}{\partial y}\right)^2 + \left(2\frac{\partial v_z}{\partial z}\right)^2\right]}. \tag{13}$$

For an incompressible material (assumption 5),

$$\nabla\cdot\mathbf{v} = 0. \tag{14}$$

Due to the symmetry of deformation in the x and y directions, Eq. (14) requires

$$\frac{\partial v_x}{\partial x} = \frac{\partial v_y}{\partial y} = -\frac{1}{2}\frac{\partial v_z}{\partial z}. \tag{15}$$

Substitution of Eq. (15) into Eq. (13) yields

$$\dot{\gamma} = \sqrt{3}\left|\frac{\partial v_z}{\partial z}\right|. \tag{16}$$

The development of the definitive rheological equation of state for web materials is of intense, on-going interest and a number of equations have been proposed. The selection of the equation of state was guided by the specific requirements of this study and other choices were possible which would not have significantly affected the conclusions of this paper.

The White-Metzner equation was used because it allows for stress relaxation, through permanent deformation; preserves material objectivity, independence of results from the coordinate system; provides the flexibility to model diverse materials such as polymers and paper; and has sufficient mathematical simplicity to allow for a solution. The White-Metzner model has also been successfully used in modeling viscoelastic behavior in extensional deformation (Fisher and Denn, 1976; Bird et al., 1987). A power-law function

$$\eta(\dot{\gamma}) = m\dot{\gamma}^{n-1} \tag{17}$$

was selected to express the viscosity in the White-Metzner model where m and n are the power-law coefficient and exponent, respectively. The value of m and n for a specific material can be determined with an extensional rheometer.

Equation (9) is a tensor equation from which the xx and zz components are of interest:

$$\tau_{xx} + 3^{(n-1)/2}\left(\frac{m}{G}\right)\left|\frac{dv_z}{dz}\right|^{n-1}\left(v_z\frac{d\tau_{xx}}{dz} + \tau_{xx}\frac{dv_z}{dz}\right) = -3^{(n-1)/2}m\left|\frac{dv_z}{dz}\right|^{n-1}\frac{dv_z}{dz}, \tag{18}$$

$$\tau_{zz} + 3^{(n-1)/2}\left(\frac{m}{G}\right)\left|\frac{dv_z}{dz}\right|^{n-1}\left(v_z\frac{d\tau_{zz}}{dz} - 2\tau_{zz}\frac{dv_z}{dz}\right) = 2\cdot 3^{(n-1)/2}m\left|\frac{dv_z}{dz}\right|^{n-1}\frac{dv_z}{dz}. \tag{19}$$

Equations (18) and (19) are derived by substituting Equations (10)–(12), (16) and (17) into Eq. (9); expanding to matrix form; writing the zz and xx components; and invoking assumption 7 to changing the partial derivatives to total derivatives. Equations (18) and (19) were used to describe the "in span" material response.

Boundary conditions for the viscoelastic response in the free span are specified as

$$v_z = v_{0^+}, \quad (\tau_{zz} - \tau_{xx}) = (\tau_{zz} - \tau_{xx})_{0^+} \quad \text{at} \quad z = 0^+, \tag{20}$$

$$v_z = v_L \quad \text{at} \quad z = L \tag{21}$$

where the subscripts "0^+" and "L" denote the positions just after the upstream roller and the end of the span, respectively. L is the length of the span.

The governing equations can be nondimensionalized for general analysis. Following Fisher and Denn (1976), the dimensionless variables were defined as

$$\xi = \frac{z}{L}, \quad \phi = \frac{v_z}{v_{0^-}}, \quad T_{ij} = \tau_{ij}\frac{A_{0^+}}{F} \tag{22}$$

where the subscript "0^-" denotes the position just before the upstream roller. Using the dimensionless variables defined above, Eqs. (8), (18), and (19) become

$$(T_{zz} - T_{xx})' = \frac{\phi'}{\phi}(T_{zz} - T_{xx}), \tag{23}$$

$$T_{xx} + D_e|\phi'|^{n-1}(\phi T'_{xx} + \phi' T_{xx}) = -N|\phi'|^{n-1}\phi', \tag{24}$$

$$T_{zz} + D_e|\phi'|^{n-1}(\phi T'_{zz} - 2\phi' T_{zz}) = 2N|\phi'|^{n-1}\phi' \tag{25}$$

where the prime indicates differentiation with respect to ξ. Two dimensionless groups, D_e and N, naturally appear in Eqs. (24) and (25)

$$D_e = 3^{(n-1)/2}\left(\frac{m}{G}\right)\left(\frac{v_{0^-}}{L}\right)^n, \tag{26}$$

$$N = D_e G\frac{A_{0^+}}{F}. \tag{27}$$

D_e is the Deborah number, which reflects the ratio of the characteristic time of the material response to the characteristic time of the operation. N is the ratio of viscous stress to the applied tensile stress in the z-direction.

Integrating Eq. (23),

$$T_{zz} - T_{xx} = c\phi \tag{28}$$

where c is an integration constant and can be determined from the boundary condition

$$\phi = \phi_{0^+}, \quad T_{zz} - T_{xx} = 1 \quad \text{at} \quad \xi = 0^+ \tag{29}$$

yielding

$$c = \frac{1}{\phi_{0^+}}. \tag{30}$$

The parameter c is of particular importance since the effect of the upstream conditions on the span of current interest enters the calculations through c. Hence, c may be thought of as a tension transfer parameter.

Subtracting Eq. (24) from Eq. (25) yields

$$(T_{zz} - T_{xx}) + D_e|\phi'|^{n-1}[\phi(T'_{zz} - T'_{xx}) - \phi'(2T_{zz} + T_{xx})] = 3N|\phi'|^{n-1}\phi'. \tag{31}$$

By noting that $2T_{zz} + T_{xx} = 3T_{zz} - (T_{zz} - T_{xx})$ and substituting Eq. (28), Equation (31) becomes

$$c\phi + D_e|\phi'|^{n-1}[c\phi\phi' - \phi'(3T_{zz} - c\phi)] = 3N|\phi'|^{n-1}\phi' \tag{32}$$

which can be solved for T_{zz}.

Downloaded 04 May 2010 to 171.66.16.28. Redistribution subject to ASME license or copyright; see http://www.asme.org/terms/Terms_Use.cfm

$$T_{zz} = \frac{c\phi}{3D_e|\phi'|^{n-1}\phi'} + \frac{2c\phi}{3} - \frac{N}{D_e}, \quad (33)$$

and differentiated with respect to ξ to give

$$T'_{zz} = c\left[\frac{1}{3D_e|\phi'|^{n-1}} - \frac{\phi(|\phi'|^{n-1})'}{3D_e|\phi'|^{2n-2}\phi'} - \frac{\phi\phi''}{3D_e|\phi'|^{n-1}(\phi')^2} + \frac{2\phi'}{3}\right], \quad (34)$$

where the double prime indicates the second derivative with respect to ξ. Equation (34) can be simplified to

$$T'_{zz} = c\left\{\frac{1}{3D_e|\phi'|^{n-1}} - \frac{n\phi\phi''}{3D_e|\phi'|^{n+1}} + \frac{2\phi'}{3}\right\}. \quad (35)$$

Equations 33 and 35 can be substituted into Equation 25 and manipulated to give the governing equation for the dimensionless velocity of a viscoelastic web in a free span

$$\phi - 2D_e^2\phi|\phi'|^{2n-2}\phi'^2 + \text{sign}\,(\phi')\left[\left(D_e\phi - \frac{3N}{c}\right)|\phi'|^n - nD_e\phi^2|\phi'|^{n-2}\phi''\right] = 0. \quad (36)$$

Boundary conditions for the governing equation are

$$\phi = \phi_{0^+} \quad \text{at} \quad \xi = 0^+, \quad (37)$$

and

$$\phi = D_R = \frac{v_L}{v_{0^-}} \quad \text{at} \quad \xi = 1 \quad (38)$$

where D_R is the draw ratio in the span.

3 Solution of the Governing Equation

The governing equation can be solved by standard numerical methods. In this paper, a fourth-order Runge-Kutta method was used.

In open-loop control, roller speeds are specified thereby resulting in a boundary value problem. A shooting method (Gerald and Wheatley, 1989) was used to transform the boundary value problem to an initial value problem. The first derivative of the dimensionless velocity at $\xi = 0^+$ is needed in this procedure:

$$\phi'_{0^+} = \text{sign}\,\{[3(T_{zz})_{0^+} - 2]D_e + 3N\} \times \left|\frac{1}{[3(T_{zz})_{0^+} - 2]D_e + 3N}\right|^{1/n}. \quad (39)$$

The derivative can be evaluated from the initial stress and the model parameters.

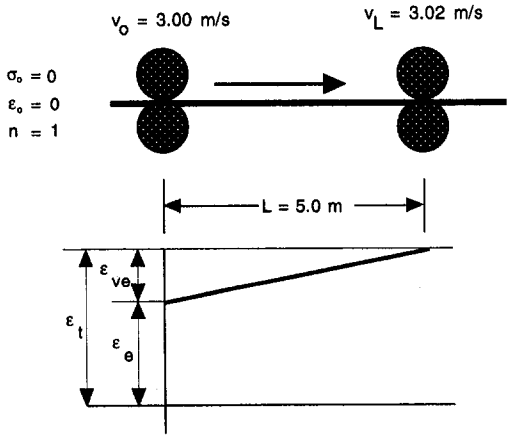
The shooting procedure is as follows: Assume c, calculate $\phi_{0^+} = 1/c$, and solve the governing equation with the corresponding initial conditions until $\phi_1 = D_R$ to the required precision.

In closed-loop control, the tension is specified. Hence, N and ϕ'_{0^+} are known and the initial value problem can be solved in a straightforward manner. In this case, a torque balance for the roller can be used to relate the velocity to the tension (Shin, 1991; Reid and Lin, 1993).

In a multispan system with mixed control, the governing equation must be solved simultaneously for each span until the entire system is unified.

4 Numerical Results and Discussion

The model equation was solved using the methods described in the previous sections for specific cases to illustrate the performance of the model and the effects of viscoelasticity. The results were also generalized to extend the applicability of the model.



Relaxation Time(sec)	$\varepsilon_{ve}/\varepsilon_t$ (%)
10	14.3
100	1.64
1000	0.165

Fig. 3 A case study of a single open span

4.1 Single Span Behavior. A single span system with typical dimensions and operating conditions is shown in Fig. 3. The initial conditions were taken as no stress, no strain, and the power-law exponent was set to 1. Figure 3 also illustrates that the total strain, ϵ_t, is the sum of a recoverable, elastic strain, ϵ_e, and a partially recoverable, viscoelastic strain, ϵ_{ve}. The elastic strain occurs instantaneously as the material enters the span, in accordance with Hooke's Law for a material experiencing a sudden change in stress. The viscoelastic deformation occurs over time as the material elements move across the span.

As would be expected, the relative contributions of the elastic and viscoelastic strains are a strong function of the relaxation time of the web material. A purely Hookean material would have an infinite relaxation time and there would be no viscoelastic contribution to the strain. The results of the model for three different relaxation times, all other conditions constant, clearly reproduce the expected trend. Typical relaxation times for web materials are of order magnitude 10^2 sec. which corresponds to a viscoelastic deformation of approximately one percent for the case shown in Fig. 3. Although the viscoelastic deformation may be small for a single span, the tension as will be demonstrated below, is very sensitive to the viscoelastic strain.

The sudden change in strain upon entering a new span followed by a gradual change in strain over the span is in agreement with the experimental observations of (Hauptmann and Cutshall, 1977). In operating web systems, most of the strain occurs at the very beginning of the span resulting in a very high strain rate. This entrance region in our model corresponds to the transient zone across the roller in an actual operation. However, we have assumed that this region is of negligible length and thus the stress and accompanying strain changes are instantaneous.

Generally, if the web is initially in an unstressed state, the irrecoverable or permanent strain at the end of the span, ϵ_p, is evaluated by

$$\epsilon_p = \epsilon_t - \Delta\epsilon_e \quad (40)$$

where $\Delta\epsilon_e$ is the elastic recovery corresponding to the tension F. If we assume that the unloading is linear and obeys Hooke's Law,

$$\Delta\epsilon_e = \frac{F}{A_L E}. \quad (41)$$

Downloaded 04 May 2010 to 171.66.16.28. Redistribution subject to ASME license or copyright; see http://www.asme.org/terms/Terms_Use.cfm

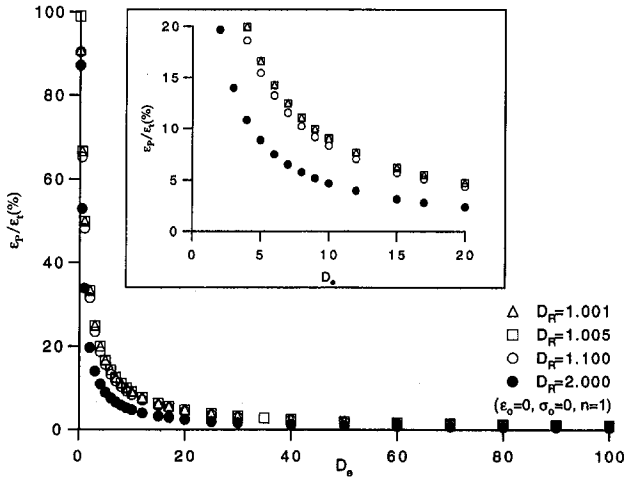


Fig. 4 Permanent deformation as a function of Deborah number with draw ratio as a parameter for a single span

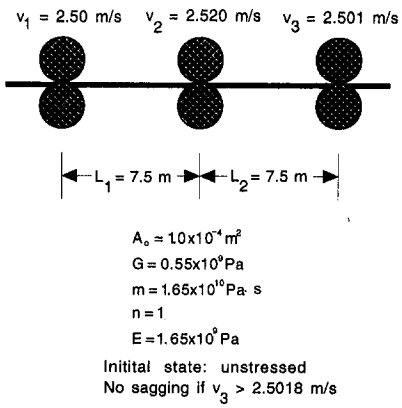


Fig. 6 Parameters for the case study of the effect of viscoelasticity for two open spans in series

The ratio ϵ_p/ϵ_t can be expressed as

$$\frac{\epsilon_p}{\epsilon_t} = \frac{cD_R - 1}{D_R - 1}. \tag{42}$$

Figure 4 shows the relationship of ϵ_p/ϵ_t to D_e with D_R as a parameter if the web is initially unstressed and $n = 1$. When D_e approaches zero (the Newtonian fluid limit) and infinity (purely elastic solid limit), the ratio reaches 100 percent and zero, respectively, as would be expected.

The total strain is closely related and all other factors being equal, is determined by D_R. As D_R increases, ϵ_e and ϵ_p will each increase. However, Fig. 4 demonstrates that ϵ_p will not increase to the same extent as ϵ_e. The degree to which the material can viscoelastically respond to the tension in the span is limited by the length of time the material remains in the span. Since increasing D_R does not significantly affect t_{span}, the viscoelastic response of the material is constrained and ϵ_e, which can be instantaneously achieved, must become proportionally larger to achieve the required total strain.

The general relationship of N, which is proportional to the reciprocal tension, to D_e and D_R for a single span, is shown in Fig. 5 for an unstressed initial state. For a fixed D_e, the tension increases (N decreases) with increasing draw ratio. Figure 5 also shows the extreme sensitivity of the tension to the draw ratio.

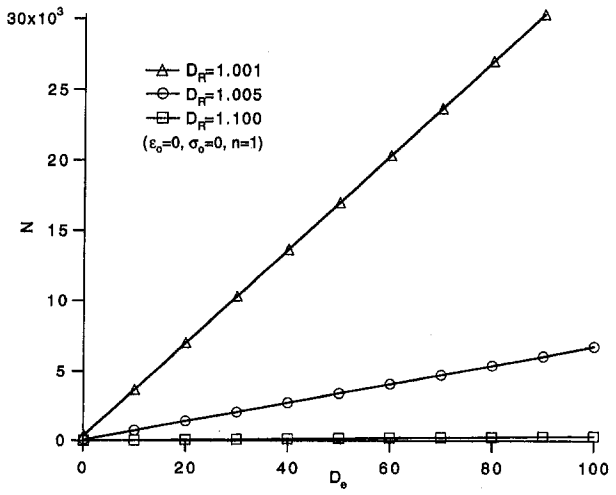


Fig. 5 Dimensionless inverse tension as a function of Deborah number with draw ratio as a parameter for a single span

4.2 Irrecoverable Deformation. In order to demonstrate the significance of the viscoelastic deformation, the configuration shown in Fig. 6 was considered with characteristic material parameters for an isotactic polypropylene film at room temperature. The system consists of two open spans with lengths of 7.5 m. The web enters the first span in an unstressed state with a cross-sectional area of 1.0×10^{-4} m^2. The material parameters are given in Fig. 6.

The speeds of the three roller sets were taken as 2.500, 2.520, and 2.501 m/s, respectively. The Deborah number of the first span, under these conditions, is 10. The draw ratio in the first span is greater than one (1.008) but, in the second span, D_R is less than one (0.992). This velocity distribution forces the web to stretch in the first span and then allows contraction in the second span.

The viscoelastic model predicts the tensions in the two spans to be 1191 N and −48 N, respectively, while Hooke's Law gives the tensions as 1310 N and 66 N, respectively. The Hookean model predicts a tension in the first span approximately ten percent greater than the viscoelastic model. This result is expected since the viscoelastic model allows for a stress relaxation mechanism which is absent from the Hookean model. However, the tensions in the second span, as predicted by the two models, are quite different. The negative tension given by the viscoelastic model indicates that the web must be compressed in order to meet the velocity specifications. Since a web cannot sustain a negative tension, the second span must be in an undesirable slack or sagging state.

The sagging in the second span is due to the irrecoverable deformation produced in the first span. The web line must be operated under conditions such that the draw ratio in the second span will be greater than some minimum value that will wind up the irrecoverable part of the deformation. However, Hooke's Law cannot predict the irrecoverable deformation and predicts that the speed of the third roller need only be equal to or greater than the speed of the first roller. In this case study, the small irrecoverable deformation in the first span due to the viscoelasticity of the material significantly affects the system behavior. These results explain the failure of some open-loop control systems that were designed with Hooke's Law and clearly illustrates the need for more realistic models of the system behavior.

The minimum draw ratio required in the second span to prevent sagging is closely related to the irrecoverable deformation and draw ratio of the previous span. If the material enters the first span in an unstressed initial state, the minimum required draw ratio, $D_{R2,min}$, in the second span can be expressed as

Downloaded 04 May 2010 to 171.66.16.28. Redistribution subject to ASME license or copyright; see http://www.asme.org/terms/Terms_Use.cfm

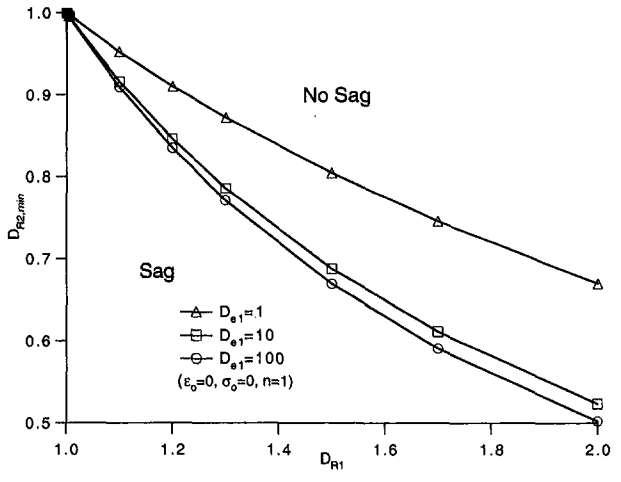


Fig. 7 Minimum required draw ratio to prevent sagging in the second span as a function of the draw ratio in the first span with Deborah number as a parameter

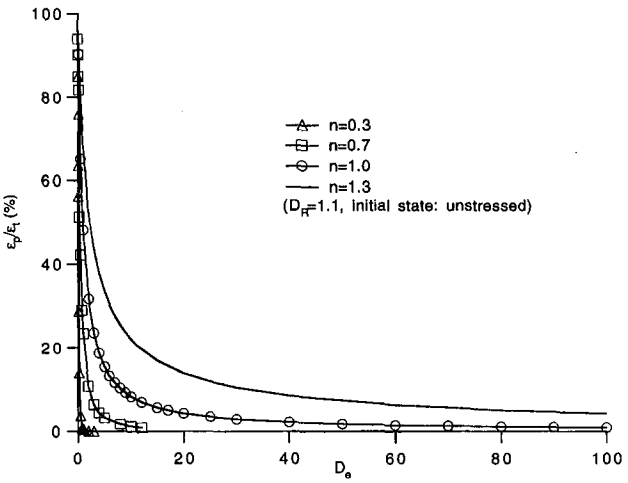


Fig. 8 Permanent deformation as a function of Deborah number with the power-law exponent as a parameter

$$D_{R2,\,\min} = c_1 = \frac{1 + \epsilon_{p1}}{D_{R1}} \tag{43}$$

where the subscript "1" means the first span. The relationship of $D_{R2,\min}$ to D_{e1} and D_{R1} is shown in Fig. 7. For a fixed D_{e1}, $D_{R2,\min}$ decreases as D_{R1} increases. Figure 7 shows that $D_{e1} = 100$ is a close approximation to the limiting case of $D_{e1} = \infty$, when $D_{R2,\min} = 1/D_{R1}$. In design, a larger D_e is desirable to reduce the tendency to sag under a given set of operating conditions. Larger Deborah numbers can be achieved by increasing the operating speed or reducing the span length.

In the example of Fig. 6, the minimum draw ratio is 0.9928 while the actual draw ratio (0.9925) is within the sagging region in Fig. 7.

4.3 Tension Transfer. The tension in the current span of interest is affected by the viscoelastic response of the material and the tension transferred from the previous span. Within any span, the tension must balance the elastic step change across the roller and the viscoelastic deformation within the span so that the kinematic conditions at the span ends can be met.

The effect of the tension in the previous span could be examined by an example with the same system configuration and operating condition as shown in Fig. 6 except that the speed of the third roller set is allowed to vary. Several cases are shown in Table 1. When $v_3 = v_2 = 2.520$ m/s, the predicted tensions in the two spans are 1191 N and 1084 N, respectively. In the second span, there is no further stretching because the two end roller sets run in the same speeds. The tension in the second span is due solely to the tension transferred from the first span. The difference in the two tensions is due to the viscoelastic stress relaxation of the web.

If the speed of the third roller set is increased to 2.530 m/s, the tension in the second span will be 1673 N. The increase of the tension is due to the further stretching in the second span since the draw ratio is greater than one. If the speed of the third roller set is lowered to 2.510 m/s, the tension will be 490 N. The decrease of the tension is due to the relaxation in the second span (draw ratio is less than one) from the previous tension. If we reduce the speed of the third roller is set back to 2.500 m/s (same as v_1), the tension in the second span will be negative (−108 N). This corresponds to a sagging state in the second span since the tension transferred from the first span could not compensate for the relaxation behavior of the material.

Table 1 Tension in the second span as a function of the velocity of the third roller set

v_3, m/s	F_1, N	F_2, N
2.520	1191	1084
2.530	1191	1673
2.510	1191	490
2.500	1191	−108
	v_1 = 2.500 m/s, v_2 = 2.520 m/s	

In these four cases, the tensions predicted by Hooke's Law in the second span are 1310 N, 1956 N, 657 N, and zero, respectively. The deviations of the Hookean results from the viscoelastic results for the tension in the second span are 20.8 percent, 16.9 percent, and 34.2 percent, respectively, in the first three cases. In the fourth case, the deviation is so great that steady-state operations would not be possible. In the first span, the deviation in tension is 9.92 percent. No matter how v_3 changes, the deviation in the second span is larger than in the first span as long as no sagging occurs. Hence, viscoelasticity is increasingly important along the web line from the beginning to the end because of the accumulation of the irrecoverable deformation.

4.4 Effect of the Power-Law Exponent, n. As a power-law parameter, n reflects the dependence of the viscosity of the material on the strain rate. The parameter n also appears in the governing equation as an independent parameter. The effect of n on system behavior can be examined by considering the relationship of ϵ_p/ϵ_t to D_e and n for a constant draw ratio, $D_R = 1.1$, as shown in Fig. 8. To achieve the fixed draw ratio, a shear thinning material ($n < 1$) responds with smaller permanent deformation than a shear thickening material ($n > 1$) for constant D_e. This result would seem to be counter intuitive. However, the explanation follows from examination of Eq. (26). For D_e to remain constant for a given material as n increases, the ratio of v_0^-/L must decrease either because v_0^- has decreased or L has increased. In either case, t_{span} will increase; resulting in a greater opportunity for the material to relax through a permanent deformation.

5 Conclusion

Although the effect of viscoelasticity may be very small in the first span of a web handling system, the effect can be dramatic in the subsequent spans. The tension predicted in the second span by the viscoelastic model differs significantly from the predictions of a model based on Hooke's law. In some cases the tension predictions of the Hookean model are so poor that a web handling system could not physically operate under the conditions specified. The importance of viscoelasticity has been

Downloaded 04 May 2010 to 171.66.16.28. Redistribution subject to ASME license or copyright; see http://www.asme.org/terms/Terms_Use.cfm

clearly demonstrated and must be given consideration in modeling web handling operations with more than one span.

Acknowledgment

The authors wish to acknowledge the Oklahoma Center for Integrated Design and Manufacture for supporting this work and Drs. Ku-Chin Lin and Karl N. Reid for many insightful discussions.

References

Akatsuka, M., 1990, "Models of Longitudinal Web Behavior in the Handling Process," M.S. Thesis, Oklahoma State University.

Alaie, S. M., and Papapastasiou, T. C., 1991, "Film Casting of Viscoelastic Liquid," *Polym. Eng. Sci.*, Vol. 31, No. 2, pp. 67–75.

Bird, R. B., Armstrong, R. C., and Hassager, O., 1987, *Dynamics of Polymeric Liquids* (Vol. 1, Fluid Mechanics), 2nd ed., John Wiley and Sons, New York.

Campbell, D. P., 1958, *Process Dynamics,* John Wiley and Sons, New York.

Fisher, R. J., and Denn, M. M., 1976, "A Theory of Isothermal Melt Spinning and Draw Resonance," *AIChE Journal,* Vol. 22, No. 2, pp. 236–246.

Gerald, C. F., and Wheatley, P. O., 1989, *Applied Numerical Analysis,* 4th ed., Addison-Wesley, Reading, PA.

Han, C. D., 1976, *Rheology in Polymer Processing,* Academic Press, New York.

Hauptmann, E. G., and Cutshall, K. A., 1977, "Dynamic Mechanical Properties of Wet Paper Webs," *Tappi,* Vol. 60, No. 10, pp. 106–108.

Reid, K. N., and Lin, K.-C., 1993, "Control of Longitudinal Tension in Multi-Span Web Transport Systems During Start Up," *Proceedings of the Second International Conference on Web Handling,* Stillwater, OK.

Shin, K.-H., 1991, "Distributed Control of Tension in Multi-Span Web Transport Systems," Doctoral Thesis, Oklahoma State University, Stillwater, OK.

Spearot, J. A., and Metzner, A. B., 1972, "Isothermal Spinning of Molten Polyethylenes," *Transactions of the Society of Rheology,* Vol. 16, No. 3, pp. 495–518.

Downloaded 04 May 2010 to 171.66.16.28. Redistribution subject to ASME license or copyright; see http://www.asme.org/terms/Terms_Use.cfm

Taylor-Couette Instability With a Continuous Spectrum

L. S. Yao

S. Ghosh Moulic[1]

Mechanical and Aerospace Engineering Department, Arizona State University, Tempe, AZ 85287

Nonlinear evolution of a continuous spectrum of unstable waves near the first bifurcation point in circular Couette flow has been investigated. The disturbance is represented by a Fourier integral over all possible axial wave numbers, and an integrodifferential equation for the amplitude-density function of a continuous spectrum is derived. The equations describing the evolution of monochromatic waves and slowly varying wave packets of classical weakly nonlinear instability theories are shown to be special limiting cases. Numerical integration of the integrodifferential equation shows that the final equilibrium state depends on the initial disturbance, as observed experimentally, and it is not unique. In all cases, the final equilibrium state consists of a single dominant mode and its harmonics of smaller amplitudes. The predicted range of wave numbers for stable supercritical Taylor vortices is found to be narrower than the span of the neutral curve from linear theory. Taylor-vortex flows with wave numbers outside this range are found to be unstable and to decay, but to excite another wave inside the narrow band. This result is in agreement with the Eckhaus and Benjamin-Feir sideband instability. The results also show that a linearly stable long wave can excite a short unstable wave through nonlinear wave interaction. An important implication of the existence of nonunique equilibrium states is that the torque induced by the fluid motion cannot be determined uniquely. The numerical results show that the uncertainty, *associated with nonuniqueness, of using any accurately measured Taylor-vortex torque slightly above the first bifurcation point in engineering practice can be as large as ten percent. The presence of multiple solutions at a fixed Reynolds number for a given geometry in Taylor-Couette flows has been known since Coles' monumental contribution in 1965. A theoretical confirmation has come only 30 years later. It is worthwhile to point out that the existence of multiple solutions, found by Coles, differs from current popular bifurcation theories. The current study indicates that the state of flows on a stable bifurcation branch can involve any wave number within a finite band and can not be determined uniquely. The multiple solutions in Coles' sense have also been found for mixed-convection flows (Yao and Ghosh Moulic, 1993, 1994) besides the Taylor-Couette flows. We believe that the nonuniqueness of Coles sense, which complements the bifurcation theories, is a generic property for all fluid flows.*

1 Introduction

Taylor (1923) showed that the flow between two concentric rotating cylinders can become unstable, resulting in a sequence of toroidal vortices spaced regularly along the axis of the cylinders. Due to its importance in the development of fluid dynamics, the instability of circular Couette flow has been the subject of many investigations. A considerable body of literature has accumulated on the linear instability eigenvalue problem and the experimental measurements of the various transition boundaries. Much of the early work on the linear instability problem is discussed by Chandrasekhar (1961). The development of finite-amplitude motions for Taylor numbers above the critical Taylor number was first studied by Stuart (1958), who used an energy-balance integral method to account for the distortion of the mean flow by the disturbance. Later, Davey (1962) used the formal expansion procedure of Stuart (1960) and Watson (1960) to compute the amplitude and form of the Taylor-vortex flow. Calculations based on the Stuart-Watson expansion can be carried out for any wave number lying in the unstable region of linear instability theory near the neutral curve. These calculations predict supercritical equilibrium states. However, Kogelman and DiPrima (1970), following the method of Eckhaus (1965), showed that, in the limit as the Taylor number approaches its critical value, Taylor-vortex flows with wave numbers outside a band of width $1/\sqrt{3}$ times the span of the neutral curve of linear theory and centered around the critical wave number k_c of linear theory are unstable to axisymmetric disturbances. This instability is due to sideband perturbations which resonate with the first harmonic of the fundamental mode to mutually reinforce each other. The Eckhaus instability mechanism for two-dimensional flows that are periodic in one spatial dimension was shown to be related to the Benjamin-Feir (1967) instability mechanism of the two-dimensional Stokes water wave by Stuart and DiPrima (1978).

As the Taylor number is increased, the Taylor vortices become unstable at a second critical Taylor number, and a new flow pattern is established with azimuthally propagating waves superposed on the Taylor vortices. This wavy instability was first systematically studied by Coles (1965), who observed that the spatial structure of doubly periodic, Taylor-vortex flow (wavy Taylor-vortex flow) was not unique. He observed different axial and azimuthal wave numbers at the same Taylor number. The nonuniqueness of wave number observed by Coles in doubly periodic flows was later shown to occur in the rotationally symmetric case by Snyder (1969) and Burkhalter and

[1] Present address: Department of Mechanical Engineering, Indian Institute of Technology, Bombay, India.

Contributed by the Applied Mechanics Division of THE AMERICAN SOCIETY OF MECHANICAL ENGINEERS for publication in the ASME JOURNAL OF APPLIED MECHANICS.

Discussion on this paper should be addressed to the Technical Editor, Professor Lewis T. Wheeler, Department of Mechanical Engineering, University of Houston, Houston, TX 77204-4792, and will be accepted until four months after final publication of the paper itself in the ASME JOURNAL OF APPLIED MECHANICS.

Manuscript received by the ASME Applied Mechanics Division, Jan. 28, 1994; final revision, June 26, 1994. Associate Technical Editor: S. A. Berger.

Copyright © 1995 by ASME

Downloaded 04 May 2010 to 171.66.16.28. Redistribution subject to ASME license or copyright; see http://www.asme.org/terms/Terms_Use.cfm

Koschmieder (1974). Snyder (1969) showed that, while the onset wavelength was unique, Taylor vortex flows of different wave numbers could be obtained at the same value of the Taylor number by varying the initial conditions. He observed that there was a band of accessible wave numbers narrower than the band that can grow according to linear theory. The extent of this band was found to be unsymmetrical about the onset wave number, with the increase occurring on the side of increasing wave number. Burkhalter and Koschmieder (1973) studied the variation of the wavelength of supercritical Taylor vortices experimentally. They found that singly periodic Taylor vortices maintained the critical wavelength over a wide range of Taylor numbers if the Taylor number was varied quasi-steadily and end effects were properly taken into account. In a later article, Burkhalter and Koschmieder (1974) reported results in which Taylor vortices were established through a sudden start of the inner cylinder. They found that a sudden start to a preset supercritical Taylor number gives the fluid a choice in the selection of the wavelength. Once established through a sudden start, a wavelength did not change its value if the Taylor number was maintained for a very long time or if the Taylor number was varied over larger intervals provided the flow was singly periodic.

In this investigation, the nonlinear interactions among Taylor vortices with different wave numbers is studied using a perturbation method. The maximum amplification rate predicted by linear instability theory is used as the expansion parameter. The disturbance is represented by a Fourier integral over all possible wavenumbers. Thus, the analysis is formulated with a continuous spectrum and therefore differs from previous theoretical studies. An integrodifferential equation describing the temporal evolution of the amplitude density of the wave components of a continuous spectrum is derived in Section 2. The evolution of monochromatic waves and slowly varying wave packets in classical weakly nonlinear instability theories are special limiting cases of the integrodifferential equation. However, the classical weakly nonlinear theories incorrectly assume a priori that the mean-flow distortion induced by nonlinear interactions is of a smaller order of magnitude compared to the amplitude of the dominant wave, as explained in the Appendix.

The choice of the small expansion parameter in the perturbation analysis in Section 2 differs from the small parameter used in the weakly nonlinear theory of monochromatic waves by Stuart (1960). The present ordering allows the possibility of nonlinear interactions among resonant triads. Such nonlinear interactions among resonant triads are absent in monochromatic waves without considering its interaction with the leading-order deformation of the mean flow, but can occur in the case of a continuous spectrum of waves. The usual ordering employed in classical weakly nonlinear theories does not consider resonant triads, and leads to a result which fails to account for proper energy exchange between the waves and the mean flow. In the special limiting cases of monochromatic waves and slowly varying wavepackets without considering the leading-order deformation of the mean flow, the final form of the amplitude equations obtained from the current formulation are the same as those in classical weakly, nonlinear instability theories.

In Section 3, results are presented for the case when the outer cylinder is at rest and has a radius which is twice that of the inner cylinder. The integrodifferential equation describing the evolution of the amplitude density of the wave components has been solved with different initial conditions. In all cases, the final equilibrium state consisted of a single dominant mode together with its harmonics and an induced mean-flow distortion. However, the final dominant mode in the equilibrium state was found to depend on the waveform of the initial disturbance and the initial wave amplitudes; consequently, the equilibrium state is nonunique. These results are in agreement with the experimental observations of Snyder (1969) and Burkhalter and Koschmieder (1974). The range of wave numbers of stable supercritical finite-amplitude Taylor vortices predicted by the present theory is found to be a subset of the linearly unstable band of wave numbers. Taylor vortex flows with wave numbers outside this subset, but within the linearly unstable band, are found to be unstable. This finding agrees with the Eckhaus and Benjamin-Feir sideband instability, and implies that a sideband instability is a consequence of nonlinear energy transfer among different interacting waves. Also, our results indicate that the selection of the equilibrium wave number is due to the intriguing nonlinear wave interactions and can be naturally determined.

The existence of multiple stable equilibrium states at the same Taylor number implies that the torque induced by the fluid motion cannot be determined uniquely. This nonuniqueness of the equilibrium state has also been observed in direct numerical simulations of mixed-convection flow in a heated vertical annulus using spectral methods employing a Fourier-Chebyshev expansion (Yao and Ghosh Moulic, 1994). We believe that multiple stable equilibrium is a generic property for all fluid flows. Consequently, any physical property transported by the fluid such as heat, salt, etc., can at best be determined within a limit of uncertainty associated with nonuniqueness.

2 Analysis

Consider the flow between two infinitely long concentric circular cylinders with radii r_1 and r_2 ($>r_1$) rotating at angular velocities Ω_1 and Ω_2, respectively. The governing equations are the continuity and Navier-Stokes equations in cylindrical polar coordinates, (r, θ, z). Let (u, v, w) denote the corresponding velocity components, p denotes the pressure, and t is the time. The flow is assumed to be rotationally symmetric so that u, v, and w are independent of the azimuthal angle, θ. All lengths have been scaled by the distance between the cylinders $d = r_2 - r_1$, the velocity components by $r_1\Omega_1$, the time by d^2/ν and the pressure by $\rho r_1^2\Omega_1^2$, where ρ is the fluid density and ν is the kinematic viscosity. The Reynolds number is defined as $R = \Omega_1 r_1 d/\nu$.

The boundary conditions are $u = w = 0$, $v = 1$ when $r = r_i$ and $u = w = 0$, $v = \mu(1 + d/r_1)$ when $r = r_0$, where $\mu = \Omega_2/\Omega_1$ is the ratio of the angular speeds of the outer and inner cylinders respectively, $r_i = r_1/d$ and $r_0 = r_1/d + 1$.

The basic state is steady laminar Couette flow, described by $u = w = 0$, $v = V(r) = A_0 r + B_0/r$, where

$$A_0 = \frac{\mu - \eta^2}{\eta(1 + \eta)}, \quad B_0 = \frac{(1 - \mu)\eta}{(1 + \eta)(1 - \eta)^2}$$

and $\eta = r_1/r_2$ is the radius ratio. The stability of this flow is studied by superposing a disturbance, which is unnecessarily to be small, on the basic state and writing the disturbed velocity field as $(u, v, w) = (u'(r, z, t), V(r) + v'(r, z, t), w'(r, z, t))$. In order to study the nonlinear interactions between the wave components of a continuous spectrum, the disturbance velocities are expressed as Fourier integrals over all possible axial wave numbers. Thus, the azimuthal velocity component is written as $v'(r, z, t) = \int_{-\infty}^{\infty} \hat{v}(k, r, t)e^{ikz}dk$. Similar expressions may be written for the other velocity components.

The linear instability of the basic state is studied by assuming the disturbance to be infinitesimal, and expressing the Fourier amplitudes of the disturbance quantities in separable form as

$$(\hat{u}(k, r, t), \hat{v}(k, r, t), \hat{w}(k, r, t), \hat{p}(k, r, t)) = [\tilde{u}(k, r), \tilde{v}(k, r), \tilde{w}(k, r), \tilde{P}(k, r)]e^{\sigma t},$$

where k is the axial wave number and σ is the amplification rate. The linearized disturbance equations may be written in terms of operators L_1, L_2, and L_3 as

$$D\tilde{u} + \frac{\tilde{u}}{r} + ik\tilde{w} = 0,$$

Downloaded 04 May 2010 to 171.66.16.28. Redistribution subject to ASME license or copyright; see http://www.asme.org/terms/Terms_Use.cfm

$$L_1(k, \sigma, \tilde{U}, \tilde{P}) = -\left(L - \frac{1}{r^2}\right)\tilde{u} - \frac{2RV(r)\tilde{v}}{r} + RD\tilde{P} + \sigma\tilde{u} = 0,$$

$$L_2(k, \sigma, \tilde{U}, \tilde{P}) = -\left(L - \frac{1}{r^2}\right)\tilde{v} + R\left(DV(r) + \frac{V(r)}{r}\right)\tilde{u} + \sigma\tilde{v} = 0,$$

$$L_3(k, \sigma, \tilde{U}, \tilde{P}) = -L\tilde{w} + ikR\tilde{P} + \sigma\tilde{w} = 0, \quad (1)$$

where $L \equiv D^2 + (1/r)\,D - k^2$, $D \equiv (d/dr)$ is the operator denoting differentiation with respect to r, and $\tilde{U} = (\tilde{u}, \tilde{v}, \tilde{w})$. The boundary conditions are

$$\tilde{u} = \tilde{v} = \tilde{w} = 0 \text{ when } r = r_i \text{ and } r = r_0. \quad (2)$$

Equations (1) with the boundary conditions (2) form an eigenvalue problem for the amplification rate, σ, for each wave number k. It is worth noting that for R not too large, the least stable eigenvalue σ_1 is real for all k, that is, the disturbed flow is nonoscillatory. The eigenfunctions $\tilde{u}$ and $\tilde{v}$ corresponding to the least stable eigenvalue are real, while the eigenfunction $\tilde{w}$ is purely imaginary. In this investigation, the eigenfunctions have been normalized so that $\int_{r_i}^{r_0} r[|\tilde{u}|^2 + |\tilde{v}|^2 + |\tilde{w}|^2]dr = 1$.

The nonlinear growth of the disturbances is studied by expanding the Fourier amplitudes in a perturbation series. The maximum amplification rate predicted by linear instability theory is used as the expansion parameter ϵ. The amplification rate predicted by linear instability theory for a wave of wave number k may be expressed in terms of ϵ as $\sigma_1(k) = \epsilon a_0(k)$, where $a_0(k)$ is a constant of order one and $\sigma_1(k)$ is the largest eigenvalue of the linear instability operator for the mode with wave number k. It may be noted that the small parameter ϵ used in the present analysis differs from the small parameter used by in the weakly nonlinear theory of monochromatic waves Stuart (1960). The wave components of a continuous spectrum may exchange energy due to nonlinear interactions among resonant triads of wavenumbers. Such nonlinear interactions among resonant triads are absent in monochromatic waves. The present ordering allows the possibility of nonlinear interactions among resonant triads, and consequently differs from the usual ordering of classical weakly nonlinear theories of monochromatic waves. In the special limiting cases of monochromatic waves and slowly varying wave packets, the final form of the amplitude equations obtained from the current formulation is the same as those in the classical theories, as demonstrated later.

The expansion for the azimuthal disturbance velocity may be written as

$$\hat{v}(k, r, t) = \epsilon\hat{v}_1(k, r, T_1, T_2) + \epsilon^2\hat{v}_2(k, r, T_1, T_2) + \epsilon^3\hat{v}_3(k, r, T_1, T_2) + \ldots. \quad (3)$$

Here, $T_1 = \epsilon t$ and $T_2 = \epsilon^2 t$ are slow time scales. Expansions for the other dependent variables are given by similar expressions.

The first-order perturbation quantities are solutions of the linearized Navier-Stokes Eq. (1). They may be expressed in the form of separation of variables as

$$\hat{v}_1(k, r, T_1, T_2) = B(k, T_1, T_2)\tilde{v}_1(k, r), \quad (4)$$

where $\tilde{v}_1(k, r)$ is the eigenfunction of the linear instability operator corresponding to the least stable eigenvalue, and $B(k, T_1, T_2)$ is a slowly varying amplitude density function of order one.

The second-order perturbation quantities are described by the equations

$$D\hat{u}_2 + \frac{\hat{u}_2}{r} + ik\hat{w}_2 = 0,$$

$$L_j(k, \sigma_1(k), \hat{U}_2, \hat{P}_2) = -\left[\frac{\partial B}{\partial T_1}(k, T_1, T_2) - a_0(k)B(k, T_1, T_2)\right]\tilde{U}_{1j}(k, r) + \int_{-\infty}^{\infty} B(k_1, T_1, T_2)B(k - k_1, T_1, T_2) F_j(k_1, k - k_1, r)dk_1, \quad (5)$$

where the inertial forcing terms F_j depend on the linear instability eigenfunctions (Ghash Moulic, 1993). It may be noted that the finite amplitude disturbance for a selected wave number, k, has been expressed as a perturbation on a state of linear stability analysis with a amplification rate, $\sigma_1(k)$ (Yao and Rogers, 1992). Thus, the operators on the left-hand sides of Eqs. (5) are the same as those of linear instability theory, and a solution exists only if the right-hand side is orthogonal to the adjoint eigenfunction which satisfies the equation adjoint to (1). If the adjoint eigenfunctions are normalized so that $\int_{r_i}^{r_0}[u_1^+\tilde{u}_1 + v_1^+\tilde{v}_1 + w_1^+\tilde{w}_1]dr = 1$, application of the integrability condition results in the following integrodifferential equation describing the evolution of the amplitude density function on the T_1 time scale:

$$\frac{\partial B}{\partial T_1}(k, T_1, T_2) = a_0(k)B(k, T_1, T_2) + \int_{-\infty}^{\infty} b_0(k_1, k - k_1)B(k_1, T_1, T_2)B(k - k_1, T_1, T_2)dk_1, \quad (6)$$

where the interacting constant $b_0(k_1, k - k_1)$ is given by

$$b_0(k_1, k - k_1) = \int_{r_i}^{r_0}[u_1^+(k, r)F_1(k_1, k - k_1, r) + v_1^+(k, r)F_2(k_1, k - k_1, r) + w_1^+(k, r)F_3(k_1, k - k_1, r)]dr. \quad (7)$$

If Eq. (6) is satisfied, the solution to Eqs. (5) may be expressed in the form

$$\hat{U}_2(k, r, T_1, T_2) = \int_{-\infty}^{\infty} B(k_1, T_1, T_2) B(k - k_1, T_1, T_2)\tilde{U}_2(k_1, k - k_1, r)dk_1, \quad (8)$$

where the functions $\tilde{U}_2 = (\tilde{u}_2, \tilde{v}_2, \tilde{w}_2)$ are independent of the amplitude density function $B(k, T_1, T_2)$ and can be determined without solving the integrodifferential Eq. (6) (Ghash Moulic, 1993).

The disturbance velocity field at third order is described by the equations

$$D\hat{u}_3 + \frac{\hat{u}_3}{r} + ik\hat{w}_3 = 0,$$

$$L_j(k, \sigma_1(k), \hat{U}_3, \hat{P}_3) = -\frac{\partial B}{\partial T_2}(k, T_1, T_2)\tilde{U}_{1j}(k, r) - \int_{-\infty}^{\infty}[a_0(k_1) + a_0(k - k_1) - a_0(k)]B(k_1, T_1, T_2) B(k - k_1, T_1, T_2)\tilde{U}_{2j}(k_1, k - k_1, r)dk_1 + \iint_{-\infty}^{\infty} B(k_1, T_1, T_2)B(k_2, T_1, T_2) B(k - k_1 - k_2, T_1, T_2)G_j(k_1, k_2, k - k_1 - k_2, r)dk_1dk_2, \quad (9)$$

where the inertial forcing terms G_j depend on the linear instability eigenfunctions, $\tilde{U}_1$, and the functions $\tilde{U}_2$ determined at sec-

Downloaded 04 May 2010 to 171.66.16.28. Redistribution subject to ASME license or copyright; see http://www.asme.org/terms/Terms_Use.cfm

ond order. As in the case of the second-order equations, a solution to Eq. (9) exists only if an integrability condition is satisfied. Application of the Fredholm alternative theory yields a integrodifferential equation describing the evolution of the amplitude density function $B(k, T_1, T_2)$ on the T_2-time scale:

$$\frac{\partial B}{\partial T_2}(k, T_1, T_2) = \int_{-\infty}^{\infty} b_1(k_1, k - k_1)B(k_1, T_1, T_2)$$
$$B(k - k_1, T_1, T_2)dk_1 + \iint_{-\infty}^{\infty} c(k_1, k_2, k - k_1 - k_2)$$
$$B(k_1, T_1, T_2)B(k_2, T_1, T_2)$$
$$B(k - k_1 - k_2, T_1, T_2)dk_1dk_2, \quad (10)$$

where the interacting constants $b_1(k_1, k - k_1)$ and $c(k_1, k_2, k - k_1 - k_2)$ are given by

$$b_1(k_1, k - k_1) = [a_0(k) - a_0(k_1) - a_0(k - k_1)]$$
$$\times \int_{r_i}^{r_0} [u_1^+(k, r)\tilde{u}_2(k_1, k - k_1, r)$$
$$+ v_1^+(k, r)\tilde{v}_2(k_1, k - k_1, r)$$
$$+ w_1^+(k, r)\tilde{w}_2(k_1, k - k_1, r)]dr,$$

$$c(k_1, k_2, k - k_1 - k_2)$$
$$= \int_{r_i}^{r_0} [u_1^+(k, r)G_1(k_1, k_2, k - k_1 - k_2, r)$$
$$+ v_1^+(k, r)G_2(k_1, k_2, k - k_1 - k_2, r)$$
$$+ w_1^+(k, r)G_3(k_1, k_2, k - k_1 - k_2, r)]dr. \quad (11)$$

The integrodifferential Eqs. (6) and (10) obtained at second and third orders, respectively, may be combined to yield a single integrodifferential equation. In terms of a physical amplitude density function $A(k) = \epsilon B(k)$, the integrodifferential equation may be written as

$$\frac{\partial}{\partial t}A(k, t) = a(k)A(k, t) + I_1(k, t) + I_2(k, t), \quad (12)$$

where

$$I_1(k, t) = \int_{-\infty}^{\infty} b(k_1, k - k_1)A(k_1, t)A(k - k_1, t)dk_1, \quad (13)$$

$$I_2(k, t) = \int_{-\infty}^{\infty}\int c(k_1, k_2, k - k_1 - k_2)A(k_1, t)A(k_2, t)$$
$$A(k - k_1 - k_2, t)dk_1dk_2, \quad (14)$$

and the interacting constants $a(k)$ and $b(k_1, k - k_1)$ are given by

$$a(k) = \epsilon a_0(k),$$
$$b(k_1, k - k_1) = b_0(k_1, k - k_1) + \epsilon b_1(k_1, k - k_1). \quad (15)$$

It is worth noting that for R to be not too large, the interacting constants $a(k)$, $b(k_1, k - k_1)$ and $c(k_1, k_2, k - k_1 - k_2)$ are real. The first interacting constant $a(k)$ represents the amplification rate of linear instability theory. The interaction integral $I_1(k, t)$ represents nonlinear interaction among all possible triads of wave numbers k_1, $k - k_1$ and k, while the interaction integral $I_2(k, t)$ represents nonlinear interactions among all possible quartets of (primary) wave numbers k_1, k_2, $k - k_1 - k_2$ and k.

The integrodifferential Eq. (12) contains as a special case the equation describing the evolution of the amplitude of a discrete monochromatic wave. The amplitude density function for a discrete wave with wave number k_0, without considering the leading-order deformation of the mean flow, has the form

$$A(k, t) = A_{k_0}\delta(k - k_0) + A_{k_0}^*\delta(k + k_0), \quad (16)$$

where $\delta(k)$ represents the Dirac delta function and the asterisk denotes complex conjugates. Substitution of (16) into Eq. (12) yields

$$\frac{dA_{k_0}}{dt} = a(k_0)A_{k_0} + a_1|A_{k_0}|^2A_{k_0}, \quad (17)$$

where

$$a_1 = c(k_0, -k_0, k_0) + c(-k_0, k_0, k_0) + c(k_0, k_0, -k_0) \quad (18)$$

is the second interacting constant and represents the resonant quartet of the disturbance wave and its complex conjugate. Equation (17) describes the evolution of the amplitude of a discrete monochromatic wave (Stuart, 1960). It is worth pointing out that there are no combinations of wave numbers involving only the waves $\pm k_0$ which form a resonant triad. Thus, there is no contribution from the integral I_1 in the amplitude Eq. (17). The integrodifferential equation (12) can also be reduced to a system of N ordinary differential equations describing the evolution of the amplitudes of a set of N discrete waves (Benney and Newell 1967).

Obviously, Eq. (12) describes the temporal evolution of the amplitude density function in wave space. However, the integral formulation does include spatial variation of the velocity disturbances in physical space through the Fourier transformation, and is not restricted to periodic disturbances. In the special case of a wave packet near the critical wave number k_c with a narrow spectral band width δ, it becomes

$$v'(r, z, t) = \tilde{A}(k_c, z, t)\tilde{v}(k_c, r)e^{ik_cz} + \text{c.c}, \quad (19)$$

where

$$\tilde{A}(k_c, z, t) = \int_{k_c-\delta}^{k_c+\delta} A(k, t)e^{i(k-k_c)z}dk$$
$$= \epsilon \int_{-\delta/\epsilon}^{\delta/\epsilon} A(k_c + \epsilon K, t)e^{i\epsilon Kz}dK, \quad (20)$$

is the envelope of the wave packet and c.c. denotes the complex conjugate. In order to derive an equation for the envelope of the wave packet, we multiply Eq. (12) by $e^{i(k-k_c)z}$ and integrate with respect to k from $k_c - \delta$ to $k_c + \delta$. Using (20) and expanding the linear amplification rate in a Taylor series around $k = k_c$, it can be shown that in the limit as $\epsilon \to 0$, Eq. (12) reduces to the equation for the spatio-temporal evolution of a wave packet derived by Newell and Whitehead (1969), Segel (1969), and Stewartson and Stuart (1971):

$$\frac{\partial \tilde{A}}{\partial t} = a(k_c)\tilde{A} + +a_1|\tilde{A}|^2\tilde{A} + a_2\frac{\partial^2\tilde{A}}{\partial z^2} \quad (21)$$

where

$$a_1 = c(k_c, -k_c, k_c) + c(k_c, k_c, -k_c) + c(-k_c, k_c, k_c)$$

and

$$a_2 = -\frac{1}{2}\frac{d^2a}{dk^2}(k_c).$$

It is worth noting that the nonlinear term in (21) which leads to an exchange of energy among the wave components is identical to that for monochromatic waves. Equation (12), on the other hand, allows nonlinear exchange of energy among the wave components of a continous band of waves with widely differing wave numbers. The advantages of this formulation are

Downloaded 04 May 2010 to 171.66.16.28. Redistribution subject to ASME license or copyright; see http://www.asme.org/terms/Terms_Use.cfm

that it is simpler than previous theories and contains information on temporal and spatial evolution of nonlinear, interacting monochromatic waves, wave trains, and waves of a continuous spectrum.

3 Numerical Solution and Results

The expansion of the azimuthal velocity component can be summarized as

$$v(r, z, t) = V(r) + \int_{-\infty}^{\infty} A(k, t)\tilde{v}_1(k, r)e^{ikz}dk + \int_{-\infty}^{\infty}\int_{-\infty}^{\infty} A(k_1, t)A(k - k_1, t)\tilde{v}_2(k_1, k - k_1, r)e^{ikz}dk_1dk + \int_{-\infty}^{\infty}\int_{-\infty}^{\infty}\int_{-\infty}^{\infty} A(k_1, t)A(k_2, t)A(k - k_1 - k_2, t) \times \tilde{v}_3(k_1, k_2, k - k_1 - k_2, r)e^{ikz}dk_1dk_2dk + \ldots . \quad (22)$$

$A(k, t)$ becomes the final small parameter for our perturbation series. Results have been obtained for the case when the outer cylinder is at rest and has a radius which is twice that of the inner cylinder. The critical Reynolds number, R_c, predicted by linear instability theory for this case is 68.1, and the critical wavenumber at the onset of instability is $k_c = 3.16$. The Taylor number for this case is related to the Reynolds number by $T = (64/9)R^2$. In this investigation, we have obtained numerical results for a Reynolds number $R = 88.1$. Linear instability analysis predicts that at this Reynolds number, circular Couette flow is unstable to disturbances with wave numbers lying between 1.6 and 5.6. Thus, the range of wave numbers permitted for supercritical Taylor vortices according to linear theory is $1.6 \leq k \leq 5.6$. The results indicate that the equilibrium state consists of monochromatic waves. The amplitude of each wave is $A_k = A\Delta k$. The values of A_k differ slightly from the prediction by the monochromatic theory. The maximum value of A_k for $R = 88.1$ is 0.1 which is small. We also calculated the kinetic energy of the base flow and the first-order perturbation terms for $k = 3$. The values are 0.1578 and 0.0096, respectively. Their ratio is about six percent. This indicates that the problem is weakly nonlinear. The results seem to demonstrate that the expansion for small ϵ, whose value is 8.34 for $R = 88.1$, may not necessarily require that ϵ is smaller than one, but it should be smaller than a threshold value which is not known at present.

The integrodifferential Eq. (12) for the evolution of the amplitude density function $A(k, t)$ was solved numerically using an implicit Euler scheme. The integrals I_1 and I_2 representing nonlinear interactions among resonant triads and quartets were discretized using the trapezoidal rule. The infinite range of integration was truncated to $-12 \leq k \leq 12$, which was found to be adequate. Most of the computations were done using a uniform mesh size $\Delta k = 0.25$ and a time step $\Delta t = 0.01$.

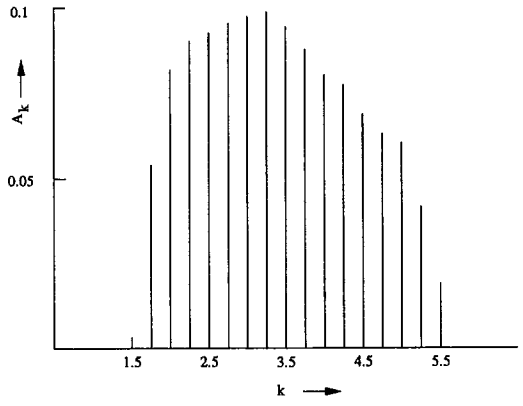


Fig. 1 Equilibrium amplitudes of Taylor vortex flows with different wave numbers for discrete monochromatic waves

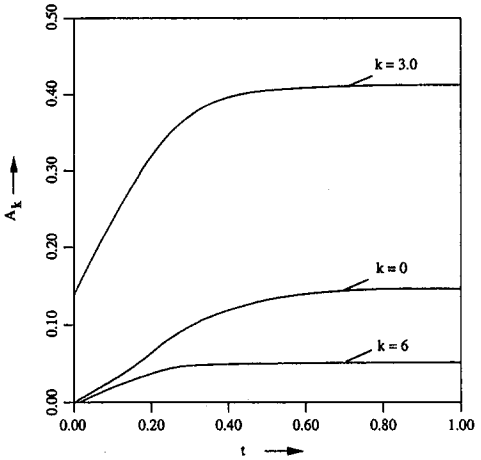


Fig. 2(*a*) Evolution of the amplitude density function for a single initial mode with wave number $k = 3$

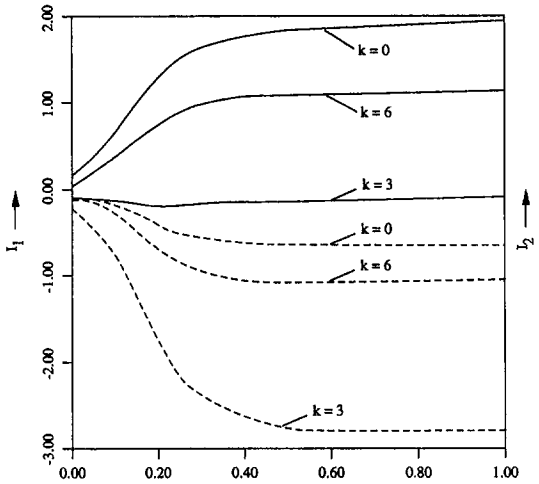


Fig. 2(*b*) Evolution of the interaction integrals I_1 and I_2 for a single initial mode with wave number $k = 3$. The solid lines indicate the integral I_1, while the dotted lines refer to the integral I_2.

Figure 1 shows the equilibrium amplitudes, A_k, for supercritical Taylor vortices, obtained by solving the Landau Eq. (17) for discrete monochromatic waves. The maximum amplitude occurs at a wave number close to the minimum critical wave number $k_c = 3.16$ of linear theory. The equilibrium amplitude is zero for modes lying in the linearly stable region.

Figure 2(*a*) shows the results of a numerical simulation of a single dominant mode with a wave number $k = 3$, obtained by solving Eq. (12) for the evolution of the amplitude density function starting with initial condition $A(k, 0) = 0.125$ for the mode $k = 3$ and zero for the other modes. The mode $k = 3$ is linearly unstable and grows by obtaining energy from the mean flow. As its amplitude increases, nonlinear effects become important and alter the linear growth rate. The figure indicates that nonlinear interactions lead to the generation of the second harmonic ($k = 6$), and distort the mean flow ($k = 0$). This may be explained by referring to Fig. 2(*b*) in which the interaction integrals I_1 and I_2 in the integrodifferential Eq. (19) have been plotted as a function of time. Figure 2(*b*) shows that I_1 is negative for the mode $k = 3$, and positive for the modes $k = 6$ and $k = 0$. Thus, energy is transferred nonlinearly from the mode $k = 3$ to its harmonic $k = 6$, and the mean flow ($k = 0$) through a three-wave resonance. The interaction integral I_2 is negative for all the modes. Thus, the four-wave resonance mechanism has a stabilizing influence on all the modes. The

Downloaded 04 May 2010 to 171.66.16.28. Redistribution subject to ASME license or copyright; see http://www.asme.org/terms/Terms_Use.cfm

mode $k = 3$ grows and eventually reaches equilibrium together with its harmonic ($k = 6$) and the mean flow ($k = 0$). In summary, the energy is transferred linearly from the mean flow to the disturbance ($k = 3$) and transferred nonlinearly from the wave ($k = 3$) to the mean flow ($k = 0$) and its harmonics ($k = 6...$). The deformation of mean flows is at same order of magnitude of the dominant wave, and is not one order of magnitude smaller than the dominant wave as assumed by the classical weakly nonlinear instability theories (see the Appendix). It is worth noting that the function $A(k, t)$ plotted in Fig. 2(a) is an amplitude density function, and the corresponding wave amplitudes of the modes are given by the area $A_k = A(k)\Delta k$. The equilibrium amplitude A_k for the mode $k = 3$ differs slightly from the equilibrium amplitude A_k predicted by the Landau Eq. (17) for a discrete monochromatic wave near the onset of the instability. This is due to the terms of the resonant triads and quartets missing from the Landau equation as explained in the Appendix. An additional computation with a smaller size of $\Delta k = 0.2$ predictes the same value of A_k. This indicates that the resolution used in our computations is adequate, although the amplitude density function $A(k, t)$ for a single dominant mode depends on the mesh size Δk used in the calculation. The dependence of the amplitude density function on the mesh size Δk for a single dominant mode is expected since in the limit as Δk approaches zero, the amplitude density function should approach a delta function. Thus, if Δk is reduced, the amplitude density $A(k)$ should increase, the area $A(k)\Delta k$ being conserved.

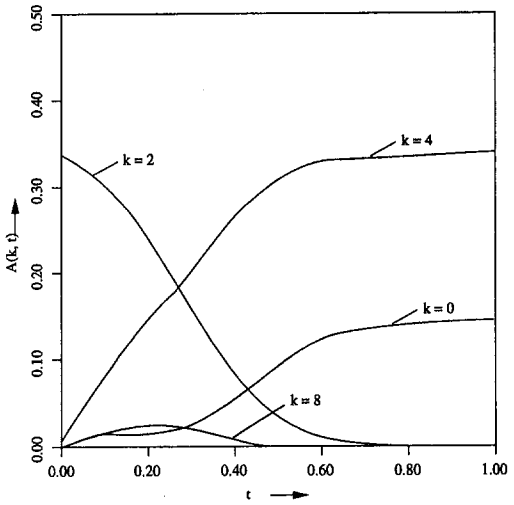


Fig. 3(a) Evolution of the amplitude density function for a single initial mode with wave number $k = 2$, illustrating sideband instability

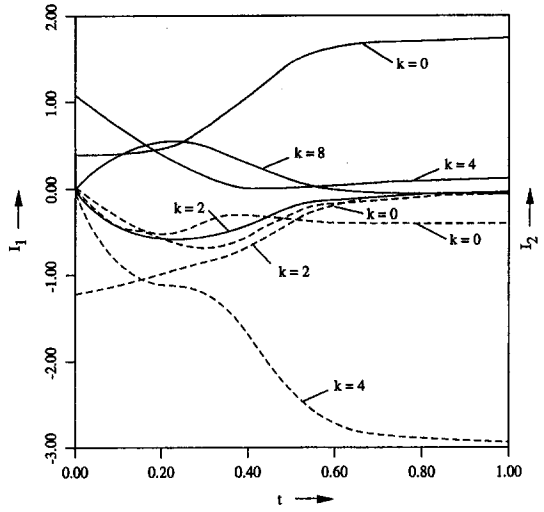


Fig. 3(b) Evolution of the interaction integrals I_1 and I_2 for a single initial mode with wave number $k = 2$. The solid lines indicate the integral I_1, while the dotted lines refer to the integral I_2.

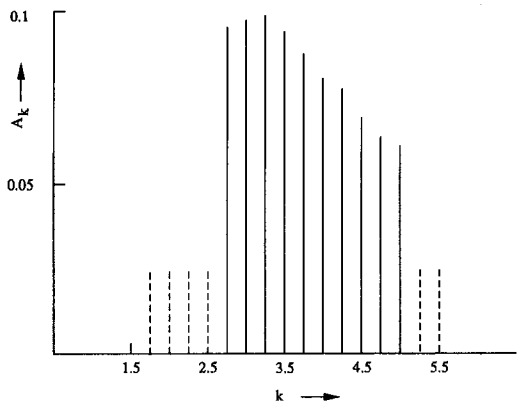


Fig. 4 Equilibrium amplitudes of dominant modes obtained with a single initial dominant mode

The results of a numerical simulation starting with a single dominant mode with wave number $k = 2$ at time $t = 0$ is presented in Fig. 3(a). The mode $k = 2$ is linearly unstable, and the weakly nonlinear theory of discrete monochromatic waves predicts a supercritical equilibrium amplitude for this mode. However, as indicated in the figure, the mode $k = 2$ decays to zero, while its harmonic $k = 4$, excited through nonlinear interactions, grows and reaches a finite-amplitude equilibrium state. This indicates that the equilibrium state predicted by the weakly nonlinear theory of discrete monochromatic waves for the mode $k = 2$ is unstable. This result is in agreement with the Eckhaus and Benjamin-Feir sideband instability. This implies that a sideband instability is a consequence of nonlinear energy transfer among different interacting waves. Figure 3(b) shows that the mode $k = 4$ receives energy through the three-wave resonance mechanism, as the interaction integral I_1 representing nonlinear interactions among triads of wave numbers is negative for the mode $k = 2$, and positive for the mode $k = 4$. This indicates that the instability is triggered by a three-wave resonance mechanism. Then, the mode $k = 4$ receives the energy linearly from the mean flow, and transfers energy to the mean flow and its harmonics nonlinearly.

Figure 4 is a summary of numerical simulations in which a single mode was given an initial amplitude density of 0.1 at time $t = 0$ and the other modes were given a small initial amplitude density of 10^{-5}. The equilibrium wave amplitude $A_k = A(k)\Delta k$ has been plotted in Fig. 4, rather than the equilibrium amplitude density function $A(k)$. The solid lines in the middle of the figure refer to modes which reach a finite-amplitude equilibrium state, while the dotted lines to the left and right indicate modes which decay to zero, their energy being transferred to other modes. The final dominant wave number in the case of initial disturbances with wave numbers $k = 1.75$, 2, 2.25 and 2.5, indicated by the dotted lines on the left of the figure, was their first harmonic $k = 3.5$, 4, 4.5, and 5, respectively. These are generated through nonlinear interaction. The final dominant wave number in the case of initial disturbances with wave numbers $k = 5.25$ and 5.5, indicated by the dotted lines on the right of the figure, was $k = 3.25$. The numerical simulations were repeated with initial conditions consisting of a larger uniform broadband spectrum with an amplitude density of 0.01 superimposed on the single dominant initial mode which was given an amplitude density of 0.1. The final equilibrium state remained unchanged in all cases except for the modes with wave numbers $k = 2.5$ and 5. In the latter cases, the final dominant mode was found to be $k = 3$. Numerical simulations starting with initial conditions consisting of a single mode at time $t = 0$ and zero background noise for the other modes

Downloaded 04 May 2010 to 171.66.16.28. Redistribution subject to ASME license or copyright; see http://www.asme.org/terms/Terms_Use.cfm

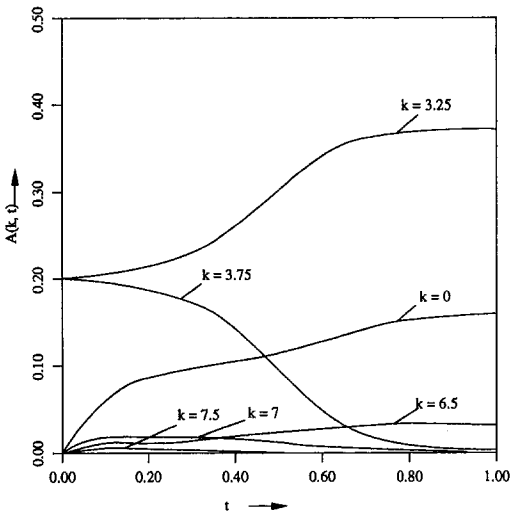


Fig. 5(*a*) Evolution of the amplitude density function for a pair of initial modes with wave numbers $k = 3.25$ and $k = 3.75$ and initial amplitudes of 0.2

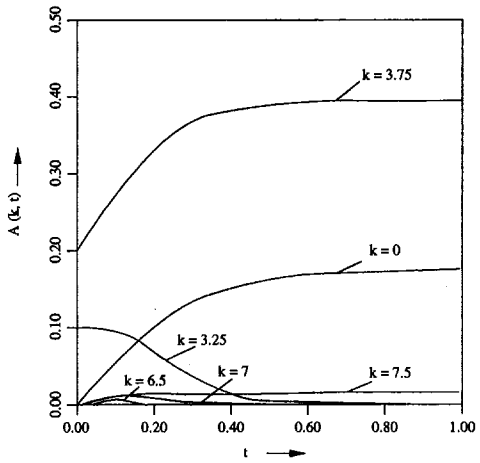


Fig. 5(*b*) Evolution of the amplitude density function for a pair of initial modes with wave numbers $k = 3.25$ and $k = 3.75$ and amplitudes of 0.2 and 0.1, respectively

yielded the same equilibrium state as with a small uniform background noise with initial amplitude density of 10^{-5} in all cases except for the modes with wave numbers $k = 5.25$ and 5.5, indicated by the dotted lines on the right end of the figure. In the absence of other modes at time $t = 0$, the modes $k = 5.25$ and 5.5 remained the dominant ones in the final equilibrium state. This is because nonlinear interactions can only generate higher harmonics. Thus, energy can be transferred to subharmonic modes through nonlinear interactions only if these modes are present at time $t = 0$, since they cannot be created through the nonlinear interactions. However, as indicated by Fig. 4, the presence of very low levels of noise in the subharmonic modes can destabilize Taylor vortex flows with wave numbers $k = 5.25$ and 5.5. Consequently, supercritical Taylor vortex flows with these wave numbers are unlikely to be observed experimentally at the Reynolds number used in our computations. Figure 4 indicates that the range of wave numbers for which our theory predicts *stable* supercritical Taylor vortices is a subset of the linearly unstable range of wave numbers.

Figure 5(*a*) shows the results of a numerical simulation in which two modes $k = 3.25$ and $k = 3.75$ were given initial amplitudes of 0.2 at time $t = 0$. The figure shows that nonlinear interactions generate the harmonics $k = 6.5$, 7 and 7.5. The mode $k = 3.75$ decays as energy is transferred to the harmonics and the mean flow, while the mode $k = 3.25$ grows as it obtains energy from the mean flow, and eventually reaches a supercritical finite amplitude equilibrium state. Figure 5(*b*) shows the results of a numerical simulation in which the mode $k = 3.25$ was given an initial amplitude of 0.1 and the mode $k = 3.75$ was given an initial amplitude of 0.2. In this case, the mode $k = 3.75$ remains the dominant one in the final equilibrium state, while the mode $k = 3.25$ decays to zero. This demonstrates that an equilibrium state can shift to a new equilibrium state by a finite disturbance. This property can have significant practical applications.

Numerical simulations starting with a uniform broadband spectrum at time $t = 0$ result in a final equilibrium state consisting of a single dominant wave and its harmonics, and an induced mean flow distortion. For initial amplitudes smaller than 0.05, the final equilibrium wave is $k = 3.5$. This is because the nonlinear terms are initially small, and hence the initial growth of the disturbances is according to linear theory. The mode $k = 3.5$ has the largest linear growth rate at the Reynolds number used in this computation. Thus, this mode grows faster than the other modes, and remains the dominant mode in the final equilibrium state. With initial amplitudes larger than 0.05, nonlinear effects become important at an earlier stage in the evolution of the waves, and the dominant wave in the final equilibrium state is $k = 3.25$, which is the one closest to the minimum critical wave number, 3.16, at the onset of instability. It is worth noting that the accuracy in the determination of the wavenumber depends on the grid size of numerical integration and is $0(\Delta k)$.

It is well known that a short Tollmien-Schlichting wave in a boundary layer can be excited by a long freestream noise (Goldstein 1989). One of the key unresolved questions concerning the boundary layer receptivity is the wavelength adjustment mechanism. The Taylor-Couette problem is not the best model to explain this mechanism. However, we demonstrate here that a long wave can indeed excite a much shorter unstable wave through nonlinear wave interactions. Figure 6 shows the results of a numerical simulation in which a single mode $k = 0.75$ was given an amplitude density of 0.1 at time $t = 0$. The mode $k = 0.75$ is linearly stable, and decays to zero as it transfers energy to the mean flow. As indicated by Fig. 6, nonlinear interactions excite the modes with wave numbers 1.5 and 3. The mode $k = 1.5$, which is also linearly stable, initially grows and then decays to zero, while the mode $k = 3$, which is linearly unstable, grows and eventually reaches a supercritical finite-amplitude equilibrium state, together with its harmonic $k = 6$. The simulations were repeated using initial amplitude densities of 0.05 and 0.01. In all the cases, the final equilibrium state was the same. Numerical simulations starting with a single mode $k = 1$ and amplitude densities of 0.1, 0.05, and 0.01 also resulted in the same equilibrium state. In this case, nonlinear

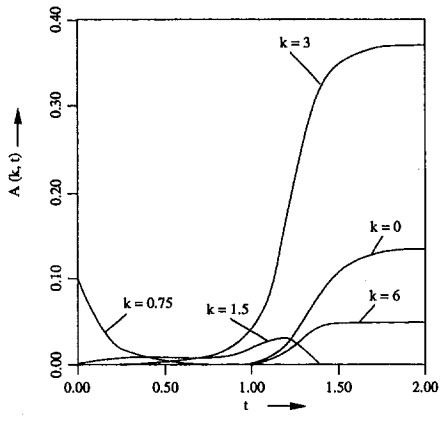


Fig. 6 Evolution of the amplitude density function for a single linearly stable initial mode with wave number $k = 0.75$

Downloaded 04 May 2010 to 171.66.16.28. Redistribution subject to ASME license or copyright; see http://www.asme.org/terms/Terms_Use.cfm

Table 1 Variation of torque with wave number

k_f	2.75	3.0	3.25	3.5	3.75	4.0	4.25	4.5	4.75	5.00
G_T/G_c	1.150	1.172	1.181	1.183	1.179	1.172	1.161	1.144	1.122	1.096

interactions generate the harmonics $k = 2$ and 3. The mode $k = 2$, although linearly unstable, does not grow to a finite amplitude equilibrium as it loses all its energy due to nonlinear interactions, as might be anticipated from the results presented in Fig. 3. The dominant mode in the final equilibrium state in this case is, however, $k = 3$, and not $k = 4$ as in Fig. 3. These results demonstrate that long wavelength disturbances can quickly excite modes that are linearly unstable and which grow to finite-amplitude equilibrium states, although they are themselves linearly damped and eventually decay to zero. It is our opinion that the mechanism of nonlinear wave interaction is a credible mechanism for boundary layer receptivity.

The selection of the equilibrium wave number is due to nonlinear wave interactions. The numerical results seem to suggest the following selection principle:

1 When the initial disturbance consists of a single dominant wave within the unstable region, the initial wave remains dominant in the final equilibrium state. Consequently, for a slowly accelerating cylinder, the critical wave is likely to be dominant.

2 When the initial condition consists of two waves with finite amplitudes in the unstable region, the final dominant wave is the one with the higher initial amplitude. If the two waves have the same initial finite amplitude, the dominant wave seems to be the one closer to the critical wave. On the other hand, if the initial amplitudes are very small, the faster growing wave becomes dominant.

3 When the initial disturbance is a uniform broadband spectrum, the final dominant wave is the fastest linearly growing wave, if the initial amplitude is small. On the other hand, if the uniform noise level is not small, the critical wave is the dominant equilibrium one.

A similar selection principle has been found to hold in mixed-convection flow in a heated vertical annulus (Yao and Rogers, 1994). Since the final equilibrium state depends on the waveform of the initial disturbance, or equivalently, on ambient noise which cannot always be controlled, any property transported by the fluid can at best be determined within a limit of uncertainty associated with nonuniqueness. Since this nonuniqueness has been found to hold for two different flow situations, we believe that this uncertainty associated with nonuniqueness of the flow solution is generic to all fluid flows.

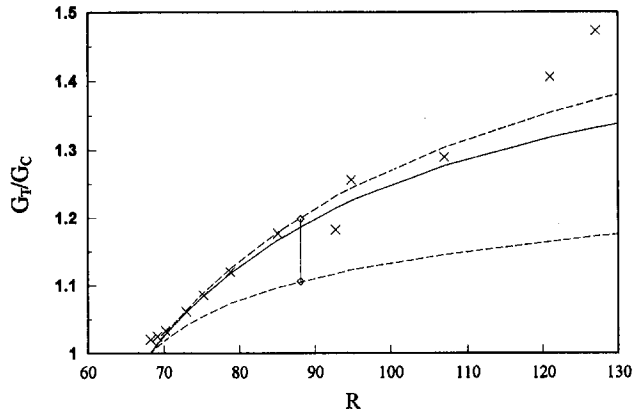


Fig. 7 Ratio of the torques of Taylor-vortex flow and Couette flow as functions of the Reynolds number. The symbol x represents the experimental data of Donnelly and Simon (1960), the curve is the prediction of Davey (1962), and the vertical line represents all the possible equilibrium states predicted by the present analysis.

The torque, obtained by integrating the shear stress over the surface of the inner cylinder, is

$$G = 2\pi r_i^3 \Omega_1 \rho \nu \int_0^{2\pi/k_f} \left[\frac{\partial v(r_i, z)}{\partial r} - \frac{v(r_i, z)}{r_i} \right] dz.$$

The ratio of Taylor-vortex torque, G_T, and that for circular Couette flow, G_C, becomes

$$\frac{G_T}{G_C} = 1 - \frac{\eta(1+\eta)}{2} \left\{ \Delta k A(k=0) \frac{\partial}{\partial r} \tilde{v}_1(k=0, r_i) + \Delta k^2 A^2(k_f) \left[\frac{\partial}{\partial r} \tilde{v}_2(k_f, -k_f, r_i) + \text{c.c.} \right] \right\},$$

where k_f is the final equilibrium wave number. Values of G_T/G_C for different wave numbers k_f are tabulated in Table 1 for $R = 88.1$. The maximum value, occurring near the minimum critical wave number at the onset of instability, is 1.183; its minimum value is 1.096 at $k_f = 5$. The ratio G_T/G_C is shown in Fig. 7 as a function of the Reynolds number. The results obtained by Davey (1962) using the Stuart-Watson expansion for $k_c = 3.16$ are compared with the experimental data of Donnelly and Simon (1960). The the dashed upper bound is extrapolated from the present calculation at Re = 88.1 and is corresponding the the critical wave number. Its values are slightly larger than the ones predicted by Davey. All possible torques predicted by the present study for different equilibrium states at $R = 88.1$ is indicated by the vertical line. The variation in the torque between its maximum and minimum values, predicted by the present study, is about ten percent at Re = 88.1. Since the equilibrium state is not unique and depends on the initial conditions which usually cannot be controlled in engineering systems, an uncertainty, associated with the nonuniqueness, should be considered when any accurately measured value of Taylor-vortex torque is used in practice.

4 Conclusion

The current study confirms that the supercritical equilibrium state of Taylor-Couette instability, slightly above the critical Taylor number, depends on the initial disturbance, as observed experimentally, and that it is not unique. Extrapolating this fact to turbulence, it is our opinion, since the *time* average will depend on the initial condition, it will not equal to the *ensemble* average even for stationary turbulence. From an application point of view, only time average has physical significance. The results also demonstrate that a long stable wave can quickly excite a much shorter unstable wave. This observation suggests that nonlinear wave interaction may be a credible mechanism for boundary layer receptivity. The integrodifferential Eq. (12) contains considerable information. In this paper, this equation was only lightly probed. The current formulation extended to traveling wave states will be reported later (Yao and Ghosh Moulic, 1995).

References

Benjamin, T. B., and Feir, J. E., 1967, "The Disintegration of Wave Trains on Deep Water, Part 1, Theory," *Journal of Fluid Mechanics,* Vol. 27, pp. 417–430.

Benney, D. J., and Newell, A. C., 1967, "The Propagation of Nonlinear Wave Envelopes," *Journal of Mathematical Physics,* Vol. 46, pp. 133–139.

Burkhalter, J. E., and Koschmieder, E. L., 1973, "Steady Supercritical Taylor Vortex Flow," *Journal of Fluid Mechanics,* Vol. 58, pp. 547–560.

Downloaded 04 May 2010 to 171.66.16.28. Redistribution subject to ASME license or copyright; see http://www.asme.org/terms/Terms_Use.cfm

Burkhalter, J. E., and Koschmieder, E. L., 1974, "Steady Supercritical Taylor Vortices After Sudden Starts," *Physics of Fluids,* Vol. 17, pp. 1929–1935.

Chandrasekhar, S., 1961, *Hydrodynamic and Hydromagnetic Stability,* Clarendon Press, Oxford, U.K.

Coles, D., 1965, "Transition in Circular Couette Flow," *Journal of Fluid Mechanics,* Vol. 21, pp. 385–425.

Davey, A., 1962, "The Growth of Taylor Vortices in Flow Between Rotating Cylinders," *Journal of Fluid Mechanics,* Vol. 14, pp. 336–368.

Donnelly, R. J., and Simon, N. J., 1960, "An Empirical Torque Relation for Supercritical Flow Between Rotating Cylinders," *Journal of Fluid Mechanics,* Vol. 7, pp. 401–418.

Eckhaus, W., 1965, *Studies in Non-linear Stability Theory,* Springer-Verlag, Berlin.

Ghosh Moulic, S., 1993, "Nonlinear Instability," Ph D Thesis, Department of Mechanical and Aerospace Engineering, Arizona State University.

Goldstein, M. E., and Hultgren, L. S., 1989, "Boundary-Layer Receptivity to Long-Wave Free-Stream Disturbances," *Annal Review of Fluid Mechanics,* Vol. 21, pp. 137–166.

Kogelman, S., and DiPrima, R. C., 1970, "Stability of Spatially Periodic Supercritical Flows in Hydrodynamics," *Physics of Fluids,* Vol. 13, pp. 1–11.

Newell, A. C., and Whitehead, J. A., 1969, "Finite Bandwidth, Finite Amplitude Convection," *Journal of Fluid Mechanics,* Vol. 38, pp. 279–303.

Segel, L. A., 1969, "Distant Side-Walls Cause Slow Amplitude Modulation of Cellular Convection," *Journal of Fluid Mechanics,* Vol. 38, pp. 203–224.

Snyder, H. A., 1969, "Wave-Number Selection at Finite Amplitude in Rotating Couette Flow," *Journal of Fluid Mechanics,* Vol. 35, pp. 273–298.

Stewartson, K., and Stuart, J. T., 1971, "A Non-Linear Instability Theory for a Wave System in Plane-Poiseuille Flow," *Journal of Fluid Mechanics,* Vol. 48, pp. 529–545.

Stuart, J. T., 1958, "On the Non-Linear Mechanics of Hydrodynamic Stability," *Journal of Fluid Mechanics,* Vol. 4, pp. 1–21.

Stuart, J. T., 1960, "On the Non-Linear Mechanics of Wave Disturbances in Stable and Unstable Parallel Flows, Part 1," *Journal of Fluid Mechanics,* Vol. 9, pp. 353–370.

Stuart, J. T., and DiPrima, R. C., 1978, "The Eckhaus and Benjamin-Feir Resonance Mechanisms," *Proceedings of Royal Society, London,* Vol. A362, pp. 27–41.

Taylor, G. I., 1923, "Stability of a Viscous Liquid Contained Between Two Rotating Cylinders," *Philosophical Transaction of Royal Society,* Vol. A223, pp. 289–343.

Watson, J., 1960, "On the Non-Linear Mechanics of Wave Disturbances in Stable and Unstable Parallel Flows, Part 2," *Journal of Fluid Mechanics,* Vol. 9, pp. 371–389.

Yao, L. S., and Rogers, B. B., 1992, "Finite-Amplitude Instability of Non-Isothermal Flow in a Vertical Annulus," *Proceedings of Royal Society,* Vol. A437, pp. 267–290.

Yao, L. S., and Ghosh Moulic, S., 1994, "Uncertainty of Convection," *International Journal of Heat and Mass Transfer,* Vol. 37, pp. 1713–1721.

Yao, L. S., and Ghosh Moulic, S., 1995, "Nonlinear Instability of Travelling Waves With a Continuous Spectrum," *International Journal of Heat and Mass Transfer,* Vol. 38, pp. 1751–1772.

APPENDIX

Amplitude Equations for Monochromatic Waves

The numerical results of (12) indicate that the energy transfers nonlinearly among the mean flow, the donminant wave and its harmonics. The modification of the mean flow is at same order of magnitude of the dominant wave. If there is no energy transfer to waves other than the selected disturbance wave, a set of simpler amplitude equations can be derived to replace Eq. (12) of a continuous spectrum. Rigorously, the expansion should include the amplitude density functions for the mean flow, the dominant disturbance wave and its harmonics. We assume that the harmonics are negligiblely small to simplify the algebra in order to demonstrate the concept clearly. Substitution of the amplitude density function

$$A(k, t) = [A_0\delta(k) + A_0^*\delta(k)] + [A_{k_0}\delta(k - k_0) + A_{k_0}^*\delta(k + k_0)] \quad (A1)$$

into equation (12) results in

$$\frac{dA_{k_0}}{dt} = a(k_0)A_{k_0} + [a_{31}A_0A_{k_0}] + [a_{41}|A_{k_0}|^2 + a_{42}|A_0|^2]A_{k_0}, \quad (A2)$$

and

$$\frac{dA_0}{dt} = a(0)A_0 + [b_{31}|A_0|^2 + b_{32}|A_{k_0}|^2] + [b_{41}|A_{k_0}|^2 + b_{42}|A_0|^2]A_0, \quad (A3)$$

where a_{ij} and b_{ij} are interacting constants. A_0 is the amplitude function for the deformation of the mean flow and A_{k_0} is for the disturbance wave. The terms inside of first square bracket on the right-hand side of (A2) and (A3) are from three-wave resonance. The terms in the second square bracket are from four-wave resonance. The terms multiplied by a_{31} and a_{42} represent the nonlinear energy transfer between the mean flow and the disturbance wave, and are not included in the Landau and Ginzburg-Landau equations. The term multiplied by a_{41} represents the self-interaction of the disturbance wave as explained in Eq. (18), and is the only nonlinear term in the Landau and Ginzburg-Landau equations.

There are two types of nonlinear interaction between two waves. One is direct interaction, if they satisfy the resonance condition, which has been pointed out by Landau. The other is *indirect* interaction in which the two waves interact simultaneously with the mean flow ($k = 0$) as indicated in (A2) and (A3). The indirect interaction always exists and has so far been overlooked. It is clear that only linear energy transfer, the terms multiplied by the growth rate, a, is considered in the Landau and Ginzburg-Landau equations. Without the terms of nonlinear energy transfer between the mean flow and the disturbance wave, they completely ignore the indirect wave interaction. Equations similar to (A2) and (A3) have been derived for the interaction of two disturbance waves, but none of them have considered an additional equation for the deformation of the mean flow.

Downloaded 04 May 2010 to 171.66.16.28. Redistribution subject to ASME license or copyright; see http://www.asme.org/terms/Terms_Use.cfm

On the Transformation Properties of the Nonlinear Hamel Equations

J. G. Papastavridis
Associate Professor of Mechanics,
School of Mechanical Engineering,
Georgia Institute of Technology,
Atlanta, GA 30332-0405

This paper discusses the transformation properties of the famous Johnsen-Hamel equations of motion of discrete mechanical systems in general nonlinear nonholonomic coordinates and constraints (i.e., the nonlinear extension of the well-known Boltzmann-Hamel equations), under general nonlinear (local) quasi-velocity transformations. It is shown that the individual kinematico-inertial terms making up the system inertia force, or system acceleration, such as the nonlinear nonholonomic Euler-Lagrange operator and nonholonomic correction (or deviation) terms, in general, do not *transform as nonholonomic covariant vectors; although taken as a whole they do, as expected. This work extends and completes the work of Papastavridis (1994), and it is strongly recommended that it be read* after *that paper.*

1 Introduction and Background

Consider a mechanical system S whose configurations of interest are determined completely and uniquely by the n holonomic *positional system parameters,* or Lagrangean coordinates $q \equiv (q_1, \ldots, q_n)$, so that the inertial position vector of a typical of its particles P is expressible as

$$\mathbf{r} = \mathbf{r}(P; t, q) \equiv \mathbf{r}(t, q). \tag{1}$$

Then, as detailed in Papastavridis (1994) and Schaefer (1951), the inertial virtual *displacement, velocity,* and *acceleration* of P [with all latin indices (except D and I, and, of course, t = time) running from 1 to n; and with *summation convention* over pairs of dummy indices (and in general, no need to distinguish between sub and superscripts)] equal

(i) In *holonomic* variables

$$\delta\mathbf{r} = \mathbf{e}_k \delta q_k, \tag{2a}$$

$$\mathbf{v} \equiv d\mathbf{r}/dt = \dot{q}_k \mathbf{e}_k + \mathbf{e}_t, \tag{2b}$$

$$\mathbf{a} \equiv d\mathbf{v}/dt = \ddot{q}_k \mathbf{e}_k + 2\dot{q}_k \dot{q}_l \mathbf{e}_{k,l} + \dot{q}_k \mathbf{e}_{k,t} + \mathbf{e}_{t,t}$$

$$= \ddot{q}_k \mathbf{e}_k + \text{terms not containing } \ddot{q}, \tag{2c}$$

where

$$\mathbf{e}_k \equiv \partial\mathbf{r}/\partial q_k = \partial\mathbf{v}/\partial\dot{q}_k = \partial\mathbf{a}/\partial\ddot{q}_k = \ldots, \tag{3a}$$

$$\mathbf{e}_{k,l} \equiv \partial\mathbf{e}_k/\partial q_l = \partial\mathbf{e}_l/\partial q_k = \mathbf{e}_{l,k}, \tag{3b}$$

$$\mathbf{e}_t \equiv \partial\mathbf{r}/\partial t,\ \mathbf{e}_{k,t} \equiv \partial\mathbf{e}_k/\partial t = \partial\mathbf{e}_t/\partial q_k = \mathbf{e}_{t,k}. \tag{3c}$$

(ii) In *nonholonomic* variables $\omega_k \equiv \omega_k(t, q, \dot{q})[\Leftrightarrow \dot{q}_k = \dot{q}_k(t, q, \omega)]$, where $\omega_k \equiv \dot{\theta}_k$, and

$$\delta\theta_k \equiv \left(\frac{\partial\omega_k}{\partial\dot{q}_l}\right)\delta q_l \leftrightarrow \delta q_l = \left(\frac{\partial\dot{q}_l}{\partial\omega_k}\right)\omega\theta_k, \tag{4a}$$

$$\delta\mathbf{r} \equiv \delta\overset{*}{\mathbf{r}} = \mathbf{a}_k \delta\theta_k, \tag{4b}$$

$$\mathbf{v} = \mathbf{v}^* = \mathbf{v}^*(t, q, \omega) = \omega_k \mathbf{a}_k + \mathbf{a}_t, \tag{4c}$$

$$\mathbf{a}_t = \mathbf{e}_t + \left[\dot{q}_k - \frac{\partial\dot{q}_k}{\partial\omega_l}\omega_l\right]\mathbf{e}_k, \tag{4d}$$

$$\mathbf{a} = \mathbf{a}^*(t, q, \omega) = \dot{\omega}_k \mathbf{a}_k + \text{terms not containing } \dot{\omega}, \tag{4e}$$

where

$$\mathbf{a}_k = \left(\frac{\partial\dot{q}_l}{\partial\omega_k}\right)\mathbf{e}_l \equiv \partial\overset{*}{\mathbf{r}}/\partial\theta_k = \partial\overset{*}{\mathbf{v}}/\partial\omega_k = \partial\overset{*}{\mathbf{a}}/\partial\omega_k = \ldots$$

$$\mathbf{e}_l = \left(\frac{\partial\omega_k}{\partial\dot{q}_l}\right)\mathbf{a}_k, \tag{4f}$$

$$\frac{\partial(\overset{*}{\ldots})}{\partial\theta_k} \equiv \frac{\partial(\overset{*}{\ldots})}{\partial q_l}\frac{\partial\dot{q}^l}{\partial\omega_k} \leftrightarrow \frac{\partial(\overset{*}{\ldots})}{\partial q_l} \equiv \frac{\partial(\overset{*}{\ldots})}{\partial\theta_k}\frac{\partial\omega_k}{\partial\dot{q}_l} \tag{4g}$$

(symbolic "quasi-chain rule")
and with the helpful *-notation, for an arbitrary (but as well behaved as needed) function

$$f = f(t, q, \dot{q}) = f[t, q, \dot{q}(t, q, \omega)]$$

$$\equiv f^*(t, q, \omega) \equiv f^*. \tag{4h}$$

Next, the variational equation of motion, i.e. Lagrange's Principle (LP), is:

$$\underbrace{\int dm\mathbf{a}\cdot\delta\mathbf{r}}_{\delta I} = \underbrace{\int d\mathbf{F}\cdot\delta\mathbf{r}}_{\delta' W}, \tag{5}$$

where: dm = mass of P, $\int(\ldots)$ = sum over the system's particles (like Stieltje's integral) for a fixed time, $d\mathbf{F}$ = total *impressed* (non constraint!) force on P; or, (i) in *holonomic* coordinates

$$\underbrace{E_k\delta q_k}_{\delta I} = \underbrace{Q_k\delta q_k}_{\delta' W}, \tag{6a}$$

$$E_k \equiv \int dm\mathbf{a}\cdot\mathbf{e}_k = \frac{d}{dt}\left(\frac{\partial T}{\partial\dot{q}_k}\right) - \frac{\partial T}{\partial q_k} \equiv E_k(T),$$

$$Q_k \equiv \int d\mathbf{F}\cdot\mathbf{e}_k \tag{6b}$$

$$T \equiv \int \frac{1}{2}\, dm\mathbf{v}\cdot\mathbf{v} = T(t, q, \dot{q}) = \text{kinetic energy}; \tag{6c}$$

Contributed by the Applied Mechanics Division of THE AMERICAN SOCIETY OF MECHANICAL ENGINEERS for publication in the ASME JOURNAL OF APPLIED MECHANICS.

Discussion on this paper should be addressed to the Technical Editor, Professor Lewis T. Wheeler, Department of Mechanical Engineering, University of Houston, Houston, TX 77204-4792, and will be accepted until four months after final publication of the paper itself in the ASME JOURNAL OF APPLIED MECHANICS.

Manuscript received by the ASME Applied Mechanics Division, Feb. 1, 1994; final revision, Sept. 27, 1994. Associate Technical Editor: P. D. Spanos.

Copyright © 1995 by ASME

Downloaded 04 May 2010 to 171.66.16.28. Redistribution subject to ASME license or copyright; see http://www.asme.org/terms/Terms_Use.cfm

and (ii) in *nonholonomic* variables (See Papastavridis (1994) for details; especially for Eq. (7*c*))

$$\underbrace{I_k\delta\theta_k}_{\delta I} = \underbrace{\Theta_k\delta\theta_k}_{\delta' W} \tag{7a}$$

$$I_k \equiv \int dm\overset{*}{\mathbf{a}}\cdot\mathbf{a}_k = \frac{d}{dt}\left(\frac{\partial T^*}{\partial\omega_k}\right) - \frac{\partial T^*}{\partial\theta_k} - \Gamma_k$$

$$\equiv E_k^*(T^*) - \Gamma_k, \tag{7b}$$

$$\Gamma_k \equiv \int dm\overset{*}{\mathbf{v}}\cdot\underbrace{\left[\frac{d}{dt}\left(\frac{\partial\overset{*}{\mathbf{v}}}{\partial\omega_k}\right) - \frac{\partial\overset{*}{\mathbf{v}}}{\partial\theta k}\right]}_{E_k^*(v)\equiv\gamma_k}$$

$$\equiv \int dm\overset{*}{\mathbf{v}}\cdot\left[\frac{d}{dt}\left(\frac{\partial\dot{q}_l}{\partial\omega_k}\right) - \frac{\partial\dot{q}_l}{\partial\theta_k}\right]\mathbf{e}_l$$

$$= \left(\int dm\overset{*}{\mathbf{v}}\cdot\mathbf{e}_l\right)E_k^*(\dot{q}_l) \equiv V^l{}_k p_l$$

$$\equiv \int dm\overset{*}{\mathbf{v}}\cdot(H_{kr}\mathbf{a}_r) = H_{kr}P_r$$

$$= \text{nonlinear nonholonomic deviation}, \tag{7c}$$

(=0, if the θ_k are genuine, or Langrangean, coordinates) where

$$H_{kr} \equiv \frac{\partial\omega_r}{\partial\dot{q}_l}E_k^*(\dot{q}_l) \equiv \frac{\partial\omega_r}{\partial\dot{q}_l}V^l{}_k$$

$$= \text{nonlinear Hamel coefficients}, \tag{7d}$$

and the system momenta, p (holonomic) and P (nonholonomic), are related by

$$P_k \equiv \int dm\overset{*}{\mathbf{v}}\cdot\mathbf{a}_k = \int dm\overset{*}{\mathbf{v}}\cdot\frac{\partial\overset{*}{\mathbf{v}}}{\partial\omega_k} = \frac{\partial T^*}{\partial\omega_k} = \frac{\partial\dot{q}_l}{\partial\omega_k}p_l, \tag{7e}$$

$$p_l \equiv \int dm\overset{*}{\mathbf{v}}\cdot\mathbf{e}_l = \int dm\mathbf{v}\cdot\frac{\partial\mathbf{v}}{\partial\dot{q}_l} = \frac{\partial T}{\partial\dot{q}_l} = \frac{\partial\omega_k}{\partial\dot{q}_l}P_k; \tag{7f}$$

and similarly for the inertia "forces" $E(T) \equiv E$ (holonomic) and $I \equiv E^*(T^*) - \Gamma \equiv E^* - \Gamma$ (nonholonomic)

$$I_k = \frac{\partial\dot{q}_l}{\partial\omega_k}E_l \leftrightarrow E_l = \frac{\partial\omega_k}{\partial\dot{q}_l}I_k \tag{7g}$$

(see also Appendix I).

If the $\delta q/\delta\theta$ are *constrained,* say by the $m(<n)$ nonlinear and generally nonholonomic (=non completely integrable) constraints

$$\omega_D \equiv f_D(t, q, \dot{q}) = 0 \quad [D = 1, \ldots, m(<n)], \tag{8a}$$

or in virtual form (recall (4*a*))

$$\delta\theta_D \equiv \left(\frac{\partial f_D}{\partial\dot{q}_k}\right)\delta q_k = \left(\frac{\partial\omega_D}{\partial\dot{q}_k}\right)\delta q_k = 0, \tag{8b}$$

then, application of the well-known method of Lagrangean multipliers to (6*a*) and (7*a*) yields, respectively,

(i) the nonlinear *Routh-Voss* equations:

$$\underbrace{\frac{d}{dt}\left(\frac{\partial T}{\partial\dot{q}_k}\right) - \frac{\partial T}{\partial q_k}}_{E_k(T)\equiv E_k} = Q_k + \sum_D \lambda_D\frac{\partial f_D}{\partial\dot{q}_k}, \tag{9a}$$

and

(ii) the nonlinear *kinetostatic* $[D = 1, \ldots, m(<n)]$ and *kinetic* $(I = m + 1, \ldots, n)$ equations

$$\underbrace{\underbrace{\frac{d}{dt}\left(\frac{\partial T^*}{\partial\omega_D}\right) - \frac{\partial T^*}{\partial\theta_D}}_{E_D^*(T^*)\equiv E_D^*}}_{I_D} - \Gamma_D = \Theta_D + \lambda_D \text{ (kinetostatic)}, \tag{9b}$$

$$\underbrace{\underbrace{\frac{d}{dt}\left(\frac{\partial T^*}{\partial\omega_I}\right) - \frac{\partial T^*}{\partial\theta_I}}_{E_I^*(T^*)\equiv E_I^*}}_{I_I} - \Gamma_I = \Theta_I \text{ (kinetic)}, \tag{9c}$$

where the m λ_D are the Lagrangean multipliers (which can be shown to equal the nonholonomic reactions corresponding to the constraints (8*a*, *b*),·(Papastavridis, 1990); and $\omega_I \equiv f(t, q, \dot{q}) \neq 0$ are arbitrary except that the q and $\dot{q}$ obtained from them and (8*a*) satisfy the latter identically. If, on the other hand, the $\delta q/\delta\theta$ are *unconstrained,* or free, then (6*a*) and (7*a*) lead, respectively, to $(k = 1, \ldots, n)$

$$\underbrace{\frac{d}{dt}\left(\frac{\partial T}{\partial\dot{q}_k}\right) - \frac{\partial T}{\partial q_k}}_{E_k(T)\equiv E_k} = Q_k, \tag{10a}$$

and

$$\underbrace{\frac{d}{dt}\left(\frac{\partial T^*}{\partial\omega_k}\right) - \frac{\partial T^*}{\partial\theta_k} - \Gamma_k}_{I_k} = \Theta_k. \tag{10b}$$

Now, a mathematically and physically important question that arises in connection with these equations is to find how the various kinematico-inertial and force terms in them transform under general local nonlinear quasivelocity transformations

$$\omega = \omega(t, q, \omega') \leftrightarrow \omega' = \omega'(t, q, \omega) \tag{11a}$$

or, in virtual form and in corresponding components,

$$\delta\theta_{k'} \equiv \frac{\partial\omega_{k'}}{\partial\dot{q}_l}\delta q_l = \frac{\partial\omega_{k'}}{\partial\dot{q}_l}\frac{\partial\dot{q}_l}{\partial\omega_k}\delta\theta_k = \frac{\partial\omega_{k'}}{\partial\omega_k}\delta\theta_k,$$

and inversely

$$\delta\theta_k = (\partial\omega_k/\partial\omega_{k'})\delta\theta_{k'}. \tag{11b}$$

This is the purpose of our investigation. To this end we may assume, for convenience, that the $\delta q/\delta\theta/\delta\theta'$ are unconstrained; the enforcement of subsequently imposed constraints can always be handled with no additional difficulty (Papastavridis, 1994).

2 Transformation of Kinematico-Inertia Terms

Below we present two derivations; one based on *system* variables, and one based on particle (Euclidean vector) variables. Here we elaborate and correct some of the results of Johnsen (1941).

2.1 System Variable Derivation. Since

$$\delta I = I_k\delta\theta_k = I_{k'}\delta\theta_{k'} = \ldots, \tag{12a}$$

and invoking (11*b*) we readily obtain the transformation equations

$$I_{k'} = \frac{\partial\omega_k}{\partial\omega_{k'}}I_k \leftrightarrow I_k = \frac{\partial\omega_{k'}}{\partial\omega_k}I_{k'}. \tag{12b}$$

Downloaded 04 May 2010 to 171.66.16.28. Redistribution subject to ASME license or copyright; see http://www.asme.org/terms/Terms_Use.cfm

Let us, next, find how the constituents of I_k i.e., $E_k^*(T^*) \equiv E_k^*$ and Γ_k, transform individually; that is how they are related to the corresponding components of $I_{k'}$, i.e., $E_{k'}^*(\overset{*}{T}') \equiv E_{k'}^*$ and $\Gamma_{k'}$, where

$$T = T(t, q, \dot{q}) = \overset{*}{T}(t, q, \omega) = \overset{*}{T}$$

$$= \overset{*}{T}[t, q, \omega(t, q, \omega')] \equiv \overset{*}{T}'(t, q, \omega') = \overset{*}{T}'. \quad (13)$$

Applying chain rule to (13) we obtain

$$\text{(i)} \qquad \frac{\partial \overset{*}{T}'}{\partial \omega_{k'}} = \frac{\partial \overset{*}{T}}{\partial \omega_k} \frac{\partial \omega_k}{\partial \omega_{k'}},$$

and therefore

$$\frac{d}{dt}\left(\frac{\partial \overset{*}{T}'}{\partial \omega_{k'}}\right) = \frac{d}{dt}\left(\frac{\partial \overset{*}{T}}{\partial \omega_k}\right) \cdot \frac{\partial \omega_k}{\partial \omega_{k'}} + \frac{\partial \overset{*}{T}}{\partial \omega_k} \cdot \frac{d}{dt}\left(\frac{\partial \omega_k}{\partial \omega_{k'}}\right); \quad (14a)$$

$$\text{(ii)} \qquad \frac{\partial \overset{*}{T}'}{\partial \theta_{k'}} \equiv \frac{\partial \overset{*}{T}'}{\partial q_l} \frac{\partial \dot{q}_l}{\partial \omega_{k'}} = \left(\frac{\partial \overset{*}{T}}{\partial q_l} + \frac{\partial \overset{*}{T}}{\partial \omega_k} \frac{\partial \omega_k}{\partial q_l}\right) \frac{\partial \dot{q}_l}{\partial \omega_{k'}}$$

$$= \frac{\partial \overset{*}{T}}{\partial \theta_k} \underline{\left(\frac{\partial \omega_k}{\partial \dot{q}_l} \frac{\partial \dot{q}_l}{\partial \omega_{k'}}\right)} + \frac{\partial \overset{*}{T}}{\partial \omega_k} \underline{\underline{\left(\frac{\partial \omega_k}{\partial q_l} \frac{\partial \dot{q}_l}{\partial \omega_{k'}}\right)}}$$

$$= \frac{\partial \overset{*}{T}}{\partial \theta_k} \underline{\frac{\partial \omega_k}{\partial \omega_{k'}}} + \frac{\partial \overset{*}{T}}{\partial \omega_k} \underline{\underline{\frac{\partial \omega_k}{\partial \theta_{k'}}}}. \quad (14b)$$

Subtracting (14b) from (14a) side by side we obtain

$$\frac{d}{dt}\left(\frac{\partial \overset{*}{T}'}{\partial \omega_{k'}}\right) - \frac{\partial \overset{*}{T}}{\partial \theta_{k'}} = \left[\frac{d}{dt}\left(\frac{\partial \overset{*}{T}}{\partial \omega_k}\right) - \frac{\partial \overset{*}{T}}{\partial \theta_k}\right]\left(\frac{\partial \omega_k}{\partial \omega_{k'}}\right)$$

$$+ \left[\frac{d}{dt}\left(\frac{\partial \omega_k}{\partial \omega_{k'}}\right) - \frac{\partial \omega_k}{\partial \theta_{k'}}\right]\left(\frac{\partial \overset{*}{T}}{\partial \omega_k}\right),$$

or, compactly, with the help of the nonholonomic Euler-Lagrange operators

$$E_{k'}^* = \underbrace{\frac{\partial \omega_k}{\partial \omega_{k'}} E_k^*}_{\text{vector-like part}} + \underbrace{E_{k'}^*(\omega_k) \frac{\partial T^*}{\partial \omega_k}}_{\text{nonvectorial part}}; \quad (14c)$$

i.e., due to the presence of the *second* right-side term, $E_{k'}^*$, in general, does *not* transform as a (covariant) vector under (11a). The transformation Eq. (14c) shows that E_k^* transforms as a vector if

$$E_{k'}^*(\omega_k) \equiv \frac{d}{dt}\left(\frac{\partial \omega_k}{\partial \omega_{k'}}\right) - \frac{\partial \omega_k}{\partial \theta_{k'}} = 0;$$

in which case ω and ω' are called, after Johnsen (1941), "relatively holonomic."

Let us, next, move to the transformation of the nonholonomic deviation Γ_k: from (7b) and (12a), and since

$$I_{k'} \equiv \underbrace{\frac{d}{dt}\left(\frac{\partial \overset{*}{T}'}{\partial \omega_{k'}}\right) - \frac{\partial \overset{*}{T}'}{\partial \theta_{k'}}}_{E_{k'}^*(\overset{*}{T}') \equiv E_{k'}^*} - \Gamma_{k'} \equiv E_{k'}^* - \Gamma_{k'}, \quad (15a)$$

we obtain

$$E_{k'}^* - \Gamma_{k'} = \frac{\partial \omega_k}{\partial \omega_{k'}}(E_k^* - \Gamma_k),$$

or, rearranging and using (14c),

$$\Gamma_{k'} = \frac{\partial \omega_k}{\partial \omega_{k'}} \Gamma_k + \left(E_{k'}^* - \frac{\partial \omega_k}{\partial \omega_{k'}} E_k^*\right),$$

or finally

$$\Gamma_{k'} = \underbrace{\frac{\partial \omega_k}{\partial \omega_{k'}} \Gamma_k + \underbrace{\left[\frac{d}{dt}\left(\frac{\partial \omega_k}{\partial \omega_{k'}}\right) - \frac{\partial \omega_k}{\partial \theta_{k'}}\right]}_{E_{k'}^*(\omega_k)} \left(\frac{\partial T^*}{\partial \omega_k}\right)}_{\text{non vectorial part}}, \quad (15b)$$

where

$$\frac{\partial T^*}{\partial \omega_k} = \frac{\partial \overset{*}{T}'}{\partial \omega_{k'}} \frac{\partial \omega_{k'}}{\partial \omega_k};$$

i.e., even though, in general, $I_k \equiv E_k^* - \Gamma_k$ does transform as a covariant vector under $\omega \leftrightarrow \omega'$ yet *individually* neither E_k^* nor Γ_k do so; they do if ω and ω' are relatively holonomic. In tensorial language such nonvectorial/nontensorial quantities are called *geometrical objects;* pretty much like the well-known Christoffel symbols (Schouten, 1954). In Appendix II we specialize (15b) to the common case of *linear* $\omega \leftrightarrow \omega'$ relationships.

In particular, if $\omega_k = \dot{q}_k$, i.e., if the ω are holonomic (Lagrangean) velocities, then

$$\overset{*}{T} \to T, E_k^* \equiv E_k^*(T^*) \to E_k(T) \equiv E_k, \Gamma_k = 0,$$

and so (15b) becomes

$$\Gamma_{k'} = \left[\frac{d}{dt}\left(\frac{\partial \dot{q}_k}{\partial \omega_{k'}}\right) - \frac{\partial \dot{q}_k}{\partial \theta_{k'}}\right]\left(\frac{\partial T}{\partial \dot{q}_k}\right), \quad (15c)$$

where $\dot{q}_k = \dot{q}_k(t, q, \omega')$; or renaming the ω', for convenience, ω:

$$\Gamma_k = \underbrace{\left[\frac{d}{dt}\left(\frac{\partial \dot{q}_l}{\partial \omega_k}\right) - \frac{\partial \dot{q}_l}{\partial \theta_k}\right]}_{\substack{\text{nonlinear Voronets/Johnsen/} \\ \text{Hamel coefficients}}} \left(\frac{\partial T}{\partial \dot{q}_l}\right) \equiv E_k^*(\dot{q}_l) p_l, \quad (15d)$$

where $\dot{q}_l = \dot{q}_l(t, q, \omega)$; while similarly, (12$a$) specializes to (7$g$).

2.2 Particle Derivation.

By the definition (7c),

$$\Gamma_{k'} \equiv \int dm \overset{*}{\mathbf{v}}' \cdot \left[\frac{d}{dt}\left(\frac{\partial \overset{*}{\mathbf{v}}'}{\partial \omega_{k'}}\right) - \frac{\partial \overset{*}{\mathbf{v}}'}{\partial \theta_{k'}}\right], \quad (16a)$$

where

$$\mathbf{v} = \mathbf{v}(t, q, \dot{q}) = \overset{*}{\mathbf{v}}(t, q, \omega)$$

$$= \overset{*}{\mathbf{v}}[t, q, \omega(t, q, \omega')] \equiv \overset{*}{\mathbf{v}}'(t, q, \omega') \equiv \overset{*}{\mathbf{v}}'. \quad (16b)$$

But by chain rule,

$$\text{(i)} \qquad \mathbf{a}_{k'} \equiv \frac{\partial \overset{*}{\mathbf{v}}'}{\partial \omega_{k'}} = \frac{\partial \overset{*}{\mathbf{v}}}{\partial \omega_k} \frac{\partial \omega_k}{\partial \omega_{k'}} \equiv \frac{\partial \omega_k}{\partial \omega_{k'}} \mathbf{a}_k,$$

Downloaded 04 May 2010 to 171.66.16.28. Redistribution subject to ASME license or copyright; see http://www.asme.org/terms/Terms_Use.cfm

and therefore

$$\frac{d}{dt}\left(\frac{\partial^* \mathbf{v}'}{\partial \omega_{k'}}\right) \equiv \frac{d\mathbf{a}_{k'}}{dt} = \frac{d}{dt}\left(\frac{\partial \omega_k}{\partial \omega_{k'}}\right)\mathbf{a}_k + \frac{\partial \omega_k}{\partial \omega_{k'}}\frac{d\mathbf{a}_k}{dt}; \quad (16c)$$

(ii)
$$\frac{\partial^* \mathbf{v}'}{\partial \theta_{k'}} \equiv \frac{\partial^* \mathbf{v}'}{\partial q_l}\frac{\partial \dot{q}_l}{\partial \omega_{k'}}$$

$$= \left(\frac{\partial^* \mathbf{v}}{\partial q_l} + \frac{\partial^* \mathbf{v}}{\partial \omega_k}\frac{\partial \omega_k}{\partial q_l}\right)\frac{\partial \dot{q}_l}{\partial \omega_{k'}}$$

$$= \frac{\partial^* \mathbf{v}}{\partial \theta_k}\left(\frac{\partial \omega_k}{\partial \dot{q}_l}\frac{\partial \dot{q}_l}{\partial \omega_{k'}}\right) + \frac{\partial^* \mathbf{v}}{\partial \omega_k}\left(\frac{\partial \omega_k}{\partial q_l}\frac{\partial \dot{q}_l}{\partial \omega_{k'}}\right)$$

$$= \frac{\partial^* \mathbf{v}}{\partial \theta_k}\frac{\partial \omega_k}{\partial \omega_{k'}} + \frac{\partial^* \mathbf{v}}{\partial \omega_k}\frac{\partial \omega_k}{\partial \theta_{k'}}. \quad (16d)$$

Inserting (16c,d) in (16a), and taking into account (16b) and the definitions of Γ_k and $\partial \overset{*}{T}/\partial \omega_k$, we obtain

$$\Gamma_{k'} = \frac{\partial \omega_k}{\partial \omega_{k'}}\left\{\int dm^* \mathbf{v}^* \cdot \left[\frac{d}{dt}\left(\frac{\partial^* \mathbf{v}}{\partial \omega_k}\right) - \frac{\partial^* \mathbf{v}}{\partial \theta_k}\right]\right\} + \left[\frac{d}{dt}\left(\frac{\partial \omega_k}{\partial \omega_{k'}}\right) - \frac{\partial \omega_k}{\partial \theta_{k'}}\right]\underbrace{\left(\int dm^* \mathbf{v}^* \cdot \frac{\partial^* \mathbf{v}}{\partial \omega_k}\right)}_{\partial \overset{*}{T}/\partial \omega_k};$$

i.e., Eq. (15b).

Remark: In the case of Appell's equations, since

$$I_k \equiv \int dm^* \mathbf{a}^* \cdot \mathbf{a}_k = \int dm^* \mathbf{a}^* \cdot \frac{\partial^* \mathbf{a}}{\partial \dot{\omega}_k} = \frac{\partial S^*}{\partial \dot{\omega}_k},$$

where

$$S^* \equiv \int \tfrac{1}{2} dm^* \mathbf{a}^* \cdot \mathbf{a}^* = \text{Appellian function},$$

and

$$\frac{\partial \dot{\omega}_k}{\partial \dot{\omega}_{k'}} = \frac{\partial \omega_k}{\partial \omega_{k'}}, \quad \frac{\partial \dot{\omega}_{k'}}{\partial \dot{\omega}_k} = \frac{\partial \omega_{k'}}{\partial \omega_k},$$

the transformation (12a) yields

$$\frac{\partial S^{*\prime}}{\partial \dot{\omega}_{k'}} = \frac{\partial \omega_k}{\partial \omega_{k'}}\frac{\partial^* S}{\partial \dot{\omega}_k} \leftrightarrow \frac{\partial^* S}{\partial \dot{\omega}_k} = \frac{\partial \omega_{k'}}{\partial \omega_k}\frac{\partial S^{*\prime}}{\partial \dot{\omega}_{k'}},$$

where

$$S = S(t, q, \dot{q}, \ddot{q})$$

$$= \overset{*}{S}(t, q, \omega, \dot{\omega})$$

$$= \overset{*}{S}[t, q, \omega(t, q, \omega'), \dot{\omega}(t, q, \omega', \dot{\omega}')]$$

$$= \overset{*}{S}'(t, q, \omega', \dot{\omega}') \equiv \overset{*}{S}'.$$

Such transformation equations may prove useful if the hitherto unconstrained, or independent, quasi-velocities $\omega_l \equiv (\omega_{m+1}, \ldots, \omega_n)$ are, later, subjected to the $m'(<n-m)$ new constraints

$$c_d(t, q, \omega_l) = 0 \quad (d = 1, \ldots, m'). \quad (17a)$$

Then, following the earlier Johnsen-Hamel approach, we may introduce n-m new quasi-velocities $\omega' \equiv (\omega_{1'}, \ldots, \omega_{(n-m)'})$ by

$$\omega'_d \equiv c_d(t, q, \omega_l) = 0 \quad (d = 1, \ldots, m'), \quad (17b)$$

$$\omega'_i \equiv c_i(t, q, \omega_l) \neq 0 \quad (i = m' + 1, \ldots, n - m), \quad (17c)$$

where the $(n-m) - m'$ $c_i(\ldots)$ are arbitrary except that when (17b,c) are solved for the $n - m$ $\omega_l = \omega_l(t, q, \omega')$ and these results are inserted in (17a) they satisfy them identically. In this case LP yields

$$\left\{\left[\frac{d}{dt}\left(\frac{\partial^* T}{\partial \omega_l}\right) - \frac{\partial^* T}{\partial \theta_l} - \Gamma_l\right] - \Theta_l\right\}\delta\theta_l = 0, \quad (17d)$$

where the $n - m$ $\delta\theta_l \equiv (\delta\theta_{m+1}, \ldots, \delta\theta_n)$ are subjected to the (virtual form of the) constraints

$$\delta\theta'_d \equiv \frac{\partial c_d}{\partial \omega_l}\delta\theta_l \equiv \frac{\partial \omega'_d}{\partial \omega_l}\delta\theta_l = 0; \quad (17e)$$

($d\theta'/dt \equiv \omega'$). From here on we proceed in well-known ways; i.e., either we *adjoin* (17e) to (17d) via (new) Lagrangean multipliers (→Routh-Voss equations in $\overset{*}{T}$ and ω_l); or we *embed* them in $\overset{*}{T}$ via the quasivariables $\delta\theta'/\omega'$ (→Maggi equations in $\overset{*}{T}$, ω_l, $\partial\omega_l/\partial\omega'$; or Hamel equations in $\overset{*}{T}'$, ω', Γ' etc.).

3 Transformation of Forces

Since

$$\delta' W = \Theta_k \delta\theta_k = \Theta_{k'}\delta\theta_{k'} = \ldots, \quad (18a)$$

invoking (11b) we readily obtain the (covariant) transformation equations

$$\Theta_{k'} = \frac{\partial \omega_k}{\partial \omega_{k'}}\Theta_k \leftrightarrow \Theta_k = \frac{\partial \omega_{k'}}{\partial \omega_k}\Theta_{k'}; \quad (18b)$$

and similarly for the constraint reactions (=Lagrangean multipliers).

Acknowledgment

The author is grateful to the unknown reviewers for their constructive comments on an earlier version of this paper.

References

Hamel, G., 1949, *Theoretische Mechanik,* Springer, Berlin, pp. 473–476.

Johnsen, L., 1941, "Dynamique Generale des Systemes Non-holonomes," *Skrifter Utgitt av det Norske Videnskaps-Akademi i Oslo I. Mathematik-Naturvidenskab Klasse,* No. 4, pp. 1–75.

Lynn, J. W., 1963, *Tensors in Electrical Engineering,* E. Arnold Ltd., London, pp. 202–203.

Papastavridis, J. G., 1990, "Maggi's Equations of Motion and the Determination of Constraint Reactions," *Journal of Guidance, Dynamics and Control,* Vol. 13, No. 2, pp. 213–220.

Papastavridis, J. G., 1991, "On Energy Rate Theorems for Linear First-Order Nonholonomic Systems," ASME JOURNAL OF APPLIED MECHANICS, Vol. 58, pp. 536–544.

Papastavridis, J. G., 1994, "On the Boltzmann-Hamel Equations of Motion: A Vectorial Treatment," ASME JOURNAL OF APPLIED MECHANICS, Vol. 61, pp. 453–459.

Schaefer, H., 1951, "Die Bewegungsgleichungen nicht holonomer Systeme," *Abhandlungen der Braunschweig Wissenschaftliche Gesellschaft,* Vol. 3, pp. 116–121.

Schouten, J. A., 1954, *Tensor Analysis for Physicists,* 2nd ed., Clarendon Press, Oxford, pp. 112, 121–123.

Downloaded 04 May 2010 to 171.66.16.28. Redistribution subject to ASME license or copyright; see http://www.asme.org/terms/Terms_Use.cfm

APPENDICES

I An Independent Derivation

of (7g); by direct differentiation of the holonomic and nonholonomic "inertia forces" $E_k \equiv E_k(T)$ and $I_k \equiv E_k^*(T^*) - \Gamma_k$. Applying the chain rule to

$$T = T(t, q, \dot{q}) = T^*(t, q, \omega) = T^*,$$

we obtain

$$\text{(i)} \qquad \frac{\partial T^*}{\partial q_l} = \frac{\partial T}{\partial q_l} + \frac{\partial T}{\partial \dot{q}_r}\frac{\partial \dot{q}_r}{\partial q_l},$$

and solving for $\partial T/\partial q_l$,

$$\frac{\partial T}{\partial q_l} = \frac{\partial T^*}{\partial q_l} - \frac{\partial T}{\partial \dot{q}_r}\frac{\partial \dot{q}_r}{\partial q_l},$$

and therefore, recalling the symbolic quasi-chain rule (4f),

$$\frac{\partial T}{\partial q_l}\frac{\partial \dot{q}_l}{\partial \omega_k} = \frac{\partial T^*}{\partial q_l}\frac{\partial \dot{q}_l}{\partial \omega_k} - \frac{\partial T}{\partial \dot{q}_r}\left(\frac{\partial \dot{q}_r}{\partial q_l}\frac{\partial \dot{q}_l}{\partial \omega_k}\right)$$

$$= \frac{\partial T^*}{\partial \theta_k} - \frac{\partial T}{\partial \dot{q}_r}\frac{\partial \dot{q}_r}{\partial \theta_k}. \qquad \text{(A1)}$$

(ii) By $(\ldots)^{\cdot}$-differentiation of the momentum transformation (7e) we obtain

$$\frac{d}{dt}\left(\frac{\partial T^*}{\partial \omega_k}\right) = \frac{d}{dt}\left(\frac{\partial T}{\partial \dot{q}_l}\right)\frac{\partial \dot{q}_l}{\partial \omega_k} + \frac{\partial T}{\partial \dot{q}_l}\frac{d}{dt}\left(\frac{\partial \dot{q}_l}{\partial \omega_k}\right),$$

and from this, rearranging,

$$\frac{d}{dt}\left(\frac{\partial T}{\partial \dot{q}_l}\right)\frac{\partial \dot{q}_l}{\partial \omega_k} = \frac{d}{dt}\left(\frac{\partial T^*}{\partial \omega_k}\right) - \frac{\partial T}{\partial \dot{q}_l}\frac{d}{dt}\left(\frac{\partial \dot{q}_l}{\partial \omega_k}\right). \qquad \text{(A2)}$$

Hence, subtracting (A1) from (A2) side by side we obtain the following fundamental kinematico-inertial identity:

$$\underbrace{\left[\frac{d}{dt}\left(\frac{\partial T}{\partial \dot{q}_l}\right) - \frac{\partial T}{\partial q_l}\right]}_{E_l}\left(\frac{\partial \dot{q}_l}{\partial \omega_k}\right) = \underbrace{\left[\frac{d}{dt}\left(\frac{\partial T^*}{\partial \omega_k}\right) - \frac{\partial T^*}{\partial \theta_k}\right]}_{E_k^*}$$

$$- \underbrace{\left[\frac{d}{dt}\left(\frac{\partial \dot{q}_l}{\partial \omega_k}\right) - \frac{\partial \dot{q}_l}{\partial q_k}\right]}_{\Gamma_k}\left(\frac{\partial T}{\partial \dot{q}_l}\right), \qquad \text{(A3)}$$

or compactly,

$$\frac{\partial \dot{q}_l}{\partial \omega_k} E_l = \underbrace{E_k^* - \Gamma_k}_{I_k};$$

i.e., Eq. (7g).

II Specialization of (15b) to Linear Nonholonomic Coordinates

Here (in exception to the rest of the paper and to Papastavridis (1994)), and for reasons that will, hopefully, become clear below, we use the general tensorial notation; i.e., subscripts and superscripts. Thus we introduce the following renamings:

$$q_k \to q^k,\ \omega_k \to \omega^{k'},\ \omega_{k'} \to \omega^{k''} \quad \text{etc.};$$

i.e., *accented (unaccented) indices denote nonholonomic* (holonomic) quantities; and the summation convention applies over *diagonal* pairs of indices. Now, it has been shown by Papastavridis (1994) that for quasivelocities $\omega^{k'}$ defined by the linear and (for algebraic convenience, but no loss in generality) *homogeneous* and invertible transformations

$$\omega^{k'} = a_k^{k'}\dot{q}^k \leftrightarrow \dot{q}^k = a_{k'}^k\omega^{k'}, \qquad \text{(A4)}$$

where the coefficients $a_k^{k'}$ and $a_{k'}^k$ are functions of the q's and satisfy the "inverseness" relationships (Papastavridis, 1990):

$$a_k^{k'}a_{l'}^k = \delta_{l'}^{k'} \quad \text{and} \quad a_k^{k'}a_{k'}^l = \delta_k^l. \qquad \text{(A5)}$$

The nonholonomic deviation becomes

$$\Gamma_{k'} \equiv \int dm\mathbf{v}^* \cdot \left[\frac{d}{dt}\left(\frac{\partial^* \mathbf{v}}{\partial \omega^{k'}}\right) - \frac{\partial^* \mathbf{v}}{\partial \theta^{k'}}\right]$$

$$= \int dm\mathbf{v}^* \cdot \underbrace{\left(\frac{\partial \mathbf{a}_{k'}}{\partial \theta^{l'}} - \frac{\partial \mathbf{a}_{l'}}{\partial \theta^{k'}}\right)}_{\gamma_{l'k'}^{s'}\mathbf{a}_{s'}}\omega^{l'}\omega^{l'}$$

$$= \left(\int dm\mathbf{v}^* \cdot \mathbf{a}_{s'}\right)\gamma_{l'k'}^{s'}\omega^{l'} = \gamma_{l'k'}^{s'}P_{s'}\omega^{l'}, \qquad \text{(A6)}$$

where

$$P_{s'} \equiv \int dm\mathbf{v}^* \cdot \mathbf{a}_{s'} = \frac{\partial T^*}{\partial \omega^{s'}}, \qquad \text{(A7)}$$

and the famous "three-index" (Hamel) transitivity, or transpositional, (nontensorial!) coefficients $\gamma_{l'k'}^{s'} = -\gamma_{k'l'}^{s'}$ are defined by the nonintegrability (nongradient) equations

$$\frac{\partial \mathbf{a}_{k'}}{\partial \theta^{l'}} - \frac{\partial \mathbf{a}_{l'}}{\partial \theta^{k'}} = \gamma_{l'k'}^{s'}\mathbf{a}_{s'} \qquad \text{(A8)}$$

and, as a result, the nonholonomic inertia (covariant) components $I_{k'}$ become

$$I_{k'} \equiv \int dm\mathbf{a}^* \cdot \mathbf{a}_{k'} = \ldots$$

$$= \frac{d}{dt}\left(\frac{\partial T^*}{\partial \omega^{k'}}\right) - \frac{\partial T^*}{\partial \theta^{k'}} - \gamma_{l'k'}^{s'}\frac{\partial T^*}{\partial \omega^{s'}}\omega^{l'} \qquad \text{(A9)}$$

$$= E_{k'}^* + \gamma_{k'l'}^{s'}P_{s'}\omega^{l'}.$$

Below, by applying (15b) between the two nonholonomic systems $\omega^{k'}$ and $\omega^{k''}$ defined, at q, by

$$\left.\begin{array}{l} \omega^{k''} = a_{k'}^{k''}\omega^{k'} = a_k^{k''}\dot{q}^k (\to a_{k'}^{k''}a_k^{k'} = a_k^{k''}) \\ \updownarrow \\ \omega^{k'} = a_{k''}^{k'}\omega^{k''} = a_k^{k'}\dot{q}^k (\to a_{k''}^{k'}a_k^{k''} = a_k^{k'}) \end{array}\right\}, \qquad \text{(A10)}$$

where the a::: coefficients are functions of the (holonomic) q's and satisfy (A5)-like relations, we will find the law of transformation between the corresponding Hamel coefficients $\gamma_{l'k'}^{s'}$ and $\gamma_{l''k''}^{s''}$. Indeed substituting, from (A6),

$$\Gamma_{k'} = \gamma_{l'k'}^{s'}P_{s'}\omega^{l'}, \quad \text{and} \quad \Gamma_{k''} = \gamma_{l''k''}^{s''}P_{s''}\omega^{l''} \qquad \text{(A11)}$$

in (15b), rewritten in nonholonomic notation as

$$\Gamma_{k''} = \frac{\partial \omega^{k'}}{\partial \omega^{k''}}\Gamma_{k'} + \left[\frac{d}{dt}\left(\frac{\partial \omega^{k'}}{\partial \omega^{k''}}\right) - \frac{\partial \omega^{k'}}{\partial \theta^{k''}}\right]P_{k'}, \qquad \text{(A12)}$$

and since, by (A10), $P_{s''} = (\partial \omega^{s'}/\partial \omega^{s''})P_{s'} = a_{s''}^{s'}P_{s'}$, we obtain

$$\omega^{l''}a_{s''}^{s'}\gamma_{l''k''}^{s''} = \omega^{l'}a_{k''}^{k'}\gamma_{l'k'}^{s'} + \left[\frac{d}{dt}\left(\frac{\partial \omega^{s'}}{\partial \omega^{k''}}\right) - \frac{\partial \omega^{s'}}{\partial \theta^{k''}}\right]. \qquad \text{(A13)}$$

Downloaded 04 May 2010 to 171.66.16.28. Redistribution subject to ASME license or copyright; see http://www.asme.org/terms/Terms_Use.cfm

Next, to isolate $\gamma^{s''}_{l''k''}$ on the left side of (A13), we

(i) multiply it with $a^{r''}_{s'}$ and sum over s' (by (A10): $a^{r''}_{s'}a^{s'}_{s''} = \delta^{r''}_{s''}$),
(ii) in the first right-side term replace $\omega^{l'}$ with $a^{l'}_{l''}\omega^{l''}$, and
(iii) notice that $(d/dt)(\partial\omega^{s'}/\partial\omega^{k''}) = a^{s'}_{k''} = (\partial a^{s'}_{k''}/\partial q^m)\dot{q}^m = [(\partial a^{s'}_{k''}/\partial\theta^{m''})(\partial\omega^{m''}/\partial\dot{q}^m)]\underbrace{(a^m_{l''}\omega^{l''})}_{\dot{q}^m}$

$$= \frac{\partial a^{s'}_{k''}}{\partial\theta^{m''}}\underbrace{(a^{m''}_{m}a^{m}_{l''})}_{\delta^{m''}_{l''}}\omega^{l''} = \frac{\partial a^{s'}_{k''}}{\partial\theta^{l''}}\omega^{l''}, \tag{A14}$$

and, recalling (4g),

$$\frac{\partial\omega^{s'}}{\partial\theta^{k''}} = \frac{\partial}{\partial\theta^{k''}}(a^{s'}_{l''}\omega^{l''}) = \frac{\partial a^{s'}_{l''}}{\partial\theta^{k''}}\omega^{l''}, \tag{A15}$$

while, in the process, renaming dummy indices if/as needed. The result is the (nontensorial!) transformation equation:

$$\gamma^{r''}_{l''k''} = \underbrace{a^{r''}_{r'}a^{l'}_{l''}a^{k'}_{k''}\gamma^{r'}_{l'k'}}_{\text{tensor-like part}} + \underbrace{\left(\frac{\partial a^{r'}_{k''}}{\partial\theta^{l''}} - \frac{\partial a^{r'}_{l''}}{\partial\theta^{k''}}\right)a^{r''}_{r'}}_{\substack{\text{nontensorial part;}\\ \text{in general, nonzero}}} \tag{A16}$$

Finally, in view of the identities

$$a^{r'}_{k''}a^{r''}_{r'} = \delta^{r''}_{k''} \rightarrow \frac{\partial a^{r'}_{k''}}{\partial\theta^{l''}}a^{r''}_{r'} = -\frac{\partial a^{r''}_{r'}}{\partial\theta^{l''}}a^{r'}_{k''} \equiv -\left(\frac{\partial a^{r''}_{r'}}{\partial\theta^{l'}}a^{l'}_{l''}\right)a^{r'}_{k''}, \tag{A17}$$

we can readily transform the nontensorial part of (A16) so that the latter takes the symmetrical form:

$$\gamma^{r''}_{l''k''} = a^{r''}_{r'}a^{l'}_{l''}a^{k'}_{k''}\gamma^{r'}_{l'k'} + \left(\frac{\partial a^{r''}_{l'}}{\partial\theta^{k'}} - \frac{\partial a^{r''}_{k'}}{\partial\theta^{l'}}\right)a^{l'}_{l''}a^{k'}_{k''}, \tag{A18}$$

in complete agreement with the result found in the (linear) nonholonomic tensor literature (Lynn, 1963). Alternative derivations of (A16, A18) based on the linear transitivity equation

$$(\delta q^k)^{\cdot} - \delta\dot{q}^k = a^k_{k'}[(\delta\theta^{k'})^{\cdot} - d\omega^{k'}] - \gamma^{k'}_{r's'}a^k_{k'}\omega^{s'}\delta\theta^{r'}$$
$$= a^k_{k''}[(\delta\theta^{k''})^{\cdot} - \delta\omega^{k''}] - \gamma^{k''}_{r''s''}a^k_{k''}\omega^{s''}\delta\theta^{r''}, \tag{A19}$$

$$\gamma^{s'}_{l'k'} = \left(\frac{\partial a^{s'}_{l}}{\partial q^k} - \frac{\partial a^{s'}_{k}}{\partial q^l}\right)a^l_{l'}a^k_{k'}, \quad \gamma^{s''}_{l''k''} = \left(\frac{\partial a^{s''}_{l}}{\partial q^k} - \frac{\partial a^{s''}_{k}}{\partial q^l}\right)a^l_{l''}a^k_{k''}$$

can also be readily obtained (Hamel, 1949; Papastavridis, 1991).

Downloaded 04 May 2010 to 171.66.16.28. Redistribution subject to ASME license or copyright; see http://www.asme.org/terms/Terms_Use.cfm

Huang Ke-Fu
Associate Professor.

Wang Min-Zhong
Professor.

Department of Mechanics
and Engineering Science,
Peking University,
Beijing 100871,
P. R. China

Complete Solution of the Linear Magnetoelasticity and the Magnetic Fields in a Magnetized Elastic Half-Space[1]

In this paper, a general solution of the equations in the linearized theory of magnetoelasticity, which was developed by Pao and Yeh (1973) on the basis of Brown's phenomenological theory of magnetoelasticity (1966), is obtained. As in some applications, the magnetic fields caused by the mechanical singularities in a magnetized elastic half-space are considered. Using the general solution and the Mindlin state of the elastic half-space (1936), the exact three-dimensional solutions for the generated magnetic fields due to various mechanical singularities, such as a single force and a doublet, are obtained in closed form.

Introduction

In 1966, a general theory of the interaction between magnetic fields and elastic deformations was thoroughly developed in a monograph by Brown (1966). In his book, he summarized his research work over the past 20 years and developed a phenomenological theory of magnetoelasticity on the basis of the large deformation theory of continuum mechanics and the classical theory of magnetism. Since such a general nonlinear theory is rather complicated, a linearized version of Brown's theory has been given by Pao and Yeh (1973). They developed a linear theory for soft ferromagnetic elastic solids and suggested a complete set of magnetoelastic field equations and boundary conditions, which were derived by means of consistent applications of the balance laws of continuum mechanics following Brown's approach (1965). A set of linearized constitutive equations governing the behavior of these materials has been also obtained from energy consideration. The linearized theory has been applied with success to investigate the magnetoelastic buckling of an isotropic plate in a transversally applied uniform magnetic induction (Pao and Yeh, 1973), and the intensification factors of cracks in ferromagnetic elastic solids (Shindo, 1977, 1978, 1980). Recently Yeh (1989) applied this theory to obtain the induced magnetic fields generated by the mechanical singularities in a magnetized elastic half-plane. The induced magnetic fields are expressed in closed form.

In the present paper we develop a general solution for the soft ferromagnetic elastic solids from Pao and Yeh's linear theory (1973), and point out that such a general solution is complete. The general solution is analogous to the Papkovich-Neuber solution in the theory of elasticity, which has been widely used in the spatial problems in elasticity (Gurtin, 1972), fracture mechanics (Kassir and Sih, 1975; Meade and Keer, 1984), etc. Using the general solution, we investigate the magnetoelastic problems for the soft ferromagnetic elastic half-space with the mechanical singularities permeated by a uniform magnetostatic field normal to the surface of the half-space. By using the Mindlin state (1936) of the elastic half-space, the problems are reduced to that of solving the Dirichlet and Neuman problems of harmonic functions. The problems are solved exactly and the induced magnetic inductions are expressed in closed form.

As a consequence, the relative plane problems considered by Yeh (1989) can be directly derived from our results by means of the finite parts technique of the divergent integrals (Wang, 1985).

The General Solution in the Linear Magnetoelasticity

Basic Equations. According to the linearized theory developed by Pao and Yeh (1973), the magnetic quantities can be decomposed into two parts as

$$B_i = \overline{B_i} + b_i \quad M_i = \overline{M_i} + m_i \quad H_i = \overline{H_i} + h_i, \tag{1}$$

where B_i, M_i, and H_i are magnetic induction, magnetization, and magnetic intensity, respectively. The barred quantities are the magnetic fields in the rigid-body state with no mechanical singularities; the quantities in lower case represent those in the perturbed state caused by the mechanical singularities and are assumed much smaller than the undisturbed state.

According to Yeh (1989), the basic equations of magnetic fields are of the form

$$e_{ijk}\overline{H}_{k,j} = 0 \quad \overline{B}_{i,i} = 0 \tag{2}$$

$$\overline{M_i} = \chi\overline{H_i} \quad \overline{B_i} = \mu_0(\overline{H_i} + \overline{M_i}) = \mu_r\mu_0\overline{H_i} \tag{3}$$

$$e_{ijk}h_{k,j} = 0 \quad b_{i,i} = 0 \tag{4}$$

$$m_i = \chi h_j \quad b_i = \mu_0(h_i + m_i) = \mu_0\mu_r h_i, \tag{5}$$

where e_{ijk} is the permutation tensor and the symbol $(,)$ denotes the partial derivative with respect to the spatial variables, and the repeated indices imply summation. χ is the magnetic susceptibility, $\mu_0 = 4\pi \times 10^{-7}$ newton/ampere^2 is the magnetic permeability of vacuum, and $\mu_r = 1 + \chi$ is the relative magnetic permeability of the materials.

The balance law of the magnetoelastic field takes the form

$$t_{ij,i} + \mu_0(\overline{M_i H_{j,i}} + \overline{M_i}h_{j,i} + m_i\overline{H}_{j,i}) + f_j = 0 \tag{6}$$

$$t_{ij} = \frac{\mu_0}{\chi}\overline{M_i M_j} + \mu(\overline{H_j}m_i + \overline{H_i}m_j) + \tau_{ij} \tag{7}$$

[1] This project was supported by the National Natural Science Foundation of China.

Contributed by the Applied Mechanics Division of THE AMERICAN SOCIETY OF MECHANICAL ENGINEERS for publication in the ASME JOURNAL OF APPLIED MECHANICS.

Discussion on this paper should be addressed to the Technical Editor, Professor Lewis T. Wheeler, Department of Mechanical Engineering, University of Houston, Houston, TX 77204-4792, and will be accepted until four months after final publication of the paper itself in the ASME JOURNAL OF APPLIED MECHANICS.

Manuscript received by the ASME Applied Mechanics Division, June 13, 1990; final revision, June 21, 1994. Associate Technical Editor: R. M. McMeeking.

Copyright © 1995 by ASME

Downloaded 04 May 2010 to 171.66.16.28. Redistribution subject to ASME license or copyright; see http://www.asme.org/terms/Terms_Use.cfm

$$\tau_{ij} = \lambda u_{k,k}\delta_{ij} + G(u_{i,j} + u_{j,i}), \quad (8)$$

where t_{ij} is the magnetomechanical stress tensor, f_j is the body force per unit volume, λ, G are the Lame constants, and δ_{ij} is the Kronecker delta symbol.

Boundary Conditions. On the boundary of the undeformed body with an outward unit normal vector n_i, we have

$$e_{ijk}n_j[\overline{H_k}] = 0 \quad n_i[\overline{B_i}] = 0 \quad (9)$$

$$e_{ijk}\{n_j[h_k] - n_p u_{p,j}[\overline{H_k}]\} = 0 \quad (10)$$

$$n_i[b_i] - n_p u_{p,i}[\overline{B_i}] = 0 \quad (11)$$

$$n_i[\tau_{ij}] = -\mu_0 n_i\left[\frac{1}{\chi}\overline{M_i M_j}\right] - \mu_0 n_i[\overline{H_j}m_i + \overline{H_i}m_j] + \frac{1}{2}\mu_0 n_j[\overline{M_n^2}] + \mu_0 n_j[\overline{M_n}m_n], \quad (12)$$

where the square brackets represent the jump of the field across the discontinuity surface and $\overline{M_n} = \overline{M_i}n_i$, $m_n = m_i n_i$.

General solutions. Here we introduce a general solution for the set of Eqs. (2)–(8).

From magnetic Eqs. (2)–(5), we have two magnetic potential functions ψ and φ:[2]

$$\overline{H_i} = \psi_{,i} \quad \overline{M_i} = \chi\psi_{,i} \quad \overline{B_i} = \mu_0\mu_r\psi_{,i} \quad (13)$$

$$h_i = \varphi_{,i} \quad m_i = \chi\varphi_{,i} \quad b_i = \mu_0\mu_r\varphi_{,i} \quad (14)$$

and

$$\psi_{,ii} = 0 \quad \varphi_{,ii} = 0. \quad (15)$$

Substituting these equations into the Eqs. (6) and (7), we have

$$t_{ij,i} + \mu_0\chi(\psi_{,i}\psi_{,ij} + \psi_{,i}\varphi_{,ij} + \psi_{,ij}\varphi_{,i}) + f_j = 0 \quad (16)$$

$$t_{ij} = \mu_0\chi(\psi_{,i}\psi_{,j} + \psi_{,i}\varphi_{,j} + \psi_{,j}\varphi_{,i}) + \tau_{ij}. \quad (17)$$

From equations (8), (15), (16), and (17) we have the general equilibrium equation represented by displacement u_i and magnetic potentials ψ and φ:

$$u_{j,ii} + \frac{1}{1-2\nu}u_{i,ij} + \frac{2\mu_0\chi}{G}(\psi_{,i}\psi_{,ij} + \psi_{,i}\varphi_{,ij} + \psi_{,ij}\varphi_{,i}) + \frac{1}{G}f_j = 0 \quad (18)$$

where $\nu = \lambda/2(\lambda + G)$ is the Poisson's ratio. Evidently Eq. (18) is very similar to the elastic equilibrium equation of displacement. Analogizing to the Papkovich-Neuber solution of elasticity (Gurtin, 1972), we have the general solution of the homogeneous equation of (18) as

$$u_j = -\frac{(1-2\nu)\mu_0\chi}{2(1-\nu)G}(\psi\psi_{,j} + \psi\varphi_{,j} + \psi_{,j}\varphi) + 4(1-\nu)\overline{P_j} - (P_0 + x_i\overline{P_i})_{,j} \quad (19)$$

where P_0 and $\overline{P_j}$ are all harmonic functions, i.e.,

$$P_{0,ii} = 0 \quad \overline{P}_{j,ii} = 0. \quad (20)$$

It is a direct result that the general solution in (19) and (20) is complete because of the completeness of the Papkovich-Neuber solution of the equilibrium equation of displacement in elasticity. Applying this solution, the problems in magnetoelasticity are reduced to the problems of solving six harmonic functions.

In the case that $\overline{H_i}$ equals a constant vector, for which we let ψ equal to $x_i\overline{H_i}$, we can simplify Eq. (19) by a transformation as

$$\overline{P_i} = P_i - \frac{(1-2\nu)\mu_0\chi}{2(1-\nu)G}\overline{H_i}\varphi + \frac{\mu_0\chi}{4(1-\nu)G}x_k\overline{H_k}\overline{H_i} \quad (21)$$

$$P_{i,jj} = 0 \quad (22)$$

and the solution (19) becomes

$$u_j = -\frac{2(1-2\nu)\mu_0\chi}{G}\overline{H_j} + 4(1-\nu)P_j - (P_0 + x_i P_i)_{,j}. \quad (23)$$

Magnetic Fields in a Magnetized Half-Space

Consider a magnetizable homogeneous, isotropic, linearly elastic, soft ferromagnetic half-space occupying the region $x_3 < 0$ in Fig. 1. Further, suppose that the half-space is subjected to a unit concentrated body force located at the point $(0, 0, -c)$ as shown in Fig. 1. The applied magnetic induction represented by $B_0 e_3$ is distributed in the whole space uniformly. From Eqs. (9) and (13), the solutions for the rigid-body state are

$$\psi^+ = x_3 B_0/\mu_0 \quad (x_3 > 0) \quad (24)$$

$$\psi = x_3 B_0/\mu_0\mu_r \quad (x_3 < 0) \quad (25)$$

where the superscript "+" represents the quantities outside the half-space. By employing Eq. (25) and introducing two harmonic potential functions as in Eqs. (14) and (15) in the upper and lower half-space, respectively, the equilibrium Eqs. (18) can be expressed as

$$u_{j,ii} + \frac{1}{1-2\nu}u_{i,ij} + \frac{2\chi B_0}{G\mu_r}\varphi_{,3j} + \frac{1}{G}f_j = 0 \quad (x_3 < 0). \quad (26)$$

The magnetic continuity conditions (10) and (11) on the surface $x_3 = 0$ are reduced to

$$\varphi^+_{,1} - \varphi_{,1} = \frac{\chi B_0}{\mu_0\mu_r}u_{3,1} \quad (\text{on } x_3 = 0) \quad (27)$$

$$\varphi^+_{,2} - \varphi_{,2} = \frac{\chi B_0}{\mu_0\mu_r}u_{3,2} \quad (\text{on } x_3 = 0) \quad (28)$$

$$\varphi^+_{,3} - \mu_r\varphi_{,3} = 0 \quad (\text{on } x_3 = 0) \quad (29)$$

and for those traction-free boundaries, Eq. (12) becomes

$$u_{1,3} + u_{3,1} = -\frac{\chi B_0}{G\mu_r}\varphi_{,1} \quad (\text{on } x_3 = 0) \quad (30)$$

$$u_{2,3} + u_{3,2} = -\frac{\chi B_0}{G\mu_r}\varphi_{,2} \quad (\text{on } x_3 = 0) \quad (31)$$

$$\nu(u_{1,1} + u_{2,2}) + (1-\nu)u_{3,3} = \frac{(1-2\nu)(\chi-2)\chi B_0}{2G\mu_r}\varphi_{,3} \quad (\text{on } x_3 = 0). \quad (32)$$

In Eq. (32) the contribution from the term $[(1-2\nu)(\chi-2)\chi/4G\mu_0\mu_r^2]B_0^2$ is neglected since it generated uniform stresses in the half-space.

To satisfy the boundary condition (29), the harmonic function φ^+ can be written by φ as

$$\varphi^+(x_1, x_2, x_3) = -\mu_r\varphi(x_1, x_2, -x_3) \quad (x_3 > 0). \quad (33)$$

Equation (33) implies that φ^+ is harmonic in the upper half-space as soon as φ is harmonic in the lower half-space. By

[2] Generally, equation $e_{ijk}h_{k,j} = 0$ may not have the potential φ. However, in our discussion, the Ampere's law can be expressed in the form as $\int_L h_i dl_i = 0$, where L is an arbitrary piecewise smooth closed curve in the space so that magnetic potential φ exists.

Downloaded 04 May 2010 to 171.66.16.28. Redistribution subject to ASME license or copyright; see http://www.asme.org/terms/Terms_Use.cfm

employing Eq. (33), boundary conditions (27) and (28) can be written as

$$(1 + \mu_r)\varphi_{,1} = \frac{\chi B_0}{\mu_0 \mu_r} u_{3,1} \quad (\text{on } x_3 = 0) \tag{34}$$

$$(1 + \mu_r)\varphi_{,2} = \frac{\chi B_0}{\mu_0 \mu_r} u_{3,2} \quad (\text{on } x_3 = 0). \tag{35}$$

For the equilibrium Eq. (26), the displacement u_i can be discomposed into two parts as

$$u_i = u_i^e + u_i^c, \tag{36}$$

where u_i^e represents the special solution corresponding to the body force f_i and u_i^c the general solution of the homogeneous equation corresponding to Eq. (26). For convenience, the special solution u_i^e is suggested by applying the Mindlin solution of the elastic half-space (Mindlin, 1936). In the Mindlin solution, the displacement satisfies the following conditions:

$$u_{1,3}^e + u_{3,1}^e = 0 \quad (\text{on } x_3 = 0) \tag{37}$$

$$u_{2,3}^e + u_{3,2}^e = 0 \quad (\text{on } x_3 = 0) \tag{38}$$

$$\nu(u_{1,1}^e + u_{2,2}^e) + (1 - \nu)u_{3,3}^e = 0 \quad (\text{on } x_3 = 0). \tag{39}$$

The general solution u_i^c is represented by Eqs. (23). In the present discussion, let $P_1 = P_2 = 0$, Eq. (23) becomes

$$u_1^c = -P_{0,1} - x_3 P_{3,1} \tag{40}$$

$$u_2^c = -P_{0,2} - x_3 P_{3,2} \tag{41}$$

$$u_3^c = (3 - 4\nu)P_3 - P_{0,3} - x_3 P_{3,3} - \frac{2(1 - 2\nu)\chi B_0}{G\mu_r}\varphi. \tag{42}$$

Substituting Eqs. (36)–(42) into the boundary conditions (30)–(32), (34), and (35), we have

$$a_1\varphi_{,1} = (1 - 2\nu)P_{3,1} - P_{0,13} \quad (\text{on } x_3 = 0) \tag{43}$$

$$a_1\varphi_{,2} = (1 - 2\nu)P_{3,2} - P_{0,23} \quad (\text{on } x_3 = 0) \tag{44}$$

$$a_2\varphi_{,3} = 2(1 - \nu)P_{3,3} - P_{0,33} \quad (\text{on } x_3 = 0) \tag{45}$$

$$a_3\varphi_{,1} = (3 - 4\nu)P_{3,1} - P_{0,13} + u_{3,1}^e \quad (\text{on } x_3 = 0) \tag{46}$$

$$a_3\varphi_{,2} = (3 - 4\nu)P_{3,2} - P_{0,23} + u_{3,2}^e \quad (\text{on } x_3 = 0) \tag{47}$$

where a_1, a_2, and a_3 are constant as

$$a_1 = (1 - 4\nu)\frac{\chi B_0}{2G\mu_r}$$

$$a_2 = (1 - 4\nu + \mu_r)\frac{\chi B_0}{2G\mu_0}$$

$$a_3 = (1 + \mu_r)\frac{\mu_0\mu_r}{\chi B_0} + 2(1 - 2\nu)\frac{\chi B_0}{G\mu_r}. \tag{48}$$

In the next section we shall prove that there exists a harmonic function $g(x_1, x_2, x_3)$ in the lower half-space satisfying the following conditions:

$$g_{,ii} = 0 \quad (x_3 < 0)$$

$$g_{,1} = u_{3,1}^e \quad g_{,2} = u_{3,2}^e \quad (\text{on } x_3 = 0)$$

$$g \text{ is finite at } x_3 \to \infty. \tag{49}$$

By employing harmonic function g defined in Eqs. (49), the harmonic functions φ, P_0, P_3, and φ^+ can be solved as

$$\varphi = \frac{\chi B_0}{\mu_0\mu_r(1 + \mu_r)\Delta} g$$

$$P_3 = \frac{\chi^2 B_0^2}{2G\mu_0\mu_r(1 + \mu_r)\Delta} g \quad (x_3 < 0)$$

$$P_{0,3} = \left(1 - 2\nu - \frac{1 - 4\nu}{\mu_r}\right)\frac{\chi^2 B_0^2}{2G\mu_0\mu_r(1 + \mu_r)\Delta} g \tag{50}$$

and

$$\varphi^+(x_1, x_2, x_3) = -\frac{\chi B_0}{\mu_0(1 + \mu_r)\Delta} g(x_1, x_2, -x_3) \quad (x_3 > 0), \tag{51}$$

where

$$\Delta = 1 - [2(1 - \nu)\mu_r - (3 - 4\nu)]\frac{\chi^2 B_0^2}{2G\mu_0\mu_r^2(1 + \mu_r)}.$$

Substituting Eqs. (50) and (51) into Eq. (14), the generated magnetic fields caused by the mechanical singularities are obtained. In the following section the magnetic induction are solved for various mechanical singularities.

Perturbation of Magnetic Fields by Mechanical Singularities

1 Magnetic Fields Generated by a Single Force Normal to the Boundary of the Half-Space. When a unit single force is applied at $(0, 0, -c)$ and acts in the x_3-direction, the displacement of the x_3-direction in the Mindlin solution of the lower half-space is (Mindlin, 1936)

$$u_3^e = \frac{1}{16\pi G(1 - \nu)}\left\{\frac{3 - 4\nu}{R_1} + \frac{1 + 4(1 - \nu)(1 - 2\nu)}{R_2} + \frac{(x_3 + c)^2}{R_1^3} + \frac{(3 - 4\nu)(x_3 - c)^2 + 2x_3 c}{R_2^3} - \frac{6x_3 c(x_3 - c)^2}{R_2^5}\right\} \quad (x_3 < 0) \tag{52}$$

where

$$R_1 = [x_1^2 + x_2^2 + (x_3 + c)^2]^{1/2},$$

$$R_2 = [x_1^2 + x_2^2 + (x_3 - c)^2]^{1/2}.$$

It is easy to show that

$$u_{3,1}^e = \frac{1}{4\pi G}\left[\frac{2(1 - \nu)}{R_2} - \frac{c(x_3 - c)}{R_2^3}\right]_{,1} \quad (\text{on } x_3 = 0) \tag{53}$$

$$u_{3,2}^e = \frac{1}{4\pi G}\left[\frac{2(1 - \nu)}{R_2} - \frac{c(x_3 - c)}{R_2^3}\right]_{,2} \quad (\text{on } x_3 = 0). \tag{54}$$

In this case, problem (49) has the solution as

$$g(x_1, x_2, x_3) = \frac{1}{4\pi G}\left[\frac{2(1 - \nu)}{R_2} - \frac{c(x_3 - c)}{R_2^3}\right] \quad (x_3 < 0). \tag{55}$$

Using Eqs. (50), (51), and (55), the magnetic potentials are

$$\varphi^+ = -\frac{k}{2\mu_0}\left[\frac{2(1 - \nu)}{R_1} + \frac{c(x_3 + c)}{R_1^3}\right] \quad (x_3 > 0) \tag{56}$$

$$\varphi = \frac{k}{2\mu_0\mu_r}\left[\frac{2(1 - \nu)}{R_2} - \frac{c(x_3 - c)}{R_2^3}\right] \quad (x_3 < 0) \tag{57}$$

where

Downloaded 04 May 2010 to 171.66.16.28. Redistribution subject to ASME license or copyright; see http://www.asme.org/terms/Terms_Use.cfm

$$k = \frac{\chi B_0}{2\pi G(1 + \mu_r)\Delta}.$$

The Papkovich-Neuber potentials P_0 and P_3 can be expressed as

$$P_0 = \left(1 - 2\nu - \frac{1 - 4\nu}{\mu_r}\right)\frac{\beta}{4\pi G} \times \left[\frac{c}{R_2} - 2(1 - \nu)\ln(R_2 - x_3 + c)\right] \quad (x_3 < 0) \quad (58)$$

$$P_3 = \frac{\beta}{4\pi G}\left[\frac{2(1 - \nu)}{R_2} - \frac{c(x_3 - c)}{R_2^3}\right] \quad (x_3 < 0) \quad (59)$$

where

$$\beta = \frac{\chi^2 B_0^2}{2G\mu_0\mu_r(1 + \mu_r)\Delta}.$$

By employing Eqs. (14), the generated magnetic inductions can be written as

$$b_1^+ = \mu_0\varphi_{,1}^+ = \frac{kx_1}{2}\left[\frac{2(1 - \nu)}{R_1^3} + \frac{3c(x_3 + c)}{R_1^5}\right] \quad (x_3 > 0) \quad (60)$$

$$b_2^+ = \mu_0\varphi_{,2}^+ = \frac{kx_2}{2}\left[\frac{2(1 - \nu)}{R_1^3} + \frac{3c(x_3 + c)}{R_1^5}\right] \quad (x_3 > 0) \quad (61)$$

$$b_3^+ = \mu_0\varphi_{,3}^+ = \frac{k}{2}\left[\frac{2(1 - \nu)(x_3 + c) - c}{R_1^3} + \frac{3c(x_3 + c)^2}{R_1^5}\right] \quad (x_3 > 0) \quad (62)$$

$$b_1 = \mu_0\mu_r\varphi_{,1} = -\frac{kx_1}{2}\left[\frac{2(1 - \nu)}{R_2^3} - \frac{3c(x_3 - c)}{R_2^5}\right] \quad (x_3 < 0) \quad (63)$$

$$b_2 = \mu_0\mu_r\varphi_{,2} = -\frac{kx_2}{2}\left[\frac{2(1 - \nu)}{R_2^3} - \frac{3c(x_3 - c)}{R_2^5}\right] \quad (x_3 < 0) \quad (64)$$

$$b_3 = \mu_0\mu_r\varphi_{,3} = \frac{k}{2}\left[\frac{-2(1 - \nu)(x_3 - c) - c}{R_2^3} + \frac{3c(x_3 - c)^2}{R_2^5}\right] \quad (x_3 < 0). \quad (65)$$

Figure 2 show the distribution of the generated magnetic inductions on the upper surface of the half-space.

2 Magnetic Fields Generated by a Single Force Parallel to the Boundary of the Half-Space. When the unit force is applied at $(0, 0, -c)$ and acts in the x_1-direction, the displacement of the x_3-direction in the Mindlin solution of the lower half-space is (Mindlin, 1936)

$$u_3^e = \frac{1}{16\pi G(1 - \nu)}\left\{\frac{x_1(x_3 + c)}{R_1^3} - \frac{4(1 - \nu)(1 - 2\nu)x_1}{R_2(R_2 - x_3 + c)} + \frac{(3 - 4\nu)x_1(x_3 + c)}{R_2^3} + \frac{6x_1x_3c(x_3 - c)}{R_2^5}\right\} \quad (x_3 < 0). \quad (66)$$

Substituting Eq. (66) into problem (49), the harmonic function g has the form

$$g(x_1, x_2, x_3) = \frac{x_1}{4\pi G}\left[\frac{c}{R_2^3} - \frac{1 - 2\nu}{R_2(R_2 - x_3 + c)}\right] \quad (x_3 < 0). \quad (67)$$

Following the same procedure as that used in the preceding case, the magnetic potentials and the Papkovich-Neuber potentials are

$$\varphi^+ = -\frac{kx_1}{2\mu_0}\left[\frac{c}{R_1^3} - \frac{1 - 2\nu}{R_1(R_1 + x_3 + c)}\right] \quad (x_3 > 0) \quad (68)$$

$$\varphi = \frac{kx_1}{2\mu_0\mu_r}\left[\frac{c}{R_2^3} - \frac{1 - 2\nu}{R_2(R_2 - x_3 + c)}\right] \quad (x_3 < 0) \quad (69)$$

$$P_0 = \left(1 - 2\nu - \frac{1 - 4\nu}{\mu_r}\right)\frac{\beta x_1[c - (1 - 2\nu)R_2]}{4\pi G R_2(R_2 - x_3 + c)} \quad (x_3 < 0) \quad (70)$$

$$P_3 = \frac{\beta x_1}{4\pi G}\left[\frac{c}{R_2^3} - \frac{1 - 2\nu}{R_2(R_2 - x_3 + c)}\right] \quad (x_3 < 0) \quad (71)$$

and the generated magnetic inductions can be written as

$$b_1^+ = \frac{k}{2}\left\{\frac{(1 - 2\nu)[R_1(R_1^2 - 2x_1^2) + (x_3 + c)(R_1^2 - x_1^2)]}{R_1^3(R_1 + x_3 + c)^2} - \frac{c(R_1^2 - 3x_1^2)}{R_1^5}\right\} \quad (x_3 > 0) \quad (72)$$

$$b_2^+ = \frac{kx_1x_2}{2}\left[\frac{3c}{R_1^5} - \frac{(1 - 2\nu)(2R_1 + x_3 + c)}{R_1^3(R_1 + x_3 + c)^2}\right] \quad (x_3 > 0) \quad (73)$$

$$b_3^+ = \frac{kx_1}{2}\left[\frac{3c(x_3 + c)}{R_1^5} - \frac{1 - 2\nu}{R_1^3}\right] \quad (x_3 > 0) \quad (74)$$

$$b_1 = \frac{k}{2}\left\{-\frac{(1 - 2\nu)[R_2(R_2^2 - 2x_1^2) - (x_3 - c)(R_2^2 - x_1^2)]}{R_2^3(R_2 - x_3 + c)^2} + \frac{c(R_2^2 - 3x_1^2)}{R_2^5}\right\} \quad (x_3 < 0) \quad (75)$$

$$b_2 = \frac{kx_1x_2}{2}\left[\frac{(1 - 2\nu)(2R_2 - x_3 + c)}{R_2^3(R_2 - x_3 + c)^2} - \frac{3c}{R_2^5}\right] \quad (x_3 < 0) \quad (76)$$

$$b_3 = \frac{kx_1}{2}\left[-\frac{3c(x_3 - c)}{R_2^5} - \frac{(1 - 2\nu)}{R_2^3}\right] \quad (x_3 < 0). \quad (77)$$

Figure 3 show the distribution of the generated magnetic inductions on the upper surface of the half-space. Solutions for the single force acts in the x_2-direction are similar to the solutions presented above.

3 Magnetic Inductions Generated by a Doublet. When a mechanical doublet is applied at the point $(0, 0, -c)$ the generated magnetic potentials and inductions can be acquired by means of the superposition principle of the linear equation. Denote φ^{1+}, φ^{2+}, and φ^{3+} the magnetic potentials generated by a single force which acts in the x_1-direction, x_2-direction, and x_3-direction, respectively, then the generated magnetic potentials due to a dipole or a couple are

- a dipole in the x_1-direction, $\varphi^{11+} = -\partial\varphi^{1+}/\partial x_1$;
- a dipole in the x_2-direction, $\varphi^{22+} = -\partial\varphi^{2+}/\partial x_2$;
- a dipole in the x_3-direction, $\varphi^{33+} = \partial\varphi^{3+}/\partial c$;
- a couple whose arm is in the x_2-direction and subjected to a pair of x_1-direction forces, $\varphi^{12+} = -\partial\varphi^{1+}/\partial x_2$;

Downloaded 04 May 2010 to 171.66.16.28. Redistribution subject to ASME license or copyright; see http://www.asme.org/terms/Terms_Use.cfm

- a couple whose arm is in the x_3-direction and subjected to a pair of x_1-direction forces, $\varphi^{13+} = \partial\varphi^{1+}/\partial c$;
- a couple whose arm is in the x_1-direction and subjected to a pair of x_2-direction forces, $\varphi^{21+} = -\partial\varphi^{2+}/\partial x_1$;
- a couple whose arm is in the x_3-direction and subjected to a pair of x_2-direction forces, $\varphi^{23+} = \partial\varphi^{2+}/\partial c$;
- a couple whose arm is in the x_1-direction and subjected to a pair of x_3-direction forces, $\varphi^{31+} = -\partial\varphi^{3+}/\partial x_1$;
- a couple whose arm is in the x_2-direction and subjected to a pair of x_3-direction forces, $\varphi^{32+} = -\partial\varphi^{3+}/\partial x_2$;

where φ^{ij+} denotes the magnetic potential induced by a dipole as $i = j$ and denotes the magnetic potential per unit moment generated by a single couple of the x_i-direction forces and the x_j-direction arm as $i \neq j$. We note that $\varphi^{ij+} \neq \varphi^{ji+}$ for $i \neq j$ because these potentials do not supply a unique characterization for the doublet states. This property is clearly the analog of the doublet states in elasticity (Gurtin, 1972, p. 178).

References

Brown, W. F., Jr., 1965, "Theory of Magnetoelastic Effects in Ferromagnetism," *J. Appl. Phys.*, Vol. 36, pp. 994–1000.

Brown, W. F., Jr., 1966, *Magnetoelastic Interactions,* Springer-Verlag, New York.

Gurtin, M. E., 1972, "The Linear Theory of Elasticity," *Encyclopedia of Physics,* Vol. VIa/2, Springer-Verlag, Berlin.

Kassir, M. K., and Sih, G. C., 1975, *Three-dimensional Crack Problems,* Noordhoff International Publishing, The Netherlands.

Meade, K. P., and Keer, L. M., 1984, "On the Problem of a Pair of Point Forces Applied to the Faces of a Semi-infinite Plane Crack," *J. Elasticity,* Vol. 14, pp. 3–14.

Mindlin, R. D., 1936, "Force at a Point in the Interior of a Semi-infinite Solid," *Physics,* Vol. 7, pp. 195–202.

Pao, Y.-H., and Yeh, C.-S., 1973, "A Linear Theory for Soft Ferromagnetic Elastic Solids," *Int. J. Engng. Sci.,* Vol. 11, pp. 415–436.

Shindo, Y., 1977, "The Linear Magnetoelastic Problem for a Soft Ferromagnetic Elastic Solid with a Finite Crack," ASME JOURNAL OF APPLIED MECHANICS, Vol. 44, pp. 47–51.

Shindo, Y., 1978, "Magnetoelastic Interaction of a Soft Ferromagnetic Elastic Solid with a Penny-Shaped Crack in a Constant Axial Magnetic Field," ASME JOURNAL OF APPLIED MECHANICS, Vol. 45, pp. 291–296.

Shindo, Y., 1980, "Singular Stresses in a Soft Ferromagnetic Elastic Solid with Two Coplanar Griffith Cracks," *Int. J. Solids and Structures,* Vol. 16, pp. 537–543.

Wang, M.-Z., 1985, "Application of the Finite Part of a Divergent Integral in the Theory of Elasticity," *Appl. Math. and Mech.,* Vol. 6, pp. 1161–1169.

Yeh, C.-S., 1989, "Magnetic Fields Generated by a Mechanical Singularity in a Magnetized Elastic Half Plane," ASME JOURNAL OF APPLIED MECHANICS, Vol. 56, pp. 89–95.

Downloaded 04 May 2010 to 171.66.16.28. Redistribution subject to ASME license or copyright; see http://www.asme.org/terms/Terms_Use.cfm

F. O. Eke
Mem. ASME.

Song-Min Wang

Department of Mechanical and Aeronautical Engineering, University of California, Davis, CA 95616

Attitude Behavior of a Variable Mass Cylinder

This paper examines the attitude motion of a cylindrical body with mass loss. It is found that mass variation can have a substantial influence on the behavior of such a system. Specifically, the initial dimensions as well as the manner in which mass loss affects system inertia are found to be key factors in the determination of the characteristics of the lateral motion of the system. In great contrast to the attitude behavior of spinning rigid bodies, oblate variable mass cylinders exhibit divergent transverse attitude motion, while the transverse motion of prolate variable mass cylinders is found to be bounded in general.

Introduction

This paper studies the attitude behavior of a cylinder, whose mass varies continuously with time as the cylinder moves in space. The principal goal is to determine whether there are circumstances under which the transverse angular velocity of such a system can become unbounded. Analyses of this kind can shed light on our understanding of the dynamics of some classes of variable mass systems, for example solid rocket motors. In fact, this study is motivated to a great extent by the Star 48 solid rocket motor problem (Eke, 1982) and the attempts that have been made to understand and resolve it (Cochran and Kang, 1991; Flandro, 1987; Kang and Cochran, 1991; Meyer, 1983; Mingori, 1986, 1993; Sevaston, 1989). The Star 48 is a solid rocket motor used to power upper stages in space missions. Each mission using this motor in the spin-stabilized mode has exhibited excessive nutation during and after motor burn. Starting from motor ignition through about the first half of the motor burn, there is a period of "stable" flight; then, there follows a period of exponential growth in nutation angle, lasting through burnout. At burnout, the motor is jettisoned, and the spacecraft starts with a relatively large residual nutation angle resulting from the motor burn. Concern for the attitude behavior of star 48 launched vehicles was heightened a few years ago, when the Air Force contemplated a launch that would require the use of two Star 48 motors in tandem. A second motor was to ignite and burn after the first had completed its burn and separated from the system. The fear then was that the second burn would be starting with very poor "initial conditions" with the danger of sending the whole system into a flat spin and possibly off course. Some of the more recent Star 48 powered flights have had to be equipped with active nutation control devices to safeguard against unacceptable growth in nutation angle.

This paper is not necessarily another attempt to "solve" the Star 48 problem. Instead, the focus of this work is on a better understanding of the impact of mass variation on the attitude dynamics of variable mass systems. In one of the early investigations of the Star 48 problem, Eke (1983) suggested that solid rocket motors with larger than normal combustion chambers and propellant grain, had inherent problems with large transverse motions, and that this phenomenon escaped detection in earlier work because of the drastic simplifying assumptions that are made whenever closed-form solutions of the equations of motion of these systems are attempted. However, his conclusions were based mostly on qualitative and sometimes heuristic arguments, because, the equations involved could not be solved in closed form. This paper revisits the issue of rotational dynamics of variable mass systems by presenting and discussing complete closed form solutions for the case of a variable mass system with a simple, yet realistic geometry—that of a cylinder.

Equations of Motion

The object of this study is a system that is initially a solid right circular cylinder as shown in dotted lines in Fig. 1, and whose motion in space is characterized by an initial angular velocity $\boldsymbol{\omega}_0$. The mass, inertia, and possibly geometric properties of this system are allowed to vary in some fashion with time because of combustion or similar processes. Thus, at some general instant of time, some parts of the system will remain solid while some other parts will have become fluid. Let B be the part of the system that is still solid. Also, consider a "control region" that consists of a closed imaginary shell C that has the same shape as the original solid cylinder and remains attached to B throughout. At any given instant, only matter located inside C will be considered part of the system of interest. It is desired to monitor the evolution with time of the angular velocity vector of C or B.

First, the equations of motion are needed, and, because the main interest here is in attitude motion, we adopt the vector equation of rotational motion derived by Eke and Wang (1993) (see also Wang, 1993) and given below as Eq. (1).

$$\mathbf{M}^* = \mathbf{I}^*\cdot\boldsymbol{\alpha} + \boldsymbol{\omega}\times\mathbf{I}^*\cdot\boldsymbol{\omega} + \left(\frac{{}^C d}{dt}\mathbf{I}_0^*\right)\cdot\boldsymbol{\omega} + \int_{S_0}\rho[\mathbf{p}\times(\boldsymbol{\omega}\times\mathbf{p})](\mathbf{v}_r\cdot\mathbf{n})dS + \int_V \rho\boldsymbol{\omega}\times(\mathbf{p}\times\mathbf{v}_r)dV + \frac{{}^C d}{dt}\int_{V_0}\rho\mathbf{p}\times\mathbf{v}_r dV + \int_{S_0}\rho[\mathbf{p}\times\mathbf{v}_r(\mathbf{v}_r\cdot\mathbf{n})]dS \quad (1)$$

This equation is obtained by applying the principle of angular momentum to the instantaneous contents of C and then expanding some of the terms by means of Reynolds Transport Theorem (White, 1986). V_0 is the constant volume of the imaginary shell, C, and S_0 is its surface area. V is the volume associated with matter that happens to be inside C at a general instant t. Note that the material found in C at time t will occupy different volumes at different times. In Eq. (1), $\mathbf{I}^*$ denotes the

Contributed by the Applied Mechanics Division of THE AMERICAN SOCIETY OF MECHANICAL ENGINEERS for presentation at the International Mechanical Engineering Congress and Exhibition, the Winter Annual Meeting of the ASME, San Francisco, CA, Nov. 12–17, 1995.

Discussion on this paper should be addressed to the Technical Editor, Professor Lewis T. Wheeler, Department of Mechanical Engineering, University of Houston, Houston, TX 77204-4792, and will be accepted until four months after final publication of the paper itself in the ASME JOURNAL OF APPLIED MECHANICS.

Manuscript received by the ASME Applied Mechanics Division, Nov. 27, 1993; final revision, June 10, 1994. Associate Technical Editor: P. D. Spanos.

Paper No. 95-WA/APM-1.

Copyright © 1995 by ASME

Downloaded 04 May 2010 to 171.66.16.28. Redistribution subject to ASME license or copyright; see http://www.asme.org/terms/Terms_Use.cfm

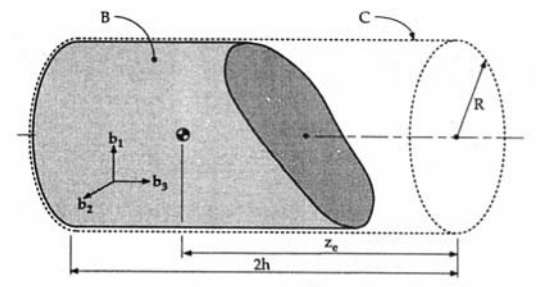


Fig. 1 Variable mass cylinder

instantaneous central inertia dyadic of the system, $\boldsymbol{\omega}$ and $\boldsymbol{\alpha}$ the angular velocity and angular acceleration respectively of C, ρ the mass density of the system, $\mathbf{v}_r$ the velocity of a generic particle of the system relative to C, and $\mathbf{p}$ is the position vector measured from the system's instantaneous mass center to a generic point of the system. Furthermore, $\mathbf{n}$ is an outwardly directed unit normal to the surface C, and the left superscript C indicates the reference frame in which the time derivative is to be taken. Note that $\mathbf{I}^*_0$ is the inertia dyadic associated with the control region C and its instantaneous contents.

Equation (1) can be simplified by making a few reasonable assumptions. First, it is assumed that the motion of the fluid particles in the system relative to the rigid part is axisymmetric, and that there is no whirling motion. This immediately leads to

$$\int_V \rho\boldsymbol{\omega} \times (\mathbf{p} \times \mathbf{v}_r)dV = \frac{{}^C d}{dt}\int_{V_0} \rho\mathbf{p} \times \mathbf{v}_r dV = \int_{S_0} \rho[\mathbf{p} \times \mathbf{v}_r(\mathbf{v}_r \cdot \mathbf{n})]dS = 0 \quad (2)$$

and Eq. (1) reduces to

$$\mathbf{M}^* = \mathbf{I}^* \cdot \boldsymbol{\alpha} + \boldsymbol{\omega} \times \mathbf{I}^* \cdot \boldsymbol{\omega} + \left(\frac{{}^C d}{dt}\mathbf{I}^*_0\right) \cdot \boldsymbol{\omega} + \int_{S_0} \rho[\mathbf{p} \times (\boldsymbol{\omega} \times \mathbf{p})](\mathbf{v}_r \cdot \mathbf{n})dS. \quad (3)$$

It is further assumed that the unburned part, B, is axisymmetric at all times, so that the instantaneous central inertia dyadic of the system has the form

$$\mathbf{I}^* = I(\mathbf{b}_1\mathbf{b}_1 + \mathbf{b}_2\mathbf{b}_2) + J\mathbf{b}_3\mathbf{b}_3 \quad (4)$$

where $\mathbf{b}_1$, $\mathbf{b}_2$, $\mathbf{b}_3$ are unit vectors fixed in B as shown in Fig. 1, and I and J are, respectively, the transverse and axial central inertia scalars of the system. If the inertial angular velocity of B at some general instant of time is taken to be

$$\boldsymbol{\omega} = \omega_1\mathbf{b}_1 + \omega_2\mathbf{b}_2 + \omega_3\mathbf{b}_3 \quad (5)$$

then, the angular acceleration is

$$\boldsymbol{\alpha} = \dot{\omega}_1\mathbf{b}_1 + \dot{\omega}_2\mathbf{b}_2 + \dot{\omega}_3\mathbf{b}_3 \quad (6)$$

and various terms of Eq. (3) become

$$\mathbf{I}^* \cdot \boldsymbol{\alpha} = I(\dot{\omega}_1\mathbf{b}_1 + \dot{\omega}_2\mathbf{b}_2) + J\dot{\omega}_3\mathbf{b}_3 \quad (7)$$

$$\boldsymbol{\omega} \times \mathbf{I}^* \cdot \boldsymbol{\omega} = (J - I)\omega_3(\omega_2\mathbf{b}_1 - \omega_1\mathbf{b}_2) \quad (8)$$

$$\left(\frac{{}^C d}{dt}\mathbf{I}^*_0\right) \cdot \boldsymbol{\omega} = \dot{I}(\omega_1\mathbf{b}_1 + \omega_2\mathbf{b}_2) + \dot{J}\omega_3\mathbf{b}_3. \quad (9)$$

In order to evaluate the last term of Eq. (3), an assumption must be made concerning the velocity field of the fluid particles of the system at the surface of the control region. Here, we anticipate the application of this analysis to rocket motion and assume that the vector $\mathbf{v}_r$ is zero everywhere on C except at one of the ends of the cylinder—the right end, say. And there,

$$\mathbf{v}_r \cdot \mathbf{n} = u(r) \quad (10)$$

because of our axisymmetry assumption. If it is further assumed that

$$u(r) = u = \text{constant} \quad (11)$$

then

$$\int_{S_0} \rho[\mathbf{p} \times (\boldsymbol{\omega} \times \mathbf{p})(\mathbf{v}_r \cdot \mathbf{n})]dS = -\dot{m}[(z_e^2 + \tfrac{1}{4}R^2)(\omega_1\mathbf{b}_1 + \omega_2\mathbf{b}_2) + \tfrac{1}{2}R^2\omega_3\mathbf{b}_3] \quad (12)$$

where m is the instantaneous mass of the system, and z_e is the distance of the mass center from the right face of the shell, C. The scalar versions of Eq. (3) constitute the dynamical equations of attitude motion for the variable mass cylinder; and they are

$$M_1 = I\dot{\omega}_1 + (J - I)\omega_2\omega_3 + \dot{I}\omega_1 - \dot{m}(z_e^2 + \tfrac{1}{4}R^2)\omega_1 \quad (13)$$

$$M_2 = I\dot{\omega}_2 - (J - I)\omega_1\omega_3 + \dot{I}\omega_2 - \dot{m}(z_e^2 + \tfrac{1}{4}R^2)\omega_2 \quad (14)$$

and

$$M_3 = J\dot{\omega}_3 + \dot{J}\omega_3 - \dot{m}\frac{R^2}{2}\omega_3 \quad (15)$$

where

$$\mathbf{M}^* = M_1\mathbf{b}_1 + M_2\mathbf{b}_2 + M_3\mathbf{b}_3 \quad (16)$$

is the sum of moments of all the external forces on the system about the system's instantaneous mass center.

Both $\dot{I}$ and $\dot{J}$ depend on how the burning process affects the mass distribution of the system. Four idealized cases will be discussed in the sequel and they will be named uniform burning, end burning, centrifugal burning, and centripetal burning. *Uniform burning* refers to the case where the overall dimensions of the unburned part of the cylinder remain equal to those of the original cylinder while the mass density varies with time. This is somewhat analogous to what happens in a rocket motor, where the external dimensions remain generally unchanged while material inside the motor casing becomes less dense with time due to combustion. In this case, however, there is the additional assumption that the density changes in the same manner everywhere within the cylinder. That is, ρ is a function of time but not of position. In *end burning,* combustion proceeds from one end of the cylinder towards the other, in such a way that the unburned part remains a cylinder of radius R at all times. The term *centrifugal burning* is used to characterize the ideal situation where combustion starts on the axis of the cylinder, and proceeds at the same rate radially outwards. Thus, at any given instant, the unburned portion of the system looks like a cylindrical pipe. Finally, the term *centripetal burning* is used here for the case where burning proceeds radially inwards from the outermost part of the cylinder. And, again, the rate of combustion is the same in all radial directions. The intermediate shape of the unburned part of the system is thus a solid cylinder whose radius is smaller than that of the original cylinder. In all computations involving the inertia dyadic, the contributions of the fluid mass will be neglected.

Uniformly Burning Cylinder

When a cylinder, whose dimensions are as given in Fig. 1, is subjected to uniform burning, its instantaneous central inertia scalars are

Downloaded 04 May 2010 to 171.66.16.28. Redistribution subject to ASME license or copyright; see http://www.asme.org/terms/Terms_Use.cfm

$$I = m\left(\frac{R^2}{4} + \frac{h^2}{3}\right) \tag{17}$$

and

$$J = m\frac{R^2}{2}. \tag{18}$$

Since R and h remain constant in this case,

$$\dot{I} = \dot{m}\left(\frac{R^2}{4} + \frac{h^2}{3}\right) \tag{19}$$

and

$$\dot{J} = \dot{m}\frac{R^2}{2}. \tag{20}$$

If we define

$$a = \frac{R^2}{4} + \frac{h^2}{3} > 0 \tag{21}$$

$$b = \frac{R^2}{4} - \frac{h^2}{3} \tag{22}$$

and

$$c = \frac{2h^2}{3} > 0, \tag{23}$$

then, the equations of attitude motion, Eqs. (13)-(15), for the case of zero external torque reduce to

$$\dot{\omega}_1 + \frac{b}{a}\omega_2\omega_3 - \frac{\dot{m}}{m}\frac{c}{a}\omega_1 = 0 \tag{24}$$

$$\dot{\omega}_2 - \frac{b}{a}\omega_1\omega_3 - \frac{\dot{m}}{m}\frac{c}{a}\omega_2 = 0 \tag{25}$$

and

$$\dot{\omega}_3 = 0. \tag{26}$$

Equation (26) leads immediately to

$$\omega_3 = \Omega = \text{constant}. \tag{27}$$

Hence, the cylinder maintains a constant spin rate. By defining the complex angular velocity

$$\omega_T = \omega_1 + j\omega_2 \tag{28}$$

where

$$j = \sqrt{-1}. \tag{29}$$

Equations (24) and (25) can be combined by adding j times Eq. (25) to Eq. (24):

$$\dot{\omega}_T - j\frac{b}{a}\Omega\omega_T - \frac{\dot{m}}{m}\frac{c}{a}\omega_T = 0. \tag{30}$$

This equation can be solved analytically. First, we observe that

$$\frac{\dot{\omega}_T}{\omega_T} = \frac{c}{a}\frac{\dot{m}}{m} + j\frac{b}{a}\Omega \tag{31}$$

thus

$$\int_{\omega_T(0)}^{\omega_T}\frac{d\omega_T}{\omega_T} = \frac{c}{a}\int_{m(0)}^{m}\frac{dm}{m} + j\frac{b}{a}\Omega\int_0^t dt \tag{32}$$

so that

$$\frac{\omega_T}{\omega_T(0)} = \left[\frac{m}{m(0)}\right]^{c/a}\exp\left(j\frac{b}{a}\Omega t\right). \tag{33}$$

Hence, although the spin rate maintains a constant value as in the case of a constant mass rigid body, the transverse attitude motion of the cylinder is oscillatory in nature with constant frequency. Since

$$\frac{m(t)}{m(0)} < 1 \tag{34}$$

and $m(t)$ decreases with time, and because

$$\frac{c}{a} > 0, \tag{35}$$

the oscillations decay with time, and the rate of decay depends on the ratio c/a. In any case, it is clear that uniform burning cannot lead to a growth in transverse angular velocity.

End Burning Cylinder

The cylinder now burns from the right end, say, as shown in Fig. 2, but the control region is unchanged. At any given instant,

$$I = m\left(\frac{R^2}{4} + \frac{z^2}{3}\right) \quad \text{and} \quad J = \frac{1}{2}mR^2. \tag{36}$$

Thus

$$\dot{I} = \dot{m}\left(\frac{R^2}{4} + z^2\right) \quad \text{and} \quad \dot{J} = \frac{1}{2}\dot{m}R^2. \tag{37}$$

The equations of attitude motion in a force-free environment then become

$$m\left(\frac{R^2}{4} + \frac{z^2}{3}\right)\dot{\omega}_1 + m\left(\frac{R^2}{4} - \frac{z^2}{3}\right)\omega_2\omega_3 + \dot{m}(z^2 - z_e^2)\omega_1 = 0 \tag{38}$$

$$m\left(\frac{R^2}{4} + \frac{z^2}{3}\right)\dot{\omega}_2 - m\left(\frac{R^2}{4} - \frac{z^2}{3}\right)\omega_1\omega_3 + \dot{m}(z^2 - z_e^2)\omega_2 = 0 \tag{39}$$

$$m\left(\frac{R^2}{2}\right)\dot{\omega}_3 = 0. \tag{40}$$

Here again,

$$\omega_3 = \Omega = \text{constant}. \tag{41}$$

As it does in the case of uniform burn, the spin rate of the cylinder stays constant under end burn.

It is easy to show that

$$\frac{\dot{m}}{m} = \frac{\dot{z}}{z} \tag{42}$$

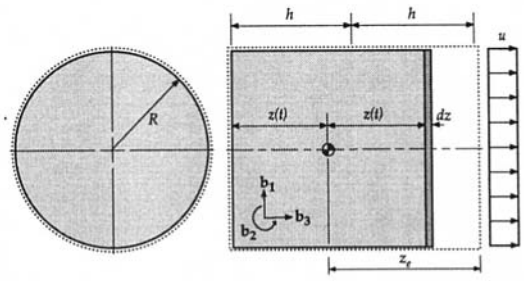


Fig. 2 End burning cylinder

Downloaded 04 May 2010 to 171.66.16.28. Redistribution subject to ASME license or copyright; see http://www.asme.org/terms/Terms_Use.cfm

so that Eqs. (38) and (39) then become, respectively,

$$\dot{\omega}_1 + \frac{(\frac{3}{4}R^2 - z^2)}{(\frac{3}{4}R^2 + z^2)}\Omega\omega_2 + \frac{\dot{z}}{z}\frac{3(z^2 - z_e^2)}{(\frac{3}{4}R^2 + z^2)}\omega_1 = 0 \quad (43)$$

and

$$\dot{\omega}_2 - \frac{(\frac{3}{4}R^2 - z^2)}{(\frac{3}{4}R^2 + z^2)}\Omega\omega_1 + \frac{\dot{z}}{z}\frac{3(z^2 - z_e^2)}{(\frac{3}{4}R^2 + z^2)}\omega_2 = 0. \quad (44)$$

As before, we introduce the complex angular velocity ω_T defined earlier, and combine Eqs. (43) and (44) into

$$\frac{\dot{\omega}_T}{\omega_T} = \frac{3(z_e^2 - z^2)}{(\frac{3}{4}R^2 + z^2)}\frac{\dot{z}}{z} + j\Omega\frac{(\frac{3}{4}R^2 - z^2)}{(\frac{3}{4}R^2 + z^2)}. \quad (45)$$

Since $z_e = 2h - z$, we can rewrite Eq. (45) as

$$\frac{d\omega_T}{\omega_T} = \left[\left(\frac{16h^2}{R^2}\right)\frac{1}{z} + \frac{-(16h^2/R^2)z - 12h}{(z^2 + 3R^2/4)}\right]dz + j\Omega\left[\frac{3R^2/2}{(z^2 + 3R^2/4)} - 1\right]dt. \quad (46)$$

Clearly, the solution of Eq. (46) depends on how z varies with t. For constant burn rate, where

$$\dot{m} = \dot{z} = \text{constant}, \quad (47)$$

the solution of Eq. (46) can be cast in the form

$$\omega_T = \omega_T(0)A(z)\exp[j\Theta(z)] \quad (48)$$

where, after some algebra, we find

$$A(z) = \left[\frac{z^2(h^2 + 3R^2/4)}{h^2(z^2 + 3R^2/4)}\right]^{8h^2/R^2} \times \exp\left\{\left(\frac{8\sqrt{3}h}{R}\right)\tan^{-1}\left[\frac{2\sqrt{3}R(z - h)}{3R^2 + 4zh}\right]\right\} \quad (49)$$

and

$$\Theta(t) = \int_0^t \Omega\frac{(\frac{3}{4}R^2 - z^2)}{(\frac{3}{4}R^2 + z^2)}dt. \quad (50)$$

Equations (48)-(50) indicate that the transverse motion is made up of damped oscillations with varying frequency. Plots of $A(z)$ as a function of $(1 - z/h)$ are shown in Fig. 3 for various values of R/h. These plots show that damping occurs much more rapidly for long and slender (prolate) cylinders than for oblate ones. There appears to be a limiting value of R/h (R/h between 2 and 5) above which the transverse motion is only slowly damped and below which damping is quite rapid. Nevertheless, the transverse angular velocity remains bounded throughout the burn, regardless of the initial dimensions of the cylinder.

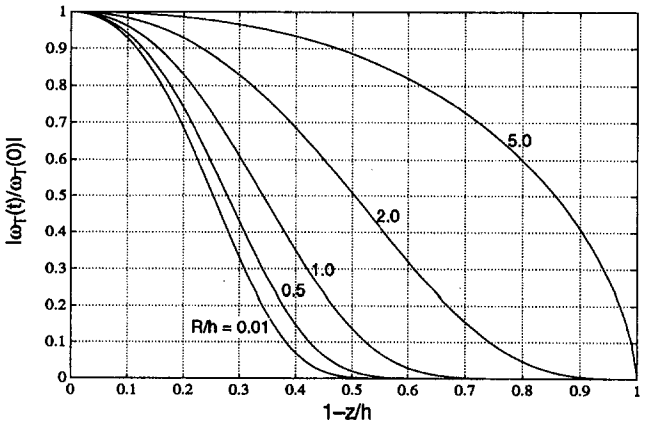


Fig. 3 Transverse angular speed for end burn

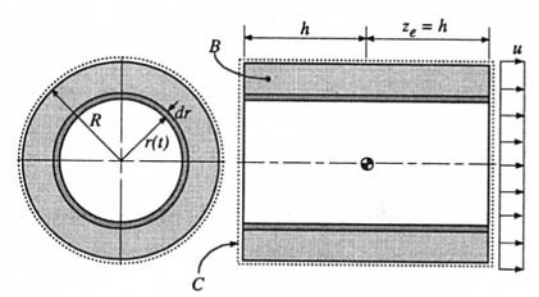


Fig. 4 Centrifugally burning cylinder

Centrifugal Burning Cylinder

We recall that in centrifugal burning, combustion starts on the axis of the cylinder and propagates radially outwards in the same manner on any plane perpendicular to the axis. In this case (see Fig. 4), it is possible to write

$$I = m\left[\frac{1}{4}(R^2 + r^2) + \frac{h^2}{3}\right] \quad \text{and} \quad J = \frac{1}{2}m(R^2 + r^2) \quad (51)$$

as well as

$$\dot{I} = \dot{m}\left[\frac{R^2}{2} + \frac{h^2}{3}\right] \quad \text{and} \quad \dot{J} = \dot{m}r^2 \quad (52)$$

and the equation of transverse attitude motion in a force-free environment, written in terms of the complex angular velocity, takes the form

$$m\left[\frac{1}{4}(R^2 + r^2) + \frac{h^2}{3}\right]\dot{\omega}_T - j\omega_3\left[\frac{1}{4}(R^2 + r^2) - \frac{h^2}{3}\right]m\omega_T + \dot{m}\left(\frac{r^2}{2} - \frac{2h^2}{3} - \frac{R^2}{4}\right)\omega_T = 0. \quad (53)$$

Similarly, the spin motion is described by

$$\dot{\omega}_3 + \frac{\dot{m}}{m}\left(\frac{2r^2 - R^2}{R^2 + r^2}\right)\omega_3 = 0. \quad (54)$$

Equation (54) can be rewritten as

$$\int_{\omega_3(0)}^{\omega_3}\frac{d\omega_3}{\omega_3} = \int_{r=0}^{r}\left[\frac{-3}{2}\left(\frac{1}{r^2 + R^2}\right) + \frac{-1}{2}\left(\frac{1}{r^2 - R^2}\right)\right]d(r^2) \quad (55)$$

which leads eventually to

$$\omega_3 = \frac{R^4}{(R^2 + r^2)\sqrt{(R^2 + r^2)(R^2 - r^2)}}\omega_3(0) \quad (56)$$

The spin motion of the cylinder under centrifugal burn no longer occurs at constant speed. Theoretically it becomes unbounded as r approaches R; but, in fact, it remains bounded (even damped) for values of r up to about 85 percent of R, and only grows beyond bounds for values of r very close to R. Note also that the parameter h does not appear in Eq. (56), so that the spin rate is independent of the cylinder's length.

The solution to the equation of transverse motion, Eq. (53), can be expressed in the form

Downloaded 04 May 2010 to 171.66.16.28. Redistribution subject to ASME license or copyright; see http://www.asme.org/terms/Terms_Use.cfm

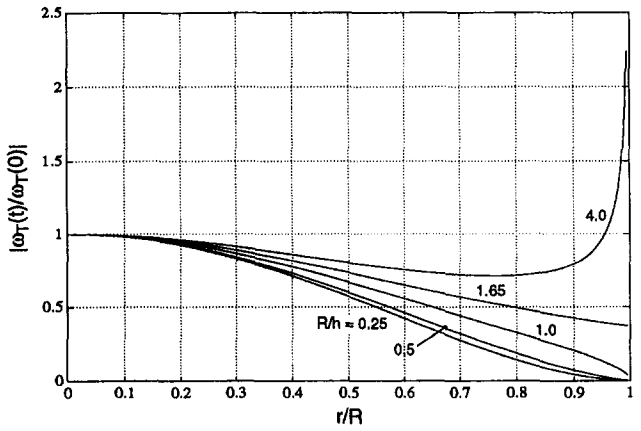


Fig. 5 Transverse angular speed for centrifugal burn

$$\omega_T = \omega_T(0)A(r)\exp[j\Theta(t)] \tag{57}$$

where, after a considerable amount of algebra, we find that

$$A(r) = \left(\frac{R^2 + 4h^2/3}{R^2 + 4h^2/3 + r^2}\right)^{(3R^2+16h^2/3)/(2R^2+4h^2/3)} \times \left(\frac{R^2 - r^2}{R^2}\right)^{(-R^2+8h^2/3)/(2R^2+4h^2/3)} \tag{58}$$

and

$$\Theta(t) = \int_0^t \frac{[\frac{1}{4}(R^2 + r^2) - \frac{1}{3}h^2]\omega_3}{[\frac{1}{4}(R^2 + r^2) + \frac{1}{3}h^2]}\,dt. \tag{59}$$

$A(r)$ is the main quantity of interest since it determines the amplitude of the transverse motion. $\Theta(t)$ governs the frequency of transverse oscillations, and will not be explored further, except to observe that the frequency is time dependent. Figure 5 shows plots of $A(r)$ as a function of r/R with R/h as parameter. This figure shows clearly that the rotational motion of the cylinder in the case of centrifugal burn depends on the relative dimensions of the cylinder. The transverse angular velocity of an oblate cylinder will grow without bounds while a prolate cylinder maintains bounded transverse motion. There appears to be a threshold value of R/h below which the transverse motion is bounded and above which it is unbounded. Figure 5 also shows that cylinders with divergent motion actually maintain apparently bounded (even damped) motion well into the burn, and the transverse motion only turns divergent towards the end of the burn—a phenomenon very similar to that observed for the Star 48 solid rocket motor.

Centripetal Burn

We now consider the case of a cylinder that burns radially inwards starting from its outermost surface. The length of the cylinder remains the same throughout but its radius decreases with time and the unburned part remains a right circular cylinder of radius r at all times.

In this case the equations of force-free attitude motion are

$$m\left(\frac{r^2}{4} + \frac{h^2}{3}\right)\dot{\omega}_1 + m\left(\frac{r^2}{4} - \frac{h^2}{3}\right)\omega_2\omega_3 + \dot{m}\left(\frac{r^2}{2} - \frac{2h^2}{3} - \frac{R^2}{4}\right)\omega_1 = 0 \tag{60}$$

$$m\left(\frac{r^2}{4} + \frac{h^2}{3}\right)\dot{\omega}_2 - m\left(\frac{r^2}{4} - \frac{h^2}{3}\right)\omega_1\omega_3 + \dot{m}\left(\frac{r^2}{2} - \frac{2h^2}{3} - \frac{R^2}{4}\right)\omega_2 = 0 \tag{61}$$

and

$$\frac{1}{2}mr^2\dot{\omega}_3 + \dot{m}\left(r^2 - \frac{R^2}{2}\right)\omega_3 = 0. \tag{62}$$

The solution to Eq. (62) is

$$\omega_3 = \omega_3(0)\left(\frac{R}{r}\right)^4 \exp\left(1 - \frac{R^2}{r^2}\right). \tag{63}$$

Although $(R/r)^4$ increases with time, it is multiplied by a term that decreases exponentially with time. The spin rate thus varies with time, but is bounded and independent of the length of the cylinder.

The transverse motion is governed by Eqs. (60) and (61), which are combined in the usual way to give

$$\frac{\dot{\omega}_T}{\omega_T} = -\frac{\dot{m}}{m}\left(\frac{\frac{r^2}{2} - \frac{2h^2}{3} - \frac{R^2}{4}}{\frac{r^2}{4} + \frac{h^2}{3}}\right) + j\omega_3\left(\frac{\frac{r^2}{4} - \frac{h^2}{3}}{\frac{r^2}{4} + \frac{h^2}{3}}\right) \tag{64}$$

where ω_T is the complex angular velocity. Following an integration strategy similar to that utilized for the centrifugal burning case, we find that the solution of Eq. (64) has the form

$$\omega_T = \omega_T(0)B(r)\exp[j\beta(t)] \tag{65}$$

where

$$\beta(t) = \int_0^t \omega_3\left(\frac{r^2/4 - h^2/3}{r^2/4 + h^2/3}\right)dt \tag{66}$$

and

$$B(r) = \left(\frac{r}{R}\right)^{[4+3R^2/(2h^2)]}\left(\frac{R^2 + 4h^2/3}{r^2 + 4h^2/3}\right)^{[4+3R^2/(4h^2)]}. \tag{67}$$

Plots of $B(r)$ versus $(1 - r/R)$ with R/h as parameter are given in Fig. 6. This figure shows that the transverse motion decays more rapidly with time for slender cylinders (small values of R/h) than for fat cylinders. However, there is a limiting value of R/h beyond which the transverse angular velocity first grows with time before reversing itself and decreasing rapidly with time. Thus, centripetal burning never really leads to unbounded transverse motion, though oblate cylinders may exhibit increasing transverse angular velocities in the early stages of the burn, thus giving the false impression of divergent motion for burns that are of limited duration.

Concluding Remarks

The results of the analyses presented in this paper indicate that mass variation can have a major impact on the attitude behavior of mechanical systems. This study shows that the transverse motion of a rotating variable mass cylinder in a force-free environment can grow or decay depending on the initial dimensions of the cylinder as well as on the burn pattern. In general, the cylinder is "well behaved" if the ratio of its diameter to its length is kept below a threshold value of about 3—this corresponds to a ratio of the axial to transverse moment of inertia of about 1.7. Above this critical value, centrifugal burns lead to divergent transverse motion. Also, centripetal burns give rise to transverse amplitudes that grow with time for a substantial portion of the burn, while end burns only produce slight

Downloaded 04 May 2010 to 171.66.16.28. Redistribution subject to ASME license or copyright; see http://www.asme.org/terms/Terms_Use.cfm

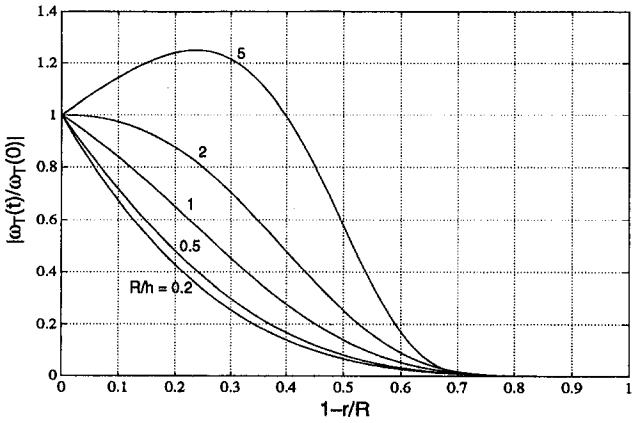


Fig. 6 Transverse angular speed for centripetal burn

damping of the transverse motions of the cylinder. Relating these results to rocket dynamics, it appears that long and slender rockets would be "better behaved" than short and fat ones. It might be useful to mention here that one of the major differences between the Star 48 motor (that produced excessive coning) and earlier motors of the same family (that did not produce coning) is that the Star 48 has a much larger diameter while maintaining about the same length.

The foregoing results differ markedly from well-known facts about the motion characteristics of spinning rigid bodies. An oblate rigid cylinder will spin stably about its axis of maximum inertia, especially if energy dissipation is present. On the other hand, the transverse angular velocity of an oblate variable mass cylinder can take on arbitrarily large values under certain circumstances. Similarly, although the transverse motion of spinning prolate rigid cylinders is divergent when energy dissipation is present, prolate variable mass cylinders do not appear to have any such problems.

Finally, it is possible to visualize the effects of a sequence or a combination of burns of different types based on the results of this study. Real systems are unlikely to undergo ideal burns such as those presented above. However, it may be possible to view a real burn as a combination of two or more ideal burns, so that the overall response can also be viewed as some combination of the responses associated with the corresponding ideal burns. For example, one may choose to view the burn of a solid rocket motor as a combination of centrifugal and end burns. Because the underlying equations are highly nonlinear, one cannot simply invoke superposition to study compound burns. Nevertheless, Figs. 3, 5, and 6 can be utilized to make an initial qualitative assessment of the behavior of real systems.

Acknowledgment

This material is based upon work supported in part by the National Science Foundation under Award No. MSS-9021549.

References

Cochran, J. E., Jr., and Kang, J. Y., 1991, "Nonlinear Stability Analysis of the Attitude Motion of a Spin Stabilized Upper Stage," AAS Paper 91-190, AAS/AIAA Spaceflight Mechanics Meeting, Houston, TX, Feb. 11–13, 1991.

Eke, F. O., 1982, "Star 48 Coning Anomaly," JPL Internal Document No. 343-82-989, Oct. 1982.

Eke, F. O., 1983, "Dynamics of Variable Mass Systems with Application to the Star 48 Solid Rocket Motor," *Advances in Astronautical Sciences,* Vol. 54, pp. 671–684.

Eke, F. O., and Wang, S. M., 1993, "Equations of Motion of Two-Phase Variable Mass Systems with Solid Base," Paper No. AAS 93-107, presented at the AAS/AIAA Space Flight Mechanics Meeting, Feb. 22–24, 1993, Pasadena, CA.

Flandro, G. A., 1987, "Fluid Mechanics of Spinning Rockets," AFRPL-TR-86-072, Final Report, Air Force Rocket Propulsion Laboratory, Edwards AFB, CA, Jan.

Kang, J. Y., and Cochran, J. E., Jr., 1991, "Further Investigation of Anomalous Attitude Motion of Spin Stabilized Upper Stage," Paper No. AAS 91-480, AAS/AIAA Astrodynamics Specialist Conference, Durango, CO, Aug. 19-22.

Meyer, R. X., 1983, "Convective Instability in Solid Propellant Rocket Motors," *Advances in the Astronautical Sciences,* Vol. 54, pp. 657–669.

Mingori, D. L., and Yam, Y., 1986, "Nutational Instability of a Spinning Spacecraft with Internal Mass Motion and Axial Thrust," Paper No. 86-2271, Proceedings of AIAA/AAS Astrodynamics Conference, Williamsburg, VA, Aug. 18-20, pp. 367–375.

Mingori, D. L., Halsmer, D. M., and Yam, Y., 1993, "Stability of Spinning Rockets with Internal Mass Motion," presented at the AAS/AIAA Spaceflight Mechanics Meeting, Pasadena, CA, Feb. 22–29.

Sevaston, G. E., ed., 1989, "Ulysses Pam-S Booster Nutation Control System Analysis," JPL Internal Document, No. D-6289, Oct. 27.

Wang, S. M., 1993, "Attitude Dynamics of Variable Mass Systems," Ph.D. Dissertation, University of California, Davis, CA, Sept.

White, F. M., 1986, *Fluid Mechanics,* 2nd ed., McGraw-Hill, New York, pp. 116–125.

Downloaded 04 May 2010 to 171.66.16.28. Redistribution subject to ASME license or copyright; see http://www.asme.org/terms/Terms_Use.cfm

R. Haberman
Professor.

E. K. Ho
Lecturer.

Department of Mathematics,
Southern Methodist University,
Dallas, TX 75275-0156

Boundary of the Basin of Attraction for Weakly Damped Primary Resonance

The dissipatively perturbed Hamiltonian system corresponding to primary resonance is analyzed in the case in which two competing stable periodic responses exist. The method of averaging fails as the trajectory approaches the unperturbed homoclinic orbit (separatrix). By using the small dissipation of the Hamiltonian (the Melnikov integral) near the homoclinic orbit, the boundaries of the basin of attraction are determined analytically in an asymptotically accurate way. The selection of the two competing periodic responses is influenced by small changes in the initial conditions. The analytic formula is shown to agree well with numerical computations.

1 Introduction

Weakly nonlinear mechanical systems exhibit primary resonance when periodically forced near their natural frequency and are summarized by many including Drazin (1992), Guckenheimer and Holmes (1983), Jordan and Smith (1987), Kevorkian and Cole (1981), and Nayfeh and Mook (1979). For a given forcing frequency near the natural frequency, perturbation methods have been used to obtain three periodic responses; the nonlinearity causes the response curve to bend yielding triple valuedness. The well-known method of multiple scales yields a coupled system of ordinary differential equations for the slow time evolution of the amplitude and phase. The three equilibria correspond to the three periodic responses: two are stable and it is important that the other is an unstable saddle point. Without damping, the time-dependent system is Hamiltonian. Nonlinear oscillations around the two periodic responses occur, exhibiting two frequencies, the forcing frequency and the frequency associated with the nonlinear oscillations. There is a double homoclinic orbit (with infinite period) connecting the saddle with itself. With damping, the homoclinic orbit is broken, and solutions approach one of the two competing stable periodic responses depending on the initial conditions. If the damping is very small, then, due to the existence of the saddle point, small changes in the initial conditions strongly influence which of the competing periodic responses eventually occurs. The boundary of the basin of attraction, the stable manifold of the saddle point, is tightly wound and spiral-like. Neishtadt (1975, 1991) computed the probability for each competing stable attractor assuming that the initial conditions were randomly distributed. For deterministic initial conditions, usually it is tacitly assumed that numerical solutions of the nonlinear differential equations must be used to determine the outcome, but in this paper we derive an analytic formula for the boundary of the basin of attraction if the damping is very weak using the method of Bourland and Haberman (1990, 1991a, b) originally developed for dissipatively perturbed double-well potentials.

The amplitude equations for primary resonance represent a strongly nonlinear oscillator and are shown in Section 2 to correspond to a dissipatively perturbed Hamiltonian system since we assume the physical damping is sufficiently small. The effects of damping on the nonlinear oscillator of primary resonance is analyzed in Section 3 by the method of averaging (slow variation theory). However, as the solution approaches the unperturbed homoclinic orbit (separatrix), the period of the unperturbed nonlinear oscillation approaches infinity, and thus, the slow variation theory fails. The change in action in crossing a separatrix was analyzed by Tennyson, Cary, and Escande (1986) and Neishtadt (1986) by introducing a large sequence of nearly homoclinic orbits following the idea of Timofeev (1978). The dissipation of the Hamiltonian along each nearly homoclinic orbit can be approximated by the Melnikov integral, as we compute for primary resonance in Section 4. Bourland and Haberman (1990) showed that the slow variation solution can be carefully matched to the sequence of nearly homoclinic orbits, resulting in an analytical formula for the boundaries of the basins of attraction for weakly damped double-well potentials. However, we follow in Section 5 the easier method of Bourland and Haberman (1991a, b). Even though the slow variation theories are not valid in general in the neighborhood of the separatrix, we show that the Hamiltonian can be approximated accurately enough by the slow variation theory at points where the phase angle is an integer or a half integer. In this way, the Hamiltonian according to the slow variation theory can be related to Melnikov ideas for nearly homoclinic orbits. Moreover, by considering the partial orbit in the slow variation theory from the last saddle approach to the predicted crossing of the unperturbed separatrix, an analytical formula for the initial Hamiltonian corresponding to the boundaries of the basins of attraction is derived for primary resonance. In Section 6 we show that our analytic criteria for the boundaries of the basin of attraction of primary resonance compare favorably with numerical computations.

2 Primary Resonance of Weakly Nonlinear Systems

We analyze here the well-known system of differential equations which models primary resonance for general dynamical systems (such as the standard Duffing equation) when the damping is exceptionally small. As described by Guckenheimer and Holmes (1983), Kevorkian and Cole (1981), and Nayfeh and Mook (1979), the amplitude response curve is triple-valued for some frequencies due to the nonlinearity, and this leads to the jump phenomena. If the forcing frequency is close to the natural frequency, then what we call primary resonance occurs, and the dynamics are well known and can be obtained by averaging over one period of the resonance, yielding

Contributed by the Applied Mechanics Division of THE AMERICAN SOCIETY OF MECHANICAL ENGINEERS for publication in the ASME JOURNAL OF APPLIED MECHANICS.

Discussion on this paper should be addressed to the Technical Editor, Professor Lewis T. Wheeler, Department of Mechanical Engineering, University of Houston, Houston, TX 77204-4792, and will be accepted until four months after final publication of the paper itself in the ASME JOURNAL OF APPLIED MECHANICS.

Manuscript received by the ASME Applied Mechanics Division, Oct. 10, 1993; final revision, Aug. 23, 1994. Associate Technical Editor: P. D. Spanos.

Copyright © 1995 by ASME

Downloaded 04 May 2010 to 171.66.16.28. Redistribution subject to ASME license or copyright; see http://www.asme.org/terms/Terms_Use.cfm

$$\frac{dq}{dt} = \frac{1}{2\mu}\left[-\Omega p - \frac{3\alpha}{4}(q^2 + p^2)p\right] - \frac{1}{2}\epsilon q, \quad (1a)$$

$$\frac{dp}{dt} = \frac{1}{2\mu}\left[\Omega q + \frac{3\alpha}{4}(q^2 + p^2)q + \gamma\right] - \frac{1}{2}\epsilon p, \quad (1b)$$

where μ is the forcing frequency, $\Omega = \omega_0^2 - \mu^2$ relates to the difference between the natural frequency (ω_0) and the forcing frequency (μ) of the original weakly nonlinear oscillator, α is the coefficient of the cubic weak nonlinearity of the original system, γ is the amplitude of the forcing, and ϵ is the parameter for the linear damping of the original system which we assume is extremely small ($0 < \epsilon \ll 1$). Here, q and p are amplitudes of oscillation for the original system, and t is actually a slow time. In this paper we only consider special values of these parameters such that three steady-state solutions coexist (the response curve is triple-valued). Two of the equilibria are stable and hence compete; the other is a saddle point.

We note that primary resonance corresponds to the following Hamiltonian system with one degree-of-freedom with small non-Hamiltonian perturbations,

$$\frac{dq}{dt} = H_p(q, p) + \epsilon h_1(q, p), \quad (2a)$$

$$\frac{dp}{dt} = -H_q(q, p) + \epsilon h_2(q, p), \quad (2b)$$

where H is the Hamiltonian, symmetric in p, given by

$$H(q, p) = \frac{1}{-4\mu}\left[\Omega(q^2 + p^2) + \frac{3\alpha}{8}(q^2 + p^2)^2 + 2\gamma q\right]. \quad (3)$$

The method we describe in this paper is valid for other kinds of damping, as long as the perturbations are purely dissipative, by which we mean that h_1 is an even function of p and h_2 is an odd function of p. For (1),

$$h_1 = -\tfrac{1}{2}q \quad \text{and} \quad h_2 = -\tfrac{1}{2}p. \quad (4a, b)$$

Without the dissipation, i.e., $\epsilon = 0$, (2) is a Hamiltonian system which permits strongly nonlinear oscillations (see Fig. 1). The unperturbed system ($\epsilon = 0$) is assumed to have two centers and a saddle point with a double homoclinic orbit connecting the saddle point. These homoclinic orbits are also referred to as separatrices.

Under the action of a positive purely dissipative perturbation, the two centers become asymptotically stable equilibria and the saddle point is preserved. However, it is well known that under a positive dissipative perturbation, the homoclinic orbits break down. The unstable and stable manifolds of the saddle point split apart, and the trajectories are no longer closed. Instead,

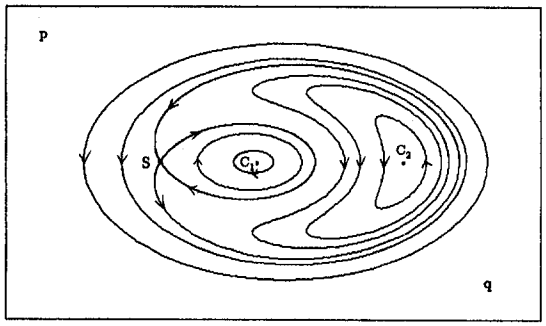


Fig. 1 Phase portrait of the unperturbed Hamiltonian system

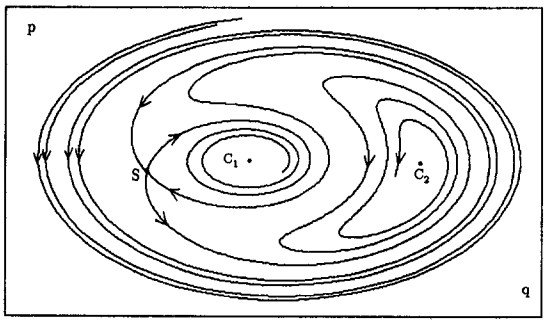


Fig. 2 Phase portrait of the slightly damped perturbed Hamiltonian system

the phase plane solution spirals inward, as sketched in Fig. 2. The boundaries of the basin of attraction are the stable manifolds of the saddle point, and we will obtain an asymptotically accurate analytic formula for them. It is well known that in this case the boundaries of the basins of attraction (stable manifold) are tightly wound and intertwining (a distance $O(\epsilon)$ apart), separating solutions getting trapped into either stable region of the stable equilibrium. Since the widths of the boundaries of the basins of attraction are well known to be $O(\epsilon)$, they depend on the $O(\epsilon)$ initial conditions. Small changes in the initial conditions affect the final outcome; in particular, they affect the competition between the two stable equilibrium solutions of (1).

3 Method of Averaging

Away from the unperturbed homoclinic orbits, the slow variation of the nonlinear oscillator, (1) or (2), can be obtained by the usual singular perturbation methods. The method of averaging for strongly nonlinear oscillators is described, for example, by Arnold, Kozlov, and Neishtadt (1988), Bourland, Haberman, and Kath (1991b), Kevorkian (1987), Sanders and Verhulst (1985), and Wiggins (1990). In order to analyze system (2) for large times, we will average the system over the fast period of oscillation. Without loss of generality, we define the fast phase ψ as

$$\frac{\psi}{\omega(H)} = \int_{q_c}^{q} \frac{dq}{H_p} = \int_0^p \frac{dp}{-H_q}, \quad (5)$$

where the frequency ω of the unperturbed oscillator depends on the Hamiltonian H in the usual way:

$$\frac{1}{\omega(H)} = \oint \frac{dq}{H_p} = \oint \frac{dp}{-H_q}. \quad (6)$$

We have normalized the period of ψ to 1 and assumed H to be an even function of p. Since the phase angle can be measured starting at any point, for convenience, we define the phase angle $\psi = 0$ to correspond to $q = q_c$ and $p = 0$ (refer to Fig. 1). The phase plane variables q, p are considered from (5) to depend on the fast phase ψ, and the Hamiltonian H: $q = q(\psi, H)$, and $p = p(\psi, H)$. Furthermore, p and q are periodic functions of ψ (with period 1) by the definition of ψ.

In the method of averaging, the perturbed Hamiltonian system (2) is first transformed into a system for the time evolution of the Hamiltonian and fast phase (standard form):

$$\frac{dH}{dt} = H_q\frac{dq}{dt} + H_p\frac{dp}{dt} = \epsilon(H_q h_1 + H_p h_2), \quad (7a)$$

according to (2). The time evolution of the fast phase requires a more nontrivial derivation. From (5), it follows that $H_p = \omega q_\psi$ and $H_q = -\omega p_\psi$. The Jacobian of the transformation can be shown to satisfy $q_\psi p_H - p_\psi q_H = 1/\omega$. Thus, the change of

Downloaded 04 May 2010 to 171.66.16.28. Redistribution subject to ASME license or copyright; see http://www.asme.org/terms/Terms_Use.cfm

variables formula may be used to derive $\psi_p = -\omega q_H$ and $\psi_q = \omega p_H$, from which the well-known expression for $d\psi/dt$ follows:

$$\frac{d\psi}{dt} = \omega\left(p_H \frac{dq}{dt} - q_H \frac{dp}{dt}\right) = \omega - \epsilon\omega(h_2 q_H - h_1 p_H). \quad (7b)$$

The leading order correction of the frequency is $-\epsilon\omega(h_2 q_H - h_1 p_H)$. The Hamiltonian system expressed as (7) is usually referred to as standard form, and it is common in the literature. It is important to note that p and q are periodic functions of ψ as are all the terms on the right-hand side of (7).

From (7a), the Hamiltonian varies slowly in time since ϵ is small. To analyze the system for large times, the following near identity transformation is introduced to facilitate the method of averaging:

$$H = e + \epsilon H_1(e, \phi) + \epsilon^2 H_2(e, \phi) + \ldots, \quad (8a)$$

$$\psi = \phi + \epsilon\psi_1(e, \phi) + \epsilon^2\psi_2(e, \phi) + \ldots. \quad (8b)$$

By this transformation, we have introduced two new dependent variables, e and ϕ, instead of H and ψ. In (8) H_i and ψ_i ($i = 1, 2, \ldots$) will be determined so that the expansions in (8) are uniform. For convenience, we choose e to be the mean of H (where e depends on ϵ) and refer to e as the averaged Hamiltonian. Similarly, ϕ is the mean of ψ. Thus H_i and ψ_i have zero averages in the fast variable ϕ. Since the dependent variables have changed, it is more convenient to express $\omega(H)$ and any needed functions $f(H, \psi)$ in terms of e and ϕ:

$$\omega(H) = \omega(e) + \epsilon H_1\omega_e + O(\epsilon^2), \quad (9a)$$

$$f(H, \psi) = f(e, \phi) + \epsilon H_1 f_e + \epsilon\psi_1 f_\phi + O(\epsilon^2). \quad (9b)$$

From here on, the functions represent the leading order term that depends on e and ϕ.

The derivatives de/dt and $d\phi/dt$ now appear linearly in both (7a) and (7b) because of (8). However, they are coupled weakly. Easily inverting a near identity matrix, yields

$$\frac{de}{dt} = \epsilon(e_q h_1 + e_p h_2 - \omega H_{1_\phi}) + \epsilon^2(M - \omega H_{2_\phi}) + O(\epsilon^3), \quad (10a)$$

$$\frac{d\phi}{dt} = \omega(e) + \epsilon(\omega h_1 p_e - \omega h_2 q_e - \omega\psi_{1_\phi} + H_1\omega_e) + O(\epsilon^2), \quad (10b)$$

where M has been introduced as

$$M = (-e_q h_1 - e_p h_2 + \omega H_{1_\phi})H_{1_e} + (\omega\psi_{1_\phi} + \omega h_1 p_e - \omega h_2 q_e - H_1\omega_e)H_{1_\phi} + (e_q h_1 + e_p h_2)_e H_1 + (e_q h_1 + e_p h_2)_\phi\psi_1. \quad (11)$$

With this near identity transformation, q, p, H_1, H_2, and ψ_1 are all functions of e and ϕ.

Since the right-hand side (rhs) of (10) are periodic functions of ϕ, all the quantities can be expressed as the sum of the mean term and an oscillatory term (ϕ dependent). Here, we introduce a notation for the average (mean) of a quantity, for example $f(e, \phi)$, with respect to the leading order phase ϕ: $\langle f\rangle \equiv \int_0^1 f(e, \phi)d\phi$. Furthermore, by assumption, the fluctuating (oscillatory) part of f is defined to be the difference between it and its mean: $\{\{f\}\} \equiv f - \langle f\rangle$. By these definitions, we also know that the average over ϕ of any oscillatory term is zero: $\langle\{\{f\}\}\rangle = 0$.

Since e is chosen as the mean of H with respect to ϕ, it follows that de/dt and $d\phi/dt$ are mean terms. Thus, averaging (10) yields

$$\frac{de}{dt} = \epsilon\langle e_q h_1 + e_p h_2\rangle + \epsilon^2\langle M\rangle + O(\epsilon^3), \quad (12a)$$

$$\frac{d\phi}{dt} = \omega(e) + \epsilon\langle\omega h_1 p_e - \omega h_2 q_e\rangle + O(\epsilon^2). \quad (12b)$$

The averaging procedure eliminates the fluctuating terms in the rhs of (10a) and (10b) and provides a method to define the near identity transformation (H_i). By comparing the $O(\epsilon)$ terms and the $O(\epsilon^2)$ terms in (10) and (12), we have

$$\omega H_{1_\phi} = \{\{e_q h_1 + e_p h_2\}\}, \quad (13a)$$

$$\omega H_{2_\phi} = \{\{M\}\}, \quad (13b)$$

$$\omega\psi_{1_\phi} = \omega\{\{h_1 p_e - h_2 q_e\}\} + \omega_e H_1. \quad (13c)$$

In order for H_1 to have zero average, integrating (13a) yields

$$H_1 = \frac{1}{\omega}\int_0^\phi \{\{e_q h_1 + e_p h_2\}\}d\phi' - \frac{1}{\omega}\left\langle\int_0^\phi \{\{e_q h_1 + e_p h_2\}\}d\phi'\right\rangle = \frac{1}{\omega}\left[\int_0^\phi \{\{e_q h_1 + e_p h_2\}\}d\phi'\right], \quad (14)$$

since we will show that $\{\{e_q h_1 + e_p h_2\}\}$ is an even function of ϕ. (Similar expressions exist for H_2 and ψ_1, but we do not need them.)

For systems in which the Hamiltonian H is symmetric in p and the $O(\epsilon)$ perturbations are purely dissipative, the time evolution of the averaged Hamiltonian e and averaged phase ϕ simplify. First, because H is even in p, it follows that the averaged term e is also even in p. Furthermore, e_p is odd in p, and e_q is even in p. Thus from (3) and (5), p is an odd function of ϕ, and q is an even function of ϕ. Consequently, e is an even function of ϕ, e_p is odd in ϕ, and e_q is even in ϕ. In a similar manner, h_1 is even in ϕ, and h_2 is odd in ϕ. Since ω depends on e, ω is even in ϕ. Since taking $\partial/\partial e$ does not change the parity, we also have that p_e is odd in ϕ and q_e is even in ϕ. Thus, $-\omega(h_2 q_e - h_1 p_e)$ is an odd function of ϕ, and we conclude that its average is zero. In this way, (12b), the equation for the evolution of the average phase simplifies: $d\phi/dt = \omega(e) + O(\epsilon^2)$. Using the same parity arguments, implies that $e_q h_1 + e_p h_2$ is an even function of ϕ.

With some care, we now show from its definition (11) that M is as odd function of ϕ. First we need the parity of H_1, H_{1_ϕ}, H_{1_e}, ψ_1, ψ_{1_ϕ}, $(e_q h_1 + e_p h_2)_e$, and $(e_q h_1 + e_p h_2)_\phi$. For the parity of H_1, we use (14). Since $e_q h_1 + e_p h_2$ is even in ϕ, $\{\{e_q h_1 + e_p h_2\}\}$ is also even in ϕ. Thus,

$\int_0^\phi \{\{e_q h_1 + e_p h_2\}\}d\phi'$ is an odd periodic function of ϕ,

and $\left\langle\int_0^\phi \{\{e_q h_1 + e_p h_2\}\}d\phi'\right\rangle = 0$,

verifying (14). From (14), H_1 is an odd function of ϕ. Consequently, H_{1_ϕ} is even in ϕ, and H_{1_e} is odd in ϕ. For the parity of ψ_1, we consider the definition (13c): $\omega\psi_{1_\phi} = \omega\{\{h_1 p_e - h_2 q_e\}\} + \omega_e H_1$. By the previous argument, $\omega(h_1 p_e - h_2 q_e)$ is odd in ϕ, and hence, $\omega\{\{h_1 p_e - h_2 q_e\}\}$ is also odd in ϕ. Since H_1 is odd in ϕ, therefore by the above definition (13c), ψ_{1_ϕ} is an odd function in ϕ. Consequently, ψ_1 is even in ϕ. Because $e_q h_1 + e_p h_2$ is an even function in ϕ, it follows that $(e_q h_1 + e_p h_2)_e$ is even in ϕ and $(e_q h_1 + e_p h_2)_\phi$ is odd in ϕ. Using these parity arguments, we derive the result that $M(e, \phi)$ is an odd function in ϕ. Thus, $\langle M\rangle = 0$ and for purely dissipative perturbations the equation for the average energy

Downloaded 04 May 2010 to 171.66.16.28. Redistribution subject to ASME license or copyright; see http://www.asme.org/terms/Terms_Use.cfm

also simplifies. We collect the equations for time evolution of both the averaged Hamiltonian and the averaged phase:

$$\frac{de}{dt} = -\epsilon\omega(e)D(e) + O(\epsilon^3), \tag{15a}$$

$$\frac{d\phi}{dt} = \omega(e) + O(\epsilon^2), \tag{15b}$$

where we have introduced the dissipation $D(e)$ of the average Hamiltonian,

$$D(e) \equiv -\langle e_q h_1 + e_p h_2\rangle/\omega(e) = \frac{1}{2\omega(\epsilon)}\langle qe_q + pe_p\rangle. \tag{16}$$

The leading-order equations for the average Hamiltonian and phase have remarkable accuracy, and hence we can use the truncated versions. The Hamiltonian H is related to its average e by (8a), where H_1 is given by (14). We also note that the difference between ψ and ϕ is small. Even though the slow variation equations fail as the separatrix is approached, we will show how to use these equations to obtain the boundaries of the basins of attraction in the next sections.

4 Transition Region With Nearly Homoclinic Orbits

As the slowly varying solution approaches the unperturbed separatrix, the period of oscillation approaches infinity. Therefore, the method of averaging fails. Instead, near the unperturbed separatrix, Timofeev (1978), Tennyson, Cary, and Escande (1986), and Bourland and Haberman (1990) have shown that the slow evolution of a system through a separatrix may be represented by a large sequence of nearly homoclinic orbits along the separatrix (see Fig. 3). It is well known (see, for example, Guckenheimer and Holmes, 1983) that along these nearly homoclinic orbits, the leading order change (dissipation) in the Hamiltonian H over a complete orbit can be approximated by M the Melnikov integral (calculated along the homoclinic orbit):

$$-\int_{-\infty}^{\infty}(H_q h_1 + H_p h_2)dt = -\oint \frac{H_q h_1 + H_p h_2}{H_p}dq = -D(e_s) \equiv M, \tag{17}$$

where e_s is the Hamiltonian associated with the separatrix (homoclinic orbit). For primary resonance, (1), as illustrated by Fig. 1, the smaller homoclinic orbit wraps around the equilibrium point C_1, and the larger homoclinic orbit wraps around the smaller homoclinic orbit and both equilibrium points. For convenience, $M_S(M_L)$ is denoted as the Melnikov integral for the smaller (larger) homoclinic orbit in the unperturbed system.

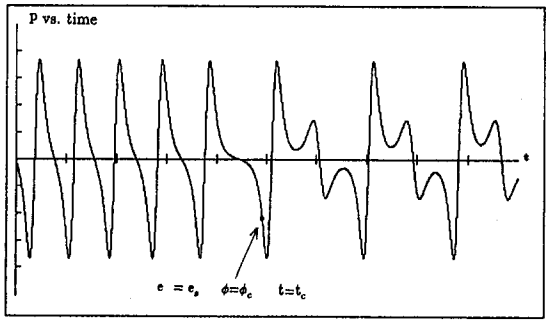


Fig. 3 Time series solution (p) as the unperturbed separatrix is crossed showing a sequence of nearly homoclinic orbits (of both kinds). Here, t_c is the critical time when the Hamiltonian predicted by averaging (the slow variation theory) is equal to e_s, the Hamiltonian of the unperturbed separatrix. The phase angle is ϕ_c at that critical time t_c.

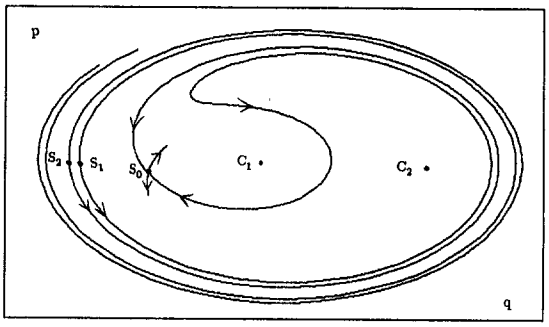


Fig. 4 Saddle approaches along the boundaries of the basins of attraction

As illustrated in Fig. 2, before the solution gets captured, the nearly homoclinic orbits are close to the larger homoclinic orbit of the unperturbed system. After the solution crosses the unperturbed separatrix, if it gets trapped in the stable region of C_1, the nearly homoclinic orbits are close to the smaller homoclinic orbit of the unperturbed system. However, if the solution is trapped in the stable region of C_2, the nearly homoclinic orbits consist of two parts: an orbit close to the larger homoclinic orbit followed by an orbit close to the smaller homoclinic orbit of the unperturbed system. Thus, the leading order dissipation of the Hamiltonian ΔH for a nearly homoclinic orbit can be approximated by its corresponding Melnikov integral:

$$\Delta H \sim \begin{cases} -\epsilon M_L & \text{(before capture)}, \\ -\epsilon M_S & \text{(captured in the stable region of } C_1\text{)}, \\ -\epsilon M_L \text{ alternates with } -\epsilon M_S & \\ \quad \text{(captured in the stable region of } C_2\text{)}. \end{cases} \tag{18}$$

The tightly wrapped boundaries of the basin of attraction sketched in Fig. 4 are the stable manifolds of the saddle point S_0. They separate solutions trapped in one stable region from the other. Trajectories which have their last saddle approach before capture between $S_0(S_2)$ and the first saddle approach S_1 will be trapped in the stable region of $C_2(C_1)$. The Hamiltonian at the saddle point S_0 is denoted e_S. As illustrated in Fig. 4, the Hamiltonian at S_1 can be approximated by $e_s + \epsilon(M_L + M_S)$, since the solution involves a smaller nearly homoclinic orbit and a larger nearly homoclinic orbit. Similarly, the Hamiltonian at S_2 can be approximated by $e_S + \epsilon M_L$. We define W_0 to be the Hamiltonian at the last saddle approach before capture. For solutions which are trapped in the stable region of $C_2(C_1)$, the last saddle approach before capture must lie between $S_0(S_2)$ and S_1, providing upper and lower limits for W_0:

$$\begin{cases} e_s < W_0 < e_s + \epsilon(M_L + M_S) & \text{capture into } C_2 \\ e_s + \epsilon(M_L + M_S) < W_0 < e_s + \epsilon M_L & \text{capture into } C_1, \end{cases} \tag{19}$$

where we have assumed that $M_L + M_S > 0$ and $M_S < 0$, in order for (19) to be valid, as can be verified for the parameter ranges of interest for primary resonance. Furthermore, $W_0 = e_S$ and $W_0 = e_S + \epsilon(M_S + M_L)$ are the stable manifolds of the saddle point corresponding to the boundaries of the basins of attraction.

5 Accurate Analytic Formula for the Boundaries of the Basins of Attraction

The method of averaging fails as the solution approaches the unperturbed separatrix. Near the unperturbed separatrix, the solution is a sequence of nearly homoclinic orbits. For double-well potentials, Bourland and Haberman (1991a, b) derived a simple method to determine the boundaries of the basin of

Downloaded 04 May 2010 to 171.66.16.28. Redistribution subject to ASME license or copyright; see http://www.asme.org/terms/Terms_Use.cfm

attraction by relating the two solutions at the last saddle approach before capture. We follow their method.

The Hamiltonian predicted by the method of averaging is given by (8a), where the fluctuating term satisfies (14). Usually as the separatrix is approached, H_1 is large since $\omega \to 0$ as $e \to e_s$. This suggests the failure of the slow variation theory as the separatrix is approached. However, if the phase is an integer or half integer, then $\int_0^{\phi} \{\{e_q h_1 + e_p h_2\}\} d\phi' = 0$ (because the period in ϕ is 1), in which case H_1 vanishes. Therefore, when the phase is an integer or a half integer, the $O(\epsilon)$ difference between H and e vanishes. Hence, we can use the averaged Hamiltonian to estimate the exact Hamiltonian at points where the phase angle is an integer or a half integer even near the separatrix.

Near the separatrix, for a complete nearly homoclinic orbit, the dissipation of the Hamiltonian predicted by the method of averaging is equal to the Melnikov integral to the leading order. Consequently, at the last saddle approach before capture (with a nearly integer phase angle), the actual Hamiltonian W_0 can be accurately approximated by the averaged Hamiltonian e there

$$e \sim W_0. \tag{20}$$

From the truncated version of (15a), we can solve for the time t_c it takes the averaged Hamiltonian e to dissipate from its initial value $e(0)$ to the Hamiltonian of the saddle point and the unperturbed separatrix which we denote as e_s:

$$\int_{e_s}^{e(0)} \frac{de}{\omega(e)D(e)} = \epsilon t_c. \tag{21}$$

The averaged phase angle at $t = t_c$ predicted by the method of averaging can be derived from (15b):

$$\phi_c = \int_0^{t_c} \omega(e)dt = \frac{1}{\epsilon}\int_{e_s}^{e(0)} \frac{de}{D(e)}, \tag{22}$$

where (15a) has been used. Since e_s is the Hamiltonian of the separatrix, the period of the oscillation corresponding to e_s is infinite. The slow variation theory (method of averaging) is not valid near e_s, so that t_c and ϕ_c do not correspond to the actual time and phase angle at which the solution intercepts the unperturbed separatrix.

To make the algebra easier, we assume that the initial conditions are at a minimum of q with p equaling zero. In this way we assume at $t = 0$ that $e = e(0)$ and $\phi = \phi(0) = 0$. Thus, from (8a) and (14), the initial Hamiltonian satisfies

$$H(0) = e(0) + O(\epsilon^2), \tag{23}$$

so that in the results to follow we do not distinguish between the initial Hamiltonian $H(0)$ and the initial averaged Hamiltonian $e(0)$.

According to (18), the Hamiltonian diminishes by the Melnikov function ϵM_L over the last complete homoclinic orbit before capture. Moreover, from (15) the average energy satisfies $de/d\phi = -\epsilon D(e)$. Thus, for partial orbits of the phase plane near the separatrix, the averaged Hamiltonian is dissipated Δe,

$$\Delta e = -\epsilon M_L \Delta\phi, \tag{24}$$

where $\Delta\phi$ represents the change in phase angle for the partial orbit. From (22) ϕ_c is defined to be the value of ϕ when e is predicted to be equal to e_s by the method of averaging. Thus, we consider a partial orbit from $e = W_0$ where $\phi = [\phi_c]$ ([ ] represents the integral part of a number) to $e = e_s$ and $\phi = \phi_c$. The modulus (fractional part) of the phase angle changes over a partial orbit from 0 to ϕ_c^{mod} ($\phi_c^{\text{mod}} \equiv \phi - [\phi]$). Hence, according to (20) and (24), the change in the Hamiltonian is

$$W_0 - e_s = \epsilon \phi_c^{\text{mod}} M_L. \tag{25}$$

ϕ_c is determined from the initial value problem of the averaged equations in Section 2, (15b). By considering the upper and lower limits of W_0, (19), we can determine the corresponding phase angle ϕ_c for the boundaries of the basins of attraction by using (25). For the solution which is captured in the stable region of C_2, $e_s < W_0 < e_s + \epsilon(M_L + M_S)$. Therefore, the fractional part of ϕ_c must be between these two values:

$$\phi_c^{\text{mod}} = 0 \quad \text{and} \quad \phi_c^{\text{mod}} = \frac{M_L + M_S}{M_L}, \tag{26}$$

where we recall that we have assumed $M_L + M_S > 0$ and $M_S < 0$. For solutions which are captured in the stable region of C_1, $e_s + \epsilon(M_L + M_S) < W_0 < e_s + \epsilon M_L$, and thus the fractional part of ϕ_c must be between these two values:

$$\phi_c^{\text{mod}} = \frac{M_L + M_S}{M_L} \quad \text{and} \quad \phi_c^{\text{mod}} = \frac{M_L}{M_L} = 1. \tag{27}$$

We can now obtain the main result of this paper, an accurate asymptotic formula for the boundaries of the basin of attraction for primary resonance. The relationship between the initial averaged Hamiltonian $e(0)$ and the critical phase angle is given by (22). However, the critical phase angle can be obtained by using (25), and hence the initial averaged Hamiltonian may be related to the energy at the last saddle approach W_0:

$$\phi_c = \frac{1}{\epsilon}\int_{e_s}^{e(0)} \frac{de}{D(e)} = [\phi_c] + \phi_c^{\text{mod}} = [\phi_c] + \frac{W_0 - e_s}{\epsilon M_L}, \tag{28}$$

where $[\phi_c]$ is the integral part of ϕ_c and is known to be the number of oscillations before the last approach to the saddle point. Again, the boundary of the basin of attraction corresponds to $W_0 = e_s$ and $W_0 = \epsilon(M_L + M_S) + e_s$ or $W_0 = e_s + \epsilon(M_L + M_S)$ and $W_0 = \epsilon M_L + e_s$ depending into which stable region the solution eventually is captured. The significance of (28) is that with the appropriate W_0 ($W_0 = e_s$ or $W_0 = \epsilon(M_L + M_S) + e_s$ or $W_0 = \epsilon M_L + e_s$) it determines the initial Hamiltonian $H(0)$ corresponding to the boundaries of the basin of attraction to sufficient accuracy since $H(0) = e(0) + O(\epsilon^2)$ under the simplifying assumption that the initial condition has a zero phase (i.e., $p = 0$ at $t = 0$). Small changes in initial conditions affect which stable equilibrium of (1) (corresponding to a stable periodic response of the resonant system) the solution approaches, and (28) has been derived to include enough accuracy to account for that.

6 Numerical Comparison

The initial Hamiltonians (with $p = 0$) $H(0)$ corresponding to the boundaries of the basin of attraction for primary resonance are given in an asymptotically accurate way by (28) with the appropriate W_0. In this section, we only compute the boundary corresponding to $W_0 = e_s$. In order for our asymptotic analysis to be valid, the initial conditions should be far away from the double homoclinic orbit with Hamiltonian e_s (for the parameter in which we compute $e_s = 0.1836473$). We let the initial Hamiltonian (with $p = 0$) be fixed; for convenience, we let $H(0) = -5$. Actually, that initial condition will usually not correspond to the boundary of the basin of attraction. Instead, we easily determine the integer $[\phi_c]$ so that the initial Hamiltonian (with $p = 0$) given by (28) is closest to -5 and then determine the initial Hamiltonian (with $p = 0$) from (28). We determine $H(0)$ this way for various small values of ϵ.

To show the accuracy of this result, we compare it to a direct numerical computation of the boundaries of the basins of attraction by integrating numerically (1) backwards in time from near the saddle point along the stable manifold for the same values of ϵ. Numerical values for the Hamiltonian when $p = 0$ are reported in Table 1.

Downloaded 04 May 2010 to 171.66.16.28. Redistribution subject to ASME license or copyright; see http://www.asme.org/terms/Terms_Use.cfm

Table 1 Comparison between analytic and numerical results for the Hamiltonian for the boundary of the basin of attraction (the initial Hamiltonian H(0) fixed near -5, $\mu = 1.5$, $\Omega = -2$, $\alpha = 1$ and $\gamma = -0.5$)

ϵ	$[\phi_c]$	Numerical Hamiltonian ($p = 0$)	Analytical Hamiltonian (28)	Difference	Bandwidth $\epsilon D(H(0))$	Difference / Bandwidth
1.0×10^{-2}	19	−4.94493851	−4.94588369	9.45×10^{-4}	0.3769	0.25%
0.9×10^{-2}	21	−4.90786698	−4.90838610	5.19×10^{-4}	0.3392	0.15%
0.8×10^{-2}	24	−5.02106368	−5.02118368	1.20×10^{-4}	0.3015	0.04%

The number of oscillations the solution undergoes from its initial condition to the saddle point is $[\phi_c]$ which can be shown to be $O(1/\epsilon)$. If ϵ is too small, the number of oscillations will be very large, and the error in the numerical integration of (1) will become too large since the solution passes near the saddle point many times. Thus, we choose $\epsilon = 0.01$, so that the number of oscillations is only moderately large, $[\phi_c] = 19$, and we vary ϵ slightly to demonstrate the effect of ϵ getting smaller.

From Table 1, we see that our asymptotic formula (28) for the initial Hamiltonian ($p = 0$) corresponding to boundary of the basin of attraction agrees quite well with the numerical integration of the backwards initial value problem. The difference between the two values of the Hamiltonian are much smaller than $O(\epsilon)$, in particular when $\epsilon = 0.01$, the difference is 9.45×10^{-4}. To appreciate how accurate our asymptotic formula is, we compare it to the width of one band of the boundaries of the basins of attraction corresponding to the initial Hamiltonian $H(0)$, which is known to be the dissipation of the Hamiltonian over one loop, $\epsilon D(H(0))$. For the initial condition we have chosen $H(0) = -5$, we obtain $D(H(0)) = 37.69\ldots$ by using (16). For example, for $\epsilon = 0.01$, in which case the band width of the Hamiltonian is $0.3769\ldots$, we see that the error between the asymptotic formula and the numerical integration divided by the bandwidth is $9.45 \times 10^{-4}/0.3769 = .0025$, which means that we have located the boundary of the basin of attraction with an error of about 1/4 percent of its width with $\epsilon = 0.01$ (assuming the numerical integration is accurate). If ϵ is less than 0.01, our asymptotic formula should be even more accurate. This agreement gives extra confidence in our analytical formula, justifying our belief that (28) can be used to accurately predict the boundary of the basin of attraction for primary resonance, determining the outcome of the competition between two stable periodic responses.

References

Arnold, V. I., Kozlov, V. V., and Neishtadt, A. I., 1988, *Mathematical Aspects of Classical and Celestial Mechanics, Dynamical Systems III,* Springer-Verlag, New York.

Bourland, F. J., and Haberman, R., 1990, "Separatrix Crossing: Time-Invariant Potentials With Dissipation," *SIAM Journal on Applied Mathematics,* Vol. 50, pp. 1716–1744.

Bourland, F. J., and Haberman, R., 1991a, "Capture and the Connection Formulas for the Transition Across a Separatrix," *Asymptotic Analysis and the Numerical Solution of Partial Differential Equations,* H. G. Kaper and M. Garbey, eds., Dekker, New York, pp. 17–30.

Bourland, F. J., Haberman, R., and Kath, W. L., 1991b, "Averaging Methods for the Phase Shift of Arbitrarily Perturbed Strongly Nonlinear Oscillators With an Application to Capture," *SIAM Journal on Applied Mathematics,* Vol. 51, pp. 1150–1167.

Drazin, P. G., 1992, *Nonlinear Systems,* Cambridge, New York.

Guckenheimer, J., and Holmes, P., 1983, *Nonlinear Oscillations, Dynamical Systems, and Bifurcations of Vector Fields,* Springer-Verlag, New York.

Jordan, D. W., and Smith, P., 1987, *Nonlinear Ordinary Differential Equations,* 2nd ed., Oxford, New York.

Kevorkian, J., 1987, "Perturbation Techniques for Oscillatory Systems With Slowly Varying Coefficients," *SIAM Review,* Vol. 29, pp. 391–461.

Kevorkian, J., and Cole, J. D., 1981, *Perturbation Methods in Applied Mathematics,* Springer-Verlag, New York.

Nayfeh, A. H., and Mook, D. T., 1979, *Nonlinear Oscillations,* John Wiley and Sons, New York.

Neishtadt, A. I., 1975, "Passage Through a Separatrix in a Resonance Problem With a Slowly-Varying Parameter," *Journal of Applied Mathematics and Mechanics,* Vol. 39, pp. 594–605.

Neishtadt, A. I., 1986, "Change of an Adiabatic Invariant at a Separatrix," *Soviet Journal of Plasma Physics,* Vol. 12, pp. 568–573.

Neishtadt, A. I., 1991, "Probability Phenomena Due to Separatrix Crossing," *Chaos,* Vol. 1, pp. 42–48.

Sanders, J. A., and Verhulst, F., 1985, *Averaging Methods in Nonlinear Dynamical Systems,* Springer-Verlag, New York.

Tennyson, J. L., Cary, J. R., and Escande, D. F., 1986, "Change of the Adiabatic Invariant Due to Separatrix Crossing," *Physical Review Letters,* Vol. 56, pp. 2117–2120.

Timofeev, A. V., 1978, "On the Constancy of an Adiabatic Invariant When the Nature of the Motion Changes," *Zh. Eksp. Teor. Fiz.,* 75, pp. 1303–1308, (In Russian), *Soviet Physics JETP,* Vol. 48, pp. 656–659.

Wiggins, S., 1990, *Introduction to Applied Nonlinear Dynamical Systems and Chaos,* Springer-Verlag, New York.

Downloaded 04 May 2010 to 171.66.16.28. Redistribution subject to ASME license or copyright; see http://www.asme.org/terms/Terms_Use.cfm

The Stiffest Wire

K. Schulgasser
Pearlstone Center for Aeronautical Engineering Studies,
Department of Mechanical Engineering,
Ben Gurion University of the Negev,
Beer Sheva, Israel

We consider a polycrystal constituted from orthorhombic single crystals for which one particular principal axis of the crystallites is always oriented parallel to a particular direction; in the plane perpendicular to this direction the crystallites are randomly oriented. Bounds are found for the Young's modulus in the axial direction. The lower *bound on the Young's modulus, which is realizable, is found to be that of the individual crystallite in the aligned direction. The* upper *bound determined is necessarily realizable when the single crystal elastic constants satisfy a certain condition. When this condition is not satisfied a bound is found; whether or not this bound is realizable must be examined using the specific elastic constants of the crystal being considered. For all physical examples considered the upper bound was indeed found to be realizable. Thus, generally speaking, a wire constituted as above, with the stiffest direction of the individual crystallites being along the wire, will have a higher Young's modulus than the maximum modulus of the individual crystallites of which it is composed.*

1 Introduction

We are concerned with a very highly textured polycrystal constituted from orthorhombic single crystals. The principal axes of the single crystal are denoted by "1," "2," and "3." Consider the case when all crystals in the polycrystal are oriented such that the 3 axes are parallel, and in the plane perpendicular to the 3 direction (the axial direction of the polycrystal) the crystal axes 1 and 2 are randomly oriented, i.e., the polycrystal is transversely isotropic. The situation is as illustrated in Fig. 1. We wish to determine the Young's modulus of such a polycrystal in the common 3 direction (or of a wire of this material, where the wire axis is the common 3 direction) as it depends on the elastic behavior of the single crystal. It will be seen that the problem as defined above has no unique solution, i.e., the mere fact of transverse isotropy is insufficient to permit determination of Young's modulus. However we will, for most cases, succeed in determining *sharp* bounds on the Young's modulus. By this we mean that there are demonstrable geometries which will exactly realize the upper and lower bounds. The lower bound is found to be exactly the Young's modulus of the single crystal in the 3 direction.

We utilize the standard 6×6 matrix notation of stiffness and compliance matrices to describe the elastic behavior of the single crystal and of the polycrystalline composite; these are denoted by $\mathbf{C}$ and $\mathbf{S}$ for the single crystal, $\mathbf{S} = \mathbf{C}^{-1}$; when referring to the polycrystal we will use an asterisk, i.e., $\mathbf{C}^*$ and $\mathbf{S}^*$. The elements of the stiffness matrix are C_{ij}, $(i, j = 1, \ldots, 6)$ and $C_{ij} = C_{ji}$. In this notation the nine constants defining the elastic behavior of a single crystal are C_{11}, C_{22}, C_{33}, C_{12}, C_{13}, C_{23}, C_{44}, C_{55}, and C_{66}. All other C's are zero. Only five constants are required to define the elastic behavior of the polycrystal. We take 1 and 2 to be any cartesian axes in the transverse plane. Then the five constants are C^*_{33}, C^*_{11}, C^*_{13}, C^*_{12}, and C^*_{44}. The other constants are given by the relationships

$$C^*_{22} = C^*_{11},\ C^*_{55} = C^*_{44},\ C^*_{23} = C^*_{13},\ C^*_{66} = \tfrac{1}{2}(C^*_{11} - C^*_{12}). \quad (1)$$

Similar statements apply to the compliance matrix, except that the last relationship of Eq. (1) now becomes

$$S^*_{66} = 2(S^*_{11} - S^*_{12}). \quad (2)$$

The results we will obtain are of course applicable when the constituting crystal is hexagonal with 2 (or 1) taken as the axial direction *of the single crystal* and 3 is simultaneously the basal direction of the single crystal and also the axial direction of the polycrystal.

Indeed the motivation for considering this problem comes from the question of the relationship between Young's modulus for carbon/graphite fibers and the degree of orientation of the basal plane of the graphite with respect to the fiber axis. The symmetry of graphite is hexagonal, i.e., a very special case of orthorhombic. Since the basal direction Young's modulus of graphite is some 30 times that in the axial direction (of the graphite), in order to obtain stiff fibers it is necessary to achieve high degrees of orientation. Attempts have been made to uniquely relate the fiber Young's modulus to the distribution of orientation angles, e.g., Reynolds (1973); the "ultimate" fiber would involve perfect alignment of the basal directions with the fiber axis. But we note that no such determination can be made; theoretically, the fiber Young's modulus can be greater than that of the graphite in the basal direction. We hasten to add two caveats. First, real fiber Young's moduli are strongly affected by the inevitable porosity of the fiber; secondly, even neglecting the porosity, for the case of graphite we will see that the ultimate Young's modulus is only very marginally higher than that of the graphite in the basal direction. However, we will give examples for other crystalline materials where the difference is appreciable.

Our analysis proceeds as follows. We find two relationships which must exist between C^*_{33}, C^*_{13}, and κ, where κ is the plane-strain (in the transverse plane) bulk modulus defined by

$$\kappa = \tfrac{1}{2}(C^*_{11} + C^*_{12}). \quad (3)$$

This we accomplish by considering the elastic behavior of the polycrystalline composite under a certain three-dimensional state of stress which results in uniform fields throughout. Secondly, we consider the plane-strain behavior in the transverse plane; sharp bounds on the plane-strain bulk modulus κ have been reported (Avellaneda and Milton, 1989). Since the axial Young's modulus of the polycrystal is given by

$$E^*_3 = C^*_{33} - \frac{C^{*2}_{13}}{\kappa}, \quad (4)$$

we will be able to determine bounds on E^*_3.

Contributed by the Applied Mechanics Division of THE AMERICAN SOCIETY OF MECHANICAL ENGINEERS for publication in the ASME JOURNAL OF APPLIED MECHANICS.

Discussion on this paper should be addressed to the Technical Editor, Professor Lewis T. Wheeler, Department of Mechanical Engineering, University of Houston, Houston, TX 77204-4792, and will be accepted until four months after final publication of the paper itself in the ASME JOURNAL OF APPLIED MECHANICS.

Manuscript received by the ASME Applied Mechanics Division, Mar. 7, 1994; final revision, Oct. 13, 1994. Associate Technical Editor: G. J. Dvorak.

Copyright © 1995 by ASME

Downloaded 04 May 2010 to 171.66.16.28. Redistribution subject to ASME license or copyright; see http://www.asme.org/terms/Terms_Use.cfm

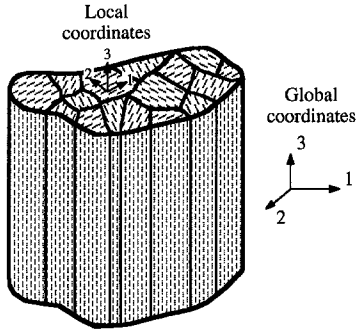


Fig. 1 Axially oriented polycrystal

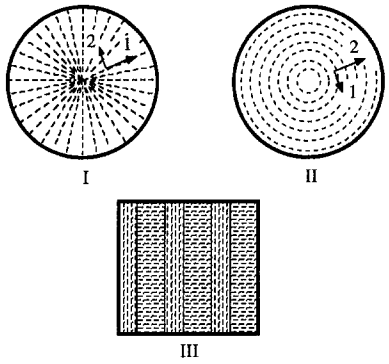


Fig. 3 Models for calculating upper bound on plane-strain bulk modulus

2 Relationship Between Coefficients

Consider the single crystal shown in Fig. 2. Suppose a traction σ_C is imposed on it directed in the 1-2 plane acting perpendicular to the vertical surface, and a traction σ_L is imposed acting in the 3 direction on the upper and lower surfaces. Clearly the state of stress in the crystal is $\sigma_3 = \sigma_L$ and in the 1-2 the stress is isotropic and equal for every direction to σ_C. Now suppose a ratio $\sigma_L{:}\sigma_C$ can be found such that the strain in the 1-2 plane is also isotropic. If so, many crystals with arbitrary orientation of the 1 and 2-axes in the 1-2 plane, all with this ratio $\sigma_L{:}\sigma_C$, can be "assembled" into a polycrystal and all traction and displacement conditions at the interfaces are fulfilled. We have the case of a polycrystal subjected to the above tractions on the outside envelope which has a uniform stress and strain field throughout. It is simple matter to find the appropriate ratio $\sigma_L{:}\sigma_C$, or the ratio of the attendant strain fields $\varepsilon_L{:}\varepsilon_C$, and then using the definition of effective properties we quickly arrive at the desired relationships.

Consider the following two constitutive equations for the crystal:

$$\sigma_1 = C_{11}\varepsilon_1 + C_{12}\varepsilon_2 + C_{13}\varepsilon_3$$

$$\sigma_2 = C_{12}\varepsilon_1 + C_{22}\varepsilon_2 + C_{23}\varepsilon_3. \qquad (5a,b)$$

Imposing the condition $\varepsilon_1 = \varepsilon_2$ and setting $\sigma_1 = \sigma_2$ we immediately find

$$\varepsilon_1 = \frac{C_{23} - C_{13}}{C_{11} - C_{22}}\,\varepsilon_3. \qquad (6)$$

The third constitutive equation of the single crystal which is of interest to us in the present context is

$$\sigma_3 = C_{13}\varepsilon_1 + C_{23}\varepsilon_2 + C_{33}\varepsilon_3. \qquad (7)$$

Now for the polycrystal we write the following constitutive equations involving the effective elastic behavior:

$$\sigma_1 = C^*_{11}\varepsilon_1 + C^*_{12}\varepsilon_2 + C^*_{13}\varepsilon_3 \qquad (8)$$

$$\sigma_3 = C^*_{13}\varepsilon_1 + C^*_{23}\varepsilon_2 + C^*_{33}\varepsilon_3. \qquad (9)$$

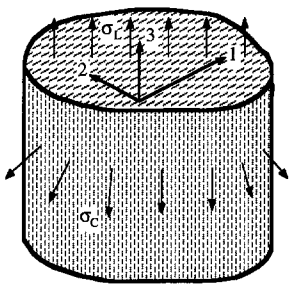


Fig. 2 Tractions for uniform field

Here the indices 1 and 2 refer to any direction in the transverse plane; $\varepsilon_1 = \varepsilon_2 = \varepsilon_C$ whether the indices refer to the single crystal or to the polycrystal by virtue a the condition imposed above. Then we can equate Eq. (5*a*) or (5*b*) to (6) and (7) to (9) in each instance writing $\varepsilon_1 = \varepsilon_2$ and expressing ε_1 in terms ε_3 of by means of Eq. (6). To maintain the symmetry of the 1 and 2 indices in the expressions to be derived it is convenient to equate the sum of Eq. (5*a*) and (5*b*) to twice Eq. (8). Then eliminating ε_3 which is arbitrary, and using Eq. (3) we find the two relationships

$$\frac{4\kappa - C_{11} - C_{22} - 2C_{12}}{C_{11} - C_{22}} = \frac{C_{13} + C_{23} - 2C^*_{13}}{C_{23} - C_{13}} \qquad (8)$$

$$\frac{2C^*_{13} - C_{13} - C_{23}}{C_{11} - C_{22}} = \frac{C_{33} - C^*_{33}}{C_{23} - C_{13}}. \qquad (9)$$

The technique used above of seeking external tractions imposed on a composite which result in uniform fields throughout in order to find relationships between effective constants was proposed and extensively exploited by Dvorak and co-workers (Dvorak and Bahei-El-Din, 1979; Dvorak, 1986; Dvorak, 1990; Benveniste and Dvorak, 1992). Alternately the results above could have been obtained using a somewhat different technique first used by Hill (1964) and further exploited by Schulgasser (1992).

3 Plane Strain

Now we consider plane-strain deformation in the transverse plane. It is convenient to consider the situation in terms of the plane strain compliance matrix defined by

$$\begin{bmatrix} \tilde{S}_{11} & \tilde{S}_{12} & 0 \\ \tilde{S}_{12} & \tilde{S}_{22} & 0 \\ 0 & 0 & \tilde{S}_{66} \end{bmatrix} \equiv \begin{bmatrix} C_{11} & C_{12} & 0 \\ C_{12} & C_{22} & 0 \\ 0 & 0 & C_{66} \end{bmatrix}^{-1}. \qquad (10)$$

Avellaneda and Milton (1989) showed that bounds on κ are given by

$$2[\sqrt{\tilde{S}_{11}\tilde{S}_{22}} + \tilde{S}_{12}] \le \frac{1}{\kappa} \le 2\left[\frac{\tilde{S}_{11} + \tilde{S}_{22}}{2} + \tilde{S}_{12}\right] \qquad (11)$$

and that these are the best bounds that can possibly be found. This latter they showed by demonstrating that geometries exist for which the bulk modulus can be calculated and which realize the above bounds. Their demonstration involved somewhat abstract constructions of realizable geometries. To make the situation concrete we present in Figs. 3 and 4 geometries which realize the upper and lower bounds, respectively. These models may seem bizarre; they are not intended to be realistic representations—they represent limiting cases.

Downloaded 04 May 2010 to 171.66.16.28. Redistribution subject to ASME license or copyright; see http://www.asme.org/terms/Terms_Use.cfm

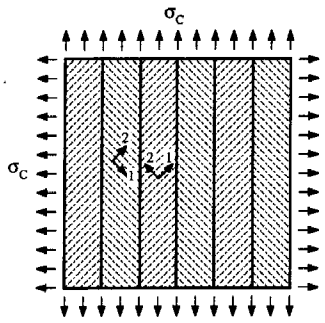


Fig. 4 Model for calculating lower bound on plane-strain bulk modulus

All the models are hierarchical of rank 2 (Milton, 1986). The usefulness of modeling composite materials via hierarchical laminating procedures was first recognized by Bruggeman (1935). For a polycrystal this technique was used by Schulgasser (1977) when considering the conductivity of polycrystals. More generally modeling composites using multiscale laminates was discussed by Milton (1986). Three schemes for realizing the upper bound are shown in Fig. 3. I and II show disks with cylindrical symmetry; in the first instance the crystalline material is arranged such that the 1 direction is radial and the 2 direction is circumferential, in II the axes are reversed. It is a simple matter to calculate the change in area of such disks when subjected to uniform radial traction. Now one can completely fill a plane with such disks of various sizes. (Sphere assemblages—or in the two-dimensional case, cylinder or disk assemblages—were first used by Hashin and Shtrikman (1962, 1963) when considering isotropic phases, and were used by Schulgasser (1983) for polycrystals in considering effective conductivity.) Geometries I and II are reminiscent of graphite arrangements in whole fiber cross sections for PAN and pitch fibers, respectively; see Avery and Herakovich (1986). Another possible construction is shown in III. Here one uses a laminate consisting of alternate layers of the crystalline material oriented such that the 1-axis is either parallel or perpendicular to the plane of the laminae. One can choose the relative thicknesses so that a uniform perpendicular traction applied to the envelope results in equal overall strain in the laminar and perpendicular directions. Now the plane can be filled by randomly oriented patches constructed as described, as long as the dimension of these areas are very large compared to lamina thickness. Calculations carried out for all three cases above lead to identical results, the left-hand side of (11), which expressed in terms of the stiffnesses is

$$\kappa = \tfrac{1}{2}[\sqrt{C_{11}C_{22}} + C_{12}]. \tag{12}$$

The lower bound on κ is achieved by the scheme shown in Fig. 4. Equal thickness laminae with the 1-axes oriented alternately at +45 deg and −45 deg are used. Clearly under uniform normal traction σ_c we will have throughout that $\sigma_1 = \sigma_2 = \sigma_c$ and the volume change is simply $\varepsilon_1 + \varepsilon_2$. Then from

$$\varepsilon_1 = \tilde{S}_{11}\sigma_1 + \tilde{S}_{12}\sigma_2 \quad \varepsilon_2 = \tilde{S}_{12}\sigma_1 + \tilde{S}_{22}\sigma_2 \tag{13a,b}$$

using

$$\sigma_c = \kappa(\varepsilon_1 + \varepsilon_2), \tag{14}$$

we have the right-hand side of Eq. (11), or in terms of the stiffnesses

$$\kappa = \frac{C_{11}C_{22} - C_{12}^2}{C_{11} + C_{22} - 2C_{12}}. \tag{15}$$

4 Bounds

We now rewrite Eqs. (8) and (9) to obtain

$$2C_{13}^* = C_{13} + C_{23} - \lambda(4\kappa - C_{11} - C_{22} - 2C_{12}) \tag{16}$$

$$C_{33}^* = C_{33} + \lambda^2(4\kappa - C_{11} - C_{22} - 2C_{12}) \tag{17}$$

where

$$\lambda = \frac{C_{23} - C_{13}}{C_{11} - C_{12}}.$$

(We will disregard for the moment the degenerate case when $C_{11} = C_{22}$.) Now if the parameter λ defined above is positive then considering the expression for E_3^* given in Eq. (4), and taking into account that for all values of κ between the limits given in Eqs. (12) and (15) the expressions in parentheses in Eqs. (16) and (17) are negative it is clear that E_3^* is a monotonically increasing function of κ. Then using the realizable lower bound on κ we have that the lower realizable limit on E_3^* is

$$E_3^* = E_3 = C_{33} - \frac{C_{11}C_{23}^2 + C_{22}C_{13}^2 - 2C_{12}C_{23}C_{13}}{C_{11}C_{22} - C_{12}^2}, \tag{18}$$

Table 1

Stiffness GPa	Single Crystal Data						Single crystal	Axial poly-crystal
Material	C_{11}	C_{22}	C_{33}	C_{12}	C_{13}	C_{23}	E_3	E_3^* (upper bound)
$CaCO_3$, Argonite‡	87	85	160	157	373	1.7	143.70	149.94
$BaSO_4$, Baryte	88.0	78.1	104	47.7	26.9	28.9	91.85	92.04
" " ‡	86.2	97.1	108	52.3	34.1	35.2	91.29	91.31
$SrSO_4$, Celestite‡	104.4	106.1	128.6	77.3	60.5	61.9	87.55	87.56
S, Sulphur‡	24.0	20.5	48.3	13.3	17.1	15.9	32.97	32.98
$Al_2(F,OH)_2SiO_4$, Topaz	295	282	349	85	88	126	283.41	286.19

Table 1. - Single crystal elastic constants, "3" direction Young's modulus of single crystal (realizable lower bound), and realizable upper bound for axial polycrystal. The single crystal is orthorhombic. ‡ indicates those crystals for which λ is negative. Data from Huntington (1958).

Downloaded 04 May 2010 to 171.66.16.28. Redistribution subject to ASME license or copyright; see http://www.asme.org/terms/Terms_Use.cfm

Table 2

Stiffness GPa	Single crystal data				Single crystal	Axial polycrystal
Material	C_{11} (= C_{33})	C_{22}	C_{23} (= C_{12})	C_{13}	C_{33} - E_3	C_{33} - E_3^* (stiffest wire)
Graphite‡	1060	36.5	15	180	34.84	34.02
Cd‡	121	51.3	44.2	48.1	39.29	34.07
Zn	161	61.0	50.1	34.2	41.55	26.60

Table 2. - Single crystal elastic constants, basal direction Young's modulus of single crystal (realizable lower bound), and realizable upper bound for axial polycrystal. The single crystal is hexagonal; "2" is *its* axial direction, but its "3" (or equivalently "1") direction is aligned with the axial direction of the polycrystal (also "3"). ‡ indicates those crystals for which λ is negative. Data from Blakslee, et al. (1970) and Huntington (1958).

i.e., exactly the 3 direction Young's modulus of the single crystal. From the realizable upper bound on κ we find the following explicit expressions:

$$C_{33}^* = C_{33} - 2\left(\frac{C_{13} - C_{23}}{C_{11} - C_{22}}\right)^2\left[\frac{C_{11} + C_{22}}{2} - \sqrt{C_{11}C_{22}}\right] \quad (19)$$

$$C_{13}^* = \tfrac{1}{2}(C_{13} + C_{23}) - \frac{C_{13} - C_{23}}{C_{11} - C_{22}}\left[\frac{C_{11} + C_{22}}{2} - \sqrt{C_{11}C_{22}}\right]. \quad (20)$$

And the upper bound on E_3^* is computed by inserting these and (12) into (4).

For a tetragonal or cubic constituting crystal for which $C_{11} = C_{22}$ and $C_{13} = C_{23}$ expressions (19) and (20) seem at first glance to be invalid. Rather than return to the derivation for this case, it is simplest to note that for $C_{11} - C_{22} = \delta$ the square brackets are of $O(\delta^2)$. So for this case it is clear the expressions reduce to

$$C_{33}^* = C_{33}, \quad C_{13}^* = C_{13}, \quad (21)$$

(12) and (15) collapse to the same value and we have, as expected, $E_3^* = E_3$.

When λ is negative it is not at all clear that E_3^* is monotonically dependent on κ. The function may have an extremum in the interval which is below the value attained for the minimum realizable κ or greater than the value attained for maximum realizable κ. Were such to be the case, and this can be easily checked for any specific crystal, the bounds on E_3^* are easily found by simply finding this extremum value; however, then the bound would not be realizable. For the lower bound on E_3^* we can immediately disregard the possibility suggested. This is so since it can readily be shown, using the theorem of minimum complementary energy whose use in the context of bounding effective elastic constants of composites was first suggested by Paul (1960), that the Young's modulus of the single crystal in the 3 direction is a lower bound on E_3^*. One simply uses as a trial function in his scheme that the stresses are uniform, σ_3 = constant, and $\sigma_1 = \sigma_2 = 0$.

5 Closure

We will see that even for cases when λ is negative it seems that for real crystals E_3^* is still monotonic in κ, and thus the upper bound is realizable. We will compare the Young's modulus of several crystals in their stiffest direction with that which could be achieved in a highly oriented polycrystal were all the axis of the crystallites arranged so that their stiffest directions were parallel. Table 1 shows the relevant elastic constants for all of the orthorhombic crystals whose properties are reported in Huntington (1958) (except those two which are either ferroelectric or piezoelectric); for some of the crystals the axis designation has been altered so that 3 is the stiffest single crystal direction. λ is negative for those crystals followed by the symbol ‡. *In every one of these cases E_3^* is found to be a monotonic function of κ*, thus the bounds are realizable in every instance. (For one material two sets of constants are reported, one with λ positive, one with λ negative.) The realizable bounds on E_3^* are shown in the table. For all of these examples the bounds are so narrow that it is clear that, given the uncertainty in the single crystal measurements, it is hard to attribute physical importance to the spread of the bounds.

In closing we consider hexagonal crystals. Counter to normal convention we label the axial direction of the single crystal 2, the basal directions are 1 and 3. (This is unfortunate, but natural in the present situation since the "axial" direction of the polycrystal is not the axial direction of the single crystal; it is the basal direction of the single crystals which is to be aligned in this global axial direction.) Table 2 shows the relevant elastic constants for graphite, cadmium, and zinc. For all three, the basal direction stiffness is greater than the axial direction stiffness, and thus they are of interest in the present context; cadmium and zinc are the only crystals listed by Huntington (1970, p. 66) which meet this condition. For both graphite and cadmium it is found that λ is negative, but again it is found that E_3^* is monotonic; hence the bounds are all realizable. For the case of graphite the difference between single crystal Young's modulus (E_3) and that for the oriented polycrystal (E_3^*) is clearly negligible, 1025.16 GPa versus 1025.98 GPa. This is well beyond the accuracy which we would expect to be detectable by any experimental technique. For cadmium these values are 81.71 GPa and 86.93 GPa, and for zinc they are 119.45 GPa and 134.40 GPa, respectively. In other words, it is theoretically possible to manufacture a zinc wire which is nearly 13 percent stiffer than the Young's modulus of a zinc crystal in its stiffest direction.

Finally we note that for the cross section geometries I and II of Fig. 3 Christensen (1994) has recently calculated the effective axial Young's modulus for the case of the hexagonal single crystal.

Acknowledgment

The author wishes to thank an unknown reviewer for clarifying the influence the parameter λ may have in some cases.

References

Avellaneda, M., and Milton, G. W., 1989, "Optimal Bounds on the Effective Bulk Modulus of Polycrystals," *SIAM Journal on Applied Mathematics*, Vol. 49, pp. 824–837.

Downloaded 04 May 2010 to 171.66.16.28. Redistribution subject to ASME license or copyright; see http://www.asme.org/terms/Terms_Use.cfm

Avery, W. B., and Herakovich, C. T., 1986, "Effect of Fiber Anisotropy on Thermal Stresses in Fibrous Composites," ASME JOURNAL OF APPLIED MECHANICS, Vol. 53, pp. 751–756.

Benveniste, Y., and Dvorak, G. J., 1992, "Uniform Fields and Universal Relations in Piezoelectric Composites," *Journal of the Mechanics and Physics of Solids,* Vol. 40, pp. 1295–1312.

Blakslee, O. L., Proctor, D. G., Seldin, E. J., Spence, G. B., and Weng, T., 1970, "Elastic Constants of Compression-Annealed Pyrolytic Graphite," *Journal of Applied Physics,* Vol. 41, pp. 3373–3382.

Bruggeman, D. A. G., 1935, "Berechnung Verschiedener Physikalischer Konstanten von Heterogenen Substanzen," *Annalen der Physik,* Vol. 5, pp. 636–664.

Christensen, R. M., 1994, "Properties of Carbon Fibers," *Journal of the Mechanics and Physics of Solids,* Vol. 42, pp. 681–695.

Dvorak, G. J., 1986, "Thermal Expansion of Elastic-Plastic Composite Materials," ASME JOURNAL OF APPLIED MECHANICS, Vol. 53, pp. 737–743.

Dvorak, G. J., 1990, "On Uniform Fields in Heterogeneous Media," *Proceedings of the Royal Society of London,* Vol. A431, pp. 89–110.

Dvorak, G. J., and Bahei-El-Din, Y. A., 1979, "Elastic-Plastic Behaviour of Fibrous Composites," *Journal of the Mechanics and Physics of Solids,* Vol. 27, pp. 51–72.

Hashin, Z., and Shtrikman, S., 1962, "A Variational Approach to the Theory of the Effective Magnetic Permeability of Multiphase Materials," *Journal of Applied Physics,* Vol. 33, pp. 1514–1517.

Hashin, Z., and Shtrikman, S., 1963, "A Variational Approach to the Theory of the Elastic Behaviour of Multiphase Materials," *Journal of the Mechanics and Physics of Solids,* Vol. 11, pp. 127–140.

Hill, R., 1964, "Theory of Mechanical Properties of Fibre-Strengthened Materials: I. Elastic Behaviour," *Journal of the Mechanics and Physics of Solids,* Vol. 12, pp. 199–212.

Huntington, H. B., 1958, *The Elastic Constants of Crystals,* Academic Press, New York, pp. 66, 72.

Milton, G. W., 1986, "Modelling the Properties of Composites by Laminates," *Homogenization and Effective Moduli of Materials and Media,* J. L. Ericksen, D. Kinderlehrer, R. Kohn, and J.-L. Lions, eds., Springer-Verlag, New York, pp. 150–174.

Paul, B., 1960, "Prediction of Elastic Constants of Multiphase Materials," *Transactions of the Metallurgical Society of AIME,* Vol. 218, pp. 36–41.

Reynolds, W. N., 1973, "Structure and Physical Properties of Carbon Fibers," *Chemistry and Physics of Carbon,* P. L. Walker, and P. A. Thrower, eds., Marcel Dekker, New York, Vol. 11, pp. 1–67.

Schulgasser, K., 1977, "Bounds on the Conductivity of Statistically Isotropic Polycrystals," *Journal of Physics C,* Vol. 10, pp. 404–417.

Schulgasser, K., 1983, "Sphere Assemblage Model for Polycrystals and Symmetric Materials," *Journal of Applied Physics,* Vol. 54, pp. 1380–1382.

Schulgasser, K., 1992, "Relationships between the Effective Properties of Transversely Isotropic Piezoelectric Composites," *Journal of the Mechanics and Physics of Solids,* Vol. 40, pp. 473–479.

Downloaded 04 May 2010 to 171.66.16.28. Redistribution subject to ASME license or copyright; see http://www.asme.org/terms/Terms_Use.cfm

A Shape Design Sensitivity Approach for Two-Dimensional Mixed-Mode Fracture Analysis Under General Loading

Tae Won Lee[1]
Associate Professor,
Department of Mechanics
and Engineering Science,
Kum-Oh National University of Technology,
188 Shinpung, Kumi, Kyungbuk,
730-701, Korea

I. R. Grosse
Department of Mechanical Engineering,
University of Massachusetts,
Amherst, MA 01003
Mem. ASME

Under general loadings including body forces and crack-face traction, the energy release rate equation for a two-dimensional cracked body is derived by a shape design sensitivity approach. Defining the virtual crack extension (VCE) as the variation of the geometry, the virtual work principle and the material derivative concept are used to obtain the final analytical equation for the energy release rate. In contrast to the results of other researchers, the functionals which appear in the derived energy release rate equation do not involve the derivative of the displacement field on the crack surface, thereby improving the numerical accuracy in the computation of the energy release rate. Although the finite element method (FEM) is applied to crack problems in this paper, any numerical analysis method can be applied to the resulting equation. In addition, if body forces and crack-face traction are constant with respect to VCE, i.e., their material derivatives are identically zero, then the energy release rate equation is domain independent for domains which exclude the crack-tip region. Three example problems are treated which demonstrate the generality, accuracy, and domain-independent nature of the derived energy release rate equation.

1 Introduction

There exist many methodologies to analyze crack problems. However, analytical solutions only exist for simple cases; numerical methods are necessary to calculate stress and displacement field for complex practical problems. For this reason the crack closure integral and J-integral, which are written mathematically and can be computed numerically, play important roles. The crack closure integral proposed by Irwin (1958) is based on an infinitesimal and virtual increment of crack length. It was first applied numerically as a method of computing energy release rates by Jerram and Hellen (1972) with subsequent improvements and extensions by Rybicki and Kanninen (1977), Buchholz (1984), Shivakumar et al. (1988), Raju et al. (1988), and Jih and Sun (1990). The virtual crack closure methods appear to require a fine mesh in the vicinity of the crack tip, especially for bimaterial cracks, to obtain accurate results. This is probably due to the fact that Irwin's crack closure integral involves taking the limit of the crack entension to zero, thereby requiring the placement of finite element nodes close to the crack tip in order to compute the work required to close the "infinitesimal" crack extension in a single analysis.

The J-integral by Eshelby (1956), Rice (1968), and Cherapnov (1979) is a closed contour integral of the strain energy density and work done by tractions around the crack tip and is equivalent to the energy release rate of the cracked body. Moreover, since the J-integral is path-independent and the terms on crack surface vanish in the absence of body forces and crack-face traction, the stress intensity factor (SIF) or energy release rate can be determined without having an accurate stress distribution near crack tip.

In spite of these advantages, it is difficult to compute the path-based J-integral with a domain-based numerical method such as the finite element method. Thus, Li et al. (1985) and Nikishkov and Atluri (1987) used the divergence theorem to convert the contour integral into the equivalent domain integral (EDI) which is equal to the energy release rate. Raju and Shivakumar (1990, 1992) extended the EDI method to the crack-face traction problem for both two-dimensional and three-dimensional mixed-mode problems. On the other hand, as the energy release rate is defined as the change in potential energy due to VCE, its equation can directly be derived, and de Lorenzi (1982, 1983) derived the equation for crack problems with body force and tractions using the VCE principle and mapping theory. However, though possible, it is cumbersome to compute the energy release rate using either the EDI or de Lorenzi's result, because the derivative of displacement field, which admits a singularity at the crack tip, is required.

We can view the crack extension as a geometry variation of the cracked body. Then, the energy release rate is the variation of the potential energy function due to geometry variation which has a direct analogy to shape design sensitivity analysis in shape optimization. Namely, the energy release rate is equal to shape design sensitivity for crack problems. However, to apply the shape design sensitivity technique, the design objective must be defined by a functional and the governing equations of the system must be differentiable with respect to the shape of the domain. There exists much research for determining the shape design sensitivity under these conditions, as explained by Phelan and Haber (1989). Shape design sensitivity can be calculated for general engineering field problems analytically and numerically, if the geometry of the domain is smooth. Hence, for crack-tip problems in which the geometry is not smooth, deriving the energy release rate by shape design sensitivity is difficult. Nevertheless, it is possible to derive the energy release rate by this approach. For example, by defining the geometry variation with a time-like variable, Budianski and Rice (1973) derived

[1] To whom all correspondence should be addressed.

Contributed by the Applied Mechanics Division of THE AMERICAN SOCIETY OF MECHANICAL ENGINEERS for publication in the ASME JOURNAL OF APPLIED MECHANICS.

Discussion on this paper should be addressed to the Technical Editor, Professor Lewis T. Wheeler, Department of Mechanical Engineering, University of Houston, Houston, TX 77204-4792, and will be accepted until four months after final publication of the paper itself in the ASME JOURNAL OF APPLIED MECHANICS.

Manuscript received by the ASME Applied Mechanics Division, Mar. 15, 1994; final revision, June 13, 1994. Associate Technical Editor: J. N. Reddy.

Copyright © 1995 by ASME

Downloaded 04 May 2010 to 171.66.16.28. Redistribution subject to ASME license or copyright; see http://www.asme.org/terms/Terms_Use.cfm

the $J-$, $L-$, and $M-$integrals in the absence of body forces and crack-face traction.

The purpose of this paper is to present the energy release rate equation under general loading case, including body forces and crack-face traction. The proposed energy release rate equation can easily be computed by a numerical method. Because of no restrictions on loading conditions, it can be applied to any general engineering problem which is described by a functional. Hence, although body forces and tractions including crack-face traction are only considered in this paper, this procedure to derive the energy release rate can be applied to any loading case and to cracked bodies involving dissimilar materials (i.e., composites). To demonstrate the generality and correctness of the derived energy release rate equation, several examples are solved using the finite element method.

2 Determination of Energy Release Rate Under General Load Conditions

2.1 Energy Release Rate by the Shape Design Sensitivity Approach. To derive the energy release rate which can be applied to general two-dimensional crack problems, we assume that the loads considered include body forces and tractions on crack surfaces and the material has hyperelastic deformation. Since initial stresses and strains can be modeled as resulting from body forces, these assumptions for loads and deformation permit a wide variety of engineering problems to be considered.

Consider the continuum domain Ω and boundary Γ to be nonlinearly elastic and finitely deformed. Then, the governing equation and the boundary conditions in fracture mechanics is, in general, given by

$$\sigma_{ij,j} + f_i = 0 \quad \text{in } \Omega \tag{1}$$

$$u_i = \bar{u}_i \quad \text{on } \Gamma_u \tag{2}$$

$$T_i = \bar{T}_i \quad \text{on } \Gamma_T \tag{3}$$

$$T_i \equiv \sigma_{ij} n_j \quad \text{on } \Gamma \tag{4}$$

where σ_{ij} is stress tensor, f_i are body forces per unit mass and n_i is the ith component of the unit outward normal vector $\hat{n}$ to the boundary Γ. In the above equations, $\bar{T}_i$ is the prescribed traction on boundary Γ_T and $\bar{u}_i$ is the prescribed displacement on boundary portion Γ_u. For the sake of mathematical convenience, only zero prescribed displacements will be considered (i.e., $\bar{u}_i = 0$).

Under small deformation and hyperelasticity assumption, the relationship of stresses and strains is as follows:

$$\epsilon_{ij} = \tfrac{1}{2}(u_{i,j} + u_{j,i}) \tag{5}$$

$$\sigma_{ij} = \frac{\partial W}{\partial \epsilon_{ij}}, \quad W = \int_{\epsilon_{ij}} \sigma_{ij} d\epsilon_{ij}. \tag{6}$$

In the above, W is the strain energy density function, and stress σ_{ij} is calculated by the partial derivative of W with respect to strain ϵ_{ij}. In this relation it can be shown that $\sigma_{ij} = \sigma_{ji}$, $\epsilon_{ij} = \epsilon_{ji}$.

The energy release rate G denotes the change of the total potential energy due to a virtual crack extension (VCE). The energy release rate in linear elasticity is the same as the J-integral in the absence of body force and crack-face traction and is path-independent. Hence, we can use the energy release rate concept in deriving the J-integral equation under the general loads. Mathematically, the energy release rate G is given by

$$G = -\frac{\partial \Pi}{\partial a} \tag{7}$$

where a is crack length and Π is total potential of system, i.e.,

$$\Pi = \int_\Omega W d\Omega - \int_{\Gamma_T} T_i u_i d\Gamma - \int_\Omega f_i u_i d\Omega. \tag{8}$$

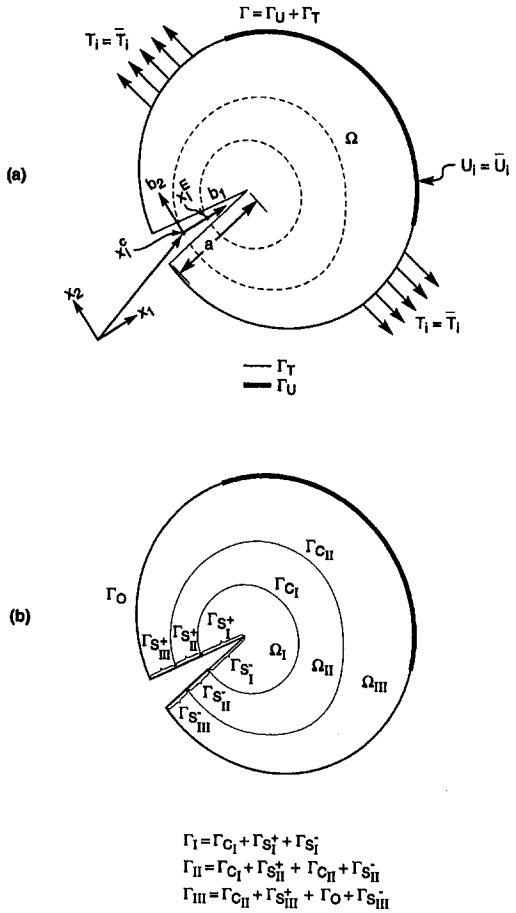


Fig. 1 The configuration of the cracked body: (*a*) geometry of the body and crack-tip coordinate system, (*b*) subdivision of body into three regions

To derive the energy release rate analytically, the domain Ω of a body is divided into the three domains Ω_I, Ω_{II}, and Ω_{III} as shown Fig. 1. The region defined by Ω_I includes the crack tip. The boundary of each region is defined by Γ_I, Γ_{II}, and Γ_{III}. The interface between region I and II is denoted as Γ_{c_I} and the interface between region II and region III is denoted by $\Gamma_{c_{II}}$, as shown Fig. 1.

It should be noted that it is mathematically permissible for region I to consist of a single point, the crack tip, for region II to consist of the remaining domain, and therefore for region III to no longer exist. However, for numerical convenience in terms of defining the design velocity, obtaining an accurate stress solution in region II, and reducing the computational effort, it is convenient to use the three finite region subdivision as illustrated in Fig. 1.

When regions I, II, and III are individually isolated, free-body equilibrium requires equal and opposite tractions to be applied on interfaces of the isolated bodies. Under these conditions the concept for VCE means that region I has rigid-body translation and region III is fixed. Therefore, these two regions do not have a variation of shape with respect to crack extension. However, the shape of region II is varied due to the rigid-body motion of region I. Accordingly, we must consider the change of potential energy due to a variation of shape of region II and solve this problem by the shape design sensitivity technique. To calculate the total energy release rate, one need only consider the change of the potential energy in region I due to rigid-body translation and the change in potential energy in region II due to shape variation.

Before deriving the energy release rate by the shape design sensitivity approach, the basic definitions are necessary. Let us

Downloaded 04 May 2010 to 171.66.16.28. Redistribution subject to ASME license or copyright; see http://www.asme.org/terms/Terms_Use.cfm

introduce a time-like variable t and define the design variables b_i, because the design variables and time-like variable are necessary for a description of the shape variation. The time-like variable is fictitious variable and a change in t implies changes in the design variables. From these definitions, the point x_i in the continuum is a function of t or design variables b_i before and after shape variation (such as a virtual crack extension). For mathematical convenience, we assume that the x-coordinate and the b-coordinate are in the same direction, that the origin of the b-coordinate is at the intersection of the crack surface and the interface $\Gamma_{c_{II}}$, and that x_1 and b_1 are in the crack direction as shown in Fig. 1. Considering b_1 as a portion of crack length, all points x_i in the cracked body can be defined by design variables. For example, all points x_i in region I are expressed by

$$x_i(\tau) = x_i(0) - x_i^E(0) + x_i^c(0) + b_i \tag{9}$$

where $x_i^c(0)$ denotes the origin of the b_i coordinate system at time $t = 0$, and $x_i^E(0)$ denotes the point at the intersection of the crack surface and the interface boundary Γ_{c_I} at $t = 0$. In Eq. (9) $t = 0$ and $t = \tau$ refer to the body shape before and after the crack extension, respectively. Then, $x_i(0)$ is the point in region I at $t = 0$, $x_i(\tau)$ is the position of the same point at $t = \tau$, and b_i describes the i–direction component of the distance from x_i^c to x_i^E at any time $t = \tau$. The design velocity is defined as (see Cea, 1981)

$$v_i \equiv \left.\frac{dx_i}{dt}\right|_{t=0} = \frac{\partial x_i}{\partial b_m}\,\delta b_m. \tag{10}$$

On the other hand, the material derivative of an arbitrary function $g(x)$ is written as follows:

$$\dot{g}(x) \equiv \frac{dg}{dt} = \frac{\partial g}{\partial t} + v_j\frac{\partial g}{\partial x_j} = g' + v_j g_{,j}. \tag{11}$$

The original body is divided into three regions, one of which contains the crack tip. Since the total potential energy is the sum of the potential energies for regions I, II, and III, the material derivative of the total potential energy is

$$\dot{\Pi} \equiv \frac{\partial \Pi}{\partial b_m}\,\delta b_m = \frac{\partial \Pi}{\partial a}\,\delta b_1 = \dot{\Pi}_I + \dot{\Pi}_{II} + \dot{\Pi}_{III}. \tag{12}$$

In Eq. (12), as region III has neither translation nor shape variation, the material derivative of its potential energy is identically equal to zero. Region I has translation without shape variation, and the variation of the potential energy function for region I does exist. Though region I includes the crack tip which admits a mathematical singularity, it is relatively simple to derive the energy release rate for it because it does not vary in shape (see Appendix A):

$$\dot{\Pi}_I = -\int_{\Omega_I} \dot{f}_i u_i\, d\Omega - \int_{\Gamma_I} \dot{T}_i u_i\, d\Omega. \tag{13}$$

The shape of region II is varied due to the rigid-body translation of region I. Considering this shape variation, the material derivative of the potential energy of region II was obtained from the shape design sensitivity technique by Haug, Choi, and Komkov (1986) (see Appendix B).

$$\begin{aligned}\dot{\Pi}_{II} = &\int_{\Gamma_{II}} W v_k n_k d\Gamma - \int_{\Gamma_{II}} \dot{T}_i u_i\, d\Gamma - \int_{\Gamma_{II}} T_i u_{i,k} v_k d\Gamma \\ &- \int_{\Gamma_{S_{II}}} T_i u_i (v_{k,k} - v_{l,m} n_l n_m) d\Gamma - \int_{\Omega_{II}} \dot{f}_i u_i\, d\Omega \\ &+ \int_{\Omega_{II}} f_{i,k} v_k u_i\, d\Omega - \int_{\Gamma_{II}} f_i u_i v_k n_k d\Gamma \end{aligned} \tag{14}$$

Because the traction on interface Γ_{c_I} between Ω_I and Ω_{II} have equal magnitudes and opposite directions, the terms involving these interfaces have been eliminated in the total energy expression. Summing up these equations, we can finally derive the following result for the variation of total potential energy:

$$\begin{aligned}\dot{\Pi} = &\int_{\Gamma_{II}} W v_k n_k d\Gamma - \int_{\Gamma_{II}} T_i u_{i,k} v_k d\Gamma - \int_{\Gamma_{S_I}+\Gamma_{S_{II}}} \dot{T}_i u_i\, d\Gamma \\ &- \int_{\Gamma_{S_{II}}} T_i u_i (v_{k,k} - v_{l,m} n_l n_m) d\Gamma - \int_{\Omega_I+\Omega_{II}} \dot{f}_i u_i\, d\Omega \\ &+ \int_{\Omega_{II}} f_{i,k} v_k u_i\, d\Omega - \int_{\Gamma_{II}} f_i u_i v_k n_k d\Gamma. \end{aligned} \tag{15}$$

In the above expression, boundary Γ_{S_I} and $\Gamma_{S_{II}}$ constitute the crack surface in domains I and II with prescribed surface traction.

Note the procedure used to derive the above equation. The material derivative of the potential energy is the variation of the response function due to the crack extension. A design variable b_1 is taken as a portion of the crack length and δb_1 denotes the crack extension. Thus, the velocity on the interface Γ_{c_I} is δb_1 and the velocity on interface $\Gamma_{c_{II}}$ is zero. Introducing these relations into Eq. (15) in the absence of body force and crack-face traction, we have the following expression:

$$\dot{\Pi} = \frac{\partial \Pi}{\partial b_1}\,\delta b_1 = \left[\int_{\Gamma_{c_I}} (W n_1 - T_i u_{i,1}) d\Gamma\right]\delta b_1. \tag{16}$$

This result is the same as the J-integral proposed by Rice (1968) for a reverse integral path. Hence, we conclude that Eq. (15) is the extended J-integral under general loading conditions.

Generally, the stresses in crack problems are calculated by numerical methods because most engineering problems are impossible to solve by analytical methods. Equation (15) involves line integrals which should be determined as accurately as possible. However, if the finite element method (FEM) is used to compute the energy release rate according to Eq. (15), computational errors are introduced due to the line integrals. In the FEM the stress and strain on the boundary have a higher order of error than at the superconvergent Gauss points inside the element. Hence, to improve numerical accuracy, the line integrals in Eq. (15) are transformed to domain integrals using Gauss's divergence theorem, yielding

$$\begin{aligned}\dot{\Pi} = &\int_{\Omega_{II}} (W v_k)_{,k} d\Omega - \int_{\Omega_{II}} (\sigma_{ij} u_{i,k} v_k)_{,j} d\Omega - \int_{\Omega_I+\Omega_{II}} \dot{f}_i u_i\, d\Omega \\ &+ \int_{\Omega_{II}} f_{i,k} v_k u_i\, d\Omega - \int_{\Omega_{II}} (f_i u_i v_k)_{,k} d\Omega - \int_{\Gamma_{S_I}+\Gamma_{S_{II}}} \dot{T}_i u_i\, d\Gamma \\ &- \int_{\Gamma_{S_{II}}} T_i u_i (v_{k,k} - v_{l,m} n_l n_m) d\Gamma. \end{aligned} \tag{17}$$

Then, introducing the relations

$$W_{,k} \equiv \frac{\partial W}{\partial x_k} = \sigma_{ij}\epsilon_{ij,k} = \sigma_{ij} u_{i,jk}, \tag{18}$$

the following equation can be derived:

$$\begin{aligned}\dot{\Pi} = &\int_{\Omega_{II}} \{(W - f_i u_i) v_{k,k} - \sigma_{ij} u_{i,k} v_{k,j}\}\, d\Omega - \int_{\Omega_I+\Omega_{II}} \dot{f}_i u_i\, d\Omega \\ &- \int_{\Gamma_{S_I}+\Gamma_{S_{II}}} \dot{T}_i u_i\, d\Gamma - \int_{\Gamma_{S_{II}}} T_i u_i (v_{k,k} - v_{l,m} n_l n_m) d\Gamma. \end{aligned} \tag{19}$$

Since the traction and the body forces are functions of b_1, the material derivatives of all loads can be obtained analytically in this final equation. Hence, Eq. (19) can be easily programmed into a finite element code once the design velocity is defined in the domain.

Downloaded 04 May 2010 to 171.66.16.28. Redistribution subject to ASME license or copyright; see http://www.asme.org/terms/Terms_Use.cfm

Either Eq. (15) or (19) can be used to calculate the energy release rate. If one can accurately obtain stresses and displacements, Eq. (15) is recommended because the design velocity in the domain with shape variation is not necessary. However, when a numerical method such as the finite element method is employed which exhibits a higher order of error on the boundary, Eq. (19) is recommended. This equation can easily be programmed into a finite element code. We note that Eq. (19) is more useful than de Lorenzi's result (1985) because it does not involve the derivative of displacements on the crack surface. On the other hand, Eq. (19) does require the design velocity in the domain, and in this paper we have assumed the design velocity to vary linearly. Although this assumption is physically reasonable, it may be possible to improve results by the selection of a different design velocity function.

In the case that the body forces and crack-face tractions do not vary during crack extension (i.e., the forces and tractions are constant with respect to spatial coordinates), the energy release rate reduces to

$$\dot{\Pi} = \int_{\Omega_{II}} \{(W - f_i u_i) v_{k,k} - \sigma_{ij} u_{i,k} v_{k,j}\} d\Omega - \int_{\Gamma_{S_{II}}} T_i u_i (v_{k,k} - v_{l,m} n_l n_m) d\Gamma. \quad (20)$$

Equation (20) involves domain integration over region II, Ω_{II}, which excludes the crack tip and path integration over a portion of the crack face $\Gamma_{S_{II}}$ which excludes the crack tip. Under these conditions the energy release rate given by Eq. (20) is independent of Ω_{II} and the associated crack-face boundary $\Gamma_{S_{II}}$. Since the definition of Ω_{II} uniquely defines Γ_{II} (and not vice versa), we refer to this energy release rate equation as being domain independent.

2.2 Determination of Domain Velocity. In the above section, we derived the energy release rate Eqs. (15) and (19) using the shape design sensitivity approach. The energy release rate can be calculated from Eq. (15) using the velocities on interface Γ_{c_I} and $\Gamma_{c_{II}}$ as δb_1 and 0, respectively. However, if Eq. (19) is employed to avoid the inaccuracy associated with line integrals in the FEM, we must determine the domain velocity for the region II. For region II the velocity of the interface boundary $\Gamma_{c_{II}}$ is zero and the velocity of the interface boundary Γ_{c_I} is the same as the velocity of region I. Therefore, velocities in the domain of the region II must exist between zero and δb_1, but it is impossible to obtain the velocity field mathematically. For this reason we assume that the design velocity varies linearly in region II. This assumption is physically reasonable. Of course, region III has zero velocity and region I has constant velocity δb_1. Thus, the velocity of all regions is as follows:

$$v_k = \delta b_k \quad \text{in } \Omega_I \quad (21)$$

$$v_k = c(s)\delta b_k \quad \text{in } \Omega_{II} \quad (22)$$

$$v_k = 0 \quad \text{in } \Omega_{III} \quad (23)$$

where $c(s)$ is a linear function and s denotes the normal distance from interface boundary Γ_{c_I} to $\Gamma_{c_{II}}$.

Although the design velocity can be calculated by linear interpolation, it is difficult to obtain the design velocity fields in the arbitrary domain except special cases. For an example, we can evaluate the velocities for a hollow circular region, defining the velocity to be inversely proportional to the distance from the center. However, relatively large computation time is needed for calculation of the design velocity in an arbitrary shape region. If we let region II be a one-element-thick layer, this problem can simply be solved. Considering a one-element-thick layer and taking an eight-noded isoparametric element as shown Fig. 2, midside nodes 6 and 8 have velocity $\frac{1}{2}\delta b_1$. The velocity field within region II can be obtained by interpolation of the boundary velocity and this velocity.

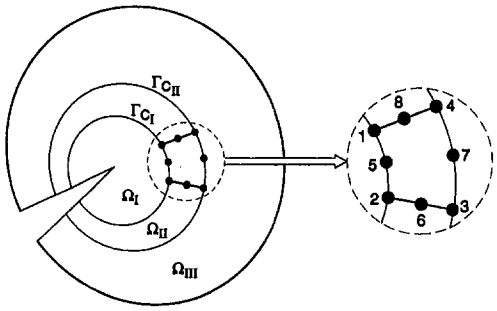


Fig. 2 Modeling of the cracked body for numerical analysis by the finite element method

3 Numerical Applications

The energy release rate equation derived in this paper is a general form which includes all loading conditions. For the case of uniform crack-face traction and body force, the resulting equation is domain independent, because the material derivatives of these loads are zero. The derived equation can be easily implemented into a finite element code. Using the decomposition method published by Ishikawa (1980), which decomposes the symmetric part and antisymmetric part of displacement and the stress field, it is possible to separate and compute mode I and mode II energy release rates for mixed-mode problems.

To show the correctness of Eqs. (15) and (19) and these observations, loads such as remote loading, crack-face traction, and gravity are treated in several examples. In all examples six-noded triangular quarter point (i.e., singular) elements were employed to model the crack-tip region and standard eight-noded quadratic quadrilateral isoparametric elements were used elsewhere.

3.1 Center Crack Problems Under Remote Loading and Crack-face Traction. Consider the center crack as shown in Fig. 3(*a*). A crack length-to-width ratio of 0.8 was taken. To show the generality of the proposed energy release rate equation, two loading cases are treated. One is the crack problem with remote uniform tensile load, and the other is the crack problem under uniform normal pressure on the crack surface. Due to the symmetry in the problems, one quarter of the body was modeled with 96 elements including eight crack-tip elements as shown in Fig. 3(*b*). In Fig. 3(*b*) the regions D_1, D_2, and D_3 denote the different domains selected to evaluate the energy release rate.

These examples are mode I fracture problems. Raju and Shivakumar (1990) solved this problem using the EDI method and a special integration rule to calculate the line integral for the derivative of displacement on the crack surface. Their results for the nondimensional J-integral ranged from 3.270 to 3.298 for the various integration paths taken. These values are taken to compare with those obtained by the shape design sensitivity approach which does not involve the derivative of displacement on crack surface. Since the material derivative of prescribed uniform crack face pressure is zero in these examples, line integration for region I with the crack tip is not needed. Hence, the resulting energy release rate Eq. (19) was completely determined from a selected domain which excluded the crack tip.

Table 1 present the value of the normalized energy release rate for various domain. As expected, the results of the remote loading case and crack-face loading case are exactly the same. From Table 1 we can see that the results by the present method

Downloaded 04 May 2010 to 171.66.16.28. Redistribution subject to ASME license or copyright; see http://www.asme.org/terms/Terms_Use.cfm

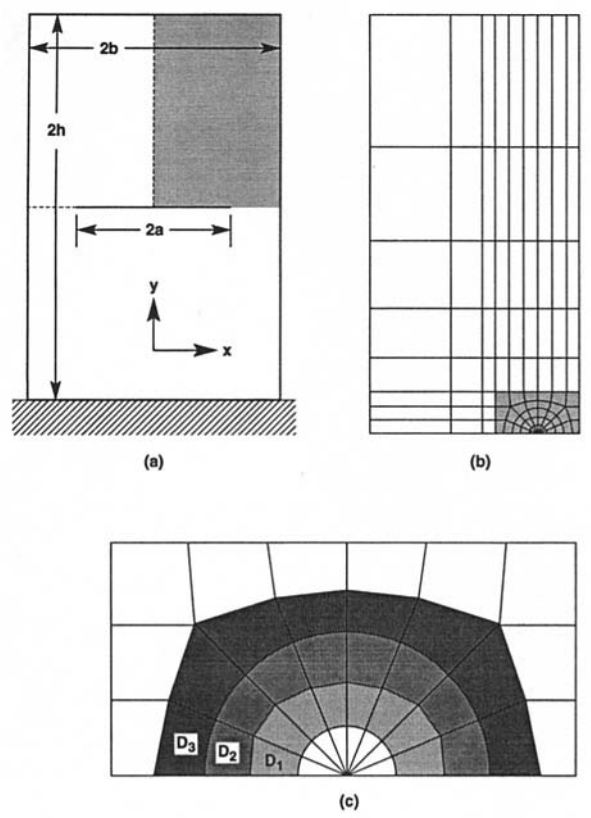


Fig. 3 The center-crack plate problem, (*a*) configuration ($h/b = 2$, $a/b = 0.8$), (*b*) finite element model, (*c*) zoom plot of crack-tip region showing the three different Ω_{ll} domains selected

are in the range of Raju and Shivakumar's results, and that the results calculated from each integral path are nearly identical; the mean value was 3.2746 and the maximum deviation was approximately 0.1 percent. As evidenced by these numerical results, we can conclude that the derived energy release rate Eq. (19) is domain independent.

3.2 Edge Crack Subject to Gravity. In the previous example, it was seen that the derived energy release rate equation can be applied to crack problems which include crack-face traction. To prove the correctness of the Eqs. (15) and (19) for the case of body forces, consider, for simplicity, a plate with an edge crack subject to gravity. As shown in Fig. 4(*a*), the width of plate to the height was taken as $\frac{7}{16}$ and the crack length as the half of the width. This problem was solved by the FEM and the plate was modeled with 38 finite element as shown in Fig. 4(*b*). The direction of gravity is the negative y-direction. Since the material derivative of the body force is zero under constant body force, the resulting energy release rate equation is domain independent.

Table 1 Comparison of G_x^* for center-crack problem under crack face and remote loading ($a/b = 0.8$; $G_x^* = (EG_x)/(p^2\pi a(1-\nu^2))$)

Domain	G_x^*	
	Crack face load	Remote load
D_1	3.271	3.271
D_2	3.276	3.276
D_3	3.277	3.277
Raju and Shivakumar	3.270–3.309	3.270–3.309

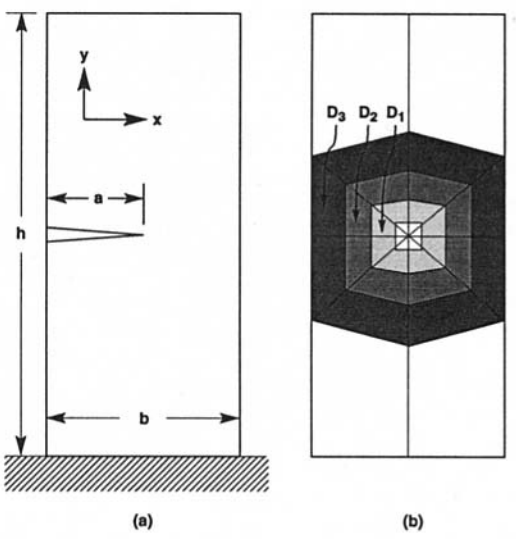


Fig. 4 The edge-crack plate problem, (*a*) configuration ($b/a = 2.0$, $b/h = \frac{7}{16}$), (*b*) finite element model showing the three different Ω_{ll} domains selected

This example has both mode I and mode II stress intensity factors. Although mode separation by the decomposition method is possible, G_x, which is the sum of mode I and mode II energy release rates, was calculated from three different domain integrals to show domain independency. The results are given in Table 2. It is seen that the computed G_x value for each integral domain are nearly identical (the average of the nondimensional $G_x = 0.9356$ with a maximum deviation of 0.16 percent). When this problem was solved using a finer mesh of 96 elements, the maximum deviation was reduced to 0.11%. This convergent behavior of the numerical results with respect to mesh refinement helps confirm that the final energy release equation (19) is correct for crack problems involving body forces.

3.3 Crack in Semi-Infinite Plane Under Crack Surface Pressure. Consider the internal crack parallel to the boundary of a semi-infinite plane. A uniform normal pressure acts on the crack surface as shown Fig. 5(*a*). A depth to crack length ratio ($h/2a$) of 0.3 was taken. Due to the symmetry in the problem, half of the body was considered. This infinite plane problem cannot be exactly solved by the FEM (without resorting to special "infinite" finite elements). However, we can approximately solve this problem by modeling the semi-infinite plane as a large finite plane. Thus, in this example we solved the finite plate problem with a crack length to radius ratio of 0.1, and the plate was modeled with 399 elements including 12 crack tip elements as shown in Figure 5(*b*). Again the notations D_1, D_2, D_3, and D_4 denote the domains used to evaluate the energy release rate.

This problem is a mixed mode one and therefore both mode I and mode II stress intensity factors must be calculated. In mixed mode crack problems without crack-face traction and body force, the decomposition method evaluates K_I and K_{II} accurately and is easily implemented into a conventional finite element code, different from other methods (e.g., see Bortman

Table 2 Comparison of G_x^* for the edge crack problem under gravity ($a/b = 0.5$; $G_x^* = (EG_x)/((\rho gh)^2\pi a(1-\nu^2))$)

Domain	G_x^*
D_1	0.9344
D_2	0.9349
D_3	0.9370

Downloaded 04 May 2010 to 171.66.16.28. Redistribution subject to ASME license or copyright; see http://www.asme.org/terms/Terms_Use.cfm

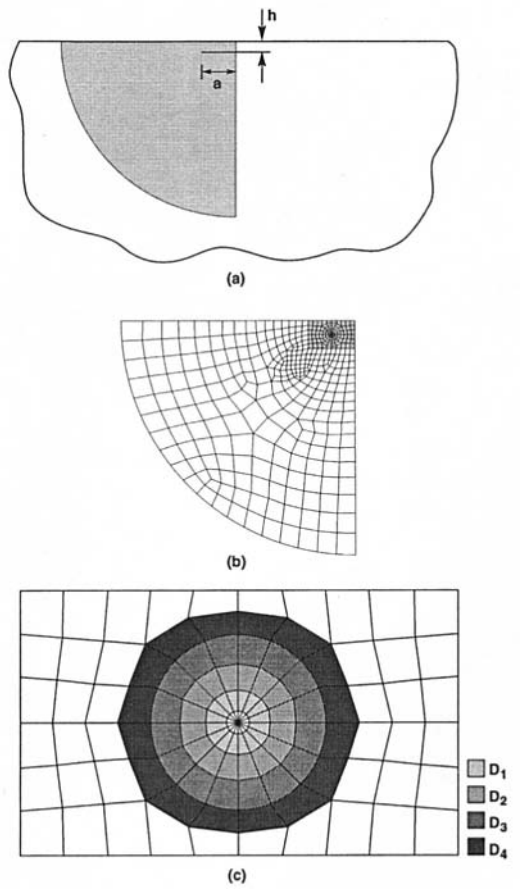


Fig. 5 Semi-infinite plane with collinear crack (*a*) configuration (h/a = 0.6), (*b*) finite element model, (*c*) zoom plot of crack-tip region showing the four different Ω_q domains selected

et al., 1983, and Yau et al., 1980). We can extend the use of the decomposition method to the crack problem with general loading conditions, because the resulting energy release rate equation (19) was derived without special assumptions and is described by a functional.

This example was previously solved by the boundary element method (Wang and Blom, 1990), by the continuously distributed dislocation method (Higashida and Kamada, 1982) and by the singularity integral equation method (Erdogan et al., 1973). Wang and Blom's and Higashida and Kamada's results are in good agreement. Therefore, Wang and Blom's results (1990) were selected as a reference. Since the crack-face pressure is uniform as previous examples, the final energy release rate equation is domain independent. Utilizing this fact, normalized K_I and K_{II} for different integral domains were obtained as shown Table 3. The numerical results given from integral domains are nearly indentical. The mean and maximum variation values were 2.0800 and 0.02 percent for K_I and 0.4931 and 0.04 percent for K_{II}. Comparing these results with the reference value, the results by the shape sensitivity have 0.4 percent and 2.7 percent error for K_I and K_{II}. However, considering the fact that the semi-infinite domain was modeled as a finite domain and solved by the FEM, the numerical results by the proposed method and the results by Wang and Blom show very good agreement.

Table 3 Comparison of K_I^* and K_{II}^* for semi-infinite plane problem under uniform crack-face traction ($K^* = (K)/(p(\pi a)^{1/2})$)

Domain	K_I^*	K_{II}^*
D_1	2.0793	0.4930
D_2	2.0802	0.4932
D_3	2.0803	0.4932
D_4	2.0803	0.4932
Wang and Bloom	2.0724	0.480

4 Conclusions

In this paper the energy release rate equation was presented for two-dimensional crack problems with general loading conditions. Defining design velocity and using the material derivative, it was analytically derived by the shape design sensitivity. Since this new approach directly used the weak governing equations and the potential energy as a funtional, its evaluation is independent of any numerical method. In contrast to other researchers' results, the proposed energy release rate equation does not include the derivative of the displacement field on the boundary, which admits a singular at the crack tip and which makes accurate numerical calculations difficult. Moreover, if body forces and crack-face tractions are constant in the cracked body with respect to the virtual crack extension, the resulting integral equation for the energy release rate involves a domain-independent integral and associated path-independent integral.

Three examples were numerically solved by the finite element method. The results show that the new method yielded accurate energy release rates for Mode I and II, even for a relatively coarse mesh. In addition, the numerical results confirmed that the derived energy release rate equation in the case of constant body forces and uniform crack-free tractions is domain independent. From these examples we conclude that the energy release rate equation derived by the shape design sensitivity approach is an accurate and efficient method for calculating mixed-mode fracture parameters under general loading conditions.

Acknowledgments

This first author thanks the Korea Science and Engineering Foundation for financial support and the Department of Mechanical Engineering at the University of Massachusetts for this Visiting Professor opportunity.

References

Bortman, Y., and Banks-Hills, L., 1983, "An Extended Weight Function Method for Mixed-Mode Elastic Crack Analysis," ASME JOURNAL OF APPLIED MECHANICS, Vol. 50, pp. 907–909.

Buchholz, F. G., 1984, "Improved formulae for the finite element calculation of strain energy release rate by the modified crack closure integral method," *Accurate Reliability and Training in FEM Technology,* Robinson and Associates, Dorset, pp. 650–659.

Budiansky, B., and Rice, J. R., 1973, "Conservation Laws and Energy Release Rates," ASME JOURNAL OF APPLIED MECHANICS, Vol. 40, pp. 201–203.

Cea, J., 1981, "Problems of Shape Optimal Designs," *The Optimization of Distributed Parameter Structures,* Sijthoff-Noordhoff, Alphen aan den Rijn, The Netherlands, pp. 1005–1048.

Cherapanov, G. P., 1979, *Mechanics of Brittle Fracture,* McGraw-Hill, New York.

de Lorenzi, H. G., 1982, "On Energy Release Rate and the *J*-integral for 3-D Crack Configuration," *International Journal of Fracture,* Vol. 19, pp. 183–192.

de Lorenzi, H. G., 1985, "Energy Release Rate Calculation by Finite Element Method," *Engineering Fracture Mechanics,* Vol. 21, pp. 129–143.

Erdogen, F., Gupta, G. D., and Cook, T. S., 1973, *Methods of Analysis and Solutions of Crack Problems,* G. C. Sih, ed., Noordhoff, Groningen, pp. 391–396.

Eshelby, J. D., 1956, "The Continuum Theory of Lattice Defects," *Solid State Physics,* Vol. 3, Academic Press, New York, pp. 79–144.

Haug, E. J., Choi, K. K., and Komkov, V., 1986, *Design Sensitivity Analysis of Structural Systems,* Academic Press, New York.

Higashida, Y., and Kamada, K., 1982, "Stress Fields Around a Crack Lying Parallel to a Free Surface," *Int. J. Fracture,* Vol. 19, pp. 39–52.

Hellen, T. K., 1975, "On the Method of Virtual Crack Extenstion," *International Journal for Numerical Metheods in Engineering,* Vol. 9, pp. 183–192.

Irwin, G. R., 1958, "Fracture Mechanics," *Structural Mechanics: Proceedings of the 1st Symposium on Naval Structural Mechanics,* J. N. Goodier and N. J. Hoff, eds., Pergamon Press, New York, 1960, pp. 557–591.

Ishikawa, H., 1980, "A Finite Element Analysis of Stress Intensity Factors for Combined Tensile and Shear Loading by Only a Virtual Crack Extension," *International Journal of Fracture,* Vol. 16, pp. R243–R246.

Downloaded 04 May 2010 to 171.66.16.28. Redistribution subject to ASME license or copyright; see http://www.asme.org/terms/Terms_Use.cfm

Jerram, K., and Hellen, T. K., 1972, "Finite element techniques in fracture mechanics," *International Conference on Welding Research Related to Power Plants,* Southampton, U.K.

Jih, C. J., and Sun, C. T., 1990, "Evaluation of a Finite Element Based Crack Closure Method for Calculating Static and Dynamic Strain Energy Release Rates," *Engineering Fracture Mechanics,* Vol. 37, No. 2, pp. 313–327.

Li, F. Z., Shih, C. F., and Needleman, A., 1985, "A Comparison of Methods for Calculating Energy Release Rate," *Engineering Fracture Mechanics,* Vol. 21, pp. 405–421.

Nikishkof, G. P., and Atluri, S. N., 1987, "Caculation of Fracture Mechanics Parameters for an Arbitray Three-dimensional Crack by Equiavalent Domain Integral Method," *International Journal for Numerical Methods in Engineering,* Vol. 24, pp. 1801–1821.

Parks, D. M., 1974, "A Stiffness Derivative Finite Element Technique for Determination of Crack Tip Stress Intensity Factors," *International Journal of Fracture,* Vol. 10, pp. 487–502.

Phelan, D. G., and Haber, R. B., 1989, "Sensitivity analysis of linear elastic system using domain parameterization and mixed multual energy principle," *Computer Methods in Applied Mechanics and Engineering,* Vol. 77, pp. 31–59.

Raju, I. S., Shivakumar, K. N., and Crews, J. H., 1988, "Three-Dimensional Static Analysis of a Composite Double Cantilever Beam Specimen," *AIAA Journal,* Vol. 26, No. 12, Dec., pp. 1493–1498.

Raju, I. S., and Shivakumar, K. N., 1990, "An Equivalent Domain Integral Method in the Two-dimensional Analysis of Mixed Mode Crack Problems," *Engineering Fracture Mechanics,* Vol. 37, pp. 707–725.

Rice, J. R., 1968, "A Path-independent Integral and Approximate Analysis of Strain Concentration by Notches and Cracks," ASME JOURNAL OF APPLIED MECHANICS, Vol. 35, pp. 376–386.

Rybicki, E. F., and Kanninen, M. F., 1977, "A finite element calculation of stress intensity factors by modified crack closure integral," *Engineering Fracture Mechanics,* Vol. 9, pp. 931–938.

Shivakumar, K. N., Tan, P. W., and Newman, J. C. Jr., 1988, "A Virtual Crack Closure Technique for Calculating Stress-Intensity Factors for Cracked Three-dimensional Bodies," *International Journal of Fracture,* Vol. 36, pp. R43–R50.

Shivakumar, K. N., and Raju, I. S., 1992, "An Equivalent Domain Integral Method for Three-dimensional Mixed Mode Fracture Problems," *Engineering Fracture Mechanics,* Vol. 42, pp. 935–959.

Wang, G. S., and Blom, A. F., 1990, "The Stress Intensity Factors for Pressed Cracks in Arbitrary Shapes," *Engineering Fracture Mechanics,* Vol. 37, pp. 1165–1181.

Yau, J. F., Wang, S. S., and Corten, H. T., 1980, "A Mixed-Mode Crack Analysis of Isotropic Solids Using Conservation Laws of Elasticity," ASME JOURNAL OF APPLIED MECHANICS, Vol. 47, pp. 335–341.

APPENDIX A

Material Derivative of Potential Energy for Region I

Consider region I which has only rigid-body motion in the direction collinear with the crack and no variation in shape. For this region the material derivative of the potential energy is

$$\dot{\Pi}_I \equiv \frac{\partial \Pi_I}{\partial b_m}\,\delta b_m = \int_{\Omega_I} \dot{W} d\Omega - \int_{\Gamma_I} (\dot{T}_i u_i + T_i \dot{u}_i) d\Gamma - \int_{\Omega_I} (\dot{f}_i u_i + f_i \dot{u}_i) d\Omega. \quad (24)$$

In this equation $\dot{W}$ means that

$$\dot{W} \equiv \frac{\partial W}{\partial \epsilon_{ij}}\,\dot{\epsilon}_{ij} = \sigma_{ij}\,\frac{\partial \epsilon_{ij}}{\partial b_m}\,\delta b_m. \quad (25)$$

From Eq. (25) and the governing system of Eqs. (1)–(6), the following relation is obtained since the domain Ω_I has the same geometry at any time:

$$\int_{\Gamma_I} \sigma_{ij} n_j \dot{u}_i d\Gamma = \int_{\Omega_I} \sigma_{ij} \dot{\epsilon}_{ij} d\Omega - \int_{\Omega_I} f_i \dot{u}_i d\Omega. \quad (26)$$

Hence, by definition of $\dot{W}$ and T_i, we can derive the functional

$$\int_{\Omega_I} \dot{W} d\Omega = \int_{\Gamma_I} T_i \dot{u}_i d\Gamma + \int_{\Omega_I} f_i \dot{u}_i d\Omega. \quad (27)$$

This equation is the virtual work principle of a body having only translation without shape variation. Substituting (27) into (24) yields

$$\dot{\Pi}_I = -\int_{\Omega_I} \dot{f}_i u_i d\Omega - \int_{\Gamma_I} \dot{T}_i u_i d\Gamma. \quad (28)$$

APPENDIX B

Material Derivative of Potential Energy for Region II

As the shape of region II is varied, we must use the shape design sensitivity technique here. Considering the variation of shape, the material derivative of the potential energy of region II is written as

$$\dot{\Pi}_{II} = \int_{\Omega_{II}} \dot{W} d\Omega + \int_{\Omega_{II}} W d\dot{\Omega} - \int_{\Gamma_{II}} (\dot{T}_i u_i + T_i \dot{u}_i) d\Gamma - \int_{\Gamma_{II}} T_i u_i d\dot{\Gamma} - \int_{\Omega_{II}} (\dot{f}_i u_i + f_i \dot{u}_i) d\Omega - \int_{\Omega_{II}} f_i u_i d\dot{\Omega} \quad (29)$$

where

$$d\dot{\Omega} = v_{k,k} d\Omega \quad (30)$$

$$d\dot{\Gamma} = (v_{k,k} - v_{l,m} n_l n_m) d\Gamma. \quad (31)$$

Considering definition (11) and Eq. (30), the first two terms of Eq. (29) are

$$\int_{\Omega_{II}} \dot{W} d\Omega + \int_{\Omega_{II}} W d\dot{\Omega} = \int_{\Omega_{II}} W' d\Omega + \int_{\Omega_{II}} W_{,k} v_k d\Omega + \int_{\Omega_{II}} W v_{k,k} d\Omega = \int_{\Omega_{II}} W' d\Omega + \int_{\Gamma_{II}} W v_k n_k d\Gamma \quad (32)$$

where the divergence theorem has been invoked to obtain the last relation. The same procedure as above can be applied to the last two terms in Eq. (29) and the final result is

$$\dot{\Pi}_{II} = \int_{\Omega_{II}} W' d\Omega + \int_{\Gamma_{II}} W v_k n_k d\Gamma - \int_{\Gamma_{II}} \{\dot{T}_i u_i + T_i (u_{i'} + u_{i,j} v_j)\} d\Gamma - \int_{\Gamma_{II}} T_i u_i d\dot{\Gamma} - \int_{\Omega_{II}} (f_i' u_i + f_i u_i') d\Omega - \int_{\Gamma_{II}} f_i u_i v_k n_k d\Gamma \quad (33)$$

We note that $v_{i,j} = 0$ on interface boundary Γ_{c_I} and $\Gamma_{c_{II}}$. Hence, the fourth term in Eq. (33) is as follows:

$$\int_{\Gamma_{II}} T_i u_i d\dot{\Gamma} = \int_{\Gamma_{S_{II}}} T_i u_i d\dot{\Gamma} \quad (34)$$

where boundary $\Gamma_{S_{II}}$ denotes the crack surface in domain II.

On the other hand, as the time-like variable t is independent of x_i in the (t, x_i) coordinate, the following virtual work expression is derived:

$$\int_{\Omega_{II}} W' d\Omega \equiv \int_{\Omega_{II}} \sigma_{ij} \frac{\partial \epsilon_{ij}}{\partial t}\, d\Omega = \int_{\Gamma_{II}} \sigma_{ij} n_j \frac{\partial u_i}{\partial t}\, d\Gamma + \int_{\Omega_{II}} f_i \frac{\partial u_i}{\partial t}\, d\Omega = \int_{\Gamma_{II}} T_i u_i' d\Gamma + \int_{\Omega_{II}} f_i u_i' d\Omega. \quad (35)$$

Substituting (35) and (31) into (33), the final equation for the material derivative of the potential energy of region II is

$$\dot{\Pi}_{II} = \int_{\Gamma_{II}} W v_k n_k d\Gamma - \int_{\Gamma_{II}} (\dot{T}_i u_i + T_i u_{i,j} v_j) d\Gamma - \int_{\Gamma_{S_{II}}} T_i u_i (v_{k,k} - v_{l,m} n_l n_m) d\Gamma - \int_{\Omega_{II}} \dot{f}_i u_i d\Omega + \int_{\Omega_{II}} f_{i,k} v_k u_i d\Omega - \int_{\Gamma_{II}} f_i u_i v_k n_k d\Gamma. \quad (36)$$

Downloaded 04 May 2010 to 171.66.16.28. Redistribution subject to ASME license or copyright; see http://www.asme.org/terms/Terms_Use.cfm

Stability of Cohesive Crack Model: Part I—Energy Principles

Z. P. Bažant
Walter Murphy Professor of Civil Engineering and Material Science, Fellow ASME.

Yuan-Neng Li
Research Assistant Professor.
Department of Civil Engineering, Northwestern University, Evanston, IL 60208

The paper deals with a cohesive crack model in which the cohesive (crack-bridging) stress is a specified decreasing function of the crack-opening displacement. Under the assumption that no part of the crack undergoes unloading, the complementary energy and potential energy of an elastic structure which has a cohesive crack and is loaded by a flexible elastic frame is formulated using continuous influence functions representing compliances or stiffnesses relating various points along the crack. By variational analysis, in which the derivatives of the compliance or stiffness functions with respect to the crack length are related to the crack-tip stress intensity factors due to various unit loads, it is shown that the minimizing conditions reduce to the usual compatibility or equilibrium equations for the cohesive cracks. The variational equations obtained can be used as a basis for approximate solutions. Furthermore, the conditions of stability loss of a structure with a growing cohesive crack are obtained from the condition of vanishing of the second variation of the complementary energy or the potential energy. They have the form of a homogeneous Fredholm integral equation for the derivatives of the cohesive stresses or crack opening displacements with respect to the crack length. Loadings with displacement control, load control, or through a flexible loading frame are considered. Extension to the analysis of size effect on the maximum load or maximum displacement are left to a subsequent companion paper.

1 Introduction

Quasi-brittle materials, such as concrete, ice (especially sea ice), rocks, ceramics, and certain composites, exhibit a large fracture process zone in which the material undergoes progressive softening damage. The process zone may be approximated by the cohesive crack model, in which the fracture process zone is represented by crack-bridging tensile stresses (cohesive stresses) which decrease with crack opening. The basic concept originated with the work of Barenblatt (1962) and Dugdale (1960), who introduced two different versions of the cohesive crack model. While Dugdale considered the cohesive stresses to be constant in order to simulate plastic behavior of metals near the crack tip, Barenblatt, in an effort to model the reduction of interatomic bond forces, introduced cohesion as a gradual softening process. Barenblatt studied equilibrium but not stability and solved only problems in which the cohesive zone is infinitesimal and the distribution of the cohesive stresses can be assumed a priori, independent of the solution of the crack opening profile. Dugdale, on the other hand, considered a cohesive zone of finite length, in the context of plastic yielding. The problem of finding the peak load for the Dugdale model was later solved by Bilby, Cottrell, and Swinden (1963), who introduced for plastic cohesive stresses a critical crack-opening displacement at which the cohesive (crack-bridging) stress drops to zero.

Later studies have led to further diversification of the cohesive stress models. Some generalizations of Barenblatt's model do not have a uniquely defined stress-displacement law. Instead, the stress distribution along the cohesive portion of the crack is assumed a priori, with a process zone which may or may not be infinitesimal. Within this category, the models of Willis (1967), Smith (1974), and Reinhardt (1985) deserve mention. In another common type of cohesive crack models, there is a stress-displacement law but the effective energy release rate is calculated according to Rice's (1968) equation which was originally developed for small-scale yielding only. Nevertheless, this equation has often been extended beyond the small-scale yielding conditions, to situations in which the cohesive zone (or damage zone) is not negligible compared to the characteristic size of the structure (e.g., Suo et al., 1992). Although one basic characteristic of the cohesive crack models introduced by Barenblatt and Dugdale is that the stress intensity factor at the crack tip is zero, some recent modified forms of the cohesive crack model admit a positive stress intensity factor at the crack tip (Foote et al., 1986; Rice, 1992). There are also differences in the definition of stress-displacement law. Normally the cohesive stress is finite as soon as a crack starts to open, being equal to the tensile strength of the material, and subsequently the stress declines. But in some recent models, the cohesive stress starts to increase from zero as the crack begins to open, and only later softening takes place. This formulation, which is not considered in the present paper, has recently been used by Needleman (1990) and Tvergaard and Hutchinson (1992) in studies of the interface between plastic materials.

This study deals with the normal case of cohesive crack model, different from that in the aforementioned studies. The basic characteristics are (1) the length of the cohesive zone is finite, i.e., not negligible compared to the structure dimensions; (2) the stress intensity factor at the crack tip is zero (which means the stress at the tip is finite); (3) the cohesive stress depends on the crack-opening displacement according to a specified softening law; and (4) the material surrounding the crack behaves in a linearly elastic manner. Such a model (under the name "fictitious crack model") was first introduced for con-

Contributed by the Applied Mechanics Division of THE AMERICAN SOCIETY OF MECHANICAL ENGINEERS for presentation at the International Mechanical Engineering Congress and Exhibition, the Winter Annual Meeting of the ASME, San Francisco, CA, Nov. 12-17, 1995.

Discussion on this paper should be addressed to the Technical Editor, Professor Lewis T. Wheeler, Department of Mechanical Engineering, University of Houston, Houston, TX 77204-4792, and will be accepted until four months after final publication of the paper itself in the ASME JOURNAL OF APPLIED MECHANICS.

Manuscript received by the ASME Applied Mechanics Division, Mar. 21, 1995; final revision, Apr. 29, 1995. Associate Technical Editor: G. J. Dvorak.

Paper No. 95-WA/APM-7.

Copyright © 1995 by ASME

Downloaded 04 May 2010 to 171.66.16.28. Redistribution subject to ASME license or copyright; see http://www.asme.org/terms/Terms_Use.cfm

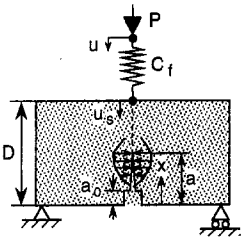


Fig. 1 Elastic structure with a cohesive crack, loaded through a spring

crete by Hillerborg, Modéer, and Petersson (1976) and extended by Petersson (1981). An equivalent crack band model was proposed by Bažant (1976, 1982, 1984), Bažant and Cedolin (1991), and Bažant and Oh (1983). All these studies were limited to the discrete finite element formulation. Although such a formulation is sufficient for numerical analysis of cracked structures, it is not well suited for characterizing the basic mathematical properties of the cohesive crack model. The aforementioned works were also limited to equilibrium analysis, but recently Li and Liang (1992, 1993) and Li and Bažant (1994) introduced a potential energy for the cohesive crack model and showed that the equilibrium conditions are the conditions of stationarity of this potential. However, the elastic strain energy of the structure and the energy of the cohesive stresses were treated in a combined manner, which does not reveal the basic mathematical properties and minimum principle.

This paper introduces continuous influence (Green's) functions along the crack in order to represent the elastic behavior of the structure separately from the cohesive stresses. The complementary energy and the potential energy of a general structure with cohesive crack is formulated and it is shown that the integral equations characterizing compatibility or equilibrium between the structure and the cohesive crack follow according to the well-known principles of minimum complementary energy or potential energy. The main objective of the paper is to present the variational derivation of these integral equations which reveals interesting relations to linear elastic fracture mechanics. The variational equations obtained could be used as a basis for approximate solutions. Finally, the conditions of stability of structures with cohesive cracks under load or displacement control and loading through a flexible frame are derived from the energy functionals in a general form. Further extensions to the analysis of size effect on the maximum load under load control and the maximum deflection under displacement control are relegated to a subsequent companion paper, and applications to sea ice will appear later.

2 Basic Energy Variables

Consider an elastic structure (or specimen) with a cohesive crack of length a (Fig. 1). For the sake of generality, we consider the structure to be loaded through an elastic loading frame of elastic compliance C_f, which is equivalent to a spring coupled in series, as in Fig. 1 (since the columns of a testing machine are placed parallel to the test specimen, a novice might think this is a parallel coupling, but it is a series coupling because the forces transmitted by the machine and by the specimen are equal and their displacements are additive). The special case $C_f = 0$ equivalent to a dead load applied directly on the structure. The problem can be formulated in terms of either stiffnesses or compliances. We first study the latter. In that case the basic variables are the forces, and the thermodynamic potential is the complementary energy Π^*, representing the Gibbs free energy in the case of isothermal conditions, or the enthalpy in the case of isentropic (or adiabatic) conditions.

According to the first law of thermodynamics (balance of energy), Π^* is additive, i.e., represents for sum of the complementary energies of all the parts of the structure-load system. Therefore,

$$\Pi^* = \Pi_s^* + \Pi_f^* + \Pi_l^*; \quad \Pi_s^* = U^* + \Pi_c^* \tag{1}$$

$$\Pi_c^* = \int_{a_0}^{a} \Gamma^*[\sigma(x)]dx \tag{2}$$

where a_0 = length of notch or initial traction-free crack; Π_s^*, Π_f^*, Π_l^*, U^*, Π_c^* = complementary energies of the structure (with the crack), the loading frame, the loading (Fig. 2(a)), the elastic structure (without crack), and the cohesive crack; and $\Gamma[\sigma(x)]$ = density of complementary energy of the crack at point of length coordinate x (Fig. 1). The elastic structure, as well as the loading frame, is assumed to be internally in equilibrium and internally compatible (which means their internal degrees of freedom are condensed out). Obviously, $\Pi_f^* = C_f P^2/2$ where C_f = compliance of the loading frame.

In the case of compliance formulation, the basic variables are the forces (e.g., Bažant and Cedolin, 1991, Sec. 10.1). So, if we want to obtain the load-point displacement u (displacement of the loading frame at the point where force P is applied), we must consider u to be constant and load P as variable (Fig. 2(c)). Thus, the complementary energy of the loading $\Pi_l^* = -W^* = -Pu$ (representing the complementary work W^* of the constant displacement u on the varying force P, which is equal to the area to the left of the vertical line in Fig. 2(c)).

The complementary energy Π^* as a potential exists, of course, if and only if the complementary energy potential exists for each part of the structure. For the crack, Π_c^* exists if we assume that no part of the crack ever undergoes unloading (i.e., the crack opens monotonically at all points x) and that the crack-opening displacement $w(x)$ at x (half the crack width) is a function of the cohesive (crack-bridging) stress $\sigma(x)$, i.e.,

$$w(x) = g[\sigma(x)] \tag{3}$$

(Fig. 3). This is the same as if the faces of the crack were held together by nonlinear continuously distributed springs following the law in Eq. (3). This law is softening (i.e., g is a decreasing function), as illustrated by the curve in Fig. 3.

The density of the potential energy of the cohesive crack is

$$\Gamma(w) = \int_0^w f(w')dw' \tag{4}$$

(Fig. 3), where $\sigma = f(\sigma)$ defines the given softening law and is inverse to function $w = g[\sigma(x)]$. The density of complementary energy is $\Pi^* = \sigma w - \Gamma$, that is

$$\Gamma^*(\sigma) = \int_{f_t}^{\sigma} g(\sigma')d\sigma' \tag{5}$$

(Fig. 3), where $w = g(\sigma)$ defines the softening law by function g that is inverse to function f; f_t' = tensile strength, which determines the σ-value at which the cohesive crack begins to open.

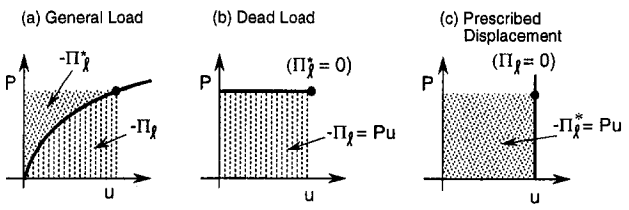


Fig. 2 Potential energy Π_l and complementary energy Π_l^* of loading

Downloaded 04 May 2010 to 171.66.16.28. Redistribution subject to ASME license or copyright; see http://www.asme.org/terms/Terms_Use.cfm

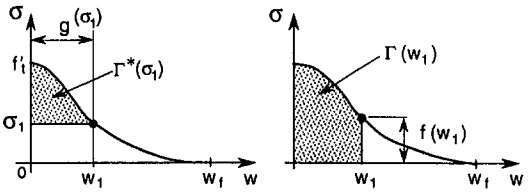


Fig. 3 Softening law relating crack-bridging (cohesive) stress σ and crack-opening displacement w

3 Complementary Energy of Structure With a Cohesive Crack

The complementary strain energy of the elastic structure, U^*, is a function of the load P as well as the surface tractions on the crack faces, which are equal to $-\sigma(x)$. Let C^{PP} = load-point compliance of the structure, $C^{\sigma\sigma}(x, x')$ = influence function representing a crack compliance function, such that the unit surface traction $\sigma(x) = \delta(x - x')$ applied at x' causes at x the opening $w = C^{\sigma\sigma}(x, x')$; $C^{\sigma P}(x)$ = influence function representing a cross-compliance function = crack-opening displacement at x caused by unit load P. Evidently, $C^{\sigma\sigma}(x, x') = C^{\sigma\sigma}(x', x)$, and $C^{\sigma P}(x)$ is equal to $C^{P\sigma}(x)$, defined so that a unit surface traction $\sigma = \delta(x - x')$ causes the load-point displacement $u = C^{P\sigma}(x)$. Expressing U^* in terms of the compliances and combining all the expressions for the complementary energies in (1) and (2), we have

$$\Pi^* = \Pi^*[\sigma(x), a, P] = \int_{a_0}^{a} \Gamma^*(x)dx + \tfrac{1}{2}\int_{a_0}^{a}\int_{a_0}^{a} C^{\sigma\sigma}(x, x')\sigma(x)\sigma(x')dx'dx - P\int_{a_0}^{a} C^{\sigma P}(x)\sigma(x)dx + \tfrac{1}{2}C^{PP}P^2 + \tfrac{1}{2}C_f P^2 - Pu \quad (6)$$

The reason for the first minus sign is that in our notation the positive directions of $\sigma(x)$ and $w(x)$ are opposite (the vector of w points toward the crack face, while the vector of σ points away from the crack face).

Equation (6) represents a function of P and $\sigma(x)$, giving the complementary energy for all the equilibrium states of the structure which are generally not compatible with the crack opening $w(x)$ and do not have the correct crack length a. The compatible crack opening is obtained by minimizing Π^* with respect to $\sigma(x)$, and the energetically correct crack length a is obtained by minimizing Π^* with respect to a. Although the equations that must result from this minimization are basically known, it will be instructive to carry out the variational procedure of minimization. Besides, the variational equations obtained by this procedure may be of interest for approximate solutions.

4 Compatibility and Minimization of Complementary Energy

A necessary condition of minimum of Π^* is that the first variation $\delta\Pi^* = 0$. We have

$$\delta\Pi^* = \left\{(C^{PP} + C_f)P - u - \int_{a_0}^{a} C^{\sigma P}(x)\sigma(x)dx\right\}\delta P + \int_{a_0}^{a}\left\{g[\sigma(x)] + \int_{a_0}^{a} C^{\sigma\sigma}(x, x')\sigma(x')dx' - C^{\sigma P}(x)P\right\}\delta\sigma(x)dx + \left\{\frac{1}{2}\int_{a_0}^{a}\int_{a_0}^{a}\frac{\partial C^{\sigma\sigma}(x, x')}{\partial a}\sigma(x)\sigma(x')dx'dx - P\int_{a_0}^{a}\frac{\partial C^{\sigma P}}{\partial a}\sigma(x)dx + \frac{1}{2}\frac{\partial C^{PP}}{\partial a}P^2 + \int_{a_0}^{a} C^{\sigma\sigma}(x, a)\sigma(x)\sigma(a)dx - PC^{\sigma P}(a)\sigma(a) + \Gamma^*[\sigma(a)]\right\}\delta a = 0. \quad (7)$$

This may be simplified by noting that we may substitute $C^{\sigma\sigma}(x, a) = C^{\sigma P}(a) = 0$ because $w = 0$ at the crack tip, and $\Gamma^*[\sigma(a)] = \Gamma^*(f_t') = 0$.

It is now necessary to relate the compliance derivatives to the energy release rate and the stress intensity factors. The energy release rate is $\partial\Pi^*/\partial a = K^2/E'$ where E' = Young's modulus E for the case of plane stress or $E' = E/(1 - \nu^2)$ for the case of plane strain, with ν = Poisson ratio. According to the principle of superposition, the total stress intensity factor is

$$K = K_P + K_\sigma = Pk_P + \int_{a_0}^{a} k_\sigma(x)\sigma(x)dx \quad (8)$$

where K_P = stress intensity factor due to load P alone and K_σ = stress intensity factor due to surface tractions $-\sigma(x)$; $k_\sigma(x)$, k_P = stress intensity factor at the crack tip ($x = a$) caused by a unit surface traction, i.e., stress $-\sigma = \delta(x - x')$, or by a unit load $P = 1$. With these notations, we have

$$\frac{\partial C^{\sigma\sigma}(x, x')}{\partial a} = \frac{\partial}{\partial a}\frac{\partial^2\Pi^*}{\partial\sigma(x)\partial\sigma(x')} = \frac{\partial^2}{\partial\sigma(x)\partial\sigma(x')}\frac{\partial\Pi^*}{\partial a} = \frac{1}{E'}\frac{\partial^2}{\partial\sigma(x)\partial\sigma(x')}\left[Pk_P + \int_{a_0}^{a} k_\sigma(x)\sigma(x)dx\right]^2 = \frac{2}{E'}k_\sigma(x)k_\sigma(x') \quad (9a)$$

$$\frac{\partial C^{\sigma P}(x)}{\partial a} = -\frac{1}{E'}\frac{\partial^2}{\partial\sigma(x)\partial P}\left[Pk_P + \int_{a_0}^{a} k_\sigma(x)\sigma(x)dx\right]^2 = -\frac{2}{E'}k_\sigma(x)k_P \quad (9b)$$

$$\frac{\partial C^{PP}}{\partial a} = \frac{2}{E'}k_P^2. \quad (9c)$$

Equations (9a, b) represent a continuous generalization of a similar well-known relation for concentrated loads given, e.g., by Tada et al. (1985).

Equation (7) must be satisfied for any variations δP, $\delta\sigma(x)$ and δa (such that $\delta\sigma \geq 0$). This requires that the expressions in brackets $\{\ldots\}$ vanish. With the aforementioned substitutions, the vanishing of the variations with respect to δP, $\delta\sigma(x)$ and δa requires that

$$\frac{\partial\Pi^*}{\partial P} = -\int_{a_0}^{a} C^{P\sigma}(x)\sigma(x)dx + (C^{PP} + C_f)P - u = 0 \quad (10)$$

$$\frac{\partial\Pi^*}{\partial\sigma(x)} = \int_{a_0}^{a} C^{\sigma\sigma}(x, x')\sigma(x')dx' - C^{\sigma P}(x)P + g[\sigma(x)] = 0 \quad (11)$$

$$E'\frac{\partial\Pi^*}{\partial a} = \int_{a_0}^{a}\int_{a_0}^{a} k_\sigma(x)k_\sigma(x')\sigma(x)\sigma(x')dx'dx + 2Pk_P\int_{a_0}^{a} k_\sigma(x)\sigma(x)dx + P^2k_P^2 = 0. \quad (12)$$

Downloaded 04 May 2010 to 171.66.16.28. Redistribution subject to ASME license or copyright; see http://www.asme.org/terms/Terms_Use.cfm

Noting that Eq. (12) may be written as

$$E' \frac{\partial \Pi^*}{\partial a} = \left[Pk_P + \int_{a_0}^{a} k_\sigma(x)\sigma(x)dx \right]^2 = 0, \qquad (13)$$

we obtain the relation $K = K_P + K_\sigma = 0$.

Equation (11) represents the crack compatibility condition, i.e., the condition that the crack openings calculated from the deformation of the elastic body match the openings obtained from the given softening law $g(\sigma)$. Equation (10) gives the load-point deflection and, in the sense of the complementary energy approach, has the meaning of the condition of compatibility of the elastic deformation of the structure with the given value of u (it is not an equilibrium condition). Equation (8) with $K = 0$, called the zero-K condition, is the basic condition of any cohesive crack model, proposed by Barenblatt (1962) and Dugdale (1960). This condition means that the stress at the crack tip must be finite, i.e., that there is no singularity. From the variational viewpoint, the condition $K = 0$ is a condition of energy rate balance between the structure and the crack. If K were positive, the rate of energy released from the structure would be larger than that dissipated in the cohesive crack (and then the propagation would be dynamic). If K were negative, propagation would be impossible.

To calculate structure displacement u_s we substitute $u = u_s + C_f P$ into (10), considering P to be positive when it puts the loading spring (Fig. 1) into compression. Then, solving for P, we get

$$u_s = C^{PP}P - \int_{a_0}^{a} C^{P\sigma}(x)\sigma(x)dx. \qquad (14)$$

5 Stability Loss in Terms of Compliance

According to the second law of thermodynamics, stability requires that the second variation $\delta^2\Pi^*$ be a positive definite functional of $\sigma(x)$, P and a (e.g., Bažant and Cedolin, 1991, Sec. 10.1). The limit of stability occurs when $\delta^2\Pi^* = 0$ for some variation $\delta\sigma(x)$, δP and δa. The variation of u cannot be considered arbitrary because displacements cannot be the variables in the complementary energy functional. Therefore, we consider loading under displacement control conditions, which is, of course, required by the form of the work term in our expression for Π^*. $\delta^2\Pi^* = 0$ means that

$$\delta(\delta_P\Pi^*) = 0, \quad \delta(\delta_\sigma\Pi^*) = 0, \quad \delta(\delta_P\Pi^*) = 0 \quad (15a, b, c)$$

for some variation. The conditions of stationary Π^*, which are necessary for min Π^*, are represented by the vanishing of (10), (11), and (12); they must be imposed only after variations δ are taken. According to the expressions for $\delta_P\Pi^*$, $\delta_\sigma\Pi^*$, and $\delta_a\Pi^*$ implied by (10), (11), and (12), with (13), Eq. (15a, b, c) read:

$$-\delta(\delta_P\Pi^*) = \left[\int_{a_0}^{a} C^{P\sigma}(x)\delta\sigma(x)dx + \int_{a_0}^{a} \frac{\partial C^{P\sigma}(x)}{\partial a}\sigma(x)dx\delta a + C^{P\sigma}(a)\sigma(a)\delta a - (C^{PP} + C_f)\delta P - \frac{\partial C^{PP}}{\partial a}P\delta a \right]\delta P = 0 \quad (16a)$$

$$-\delta(\delta_\sigma\Pi^*) = \int_{a_0}^{a} \left[\int_{a_0}^{a} C^{\sigma\sigma}(x, x')\delta\sigma(x')dx' + \int_{a_0}^{a} \frac{\partial C^{\sigma\sigma}(x, x')}{\partial a}\sigma(x')dx'\delta a - C^{\sigma\sigma}(x, a)\sigma(a)\delta a - \frac{\partial C^{\sigma P}(x)}{\partial a}P\delta a - C^{\sigma P}(x)\delta P + \frac{dg[\sigma(x)]}{d\sigma}\delta\sigma(x) \right]\delta\sigma(x)dx = 0 \quad (16b)$$

$$E'\delta(\delta_a\Pi^*) = 2(K_P + K_\sigma)(\delta K_P + \delta K_\sigma)\delta_a = 0. \quad (16c)$$

The last equation is automatically satisfied because $K_P + K_\sigma = 0$ at min Π^*. The other equations may again be simplified using Eq. (9a, b, c) and, noting that,

$$C^{\sigma\sigma}(x, a) = C^{P\sigma}(a) = 0, k_P P = K_P, \quad -\int_{a_0}^{a} k_\sigma(x)\sigma(x)dx = K_\sigma$$

we get

$$-\delta(\delta_P\Pi^*) = \left[\int_{a_0}^{a} C^{P\sigma}(x)\delta\sigma(x)dx - \frac{2}{E'}k_P(K_P + K_\sigma)\delta a - (C^{PP} + C_f)\delta P \right]\delta P = 0 \quad (17a)$$

$$\delta(\delta_\sigma\Pi^*) = \int_{a_0}^{a} \left[\int_{a_0}^{a} C^{\sigma\sigma}(x, x')\delta\sigma(x')dx' + \frac{2}{E'}k_\sigma(x)(K_P + K_\sigma)\delta a - C^{\sigma P}(x)\delta P + \frac{dg[\sigma(x)]}{d\sigma}\delta\sigma(x) \right]\delta\sigma(x)dx = 0. \quad (17b)$$

Here again we may set $K_P + K_\sigma = 0$. Eliminating δP from the last two equations, we obtain

$$-\frac{dg[\sigma(x)]}{d\sigma}v(x) = \int_{a_0}^{a} \bar{C}^{\sigma\sigma}(x, x')v(x')dx' \qquad (18)$$

in which we introduced the notations $\delta\sigma(x)/\delta a = v(x)$ and

$$\bar{C}^{\sigma\sigma}(x, x') = C^{\sigma\sigma}(x, x') - \frac{C^{\sigma P}(x)C^{\sigma P}(x')}{C^{PP} + C_f}. \qquad (19)$$

Equation (18) is a homogeneous Fredholm integral equation for function $v(x)$. It is linear if function $g(\sigma)$ is linear. It characterizes the loss of stability under displacement control with a flexible loading frame. Note that $\bar{C}^{\sigma\sigma}(x, x')$ represents the crack compliances of the system consisting of the structure and the loading frame combined.

The special case $C_f = 0$ is equivalent to loading the structure under displacement control at the point of transmission of load P into the structure (rather than at the loading frame). In this case, the stability limit determines the maximum deflection of the structure, corresponding to the onset of snapback instability. Of course, the condition of maximum deflection could have been obtained more directly, simply by considering a structure without any loading frame from the outset ($C_f = 0$).

The special case $C_f \to \infty$ (with $u \to \infty$), for which $\bar{C}^{\sigma\sigma}(x, x') = C^{\sigma\sigma}(x, x')$, is equivalent to loading the structure under conditions of load control (dead load). In that case, the structure and the crack become unstable at maximum load, and so Eq. (18) becomes the condition of maximum load, which is obtained from Eq. (14).

The condition of maximum load ($C_f \to \infty$) could have been, of course, also obtained more directly, namely by considering the structure without any loading frame, loaded directly by P. In that case, we would have had to discard the term $-Pu$ from Eq. (6) defining Π^*. This term represents the complementary energy for load P varying at constant displacement u. For displacement u varying at constant P (i.e., dead load), the complementary energy of load is zero (Fig. 2(b)).

Downloaded 04 May 2010 to 171.66.16.28. Redistribution subject to ASME license or copyright; see http://www.asme.org/terms/Terms_Use.cfm

6 Potential Energy of Structure With Cohesive Crack

Second, we study the stiffness formulation. In that case the thermodynamic potential is the potential energy Π, representing the Helmholtz free energy in the case of isothermal conditions or the total energy in the case of isotropic (adiabatic) conditions. According to the first law of thermodynamics,

$$\Pi = \Pi_s + \Pi_f + \Pi_l, \quad \Pi_s = U + \Pi \tag{20}$$

where

$$\Pi = \int_{a_0}^{a} \Gamma[w(x)]dx, \quad \Gamma(w) = \int_0^w f[w]dw. \tag{21}$$

The notations Π_s, Π_f, Π_l, and U are analogous to Π_s^*, Π_f^*, Π_l^*, and U^* (U = strain energy of structure, $-\Pi_l = W$ = work of load). Obviously, $\Pi_f = R_f(u - u_s)^2/2$ where $R_f = 1/C_f$ = stiffness of the loading frame, and u_s = displacement of structure at point of contact with the loading frame.

In the case of stiffness formulation, the basic variables are the displacements. If we consider load-control, then P is fixed (dead load) and u is variable, in which case the potential energy of the loading is $\Pi_l = -W = -Pu$. This happens to be the same expression as before but W represents the work of load P on displacement u, which is the area below the horizontal line in Fig. 1 (b). However, we will be more interested in displacement control, in which case $\Pi_l = 0$, because u is fixed ($du = 0$) and P is varied (in which case $dW = Pdu = 0$); Fig. 2(c).

7 Equilibrium and Minimization of Potential Energy

Under our assumptions, the potential exists separately for the load, the frame, the structure, and the cohesive crack. Therefore, it must also exist for the entire system, as given by Eq. (21). The potential energy of the elastic structure (i.e., strain energy) is a function of u_s and $w(x)$ (all the internal displacements of the structure are assumed to be condensed out). Let $R^{ww}(x, x')$ = influence function = crack stiffness function representing the stress at x caused by a unit displacement $w = \delta(x - x')$; $R^{wu}(x)$ = influence function (or stiffness function) representing the stress at x caused by a unit displacement $u_s = 1$; and R^{uu} = load-point stiffness representing the force at the point of contact with the loading frame caused by $u_s = 1$. The potential energy expression for the case of displacement control may now be rewritten as

$$\Pi = \int_{a_0}^{a} \Gamma[w(x)]dx + \tfrac{1}{2}\int_{a_0}^{a}\int_{a_0}^{a} R^{ww}(x, x')w(x)w(x')dx'dx - u_s\int_{a_0}^{a} R^{uw}(x)w(x)dx + \tfrac{1}{2}R^{uu}u_s^2 + \tfrac{1}{2}R_f(u - u_s)^2 \tag{22}$$

(Note that $\Pi_l = 0$ because the load varies at prescribed displacement.) The first variation of this expression is

$$\delta\Pi = \left\{(R^{uu} + R_f)u_s - R_f u - \int_{a_0}^{a} R^{uw}(x)w(x)dx\right\}\delta u_s + \int_{a_0}^{a}\left\{f[w(x)] + \int_{a_0}^{a} R^{ww}(x, x') \times w(x')dx' - u_s R^{uw}(x)\right\}\delta w(x)dx + \left\{\frac{1}{2}\int_{a_0}^{a}\int_{a_0}^{a}\frac{\partial R^{ww}(x, x')}{\partial a}w(x)w(x')dx'dx - u_s\int_{a_0}^{a}\frac{\partial R^{uw}(x)}{\partial a}w(x)dx + \frac{1}{2}\frac{\partial R^{uu}}{\partial a}u_s^2 + \int_{a_0}^{a} R^{ww}(x, a)w(a)dx - u_s R^{uw}(a)w(a) + \Gamma[w(a)]\right\}\delta a = 0. \tag{23}$$

Now we note that $w(a) = \Gamma(0) = 0$ and, in analogy to Eq. (9a, b, c), we could prove that

$$\frac{\partial R^{ww}(x, x')}{\partial a} = -\frac{2}{E'}k_w(x)k_w(x'), \quad \frac{\partial R^{wu}(x)}{\partial a} = \frac{2}{E'}k_w(x)k_u, \quad \frac{\partial R^{uu}}{\partial a} = -\frac{2}{E'}k_u^2 \tag{24}$$

where $k_w(x)$ and k_u are the stress intensity factors at $x = a$ caused by unit displacement $w(x') = \delta(x' - x)$ or by unit displacement $u_s = 1$. The condition of minimum potential energy requires that the expression in the brackets $\{\ldots\}$ multiplied by δu_s, $\delta w(x)$, and δa vanish. This yields three equations:

$$u_s = \frac{1}{R^{uu} + R_f}\left[R_f u + \int_{a_0}^{a} R^{uw}(x)w(x)dx\right] \tag{25}$$

$$f[w(x)] = -\int_{a_0}^{a} R^{ww}(x, x')w(x')dx' + R^{uw}(x)u_s \tag{26}$$

$$-\frac{\partial\Pi}{\partial a} = \frac{1}{E'}\int_{a_0}^{a}\int_{a_0}^{a} k_w(x)k_w(x')w(x)w(x')dx'dx + \frac{u_s}{E'}\int_{a_0}^{a} k_w(x)k_u dx + \frac{1}{E'}k_u^2u_s^2 = \frac{1}{E'}\left[k_u u_s + \int_{a_0}^{a} k_w(x)w(x)dx\right]^2 = 0.$$

The last equation may be rewritten as

$$K = K_u + K_w = 0, \quad K_u = k_u u_s, \quad K_w = \int_{a_0}^{a} k_w(x)w(x)dx. \tag{28a, b, c}$$

This means that the total stress intensity factor K caused by load-point displacement and crack opening must vanish. This is the same well-known condition as we obtained before, but expressed in terms of the displacement-caused stress intensity factors k_u and k_w.

To calculate load P, we substitute $u = u_s + (P/R_f)$ into (25), and solve the equation for P:

$$P = R^{uu}u_s - \int_{a_0}^{a} R^{uw}(x)w(x)dx. \tag{29}$$

Equation (26) gives the equilibrium value of displacement of the structure at the point of loading by the frame. Equations (27) or (28) give the condition of equilibrium (static) propagation, at which the energy release and energy dissipation rates are equal.

8 Stability Loss in Terms of Stiffness

Let us now consider stability at prescribed displacement u. According to the Lagrange-Dirichlet theorem (which is a consequence of the second law of thermodynamics under the hypothesis of a tangentially equivalent elastic structure, Bažant and Cedolin, 1991, Sec. 10.1), stability requires that $\delta^2\Pi$ be positive definite. The limit of stability is reached when $\delta^2\Pi = 0$ becomes possible. To simplify the calculations, let us eliminate displacement u_s by substituting Eq. (26) into (27) and (28). This yields

Downloaded 04 May 2010 to 171.66.16.28. Redistribution subject to ASME license or copyright; see http://www.asme.org/terms/Terms_Use.cfm

$$f[w(x)] = -\int_{a_0}^{a} \bar{R}^{ww}(x, x')w(x')dx' + \bar{R}^{uw}(x)u \quad (30)$$

$$\bar{K}_u + \bar{K}_w = 0, \quad \bar{K}_u = \bar{k}_u u, \quad \bar{K}_w = \int_{a_0}^{a} \bar{k}_w(x)w(x)dx. \quad (31)$$

Here we introduced the notations

$$\bar{R}^{ww}(x, x') = R^{ww}(x, x') - \frac{R^{uw}(x)R^{uw}(x')}{R^{uu} + R_f}, \quad (32)$$

$$\bar{R}^{uw}(x) = \frac{R_f}{R^{uu} + R_f} R^{uw}(x) \quad (32)$$

$$\bar{k}_w = k_w(x) + \frac{R^{uw}(x)k_u}{R^{uu} + R_f}, \quad \bar{k}_u = \frac{R_f k_u}{R^{uu} + R_f} \quad (33)$$

which have the meaning of stiffnesses and unit stress intensity factors of the system of the structure and the loading frame combined. The stability limit is reached when $\delta^2\Pi = 0$ for some variation $\delta w(x)$ and δa. This means that

$$\delta(\delta_w\Pi) = \int_{a_0}^{a} \frac{df[w(x)]}{dw} [\delta w(x)]^2 dx + \int_{a_0}^{a}\int_{a_0}^{a} \bar{R}^{ww}(x, x')\delta w(x)\delta w(x')dx'dx + \frac{\bar{K}_u + \bar{K}_w}{E'} \int_{a_0}^{a} \bar{k}_w(x)\delta w(x)dx\delta a = 0 \quad (34a)$$

$$\delta(\delta_a\Pi) = \frac{\bar{K}_u + \bar{K}_w}{E'} \int_{a_0}^{a} \bar{k}_w(x)\delta w(x)dx\delta a + \frac{\bar{K}_u + \bar{K}_w}{E'} \frac{\partial(\bar{K}_u + \bar{K}_w)}{\partial a} (\delta a)^2 = 0. \quad (34b)$$

We find that Eq. (34*b*) is automatically satisfied because $\bar{K}_u + \bar{K}_w = 0$. Furthermore, denoting $\mu(x) = \delta w(x)/\delta a$, we get from Eq. (34*a*) the condition for the loss of stability under displacement control occurs:

$$-\frac{df[w(x)]}{dw} \mu(x) = \int_{a_0}^{a} \bar{R}^{ww}(x, x')\mu(x')dx'. \quad (35)$$

Similar to Eq. (18), this is again a homogeneous Fredholm integral equation for function $\mu(x)$. It is linear if function $f(w)$ is linear.

The special case for $R_f \to \infty$ (with $u = u_s$) represents direct displacement control of the structure (no flexible loading frame). In that case Eq. (35) decides the maximum deflection of the structure, i.e., the onset of snapback instability.

The special case $R_f \to 0$ (with $u \to \infty$) represents loading of the structure under load control. Of course, the case of load control can also be obtained directly. To that end, one must set $R_f = 0$, $u_s = u$ and add to Eq. (22) the term $\Pi_l = -Pu$ representing the potential energy of dead load.

9 Conclusion

Under the assumption of no unloading anywhere within the crack, the cohesive crack model can be formulated in terms of minimization of either the complementary energy or the potential energy of the system. Using the relation of the compliance or stiffness derivatives with respect to the crack length to the unit stress intensity factors, the minimum condition yields the usual compatibility or equilibrium relations for the opening displacements and the cohesive (crack-bridging) stresses in the cohesive crack, and the condition of zero stress intensity factor at the crack tip. The energy formulation also provides the conditions for the loss of stability of a structure with a growing cohesive crack. They have the form of a homogeneous Fredholm integral equation for the derivative of the cohesive stresses or crack opening displacements with respect to the crack length. The variational equations obtained can be used for formulation or approximate solutions.

Acknowledgment

Partial financial support under ONR grant N0014-91-J-1109 to Northwestern University, dealing with applications to sea ice, is gratefully acknowledged. Further support for applications to concrete has been obtained from the Center of Advanced Cement Based Materials at Northwestern University.

References

Barenblatt, G. I., 1962, "The mathematical theory of equilibrium cracks in brittle fracture," *Advances in Applied Mechanics,* Vol. 7, pp. 55–129.

Bažant, Z. P., 1976, "Instability, ductility, and size effect in strain softening concrete," ASCE *Journal of Engineering Mechanics,* Vol. 102, No. 2, pp. 331–344.

Bažant, Z. P., 1982, "Crack band model for fracture geomaterials," *Proceedings of the 4th International Conference on Numerical Method in Geomechanics,* Z. Eisenstein, ed., Edmonton, Alberta, Vol. 3, pp. 1137–1152.

Bažant, Z. P., and Oh, B. H., 1983, "Crack band theory for fracture concrete," *Material and Structures* (RILEM, Paris), Vol. 16, pp. 155–177.

Bažant, Z. P., 1984, "Size effect in blunt fracture: Concrete, Rock, Metal," *ASCE Journal of Engineering Mechanics,* Vol. 110, No. 4, pp. 518–535.

Bažant, Z. P., and Cedolin, L., 1991, *Stability of Structures: Elastic, Inelastic, Fracture, and Damage Theories,* Oxford University Press, Oxford, U.K.

Bilby, B. A., Cottrell, A. H., and Swinden, K. H., 1963, "The spread of plastic yield form a notch," *Proceedings of Royal Society London,* Vol. A272, pp. 304–314.

Dugdale, D. S., 1960, "Yielding of steel sheets containing slits," *Journal of the Mechanics and Physics of Solids,* Vol. 8, pp. 100–104.

Foote, R. M. L., Mai, Y.-W., and Cottrell, B., 1986, "Crack growth resistance curves in strain-softening materials," *Journal of the Mechanics and Physics of Solids,* Vol. 34, No. 6, pp. 593–607.

Hillerborg, A., Modéer, M., and Petersson, P. E., 1976, "Analysis of crack formation and crack growth in concrete by means of fracture mechanics and finite elements," *Cement and Concrete Research,* Vol. 6, pp. 773–782.

Li, Y. N., and Bažant, Z. P., 1994, "Eigenvalue analysis of size effect for cohesive crack model," *International Journal of Fracture,* Vol. 66, pp. 213–226.

Li, Y. N., and Liang, R. Y., 1992, "Stability theory of the cohesive crack model," ASCE *Journal of Engineering Mechanics,* Vol. 118, No. 3.

Li, Y. N., and Liang, R. Y., 1993, "The theory of boundary eigenvalue problem in the cohesive crack model and its application," *Journal of the Mechanics and Physics of Solids,* Vol. 41, pp. 331–350.

Needleman, A., 1990, "An analysis of tensile decohesion along an interface," *Journal of the Mechanics and Physics of Solids,* Vol. 38, No. 3, pp. 289–324.

Petersson, P.-E., 1981, "Crack growth and development of fracture zones in plain concrete and similar materials," Doctoral Dissertation, Lund Institute of Technology, Sweden.

Rice, J. R., 1968, "Path Independent Integral and Approximate Analysis of Strain Concentration by Notches And Cracks," ASME JOURNAL OF APPLIED MECHANICS, Vol. 35, pp. 379–386.

Rice, J. R., 1992, "Dislocation nucleation from a crack tip: An analysis based on the Peierls concept," *Journal of the Mechanics and Physics of Solids,* Vol. 40, No. 2, pp. 239–271.

Reinhardt, H. W., 1985, "Crack softening zone in plain concrete under static loading," *Cement and Concrete Research,* Vol. 15, pp. 42–52.

Smith, E., 1974, "The structure in the vicinity of a crack tip: A general theory based on the cohesive zone model," *Engineering Fracture Mechanics,* Vol. 6, pp. 213–222.

Suo, Z., Bao, G., and Fan, B., 1992, "Delamination *R*-curve phenomena due to damage," *Journal of the Mechanics and Physics of Solids,* Vol. 40, No. 1, pp. 1–16.

Tada, H., Paris, P. C., and Irwin, G. R., 1985, *The stress analysis of cracks handbook,* Del Research Corp., Hellertown, PA.

Tvergaard, V., and Hutchinson, J. W., 1992, "The relation between crack growth resistance and fracture process parameters in elastic-plastic solids," *Journal of the Mechanics and Physics of Solids,* Vol. 40, No. 6, pp. 1377–1397.

Willis, J. R., 1967, "A comparison of the fracture criteria of Griffith and Barenblatt," *Journal of the Mechanics and Physics of Solids,* Vol. 15, pp. 151–162.

Downloaded 04 May 2010 to 171.66.16.28. Redistribution subject to ASME license or copyright; see http://www.asme.org/terms/Terms_Use.cfm

Stability of Cohesive Crack Model: Part II—Eigenvalue Analysis of Size Effect on Strength and Ductility of Structures

Z. P. Bažant
Walter Murphy Professor of Civil Engineering and Material Science, Fellow ASME.

Yuan-Neng Li
Research Assistant Professor.

Department of Civil Engineering, Northwestern University, Evanston, IL 60208

The preceding paper is extended to the analysis of size effect on strength and ductility of structures. For the case of geometrically similar structures of different sizes, the criterion of stability limit is transformed to an eigenvalue problem for a homogeneous Fredholm integral equation, with the structure size as the eigenvalue. Under the assumption of a linear softening stress-displacement relation for the cohesive crack, the eigenvalue problem is linear. The maximum load of structure under load control, as well as the maximum deflection under displacement control (which characterizes ductility of the structure), can be solved explicitly in terms of the eigenfunction of the aforementioned integral equation.

1 Introduction

As explained in the preceding paper (Bažant and Li, 1995), the cohesive crack model is a nonlinear theory of fracture mechanics in which the condition of stability limit is expressed in terms of the singularity condition of the second variation of the energy potential with respect to cohesive stresses or crack-opening displacements. Although the criterion of stability limit can also be formulated in terms of energy variation with respect to the crack length, the resulting equation is not very useful, since the energy release rate in the cohesive crack model depends on the cohesive stresses or crack-opening displacements.

For a given structure, the criterion of stability limit leads to a highly nonlinear equation for crack length. However, when a class of geometrically similar structures of different sizes is considered and the relative crack length is given, the criterion of stability limit can be treated as an equation for the structure size at which the stability limit occurs at the given relative crack length. In this manner, the criterion of the stability limit is transformed into an eigenvalue problem, with the structure size as the eigenvalue. In the special case of linear softening, the eigenvalue problem is linear. It can be solved independently of the solution of the cohesive crack model. Furthermore, the corresponding maximum value of the load or loading parameter can be expressed explicitly in terms of the eigenfunction. In this way, the size effect curve can be obtained readily, without having to calculate the load-deflection curves for structures of various sizes.

The eigenvalue problem of the cohesive crack model was studied by Li and Hong (1992), Li and Liang (1993) and Li and Bažant (1993). However, only the peak-load solution was discussed in these previous papers. In the present paper, the influence functions are used to formulate the condition of stability limit of a structure with a cohesive crack in the form of a homogenous Fredholm integral equation. The peak load, as well as the maximum displacement (which corresponds to snap-back instability), is obtained. In addition, the cases of a structure loaded through a spring coupled in series (i.e., the case of a soft loading device) and a structure restrained by a spring coupled in parallel are analyzed. Finally, some computational techniques are discussed and a numerical example of the size effect curves for maximum deflection is given.

2 Dimensionless Process Zone Equations

We consider a two-dimensional structure of a unit thickness and introduce the following dimensionless variables:

$$\bar{C} = CE, \quad \alpha = \frac{a}{D}, \quad \xi = \frac{x}{D}, \quad \bar{\sigma} = \frac{\sigma}{f_t},$$

$$\bar{w} = \frac{w}{w_c}, \quad \bar{P} = \frac{P}{Df_t}, \quad \bar{D} = \frac{D}{2L_0} \quad (1)$$

where $L_0 = EG_f/f_t^2$ = characteristic size of the process zone, f_t = direct tensile strength of the material, and w_c = threshold value of the crack-opening displacement. All the notations from the preceding paper (Bažant and Li, 1994) are retained. To simplify notations in the following text, we will drop the bars, with the understanding that all the variables are dimensionless unless specified otherwise.

For a generic elastic structure, the crack-opening displacement w, the load-line displacement u, the load P, and the crack-bridging stress σ must satisfy the compatibility equations:

$$\frac{w(\xi)}{D} = -\int_{\alpha_0}^{\alpha} C^{\sigma\sigma}(\xi, \xi')\sigma(\xi')d\xi' + C^{\sigma P}(\xi)P \quad (2)$$

$$\frac{u}{D} = -\int_{\alpha_0}^{\alpha} C^{P\sigma}(\xi')\sigma(\xi')d\xi' + C^{PP}P \quad (3)$$

which represent the special case of Eqs. (11) and (10) or (14) of the preceding paper for $C_f = 0$; $C^{\sigma\sigma}(\xi, \xi')$, $C^{\sigma P}(\xi)$, $C^{P\sigma}(\xi)$, C^{PP} are dimensionless compliance influence functions (Green's functions). The lower integration limit α_0 is the relative length

Contributed by the Applied Mechanics Division of THE AMERICAN SOCIETY OF MECHANICAL ENGINEERS for presentation at the International Mechanical Engineering Congress and Exhibition, the Winter Annual Meeting of the ASME, San Francisco, CA, Nov. 12-17, 1995.

Discussion on this paper should be addressed to the Technical Editor, Professor Lewis T. Wheeler, Department of Mechanical Engineering, University of Houston, Houston, TX 77204-4792, and will be accepted until four months after final publication of the paper itself in the ASME JOURNAL OF APPLIED MECHANICS.

Manuscript received by the ASME Applied Mechanics Division, Mar. 21, 1995; final revision, Apr. 29, 1995. Associate Technical Editor: G. J. Dvorak.

Paper No. 95-WA/APM-8.

Copyright © 1995 by ASME

Downloaded 04 May 2010 to 171.66.16.28. Redistribution subject to ASME license or copyright; see http://www.asme.org/terms/Terms_Use.cfm

of the initial traction-free crack (notch); α is the total relative crack length which includes both the process zone (crack-bridging zone) and the stress-free crack. The problem can also be formulated as equilibrium conditions written in terms of stiffness influence functions:

$$D\sigma(\xi) = \int_{\alpha_0}^{\alpha} R^{ww}(\xi, \xi')w(\xi')d\xi' + R^{wu}(\xi)u \quad (4)$$

$$DP = \int_{\alpha_0}^{\alpha} R^{uw}(\xi)w(\xi)d\xi + R^{uu}u. \quad (5)$$

These equations represent the special case of Eqs. (26) and (25). Equation (4) for prescribed load P ensues by solving u from Eq. (5) and substituting it into Eq. (4). The dimensionless stiffness functions are here defined with a unit value of Young's modulus.

In the cohesive crack model, the cohesive stress σ is related to the crack-opening displacement w by the stress-displacement relation, which can be described by either of the following forms

$$w = g(\sigma), \quad \sigma = f(w). \quad (6a, b)$$

Substituting (6a) into (2), we obtain what we call the crack compatibility equation in terms of compliance functions:

$$\frac{1}{D}g[\sigma(\xi)] = -\int_{\alpha_0}^{\alpha} C^{\sigma\sigma}(\xi, \xi')\sigma(\xi')d\xi' + C^{\sigma P}(\xi)P \quad (7)$$

Substituting (6b) into (4), we obtain the crack equilibrium equation in terms of stiffness functions:

$$Df[w(\xi)] = -\int_{\alpha_0}^{\alpha} R^{ww}(\xi, \xi')w(\xi')d\xi' + R^{wu}(\xi)u. \quad (8)$$

3 Peak-Load Solution by the Condition of Structural Stability Limit

As established in Bažant and Li (1995), the singularity condition for the compliance formulation under load control can be expressed as the condition of finding a nonzero solution $v(\xi)$ of the following homogenous equation:

$$D\int_{\alpha_0}^{\alpha} C^{\sigma\sigma}(\xi', \xi)v(\xi')d\xi' = -\frac{dg[\sigma(\xi)]}{d\sigma}v(\xi). \quad (9)$$

Since we are considering geometrically similar structures only, (9) can be regarded as an eigenvalue problem if the relative crack length α is given. The dimensionless quantity D plays the role of an eigenvalue. In the actual calculation, the singularity condition should be solved simultaneously with the basic equations to obtain the nominal strength as the maximum load parameter and the corresponding size for a given relative crack length. Calculation of size effect curves in this manner is very efficient. A discussion of the discrete form of the present formulation has been given by Li and Bažant (1994).

In the following, we restrict attention to the case of linear softening, which is defined as

$$w = g(\sigma) = 1 - \sigma, \quad \sigma = f(w) = 1 - w. \quad (10)$$

Since for linear softening $dg/d\sigma = -1$, the eigenvalue is no longer coupled with the basic equations of the cohesive crack. The eigenvalue problem can now be written as

$$D\int_{\alpha_0}^{\alpha} C^{\sigma\sigma}(\xi', \xi)v(\xi')d\xi' = v(\xi). \quad (11)$$

If the relative crack length is specified and geometrically similar structures are considered, Eq. (11) represents a linear homogeneous Fredholm integral equation (Tricomi, 1957) for function $v(\xi)$, with size D as the eigenvalue. The size D for which the given α corresponds to the maximum load is the largest eigenvalue of (11). This approach, proposed by Li and Bažant (1994), makes it possible to avoid solving the load-deflection curves for various sizes D. It represents an efficient method of calculating the size effect curve.

The dimensionless crack compatibility equation can be written as

$$\frac{1 - \sigma(\xi)}{D} = -\int_{\alpha_0}^{\alpha} C^{\sigma\sigma}(\xi, \xi')\sigma(\xi')d\xi' + C^{\sigma P}(\xi)P. \quad (12)$$

Multiplying this with the eigenfunction $v(\xi)$ and then integrating with respect to ξ, we obtain

$$\int_{\alpha_0}^{\alpha}\left[\frac{1}{D} - C^{\sigma P}(\xi)P\right]v(\xi)d\xi = \int_{\alpha_0}^{\alpha}\sigma(\xi)\int_{\alpha_0}^{\alpha}\left[\frac{\delta(\xi - \xi')}{D} - C^{\sigma\sigma}(\xi, \xi')\right]v(\xi')d\xi'd\xi. \quad (13)$$

If the singularity condition is satisfied, then the applied load is at its maximum. This maximum value is found to be

$$P = \frac{1}{D}\frac{\int_{\alpha_0}^{\alpha} v(\xi)d\xi}{\int_{\alpha_0}^{\alpha} C^{\sigma P}(\xi)v(\xi)d\xi}. \quad (14)$$

An equivalent expression for the peak load was obtained by Li and Hong (1992), and by Li and Bažant (1994). The eigenvalue problem (11) and the peak load solution (14) provide a powerful set of equations for solving the size-effect curve of the cohesive crack model directly, without any need to solve the load-deflection curve from the basic equations.

The solution can also be generalized to include the case of multiple (conservative) loads. They can vary arbitrarily but in such a manner that there is no crack closure. Then the relation among the load values at the stability limit of the structure is linear. For instance, when a beam is subjected to combined action of lateral load P and axial load N, as shown in Fig. 1, the crack compatibility equation can be written as

$$\frac{1 - \sigma(\xi)}{D} = -\int_{\alpha_0}^{\alpha} C^{\sigma\sigma}(\xi, \xi')\sigma(\xi')d\xi' + C^{\sigma P}(\xi)P + C^{\sigma N}(\xi)N \quad (15)$$

where the symbols are self-explanatory. Since the loading terms do not enter the criterion of stability limit, the equation for the structural stability limit remains the same. If the condition for the stability limit is satisfied, the relation between these two loads is found to be linear:

$$\frac{P}{P^*} + \frac{N}{N^*} = 1 \quad (16)$$

where the denominators, defined as

$$P^* = \frac{1}{D}\frac{\int_{\alpha_0}^{\alpha} v(\xi)d\xi}{\int_{\alpha_0}^{\alpha} C^{\sigma P}(\xi)v(\xi)d\xi}$$

$$N^* = \frac{1}{D}\frac{\int_{\alpha_0}^{\alpha} v(\xi)d\xi}{\int_{\alpha_0}^{\alpha} C^{\sigma N}(\xi)v(\xi)d\xi}, \quad (17)$$

represent the critical loads when P and N are applied to the structure separately. Equation (16) is the general interaction relation when the structure fails by tensile fracture and the

Downloaded 04 May 2010 to 171.66.16.28. Redistribution subject to ASME license or copyright; see http://www.asme.org/terms/Terms_Use.cfm

softening stress-displacement law is linear. A relation of this type was also reported by Li, Müller, and Wörner (1994) in a discrete (matrix) form. Generalization to an arbitrary number of applied loads is self-evident.

When the stress-displacement relation for a cohesive crack is nonlinear, one can use an iterative succession of linear approximations representing tangents of the stress-displacement curve according to the preceding approximation (this approach was formulated for the maximum load in Li and Bažant, 1994).

4 Solution of Maximum Deflection

If the structure is loaded by controlled displacement (i.e., with a rigid grip), the stability limit is reached when there is a snap back in the diagram of load P versus load-line displacement u. The crack equilibrium equation for this case is Eq. (30) of the preceding paper which, in the case of linear softening, yields

$$[1 - w(\xi)]D = -\int_{\alpha_0}^{\alpha} R^{ww}(\xi, \xi')w(\xi')d\xi' + R^{wu}(\xi)u. \quad (18)$$

The dimensionless condition of stability limit may now be written as

$$\frac{1}{D}\int_{\alpha_0}^{\alpha} R^{ww}(\xi, \xi')v(\xi)d\xi = v(\xi'). \quad (19)$$

Since α is constant for geometrically similar structures, (19) is a linear homogeneous Fredholm integral equation for the unknown cohesive stress $v(\xi)$ in the process zone. This represents an eigenvalue problem with $1/D$ as the eigenvalue. Only the smallest eigenvalue $1/D$ represents a stability limit. The maximum deflection, characterizing snap back, is found to be

$$u = \frac{D\int_{\alpha_0}^{\alpha} v(\xi)d\xi}{\int_{\alpha_0}^{\alpha} S^{wu}v(\xi)d\xi}. \quad (20)$$

However, the maximum deflection can also be solved in terms of the compliance functions. To this end, we eliminate the load parameter P from (3) and (7) and obtain the following crack compatibility equation under displacement control:

$$1 - \sigma(\xi) = -D\int_{\alpha_0}^{\alpha} \tilde{C}^{\sigma\sigma}(\xi, \xi')\sigma(\xi')d\xi' + \frac{C^{\sigma P}(\xi)}{C^{PP}}u \quad (21)$$

where

$$\tilde{C}^{\sigma\sigma}(\xi, \xi') = C^{\sigma\sigma}(\xi, \xi') - C^{\sigma P}(\xi)C^{P\sigma}(\xi')\frac{1}{C^{PP}}. \quad (22)$$

The corresponding eigenvalue problem now becomes

$$v(\xi) = D\int_{\alpha_0}^{\alpha} \tilde{C}^{\sigma\sigma}(\xi', \xi)v(\xi')d\xi'. \quad (23)$$

This is equivalent to the eigenvalue problem (19) of stiffness formulation, because the modified compliance function is the inverse of the stiffness function R^{ww}. The maximum deflection can be expressed as

$$u = C^{PP}\frac{\int_{\alpha_0}^{\alpha} v(\xi)d\xi}{\int_{\alpha_0}^{\alpha} C^{\sigma P}v(\xi)d\xi}. \quad (24)$$

The compliance formulation is of course equivalent to the stiffness formulation. In a similar way, we can also express the maximum load in terms of the stiffness influence functions. The details will not be given because the derivation is analogous.

5 Stability Limit of Structure Loaded Through a Spring

If the device that controls loading (e.g., the testing machine) has finite compliance C_f, the device can be represented as a spring connected to the structure in series. In such a connection, the device and the structure share the same force. Denote as u the total deflection that is controlled, which is the sum of the deflection u_s of the structure and the deflection of the device $u - u_s$. Using (3), we can solve load P in terms of u as

$$P = (C^{PP} + C^f)^{-1}\left[\frac{u}{D} - \int_{\alpha_0}^{\alpha} C^{P\sigma}(\xi)\sigma(\xi)d\xi\right] \quad (25)$$

In the dimensionless form, the process zone equation is

$$1 - \sigma(\xi) = -D\int_{\alpha_0}^{\alpha} \tilde{C}^{\sigma\sigma}(\xi, \xi')\sigma(\xi')d\xi' + C^{\sigma P}(\xi)(C^{PP} + C_f)^{-1}u \quad (26)$$

where

$$\tilde{C}^{\sigma\sigma}(\xi, \xi') = C^{\sigma\sigma}(\xi, \xi') - C^{\sigma P}(\xi)(C^{PP} + C_f)^{-1}C^{P\sigma}(\xi'). \quad (27)$$

The form of the eigenvalue problem is the same as (23) except that the modified compliance function is defined by (27). The maximum deflection is found to be

$$u = (C^{PP} + C_f)\frac{\int_{\alpha_0}^{\alpha} v(\xi)d\xi}{\int_{\alpha_0}^{\alpha} C^{\sigma P}v(\xi)d\xi}. \quad (28)$$

This formula reduces to (24) when compliance C_f approaches zero.

On the other hand, if the spring is connected to the structure in parallel, it shares the same deflection with the structure. Denote by P the total load applied to the structure-spring system, which is the sum of the load P_s which acts on the structure and $S_f u$ where $S_f = 1/C_f$. Using (5) we can express u in terms of P as

$$u = \left[\int_{\alpha_0}^{\alpha} R^{uw}(\xi)w(\xi)d\xi + DP\right](R^{uu} + R_f)^{-1}. \quad (29)$$

Substituting (29) into (8), one obtains the following crack compatibility equation:

$$1 - w(\xi) = -\frac{1}{D}\int_{\alpha_0}^{\alpha} \tilde{R}^{ww}(\xi, \xi')w(\xi')d\xi' + R^{wu}(\xi)P(R^{uu} + R_f)^{-1} \quad (30)$$

where the modified stiffness function is defined as

$$\tilde{R}^{ww}(\xi, \xi') = R^{ww}(\xi, \xi') - R^{wu}(\xi)R^{uw}(\xi')(R^{uu} + R_f)^{-1}. \quad (31)$$

The eigenvalue problem is to find a nonzero eigenfunction satisfying

$$v(\xi) = \frac{1}{D}\int_{\alpha_0}^{\alpha} \tilde{R}^{ww}(\xi, \xi')v(\xi')d\xi'. \quad (32)$$

The maximum total applied load can be calculated from the following equation:

$$P = (R^{uu} + R_f)\frac{\int_{\alpha_0}^{\alpha} v(\xi)d\xi}{\int_{\alpha_0}^{\alpha} R^{wu}v(\xi)d\xi}. \quad (33)$$

Of course when the spring constant of the connected spring

Downloaded 04 May 2010 to 171.66.16.28. Redistribution subject to ASME license or copyright; see http://www.asme.org/terms/Terms_Use.cfm

approaches zero, (33) becomes the peak-load solution in the stiffness formulation without a spring.

6 Numerical Implementation

As a numerical example, a three-point bent fracture specimen (Fig. 1) is analyzed. The finite element method is used to obtain the compliance functions in a discretized form (although other methods, such as the boundary element method, might also be suitable). The four-node finite element, which is the simplest, is chosen to discretize one half of the beam. To determine the nodal compliance matrix, the displacement solutions are obtained for one unit load applied successively at each node along the potential crack path or at the load point.

Each column of matrix $C^{\sigma\sigma}$ represents nodal displacements on the crack line when a unit load is applied to one node in the process zone, $C^{\sigma P}$ represents the nodal displacements in the process zone when a unit load is applied at the load point, and C^{PP} represents the load-line displacement when a unit load is applied at the load point. During the calculation, the total relative crack length α is first taken to correspond to the node that is farthest from the crack mouth as allowed by the compliance matrix, and then cracks reaching successively to nodes closer and closer to the crack mouth are considered. In each case the nodal displacements that lie in the uncracked ligament are eliminated. In this way, the dependence of the compliance function on the crack length is reflected by the sizes of the compliance matrices.

Starting with Hillerborg (1976), the zero-K condition has been approximated by the condition that the elastic stress ahead of the cohesive crack tip be equal to the tensile strength. So in our dimensionless definition, $\sigma_{tip} = 1$. In the space of continuous functions, this condition is mathematically equivalent to the condition that the stress intensity factor K at the crack tip be zero (Barenblatt, 1962). After discretization, however, these two conditions are equivalent only approximately. Thus the use of the condition $\sigma_{tip} = 1$ inevitably introduces additional numerical error into the discrete solution. But this small price is quite justifiable, because we do not need the corresponding stress intensity factors, which are not easy to calculate anyway.

However, numerical results (Li and Bažant, 1994) show that, in order to obtain good accuracy for large (dimensionless) structural sizes, it seems important to assume the cohesive stress to vary linearly from node to node in the process zone, rather than a piece-wise constant manner. The assumption of linear variation of cohesive stress between the nodes leads to a tridiagonal matrix connecting the nodal values of cohesive stresses to the cohesive nodal forces (in detail, see Li and Bažant, 1994). Numerically, the differences in the maximum load values calculated by the eigenvalue analysis and by the load-deflection curves are usually in the fifth or sixth digit for linear (or nearly linear) softening laws.

7 Numerical Solution of the Maximum Deflection

Numerical examples for the peak load solution using the eigenvalue approach have been given in previous papers (e.g., Li and Hong, 1992; Li and Bažant, 1994). Therefore, we will discuss only the numerical solution of maximum deflection, which characterizes ductility of a structure. Although the maximum load solution and the maximum deflection solution are

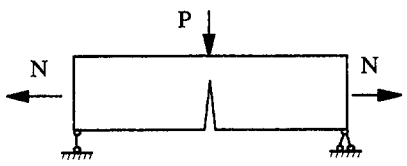


Fig. 1 Beam under combined lateral load and axial load

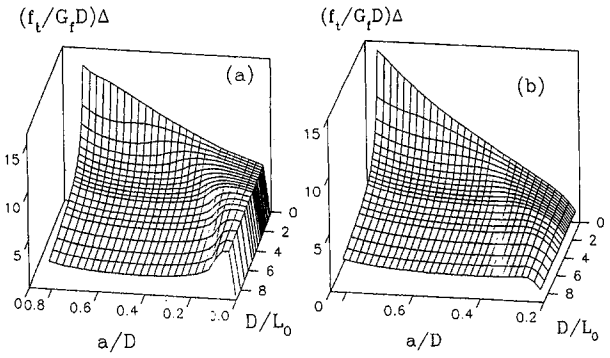


Fig. 2 Dimensionless deflection for (*a*) $\alpha_0 = 0$ and (*b*) $\alpha_0 = 0.2$

mathematically similar, there exists one important difference. For three-point-bent beams, the maximum load always exists, no matter how large the relative process zone length $\alpha - \alpha_0$ is, or how small the dimensionless size D/L_0 is. However, for maximum deflections, the situation is different. As shown in Fig. 2, there is no maximum deflection if the relative length α of the cohesive crack is large enough. The smallest dimensionless size D below which there is no snap back will be called the critical size of the structure. The critical size is a function of relative notch depth α_0 as well as the slenderness ratio (span-to-depth ratio of the beam).

The dependence of the critical size on the relative notch depth can also be seen in Fig. 2. Fig. 2(*a*) gives the deflection for beams without a notch ($\alpha_0 = 0$), and Fig. 2(*b*) for beams with relative notch depth $\alpha_0 = 0.2$. For $\alpha_0 = 0$, the critical size is found to be approximately 0.43 and for $\alpha_0 = 0.2$ approximately 1.4.

According to Eqs. (23) and (24), we can obtain the size effect curves for maximum deflection for any given relative length α of the cohesive crack. Figure 3 shows the size effect curves for different initial notch ratios. Note that, paradoxically, the curves extend even to the left of the critical sizes (dashed lines); these portions of the curves are of course physically meaningless since there exists no maximum deflection at all. The explanation is that these portions correspond to cases with negative σ, whereas our analytical expressions are valid only when the crack-opening displacement in the process zone is less than the crack-opening threshold w_c (at which the stress is reduced to zero). With careful observation, one finds that, when the condition of stability limit is satisfied, the critical size D is actually the size at which the crack-mouth-opening displacement becomes equal to the threshold w_c. Above the critical size (i.e., on right portions of the curves in Fig. 3), the obtained maximum deflections are exactly what one would obtain if the load-deflection curve were solved by the conventional method, that is, by solving the basic equations step by step for each different cohesive crack lengths.

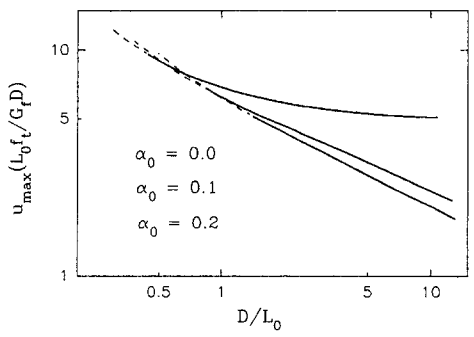


Fig. 3 Size effect curve for maximum deflection

Downloaded 04 May 2010 to 171.66.16.28. Redistribution subject to ASME license or copyright; see http://www.asme.org/terms/Terms_Use.cfm

As a check, we select, from the size effect curve, a maximum deflection value with its corresponding relative crack length α and its dimensionless size D. Then we use this dimensionless size as the input and solve the process zone equation together with the crack-tip equation ($\sigma_{tip} = 1$) for different crack lengths. In all the cases examined, the maximum deflection is found to be the same (within the numerical precision of the calculation) and to occur at the same relative crack length.

8 Final Remarks and Conclusions

The cohesive crack model can be effectively analyzed in terms of continuous influence functions. Under the assumption of a linear softening stress-displacement law, the criterion of stability limit, which has been analyzed by Bažant and Li (1995), becomes a linear eigenvalue problem when geometrically similar structures are considered. The peak value of the load parameter can be determined by solving the eigenvalue problem. In this manner, the size effect of the cohesive crack model becomes intimately related to the solutions of the eigenvalue problem. There are some similarities between the eigenvalue problem studied here and the eigenvalue problem for the buckling load of a structure. Both eigenvalue problems are derived from the criterion of structural stability limit. Whereas, in the buckling problem, the eigenvalue is Euler's critical load, in the cohesive crack model the eigenvalue is the structure size for which the loading parameter is maximized at a given relative cohesive crack length. The maximum load or load parameter can be calculated from the eigenfunctions. The following conclusions can be drawn:

1 When geometrically similar structures are considered, the criterion of stability limit becomes an eigenvalue problem. The size for which a given relative crack length corresponds to either the maximum load or the maximum displacement is the first eigenvalue of a homogeneous Fredholm integral equation. The size effect curve can thus be calculated efficiently.

2 If the softening stress-displacement law for the cohesive crack is linear, the eigenvalue problem becomes linearized and can be solved independently. The critical value of the loading parameter (either the maximum load or the maximum load-line deflection), can be determined through the eigenfunction obtained.

3 Numerical examples of the solution of the maximum deflection as a function of the dimensionless beam depth demonstrate that the maximum deflection solution ceases to be valid if the structure dimension (e.g., beam depth) becomes smaller than a certain critical value. This critical value is characterized by the condition that the crack opening at the stability limit reaches the threshold value at which the cohesive stress gets reduced to zero.

Acknowledgment

Partial financial support for the present theory (in both Parts I and II of the present study) was obtained under ONR grant No. N00014-91-J-1109 to Northwestern University (monitored by Dr. Yapa Rajapakse). Additional financial support for some ramifications to concrete fracture was obtained from the Center for Advanced Cement Based Materials at Northwestern University.

References

Barenblatt, G. I., 1962, "The mathematical theory of equilibrium cracks in brittle fracture," *Advances in Applied Mechanics,* Vol. 7, pp. 55–129.

Bažant, Z. P., and Cedolin, L., 1991, *Stability of Structures: Elastic, Inelastic, Fracture and Damage Theories,* Oxford University Press, Oxford, U.K.

Bažant, Z. P., and Li, Y. N., 1995, "Stability of Cohesive Crack Model: I. Energy Principles," ASME JOURNAL OF APPLIED MECHANICS, submitted for publication.

Hillerborg, A., Modéer, M., and Petersson, P.-E., 1976, "Analysis of crack formation and crack growth in concrete by means of fracture mechanics and finite elements," *Cement and Concrete Research,* Vol. 6, pp. 773–782.

Li, Y. N., and Hong, A. P., 1992, "Prediction of failure in notched infinite strips by the cohesive crack model," *International Journal of Solids and Structures,* Vol. 29, No. 23, pp. 2815–2828.

Li, Y. N., and Liang, R. Y., 1993, "The theory of boundary eigenvalue problem in the cohesive crack model and its application," *Journal of the Mechanics and Physics of Solids,* Vol. 41, No. 2, pp. 331–350.

Li, Y. N., and Bažant, Z. P., 1994, "Eigenvalue analysis of size effect in cohesive crack model," *International Journal of Fracture,* Vol. 66, pp. 213–226.

Li, Y. N., Müller, M., and Wörner, J.-D., 1994, "Two new approaches in the fictitious crack model and their applications," *Journal of Engineering Mechanics ASCE,* Vol. 120, No. 12, pp. 2604–2620.

Petersson, P.-E., 1981, "Crack growth and development of fracture zones in plain concrete and similar materials," Doctoral Dissertation, Lund Institute of Technology, Sweden.

Tricomi, F. G., 1957, *Integral equations,* Interscience Publishers, New York, (also Dover, 1985).

Downloaded 04 May 2010 to 171.66.16.28. Redistribution subject to ASME license or copyright; see http://www.asme.org/terms/Terms_Use.cfm

S.-M. Wang
Mikuni Berkeley R & D Corporation,
4000 Lakeside Drive,
Richmond, CA 94806

F. O. Eke
Department of Mechanical and
Aeronautical Engineering,
University of California,
Davis, CA 95616
Mem. ASME

Rotational Dynamics of Axisymmetric Variable Mass Systems

This paper studies the attitude dynamics of variable mass systems that have axisymmetric mass distribution and that are subjected to continuous mass variation while in motion. The equations of rotational motion for such systems are solved analytically under the assumption of zero external torque. It is found that such systems can spin up or spin down in free motion, and that the transverse angular velocity magnitude can increase or decrease with time. The analytical conditions for growth or decay of spin rate and lateral angular speed are presented, and these conditions are related to practical design criteria for rocket-type systems.

Introduction

The first documented study of the dynamics of bodies with varying mass was performed in the 18th century by Bernoulli (1738) in a monograph that included a section on hydroreactive propulsion. This first study was followed by a long period of only sporadic activity in this field, and it was not until the 20th century that a resurgence of activity in this area occurred, mostly in connection with rocketry. Early studies of variable mass systems focused on the translational motion of such systems. In the mid 20th century, researchers started to grapple with rotational equations of motion for variable mass systems (Rosser et al., 1947; Ellis and McArthur, 1959). The equations derived have forms similar to Euler's equations for rigid bodies, with extra terms accounting for mass variability. Thomson (1963) studied the free transverse attitude motion of a nonspinning axisymmetric rocket. Assuming negligible change in system radius of gyration, as well as a constant distance between system mass center and nozzle exit plane, he showed that the transverse rotation rate depends on the ratio of the distance of the system mass center from the nozzle exit, to the transverse radius of gyration of the rocket. If this ratio is greater than one (the most common case), the transverse angular velocity decreases with time; and when the ratio is less that one, the transverse angular velocity increases with time. Warner and Snyder (1968) examined the effects of mass variation on the spin rate of a rolling rocket under radial burn. They compared the results obtained by assuming constant radius of gyration to those obtained for varying radius of gyration, and found that attitude motion predictions can differ considerably depending on the assumptions made. Recently, Eke and Wang (1995) presented elaborate closed-form solutions of the equations of attitude motion of a variable mass cylinder. Their study assumed symmetric internal fluid flow with negligible whirling motion; its main conclusion was that the time history of the angular velocity of a variable mass cylinder depends on the initial dimensions of the cylinder, as well as on the manner in which its geometry changes as mass is lost.

This paper deals with an extension of the cylinder problem; it generalizes the problem to an axisymmetric system that has two equal central principal moments of inertia at all times, without necessarily being a body of revolution. As in previous studies, the goal here is to examine how the system's attitude motion is affected by the process of mass loss. Specifically, the equations of torque-free attitude motion are solved analytically, and the effect of mass variation on the various components of the angular velocity vector for the solid portion of the system is examined in detail.

Equations of Attitude Motion

A model of the type of system under consideration is shown in Fig. 1. This system consists of a solid portion, B, as well as the fluid portion comprising mostly products of combustion. An imaginary closed shell, C, of constant shape and volume is attached to B, and serves to delimit the system. Thus, everything within C at any given instant constitutes the system, S, at that instant. Several versions of the equations of motion for such a system exist in the literature (see, for example, Thomson and Reiter, 1965; Meirovitch, 1970; Eke and Wang, 1994; Wang, 1993). We adopt here, one of the vector equations of attitude motion derived by Eke and Wang (1994):

$$\mathbf{M} = \mathbf{I}_c\cdot\boldsymbol{\alpha} + \boldsymbol{\omega}\times\mathbf{I}_c\cdot\boldsymbol{\omega} + \left(\frac{{}^{B}d\mathbf{I}_c}{dt}\right)\cdot\boldsymbol{\omega} + \int_{S_c}\rho[\mathbf{p}\times(\boldsymbol{\omega}\times\mathbf{p})](\mathbf{v}_r\cdot\mathbf{n})dS + \int_{V}\rho[\boldsymbol{\omega}\times(\mathbf{p}\times\mathbf{v}_r)]dV + \frac{{}^{B}d}{dt}\int_{V_c}\rho(\mathbf{p}\times\mathbf{v}_r)dV + \int_{S_c}\rho(\mathbf{p}\times\mathbf{v}_r)(\mathbf{v}_r\cdot\mathbf{n})dS \quad (1)$$

with mass outflow rate from C, $\dot{m}_c$, satisfying the continuity equation

$$\dot{m}_c = -\int_{S_c}\rho(\mathbf{v}_r\cdot\mathbf{n})dS. \quad (2)$$

In these equations, $\boldsymbol{\omega}$ and $\boldsymbol{\alpha}$ are, respectively, the angular velocity and angular acceleration of the solid part of the system; $\mathbf{I}_c$ is the instantaneous central inertia dyadic of everything contained within the control region C; $\mathbf{p}$ is the position vector from the instantaneous mass center of S to a generic point, P, inside C; $\mathbf{v}_r$ is the velocity of point P relative to B; S_c is the area of C; $\mathbf{n}$ is an outward unit normal to C; ρ is the density function of S; V_c is the region of constant volume occupied by C; V is the region occupied by matter that happens to be inside C at the

Contributed by the Applied Mechanics Division of THE AMERICAN SOCIETY OF MECHANICAL ENGINEERS for presentation at the International Mechanical Engineering Congress and Exhibition, the Winter Annual Meeting of the ASME, San Francisco, CA, Nov. 12-17, 1995.

Discussion on this paper should be addressed to the Technical Editor, Professor Lewis T. Wheeler, Department of Mechanical Engineering, University of Houston, Houston, TX 77204-4792, and will be accepted until four months after final publication of the paper itself in the ASME JOURNAL OF APPLIED MECHANICS.

Manuscript received by the ASME Applied Mechanics Division, Nov. 4, 1994; final revision, Apr. 4, 1995. Associate Technical Editor: J. W. Shaw.

Paper No. 95-WA/APM-5.

Copyright © 1995 by ASME

Downloaded 04 May 2010 to 171.66.16.28. Redistribution subject to ASME license or copyright; see http://www.asme.org/terms/Terms_Use.cfm

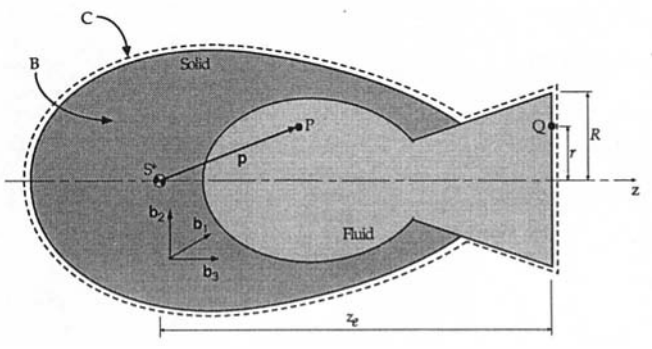


Fig. 1 Variable mass system

instant under consideration; the left superscript B indicates that the time derivative is to be taken in B; and $\mathbf{M}$ is the sum of moments of all the external forces on S about the system mass center, S^*. We note here that the mass center, S^*, is not necessarily fixed in B.

To make (1) somewhat more tractable, a number of assumptions are made. First, the solid portion of the system is assumed to be rigid, and the overall system is taken to be axisymmetric with respect to the longitudinal axis, z, of the system. By this, we mean that the z-axis is a central principal axis for the system at every instant, and that the moments of inertia for the other two (transverse) central principal axes are equal. Next, it is assumed that fluid flow within the system is steady as well as symmetrical about the z-axis; and, at this stage of the analysis, the fluid particles are assumed to have no whirling motion relative to the solid portion of the system. Because of the above assumptions, the last three terms of (1) vanish, and we are left with

$$\mathbf{M} = \mathbf{I}_c \cdot \boldsymbol{\alpha} + \boldsymbol{\omega} \times \mathbf{I}_c \cdot \boldsymbol{\omega} + \frac{{}^B d\mathbf{I}_c}{dt} \cdot \boldsymbol{\omega} + \int_{S_c} [\mathbf{p} \times (\boldsymbol{\omega} \times \mathbf{p})](\rho \mathbf{v}_r \cdot \mathbf{n}) dS \quad (3)$$

with

$$\mathbf{I}_c = I(\mathbf{b}_1\mathbf{b}_1 + \mathbf{b}_2\mathbf{b}_2) + J\mathbf{b}_3\mathbf{b}_3 \quad (4)$$

where I and J are the transverse and axial central inertia scalars of the system, respectively; and, $\mathbf{b}_1$, $\mathbf{b}_2$, $\mathbf{b}_3$ form a right-handed set of mutually perpendicular unit vectors fixed in B, and directed as shown in Fig. 1.

If, at any given instant, the inertial angular velocity of B is written as

$$\boldsymbol{\omega} = \omega_x\mathbf{b}_1 + \omega_y\mathbf{b}_2 + \omega_z\mathbf{b}_3, \quad (5)$$

then the first three terms on the right-hand side of (3) can be expressed, respectively, as

$$\mathbf{I}_c \cdot \boldsymbol{\alpha} = I(\dot{\omega}_x\mathbf{b}_1 + \dot{\omega}_y\mathbf{b}_2) + J\dot{\omega}_z\mathbf{b}_3 \quad (6)$$

$$\boldsymbol{\omega} \times \mathbf{I}_c \cdot \boldsymbol{\omega} = (J - I)\omega_z(\omega_y\mathbf{b}_1 - \omega_x\mathbf{b}_2) \quad (7)$$

and

$$\left(\frac{{}^B d}{dt}\mathbf{I}_c\right) \cdot \omega = \dot{I}(\omega_x\mathbf{b}_1 + \omega_y\mathbf{b}_2) + \dot{J}\omega_z\mathbf{b}_3. \quad (8)$$

The symmetry and steadiness of the flow field imply that the velocity $\mathbf{v}_r$ at a general point, Q, on the fluid exit plane satisfies the relation

$$\mathbf{v}_r \cdot \mathbf{n} = u(r). \quad (9)$$

As a result, the continuity equation, (2) takes the form

$$\dot{m}_c = -2\pi \int_0^R \rho u(r) r dr \quad (10)$$

where R is the radius of the fluid exit surface (see Fig. 1), that is assumed to be circular.

To evaluate the last term on the right-hand side of (3), we express the position vector $\mathbf{p}$, of a point, Q, on the exit plane, in cylindrical coordinates as

$$\mathbf{p} = r\cos\theta\mathbf{b}_1 + r\sin\theta\mathbf{b}_2 + z_e\mathbf{b}_3 \quad (11)$$

and the term then simplifies to

$$\int_{S_c} [\mathbf{p} \times (\boldsymbol{\omega} \times \mathbf{p})](\rho \mathbf{v}_r \cdot \mathbf{n}) dS = \int_0^R \pi\rho[(2z_e^2 + r^2)(\omega_x\mathbf{b}_1 + \omega_y\mathbf{b}_2) + 2r^2\omega_z\mathbf{b}_3]u(r)rdr. \quad (12)$$

This integral can then be evaluated once the velocity profile, $u(r)$, at the fluid exit surface is given. Here, three types of velocity distribution are examined: uniform, linear, and parabolic, as shown in Figs. 2(*a*), 2(*b*), and 2(*c*), respectively. In the case of uniform distribution,

$$u(r) = u_u = \text{constant}, \quad (13)$$

and, assuming ρ has the constant value, ρ_e, over the exit surface,

$$\dot{m}_c = -\pi\rho_e u_u R^2 \quad (14)$$

and

$$\int_{S_c} [\mathbf{p} \times (\boldsymbol{\omega} \times \mathbf{p})](\rho \mathbf{v}_r \cdot \mathbf{n}) dS = -\dot{m}_c\left[\left(z_e^2 + \frac{R^2}{4}\right)(\omega_x\mathbf{b}_1 + \omega_y\mathbf{b}_2) + \frac{R^2}{2}\omega_z\mathbf{b}_3\right]. \quad (15)$$

For linear velocity distribution,

$$u(r) = u_L\left(1 - \frac{r}{R}\right), \quad (16)$$

where u_L is a constant. Hence,

$$\dot{m}_c = -\tfrac{1}{3}\pi\rho_e u R^2 \quad (17)$$

and

$$\int_{S_c} [\mathbf{p} \times (\boldsymbol{\omega} \times \mathbf{p})](\rho \mathbf{v}_r \cdot \mathbf{n}) dS = -\dot{m}_c[(z_e^2 + \tfrac{3}{20}R^2)(\omega_x\mathbf{b}_1 + \omega_y\mathbf{b}_2) + \tfrac{3}{10}R^2\omega_z\mathbf{b}_3]. \quad (18)$$

Finally, parabolic velocity distribution at the exit plane leads to

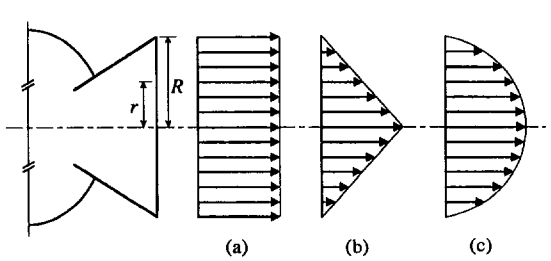


Fig. 2 Velocity profile at exit plane: (*a*) uniform; (*b*) linear; (*c*) parabolic

Downloaded 04 May 2010 to 171.66.16.28. Redistribution subject to ASME license or copyright; see http://www.asme.org/terms/Terms_Use.cfm

$$u(r) = u_p\left(1 - \frac{r^2}{R^2}\right) \tag{19}$$

so that

$$\dot{m}_c = -\tfrac{1}{2}\pi\rho_e u_p R^2 \tag{20}$$

and

$$\int_{S_c} [\mathbf{p} \times (\boldsymbol{\omega} \times \mathbf{p})](\rho \mathbf{v}_r \cdot \mathbf{n}) dS = -\dot{m}_c\left[\left(z_e^2 + \frac{R^2}{6}\right)(\omega_x \mathbf{b}_1 + \omega_y \mathbf{b}_2) + \frac{R^2}{3}\omega_z \mathbf{b}_3\right]. \tag{21}$$

Taken together, the above results yield the following equations of force-free attitude motion for axisymmetric variable mass systems:

$$\dot{\omega}_x = (1 - J/I)\omega_y\omega_z - \frac{1}{I}[\dot{I} - \dot{m}_c f(t)]\omega_x \tag{22}$$

$$\dot{\omega}_y = -(1 - J/I)\omega_x\omega_z - \frac{1}{I}[\dot{I} - \dot{m}_c f(t)]\omega_y \tag{23}$$

and

$$\dot{\omega}_z = -\frac{1}{J}[\dot{J} - \dot{m}_c\delta]\omega_z \tag{24}$$

where

$$f(t) = \begin{cases} z_e^2 + R^2/4 & \text{for uniform velocity profile} \\ z_e^2 + 3R^2/20 & \text{for linear velocity profile} \\ z_e^2 + R^2/6 & \text{for parabolic velocity profile} \end{cases} \tag{25}$$

and

$$\delta = \begin{cases} R^2/2 & \text{for uniform velocity profile} \\ 3R^2/10 & \text{for linear velocity profile} \\ R^2/3 & \text{for parabolic velocity profile.} \end{cases} \tag{26}$$

The function $f(t)$ and the constant δ depend on the actual velocity profile at the exit surface. Note, however, that for the three velocity distributions studied, $f(t)$ takes on its highest value when the velocity distribution at the exit plane is uniform, and its lowest value for a linear velocity profile. The same is true for δ. The actual velocity profile is likely to be somewhere between the aforementioned uniform and linear profiles. Thus, the actual $f(t)$ and δ are bounded by the expressions for the uniform and linear profiles in (25) and (26). The time rates of change of the inertia scalars ($\dot{I}$ and $\dot{J}$) depend mainly on the manner in which mass is lost from the system. For example, in the case of solid rocket motors, $\dot{I}$ and $\dot{J}$ would depend on the geometry of the propellant grain as well as the burning process.

Motion Characteristics

Spin Motion. The Eqs. (22), (23), and (24) derived in the previous section govern the attitude motion of the system. As in the axisymmetric rigid body case, the spin equation of motion, (24), is decoupled from the equations of transverse motion—(22) and (23). To characterize the attitude motion, we start by solving the equation of spin motion. Letting

$$H(t) = -\frac{1}{J}[\dot{J} - \dot{m}_c\delta] \tag{27}$$

(24) can be integrated to yield

$$\omega_z(t) = \omega_z(0) \cdot \exp\left[\int_0^t H(t)dt\right]. \tag{28}$$

Therefore, the time history of spin angular velocity, ω_z, is determined totally by the function $H(t)$. Now, let

$$\Phi(t) = \int_0^t H(t)dt = -\int_0^t [(\dot{J} - \dot{m}_c\delta)/J]dt = \Phi_1(t) + \Phi_2(t) \tag{29}$$

where

$$\Phi_1(t) = -\int_0^t (\dot{J}/J)dt = Ln(J_0/J) \tag{30}$$

$$\Phi_2(t) = \delta\int_0^t (\dot{m}_c/J)dt \tag{31}$$

and J_0 is the initial value of the axial moment of inertia, J. Because J must decrease with time as mass is lost, $\Phi_1(t)$ is always positive and monotonically increasing with time. On the other hand, $\dot{m}_c$ is a negative quantity that can be taken to be approximately constant. Hence, $\Phi_2(t)$ is negative at all times and is a monotonically decreasing function of time. All of this means that $\Phi(t)$ can grow, decay, remain stationary, or fluctuate with time, depending on the relative magnitudes of Φ_1 and Φ_2. In other words, the spin rate can grow or decay, or even fluctuate with time. $\omega_z(t) > \omega_z(0)$ whenever $\Phi_1(t) > |\Phi_2|$; similarly, $\omega_z(t) < \omega_z(0)$ anytime that $\Phi_1(t) < |\Phi_2(t)|$, and $\omega_z(t) = \omega_z(0)$ wherever $\Phi_1(t) = |\Phi_2(t)|$.

In the case of axisymmetric rigid bodies, $J = J_0$ and $\dot{m}_c = 0$, so that $\Phi_1 = \Phi_2 = \Phi = 0$ at all times. Thus, the criteria predict constant spin rate, in agreement with well known results. For an axisymmetric variable mass system with constant axial radius of gyration, k,

$$\Phi_1 = Ln(m_0/m) \tag{32}$$

and

$$\Phi_2 = \frac{\delta}{k^2}\int_0^t (\dot{m}/m)dt = -\frac{\delta}{k^2}Ln(m_0/m) \tag{33}$$

Hence

$$\left|\frac{\Phi_1}{\Phi_2}\right| = \frac{k^2}{\delta}. \tag{34}$$

Since this ratio is independent of time, the spin rate can grow continuously with time, or it can decay monotonically with time. It can also remain equal to its initial value throughout, but it cannot fluctuate with time. For the spin rate to grow at some instants and decay at other instants, the system under consideration must have varying axial radius of gyration. These statements are consistent with the observations of Warner and Snyder (1968), as well as with our recent results for the cylinder (Eke and Wang, 1995).

Transverse Motion. Once ω_z is obtained, further progress can be made with (22) and (23) by combining them into the complex form

$$\dot{\omega}_c = [F(t) - i(1 - J/I)\omega_z]\omega_c \tag{35}$$

where $i = \sqrt{-1}$, and

$$F(t) = -\frac{1}{I}[\dot{I} - \dot{m}_c f(t)] \tag{36}$$

with

$$\omega_c = \omega_x + i\omega_y \tag{37}$$

Downloaded 04 May 2010 to 171.66.16.28. Redistribution subject to ASME license or copyright; see http://www.asme.org/terms/Terms_Use.cfm

as the complex transverse angular velocity. Since ω_c would then be the only unknown in (35), this equation can be solved by separation of variables. If we define

$$\Gamma(t) = \exp\left[\int_0^t F(t)dt\right] \tag{38}$$

and

$$\Theta(t) = \int_0^t (1 - J/I)\omega_z(t)dt \tag{39}$$

then, the solution of (35) can be presented in the form

$$\omega_c(t) = \omega_c(0)\cdot\Gamma(t)\cdot\exp[-i\Theta(t)]. \tag{40}$$

Note that (40) implies that

$$\left|\frac{\omega_c(t)}{\omega_c(0)}\right| = \Gamma(t). \tag{41}$$

That is, the amplitude of the transverse angular velocity of the system depends solely on the function $F(t)$. Whether the transverse angular velocity grows or decays with time is determined completely by $F(t)$. The transverse angular velocity grows without bounds if $\int_0^t F(t)dt$ is a monotonically increasing function of time, and remains bounded otherwise. For the lateral angular speed to decay with time, $\int_0^t F(t)dt$ must decay monotonically with time. From (36),

$$\int_0^t F(t)dt = -\int_0^t \frac{1}{I}[\dot{I} - \dot{m}f(t)]dt$$

$$= Ln\left(\frac{I_0}{I}\right) + \int_0^t \frac{\dot{m}}{I} f(t)dt = \Sigma_1 + \Sigma_2 = \Sigma \tag{42}$$

where I_0 is the initial value of the transverse, central, moment of inertia, and

$$\Sigma_1 = Ln\left(\frac{I_0}{I}\right) \tag{43}$$

with

$$\Sigma_2 = \int_0^t \frac{\dot{m}}{I} f(t)dt. \tag{44}$$

We recall that the value of the function $f(t)$ depends on the velocity profile at the fluid exit plane. However, $f(t)$ is always positive, and thus Σ_2 is always negative and decreasing for systems with mass loss, and will tend to have a damping effect on the transverse angular velocity of rocket-like systems. On the other hand, Σ_1 is positive, and is a monotonically increasing function of time.

The normal desire is to have the transverse angular velocity decay rapidly to zero. To achieve this passively, I should be kept as close to I_0 as possible so that Σ_2 completely overshadows Σ_1. An example of how this can be done for a solid rocket is to give the propellant grain a prolate shape, have its mass center positioned as close as possible to the mass center of the rocket and its potential payload, and implement a radial burn. These results are in agreement with our recent findings (Eke and Wang, 1995) for a variable mass cylinder. For example, it was found that the transverse angular velocity of a prolate cylinder in end burn is damped much more rapidly than that of an oblate cylinder. That makes sense in light of the above criteria because the transverse central moment of inertia decreases much more slowly for the prolate shape. It was also found that if centrifugal (radial) burn is utilized instead, the transverse angular velocity of the oblate cylinder actually grows without bounds while that of the prolate cylinder is damped. This is also in agreement with the moment of inertia criterion given above. We note also that the actual values of the instantaneous inertia scalars (I and J) are of little value in determining whether the amplitude of the transverse angular velocity increases or decreases with time; they have much greater influence on (see (40) and (39)) the frequency of this motion. This is a very important observation because it points out the fact that it is not so much the overall size and shape of the system that determines whether the transverse angular velocity grows or decays; the more important factors are the amount of fuel, its geometric arrangement, and the depletion geometry. Finally, the growth or decay of the transverse angular velocity is not tied to the behavior of the spin rate. Hence, it is possible to have the transverse rate growing without bounds and the spin rate either increasing or decreasing.

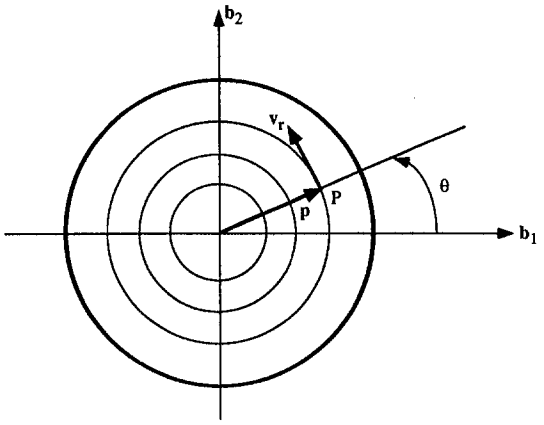


Fig. 3 Centered steady vortex flow

Effects of Centered Vortex Flow

We conclude this paper by relaxing—somewhat—one of the main assumptions made in this study. The results presented so far are valid for axisymmetric systems with internal fluid flow that is symmetric with respect to the longitudinal axis. However, whirling motion of fluid particles is precluded; that is, flows which allow fluid particles to move towards the exit plane along spiral curves centered on or off the longitudinal axis are not allowed. Since such spiral motion is not only possible but is in fact most likely to occur for spinning systems, we now consider the case where such flows occur along spiral curves centered on the longitudinal axis of the system. Thus, the velocity of a typical fluid particle P will not only have axial and radial components, but a transverse component will also be present. We assume steady flow so that the cross section of the flow lines is as shown in Fig. 3 at any instant of time. Then, in cylindrical coordinates, the position vector of the generic particle P can be written as

$$\mathbf{p} = r\cos\theta\mathbf{b}_1 + r\sin\theta\mathbf{b}_2 + z\mathbf{b}_3 \tag{45}$$

where z is the axial distance of the particle from the instantaneous mass center. We also have that

$$\mathbf{v}_r = -v\sin\theta\mathbf{b}_1 + v\cos\theta\mathbf{b}_2 + u\mathbf{b}_3. \tag{46}$$

The scalar v is the speed of the in-plane vortex motion, and it may vary with r, the radial position of P. Scalar u is the axial component of the velocity vector, and it may also vary with r.

To properly handle vortex fields, the more general form of the vector equation of attitude motion, (1), is now needed. The first three terms on the right-hand side of this equation are unaffected by the vortex flow; their expressions are therefore identical to those given in (6), (7), and (8). The fourth term also does not change. This is because $\mathbf{v}_r\cdot\mathbf{n} = u(r)$ as before at

Downloaded 04 May 2010 to 171.66.16.28. Redistribution subject to ASME license or copyright; see http://www.asme.org/terms/Terms_Use.cfm

the exit plane. The term $({}^{B}d/dt)\int_{V_c}\rho(\mathbf{p}\times\mathbf{v}_r)dV$ still vanishes, since the flow field inside the control region is steady. To evaluate the other two terms of (1), we start with

$$\mathbf{p}\times\mathbf{v}_r = (ru\sin\theta - zv\cos\theta)\mathbf{b}_1 - (ru\cos\theta - zv\sin\theta)\mathbf{b}_2 + rv\mathbf{b}_3 \quad (47)$$

so that

$$\begin{aligned}\int_{S_c}\rho(\mathbf{p}\times\mathbf{v}_r)(\mathbf{v}_r\cdot\mathbf{n})dS &= \int_0^R\int_0^{2\pi}[(ru\sin\theta - zv\cos\theta)\mathbf{b}_1 \\ &\quad - (ru\cos\theta - zv\sin\theta)\mathbf{b}_2 + rv\mathbf{b}_3]\rho urd\theta dr \\ &= \left(\int_0^R 2\pi\rho uvr^2dr\right)\mathbf{b}_3. \end{aligned} \quad (48)$$

This expression can be integrated exactly, once $u(r)$ and $v(r)$ are known. Note that only the $\mathbf{b}_3$ component survives, and that the z coordinate does not appear in this expression. Hence, this term will have no effect on lateral motion, although it will influence the spin rate. If we let

$$A(R) = \int_0^R 2\pi\rho uvr^2dr \quad (49)$$

it then becomes possible to show that

$$\begin{aligned}\int_{V_c}\rho[\boldsymbol{\omega}\times(\mathbf{p}\times\mathbf{v}_r)]dV &= \boldsymbol{\omega}\times\left(\int_0^{z_e}\int_0^R 2\pi\rho uvr^2drdz\right)\mathbf{b}_3 \\ &= (\omega_x\mathbf{b}_1 + \omega_y\mathbf{b}_2 + \omega_z\mathbf{b}_3)\times[A(R)z_e\mathbf{b}_3] \\ &= A(R)z_e(-\omega_x\mathbf{b}_2 + \omega_y\mathbf{b}_1). \end{aligned} \quad (50)$$

Observe that ω_x appears as one of the coefficients of $\mathbf{b}_2$ and ω_y appears as a coefficient of $\mathbf{b}_1$. Furthermore, the factors that multiply $\omega_x\mathbf{b}_2$ and $\omega_y\mathbf{b}_1$ have the same magnitude, but opposite signs. Therefore, when the differential equation of transverse motion is written in terms of the complex angular velocity ω_c, the contribution of (49) will appear in the imaginary part. Hence, the effect of this term, and thus of steady vortex, manifests itself in the frequency of transverse motion and not on the amplitude. In other words, the criteria established for the growth or decay of the transverse angular velocity magnitude remain valid under steady vortex flow.

Conclusion

The free attitude motion of an axisymmetric variable mass system differs markedly from that of rigid bodies of similar shape. Although an axisymmetric rigid body in free flight maintains a constant spin rate throughout, variable mass systems can spin up, spin down, or maintain a constant spin rate. The magnitude of the transverse angular velocity of variable mass systems can also grow or decay with time, depending on how the system's central transverse moment of inertia varies with time. In order for the lateral angular velocity to decay rapidly with time, the transverse moment of inertia should not be allowed to vary much. In the case of rockets, variation in inertia is a result of fuel depletion. It is thus possible to influence the attitude motion to one's advantage by making judicious choices for the mass, shape, location and depletion strategy for the rocket's propellant.

Acknowledgment

This material is based upon work supported by NASA under award No. NAG-2-4003.

References

Bernoulli, D., 1738, *Hydrodynamica,* Argentorati.

Eke, F. O., and Wang, S. M., 1994, "Equations of Motion of Two-Phase Variable Mass Systems with Solid Base," ASME JOURNAL OF APPLIED MECHANICS, Vol. 61, pp. 855–860.

Eke, F. O., and Wang, S. M., 1995, "Attitude Behavior of A Variable Mass Cylinder," ASME JOURNAL OF APPLIED MECHANICS, to appear.

Ellis, J. W., and McArthur, C. W., 1959, "Applicability of Euler's Dynamical Equations to Rocket Motion," *ARS Journal,* Vol. 29, No. 11, pp. 863–864.

Meirovitch, L., 1970, "General Motion of a Variable Mass Flexible Rocket with Internal Flow," *Journal of Spacecraft and Rockets,* Vol. 7, No. 2, pp. 186–195.

Rosser, J. B., Newton, R. R., and Cross, G. L., 1947, *Mathematical Theory of Rocket Flight,* McGraw-Hill, New York.

Thomson, W. T., 1963, *Introduction to Space Dynamics,* John Wiley and Sons, New York.

Thomson, W. T., and Reiter, G. S., 1965, "Jet Damping of a Solid Rocket: Theory and Flight Results," *AIAA Journal,* Vol. 3, No. 3, pp. 413–417.

Wang, S. M., 1993, "Attitude Dynamics of Variable Mass Systems," Ph.D. Dissertation, University of California, Davis, CA.

Warner, G. G., and Snyder, V. W., 1968, "A Re-Evaluation of Jet Damping," *J. Spacecraft,* Vol. 5, No. 3, pp. 364–366.

Downloaded 04 May 2010 to 171.66.16.28. Redistribution subject to ASME license or copyright; see http://www.asme.org/terms/Terms_Use.cfm

Optimal Design Problems in Mechanics of Growing Composite Solids, Part I: Preload Optimization

A. D. Drozdov
Institute for Industrial Mathematics,
Ben-Gurion University of the Negev,
Beer-Sheva, Israel

A. L. Kalamkarov
Department of Mechanical Engineering,
Technical University of Nova Scotia,
P. O. Box 1000,
Halifax, Nova Scotia B3J 2X4,
Canada
Mem. ASME

Optimal design problems arising in mechanics of growing composite viscoelastic and elastic solids subjected to aging are considered. The growth means a continuous mass influx to the body surface. Due to this process, the size of the body increases in time. The mass influx with pretensioning causes the rise of stresses in the growing body. The purpose of the current study is to propose a new class of the optimal design problems for the growing viscoelastic composite solids subjected to aging, and to solve the mechanical design problems of this new type. In the current paper, we analyze the optimal preload distribution in the winding process for cylindrical solids. The proposed approach and the obtained new solutions are of a special interest and importance for the optimization of winding of composite pressure vessels.

1 Introduction

The paper is devoted to the study of a new class of optimal design problems in mechanics of growing viscoelastic bodies subjected to aging. The growth means that the mass of a body increases monotonously in time due to the material influx from environment. The process of growth is treated as a process of successive accretion of thin layers of a material to the surface of a growing body. During the process of accretion, successive layers (built-up portions) are applied to a deformed boundary. This leads to dependence of the final stresses on the rate of growth and on the loading history.

The theory of growing elastic bodies was originated in the 1950s and 1960s. To our knowledge, the first problems in mechanics of growing elastic bodies were formulated and derived by Rashba (1953) and, independently, by Brown and Goodman (1963) and Goodman and Brown (1963). These problems were initiated by the practical civil engineering problems. Rashba (1953) analyzed the stress distribution in a concrete dam built up in successive layers. Goodman and Brown (1963) studied the effect of placing layers of a material to build up an embankment with one horizontal and one inclined face. Brown and Goodman (1963) investigated the stresses and the strains in a gravitating sphere that has grown to its final size by continuous accretion of a linear elastic material. This problem is connected with the well-known theory of planetary origin due to an accretion process on the surface of a central protoplanet at temperatures below the melting point of the planet material. The solution obtained by Brown and Goodman was later generalized to the case of a nonlinear viscoelastic material with finite strains by Arutyunyan and Drozdov (1984).

Interaction of engineering structures with accreted foundations was analyzed by Brown (1967) and Cristiano and Chantranuluck (1974). The stress state in an accreted snow plate was considered by Brown et al. (1972).

Mechanical problems of growing thin films were discussed by Hearn et al. (1986) and Tsai and Dillon (1987). Mathur et al. (1989) considered droplet consolidation of metallic materials, when the material in the form of a spray of droplets impinges on a substrate to produce a thick deposit. In the paper by Anestiev (1989), the formation of a thin ribbon by rapid quenching from the melt was analyzed.

All these problems were considered in the framework either of the model of a linear elastic body or of the model of a Newtonian fluid. According to these models, the mechanical properties of a material are independent of time, and the growing body is assumed to be homogeneous.

An essentially different situation arises when the growing body is made of an aging material. The aging of a material means the change of its mechanical properties in time due to some physical or chemical transformations. Typical examples of this phenomenon are the aging of polymers (due to the reconstruction of "long" moleculae) and the aging of concrete (due to the chemical interaction of concrete and water). A model of an aging viscoelastic material was proposed by Arutyunyan (1952). Some experimental data about the aging process in polymer materials are represented in Struik (1978).

For a growing body subjected to aging, the specific inhomogeneity arises because the different points of a body are born at the different moments of time. This inhomogeneity is characterized by the function $\kappa(x)$, where $\kappa(x)$ is the birth moment for the element with the coordinate x. Internal inhomogeneity is a typical feature of composite materials. The new models describing the effective and local properties of the composite solids were developed by Kalamkarov (1992). The model of inhomogeneously aging viscoelastic body was introduced by Arutyunyan (1976) and developed by Arutyunyan and Kolmanovskii (1983). This model was employed by Arutyunyan (1987) in the study of the growth process in aging viscoelastic bodies for infinitesimal strains, and by Arutyunyan and Drozdov (1984) in the case of finite strains. Detailed description of this theory and its applications can be found in Arutyunyan et al. (1987).

The main conclusion of the previous investigations can be formulated as follows. The final stress distribution in a growing body subjected to aging depends on the following factors: (i) the loading history, (ii) the rate of the material influx, (iii) the rheological properties of a viscoelastic material, and (iv) the rate of aging.

Contributed by the Applied Mechanics Division of THE AMERICAN SOCIETY OF MECHANICAL ENGINEERS for publication in the ASME JOURNAL OF APPLIED MECHANICS.

Discussion on this paper should be addressed to the Technical Editor, Professor Lewis T. Wheeler, Department of Mechanical Engineering, University of Houston, Houston, TX 77204-4792, and will be accepted until four months after final publication of the paper itself in the ASME JOURNAL OF APPLIED MECHANICS.

Manuscript received by the ASME Applied Mechanics Division, July 7, 1993; final revision, July 7, 1994. Associate Technical Editor: G. J. Dvorak.

Copyright © 1995 by ASME

Downloaded 04 May 2010 to 171.66.16.28. Redistribution subject to ASME license or copyright; see http://www.asme.org/terms/Terms_Use.cfm

For the technological processes of growth in engineering practice, these characteristics can be chosen under some restrictions. Therefore, the problem of their optimal choice naturally arises.

The first optimization problem in the theory of growing viscoelastic bodies subjected to aging was formulated and solved by Drozdov (1986). In this paper, the optimal rate of the material influx to a cantilevered viscoelastic beam was obtained. This rate ensures the minimum time of the fabrication process under the given restrictions on the beam deflection due to the action of external loads. The problem of the rate optimization for three-dimensional viscoelastic bodies was studied by Arutyunyan and Drozdov (1988). A stochastic problem of optimizing the rate of the material influx was proposed and solved by Drozdov (1988).

Another class of the optimal design problems in mechanics of growing bodies consists in determining the optimal conditions for the solidification process. It is worth to mention here the paper by Arutyunyan and Drozdov (1988), where the optimal temperature regime was obtained for the process of castings' solidification.

In the present work we propose two new classes of the optimal design problems for the growing viscoelastic bodies subjected to aging. In the current first part of the work we consider the problem of optimal winding of layers of ribbon for fabrication of the multilayered composite cylindrical solids. The winding is realized with pretensioning. The problem consists in determining the optimal preload in the ribbon that ensures the maximum load-carrying capacity of the vessel under the action of internal pressure.

In the second part of the work we analyze the problem of optimal design of the shape for the reinforced engineering structures on account of the process of their growth.

2 Optimal Preload of a Growing Cylindrical Solid

The winding of layers of narrow strips or fibers with pretensioning is probably the most comprehensive technological process in the modern manufacturing of composite pressure vessels. During the winding process some external loads are applied. These loads and the preload in built-up portions can be chosen to minimize the total weight or volume of the unit of a fixed load-carrying capacity. For cylindrical and spherical vessels under the action of internal pressure this minimum is attained if the stress intensity is uniform in all layers, cf. Banichuk (1980).

In this section, we consider the problem of determination of the optimal preload in a growing, multilayered, composite, thick-walled cylindrical vessel under the action of internal pressure. Our purpose is to provide a uniform stress intensity in the pressure vessel under the action of the main load.

2.1 Formulation of the Problem and Basic Relations. The growing body before the deformations is a hollow cylinder with the length l, the internal radius a_0 and the external radius a_1. The accretion of material on the external boundary surface of the cylinder begins at the moment $t = 0$ and occurs in the interval of time $[0, T]$. Due to the material influx, the external radius of the cylinder a changes according to the law: $a = a(t)$, with $a(0) = a_1$ and $a(T) = a_2$. We assume that there are no external forces and the state of plane deformation is realized in the cylindrical solid.

Let us introduce the cylindrical coordinates $\{r, \theta, z\}$, where the axis z coincides with the longitudinal axis of the cylinder. At the moment t, the growing cylinder occupies the domain

$$\{a_0 \le r \le a(t), \quad 0 \le \theta < 2\pi, \quad 0 \le z \le l\}.$$

In the interval $[t, t + dt]$, a cylindrical layer

$$\{a(t) < r \le a(t) + da(t), \quad 0 \le \theta < 2\pi, \quad 0 \le z \le l\},$$

joins the cylinder.

For better understanding we recall here some basic assertions of the theory of growing deformable solids. In mechanics of nongrowing deformable solids two basic configurations are introduced for the description of the deformation process. First is a natural configuration. An element of a body is in its natural configuration if all components of the stress tensor σ equal zero. It is assumed that a body can maintain its natural configuration during an arbitrary interval of time before the external forces will be applied. The other configuration is the actual configuration. The actual configuration of an element of a body is the configuration where this element is in equilibrium at the current moment of time under the action of external load. The natural configuration determines the shape of the body under consideration before the deformations, and the actual configuration determines the shape of this body during the deformation process. In the theory of growing bodies these two configurations are not sufficient for the description of the growth process because a built-up portion with different preloading can merge with the main (growing) body. Therefore, a third type of configuration, called the initial configuration, must be introduced. This new configuration determines the "schedule" or "plan" of growth. Namely, we introduce the Lagrange coordinate system and for any moment t, determine the domain occupied by a growing body in this coordinate system. On the boundary of this domain we describe the points of the main body and the built-up portions which coincide when the built-up element joins the growing body. The domain occupied by the growing body in the initial configuration increases monotonously in time (contrary to the domain occupied in the actual configuration which can decrease under the action of compressive forces). For a nongrowing body, the initial configuration coincides with the natural one. For a growing body this is true only for the main body at the initial moment of time. For built-up portions, the initial and the natural configurations can be different. This difference implies the preload needed for merging a built-up portion with the main body.

In our study we utilize the geometrical approach and introduce the transformation from the initial configuration of a built-up portion to its natural configuration. The preload corresponding to this transformation can be calculated using the constitutive equations of material.

In the problem of winding of a cylindrical solid we assume that the built-up layer is first deformed under the action of an internal pressure so that its internal radius (in the actual configuration, under the action of this pressure) coincides with the external radius of the growing body in the actual configuration. After this operation, layer is wrapped around the growing cylinder and instantly merges with it.

We assume that the mechanical behavior of the material obeys the following constitutive equations of an incompressible elastic body subject to aging, cf. Arutyunyan et al. (1987):

$$\sigma(t, r) = -p(t, r)I + 2\left[G(t - \kappa(r))e^o(t, r) - \int_{\kappa(r)}^{t} \dot{G}(s - \kappa(r))e^o(s, r)ds\right]. \quad (1)$$

Here σ is the stress tensor, p is the pressure, e^o is the strain tensor for the transition from the natural configuration of an element to its actual configuration at the current moment of time, I is the unit tensor, $G(t)$ is the current shear modulus, $\kappa(r)$ is the birth moment of the element with a polar radius r, and the upper dot denotes the differentiation with respect to time. A detailed discussion on the constitutive Eq. (1) is provided in the Appendix. For the main body ($a_0 \le r \le a_1$), κ coincides with the initial moment of time. For built-up portions, κ coincides with the moment of their merger with the main body:

Downloaded 04 May 2010 to 171.66.16.28. Redistribution subject to ASME license or copyright; see http://www.asme.org/terms/Terms_Use.cfm

$$\kappa(r) = \begin{cases} 0 & a_0 \le r \le a_1, \\ t & r = a(t). \end{cases}$$

We assume that an axisymmetrical deformation is realized in the growing cylindrical body, and denote by $u(t, r)$ the radial displacement for the transition from the initial to the actual configuration. The incompressibility condition $du/dr + u/r = 0$ yields

$$u = D(t)r^{-1}, \tag{2}$$

where $D = D(t)$ is an unknown function. According to Eq. (2) the nonzero components of the deviatoric part of the strain tensor for the transition from the initial to the actual configuration, e, can be represented as follows:

$$e_{11} = -D(t)r^{-2}, \quad e_{22} = D(t). \tag{3}$$

Let us represent the radial displacement for the transition from the initial to the actual configuration $u^*(r)$ and the nonzero components of the strain tensor for this transition e^* in the form (2), (3), respectively, in which the function $D(t)$ is replaced by a function $D^*(r)$.

Substituting (2) and (3) into Eq. (1) and using the identity $e^o(t, r) = e(t, r) - e^*(r)$ we find the following nonzero physical components of the stress tensor σ:

$$\sigma_r = -p(t, r) - 2r^{-2}\left[G(t - \kappa(r))(D(t) - D^*(r)) - \int_{\kappa(r)}^{t} \dot{G}(s - \kappa(r))(D(s) - D^*(r))ds \right],$$

$$\sigma_\theta = -p(t, r) + 2r^{-2}\left[G(t - \kappa(r))(D(t) - D^*(r)) - \int_{\kappa(r)}^{t} \dot{G}(s - \kappa(r))(D(s) - D^*(r))ds \right],$$

$$\sigma_z = -p(t, r). \tag{4}$$

For the main body, the initial and the natural configurations coincide. Therefore, $D^*(r) = 0$ for $a_0 \le r \le a_1$. In order to determine the function $D^*(r)$ for $a_1 < r \le a_2$, we consider the deformation of a built-up portion at the moment of its merger with the main body. It follows from Eqs. (2) and (4) that the following stresses arise in the cylindrical shell for an instant transition from the natural to the actual configuration:

$$\sigma_r(r) = -p(r) - 2G(0)[D(\kappa(r)) - D^*(r)]r^{-2},$$

$$\sigma_\theta(r) = -p(r) + 2G(0)[D(\kappa(r)) - D^*(r)]r^{-2},$$

$$\sigma_z(r) = -p(r).$$

Setting $\sigma_r(r) = 0$, $\sigma_\theta(r) = \xi(r)$, where $\xi(r)$ is the intensity of the preload, we obtain

$$D^*(r) = D(\kappa(r)) - \xi(r)r^2[4G(0)]^{-1}, \quad a_1 < r \le a_2. \tag{5}$$

Function $\xi(r)$ characterizes the preload in winding layers or strips. This function is not fixed and can be chosen to optimize the properties of the structure. We are looking for such function $\xi(r)$ that ensures the uniform stress intensity in all layers after application of the main load.

Integrating the equilibrium equation

$$\frac{d\sigma}{dr} + \frac{\sigma_r - \sigma_\theta}{r} = 0 \tag{6}$$

with respect to r from a_0 to $a(t)$, and using the expressions (4) and (5) and the boundary conditions $\sigma_r(t, a_0) = 0$ and $\sigma_r(t, a(t)) = 0$ we get

$$\left[G(t)\int_{a_0}^{a_1} \frac{dr}{r^3} + \int_{a_0}^{a(t)} G(t - \kappa(r))\frac{dr}{r^3} \right] D(t) - \left[\int_{a_0}^{a_1} \frac{dr}{r^3}\int_0^t \dot{G}(s)D(s)ds + \int_{a_1}^{a(t)} \frac{dr}{r^3}\int_{\kappa(r)}^t \dot{G}(s - \kappa(r))D(s)ds \right] = G(0)\int_{a_1}^{a(t)} D^*(r)\frac{dr}{r^3}.$$

Replacing the integrals with respect to r by integrals with respect to $\tau = \kappa(r)$, where $r = a(\tau)$, and using Eq. (5) we obtain

$$\left[\frac{1}{2}\left(\frac{1}{a_0^2} - \frac{1}{a_1^2}\right)G(t) + \int_0^t G(t - \tau)\frac{\dot{a}(\tau)}{a^3(\tau)}d\tau \right] D(t) - \int_0^t \left[\frac{1}{2}\left(\frac{1}{a_0^2} - \frac{1}{a_1^2}\right)\dot{G}(s) + \int_0^s \dot{G}(s - \tau)\frac{\dot{a}(\tau)}{a^3(\tau)}d\tau + G(0)\frac{\dot{a}(s)}{a^3(s)} \right] D(s)ds = -\frac{1}{4}\int_0^t \xi(a(\tau))\frac{\dot{a}(\tau)}{a(\tau)}d\tau.$$

Differentiation of this relationship with respect to t yields

$$\left[\frac{1}{2}\left(\frac{1}{a_0^2} - \frac{1}{a_1^2}\right)G(t) + \int_0^t G(t - \tau)\frac{\dot{a}(\tau)}{a^3(\tau)}d\tau \right] \dot{D}(t) = -\frac{1}{4}\xi(a(t))\frac{\dot{a}(t)}{a(t)}. \tag{7}$$

For a given preload intensity $\xi(r)$, this relation is a linear differential equation for the function $D(t)$ with the initial condition $D(0) = 0$.

Suppose that the vessel which has been manufactured in the way described above is loaded by the internal pressure P immediately after fabrication. Integrating equalibrium Eq. (6) from a_0 to $a_2 = a(T)$, and using the boundary conditions $\sigma_r(t, a_0) = -P$ and $\sigma_r(t, a_2) = 0$, we find that

$$P = \int_{a_0}^{a_2} \frac{\sigma_\theta - \sigma_r}{r}dr. \tag{8}$$

Substitution of the expression (4) into Eq. (8) yields

$$\frac{P}{2} = \left(\frac{1}{a_0^2} - \frac{1}{a_1^2}\right)\left[G(t)D(t) - \int_0^t \dot{G}(s)D(s)ds \right] + 2\int_0^T \left[G(t - \tau)(D(t) - D^*(a(\tau))) - \int_\tau^t \dot{G}(s - \tau)(D(s) - D^*(a(\tau)))ds \right] \frac{\dot{a}(\tau)}{a^3(\tau)}d\tau. \tag{9}$$

Differentiating Eq. (9) with respect to time we obtain

$$\left[\left(\frac{1}{a_0^2} - \frac{1}{a_1^2}\right)G(t) + 2\int_0^t G(t - \tau)\frac{\dot{a}(\tau)}{a^3(\tau)}d\tau \right] \dot{D}(t) = 0.$$

This relation implies that

$$D(t) = D(T + 0), \quad t \ge T, \tag{10}$$

where $D_1 = D(T + 0)$ satisfies the equation

$$\frac{P}{2} = \left[\left(\frac{1}{a_0^2} - \frac{1}{a_1^2}\right)G(T) + 2\int_0^T G(T - \tau)\frac{\dot{a}(\tau)}{a^3(\tau)}d\tau \right] D_1 - \left\{ \left(\frac{1}{a_0^2} - \frac{1}{a_1^2}\right)\int_0^T \dot{G}(s)D(s)ds \right.$$

Downloaded 04 May 2010 to 171.66.16.28. Redistribution subject to ASME license or copyright; see http://www.asme.org/terms/Terms_Use.cfm

$$+ 2\int_0^T \frac{\dot{a}(\tau)}{a^3(\tau)}\,d\tau\Bigg[G(T-\tau)D^*(a(\tau)) + \int_\tau^T \dot{G}(s-\tau)(D(s)-D^*(a(\tau)))\Bigg]ds\Bigg\}.$$

It follows from Eqs. (4) and (5) that the stress intensity in the cylindrical pressure vessel is equal to

$$S = \sigma_\theta - \sigma_r = \frac{4}{r^2}\left[G(t-\kappa(r))(D(t)-D^*(r)) - \int_0^t \dot{G}(s-\kappa(r))(D(s)-D^*(r))ds\right] \quad (11)$$

Differentiation of this expression with respect to t yields $\dot{S} = 4r^{-2}G(t-\kappa(r))\dot{D}(t)$. It follows from this relation and Eq. (10) that the following expression is valid for any moment of time $t \geq T$:

$$S(t,r) = S(T,r) = \frac{4}{r^2}\left[G(T-\kappa(r))(D_1 - D^*(r)) - \int_{\kappa(r)}^T \dot{G}(s-\kappa(r))(D(s)-D^*(r))ds\right].$$

Integrating by parts we obtain

$$S(t,r) = \frac{4}{r^2}\left[G(T-\kappa(r))(D_1 - D(T)) + G(0)(D(\kappa(r)) - D^*(r)) + \int_{\kappa(r)}^T G(s-\kappa(r))\dot{D}(s)ds\right].$$

Substitution of Eqs. (5) and (7) into this relation yields

$$S(t,r) = \xi(r) + \frac{4}{r^2}\left[G(T-\kappa(r))(D_1 - D(T)) - \frac{1}{2}\int_{\kappa(r)}^T \frac{G(s-\kappa(r))\xi(a(s))\dot{a}(s)a^{-1}(s)ds}{(a_0^{-2}-a_1^{-2})G(s) + 2\int_0^s G(s-\tau)\dot{a}(\tau)a^{-3}(\tau)d\tau}\right].$$

Finally, transforming the integral term we find that

$$S(t,r) = \xi(r) + \frac{4}{r^2}\left[G(T-\kappa(r))(D_1 - D(T)) - \frac{1}{2}\int_r^{a_2} \frac{G(\kappa(\rho)-\kappa(r))\xi(\rho)\rho^{-1}d\rho}{(a_0^{-2}-a_1^{-2})G(\kappa(\rho)) + 2\int_{a_1}^\rho G(\kappa(\rho)-\kappa(\beta))\beta^{-3}d\beta}\right]. \quad (12)$$

Let us assume that $S = S^*$, where S^* is given. Parameter S^* can be treated as a critical value of the stress intensity which is "permitted" by the material without being destroyed. Then Eq. (12) implies

$$\frac{r^2}{4}[S^* - \xi(r)] = G(T-\kappa(r))(D_1 - D(T)) - \frac{1}{2}\int_r^{a_2} \frac{G(\kappa(\rho)-\kappa(r))\xi(\rho)\rho^{-1}d\rho}{(a_0^{-2}-a_1^{-2})G(\kappa(\rho)) + 2\int_{a_1}^\rho G(\kappa(\rho)-\kappa(\beta))\beta^{-3}d\beta}. \quad (13)$$

It follows from Eqs. (4) and (8) that the following expression is valid for any moment of time $t \geq T$:

$$P = 4\int_{a_0}^{a_1}\left[G(t)D(t) - \int_0^t \dot{G}(s)D(s)ds\right]\frac{dr}{r^3} + \int_{a_1}^{a_2} S(t,r)\frac{dr}{r}.$$

This equality together with the formula (10) and the assumption $S = S^*$ leads to the formula

$$P = 2\left(\frac{1}{a_0^2} - \frac{1}{a_1^2}\right)\left[G(T)D_1 - \int_0^T \dot{G}(s)D(s)ds\right] + S^*\ln\frac{a_2}{a_1}.$$

Integrating by parts and employing Eq. (7) we get

$$P - S^*\ln\frac{a_2}{a_1} = 2\left(\frac{1}{a_0^2} - \frac{1}{a_1^2}\right)\left[G(T)(D_1 - D(T)) - \frac{1}{2}\int_0^T \frac{G(s)\xi(a(s))\dot{a}(s)a^{-1}(s)ds}{(a_0^{-2}-a_1^{-2})G(s) + 2\int_0^s G(s-\tau)\dot{a}(\tau)a^{-3}(\tau)d\tau}\right].$$

Therefore, we find that

$$\frac{P - S^*\ln(a_2/a_1)}{2(a_0^{-2}-a_1^{-2})} = G(T)(D_1 - D(T)) - \frac{1}{2}\int_{a_1}^{a_2} \frac{G(\kappa(\rho))\xi(\rho)\rho^{-1}d\rho}{(a_0^{-2}-a_1^{-2})G(\kappa(\rho)) + 2\int_{a_1}^\rho G(\kappa(\rho)-\kappa(\beta))\beta^{-3}d\beta}. \quad (14)$$

Excluding $D_1 - D(T)$ from Eqs. (13) and (14) we obtain the following integral equation for the function $\xi(r)$:

$$\frac{r^2}{2}[S^* - \xi(r)] + \int_r^{a_2} \frac{G(\kappa(\rho)-\kappa(r))\xi(\rho)\rho^{-1}d\rho}{(a_0^{-2}-a_1^{-2})G(\kappa(\rho)) + 2\int_{a_1}^\rho G(\kappa(\rho)-\kappa(\beta))\beta^{-3}d\beta} = \frac{G(T-\kappa(r))}{G(T)}\left[\frac{(P - S^*\ln(a_2/a_1)}{a_0^{-2}-a_1^{-2}} + \int_{a_1}^{a_2} \frac{G(\kappa(\rho))\xi(\rho)\rho^{-1}d\rho}{(a_0^{-2}-a_1^{-2})G(\kappa(\rho)) + 2\int_{a_1}^\rho G(\kappa(\rho)-\kappa(\beta))\beta^{-3}d\beta}\right]. \quad (15)$$

2.2 Growing of the Nonaging Cylindrical Solid. In the case of a nonaging elastic material, $G(t) = G$, Eq. (15) can be simplified and written as follows:

$$r^2[S^* - \xi(r)] = \frac{2a_0^2a_1^2}{a_1^2 - a_0^2}\left(P - S^*\ln\frac{a_2}{a_1}\right) + 2a_0^2\int_{a_1}^r \frac{\xi(\rho)\rho d\rho}{\rho^2 - a_0^2}.$$

Differentiation of this relationship with respect to r yields

$$r\frac{d\xi}{dr} + \frac{2r^2\xi}{r^2 - a_0^2} = 2S^*. \quad (16)$$

Setting $r = a_1$ we get

$$\xi(a_1) = \xi_0 = S^* + \frac{2a_0^2}{a_1^2 - a_0^2}\left(S^*\ln\frac{a_2}{a_1} - P\right). \quad (17)$$

Downloaded 04 May 2010 to 171.66.16.28. Redistribution subject to ASME license or copyright; see http://www.asme.org/terms/Terms_Use.cfm

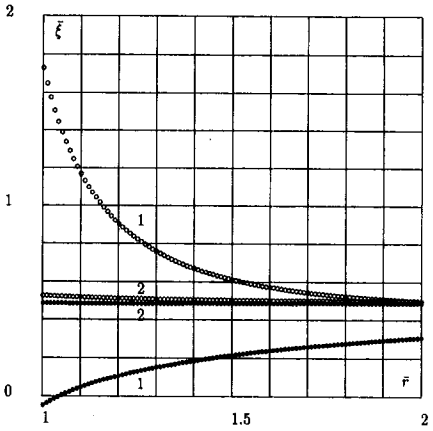


Fig. 1 Optimal preload intensity $\bar{\xi}$ versus radius $\bar{r}$ in the case of a non-aging material

Solution of Eq. (16) with the initial condition (17) has the form

$$\xi(r) = S^*\left[1 + \frac{a_0^2}{r^2 - a_0^2}\ln\left(\frac{a_2}{r}\right)^2\right] - \frac{2Pa_0^2}{r^2 - a_0^2}. \quad (18)$$

It will be more convenient to use the following dimensionless variables:

$$\bar{r} = \frac{r}{a_1}, \quad \bar{\xi} = \frac{\xi}{S^*}, \quad \bar{P} = \frac{P}{S^*}, \quad \eta_1 = \frac{a_1}{a_0}, \quad \eta_2 = \frac{a_2}{a_1}.$$

In this new notation, formula (18) implies

$$\bar{\xi}(\bar{r}) = 1 + \frac{2}{\eta_1^2\bar{r}^2 - 1}\left(\ln\frac{\eta_2}{\bar{r}} - \bar{P}\right).$$

Dependence of the calculated optimal preload intensity $\bar{\xi}$ on the dimensionless radial coordinate $\bar{r}$ is plotted in Fig. 1. The calculations are carried out for $\eta_2 = 2$. Light points correspond to $\bar{P} = 0$, and black points correspond to $\bar{P} = 1$. Curves 1 are obtained for a thin initial body ($\eta_1 = 1.25$, $a_0 = 0.8a_1$), and curves 2 are obtained for a thick one ($\eta_1 = 5$, $a_0 = 0.2a_1$).

The data of Fig. 1 show that in the case of a thick initial body, the optimal preload intensity $\bar{\xi}$ is practically independent of the radial coordinate r as well as of the internal pressure P. In the case of a thin initial body and the zero internal pressure P, the optimal preload intensity $\bar{\xi}$ diminishes significantly with the growth of the radial coordinate r and tends to a constant value for large r values. That means that the preload does not depend on the coordinate in a region far from the initial body. With the growth of the internal pressure P this behavior changes crucially. For $\bar{P} = 1$, the optimal pretensioning $\bar{\xi}$ increases monotonously with the increase of the radius r. For a fixed coordinate r, the preload intensity decreases with the growth of the internal pressure P.

It is worth to note that for a thin initial cylinder and a large internal pressure $\bar{P}$ we have obtained a region where the preload ξ is negative. This region appears for $\bar{P} \approx 0.95$ and grows with the increase of $\bar{P}$. It is impossible in practice to provide the negative preloading in a winding strip. That means that our optimization problem has a solution only for a sufficiently thick initial body or for a sufficiently small intensity of internal pressure.

2.3 Growing of the Aging Cylindrical Solid. In the general case of aging composite material, the differentiation of Eq. (15) with respect to r yields

$$r\frac{d\xi}{dr}(r) + 2\xi(r)\left[1 + \frac{r}{2}\frac{d\kappa}{dr}(r)\frac{\dot{G}(T-\kappa(r))}{G(T-\kappa(r))} + \frac{G(0)r^{-2}}{(a_0^{-2} - a_1^{-2})G(\kappa(r)) + 2\int_{a_1}^{r} G(\kappa(r) - \kappa(\rho))\rho^{-3}d\rho}\right]$$
$$- \frac{2}{r}\frac{d\kappa}{dr}(r)\int_r^{a_2}\left[\frac{\dot{G}(\kappa(\rho) - \kappa(r))}{G(\kappa(\rho) - \kappa(r))} - \frac{\dot{G}(T-\kappa(r))}{G(T-\kappa(r))}\right]$$
$$\times \frac{G(\kappa(\rho) - \kappa(r))\xi(\rho)\rho^{-1}d\rho}{(a_0^{-2} - a_1^{-2})G(\kappa(\rho)) + 2\int_{a_1}^{\rho} G(\kappa(\rho) - \kappa(\beta))\beta^{-3}d\beta}$$
$$= 2S^*\left[1 + \frac{r}{2}\frac{d\kappa}{dr}(r)\frac{\dot{G}(T-\kappa(r))}{G(T-\kappa(r))}\right]. \quad (19)$$

Suppose that during the growth process the function $G(t)$ does not change significantly, i.e., that there exists a small parameter $\mu \in (0, 1]$ such that $G(t) = G(0)[1 + \mu g(t)]$, where $g(t)$ is a bounded function in $[0, T]$. Substitution of this expression into Eq. (19) yields

$$r\frac{d\xi}{dr}(r) + \frac{2r^2}{r^2 - a_0^2}\xi(r)[1 + \mu A(r, \mu)] - \mu\int_r^{a_2} B(r, \rho, \mu)\xi(\rho)d\rho = 2S^*[1 + \mu F(r, \mu)], \quad \xi(a_1) = \xi_0, \quad (20)$$

where

$$A(r, \mu) = \frac{r^2 - a_0^2}{2r}\frac{d\kappa(r))}{dr}\frac{\dot{g}(T-\kappa(r))}{1 + \mu g(T-\kappa(r))} - \frac{a_0^2}{r^2}\frac{(a_0^{-2} - a_1^{-2})g(\kappa(r)) + 2\int_{a_1}^{r} g(\kappa(r) - \kappa(\rho))\rho^{-3}d\rho}{(a_0^{-2} - r^{-2}) + \mu[(a_0^{-2} - a_1^{-2})g(\kappa(r)) + 2\int_{a_1}^{r} g(\kappa(r) - \kappa(\rho))\rho^{-3}d\rho]},$$

$$B(r, \rho, \mu) = \frac{2}{r\rho}\frac{d\kappa(r)}{dr}\left[\frac{\dot{g}(\kappa(\rho) - \kappa(r))}{1 + \mu g(\kappa(\rho) - \kappa(r))} - \frac{\dot{g}(T-\kappa(r))}{1 + \mu g(T-\kappa(r))}\right]$$
$$\times \frac{1 + \mu g(\kappa(\rho) - \kappa(r))}{(a_0^{-2} - \rho^{-2}) + \mu[(a_0^{-2} - a_1^{-2})g(\kappa(\rho)) + 2\int_{a_1}^{\rho} g(\kappa(\rho) - \kappa(\beta))\beta^{-3}d\beta]},$$

$$F(r, \mu) = \frac{r}{2}\frac{d\kappa(r)}{dr}\frac{\dot{g}(T-\kappa(r))}{1 + \mu g(T-\kappa(r))}.$$

Downloaded 04 May 2010 to 171.66.16.28. Redistribution subject to ASME license or copyright; see http://www.asme.org/terms/Terms_Use.cfm

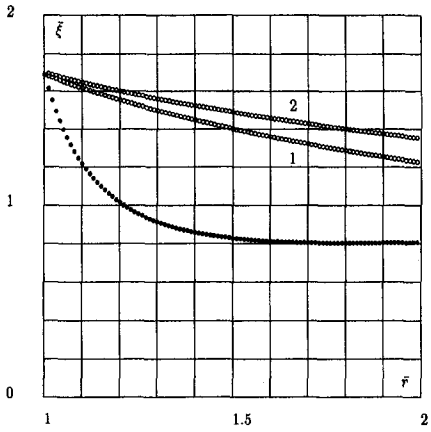


Fig. 2 Optimal preload intensity $\bar{\xi}$ versus radius $\bar{r}$ in the case of an aging material

Let us seek solution of Eq. (20) in the following form:

$$\xi(r, \mu) = \xi^{(0)}(r) + \mu\xi^{(1)}(r) + \ldots. \tag{21}$$

Substituting the formula (21) into Eq. (20) we find out that the function $\xi^{(0)}(r)$ satisfies the problem (16), (17), and, therefore, has the form (18). Function $\xi^{(1)}(r)$ satisfies the following problem:

$$r\frac{d\xi^{(1)}}{dr}(r) + \frac{2r^2}{r^2 - a_0^2}\xi^{(1)}(r) = F^{(1)}(r),$$

$$\xi^{(1)}(a_1) = 0, \tag{22}$$

where

$$F^{(1)}(r) = 2S^* f(r, 0) - \frac{2r^2\xi^{(0)}(r)A(r, 0)}{r^2 - a_0^2}$$

$$+ \int_r^{a_2} B(r, \rho, 0)\xi^{(0)}(\rho)d\rho$$

$$= r\frac{d\kappa(r)}{dr}\left\{\dot{g}(T - \kappa(r))[S^* - \xi^{(0)}(r)]\right.$$

$$\left. + \frac{2a_0^2}{r^2}\int_r^{a_2}\frac{\dot{g}(\kappa(\rho) - \kappa(r)) - \dot{g}(T - \kappa(r))}{\rho^2 - a_0^2}\rho\xi^{(0)}(\rho)d\rho\right\}$$

$$+ \frac{2r^2a_0^4}{(r^2 - a_0^2)^2}\xi^{(0)}(r)\left[(a_0^{-2} - a_1^{-2})g(\kappa(r))\right.$$

$$\left. + 2\int_{a_1}^r g(\kappa(r) - \kappa(\rho))\rho^{-3}d\rho\right].$$

The standard dependence of the current shear modulus $G(t)$ for an aging elastic material can be written as $G(t) = G_0 + (G_\infty - G_0)[1 - \exp(-\gamma t)]$, where G_0 is the initial elastic modulus, G_∞ is the limiting elastic modulus, and γ^{-1} is the characteristic time of the material aging. This dependence has been introduced for the description of the mechanical behavior of concrete; see Arutyunyan (1952), and later was employed for other materials demonstrating aging; see, e.g., Struik (1978).

In this case, we get $\mu = G_\infty/G_0 - 1$, $g(t) = 1 - \exp(-\gamma t)$. Let us assume that the growth is carried out with a constant rate u of the material influx: $u = 2\pi a(t)d(t)l$. The constant u is determined from the condition $uT = \pi l(a_2^2 - a_1^2)$. It follows from these formulae that

$$a(t) = a_1\sqrt{1 + \frac{(a_2^2 - a_1^2)t}{a_1^2T}}, \quad \kappa(r) = T\frac{r^2 - a_1^2}{a_2^2 - a_1^2}.$$

These relationships imply $F^{(1)}(r) = 2S^*\bar{F}^{(1)}(\bar{r})$, where

$$\bar{F}^{(1)}(\bar{r}) = \eta\left[\frac{\bar{r}^2}{\eta_2^2 - 1}(1 - \bar{\xi}^{(0)}(\bar{r}))\exp\left(-\eta\frac{\eta_2^2 - \bar{r}^2}{\eta_2^2 - 1}\right)\right.$$

$$+ \frac{1}{\bar{r}^2}\int_{\bar{r}}^{\eta_2}\left(\exp\left(-\eta\frac{\rho^2 - \bar{r}^2}{\eta_2^2 - 1}\right)\right.$$

$$\left.\left. - \exp\left(-\eta\frac{\eta_2^2 - \bar{r}^2}{\eta_2^2 - 1}\right)\right)\frac{\rho\bar{\xi}^{(0)}(\rho)d\rho}{\eta_1^2\rho^2 - 1}\right]$$

$$+ \frac{\bar{r}^2\bar{\xi}^{(0)}(\bar{r})}{(\eta_1^2\bar{r}^2 - 1)^2}\left[(\eta_1^2 - 1)\left(1 - \exp\left(-\eta\frac{\bar{r}^2 - 1}{\eta_2^2 - 1}\right)\right)\right.$$

$$\left. + 2\int_1^{\bar{r}}\left(1 - \exp\left(-\eta\frac{\bar{r}^2 - \rho^2}{\eta_2^2 - 1}\right)\right)\frac{d\rho}{\rho^3}\right],$$

and $\eta = \gamma T$. Introducing the dimensionless quantity $\bar{\xi}^{(1)}(\bar{r}) = \xi^{(1)}(r)/S^*$ we can rewrite Eq. (22) as follows:

$$\frac{d\bar{\xi}^{(1)}}{d\bar{r}} = \frac{2}{\bar{r}}\left[\bar{F}^{(1)}(\bar{r}) - \frac{\eta_1^2\bar{r}^2}{\eta_1^2\bar{r}^2 - 1}\bar{\xi}^{(1)}\right], \quad \bar{\xi}^{(1)}(1) = 0.$$

Dependence of the calculated optimal preload intensity $\bar{\xi}$ versus the dimensionless radius $\bar{r}$ is plotted in Fig. 2. Numerical analysis is carried out for $\eta_1 = 1.25$, $\eta_2 = 2.0$, $\mu = 0.2$, and $\bar{P} = 0.5$. Black points correspond to the zero approximation $\bar{\xi}^{(0)}$, and light points correspond to the first approximation $\bar{\xi}^{(0)} + \mu\bar{\xi}^{(1)}$ in our calculations of the optimal pretension $\bar{\xi}$. Curve 1 is obtained in the case $\eta = 1$, and curve 2 is obtained for $\eta = 100$. The data of Fig. 2 show that the optimal pretension $\bar{\xi}$ is a monotonously decreasing function of the radius. The rate of decrease is maximum for a nonaging material and diminishes with the growth of η. For a fixed time of winding, T, this means that the increase of the rate of aging γ implies the increase of the optimal preload intensity at any point of the growing cylinder. For any polar radius r, the preload intensity for a pressure vessel made of a nonaging material is less than the preload intensity for a pressure vessel made of an aging material.

3 Conclusions

A new class of the optimal design problems arising in mechanics of growing viscoelastic composite bodies subjected to aging is proposed.

In the current paper, we consider the problem of the optimal pretensioning in fabrication of composite pressure vessels by winding layers of a ribbon. In this problem, we derive an explicit solution (the dependence of the optimal preload intensity ξ versus the polar radius r) for a nonaging material and an asymptotic analytical solution for an aging material of the ribbon. By numerical analysis, we have studied the influence of the rheological characteristics of material on the optimal pretensioning and have formulated the following recommendations:

(i) for a thick initial pressure vessel, the optimal preload intensity ξ is practically independent of the radius r as well as of the internal pressure P;
(ii) for a thin initial pressure vessel and sufficiently small internal pressure P, the optimal preload intensity ξ monotonously decreases with the growth of the radius r and tends to a constant value in the region far enough from initial body;
(iii) the rate of decrease is maximum for a nonaging material, and diminishes with the growth of the rate of aging. For a fixed time of the winding process, the increase of the rate of aging

Downloaded 04 May 2010 to 171.66.16.28. Redistribution subject to ASME license or copyright; see http://www.asme.org/terms/Terms_Use.cfm

implies the increase of the optimal preload intensity at any point of the growing cylindrical body; and

(iv) for a thin initial pressure vessels and sufficiently large internal pressure P, the optimal preload intensity ξ monotonously increases with the growth of the radius r.

Acknowledgments

This work has been supported by the Natural Sciences and Engineering Research Council of Canada.

References

Anestiev, L. A., 1989, "An Analysis of Heat and Mass Transfer and Ribbon Formation by Rapid Quenching from the Melt," *Materials Science and Engineering,* Vol. A110, pp. 131–138.

Arutyunyan, N. Kh., 1952, *Some Problems in the Creep Theory,* Gostechizdat, Moscow (in Russian).

Arutyunyan, N. Kh., 1976, "Theory of Creep in Nonuniformly Hereditary-Aging Media," *Soviet Physics Doklady,* Vol. 21, No. 7, pp. 385–386.

Arutyunyan, N. Kh., 1977, "Boundary Problem in the Creep Theory for a Built-up Body," *Applied Mathematics and Mechanics,* Vol. 41, pp. 783–789.

Arutyunyan, N. Kh., and Drozdov, A. D., 1984, "Mechanics of Growing Viscoelastic Bodies Subjected to Aging with Finite Deformations," *Soviet Physics Doklady,* Vol. 29, pp. 450–452.

Arutyunyan, N. Kh., and Drozdov, A. D., 1984, "Accreting Gravitating Viscoelastic Sphere with Finite Deformations," *Mechanics of Solids,* Vol. 19, No. 4, pp. 121–134.

Arutyunyan, N. Kh., and Drozdov, A. D., 1988, "Optimization Problems in the Mechanics of Growing Solids," *Mechanics of Composite Materials,* Vol. 24, pp. 359–369.

Arutyunyan, N. Kh., and Drozdov, A. D., 1988, "Optimization of the Crystallization Process for a Spherical Casting," *Doklady Akademii Nauk Arm. SSR,* Vol. 87, pp. 212–215 (in Russian).

Arutyunyan, N. Kh., Drozdov, A. D., and Naumov, V. E., 1987, *Mechanics of Growing Viscoelastoplastic Bodies,* Nauka, Moscow (in Russian).

Arutyunyan, N. Kh., and Kolmanovskii, V. B., 1983, *Creep Theory for Heterogeneous Bodies,* Nauka, Moscow (in Russian).

Banichuk, N. V., 1980, *Shape Optimization for Elastic Bodies,* Nauka, Moscow (in Russian).

Brown, C. B., 1967, "Forces on Rigid Culverts under High Fills," *Journal of the Structural Division, ASCE,* Vol. 93, pp. 195–215.

Brown, C. B., Evans, R. J., and LaChapelle, E. R., 1972, "Slab Avalanching and State of Stress in Fallen Snow," *Journal of Geophysical Research,* Vol. 77, pp. 4570–4580.

Brown, C. B., and Goodman, L. E., 1963, "Gravitational Stresses in Accreted Bodies," *Proceedings of the Royal Society of London,* Vol. A276, pp. 571–576.

Christensen, R. M., 1982, *Theory of Viscoelasticity. An Introduction,* Academic Press, New York.

Christiano, P. P., and Chantranuluck, S., 1974, "Retaining Wall under Action of Accreted Backfill," *Journal of Geotechnical Engineering Division, ASCE,* Vol. 100, pp. 471–476.

Drozdov, A. D., 1986, "The Time-Optimal Regime for Manufacturing Rods of an Inhomogeneous, Aging, Viscoelastic Material," *Izvestiya Akademii Nauk Arm. SSR. Mekhanika,* Vol. 37, pp. 48–64 (in Russian).

Drozdov, A. D., 1988, "Optimization of the Process of Growth of Elastic Bodies," *Journal of Applied Mechanics and Technical Physics,* Vol. 29, pp. 911–914.

Fabrizio, M., and Morro, A., 1992, *Mathematical Problems in Linear Viscoelasticity,* SIAM Studies in Applied Mathematics, Vol. 12, Philadelphia, PA.

Goodman, L. E., and Brown, C. B., 1963, "Dead Load Stresses and the Instability of Slopes," *Journal of the Soil Mechanics and Foundations Division: Proceedings of the American Society of Civil Engineers,* Vol. 89, ASCE, New York, pp. 103–134.

Hearn, E. W., Werner, D. J., and Doney, D. A., 1986, "Film-Induced Stress Model," *Journal of Electrochemical Society,* Vol. 133, pp. 1749–1751.

Kalamkarov, A. L., 1992, *Composite and Reinforced Elements of Construction,* Wiley, Chichester, U.K.

Mathur, P., Apelian, D., and Lawley, A., 1989, "Analysis of the Spray Deposition Process," *Acta Metallurgica,* Vol. 37, pp. 429–443.

McKenna, G. B., and Kovacs, A. J., 1984, "Physical Aging of Poly(Methyl Methacrylate) in the Nonlinear Range: Torque and Normal Force Measurements," *Polymer Engineering and Science,* Vol. 24, pp. 1138–1141.

Rashba, E. I., 1953, "The Influence of the Construction Schedule on Stresses in Heavy Dams," *Proceedings of the Institute for Civil Engineering (Ukr. SSR),* Vol. 18, pp. 23–27.

Renardy, M., Hrusa, W. J., and Nohel, J. A., 1987, *Mathematical Problems in Viscoelasticity,* Longmans Press, Essex, U.K.

Ross, A. D., 1958, "Creep in Concrete under Variable Stress," *Journal of the American Concrete Institute,* Vol. 29, pp. 739–758.

Struik, L. C. E., 1978, *Physical Aging in Amorphous Polymers and Other Materials,* Elsevier, Amsterdam.

Tsai, C. T., and Dillon, O. W., 1987, "Thermal Viscoplastic Buckling During the Growth of Silicon Ribbon," *International Journal of Solids and Structures,* Vol. 23, pp. 387–402.

APPENDIX

The constitutive Eq. (1) that provides the basis for our study is written in a nonstandard form. In this Appendix we deduce it from the well-known constitutive relations (see, e.g., Christensen (1982), Fabrizio and Morro (1992), Renardy et al. (1987)).

The standard constitutive equation for an incompressible, linearly viscoelastic medium is written as follows:

$$\bar{\sigma} = -3p, \quad s = 2G\left(e - \int_0^t Red\tau\right), \tag{A1}$$

where $\bar{\sigma}$ and s are the spherical and deviatoric parts of the stress tensor σ, and e is the deviatoric part of the strain tensor ϵ (it follows from the incompressibility condition that the spherical part of the strain tensor equals zero, so that $e = \epsilon$), p is pressure, G is the shear modulus, and R is the relaxation kernel.

Materials with a constant modulus G and a function R depending only on the difference of arguments $(t - \tau)$ are called nonaging, whereas materials with a time-varying modulus G and a function R depending on two arguments t and τ separately, are called aging.

Below we focus our attention on aging viscoelastic materials whose mechanical properties are studied in a number of experimental works (see, e.g., Ross (1958), Struik (1978)).

It is common to introduce the following relaxation measure Q, instead of the relaxation kernel R:

$$R(t, \tau) = \frac{1}{G(t)} \frac{\partial}{\partial \tau} [G(\tau) + Q(t, \tau)]. \tag{A2}$$

We confine ourselves to regular relaxation measures and assume that functions in the right-hand side of Eq. (A2) are sufficiently smooth.

Substitution of expressions (A1) and (A2) into the formula for the stress tensor

$$\sigma = \tfrac{1}{3}\bar{\sigma} I + s,$$

implies that

$$\sigma(t) = -p(t)I + 2\left\{G(t)e(t) - \int_0^t \frac{\partial}{\partial \tau}[G(\tau) + Q(t, \tau)]e(\tau)d\tau\right\}, \tag{A3}$$

where I is the unit tensor.

The constitutive model, Eq. (A3), describes the behavior of an aging viscoelastic material. Function $G(t)$ in Eq. (A3) determines the instant response in the material, and function $Q(t, \tau)$ determines the stress relaxation.

An aging elastic material is a particular case of an aging viscoelastic material with zero relaxation measure. Equation (A3) implies that the constitutive law of an aging elastic material can be written as follows:

$$\sigma(t) = -p(t)I + 2\left[G(t)e(t) - \int_0^t \dot{G}(\tau)e(\tau)d\tau\right], \tag{A4}$$

where the upper dot denotes the differentiation with respect to time.

Equation (A4) can be also written in the form similar to Eq. (A1),

$$\bar{\sigma}(t) = -3p(t), \quad s(t) = 2\left[G(t)e(t) - \int_0^t \dot{G}(\tau)e(\tau)d\tau\right].$$

Differentiation of the latter equality with respect to time yields

$$\dot{s}(t) = 2G(t)\dot{e}(t). \tag{A5}$$

Downloaded 04 May 2010 to 171.66.16.28. Redistribution subject to ASME license or copyright; see http://www.asme.org/terms/Terms_Use.cfm

The question of natural interest is to compare this relationship with another constitutive equation which is also used to describe the mechanical behavior of viscoelastic solids; see, e.g., McKenna and Kovacs (1984),

$$s(t) = 2G(t)e(t). \tag{A6}$$

Formally, both expressions (A5) and (A6) can be employed to describe the aging elastic material. Nevertheless, we use Eq. (A5) in our work referring to the following arguments:

(i) Equation (A6) is usually utilized in experimental research as a model for the description of the viscoelastic behavior. In this case, strain e is assumed to be time independent, and the secant stress-relaxation modulus $G(t)$ is defined as the ratio of the stress $\sigma(t)$ to the uniform in time strain e. This ratio is not divided into the instant modulus and the relaxation kernel, as in Eq. (A1), and it contains the entire information about the viscoelastic response, see Struik (1978). So far, for time-dependent deformations, function $G(t)$ cannot serve as a material characteristics, since it depends essentially on the history of strains.

(ii) One of the basic principles of the theory of aging elastic materials states that modulus $G(t)$ grows in time. This fact has been approved by several experimental data; see, e.g., Arutyunyan (1952), Ross (1958). All the known interpretations of experiments based on Eq. (A6) demonstrate that coefficient $G(t)$ in (A6) decreases in time due to the stress relaxation; see, e.g., McKenna and Kovacs (1984), Struik (1978). This is another reason why Eq. (A6) cannot be used for adequate modeling of aging elastic materials.

(iii) For the shear modulus $G(t)$ monotonously increasing in time, only model (A5) provides a correct thermodynamic description of the material behavior. To verify this statement, let us calculate work of internal forces for a closed circle in the interval $[0, T]$ when dilatation is absent, and shear strain starts and finishes at point $e = 0$. By using Eq. (A5), and the standard technique of integrating by parts, we find

$$\int_0^T \sigma(t)\cdot\dot{e}(t)dt = \int_0^T s(t)de(t) = s(t)e(t)\Big|_{t=0}^{t=T}$$

$$- \int_0^T \dot{s}(t)\cdot e(t)dt = -2\int_0^T G(t)e(t)\cdot\dot{e}(t)dt$$

$$= -2\int_0^T G(t)d(e(t)\cdot e(t)) = -G(t)(e(t)\cdot e(t))\Big|_{t=0}^{t=T}$$

$$+ \int_0^T \dot{G}(t)(e(t)\cdot e(t))dt \geq 0.$$

By applying Eq. (A6) and repeating a similar procedure, we can obtain both positive and negative values, but the negative values contradict the second law of thermodynamics.

Concluding the foregoing consideration, we adopt the constitutive model (A4) equivalent to Eq. (A5) for our analysis.

Equation (A4) determines the response in an aging elastic body without accretion. For a built-up solid this equation is valid only for its main part which exists at the initial moment of time. For a built-up portion in the neighborhood of the point with coordinate r, time t should be replaced by the eigentime of the element which is equal to the difference between the time t and the moment of material creation $\kappa(r)$. Moreover, strain tensor e, that characterizes transition from the initial to the actual configuration, should be replaced by the eigenstrain tensor e^o that characterizes transition from the natural (stress-free) configuration of the accreted element to the actual configuration for the growing body. For the growth without prestressing the eigenstrain is equal to the difference between the strain at moment t and the strain at the moment when the built-up portion merges with the growing solid,

$$e^o(t, r) = e(t, r) - e(\kappa(r), r).$$

On account of these transformations, Eq. (A4) turns into the constitutive Eq. (1).

Downloaded 04 May 2010 to 171.66.16.28. Redistribution subject to ASME license or copyright; see http://www.asme.org/terms/Terms_Use.cfm

Optimal Design Problems in Mechanics of Growing Composite Solids, Part II: Shape Optimization

A. D. Drozdov
Institute for Industrial Mathematics,
Ben-Gurion University of the Negev,
Beer-Sheva, Israel

A. L. Kalamkarov
Department of Mechanical Engineering,
Technical University of Nova Scotia,
P. O. Box 1000,
Halifax, Nova Scotia B3J 2X4,
Canada
Mem. ASME

Optimal design problems arising in mechanics of growing composite viscoelastic and elastic solids subjected to aging are considered. The growth means a continuous mass influx to the body surface. Due to this process, the size of the body increases in time. The mass influx with pretensioning causes the rise of stresses in the growing body. The purpose of the current study is to propose a new class of the optimal design problems for the growing viscoelastic composite solids subjected to aging, and to solve the mechanical design problems of this new type. In the current paper we analyze the optimal design of the shape of growing reinforced beams which minimizes their maximum deflection. The proposed approach and the obtained new solutions are of a special interest and importance for the design of the reinforced cantilevers and bridges.

1 Introduction

In the present work we study the problem of optimal design of the shape of engineering structures on account of their growth. The problem of shape optimization for elastic and elastoplastic thin-walled elements of construction with fixed mass were analyzed, e.g., by Banichuk (1980) and Troitskii and Petukhov (1982). Optimization of the thickness of a nongrowing, heterogeneously aging, viscoelastic beam was studied by Arutyunyan and Kolmanovskii (1983) and by Drozdov and Kolmanovskii (1984). The shape optimization problems for a three-dimensional, aging, viscoelastic body were analyzed by Zevin (1979). The problems of the numerical design of wafer and honeycomb-like shells with the optimal shape and strength are solved by Kalamkarov and Kolpakov (1993). Their consideration is based on the general homogenization composite shell model developed by Kalamkarov (1992).

The purpose of current work is to analyze a correlation between the rate of growth and the optimal final shape of an accreted solid. We analyze the problem of thickness optimization for a growing reinforced beam subjected to aging, and we obtain the optimal thickness distribution for a cantilevered beam under the action of its weight. In our study we employ the model of an aging elastic medium. This model is sufficiently simple (with respect to the model of a viscoelastic material with an arbitrary relaxation kernel), and it allows to take into account the material aging. The process of growth is considered as quasi-static with infinitesimal strains.

2 Optimal Shape of a Growing Reinforced Beam

In this section we analyze the influence of the build-up process on the optimal shape of a growing body. For this purpose, we consider the optimization problem for a growing beam made of an aging elastic material.

Contributed by the Applied Mechanics Division of THE AMERICAN SOCIETY OF MECHANICAL ENGINEERS for publication in the ASME JOURNAL OF APPLIED MECHANICS.

Discussion on this paper should be addressed to the Technical Editor, Professor Lewis T. Wheeler, Department of Mechanical Engineering, University of Houston, Houston, TX 77204-4792, and will be accepted until four months after final publication of the paper itself in the ASME JOURNAL OF APPLIED MECHANICS.

Manuscript received by the ASME Applied Mechanics Division, July 7, 1993; final revision, July 7, 1994. Associate Technical Editor: G. J. Dvorak.

2.1 Formulation of the Problem.

Let us consider the bending of a reinforced elastic beam. The beam has the rectangular cross section with a uniform width b. Thickness of the beam is described by the unknown function $h(x)$ of the longitudinal coordinate x. This function is assumed to be piecewise continuous and bounded,

$$h_1 \le h(x) \le h_2, \tag{1}$$

where h_1 is minimum and h_2 is maximum admissible values of the beam thickness.

Reinforcement fills the domain with the thickness $h_0 < h_1$ in the vicinity of the longitudinal axis. The rest of the beam volume is filled by the main material.

The growth begins at the moment $t = 0$ and occurs in the interval $[0, T]$. It consists in joining portions of the reinforcement and portions of the main material. Denote by $l_0(t)$ the length of the reinforcement and by $l(t)$ the length of the part filled by the main material (see Fig. 1). Functions $l_0(t)$ and $l(t)$ increase monotonously, and satisfy the inequality $l_0(t) \ge l(t)$ and the boundary conditions $l(0) = 0$, $l_0(0) = l_0$, $l(T) = l_0(T) = l_1$.

As a practical example of the growth process we consider a construction of a reinforced steel-concrete beam. We assume that the mechanical behavior of the main material (concrete) obeys the constitutive equation of an aging elastic body; see, e.g., Arutyunyan et al. (1987), and the behavior of reinforcement (steel) is governed by the constitutive law of a nonaging elastic material. For an uniaxial stress state, stress σ is expressed in terms of strain e by the following relationships:

- in the reinforcement

$$\sigma(t, x) = E_0 e^o(t, x), \tag{2}$$

- in the main material

$$\sigma(t, x) = E(t - \kappa(x))e^o(t, x) - \int_{\kappa(x)}^{t} \dot{E}(s - \kappa(x))e^o(s, x)ds. \tag{3}$$

Here E_0 is the uniform Young's modulus of the reinforcement material, $E(t)$ is the current elastic modulus of the main mate-

Copyright © 1995 by ASME

Downloaded 04 May 2010 to 171.66.16.28. Redistribution subject to ASME license or copyright; see http://www.asme.org/terms/Terms_Use.cfm

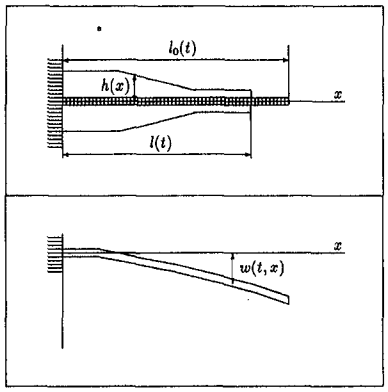


Fig. 1 Growing reinforced beam

rial, and the moment $\kappa(x)$ coincides with the moment when the built-up portion at the point x merges with the growing beam.

We consider the growth without pretensioning. That means that strain in a built-up portion at the point x for the transition from the initial to the natural configuration coincides with the strain on the boundary of the growing body at the same point x at the moment $\kappa(x)$. Suppose that one end of the beam, $x = 0$, is clamped, and the other end, $x = l_0(t)$, is free. Since the strain from the initial to the actual configuration vanishes at the free end, the strain $e^o(t, x)$ in the formula (2) coincides with the strain $e(t, x)$ for the transition from the initial to the actual configuration. For the built-up portions of the main material, which joins the deformed lateral surface of the beam, the strain $e^o(t, x)$ in the formula (3) equals the difference $e(t, x) - e(\kappa(x), x)$.

Denote by $w(t, x)$ the beam deflection at the point x at the moment t. We assume that (i) the deflection is sufficiently small and we can neglect the nonlinear terms in the expression for the curvature of the longitudinal axis; and (ii) the hypothesis regarding plane sections in the bending is fulfilled. It follows from Eqs. (2), (3), and the technical theory of bending that the bending moment $M(t, x)$ can be represented as follows:

$$M(t,x) = \tfrac{1}{12}\Big[E_0h_0^3w''(t,x) + E(t-\kappa(x))\times(h^3(x)-h_0^3)(w''(t,x) - w''(\kappa(x),x)) - \int_{\kappa(x)}^{t}\dot{E}(\tau-\kappa(x))(h^3(x)-h_0^3)\times(w''(\tau,x)-w''(\kappa(x),x))d\tau\Big],\quad 0\le x\le l(t),$$

$$M(t,x) = \tfrac{1}{12}E_0h_0^3w''(t,x),\quad l(t) < x \le l_0(t). \qquad (4)$$

Suppose that the longitudinal axis of the beam is horizontal, and that the weight is the only force applied to the beam. Then the moment M can be calculated as follows:

$$M(t,x) = bg\Big[\tfrac{1}{2}\rho_0h_0(l(t)-x)^2 + \rho\int_x^{l(t)}(h(s)-h_0)(s-x)ds\Big],\quad 0\le x\le l(t),$$

$$M(t,x) = \tfrac{1}{2}bg\rho_0h_0(l_0(t)-x)^2,\quad l(t) < x \le l_0(t), \qquad (5)$$

where ρ_0, ρ are the mass densities of the reinforcement and the main material, respectively, and g is the gravity acceleration. Equating (4) and (5), we find

$$[E_0h_0^3 + E(t-\kappa(x))(h^3(x)-h_0^3)]w''(t,x) = (h^3(x)-h_0^3)\int_{\kappa(x)}^{t}\dot{E}(\tau-\kappa(x))w''(\tau,x)d\tau + 6bg\Big\{\rho_0h_0\Big[(l_0(t)-x)^2 + \frac{E(0)}{E_0h_0^3}(h^3(x)-h_0^3)\times(l_0(\kappa(x))-x)^2\Big] + 2\rho\int_x^{l(t)}(h(s)-h_0)(s-x)ds\Big\}. \qquad (6)$$

For a cantilevered growing beam the boundary conditions for Eq. (6) are the following: $w(t, 0) = 0$, $w'(t, 0) = 0$.

Denote by $V(t)$ the volume of the part filled by the main material,

$$V(t) = b\int_0^{l(t)}(h(x)-h_0)dx, \qquad (7)$$

and by $u = dV/dt$ the rate of influx of the main material. It is assumed below that u is constant.

It is convenient to introduce the following dimensionless variables and parameters:

$$x_* = \frac{x}{l_1},\quad t_* = \frac{t}{T},\quad h_* = \frac{h}{h_0},\quad E_* = \frac{E}{E_0},\quad l_{0*} = \frac{l_0}{l_1},$$

$$l_* = \frac{l}{l_1},\ u_* = \frac{uT}{bh_0l_1},\quad V_* = \frac{V}{bh_0l_1},\quad \kappa_* = \frac{\kappa}{T},$$

$$\beta = \frac{\rho}{\rho_0},\quad z = \frac{6bg\rho_0l_1^4}{E_0h_0^3}w''.$$

In this new notation, Eq. (6) can be rewritten as follows (for simplicity the subscript asterisks are omitted):

$$[1 + E(t-\kappa(x))(h^3(x)-1)]z(t,x) = (h^3(x)-1)\int_{\kappa(x)}^{t}\dot{E}(\tau-\kappa(x))z(\tau,x)d\tau + (l_0(t)-x)^2 + E(0)(h^3(x)-1)(l_0(\kappa(x))-x)^2 + 2\beta\int_x^{l(t)}(h(s)-1)(s-x)ds. \qquad (8)$$

Differentiating Eq. (7) with respect to time and using the above boundary conditions we obtain

$$\frac{dl}{dt} = \frac{u}{h(l(t))-1},\quad l(0) = 0,\quad l(1) = 1. \qquad (9)$$

The maximum deflection of the growing beam is

$$w(T, l_1) = \frac{E_0h_0^3\Phi}{6bg\rho_0l_1^2},$$

where

$$\Phi = \int_0^1 (1-x)z(1,x)dx. \qquad (10)$$

The optimization problem of interest consists in determining of the function $h^o(x)$ which obeys the geometrical restrictions (1) and minimizes the functional (10) on the set of solutions to the boundary problem (8), (9).

Downloaded 04 May 2010 to 171.66.16.28. Redistribution subject to ASME license or copyright; see http://www.asme.org/terms/Terms_Use.cfm

2.2 Optimal Thickness of a Nonaging Elastic Beam. In this subsection we consider the case of a nonaging elastic material, when we can assume $E(t) = 1$. Equations (8) and (10) imply

$$\Phi = \int_0^1 (1 - x)(l_0(\kappa(x)) - x)^2 dx + \beta\Phi_0,$$

where

$$\Phi_0 = \int_0^1 (1 - x)\{2y_1(x) + \beta^{-1}[(1 - x)^2 - (l(\kappa(x)) - x)^2]\}h^{-3}(x)dx.$$

Function

$$y_1(x) = \int_x^1 (h(s) - 1)(s - x)ds$$

satisfies the following differential equations:

$$y_1' = -y_2, \quad y_2' = 1 - h(x),$$
$$y_1(1) = 0, \quad y_2(1) = 0. \tag{11}$$

Our purpose is to determine the function $h^o(x)$ which minimizes the functional Φ_0 on the set of solutions to the problem (11) and satisfies the conditions (1) and

$$\int_0^1 h(x)dx = V_1, \tag{12}$$

where $V_1 = 1 + V_*(T)$.

Let us calculate the increments $\Delta y_1(x)$, $\Delta y_2(x)$ of the functions $y_1(x)$, $y_2(x)$ caused be the increment $\Delta h(x)$ of thickness $h(x)$. According to Eq. (11) we find

$$\Delta y_1' + \Delta y_2 = 0, \quad \Delta y_2' + \Delta h(x) = 0,$$
$$\Delta y_1(1) = 0, \quad \Delta y_2(1) = 0. \tag{13}$$

Let us take into account the isoperimetric condition (12) using the penalty method; see, e.g., Vanderplaats (1984), and consider the minimization problem for the functional

$$\Phi_1 = \Phi_0 + \mu\left[\int_0^1 h(x)dx - V_1\right]^2,$$

where μ is a sufficiently large positive constant.

The increment $\Delta\Phi_1$ of this functional caused by the increment $\Delta h(x)$ of the function $h(x)$ can be represented as follows:

$$\Delta\Phi_1 = -3\int_0^1 \frac{(1 - x)\Delta h(x)}{h^4(x)} \times \left\{2y_1(x) + \frac{1}{\beta}[(1 - x)^2 - (l_0(\kappa(x)) - x)^2]\right\}dx + 2\int_0^1 \frac{(1 - x)\Delta y_1(x)}{h^3(x)}dx + 2\mu\left[\int_0^1 h(x)dx - V_1\right]\int_0^1 \Delta h(x)dx. \tag{14}$$

Let us introduce the functions $\psi_1(x)$, $\psi_2(x)$ which satisfy the differential equations

$$\psi_1' = 2(1 - x)h^{-3}(x), \quad \psi_2' = \psi_1,$$
$$\psi_1(0) = 0, \quad \psi_2(0) = 0. \tag{15}$$

We multiply the first Eq. (13) by $\psi_1(x)$, the second Eq. (13) by $\psi_2(x)$, integrate from 0 to 1 and add to the relationship (14). After the integration by parts and with use of Eq. (15), we finally obtain

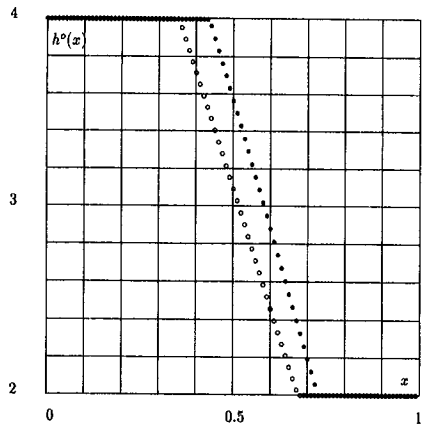


Fig. 2 Optimal thickness of a growing nonaging reinforced cantilever; $\beta = 1$, ○—regime (*a*), ●—regime (*b*)

$$\Delta\Phi_1 = \int_1^1 N(x)\Delta h(x)dx, \tag{16}$$

where

$$N(x) = 2\mu\left[\int_0^1 h(x)dx - V_1\right] + \psi_2(x) - \frac{3(1 - x)}{h^4(x)} \times \left\{2y_1(x) + \frac{1}{\beta}[(1 - x)^2 - (l_0(\kappa(x)) - x)^2]\right\}.$$

To solve the optimization problem we employ the gradient projection method, cf. Vasiliev (1980). First, we fix an admissible thickness of the beam, $h^{(1)}(x)$. Then, using thickness $h^{(k)}(x)$ at the kth step of the iterative process, we calculate the thickness $h^{(k+1)}(x)$ at the $(k + 1)$th step according to the following algorithm:

$$h^{(k+1)}(x) = \begin{cases} H^k(x), & h_1 \le H^k(x) \le h_2, \\ h_1, & H^k(x) < h_1, \\ h_2, & H^k(x) > h_2, \end{cases} \tag{17}$$

where $H^k(x) = h^{(k)}(x) - \alpha N^{(k)}(x)$, α is a positive constant and $N^{(k)}(x)$ is the function $N(x)$ corresponding to the thickness $h^{(k)}(x)$.

At the kth step, we first set $\alpha = \alpha_0$, where α_0 is a given constant. Then we calculate the functional Φ_1 for $h^{(k)}(x)$ and for $h^{(k+1)}(x)$, where the function $h^{(k+1)}(x)$ is determined by the formula (17). If $\Phi_1(h^{(k+1)}) < \Phi_1(h^{(k)})$, then we pass from the kth to the $(k + 1)$th step of the iterative process. If $\Phi(h^{(k+1)}) \ge \Phi(h^{(k+1)})$, then we reduce α twice and repeate the same procedure with the new α value.

For analysis we choose two different regimes of growth, (*a*) $l_0(\kappa(x)) = 1$, and (*b*) $l_0(\kappa(x)) = x$. Regime (*a*) corresponds to the case when all reinforcement is established at the moment $t = 0$, and regime (*b*) corresponds to the case when at any moment t, the reinforcement length coincides with the length of the part filled by the main material.

The calculations are carried out for the following parameters:

$$h_1 = 2.0, \quad h_2 = 4.0, \quad V_1 = 3.0, \quad \alpha_0 = 0.05, \quad \mu = 0.002.$$

The iterative algorithm demonstrates sufficiently good convergence. The numerical results show that 3500 iterations ensure the minimum value of the functional Φ_1 with the accuracy higher than 99 percent. We also carried out calculations with 6000 iterations, that ensures the accuracy higher than 99.9 percent.

The dependences $h^o(x)$ are plotted in the Figs. 2 and 3. Figure 2 is obtained for $\beta = 1.0$, and Fig. 3 is obtained for $\beta = 0.3$. We recall here that the parameter β determines the ratio

Downloaded 04 May 2010 to 171.66.16.28. Redistribution subject to ASME license or copyright; see http://www.asme.org/terms/Terms_Use.cfm

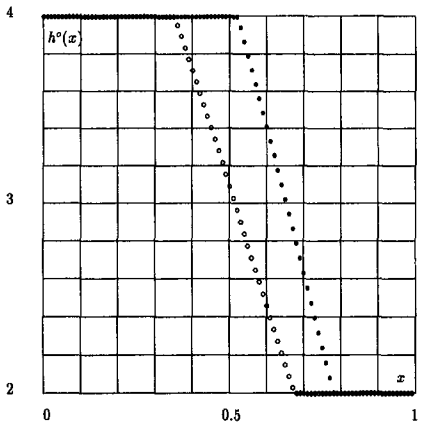


Fig. 3 Optimal thickness of a growing nonaging reinforced cantilever $\beta = 0.3$, ○—regime (a), ●—regime (b)

of the mass densities of the main material and the reinforcement. Light points correspond to the regime (a) and black points correspond to the regime (b) of growth.

Numerical results show that the shape of the function $h^o(x)$ practically coincides for the regime (a) and the regime (b). The optimal curve $h^o(x)$ for the regime (b) can be obtained from the same curve for the regime (a) by shifting along the x-axis. Therefore, the transition from the regime (a) the regime (b) of growth leads only to increase of the total mass of the beam. Obviously, that for the regime (b), the isoperimetric condition (12) holds with less accuracy than for the regime (a).

Decrease of β value, i.e., the decrease of the mass density of the main material, leads to increase of the difference between the optimal thicknesses for the regime (a) and for the regime (b). This increase is substantial near the clamped end of the beam, and it diminishes with the growth of x coordinate.

2.3 Optimal thickness of an aging elastic beam. In this subsection we consider the optimization problem for a growing reinforced elastic cantilever subjected to aging. We restrict ourselves by the case when all reinforcement is established at the initial moment, i.e., $l_0(t) = 1$, $(t > 0)$. For $t = \kappa(x)$, Eq. (8) implies

$$z(\kappa(x), x) = (1 - x)^2.$$

Differentiating Eq. (8) with respect to time and using Eq. (9) we obtain

$$\frac{\partial z}{\partial t}(t, x) = \frac{2\beta u(l(t) - x)}{1 + E(t - \kappa(x))(h^3(x) - 1)}.$$

Integrating this equation from $\kappa(x)$ to 1 we find

$$z(1, x) = (1 - x)^2 + 2\beta u \int_{\kappa(x)}^{1} \frac{(l(t) - x)dt}{1 + E(t - \kappa(x))(h^3(x) - 1)}. \quad (18)$$

By the differentiation of the identity $\kappa(l(t)) = t$ with respect to time, and the application of Eq. (9), we obtain the following equation for the function $\kappa(x)$:

$$\kappa' = \frac{h(x) - 1}{u} \quad (19)$$

with the boundary conditions

$$\kappa(0) = 0, \quad \kappa(1) = 1. \quad (20)$$

Substituting Eq. (18) into Eq. (10), setting $t = \kappa(y)$, and using (19) we find that

$$\Phi = \tfrac{1}{4} + 2\beta\Phi_0,$$

where

$$\Phi_0 = \int_0^1 (1 - x)dx \int_x^1 \frac{(y - x)(h(y) - 1)dy}{1 + E(\kappa(y) - \kappa(x))(h^3(x) - 1)}.$$

The optimization problem under consideration consists in determining the function $h^o(x)$ which satisfies the condition (1) and minimizes the functional Φ_0 on the set of solutions to the problem (19) and (20). The latter condition (20) will be taken into account by means of the penalty method. We consider the minimization problem for the functional

$$\Phi_1 = \Phi_0 + \mu[\kappa(1) - 1]^2,$$

where μ is a sufficiently large constant, and the function $\kappa(x)$ satisfies the differential Eq. (19) with the initial condition $\kappa(0) = 0$.

The increment $\Delta\Phi_1$ of the functional Φ_1 caused by the increment $\Delta h(x)$ of the function $h(x)$ can be represented as follows:

$$\Delta\Phi_1 = 2\mu(\kappa(1) - 1)\Delta\kappa(1) + \int_0^1 (1 - x)dx \times \int_x^1 \{\Delta h(y)[1 + E(\kappa(y) - \kappa(x))(h^3(x) - 1)] - (h(y) - 1)[\dot{E}(\kappa(y) - \kappa(x))(h^3(x) - 1)(\Delta\kappa(y) - \Delta\kappa(x)) + 3E(\kappa(x) - \kappa(y))h^2(x)\Delta h(x)]\} \times \frac{(y - x)dy}{[1 + E(\kappa(y) - \kappa(x))(h^3(x) - 1)]^2}.$$

Changing the order of integration we transform this equality to the form

$$\Delta\Phi_1 = 2\mu(\kappa(1) - 1)\Delta\kappa(1) + \int_0^1 \Delta h(x)dx \times \left\{\int_0^x \frac{(1 - y)(x - y)dy}{1 + E(\kappa(x) - \kappa(y))(h^3(y) - 1)} - 3(1 - x)h^2(x) \times \int_x^1 \frac{(h(y) - 1)(y - x)E(\kappa(x) - \kappa(y))dy}{[1 + E(\kappa(y) - \kappa(x))(h^3(x) - 1)]^2}\right\} - \int_0^1 R(x)\Delta\kappa(x)dx. \quad (21)$$

Here

$$R(x) = (h(x) - 1) \times \int_0^x \frac{(x - y)(1 - y)(h^3(y) - 1)\dot{E}(\kappa(x) - \kappa(y))dy}{[1 + E(\kappa(x) - \kappa(y))(h^3(y) - 1)]^2} - (1 - x)(h^3(x) - 1) \times \int_x^1 \frac{(y - x)(h(y) - 1)\dot{E}(\kappa(y) - \kappa(x))dy}{[1 + E(\kappa(y) - \kappa(x))(h^3(x) - 1)]^2}.$$

Equation (19) implies

$$\Delta\kappa' = \frac{\Delta h(x)}{u}, \quad \Delta\kappa(0) = 0. \quad (22)$$

Let us introduce the function $\psi(x)$ which obeys the differential equation

$$\psi' = R(x), \quad \psi(1) = 2\mu(\kappa(1) - 1). \quad (23)$$

We multiply Eq. (22) by $\psi(x)$, integrate from 0 to 1, and add to expression (21). After the integration by parts of the obtained

Downloaded 04 May 2010 to 171.66.16.28. Redistribution subject to ASME license or copyright; see http://www.asme.org/terms/Terms_Use.cfm

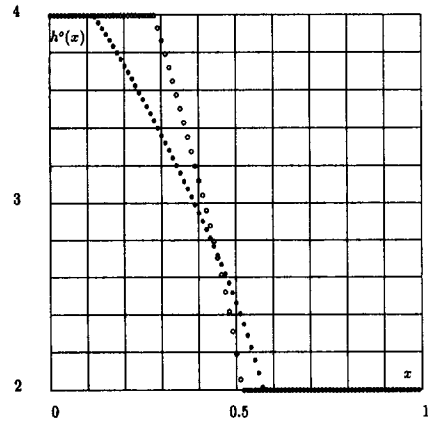


Fig. 4 Optimal thickness of a growing reinforced cantilever made of an aging elastic material. ●— $\gamma = 1.0$; ○— $\gamma = 0.1$.

expression, and with use of Eq. (23), we finally obtain the formula (16) with the following expression for the function $N(x)$:

$$N(x) = \frac{\psi(x)}{u} + \int_0^x \frac{(1-y)(x-y)dy}{1 + E(\kappa(x) - \kappa(y))(h^3(y) - 1)} - 3(1-x)h^2(x) \times \int_x^1 \frac{(h(y) - 1)(y - x)E(\kappa(x) - \kappa(y))dy}{[1 + E(\kappa(y) - \kappa(x))(h^3(x) - 1)]^2}.$$

To determine the optimal shape of a growing beam we employ the gradient projection method with the algorithm (17). Numerical analysis is carried out in the following case:

$$h_1 = 2.0, \quad h_2 = 4.0, \quad u = 1.0,$$

$$\mu = 0.005, \quad E(t) = 0.1 + 0.6[1 - \exp(-\gamma t)].$$

The latter formula means that the ratio of the initial Youngs modulus of the main material to the elastic modulus of the reinforcement equals 0.1, and the ratio of the limiting Youngs modulus of the main material to the elastic modulus of the reinforcement equals 0.7.

The dependences $h^o(x)$ are plotted in the Fig. 4. Black points correspond to $\gamma = 1.0$, and light points correspond to $\gamma = 0.1$. We recall here that γ^{-1} is the characteristic time of the material aging.

Numerical analysis shows that the optimal shape of a growing elastic beam subject to aging depends essentially on the rate of material aging. For a slow aging ($\gamma = 0.1$), most of the material concentrates at the cantilevered end of a beam. For a rapid aging ($\gamma = 1.0$), the optimal thickness in the neighborhood of the clamped end decreases and an additional part of the material passes to the middle of the beam where the optimal thickness grows.

In the beginning, when we formulated the problem of shape optimization, we did not impose any specific restrictions on the behavior of the function $h^o(x)$. In a general case, the above statement of the optimization problem could lead to a solution, which would be very difficult to realize in practice. Nevertheless, we have obtained the formula for the optimal thickness $h^o(x)$ which is relatively simple to apply in construction. Namely, a quasi-optimal thickness $h^*(x)$ of a growing cantilevered beam (whose maximum difference from the optimal thickness $h^o(x)$ is less than five percent) is as follows. This function takes the maximum value h_2 in the vicinity of the cantilevered end, diminishes linearly to the minimum value h_1, and takes the value h_1 in the vicinity of the free end of the beam:

$$h^*(x) = \begin{cases} h_2, & 0 \le x \le x_1, \\ h_2 - \dfrac{h_2 - h_1}{x_2 - x_1}(x - x_1), & x_1 \le x \le x_2, \\ h_1, & x_2 \le x \le 1. \end{cases}$$

The points x_1 and x_2, where the derivatives of the function $h^*(x)$ are discontinuous, can be determined from a very simple optimization problem. The above numerical results show that for an aging material, the growth of the rate of aging, γ, leads to increase of the parameter x_2, and leads to decrease of the parameter x_1.

3 Conclusions

A new class of the optimal design problems arising in mechanics of growing viscoelastic composite bodies subjected to aging is proposed.

In the current paper we analyze the problem of shape optimization for growing reinforced elements of construction. It is studied on the example of a growing cantilevered reinforced beam under the action of its weight. The problem consists in determining of the optimal thickness $h^o(x)$ of the beam which minimizes the maximum deflection on account of geometrical restrictions and limitations on the total volume of the beam. We propose a semi-analytical solution to this problem, and we have obtained the optimal thickness of the beam using numerical techniques. It is shown that

(i) the optimal thickness of the growing cantilevered beam is a piecewise continuously differentiable function of the longitudinal coordinate. In the vicinity of the clamped end, the optimal thickness is uniform, and it is equal to the maximum admissible thickness, h_2; in the middle of the beam, function $h^o(x)$ decreases (practically linearly); and it is uniform and takes the minimum admissible value h_1 in the vicinity of the free end of the beam;

(ii) for a nonaging material of the beam, the optimal thickness depends very weakly on the regime of construction of the reinforcement. For a fixed cost functional, the regime when the length of the reinforcement coincides with the length of the part filled by the main material demands an additional volume of the main material with respect to other regimes of growth, when the reinforcement is established before the construction of the main material;

(iii) decrease of the mass density of the main material leads to additional material influx in the vicinity of the clamped end of the growing cantilever. This decrease shifts the optimal function $h^o(x)$ closer to free end of the beam; and

(iv) aging of the main material essentially changes the optimal thickness of the growing beam. For relatively slow aging, the main material is concentrated in the vicinity of the cantilevered end of the beam. The growth of the rate of aging leads to increase of thickness in the middle part of the beam without significant changes of the total volume.

Acknowledgments

This work has been supported by the Natural Sciences and Engineering Research Council of Canada.

References

Arutyunyan, N. Kh., and Drozdov, A. D., 1984, "Mechanics of Growing Viscoelastic Bodies Subjected to Aging with Finite Deformations," *Soviet Physics Doklady*, Vol. 29, pp. 450–452.

Downloaded 04 May 2010 to 171.66.16.28. Redistribution subject to ASME license or copyright; see http://www.asme.org/terms/Terms_Use.cfm

Arutyunyan, N. Kh., and Drozdov, A. D., 1988, "Optimization Problems in the Mechanics of Growing Solids," *Mechanics of Composite Materials,* Vol. 24, pp. 359–369.

Arutyunyan, N. Kh., Drozdov, A. D., and Naumov, V. E., 1987, *Mechanics of Growing Viscoelastoplastic Bodies,* Nauka, Moscow (in Russian).

Arutyunyan, N. Kh., and Kolmanovskii, V. B., 1983, *Creep Theory for Heterogeneous Bodies,* Nauka, Moscow (in Russian).

Banichuk, N. V., 1980, *Shape Optimization for Elastic Bodies,* Nauka, Moscow (in Russian).

Drozdov, A. D., and Kolmanovskii, V. B., 1984, "An Approximate Method for Optimizing the Shape of Reinforced Rods in Nonuniformly Aging Materials," *Applied Mathematics and Mechanics,* Vol. 48, pp. 33–40.

Kalamkarov, A. L., 1992, *Composite and Reinforced Elements of Construction,* Wiley, Chichester, U.K.

Kalamkarov, A. L., and Kolpakov, A. G., 1993, "Numerical Design of Thin-Walled Structural Members on Account of their Strength," *International Journal for Numerical Methods in Engineering,* Vol. 36, pp. 3441–3449.

Troitskii, V. A., and Petukhov, L. V., 1982, *Shape Optimization for Elastic Bodies,* Nauka, Moscow (in Russian).

Vanderplaats, G. N., 1984, *Numerical Optimization Techniques for Engineering Design,* McGraw-Hill, New York.

Vasiliev, F. P., 1980, *Numerical Methods for Solving Extremal Problems,* Nauka, Moscow (in Russian).

Zevin, A. A., 1979, "Optimum Shape of an Aging Hereditary Solid," *Mechanics of Solids,* Vol. 14, No. 3, pp. 127–134.

Downloaded 04 May 2010 to 171.66.16.28. Redistribution subject to ASME license or copyright; see http://www.asme.org/terms/Terms_Use.cfm

The Contact Problem at Delamination

A. E. Giannakopoulos
Department of Solid Mechanics,
Royal Institute of Technology,
S-10044 Stockholm, Sweden

K.-F. Nilsson
Aeronautical Research Institute of Sweden,
S-16111 Bromma, Sweden

G. Tsamasphyros
Department of Theoretical and Applied Mechanics,
National Technical University of Athens,
Athens 15774, Greece

The important phenomenon of delamination buckling is examined subjected to the condition of frictionless contact. Buckled delamination is examined in particular, because in-plane compressive loading is typical and detrimental. Two types of contact can be distinguished, local and global. The latter may occur everywhere in the plate while the local contact is limited to the crack front (negative K_I stress intensity factors). Both local and global contact conditions were considered using a finite element scheme which employed nonlinear plate theory. The global contact problem is formulated as it appears in post-buckling of delamination. The case of simultaneous buckling and contact is also addressed in this paper. Two particularly interesting examples of thin film delaminations are presented. In the first, the contact at buckling is due to the material anisotropy. In this case the bucking load and the post-bucking analysis were very well supported by experiments. In the second example, contact at buckling arises because of a pin that holds down the delaminated layer at its center. The treated cases indicated that contact may significantly affect the fracture parameters along the delamination front, and is, therefore, important for delamination arrest.

Introduction

Besides those of panels and laminated composites, delamination problems may also occur in thin film coatings such as paints, thermal insulators, and electric conductors. These devices are of prime interest in a variety of applications in microelectronics, aerospace, naval structures, and bioengineering. Protecting and restoring old master's paintings could be another important area of delamination problems. Two important questions are pertinent to the previously mentioned cases: (1) how to select the right type of laminate materials to prolong their life time, and (2) how to detect and repair delamination.

When the delaminated section buckles under some external thermomechanical load, it may cause high interlaminar stresses which tend to enlarge it. This may alter the overall strength and proper function of the structure. A complete fracture mechanics analysis requires in general three-dimensional computations. However, three-dimensional finite elements often give ill-conditioned matrices when they are very thin (large aspect ratio), and furthermore, the number of degrees-of-freedom required is generally very large. Given the complexity of the problem, it is assumed that a nonlinear elastic plate theory provides a good approximation to the stored energy in the whole laminate and therefore the delamination growth can be analyzed with energetic considerations particularized to plates. It is assumed that the delaminated plates undergo small lateral deflections, but moderate rotations, and the deformation across the plate thickness is assumed negligible (von Karman kinematic approximations). The computational economy achieved by such simplification makes possible to model contact, growth, and material nonlinearities that exist in the delamination problem.

In our previous work, Nilsson and Giannakopoulos (1990), only contact-free cases were analyzed. The unconstrained buckling mode may have regions of interpenetration (nodal lines) which is, of course, physically unacceptable. In a recent paper, Chai (1990b) used the Rayleigh-Ritz method to predict buckling and post-buckling behavior of elliptical plates. Chai's results are very important because it is there realized that contact analysis is needed for certain geometries and loadings. Chai also showed cases where contact can occur at buckling. Furthermore, he attempted to include contact analysis at buckling, but he admitted very poor convergence and low accuracy for those results. General delamination shapes with material anisotropy have not been addressed so far. Based on the present analysis, the effect of contact on delamination growth was examined by Nilsson et al. (1993), where comparisons with experiments were made. The present work deals with the buckling and post-buckling range of a laminated plate which contains a delamination. The interaction between post-buckling and local delamination growth is analysed, using an analytical formula for computing the energy release rate along the delamination front, Storåkers and Andersson (1988). The present formulation accounts for geometric nonlinearity and hyperelasticity.

1 Problem Formulation

1.1 Global Contact. A single delamination, Ω, on a semi-infinite stratum ($x_3 \leq 0$) is considered. The points of the middle plane of the undeformed, delaminated flat plate are related to a fixed right-hand Cartesian system ($Ox_1x_2x_3$), with the out-of-plane coordinate $x_3 = 0$ (Fig. 1). In-plane load is imposed along the delamination boundary line, $\partial\Omega$, which suffices to be Lipschitzian.

Regarding global contact, the contacting support will be considered rigid, and the candidate contact surface is included in the delaminated area Ω. Unilateral contact without friction will be examined (Signorini-Fichera problem) under quasi-static conditions. Both delaminated plate and rigid support are constrained against rigid body motion. The problem may develop multiple connected contact locations. Solution of the problem entails the satisfaction of equilibrium together with the following constraint condition which concerns the vertical displacement of the mid-surface of the plate:

$$u_3(x_\alpha) \geq 0 \qquad (1)$$

which must be H^2-continuous. Due to plate continuity, there is contact of at least first order. That is, at the contact region, Ω_c,

Contributed by the Applied Mechanics Division of THE AMERICAN SOCIETY OF MECHANICAL ENGINEERS for publication in the ASME JOURNAL OF APPLIED MECHANICS.

Discussion on this paper should be addressed to the Technical Editor, Professor Lewis T. Wheeler, Department of Mechanical Engineering, University of Houston, Houston, TX 77204-4792, and will be accepted until four months after final publication of the paper itself in the ASME JOURNAL OF APPLIED MECHANICS.

Manuscript received by the ASME Applied Mechanics Division, July 17, 1992; final revision, June 20, 1994. Associate Technical Editor: D. M. Parks.

Copyright © 1995 by ASME

Downloaded 04 May 2010 to 171.66.16.28. Redistribution subject to ASME license or copyright; see http://www.asme.org/terms/Terms_Use.cfm

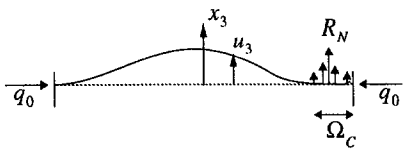


Fig. 1 Delamination buckling with contact

$$u_3(x_\alpha) = 0, \quad u_{3,\beta}(x_\alpha) = 0 \quad (\alpha, \beta = 1, 2); \quad x_\alpha \in \Omega_c \quad (2)$$

(the comma indicates differentiation with respect to x_α-plane coordinates).

The assumption of a contact domain leads to contact reactions acting on the delaminated plate. The normal reactions, R_N (Fig. 1), associated with contact are

$$R_N u_3 = 0, \quad R_N(x_\alpha) \geq 0; \quad x_\alpha \in \Omega_c \quad (3)$$

and are assumed to be maximal monotone. Note that R_N is smooth according to the smoothness of u_3, and the resultant of all R_N is in the interior of Ω_c.

The plate is initially unconstrained ($\Omega_c^o = \phi$), and the contact region is permitted to advance and recede freely until equilibrium is achieved without interpenetration (spontaneous contact is excluded). A useful global contact relation (essentially a negative L^1-norm), suitable for a FEM contact convergence criterion, is

$$\left| \int_\Omega u_3 d\Omega \right| = a \int_\Omega |u_3| \, d\Omega, \quad (4)$$

where $a = 1$ means no contact, and $0 \leq a < 1$ indicates contact.

1.2 Static Buckling of Delamination With Contact. The static buckling of a delamination will be studied by assuming the application of in-plane proportional loading along the delamination boundary line $\partial\Omega$:

$$q_\alpha = \lambda q_\alpha^o; \quad \alpha = 1, 2 \quad (5)$$

where q_α^o is a self-equilibrating load distribution which is L^2-continuous (Fig. 1). The scalar multiplier, λ, is supposed to increase monotonically from zero to a critical (assumed unique) value, λ_c, at which point the delamination buckles. A total Lagrangian formulation (undeformed state) is considered.

At $\partial\Omega$, the clamped kinematic constraints $u_3 = 0$ and $u_{3,\alpha} = 0$ hold. Within von Karman theory, the nonzero generalized strains read as

$$\epsilon_{\alpha\beta}^m = (u_{\alpha,\beta} + u_{\beta,\alpha} + u_{3,\alpha}u_{3,\beta})/2 \quad (6)$$

$$\kappa_{\alpha\beta} = -u_{3,\alpha\beta}; \quad \alpha, \beta = 1, 2, \quad (7)$$

where u_α are the in-plane displacements that must be H^1-continuous.

The membrane forces, $N_{\alpha\beta}$, and bending moments, $M_{\alpha\beta}$, are work conjugate functions of the membrane strains, $\epsilon_{\alpha\beta}^m$, and the curvatures, $\kappa_{\alpha\beta}$, respectively, with a convex, positive definite, strain energy density $W(\epsilon_{\alpha\beta}^m, \kappa_{\gamma\delta})$. The constitutive equations, $N_{\alpha\beta} = \partial W/\partial\epsilon_{\alpha\beta}^m$, $M_{\alpha\beta} = \partial W/\partial\kappa_{\alpha\beta}$, satisfy the usual symmetry and ellipticity conditions.

The equilibrium equations are

$$N_{\alpha\beta,\beta} = 0 \quad \text{(in-plane)} \quad (8)$$

$$M_{\alpha\beta,\alpha\beta} + N_{\alpha\beta}u_{3,\alpha\beta} = 0 \quad \text{(out-of-plane)}. \quad (9)$$

Repeated indices imply summation. The transmition relations at the contact boundary $\partial\Omega_c$ are Eqs. (2). The normal contact tractions are

$$R_N = -(M_{\alpha\beta,\alpha\beta} + N_{\alpha\beta}u_{3,\alpha\beta}), \quad (10)$$

with $R_N = 0$ at $x_\alpha \in \partial\Omega_c$.

Assume that before buckling an initial state ($u_3^o = 0$, $M_{\alpha\beta}^o = 0$) was in equilibrium with $q_\alpha^o(\int_\Omega N_{\alpha\beta}^o \delta e_{\alpha\beta}^o d\Omega = \int_{\partial\Omega} q_\alpha^o \delta u_\alpha^o ds)$, giving a unique solution u_α^o for the plane elasticity problem. In such state, only the linear terms exist. When contact develops in the post-buckling regime, the stationary condition for virtual work becomes an elliptic variational inequality of the first kind. According to Lions and Stampacchia (1967), such variational inequality has a unique solution. On the other hand, the variational inequality characterizing the problem of contact at buckling reads as

$$\int_\Omega (M_{\alpha\beta}\delta u_{3,\alpha\beta} - N_{\alpha\beta}u_{3,\alpha}\delta u_{3,\beta}) d\Omega - \lambda \int_\Omega (N_{\alpha\beta}^o u_{3,\alpha}\delta u_{3,\beta}) d\Omega \geq 0. \quad (11)$$

The following Rayleigh quotients may be defined:

$$\frac{1}{\lambda_c^1} = \sup_{u_3 \geq 0} \frac{\int_\Omega N_{\alpha\beta}^o u_{3,\alpha}u_{3,\beta} d\Omega}{\int_\Omega M_{\alpha\beta}u_{3,\alpha\beta} d\Omega}, \quad (12)$$

$$\frac{1}{\lambda_c^2} = \inf_{u_3 \geq 0} \frac{\int_\Omega N_{\alpha\beta}^o u_{3,\alpha}u_{3,\beta} d\Omega}{\int_\Omega M_{\alpha\beta}u_{3,\alpha\beta} d\Omega}. \quad (13)$$

When $\lambda_c^1 < \lambda < \lambda_c^2$, there is at least one solution, λ_c, to (11) which gives the smallest buckling load in presence of contact. It is clear that λ_c is larger when there is simultaneous contact and buckling than when unconstraint buckling occurs. Therefore, contact stiffens the delamination. Generally, the solution to this problem is not uniquely determined because of the geometric nonlinearity of the adopted model.

1.3 Local Contact. According to the plate model, the stress field is not singular at the delamination front, $\partial\Omega$, but discontinuous. This discontinuity is transported with the delamination front as it grows. However, a crack-type singularity has still to be dealt with. To this end, a crack-tip criterion for contact has to be considered as proposed by Chai (1990a). This situation is called contact in the small (or local), to distinguish it from contact in the large (or global). Attention will be directed to isotropic, linear elastic fracture analysis of bimaterial beam configurations, in accord with the overall elastic plate analysis. As for the global contact, no frictional dissipation will be accounted for the local contact.

It will be assumed that the total energy release rate can be decomposed into modes I, II, III. Mode III can be decomposed for linear elastic materials, if the mode III shear resultant does not couple with the other plate resultant forces and moments (Nilsson and Storåkers, 1992). Mode decomposition, in the Irwin's spirit, may not be always possible, or may be possible in an approximate way, depending on the elastic properties of the material close to the interface. The mode decomposition, in absence of local contact, is given by Suo and Hutchinson (1988):

$$\frac{K_{II}}{K_I} = \frac{\cos\omega - (hP/(M\sqrt{12}))\sin\omega}{-\sin\omega - (hP/(M\sqrt{12}))\cos\omega}, \quad (14)$$

where P and M are the axial force and bending moment at the vicinity of the delamination front, and h is the plate's thickness. In general, ω depends on the Dundurs' elastic mismatch parameters. Expressions analogous to (14) can be stated for linear elastic, orthotropic materials with dissimilar elastic properties across the delamination plane (e.g., Suo, 1990).

The contact zone model, which is used in this work, has been examined by Comninou (1990) and has been shown to give a

Downloaded 04 May 2010 to 171.66.16.28. Redistribution subject to ASME license or copyright; see http://www.asme.org/terms/Terms_Use.cfm

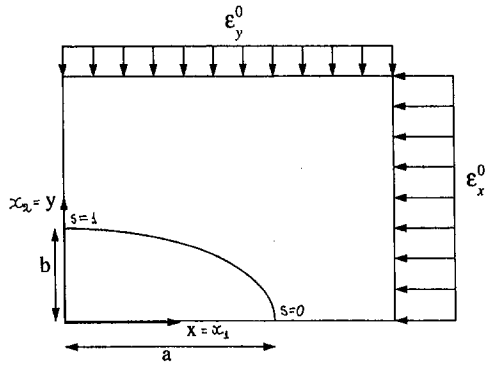


Fig. 2 Elliptic film delamination

unique solution. Following Comninou (1990), local closure requires $K_I = 0$; this may not be true for certain orthotropic bimaterials (Ni and Nemat-Nasser, 1991). In this formulation, the energy release rate is preserved and, in case of local contact, is entirely attributed to mode II. Note that the extent of local contact cannot be found from the present consideration.

2 Global Contact Algorithm

The solution of the delamination problem subjected to a frictionless contact is obtained by a programming method which is suggested by the Kuhn-Tucker contact conditions (1) and (3). By this approach, the need for artificial interface elements based on the penalty resolution of contact is circumvented, since the usually large ratio of interface to plate element stiffness will make the global stiffness ill-conditioned, affecting negatively the FEM solution (Gallagher, 1975). The problem is solved numerically as a sequence of bilateral problems by tracking only the vertical displacements. In turn, the interface normal tractions follow as a consequence of the procedure, and ensure subsequent possible separation (reverse contact).

Loading is imposed incrementally. The growth of the contact region is monitored at the end of each loading step by imposing or lifting nodal kinematic boundary restrictions corresponding to Eqs. (2). This stage of the numerical proceeding is called contact prediction. The global stiffness matrix is updated at the end of the load step to account for the activation of the new contact constraints.

The interface normal tractions in the contact region are the corresponding reactions to the kinematic constrains. If among the nodes with prescribed contact constraints there are some with negative normal reaction (inconsistent with the contact conditions (3)), then these constraints are released. This stage is called contact correction. A final optimality test is performed to ensure that the imposed final constrained nodes are the minimum possible ones. The contact algorithm at buckling is discussed in detail in the Appendix.

The procedure was integrated in an already existing FEM code (Nilsson and Giannakopoulos, 1990). The four-noded type of element used is described by Bathe and Dvorkin (1985). In the FEM formulation, the imminence of buckling was sensed by monitoring the determinant of the tangent stiffness matrix as it approached zero. The buckling mode was determined by the Lanczos algorithm, Bathe and Wilson (1976). The post-buckling analysis was based on perturbating the initial configuration with a very small amplitude of the buckling mode. When a fairly uniform mesh is used, the convergence of the FEM solution is established by examining an approximation of (4). Convergence is assumed when a is close to 1. In the present FEM calculations, a was taken as 0.9999. The smaller Ω_c is, the faster the convergence.

3 Examples

In the following examples, laminates which are well constrained (embedded thin films), or completely symmetric about the delamination plane are examined. Unless otherwise stated, the material is linear elastic and isotropic with Poisson's ratio $\nu = 0.3$. The film thickness is h and the Young's modulus is $E = 70$ GPa. Due to symmetry, only a quarter of the delamination is discretized. The loading was a given ratio of biaxial compressive strain controlled by a single amplitude parameter (x, y are the in-plane coordinates). The post-buckling load increment was taken to be $\epsilon_y^b/50$ (ϵ_y^b is the buckling load). The delamination front, s, used in the analysis was normalized to vary from 0 to 1, as shown in Fig. 2. In these examples it can be shown (Nilsson and Storåkers, 1992) that $K_{III} \simeq 0$, which was also verified by the computations. From a broad variety of examples we solved, we depicted four characteristic cases for the purpose of illustrating the local and global contact effect at delamination.

Case (i): Isotropic Circular Film. In the first case, a circular film ($b/a = 1$) with $\epsilon_x^0/\epsilon_y^0 = -0.3$ (ϵ_y^0 is compressive) and $h/a = 1/20$ was considered. The FEM mesh is shown in Fig. 3(a). The number of nodes of the delaminated plate is 252, the number of elements is 223, and 28 elements are used along the delamination front.

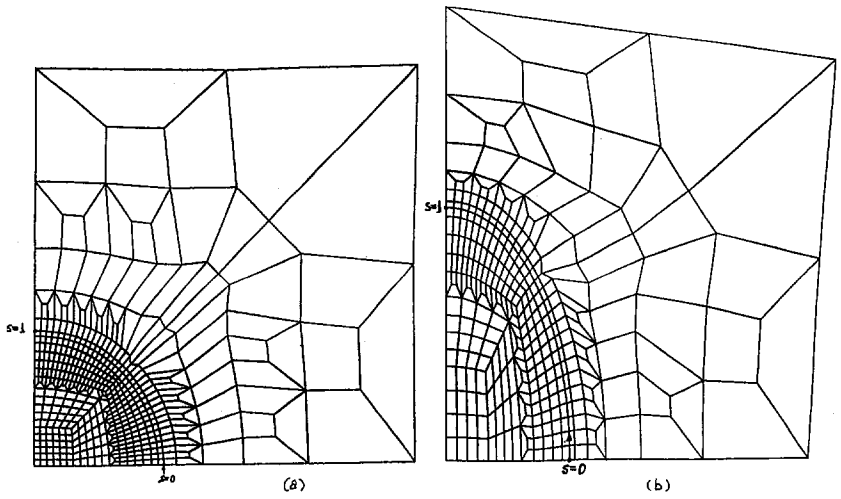


Fig. 3(a) FEM mesh used for the circular delamination under uniaxial compression; (b) FEM mesh used for the elliptical delamination (b/a = 0.5) under biaxial uniform strain

Downloaded 04 May 2010 to 171.66.16.28. Redistribution subject to ASME license or copyright; see http://www.asme.org/terms/Terms_Use.cfm

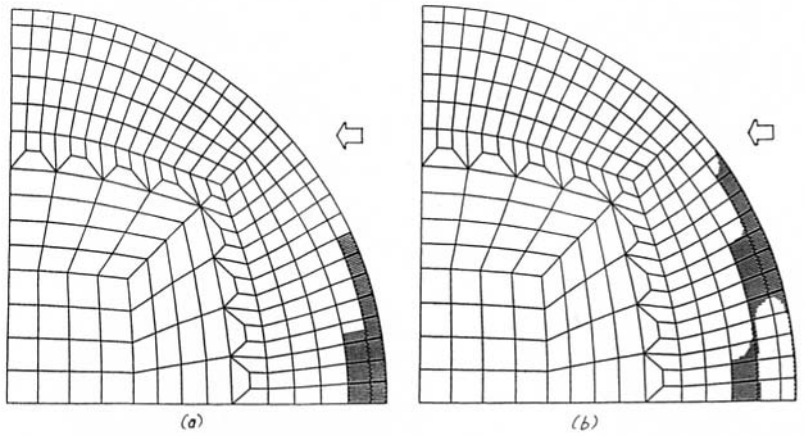


Fig. 4 Evolution of the contact region for a circular film under uniaxial load; (*a*) $\bar{\epsilon}_y^o = 1.755$, (*b*) $\bar{\epsilon}_y^o = 2.395$. The contact region is shown shaded.

The buckling strain was computed to be $\epsilon_y^b = 2.47(h/a)^2$. Local overlap was detected when $\bar{\epsilon}_y^o = 1.235(\bar{\epsilon}_y^o = \epsilon_y^o/\epsilon_y^b)$. Global (plate) overlap was detected when $\bar{\epsilon}_y^o = 1.635$. In Chai (1990b), and Nilsson and Storåkers (1992), the corresponding values were $2.51(h/a)^2$, 1.25, and 1.65, respectively.

In Fig. 4, the global contact is shown as shaded regions for $\bar{\epsilon}_y^o = 1.755$ (Fig. 4(*a*)) and for $\bar{\epsilon}_y^o = 2.395$ (Fig. 4(*b*)). Global contact starts at point $s = 0$ of $\partial\Omega$, and advances to the interior of the delamination. At $\bar{\epsilon}_y^o = 2.135$, some area previously in contact rebounds, and this indicates that the contact area is not monotonically spreading with load. For $\bar{\epsilon}_y^o > 2.135$ there is both an advance and a retreat of the contact area. These results indicate lack of any pattern for the contact evolution due to the strongly nonlinear character of the problem.

In Fig. 5, the normalized energy release rate, $\bar{G} = G/(Eh(\epsilon_y^b)^2)$, computed locally along the normalized delamination boundary line, s, is shown for $\bar{\epsilon}_y^o = 1.235, 1.755, 2.395$. Note that the maximum, $G_{\max}$, is always at $s = 1$, but the minimum, $G_{\min}$ is not always at $s = 0$. It should be noted that the G-distributions are in relative good agreement with Chai's (1990b) results. However, close examination of Chai's results reveals intersection of the G-curves for various loads, which was not observed in the present work.

In Fig. 6, the normalized stress intensity factors, $\bar{K}_{I,II} = K_{I,II}(1 - \nu^2)^{1/2}/(E\epsilon_y^b(2h)^{1/2})$, along the normalized delamination front, s, are shown for $\bar{\epsilon}_y^o = 1.235, 1.755, 2.395$.

In Fig. 7, the $\bar{K}_I$ and $\bar{K}_{II}$ values at $s = 0$ and $s = 1$ are shown as functions of $\bar{\epsilon}_y^o$ $(=\epsilon_y^o/\epsilon_y^b)$. Note that $|K_{II}|$ is always larger than K_I for all $s \in \lfloor 0, 1 \rfloor$ and $\bar{\epsilon}_y^o \geq 1$. For $1 < \bar{\epsilon}_y^o < 1.235$, K_I $(s = 0) > 0$, but very small as compared with K_{II}. For $\bar{\epsilon}_y^o \geq 1.235$, K_I $(s = 0) = 0$ due to local contact. So in this example, local contact precedes global contact and persists with loading. The maxima of K_I, $|K_{II}|$ always occurred at $s = 1$. However, the minima of K_I, $|K_{II}|$ were not always at $s = 0$. The part of the delamination front in local contact is increasing with the load, but with decreasing rate.

Case (ii): Isotropic Elliptical Film. In the second example, an elliptical film $(b/a = 0.5)$ with $\epsilon_x^o/\epsilon_y^o = 1$ and $h/a = 1/20$ was examined. The FEM mesh is shown in Fig. 3(*b*)).

The buckling strain was computed to be $\epsilon_y^b = 0.665(h/a)^2$, in agreement with Chai (1990b). Local overlap develops immediately upon buckling. No global overlap was found, as was also shown by Chai.

The normalized energy release rate, as well as the stress intensity factors, were computed along the normalized delamination quarter front line, $s \in \lfloor 0, 1 \rfloor$, for $\bar{\epsilon}_y^o = 1.235, 2.467, 4.917$. It was found that $G_{\min}$ is always at $s = 1$, but $G_{\max}$ is not always at $s = 0$. In this case, our G-distribution results were in departure with Chai's (1990b) results, especially at high loads. The plots are not shown herein for brevity.

$|K_{II}|$ is always larger than K_I for all $s \in \lfloor 0, 1 \rfloor$ and $\bar{\epsilon}_y^o \geq 1$. What is interesting in this case is that local contact appears

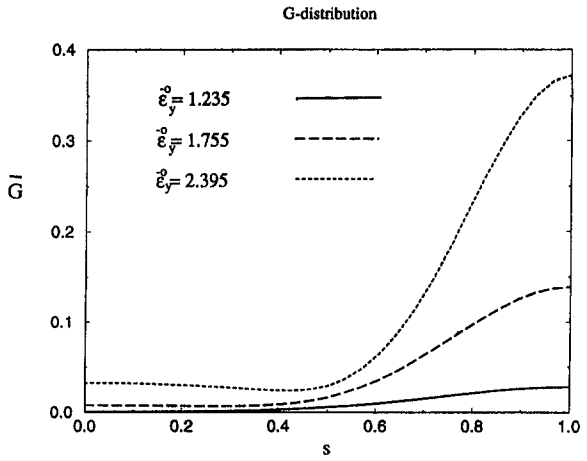


Fig. 5 Normalized energy release rate, $\bar{G}$ along the normalized delamination front line, s, for loads $\bar{\epsilon}_y^o = 1.235, 1.755, 2.395$ (circular delamination)

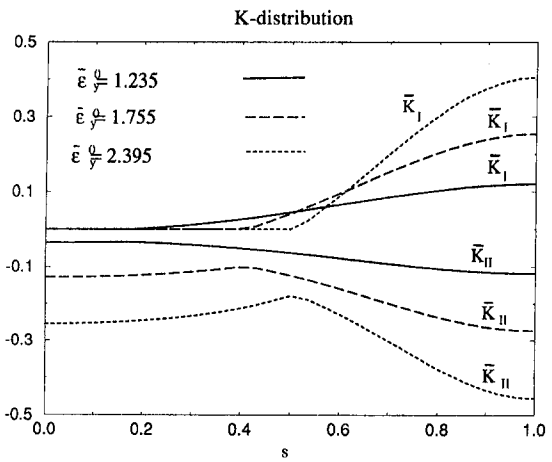


Fig. 6 Normalized stress intensity factors, $\bar{K}_{I,II}$, along the normalized delamination front line, s, for $\bar{\epsilon}_y^o = 1.235, 1.755, 2.395$ (circular delamination)

Downloaded 04 May 2010 to 171.66.16.28. Redistribution subject to ASME license or copyright; see http://www.asme.org/terms/Terms_Use.cfm

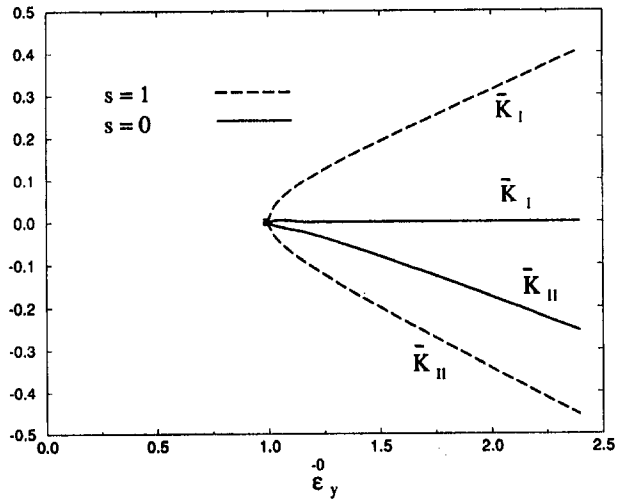


Fig. 7 Normalized stress intensity factors, $K_{I,II}$, at $s = 0$ and $s = 1$, as functions of ε_y^0 (circular delamination)

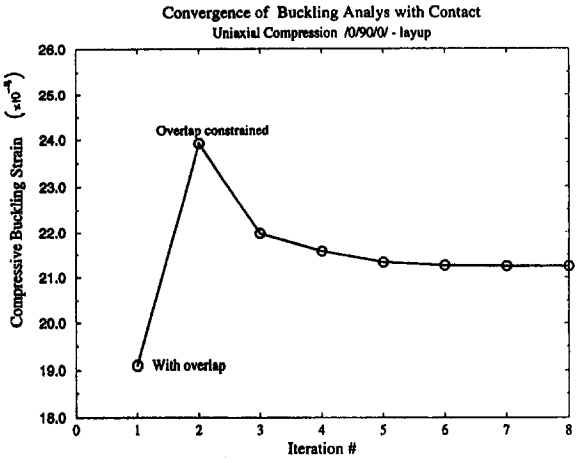


Fig. 8 Convergence of the buckling load for the orthotropic circular case

initially near the end of the long axis, and disappears with load. The minima of K_I, $|K_{II}|$ always occurred at $s = 1$. However, the maxima of K_I, $|K_{II}|$ were not always at $s = 0$, but shifted towards $s = 1$ as the load increased.

Some general remarks can be stated when the ellipse is uniaxially loaded along its long axis. Global overlap occurs right at buckling and becomes more pronounced with increasing load. This problem (contact at buckling) was addressed in the remaining examples of this paper.

Case (iii): Orthotropic Circular Film. The delaminated part consisted of an orthotropic material (graphite-epoxy) with the following properties. The ply thickness was 0.127 mm, i.e., 0.0402 mm for each of the three layers constituting the delaminated film. The layup was (0 deg/90 deg/0 deg). The material constants of each layer (with fibers oriented along, say, 1-direction of a Cartesian system) were: (Young's moduli) $E_{11} = 145.6$ GPa, $E_{22} = E_{33} = 10.5$ GPa, (Poisson's ratios) $\nu_{12} = \nu_{13} = 0.3$, $\nu_{23} = 0.51$, (Shear moduli) $G_{12} = G_{13} = 5.25$ GPa, $G_{23} = E_{22}/(2(1 + \nu_{23}))$. The radius of the delamination front was 10 mm. The delaminated layer was assumed to be clamped to the substrate. The substrate consisted of 48 layers, $(0 \text{ deg}/90 \text{ deg}/0 \text{ deg})_{16}$, subjected to uniaxial strain compression $\epsilon_y = \epsilon_y^0$ and $\epsilon_x = -0.05\epsilon_y^0$. The y-loading was along the 90 deg fiber direction (x and y in-plane directions correspond to x_1 and x_2, respectively). Standard laminate theory was used to calculate the homogenized membrane and bending stiffness. The coupling stiffness is zero, because a symmetric layup was used. Transverse shear factors were calculated from the cylindrical bending case. The FEM mesh used in the numerical simulation is shown in Fig. 3(a).

The buckling strain converged to $\epsilon_y^b = 2.12 \times 10^{-3}$, about 12 percent higher than the case where contact is not taken into account. Figure 8 shows the convergence of the algorithm described in the Appendix. The experiments of Nilsson et al. (1993) gave $\epsilon_y^b \approx 2.2 \times 10^{-3}$, in four percent error with the analysis. Figure 9(a) shows the nodes in contact at buckling. The computed post-buckling displacement of the delamination center was also in excellent agreement with the experimental one.

For $\epsilon_y \approx 3.3 \times 10^{-3}$, the experiments showed a clear tendency for the delamination to grow. The maximum energy release rate at this critical load was computed to be 217 J/m^2. This value is eight percent higher than the one computed without taking into account contact. Independent experiments evaluated the critical G to be 196 J/m^2 in pure mode I, and 596 J/m^2 in mode II (Nilsson et al., 1993). The computed $G_{\max}$ appears always at point $s = 1$, transverse to the loading direction. Therefore, the delamination is expected to start growing at that point, and, indeed, the experiments verified that. Some G distributions along the delamination front are plotted in Fig. 10 for various values of ϵ_y. It can be observed that the energy release rate along the delaminated boundary has a sharp gradient at $G_{\max}$. This gradient becomes sharper with load, in departure with the isotropic case (Fig. 5). The anisotropic delamination propagate stably (increasing load to drive the delamination), whereas the

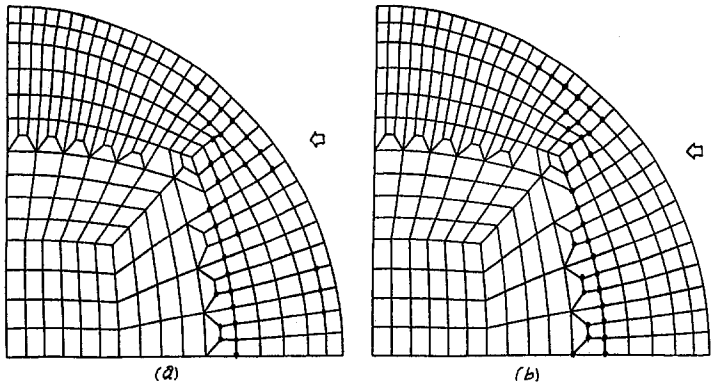


Fig. 9(a) Nodes in contact at buckling (Ω_{cc}) for the orthotropic circular case; (b) nodes in contact at $\varepsilon_y^0 = 1.556$

Downloaded 04 May 2010 to 171.66.16.28. Redistribution subject to ASME license or copyright; see http://www.asme.org/terms/Terms_Use.cfm

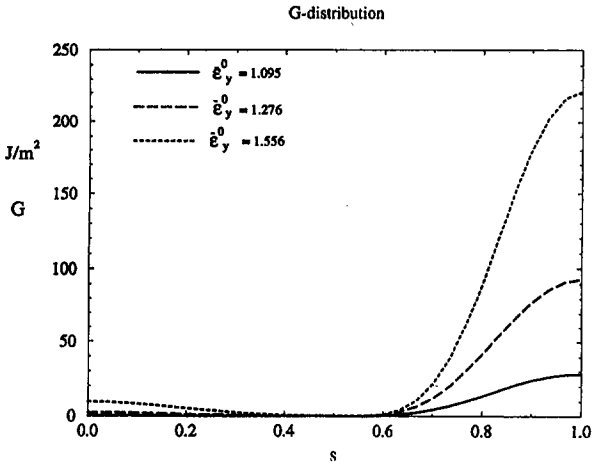


Fig. 10 The energy release rate distributions G for various load levels (orthotropic case)

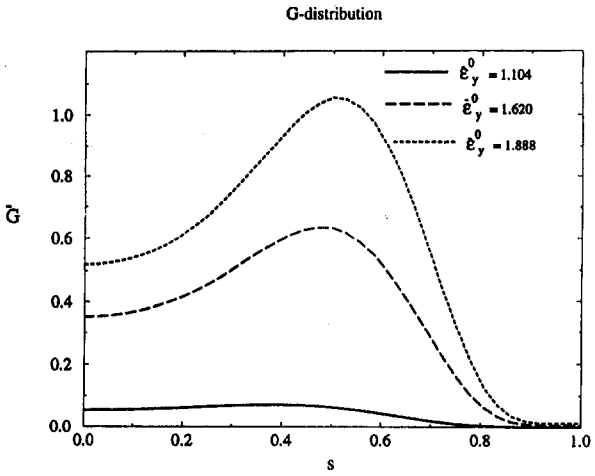


Fig. 12 The normalized energy release rate distributions, $\bar{G}$, for various normalized load levels, $\bar{\epsilon}_y^0$ = 1.104, 1.620, 1.888 (pinned delamination case)

isotropic delamination grows unstably, as was also shown experimentally and numerically by Nilsson et al. (1993).

The contact area evolves slightly with load. In Fig. 9(b), the nodes at contact for $\epsilon_y = 3.305 \times 10^{-3}$ are shown. Clearly, the contact area appears slightly larger than the initial one (Fig. 9(a)), and shifted a little to the delamination's center. The difference with the isotropic case (i) is that in the present case contact appears at buckling, and does not change as much with load (Fig. 4).

Case (iv): The Pinning Problem. In this example, the isotropic, linear elastic circular delamination film was examined. However, the center of the delamination was "pinned"; that is zero out-of-plane displacement and zero slopes were imposed at that point. The delamination material, geometry and loading was as in case (i). This configuration is an idealization of a possible attempt to repair a delamination by "nailing" its center to the parent substrate.

The FEM mesh used is shown in Fig. 3(a). The computed unconstrained buckling mode indicates severe interpenetration. The buckling load and the contact area at buckling were then computed by the proposed general algorithm discussed in the Appendix. The convergence of the solution is shown in Fig. 11. The buckling load converged to $\epsilon_c^b \approx 5.147(h/a)^2$, which is about twice the buckling load for the unpinned case. As expected from the general analysis, the pin stiffens the delamination. The initial contact area is shown in Fig. 11; as illustrated, the contact region at buckling has the form of a thin strip along the delamination diameter normal to the load. Furthermore, it was found that the contact area changes very little with load.

In Fig. 12, the normalized energy release rate $\bar{G} = G/(Eh(\epsilon_y^b)^2)$ is plotted for various values of the normalized strain $\bar{\epsilon}_y^0$ $(=\epsilon_y^0/\epsilon_y^b)$ = 1.104, 1.620, 1.888. It can be observed that $G_{\min}$ appeared at $s = 1$, transverse to the load direction. However, $G_{\max}$ appeared around $s \approx 0.5$, in the middle of the quarter of the delamination front. This is a clear departure from the unpinned case (i) where $G_{\max}$ was found to be always at $s = 1$ (Fig. 5).

The normalized stress intensity factors, $\bar{K}_{I,II} = K_{I,II}(1-\nu^2)^{1/2}/(E\epsilon_y^b(2h)^{1/2})$, along the delamination front, s, are shown in Fig. 13 for various values of the normalized strain $\bar{\epsilon}_y^0$. In this case it was found that $\bar{K}_{III} \approx 0$. Note that $\bar{K}_I = 0$ for some region of the front close to $s = 1$, corresponding to local contact conditions, as discussed in Section 1.3. The local contact region remains almost constant with the load as it is expected, because local and global contact share in this case the same part of $\partial\Omega$, and global contact was found to change little with load. On the contrary, in the unpinned case (i) the local contact area varied substantially with the load (Fig. 6).

The location of the absolute maxima for $\bar{K}_I$ and $\bar{K}_{II}$ are close to that of $\bar{G}_{\max}$, i.e., $s \approx 0.5$, and are increasing with load. There is not much fluctuation of this position which is expected to be

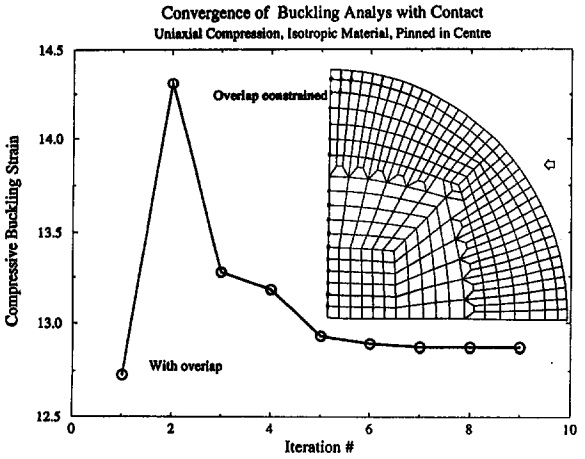


Fig. 11 Convergence of the buckling load for the centrally pinned circular delamination case

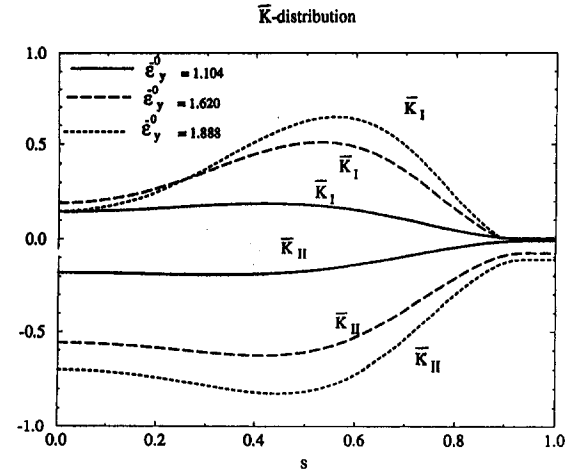


Fig. 13 The normalized stress intensity factors, $\bar{K}_{I,II}$, for various load levels, $\bar{\epsilon}_y^0$ = 1.104, 1.620, 1.888 (pinned delamination case)

Downloaded 04 May 2010 to 171.66.16.28. Redistribution subject to ASME license or copyright; see http://www.asme.org/terms/Terms_Use.cfm

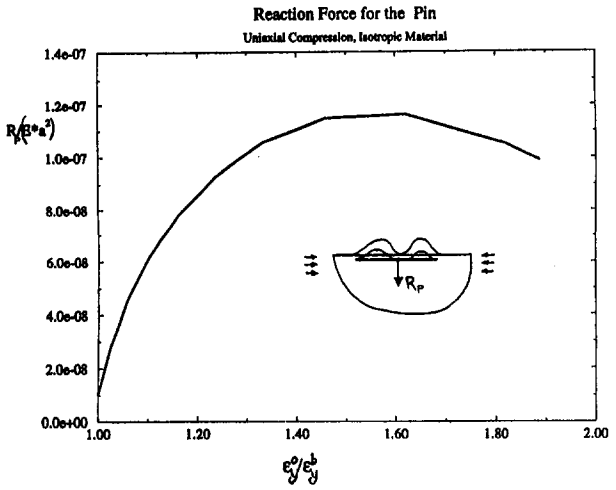


Fig. 14 The normalized reaction force, $\bar{R}_p$, of the pin as a function of the normalized load $\bar{\epsilon}_y^o$

the starting point for delamination growth. The absolute maxima of $\bar{K}_{II}$ are always bigger than the absolute maxima of $\bar{K}_I$. The absolute minima of $\bar{K}_I$ and $\bar{K}_{II}$ are at $s = 1$. The G and $K_{I,II}$ distributions for the pinned case are completely different from the unpinned case. Another interesting point is that these distributions become steeper with load.

Finally, in Fig. 14 the normalized reaction force for the pin, $\bar{R}_p = R_p/(Ea^2)$, is plotted as a function of the increasing normalized load $\bar{\epsilon}_y^o$. At buckling, $\bar{R}_p = 0$, but cumulative numerical error close to the buckling load ($\bar{\epsilon}_y^o = 1$) gave a value for $\bar{R}_p$ which is not exactly zero. The pin's reaction force has a maximum value $\bar{R}_p^{\max} \approx 1.15 \times 10^{-7}$ at $\bar{\epsilon}_y^o \approx 1.62$. Then, $\bar{R}_p$ declines, indicating that the delamination folding relaxes this force as the contact forces become comparable to it. $\bar{R}_p$ may actually decrease substantially, but the analysis was terminated at $\bar{\epsilon}_y^o = 2$.

The existance of $\bar{R}_p^{\max}$ is of great importance for the design of such delamination repair. It implies that a good pin has to be designed only for this maximum load. The pin clearly stiffens and strengthens the delamination.

Conclusions

A direct procedure (augmented Lagrange multiplier method) particularly suited for the solution of frictionless global contact encountered in delamination problems has been presented. The method is conceptually simple and the required codes may be easily appended to existing FEM programs. Some interesting delamination problems which exhibited contact at buckling were analyzed, and a general computational technique to treat such problems was presented. The problems involved different material properties, delaminations shapes, and loads.

For delamination buckling problems, global contact must be examined with care. In the present cases, contact is a phenomenon which can be modeled well only after buckling has occured. However, it was shown that a numerical method is applicable to cases where there is contact at buckling, provided that a stable post-buckling path exists. Contact increases the buckling load and stiffens the delamination.

In many cases, however, the subsequent development of global contact with increasing load may involve a spread as well as a retreat of the contact zone, the details depending strongly on the delamination geometry and loading.

Local contact can be treated separately following a treatment of global contact. As it is true for many cases, the three fracture modes may be decomposed using plate variables. Assuming small-scale contact, Comninou's contact zone model may serve to update the stress intensity factors and complete the analysis. Overlap prevention by the substrate affects drastically the energy available for delamination propagation, as well as the distributions of the stress intensity factors along the delamination front. The consequences are important regarding delaminations where their critical energy release rate depends on the mode mixity. Elastic anisotropy is significant both in the contact problem and the delamination growth, as verified by experiments.

By imposing a pinning condition at the delamination center, a substantial increase in the delamination stiffness was found. The force required to keep the delamination pinned showed a maximum value for the case of uniaxial load. This value is very important in designing for delamination arrest. Other possibilities for repairing delaminations of different shapes and under various loads and constraints will be discussed elsewhere.

Acknowledgments

The authors want to express their gratitude to Prof. B. Storåkers for his valuable comments on this work.

References

Bathe, K. J., and Dvorkin, E., 1985, "A Four-Node Plate Bending Element Based on Mindlin/Reissner Plate Theory and a Mixed Interpolation," *Int. J. Num. Meth. in Engng.*, Vol. 21, pp. 367–383.

Bathe, K. J., and Wilson, E. L., 1976, *Numerical Methods in Finite Element Analysis*, Prentice-Hall, Englewood Cliffs, NJ.

Chai, H., 1990, "Three-Dimensional Fracture Analysis of Thin-Film Debonding," *Int. J. of Fracture*, Vol. 46, pp. 237–256.

Chai, H., 1990, "Buckling and Post-Buckling Behavior of Elliptical Plates: Part II—Results," ASME JOURNAL OF APPLIED MECHANICS, Vol. 57, pp. 989–994.

Comninou, M., 1990, "An Overview of Interface Cracks," *Eng. Fracture Mechanics*, Vol. 37, pp. 197–208.

Gallagher, R. H., 1975, *Finite Element Analysis—Fundamentals*, Prentice-Hall, Englewood Cliffs, NJ.

Lions, J. L., and Stampacchia, G., 1967, "Variational Inequalities," *Comm. Pure Appl. Math.*, Vol. 20, pp. 493–519.

Ni, L., and Nemat-Nasser, S., 1991, "Interface Crack in Anisotropic Dissimilar Materials: An Analytic Solution," *J. Mech. Phys. Solids*, Vol. 39, pp. 113–144.

Nilsson, K.-F., and Giannakopoulos, A. E., 1990, "Finite Element Simulation of Delamination Growth," *The First International Conference on Computer Aided Assessment and Control of Localized Damage*, M. H. Aliabadi, C. A. Brebbia, and D. J. Cartwright, eds., Springer Verlag, Portsmouth UK, Vol. 2, pp. 299–313.

Nilsson, K.-F., and Storåkers, B., 1992, "On Interface Crack Growth in Composite Plates," ASME JOURNAL OF APPLIED MECHANICS, Vol. 59, pp. 530–538.

Nilsson, K.-F., Thesken, J. C., Sindelar, P., Giannakopoulos, A. E., and Storåkers, B., 1993, "A Theoretical and Experimental Investigation of Buckling Induced Delamination Growth," *J. Mech. Phys. Solids*, Vol. 41, pp. 749–782.

Storåkers, B., and Andersson, B., 1988, "Nonlinear Plate Theory Applied to Delamination in Composites," *J. Mech. Phys. Solids*, Vol. 36, pp. 689–718.

Suo, Z., and Hutchinson, J. W., 1988, "Interface Crack Between Two Elastic Layers," *Int. J. of Fracture*, Vol. 43, pp. 1–22.

Suo, Z., 1990, "Delamination Specimens for Orthotropic Materials," ASME JOURNAL OF APPLIED MECHANICS, Vol. 57, pp. 627–634.

Villaggio, P., 1979, "Buckling Under Unilateral Constraints," *Int. J. Solids Structures*, Vol. 15, 193–201.

APPENDIX

The Contact Algorithm at Buckling

Let λ_c^1 be the buckling load coefficient for the initial case where no contact constraint is imposed, and u_3^1 be the buckling mode corresponding to the load λ_c^1. When a nodal line for u_3^1 exists, then from (4),

$$a_1 = \left| \int_\Omega u_3^1 d\Omega \right| \Big/ \int_\Omega |u_3^1| \, d\Omega \quad 0 < a_1 < 1. \tag{A1}$$

The coefficient a_1 is a measure of the severity of contact at buckling. In the present method it is important that a_1 not be zero, and that for the initial contact area, $\Omega_c^1 \subset \Omega$:

$$\left| \int_{\Omega - \Omega_c^1} u_3^1 d\Omega \right| > \int_{\Omega_c^1} |u_3^1| \, d\Omega. \tag{A2}$$

From (12), it can be easily shown that λ_c^1 is the lowest bound of the true buckling load, $\lambda_c (\lambda_c^1 \leq \lambda_c)$. Next it is assumed the

Downloaded 04 May 2010 to 171.66.16.28. Redistribution subject to ASME license or copyright; see http://www.asme.org/terms/Terms_Use.cfm

predicted contact area Ω_c^1 to be the first approximation of the true contact area at buckling, Ω_{cc}. The kinematic contact conditions (2) are imposed for all (x_1, x_2) in Ω_c^1, $u_3^1 = 0$, $\partial u_3^1/\partial x_1 = 0$, $\partial u_3^1/\partial x_2 = 0$, and the buckling analysis is repeated. The second iteration will give a new buckling load, λ_c^2, and a new buckling mode, u_3^2. Next, the contact norm, $a_2 = a(u_3^2)$, formulated after (4), is examined. If $0 < a_2 < 1$, then there is some area, Ω_c^n, satisfying $u_3 < 0$ which is outside Ω_c^1. A new contact area, Ω_c^2, is defined as $\Omega_c^2 = \Omega_c^1 \cup \Omega_c^n$. The buckling analysis has to be repeated, imposing the contact conditions (2) to Ω_c^2. However, in most cases this step is never reached. The term "area" here is used to indicate a topological region, not a particular scalar measure.

Suppose that $a_2 = 1$, either from the beginning, or from repeated steps. Then, $\Omega_c^2 = \Omega_c^1$, and λ_c^2 is taken as the upper bound of the true buckling load, Eq. (13), $(\lambda_c \le \lambda_c^2)$. It remains to find $\Omega_{cc} \subseteq \Omega_c^2$ for which it holds: $\Omega_c = \Omega_{cc} \equiv$ contact area at buckling load λ_c.

This can be done, if a bounded and monotonically decreasing sequence of contact areas, Ω_c^i; $\Omega_c^i \subseteq \Omega_c^{i-1} \subseteq \Omega_c^2$ $(i = 1, 2, 3, \ldots)$, can be established, corresponding to the bounded and monotonically decreasing sequence of the buckling loads, λ_c^i, uniquely associated with Ω_c^i; $0 < \lambda_c^1 \le \lambda_c^i \le \lambda_c^{i-1} \le \lambda_c^2$ $(i = 3, 4, 5, \ldots)$. The uniqueness of Ω_{cc} is assumed, which in turn implies the uniqueness of λ_c. In the limit $(i \to +\infty)$: $\Omega_c^i \to \Omega_{cc}$ and is Cauchy equivalent to $\lambda_c^i \to \lambda_c$, under the norm, b_i:

$$b_i = (\lambda_c^{i-1} - \lambda_c^i)/\lambda_c^i, \quad b_i \to 0. \tag{A3}$$

It follows that $b_i \ge 0$, $i = 3, 4, \ldots$. Then, λ_c is the buckling load and Ω_{cc} is the contact region at buckling. The buckling mode shape u_3^i converges to its limiting value u_3^c $(u_3^c \ge 0)$, under the norm:

$$a_i = \left| \int_\Omega u_3^i d\Omega \right| \Big/ \int_\Omega |u_3^i| \, d\Omega; \; a_i \to 1, \text{ when } i \to +\infty. \tag{A4}$$

Note that $a_i > 0$, for $i = 1, 2, 3, \ldots$ because of (A2).

After the upper bound of Ω_{cc} and the bounds of λ_c have been estimated, a repeated buckling analysis $(i = 3, 4, 5, \ldots)$ is performed. At each iteration, the initial contact area is the one that was computed previously (Ω_c^{i-1}). Then a new buckling analysis is performed to compute λ_c^i. With λ_c^i been computed, a first order correction to Ω_c^{i-1} is made by performing a step of post-buckling analysis (close to the computed buckling load) in order to assert the complementary contact condition, $R_N > 0$. This correction will give Ω_c^i at the end of the ith iteration. At the element level, the minimization of the contact area corresponds to sequential constraining the element's degrees of freedom according to the algorithm (Villaggio, 1979). The assumed uniqueness implies configurational stability of the contact area at buckling. In all the examples encountered in the present work, the configuration stability of Ω_{cc} was numerically asserted. The analysis is truncated when b_i becomes a very small positive number (e.g., 10^{-6}). At the end of the analysis, approximations of λ_c and Ω_{cc} at buckling are obtained. The computation of Ω_{cc} is a necessary step before proceeding to the post-buckling analysis, otherwise there may be no convergence of the solution.

Downloaded 04 May 2010 to 171.66.16.28. Redistribution subject to ASME license or copyright; see http://www.asme.org/terms/Terms_Use.cfm

J. S. Epstein
Fracture Behavior Group,
The Idaho National Engineering Laboratory,
P. O. Box 1625,
Idaho Falls, ID 83415-2218
Assoc. Mem. ASME

S. M. Graham
Materials Engineering Associates,
9700B M. L. King Jr. Highway,
Lanham, MD 20706-1837

K. E. Perry

W. G. Reuter

Fracture Behavior Group,
The Idaho National Engineering Laboratory,
P. O. Box 1625,
Idaho Falls, ID 83415-2218

Displacement and Strain Fields for a Bimetallic Strip Under Remote Tension

Experimental displacement and strain fields are presented for a generalized plane stress tensile specimen consisting of commercially pure titanium diffusion bonded to 6Al-4V titanium. Plastic flow initiates at the intersection of the interface with the specimen free edge. Further deformation results in concentrated shear bands emanating from the interface at both free edges. Interactions of the interface-free edge shear bands force a state of plane strain in the center of the specimen. These interface constraint effects have practical relevance on the testing of joined metals with property mismatch.

1 Introduction

Nonstrain hardening flow in a uniaxial strip has been well documented by Nadai (1950), Onat and Prager (1954), and Hart (1955). Strain hardening complicates the analysis, typically requiring computational methodologies (Storen and Rice, 1975; Hill and Hutchinson, 1975; Burke and Nix, 1979; Ortiz et al., 1987). Of particular importance with strain hardening is the prediction of the onset of plastic localization zones and the distribution of strain within these zones.

An experimental study is described that maps the deformation surrounding the onset of plastic localization for a bimetallic strip with mechanically aligned tensile end conditions (Fig. 1). For this geometry, one side of the interface remains elastic while the other side yields with strain hardening.

There are a number of reasons for the geometry and material combination shown in Fig. 1. It is important to understand the initiation of slip and plasticity along the interface for a planar uniaxial geometry and how the spatial inhomogeneity of the plasticity process affects the interpretation of a bimaterial tension test based upon far field bulk measurements. The interface creates an elastic singularity when it intersects a traction-free edge (Bogy, 1971; Blum and Shih, 1989; Kishimoto et al., 1993), thus presenting a specific region where plastic localization can initiate. The resultant conditions of plastic flow from the interface are relevant to the testing of joined metals with property mismatch. The biaxial constraint developed by the shear bands emanating from bondline free-edge intersection region can significantly affect the overall bulk deformation and failure processes in the sample.

This article will take the following outline, the specimen geometry and material system will be discussed with close attention to the method of bonding and creating a sharp interface. The experimental procedure will be described which includes moire interferometry and a loading fixture to mechanically ensure tensile end pin alignment. The moire data analysis will be presented with attention to accuracy. A discussion of the results which include the X and Y displacement as well as strain fields and the shear strain fields will be provided. The displacement kinematics of the shear banding will be described from the moire displacement fields. The strain fields will focus upon the development of the slip bands emanating from the interface-free edge region. Finally, the constraint on the plastic flow process due to the interface and its implications on the interpretation of bulk stress-strain data for the bimetallic tensile geometry will be discussed.

2 Experimental Procedure

The experimental procedure consisted of three elements, the specimen material and geometry selection, the loading fixture design, and the fringe reduction method to obtain strain fields.

2.1 Material Systems. The material system chosen for this study consists of commercially pure titanium (CP Ti) diffusion bonded to 6Al-4V titanium (6Al-4V Ti). The stress-strain response for the two titaniums was measured and is shown in Figs. 2(a) and (b). Averaged material parameters for the two titaniums are found in Table 1.
where

$$\epsilon/\epsilon_0 = \alpha(\sigma/\sigma_0)^n \tag{1}$$

and the subscript "0" denotes 0.2 percent offset yield stress and strain and ϵ_0 is the engineering strain.

The advantage of this diffusion bonded material system is that the elastic modulii and coefficients of thermal expansion are close while the yield strengths differ. The thermal coefficient of expansion at the bonding temperature (870°C) ranges between $5-6 \times 10^{-6}$ for both materials. Under loading, the CP Ti yields while the 6Al-4V remains essentially elastic. The proportional limit for the CP Ti is 300 MPa while for the 6Al-4V it is 886 MPa. The J_{IC} of the 6Al-4V and CP Ti are 62.7 and 110.0 kJ/m^2, respectively. The CP Ti is a TIMET grade 50A with a maximum impurity content by weight of 0.08 percent carbon, 0.3 percent iron, 0.05 percent nitrogen, and 0.2 percent oxygen, the remainder being titanium. Diffusion bonding is used

Contributed by the Applied Mechanics Division of THE AMERICAN SOCIETY OF MECHANICAL ENGINEERS for publication in the ASME JOURNAL OF APPLIED MECHANICS.

Discussion on this paper should be addressed to the Technical Editor, Professor Lewis T. Wheeler, Department of Mechanical Engineering, University of Houston, Houston, TX 77204-4792, and will be accepted until four months after final publication of the paper itself in the ASME JOURNAL OF APPLIED MECHANICS.

Manuscript received by the ASME Applied Mechanics Division, Jan. 5, 1993; final revision, May 16, 1994. Associate Technical Editor: M. E. Fourney.

Copyright © 1995 by ASME

Downloaded 04 May 2010 to 171.66.16.28. Redistribution subject to ASME license or copyright; see http://www.asme.org/terms/Terms_Use.cfm

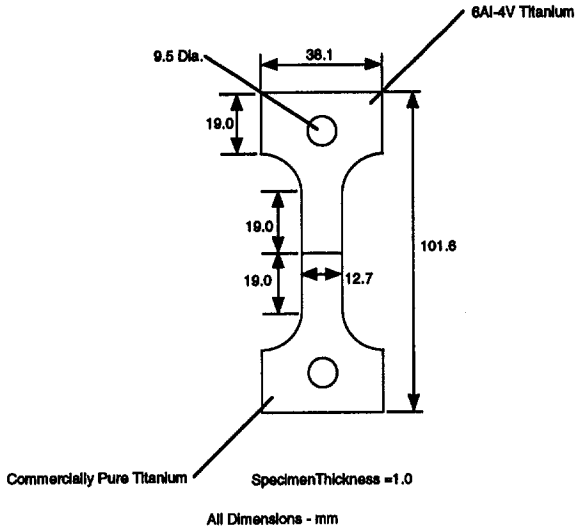


Fig. 1 The tensile bimaterial specimen (all dimensions in mm)

to create a mathematically sharp (continuum scale) interface between the two materials.

The diffusion bonding process begins with 50 mm dia, 50 mm long blanks of CP and 6Al-4V Ti whose ends are machined parallel and flat. The blanks are then polished with a 1 micron diamond paste, their surface oxide removed and inserted into a 178 kN capacity hot press for diffusion bonding in an argon environment. Diffusion bonding was performed at 870°C with a nominal pressure of 1.06 MPa for 40 minutes. Figure 3 shows

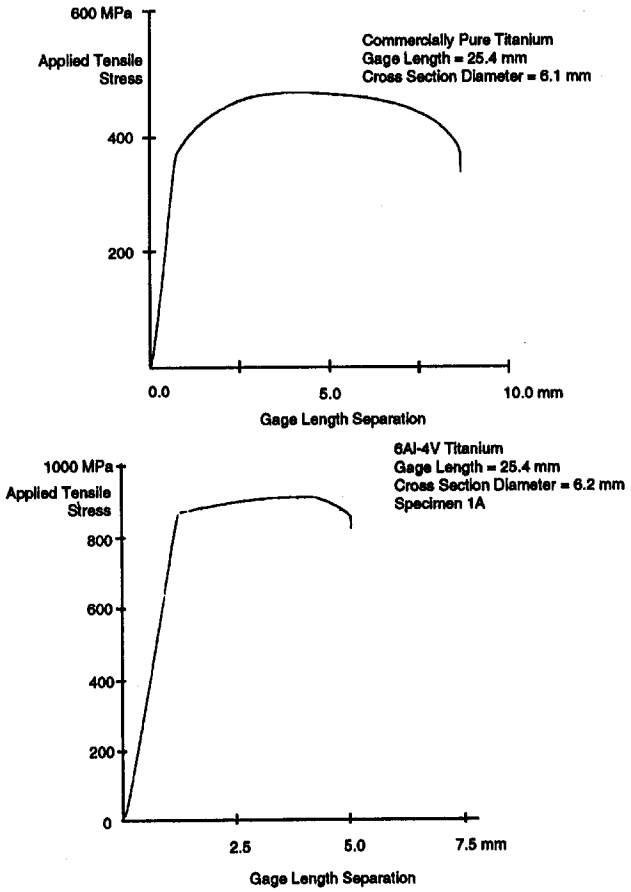


Fig. 2 The overall stress strain response for the CP and 6Al-4V titaniums (note figures are not the same scale)

Table 1

Material	E (GPa)	Poisson's ratio	ϵ_0 (%)	σ_0 (MPa)	α	n
CP Ti	112.3	0.24	0.33	366	0.60	11.0
6Al-4V Ti	115.1	0.28	0.72	886	0.349	31.8

a micrograph of the bondline region using Kellars etch. The large alpha grains in the CP Ti are evident as well as the long alpha structure interdispersed with the darker beta phases in the 6Al-4V. The bond is well defined with no evidence of diffusion across it.

As noted in the Introduction, Fig. 1 shows the specimen geometry. The geometry has a width to thickness ratio to 12:1 to approximate a generalized plane stress state. The principal reason for choosing this thin geometry was to minimize three-dimensional effects that would be inherent in thicker plane strain geometries. The planar aspects of the geometry facilitated the use of moire interferometric gratings that would be applied to the surface. Finally, the thin geometry implies that the principal plastic constraint effect to be studied will be in the X displacement along the width of the specimen bond line. There are a number of disadvantages to this thin geometry; they will be discussed in the following section.

2.2 Loading and Data Recording. Because the generalized plane stress specimen is thin and an interferometric moire method is employed, a loading fixture was designed to restrain the specimen from out-of-plane warping and to keep the end loading pins aligned during a tensile test. The loading fixture is detailed in Fig. 4. The alignment requirements are met by two sliding flat plates inside a carefully machined inner shell that aligns the loading pins. Such fixtures are common for interferometric specimen loading to minimize specimen rigid body rotation (Post 1987). This loading fixture was mounted inside a fixed displacement load frame. The remote load was monitored with 9 kN load cell. The relative end pin separation was monitored with a LVDT.

The surface displacements were recorded using moire interferometry (Post 1987). A 600 l/mm aluminized crossed diffraction grating was replicated onto the specimen surface in the bond line region. An effective frequency multiplication of 2 was utilized for a displacement sensitivity of 0.8 microns per fringe contour. Two fiber optic moire systems were coupled to monitor the X and Y displacements. A schematic of a single

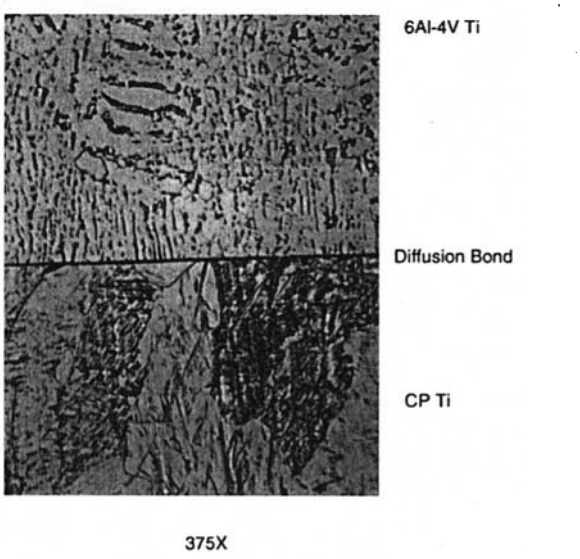


Fig. 3 The microstructure of the diffusion bond region (375×)

Downloaded 04 May 2010 to 171.66.16.28. Redistribution subject to ASME license or copyright; see http://www.asme.org/terms/Terms_Use.cfm

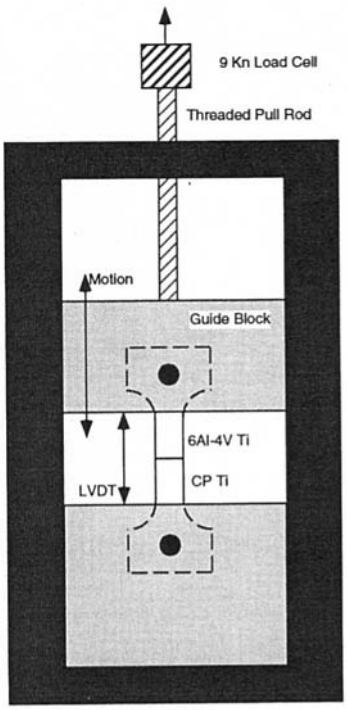


Fig. 4 The tensile testing fixture to insure proper pin alignment

two-beam system is shown in Fig. 5 (Deason, 1989). 100 × 125 mm Kodak Tmax 400 ASA film was employed to photograph the interferograms. A Pulnix CCD camera was employed to capture the interferograms for digital image processing. Figure 6 shows the experimental setup. Figure 7 details the remote stress applied to the end pins verses remote strain as measured by the LVDT—early in the displacement history some specimen seating is evidenced. The LVDT was mounted between the upper and lower guide blocks of Fig. 4; hence, the strain in Fig. 7 represents strain on the overall specimen test section.

2.3 *X* and *Y* Interferograms. Figure 8 shows the *X* and *Y* displacement fringes as a function of load. The tensile stress states in Fig. 8 are derived from the undeformed cross section. Figure 8 shows graphically the evolution of the shear bands emanating from the intersection of the bondline with the free edge as well as the gradient in displacement between the rigid

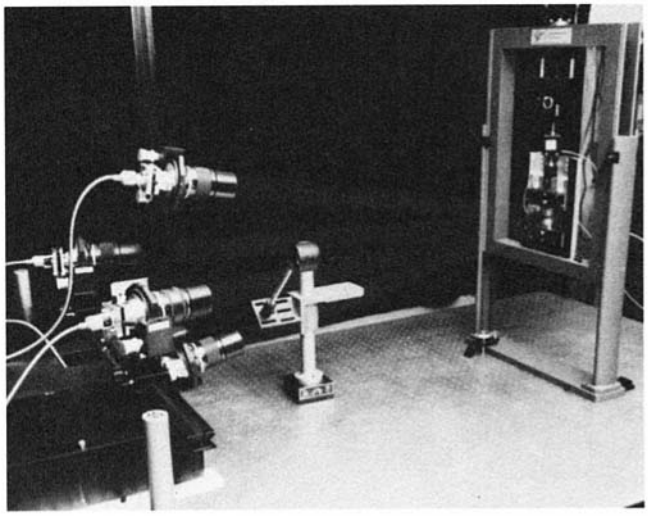


Fig. 6 A beam trace of a typical four-beam unit

6Al-4V Ti and the yielding CP Ti. The interpretation of the interferograms is essentially the same as mechanical moire (Post and Livnat 1985):

$$U_i = N_i / F$$

where

U_i is the X or Y displacement,
N_i is the fringe order from a known datum, and
F is the frequency of the grating usually in lines/mm or in.

Thus each fringe is a line of constant displacement in the direction perpendicular to the reference grating held constant in space.

Three regions are of particular interest in the X displacement fields shown in Fig. 8: the 345.1, 365.8, and 0 (residual) MPa stress states. The 345.1 and 365.8 MPa stress states correspond to ratios of far field applied tensile stress to the CP Ti proportional limit of 1.15 and 1.22. The proportional limit is used as it is a better physical indicator of yield in the CP Ti than the 0.2 percent offset strain. Overlay lines are also shown in Fig. 8 to highlight the slip bands. These bands are defined by the angular shift in the X displacement fringes as compared to the vertical X fringes due to Poisson contraction. For deforma-

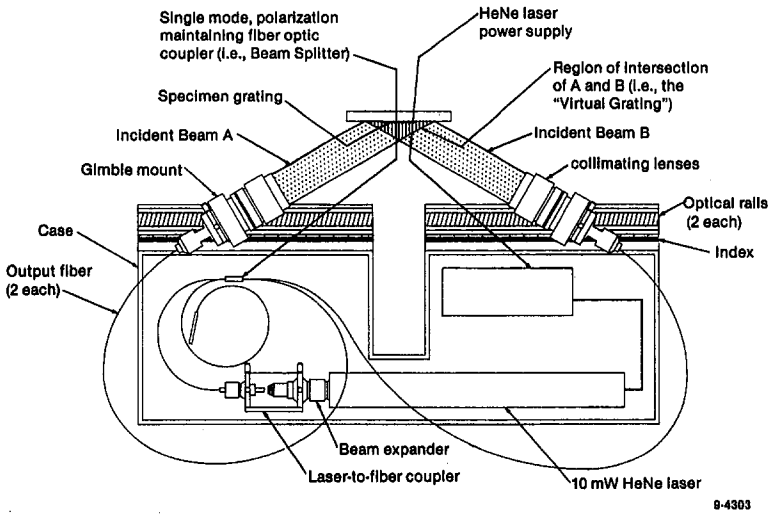


Fig. 5 The fiber optic two-beam moire interferometer

Downloaded 04 May 2010 to 171.66.16.28. Redistribution subject to ASME license or copyright; see http://www.asme.org/terms/Terms_Use.cfm

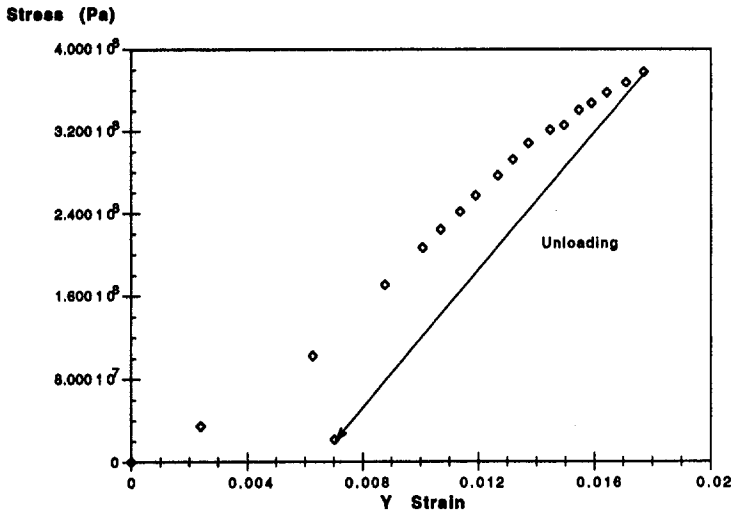


Fig. 7 The bulk stress strain response for the tensile specimen

tion below 345.1 MPa, two symmetric shear bands emanate from the bondline-free edge region in the CP Ti. The *X* contours of displacement far field from the bond are parallel to the contraction direction as expected. At 365.8 MPa the overall specimen tensile deformation is dominated by the right side CP Ti interface shear band. The angle produced by this dominate band is 58 deg. from the vertical in close agreement with the plane stress angle of 54 deg. based upon two-dimensional Mohr's circle analysis. Higher frequency perturbations are evident in the CP Ti *X* fringes which is a result of individual grain shear (the average grain size in the CP Ti is 30–40 microns which correlates with the perturbation size). Also the interior portion of the bondline shows essentially little if any change in the vertical *X* fringe direction, indicating that uniform plane strain like conditions exist along the interior portion of the bondline.

The low fringe density region in the 0 MPa plastic residual *X* field in Fig. 8 is the neutral axis from the asymmetric shear

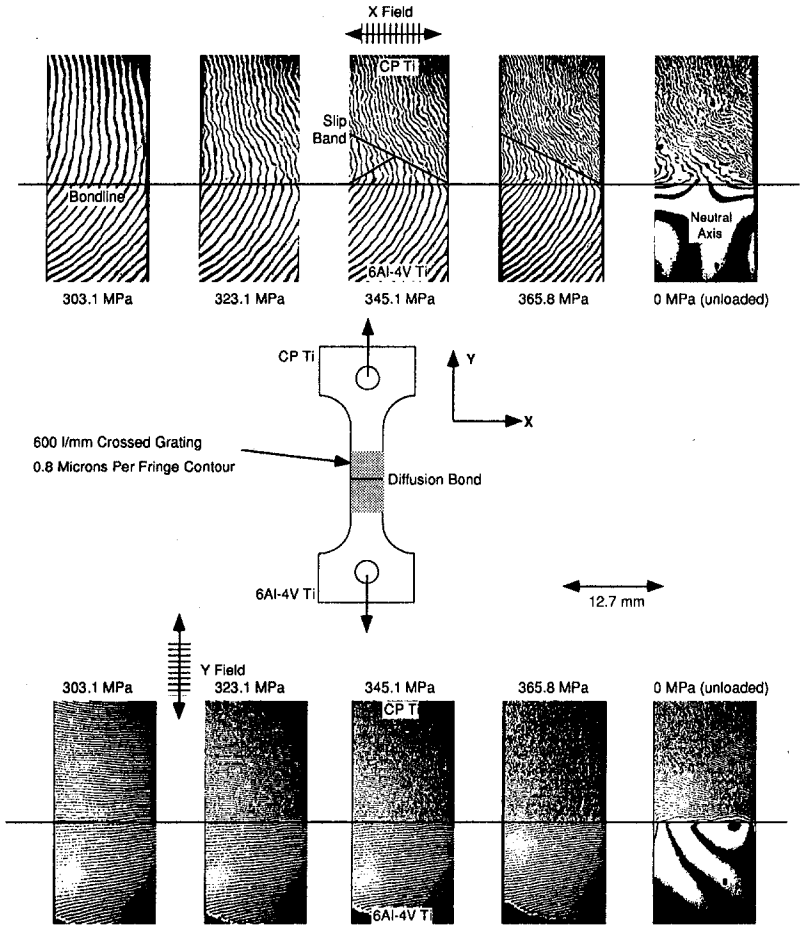


Fig. 8 The *X* and *Y* fringe moire fringe patterns for the deforming tensile specimen

Downloaded 04 May 2010 to 171.66.16.28. Redistribution subject to ASME license or copyright; see http://www.asme.org/terms/Terms_Use.cfm

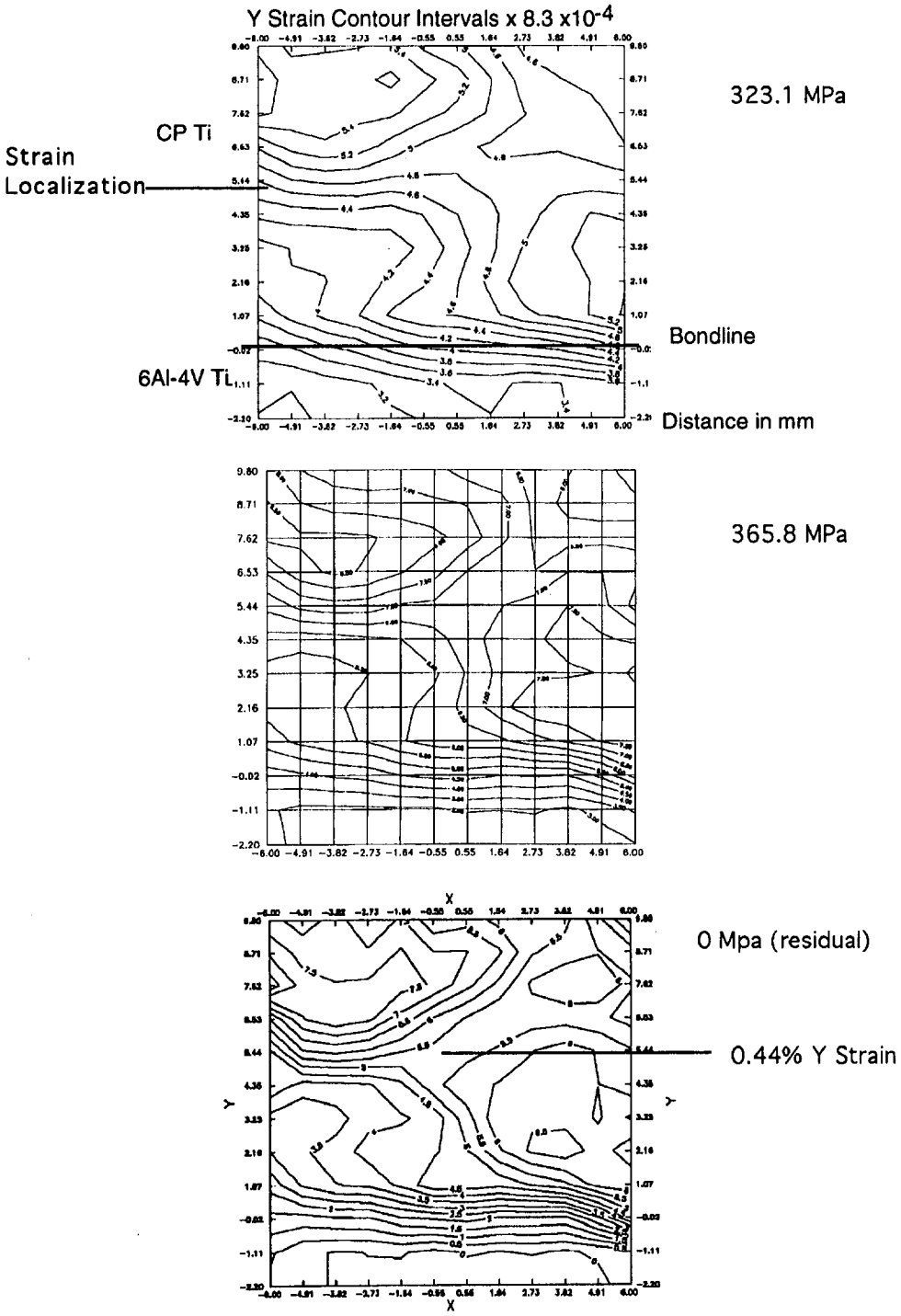


Fig. 9 The *Y* strain contours—note the contours are generated in terms of fringe order—multiply by 8.3 × 10^{-4} to obtain strain

banding process which in turn produces a bending moment in the tensile specimen.

3 Data Reduction and Strain Analysis

To extract strain from the *X* and *Y* interferograms, a three-step process is used. First the interferograms are digitized, second the digitized points are fit to a grid of regular spacing and third, a tensioned spline surface with the fringe order as the surface elevation is fit to the grid coordinates from step two. Two commercial PC based packages were employed. Surfer[1] first converts the random digitized points along the fringe orders to a fitted regular or gridded array. Fitlib[2] takes the gridded Surfer array and fits a tensioned splinned surface of (N_i, X, Y), (where N_i are the fringe orders). From this surface, derivatives may be taken to obtain the *X*, *Y* and shear strain.

Three checks are performed throughout the fitting process. The first check is to overlay the Surfer fringe pattern on the

[1]Golden Software Inc., P. O. Box 281, Golden, CO, 80402-0281.
[2]Fitlib, PC Scientific, Inc., 6 Pine Tree Dr., Suite 250, St. Paul, MN, 55112.

Downloaded 04 May 2010 to 171.66.16.28. Redistribution subject to ASME license or copyright; see http://www.asme.org/terms/Terms_Use.cfm

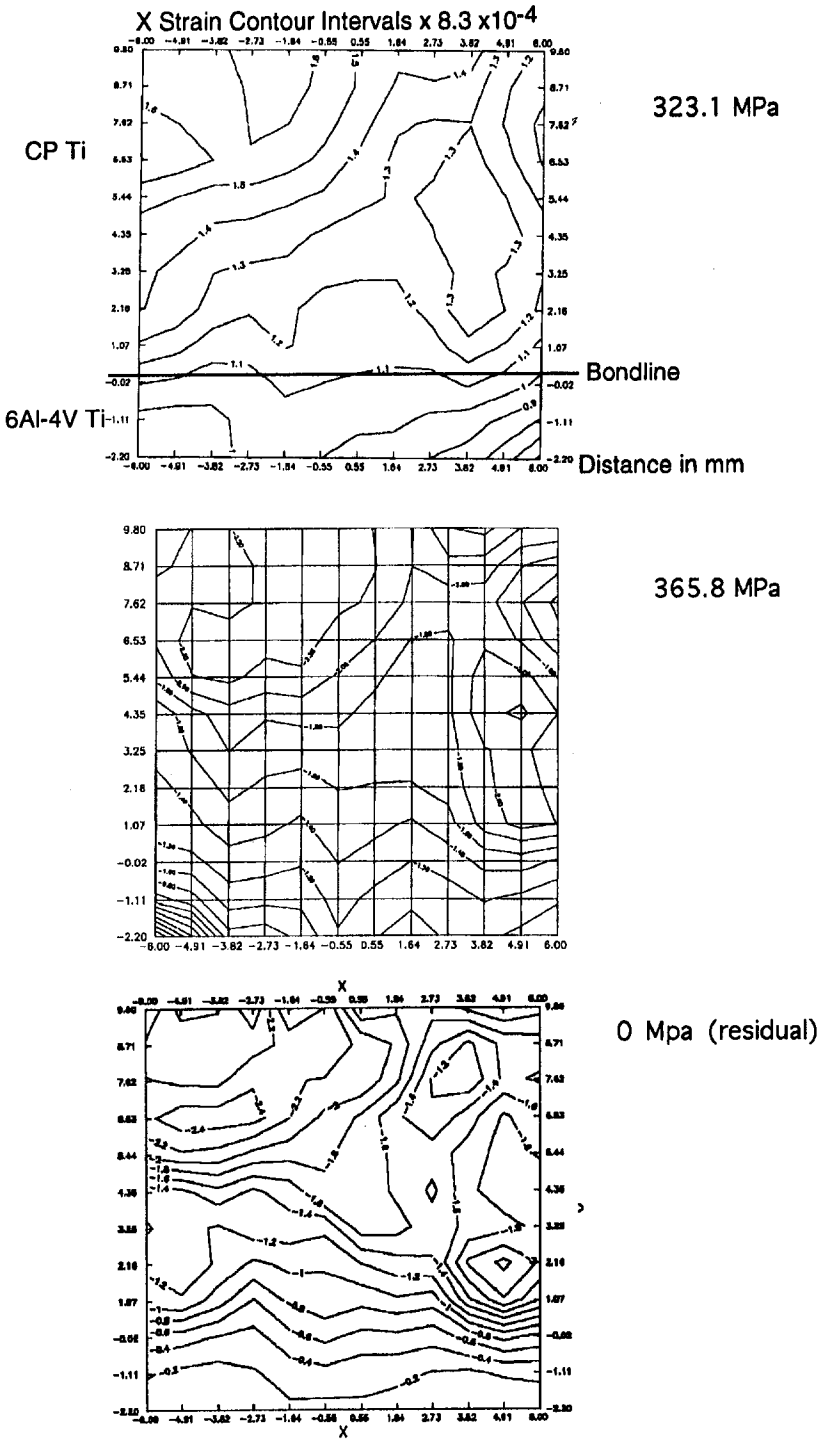


Fig. 10 The *X* strain contours—note the contours are in generated in terms of fringe order—multiply by 8.3 × 10^{-4} to obtain strain.

actual moire pattern. The second check is to overlay the Fitlib displacement field on the actual fringe patterns. The higher frequency grain shear or perturbations in the moire fringe patterns were not fitted in the bulk fringe fitting process. Capturing this finer detail requires a subset fitting local to the higher frequency information. The third and final check was to hand check the Fitlib strain fields with randomly selected points in the interferograms.

A key feature of the fitting process was to over sample, that is, to have at least twice the number of data points as actual grid points. This over sampling was feasible given the well-populated data sets in the moire interferograms. Despite the manual nature of this data reduction, we found that the process to be robust.

4 Strain Field Analysis

The *Y*, *X*, and *X*-*Y* (shear) strain fields are found in Figs. 9, 10, and 11, respectively. Each figure contains the strain field according to three remote applied stress states of Figure 8, 323.1, 365.1, and 0 (residual) MPa.

The *Y* strain fields in Fig. 9 show the same trend for all three stress levels, that is, there is a sharp strain gradient moving

Downloaded 04 May 2010 to 171.66.16.28. Redistribution subject to ASME license or copyright; see http://www.asme.org/terms/Terms_Use.cfm

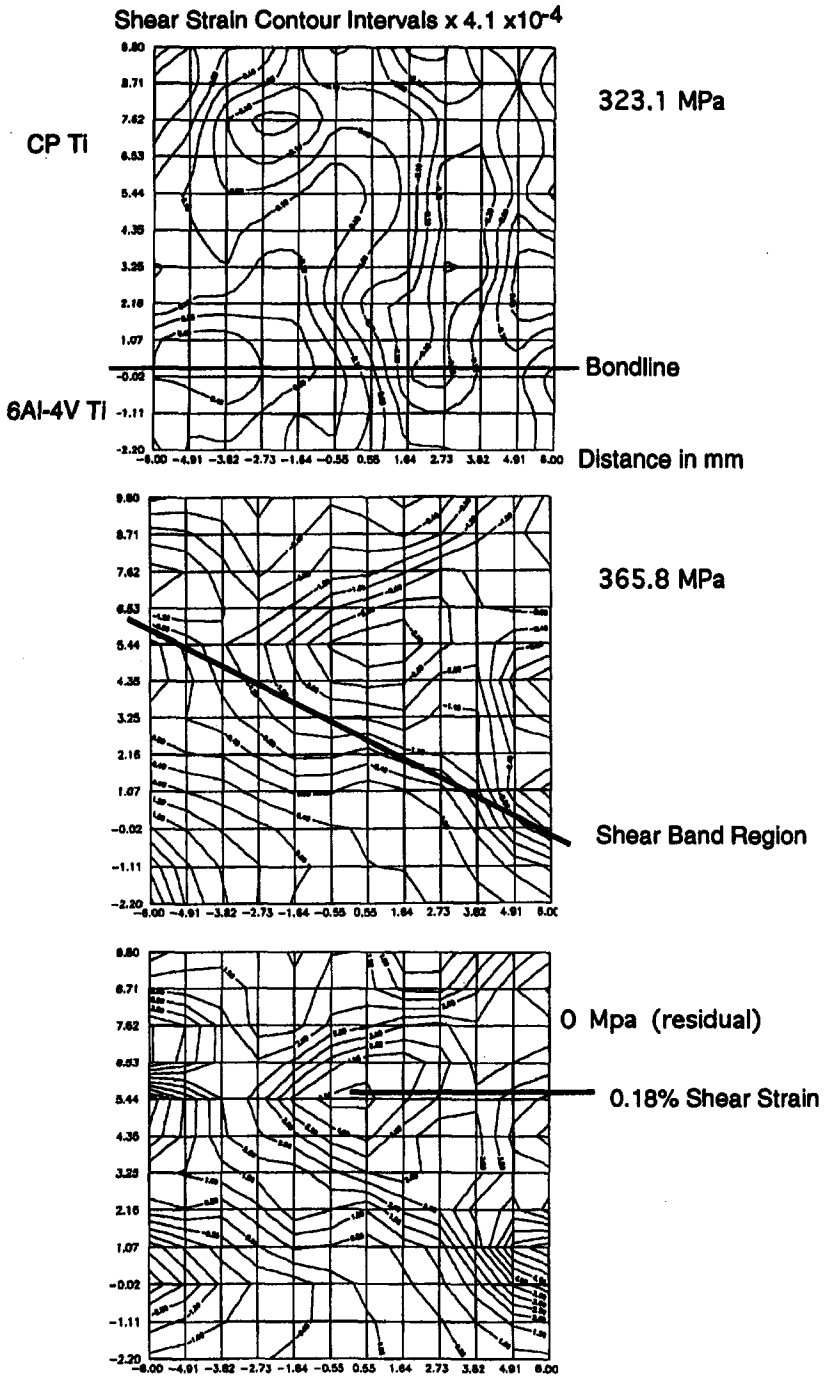


Fig. 11 The shear strain contours ($\frac{1}{2}(\partial u/\partial y + \partial v/x)$)—note the contours are in generated in terms of fringe order—multiply by 4.1×10^{-4} to obtain strain.

away from the interface, a relatively quiet region and then a localization region 5-6 mm from the interface on the left hand side. Likewise the X strain fields, Fig. 10, again show the presence of contraction strain or necking, above the bondline region as well as the localization of strain in the unloaded 0 MPa residual state on the right-hand side of the specimen (in the same region as was for the Y strain). The interior portion of the bondline clearly shows its plane strain nature as the X strain is nearly constant along the center of the specimen. Figure 11 details the shear strain field. For the unloaded 0 MPa residual state, the shear strain within the shear band is as high as 0.18 percent in Fig. 11. The Y strain at the same 0 MPa state in the same spatial region is 0.44 percent (Fig. 9). It is also evident that the shear strain along the middle of the bond line region ($X = Y = 0$) for stress states in Fig. 11 are nearly zero confirming the strong biaxial stress state present there.

5 Discussion

Evident in the shear strain (Fig. 11) and X displacement fields, (Fig. 8) is the nonhomogeneous nature of the slip process. Slip starts, as expected, from the interface-free surface intersection singularity region. It progresses into the specimen with continued bulk tensile deformation until the right-hand slip band dominates the deformation process. Single grain shear is evidenced as higher frequency perturbations in the X displacement fields, Fig. 8. It should be noted that the interface singularities described by Bogy (1971) are due to elastic mismatch.

Downloaded 04 May 2010 to 171.66.16.28. Redistribution subject to ASME license or copyright; see http://www.asme.org/terms/Terms_Use.cfm

Because the elastic modulii are close for these specimens, slip initiation is due to a yield strength mismatch and most likely a lower strength singularity than in the elastic case. One may ask whether the slip is a microstructural or mechanical phenomena. The bond line shown in Fig. 3 is relatively intact, that is there is no evidence of void nucleation or impurities. Further, the yielding material is nonalloyed, i.e., it is commercially pure titanium (99.5 percent), thus denying void nucleation from impurity elements. Finally, the CP Ti is hydrostatically constrained at the interface by the higher yield strength 6Al-4V Ti further lowering the possibility of void nucleation. Thus, one may conclude that the yielding is predominately due to the mechanical properties of the CP Ti. The observation that the right-hand band dominates the right-hand slip process during later stages of deformation may be attributed to a number factors such as a number of grains in the right-hand interface-slip band region having their slip systems preferentially oriented, a small machining mark, etc. The exact mechanism is left to conjecture. Finally, the 0 MPa X displacement field in Fig. 8 shows that upon unloading, this asymmetric slip process results in a residual bending field as evidenced by the labeled neutral axis in the 6Al-4V alloy side.

The shear strain within the slip band of Fig. 11 is not constant as is classically predicted for nonstrain hardening materials. This gradient in shear strain is attributable to strain hardening in the CP Ti and the possibility of out-of-plane three-dimensional deformation even in this very thin sample.

Practical questions arise regarding the nature of testing any joined specimen, in particular a weld joint under tension and the implications of what would occur if a crack existed at the bondline and what would be its most severe location along that interface.

These results show that for a mismatch yield strength weldment or bond of any kind, a tension test does not necessarily provide a uniform tensile field at the interface. This lack of uniformity is due to the finite geometry of the specimen and the yielding created at the free edge region of the interface. These singularities impose shear bands that progress into the interior of the specimen as shown in the X displacement field patterns of Fig. 8. Due to the shear banding instability, one of the bands eventually dominates and the specimen exhibits a strong shear from the bondline into the interior of the specimen. The result of this asymmetric shear banding process is that the specimen develops a bending moment (see the 0 MPa X field in Fig. 8) even though it is pulled under remote tension.

The shear banding in turn creates a generalized plane strain region in the X direction along the middle of the bond line region, as evidenced by the relatively low but constant X strains in Fig. 10. This interior plane strain constraint region can result in initiation of a brittle interface crack under remote tension provided that the bond strength is low enough compared to the interface-free surface intersection region where plastic flow occurs. (Indeed this happened with an earlier specimen). Likewise if the bond strength is high thereby denying interior interface separation, then ductile failure can occur at the interface-free edge region where the unconstrained plastic flow occurs.

Thus one may observe two completely different responses from the bimetallic specimen depending on the bond strength. Brittle fracture via interface separation (or debonding) can occur under high constraint in the middle region or ductile crack initiation can occur at the interface-free edge region under low constraint. In terms of assessing the bondline strength of a weldment, one would have to ensure that fracture initiated in the interior or middle region of the specimen and not the free edge region where low constraint exists. In terms of placement of a crack, one would have to make the specimen wide enough so the near crack-tip plastic fields do not interact with the shear bands emanating from the free edge. Finally, placing a crack along the bondline in the middle constrained region can give a conservative fracture energy due to the generalized plane strain like constraint in the X direction on the crack-tip plastic zones.

6 Conclusions

The deformations and strains in a bimetallic strip under remote tension have been measured and analyzed. Shear banding was observed to emanate from the interface-free edge singularity region. During later stages of deformation, plastic localization and instability permitted one of the shear bands to dominate thus creating a bending field in the tension sample. A robust fringe data reduction technique has been developed that determines the strain fields in the sample. Large grain shear is evidenced as higher order perturbations in the X field fringe patterns. The strain field analysis indicates two forms potential of failure, elastic debonding in the middle of the specimen along the interface or ductile flow initiated failure along the interface-free edge region.

In conclusion, one would anticipate a valid tension test of the bond line provided the failure occurs in the middle portion of the sample and not the free edge. In terms of placing a crack along the bond line one would have to insure that the tip plastic zones are not perturbed by the interface-free edge shear bands and that the overall energy to fracture would be conservative due to the interior generalized plane strain constraint. Finally, in both uncracked and cracked tension tests one would have to ensure that fracture initiated before the asymmetric deformation process creating a bending field in the tensile sample occurs.

Acknowledgments

This work was funded by the U.S. Department of Energy, Office of Basic Energy Sciences under contact DE-AC07-76ID01570, Dr. O. P. Manley program manager. The assistance of Mr. W. R. Lloyd is gratefully acknowledged.

References

Blum, J. A., and Shih, F., 1989, "The Singular Behavior of a Bimaterial Strip," *Proceedings, 7th ASCE Engineering Mechanics Conf.*, R. A. Heller and M. P. Sing, ed., ASCE, NY, p. 72.

Bogy, D. B., 1971, "Two Edge Bonded Elastic Wedges of Different Materials and Wedge Angles Under Surface Tractions," ASME JOURNAL OF APPLIED MECHANICS, Vol. 35, pp. 377–386.

Burke, M. A., and Nix, W. D., 1979, "A Numerical Study of Necking in the Plane Tension Test," *International Journal Solids and Structures,* Vol. 15, pp. 379–393.

Deason, V. A., and Ward, M. B., 1989, "A Compact Portable Diffraction Moire Interferometer," *Proceedings, Laser Interferometry, Quantitative Analysis of Interferograms,* Vol. 1162, Society for Photo Optical Instrumentation Engineers, Bellingham, WA, pp. 26–35.

Hart, E. W., 1955, "A Uniaxial Strain Model for a Lüder's Band," *Acta Metallurgica,* Vol. 3, Mar. pp. 146–49.

Hill, R., and Hutchinson, J. W., 1975, "Bifurcation Phenomena in the Plane Tension Test," *Journal of the Mechanics and Physics of Solids,* Vol. 23, pp. 239–264.

Kishimoto, K., Sugita, T., Noyomi, M., and Koizumi, T., 1993, "Elastic-Plastic Finite Element Analysis on Bonding Edge of Dissimilar Materials," *Japan Society of Mechanical Engineers International Journal,* Ser. A, Vol. 36, No. 4, pp. 382–389.

Livnat, A., and Post, D., 1985, "The Grating Equations for Moire Interferometry and Their Identity to Equations of Geometrical Moire," *Experimental Mechanics,* Vol. 25, No. 4, pp. 360–366.

Nadai, A., 1950, *Theory of Flow and Fracture of Solids,* Vol. 1, 2nd ed., McGraw-Hill, New York, pp. 289–327.

Onat, E. T., and Prager, W., 1954, "Necking of a Tension Specimen in Plastic Flow," *Journal of Applied Physics,* Vol. 25, No. 4, Apr., pp. 491–93.

Ortiz, M., Leroy, Y., and Needleman, A., 1987, "A Finite Element Method for Localized Failure Analysis," *Computer Methods in Applied Mechanics,* Vol. 61, pp. 189–214.

Post, D., 1987, "Moire Interferometry," *Handbook on Experimental Mechanics,* A. Kobayashi, ed., McGraw-Hill, New York, Chapter 7.

Storen, S., and Rice, J. R., 1975, "Localized Necking in Thin Sheets," *Journal of the Mechanics and Physics of Solids,* Vol. 23, pp. 421–41.

Downloaded 04 May 2010 to 171.66.16.28. Redistribution subject to ASME license or copyright; see http://www.asme.org/terms/Terms_Use.cfm

Analysis of Ring-Stiffened Cylindrical Shells

Bingen Yang
Associate Professor,
Mechanical Engineering,
Mem. ASME.

Jianping Zhou[1]
Visiting Scholar.

University of Southern California,
Los Angeles, CA 90089-1453

A new analytical and numerical method is presented for modeling and analysis of cylindrical shells stiffened by circumferential rings. This method treats the shell and ring stiffeners as individual structural components, and considers the ring eccentricity with respect to the shell middle surface. Through use of the distributed transfer functions of the structural components, various static and dynamic problems of stiffened shells are systematically formulated. With this transfer function formulation, the static and dynamic response, natural frequencies and mode shapes, and buckling loads of general stiffened cylindrical shells under arbitrary external excitations and boundary conditions can be determined in exact and closed form. The proposed method is illustrated on a Donnell-Mushtari shell, and compared with finite element method and two other modeling techniques.

1 Introduction

Cylindrical shells stiffened by stringers and rings have wide engineering applications. The modeling techniques for such structure systems can be divided into two categories. The first category smears the stiffness of the stiffeners on the shell, and treats the stiffened shell as an orthotropic one; for instance, see Wang (1970) and the references therein. Such treatment is fine when the stiffeners are densely placed. However, if stiffeners are sparsely spaced that there are not enough stiffeners in each half wavelength in the circumferential and longitudinal directions of the shell, or if the actual deformation and stress distributions of the stiffened shell are needed, orthotropic approximation will loose accuracy. In this case, it is necessary to consider stiffeners as individual structural components, which gives rise to the second category of modeling techniques, namely, the analysis of combined shell-stiffener component systems.

Modeling stiffened cylindrical shells as combined component systems has been studied by many authors. Of various static and dynamic problems, free vibration of different stiffened shells has received great attention. Garnet and Goldberg (1962) and Godzvich and Ivanova (1965) considered ring-stiffened cylindrical shells. Schnell and Heinrichsbauer (1964) studied longitudinally stiffened thin-walled cylindrical shells. Egle and Sewall (1968) analyzed a ring-and-stringer-stiffened circular cylindrical shell by a Rayleigh-Ritz procedure. Wang and Rinehart (1974) modeled longitudinally stiffened cylindrical shells with arbitrary edge boundary conditions. Wang and Hsu (1985) proposed a model for stiffened composite cylindrical shells. Mead and Bardell (1987) investigated periodically stiffened cylindrical shells.

Among other problems, Wang and Lin (1973) examined the stability of stringer-stiffened cylindrical shells under axial pressure and simply supported boundary conditions; Reddy (1980) presented a bifurcation analysis for stringer-stiffened cylinders sustaining elastic-plastic deformation; and Sridharan et al. (1992) studied post-buckling of stiffened composite shells.

Several analytical and numerical methods for stiffened cylindrical shells have been developed. Forsberg (1969) obtained an exact solution for natural frequencies of ring-stiffened cylinders subjected to different boundary conditions. Al-Najafi and Warburton (1970) applied the finite element method to evaluate the natural frequencies and mode shapes of ring-stiffened cylindrical shells with each stiffening ring treated as a discrete element. Wang (1970) yielded a Fourier series solution of ring-and-stringer-stiffened cylindrical shells by treating the shell, rings, and stringers as structural components, and imposing deformation compatibility among those components. Wilken and Soedel (1976) used a receptance method to describe the modal characteristics of ring-stiffened shells. By Laplace transform and numerical inverse Laplace transform, Dekos and Oates (1981) predicted the dynamic response of ring-stiffened circular cylindrical shells subjected to axis-symmetric loading and boundary restriction conditions. Rigo (1992) developed the stiffened sheathing method and LBR-3 software for computing the response of orthotropic cylindrical shells. Combining wave propagation method and transfer matrix method, Huntington and Lyrintzis (1992) developed a modified wave method for analysis of skin-stringer panels which improves the numerical stability of transfer matrix method.

This paper proposes a new analytic and numerical method for constrained/combined, ring-stiffened cylindrical shells, which falls in the second category of modeling techniques. A typical example is shown in Fig. 1, where the shell consists of several serially connected segments of different geometry and material parameters, each shell segment may be constrained by springs and dampers that are circumferential distributed, the ring stiffeners are placed either inwardly, or outwardly, or symmetrically with respect to the shell middle surface, and the whole shell is subject to arbitrary external excitations and boundary conditions. The distributed transfer function formulation proposed in Yang (1992, 1994) is extended to model stiffened shells. In the analysis, the shell and stiffeners are modeled as individual structural components. Through both Fourier expansion and Laplace transform of the shell displacements, the initial and boundary value problem of the shell is cast into a spatial state-space form in the s-domain. The distributed transfer functions of the shell segments are then derived, based on which the shell and stiffeners are assembled by imposing displacement continuity and force balance on the shell-stiffener contact surface, leading to a global dynamic equilibrium equation. Solution of the equilibrium equation gives accurate estimation of the static deflection, natural frequencies and mode shapes, bucking loads, and forced response of stiffened cylindrical shells under arbitrary boundary conditions and external excitations.

The proposed method has the following advantages. First, the transfer function method provides exact and closed-form

[1] Currently at the National University of Defense Technology, China.

Contributed by the Applied Mechanics Division of THE AMERICAN SOCIETY OF MECHANICAL ENGINEERS for publication in the ASME JOURNAL OF APPLIED MECHANICS.

Discussion on this paper should be addressed to the Technical Editor, Professor Lewis T. Wheeler, Department of Mechanical Engineering, University of Houston, Houston, TX 77204-4792, and will be accepted until four months after final publication of the paper itself in the ASME JOURNAL OF APPLIED MECHANICS.

Manuscript received by the ASME Applied Mechanics Division, May 13, 1994; final revision, Sept. 23, 1994. Associate Technical Editor: J. N. Reddy.

Copyright © 1995 by ASME

Downloaded 04 May 2010 to 171.66.16.28. Redistribution subject to ASME license or copyright; see http://www.asme.org/terms/Terms_Use.cfm

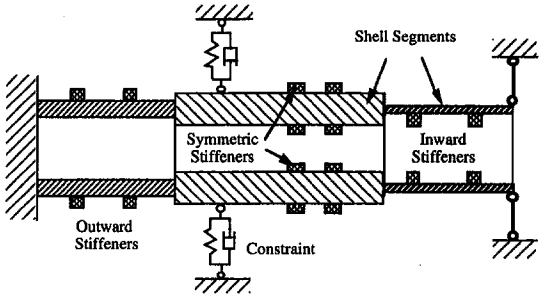


Fig. 1 A constrained/combined, ring-stiffened cylindrical shell

solutions for various static, dynamic, and control problems of stiffened cylindrical shells. Second, the transfer function method systematically treats different shell models (Love-Timoshenko or Donnell-Mushtari type, elastic or viscoelastic, stationary or spinning shells, etc.), and arbitrary boundary conditions and external excitations in a simple and unified manner, rendering numerical simulation and computer coding extremely convenient. Third, the transfer functions is especially capable of synthesizing combined cylindrical shells as shown in Fig. 1. All these will be demonstrated in the subsequent analysis and the numerical simulation.

2 Distributed Transfer Functions of Cylindrical Shells

The response of the homogeneous cylindrical shell in Fig. 2 is governed by

$$\sum_{k=1}^{3}\sum_{i=0}^{n_k}\sum_{j=0}^{i}\left[A_{mkij}\frac{\partial^2}{\partial t^2}+B_{mkij}\frac{\partial}{\partial t}+C_{mkij}\right]\frac{\partial^i u^k(x,\theta,t)}{\partial x^{i-j}\partial\theta^j}=f^m(x,\theta,t),\quad m=1,2,3 \tag{1}$$

where u^k ($k = 1, 2, 3$) are the shell displacements in the longitudinal (x-), circumferential (θ-) and radial (z-) coordinate directions, respectively, n_k is the highest order of differentiation of u^k, A_{mkij}, B_{mkij}, and C_{mkij} are constants of the shell, and $f^m(x, \theta, t)$ are the external loads acted on the shell. Here, Eq. (1) has been nondimensionalized so that $x = 0$ and $x = 1$ are the left and right boundaries of the shell. The boundary and initial conditions of the shell are

$$\left[\sum_{k=1}^{3}\sum_{i=0}^{n_k-1}\sum_{j=0}^{i}\beta_{lkij}\frac{\partial^i u^k(x_\alpha,\theta,t)}{\partial x^{i-j}\partial\theta^j}\right]_{x=x_\alpha}=\lambda^l(\theta,t),\quad l=1,2,\ldots,n_b \tag{2a}$$

and

$$u^k(x,\theta,t)|_{t=0}=u_0^k(x,\theta),\qquad \frac{\partial}{\partial t}u^k(x,\theta,t)\bigg|_{t=0}=u_0^{k,t}(x,\theta),\quad k=1,2,3 \tag{2b}$$

where $x_\alpha = 0$ and 1 for $\alpha = 1$ and 2, respectively, β_{lkij} are constants, and $\lambda^l(\theta, t)$, $u_0^k(x, \theta)$ and $u_0^{k,t}(x, \theta)$ are those proposed by given functions representing the boundary and initial disturbances. The number of boundary conditions $n_b = n_1 + n_2 + n_3$, and is 8 in most situations. Equations (1) and (2) represent many shell models, such as Donnell-Mushtari, Love-Timoshenko, Flugge-Novozhilov, Reissner, Vlasov, and Sanders.

To find the solution of the initial-boundary value problem formed by (1) and (2), the shell displacements and all the given functions of disturbances are expanded into Fourier series in circumferential direction θ

$$u^k(x,\theta,t)=\sum_{n=0}^{\infty}[u_{1,n}^k(x,t)\cos n\theta+u_{2,n}^k(x,t)\sin n\theta],\quad k=1,3 \tag{3a}$$

$$u^2(x,\theta,t)=\sum_{n=0}^{\infty}[u_{1,n}^2(x,t)\sin n\theta+u_{2,n}^2(x,t)\cos n\theta] \tag{3b}$$

$$f^m(x,\theta,t)=\sum_{n=0}^{\infty}[f_{1,n}^m(x,t)\cos n\theta+f_{2,n}^m(x,t)\sin n\theta],\quad m=1,2,3 \tag{3c}$$

$$u_0^k(x,\theta)=\sum_{n=0}^{\infty}[u_{1,n}^{k,0}(x)\cos n\theta+u_{2,n}^{k,0}(x)\sin n\theta],\quad k=1,3 \tag{3d}$$

$$u_0^2(x,\theta)=\sum_{n=0}^{\infty}[u_{1,n}^{2,0}(x)\sin n\theta+u_{2,n}^{2,0}(x)\cos n\theta] \tag{3e}$$

$$u_0^{k,t}(x,\theta)=\sum_{n=0}^{\infty}[u_{0,1,n}^{k,t}(x)\cos n\theta+u_{0,2,n}^{k,t}(x)\sin n\theta] \tag{3f}$$

$$u_0^{2,t}(x,\theta)=\sum_{n=0}^{\infty}[u_{0,1,n}^{2,t}(x)\sin n\theta+u_{0,2,n}^{2,t}(x)\cos n\theta] \tag{3g}$$

$$\lambda^l(\theta,t)=\sum_{n=0}^{\infty}[\lambda_{1,n}^l(t)\cos n\theta+\lambda_{2,n}^l(t)\sin n\theta],\quad l=1,2,\ldots,n_b. \tag{3h}$$

Here, the subscripts $(1, n)$ and $(2, n)$ indicate that the terms in Fourier series are related to $\cos n\theta$ and $\sin n\theta$, respectively. If all excitations are symmetric with respect to $\theta = 0$ and the shell is homogeneous and isotropic, each of the above Fourier series will only contain either cosine or sine- terms, thus reducing the number of unknowns by half.

Substituting the Fourier series into Eqs. (1) and (2), conducting Laplace transform with time t, and setting the coefficients of $\cos n\theta$ and $\sin n\theta$ to be equal on the both sides of the resulting equations, lead to an infinite number of equations ($m = 1, 2, 3, n = 0, 1, 2, \ldots$)

$$\sum_{k=1}^{3}\sum_{i=0}^{n_k}\left\{\sum_{j=0}^{[i/2]}D_{mki(2j)}(s)(-1)^j\frac{\partial^{i-2j}U_{1,n}^k}{\partial x^{i-2j}}+\sum_{j=1}^{[(i+1)/2]}D_{mki(2j-1)}(s)(-1)^{j+1}\frac{\partial^{i-(2j-1)}U_{2,n}^k}{\partial x^{i-(2j-1)}}\right\}=\tilde f_{1,n}^m(x,s)+\tilde g_{1,n}^m(x,s)$$

$$\sum_{k=1}^{3}\sum_{i=0}^{n_k}\left\{\sum_{j=0}^{[i/2]}D_{mki(2j)}(s)(-1)^j\frac{\partial^{i-2j}U_{2,n}^k}{\partial x^{i-2j}}+\sum_{j=1}^{[(i+1)/2]}D_{mki(2j-1)}(s)(-1)^j\frac{\partial^{i-(2j-1)}U_{1,n}^k}{\partial x^{i-(2j-1)}}\right\}=\tilde f_{2,n}^m(x,s)+\tilde g_{2,n}^m(x,s)$$

where $U_{j,n}^k = \tilde u_{j,n}^k$ for $k = 1$ and 3, and $U_{1,n}^2 = \tilde u_{2,n}^2$ and $U_{2,n}^2 = \tilde u_{1,n}^2$, $\tilde u_{i,n}^k$ and $\tilde f_{j,n}^m(x, s)$ are the Laplace transforms of $f_{j,n}^m(x, t)$

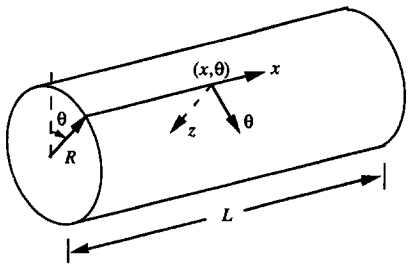


Fig. 2 A homogeneous cylindrical shell

Downloaded 04 May 2010 to 171.66.16.28. Redistribution subject to ASME license or copyright; see http://www.asme.org/terms/Terms_Use.cfm

and $u^k_{i,n}$, respectively; $\tilde{g}^m_{j,n}(x, s)$ are given in terms of $u^{k,0}_{j,n}(x)$; the complex numbers $D_{mkij}(s) = (A_{mkij}s^2 + B_{mkij}s + C_{mkij})n^j$; and s is the complex Laplace transform parameter. Note that the displacement functions $\tilde{u}^k_{i,n}$ and $\tilde{u}^k_{i,m}$ do not couple if n is not equal to m.

The above equations are cast in a state-space form

$$\frac{\partial \eta_n(x, s)}{\partial x} = F_n(s)\eta_n(x, s) + \tilde{f}_n(x, s) + \tilde{g}_n(x, s), \qquad n = 0, 1, \ldots \quad (4)$$

where the state-space vector contains the displacement functions $\tilde{u}^k_{i,m}$; i.e.,

$$\eta_n = \{\eta^T_{1,1,n} \quad \eta^T_{2,1,n} \quad \eta^T_{3,1,n} \quad \eta^T_{1,2,n} \quad \eta^T_{2,2,n} \quad \eta^T_{3,2,n}\}^T \in C^{2n_b} \quad (5a)$$

$$\eta_{k,i,n} = \left\{\tilde{u}^k_{i,n} \frac{\partial \tilde{u}^k_{i,n}}{\partial x} \cdots \frac{\partial^{n_k-1}\tilde{u}^k_{i,n}}{\partial x^{n_k-1}}\right\}^T \in C^{n_k}, \qquad k = 1, 2, 3, \quad i = 1, 2. \quad (5b)$$

$F_n(s)$ is a $2n_b \times 2n_b$ complex matrix containing the coefficients A_{mkij}, B_{mkij}, and C_{mkij} of (1), and the complex $2n_b$-vectors $\tilde{f}_n(x, s)$ and $\tilde{g}_n(x, s)$ are composed of $\tilde{f}^m_{j,n}(x, s)$ and $\tilde{g}^m_{j,n}(x, s)$, respectively. Similarly, the boundary conditions (2a) can be transformed into the form

$$M_n(s)\eta_n(0, s) + N_n(s)\eta_n(1, s) = \gamma_n(s) \quad (6)$$

where the boundary matrices $M_n(s)$ and $N_n(s)$ ($\in C^{2n_b \times 2n_b}$) contain the coefficients β_{lkij} in (2a), and the vector $\gamma_n(s)$ contain the Laplace transforms of the boundary excitation functions $\lambda^k_{j,m}$. One example of the above state-space form will be illustrated in Section 4.

The solution of the Eqs. (4) and (6) is (Yang and Tan, 1992)

$$\eta_n(x, s) = \int_0^1 G_n(x, \xi, s)(\tilde{f}_n(\xi, s) + \tilde{g}_n(\xi, s))d\xi + H_n(x, s)\gamma_n(s) \quad (7)$$

where the $2n_b \times 2n_b$ complex matrices

$$G_n(x, \xi, s) = \begin{cases} H_n(x, s)M_n(s)e^{-F_n(s)\xi}, & \xi \le x \\ -H_n(x, s)N_n(s)e^{F_n(s)(1-\xi)}, & \xi > x \end{cases} \quad (8a)$$

$$H_n(x, s) = e^{F_n(s)x}(M_n(s) + N_n(s)e^{F_n(s)})^{-1} \quad (8b)$$

are the distributed transfer functions of the shell. The displacement functions are found from η_n:

$$u^1(x, s) = \sum_{n=0}^{\infty} [\eta_{n,1}(x, s) \cos n\theta + \eta_{n,n_1+n_2+n_3+1}(x, s) \sin n\theta] \quad (9a)$$

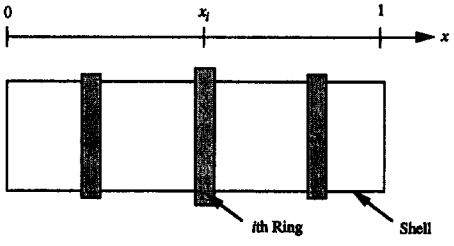


Fig. 3 A cylindrical shell stiffened by circumferential rings

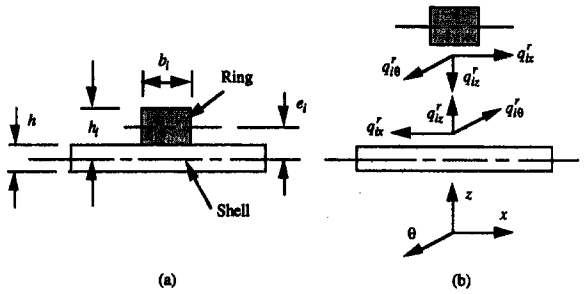


Fig. 4 Interaction between the shell and the ith ring: (a) geometry; (b) tractions

$$u^2(x, s) = \sum_{n=0}^{\infty} [\eta_{n,n_1+1}(x, s) \sin n\theta + \eta_{n,2n_1+n_2+n_3+1}(x, s) \cos n\theta] \quad (9b)$$

$$u^3(x, s) = \sum_{n=0}^{\infty} [\eta_{n,n_1+n_2+1}(x, s) \cos n\theta + \eta_{n,2n_1+2n_2+n_3+1}(x, s) \sin n\theta] \quad (9c)$$

where $\eta_{n,j}$ is the jth element of η_n.

In the above derivation, no approximation has been made; the transfer function formulation provides an exact and closed-form solution. The result here is quite general because different shell models and arbitrary boundary and initial conditions are dealt with by the same formula.

The transfer function formulation is directly applicable to the eigenvalue problems associated with free vibration and buckling of cylindrical shells, which are described by

$$[M_n(s; \bar{p}) + N_n(s; \bar{p})e^{F_n(s;\bar{p})}]\psi = 0 \quad (10)$$

with $\bar{p}$ being a load parameter and ψ a nonzero complex vector. The eigenvalues are the roots of the characteristic equation

$$\det [M_n(s; \bar{p}) + N_n(s; \bar{p})e^{F_n(s;\bar{p})}] = 0. \quad (11)$$

For free vibration of the shell, $\bar{p} = 0$ and s is the eigenvalue; the corresponding mode shape is determined by $\eta_n(x, s) = e^{F_n(s;0)x}\psi$ and (9). For a static buckling problem, $s = 0$ and $\bar{p}$ is the eigenvalue; the bucking mode shape is given by $\eta_n(x, \bar{p}) = e^{F_n(0;\bar{p})x}\psi$. For free vibration of a prestressed cylindrical shell, $\bar{p}$ is a nonzero constant and the s is the eigenvalue; the mode shape is given by $\eta_n(x, s) = e^{F_n(s;\bar{p})x}\psi$.

The transfer functions can also be used to determine the dynamic response and stability of the cylindrical shell under various forcing sources, and to design active vibration controllers and smart structure mechanism (Yang, 1994).

3 Analysis of Ring-Stiffened Cylindrical Shells

In Fig. 3, a homogeneous cylindrical shell is stiffened by N^r circumferential rings at $x = x_i$, $i = 1, \ldots, N^r$. Assume that the influence of the ring width is negligible. Denote the middle surface displacement of the ith ring by $u^r_{ik}(\theta, t)$, where the subscript refers to the ith stiffening ring, and the superscript r indicates that the parameters are related to the rings. The dynamic equations of the stiffening ring in general are

$$\sum_{k=1}^{3}\sum_{j=0}^{n_k}\left(\alpha_{imkj}\frac{\partial^2}{\partial t^2} + \beta_{imkj}\frac{\partial}{\partial t} + \gamma_{imkj}\right)\frac{\partial^j u^r_{ik}(\theta, t)}{\partial \theta^j} = q^r_{im} + q^e_{im} \quad (12)$$

where $m = 1, 2, 3$, $i = 1, \ldots, N^r$, the constants α_{imkj}, β_{imkj}, and γ_{imkj} are related to the geometry and material parameters of the rings, and q^e_{im} are the external loads applied to the ith ring. Here q^r_{im} are the tractions between the shell and the ith ring; see Fig. 4, where $q^r_{i1} = q^r_{ix}$, $q^r_{i2} = q^r_{i\theta}$ and $q^r_{i3} = q^r_{iz}$. Like

Downloaded 04 May 2010 to 171.66.16.28. Redistribution subject to ASME license or copyright; see http://www.asme.org/terms/Terms_Use.cfm

Eq. (1), (12) is quite general and represents many different curved beam models.

For thin-walled cylindrical shells, the Kirchhoff hypothesis holds and the displacements of the shell and rings satisfy the following matching conditions:

$$u^r_{i1}(\theta, t) = [u^1 - e_i u,^3_x]_{x=x_i} \tag{13a}$$

$$u^r_{i2}(\theta, t) = \left[u^2 - e_i \frac{1}{R} u,^3_\theta\right]_{x=x_i} \tag{13b}$$

$$u^r_{i3}(\theta, t) = u^3(x_i, \theta, t) \tag{13c}$$

where $u,^3_x = \partial u^3/\partial x$, $u,^3_\theta = \partial u^3/\partial\theta$, and e_i is the eccentricity of the centroid of the ith stiffening ring from the middle surface of the shell; see Fig. 4(a). The e_i is positive (negative or zero) if the ring is inward (outward or symmetric).

The analysis of the stiffened shell follows three steps: Fourier expansion, Laplace transform, and state-space formulation. The Fourier series of the displacements and loads are

$$u^r_{ik}(\theta, t) = \sum_{n=0}^{\infty} [u^{i,k}_{r,1,n}(t) \cos n\theta + u^{i,k}_{r,2,n}(t) \sin n\theta], \quad k = 1, 3 \tag{14a}$$

$$u^r_{i,2}(\theta, t) = \sum_{n=0}^{\infty} [u^{i,2}_{r,1,n}(t) \sin n\theta + u^{i,2}_{r,2,n}(t) \cos n\theta] \tag{14b}$$

$$q^r_{ik}(\theta, t) = \sum_{n=0}^{\infty} [q^{i,k}_{r,1,n}(t) \cos n\theta + q^{i,k}_{r,2,n}(t) \sin n\theta], \quad k = 1, 2, 3 \tag{14c}$$

$$q^e_{ik}(\theta, t) = \sum_{n=0}^{\infty} [q^{i,k}_{e,1,n}(t) \cos n\theta + q^{i,k}_{e,2,n}(t) \sin n\theta], \quad k = 1, 2, 3. \tag{14d}$$

Substituting (3a, b), (14a, b) into (12) and (13), one has

$$\begin{aligned} q^{i,m}_{r,1,n} \cos n\theta + q^{i,m}_{r,2,n} \sin n\theta &= -q^{i,m}_{r,1,n} \cos n\theta - q^{i,m}_{r,2,n} \sin n\theta \\ &+ \sum_{k=1}^{3} \sum_{j=0}^{n_k} \left(\alpha_{imkj} \frac{\partial^2}{\partial t^2} + \beta_{imkj} \frac{\partial}{\partial t} + \gamma_{imkj}\right) \frac{\partial^j u^k_n}{\partial \theta^j}\bigg|_{x=x_i} \\ &- \frac{ne_i}{R} \sum_{j=0}^{n_2} \left(\alpha_{im2j} \frac{\partial^2}{\partial t^2} + \beta_{im2j} \frac{\partial}{\partial t} + \gamma_{im2j}\right) \frac{\partial^j}{\partial \theta^j} \\ &\times (u^3_{2,n} \cos n\theta - u^3_{1,n} \sin n\theta)|_{x=x_i} - e_i \\ &\times \sum_{j=0}^{n_1} \left(\alpha_{im1j} \frac{\partial^2}{\partial t^2} + \beta_{im1j} \frac{\partial}{\partial t} + \gamma_{im1j}\right) \\ &\times \frac{\partial}{\partial x} \frac{\partial^j}{\partial \theta^j} (u^3_{1,n} \cos n\theta + u^3_{2,n} \sin n\theta)|_{x=x_i} \end{aligned} \tag{15}$$

for $m = 1, 2$ and 3, where n is the circumferential wave number of the shell. Laplace transform of (15) and application of the state-space form (4) lead to

$$\tilde{q}^{r,n}_i(s) = L^{i,n}(s)\eta_n(x_i, s) - \tilde{q}^{e,n}_i(s) \tag{16}$$

where $\tilde{q}^{r,n}_i(s)$ is the vector of the tractions between the shell and rings, $\tilde{q}^n_i(s)$ is the vector of the external loads, including the initial disturbances, and the matrix $L^{i,n}(s)$ consists of the parameters of the ith ring (see the Appendix).

Since the traction forces $\tilde{q}^{r,n}_i$ are pointwise along the x-direction, the total forces π_n applied to the shell can be expressed by

$$\pi_n(x, s) = \hat{f}_n(x, s) + \sum_{i=1}^{N^r} T^r_i L^{i,n}(s)\eta_n(x_i, s)\delta(x - x_i) \tag{17}$$

where $\delta(x - x_i)$ is the delta function, $\hat{f}_n(x, s)$ is the resultant of the external loads on the shell and rings, and the equivalent forces due to the initial disturbances of the rings, T^r_i are scaling matrices guaranteeing the same dimension of $\tilde{q}^{r,n}_i$ in (16) and $\tilde{f}_n$ in (4). By (4), we have

$$\eta_n(x, s) = e^{F_n(s)x}\left\{\int_0^x e^{-F_n(s)\xi}[\pi_n(\xi, s) + \tilde{g}_n(\xi, s)]d\xi + \eta_n(0, s)\right\}. \tag{18}$$

Substituting (17) into the above gives

$$\eta_n(x, s) = A^{(0)}_n(x, s) + \sum_{j=1}^{N^r} B_{n,j}(x, s)\eta_n(x_j, s) + C^{(0)}_n(x, s)\eta_n(0, s) \tag{19}$$

where

$$A^{(0)}_n(x, s) = e^{F_n(s)x} \int_0^x e^{-F_n(s)\xi}[\hat{f}_n(\xi, s) + \tilde{g}_n(\xi, s)]d\xi$$

$$B_{n,j}(x, s) = e^{F_n(s)(x-x_j)} T^r_i L^{j,n}(s) u(x - x_j), \quad j = 1, \ldots, N^r$$

$$C^{(0)}_n(x, s) = e^{F_n(s)x}$$

and $u(x - x_j)$ is the unit step function. Eliminating $\eta_n(x_j, s)$ from (19) by setting $x = x_i$, $i = 1, \ldots, N^r$, and solving the N^r resulting equations yield

$$\eta_n(x, s) = \bar{A}_n(x, s) + \bar{C}_n(x, s)\eta_n(0, s) \tag{20}$$

where the matrices $\bar{A}_n(x, s)$ and $\bar{C}_n(x, s)$ are obtained from the N^r-step recurrence procedure

$$A^{(i)}_n(x, s) = A^{(i-1)}_n(x, s) + B_{n,i}(x, s)[I - B_{n,i}(x_i, s)]^{-1} A^{(i-1)}_n(x_i, s) \tag{21a}$$

$$C^{(i)}_n(x, s) = C^{(i-1)}_n(x, s) + B_{n,i}(x, s)[I - B_{n,i}(x_i, s)]^{-1} C^{(i-1)}_n(x_i, s) \tag{21b}$$

for $i = 1, 2, \ldots, N^r$, with $\bar{A}_n(x, s) = A^{(N^r)}_n(x, s)$ and $\bar{C}_n(x, s) = C^{(N^r)}_n(x, s)$.

Finally, by plugging (20) into the boundary conditions (6), we obtain the response of the ring-stiffened cylindrical shell under various external loads, and initial and boundary conditions

$$\eta_n(x, s) = \bar{A}_n(x, s) + \bar{C}_n(x, s)[M_n(s) + N_n(s)\bar{C}_n(1, s)]^{-1} \times [\gamma_n(s) - N_n(s)\bar{A}_n(1, s)]. \tag{22}$$

For the eigenvalue problems of the stiffened shell, the characteristic equation by (22) is

$$\det [M_n(s; \bar{p}) + N_n(s; \bar{p})\bar{C}_n(1, s; \bar{p})] = 0 \tag{23}$$

and the discussion after Eq. (11) applies.

Constrained cylindrical shells can be viewed as the degenerate cases of stiffened shells. Assume that the shell is constrained by N^s pairs of uniformly distributed springs and dampers, located at $x = x_i$ ($i = 1, \ldots, N^s$) and along the circle $0 \le \theta \le 2\pi$. At $x = x_i$, the constraint forces by the springs and dampers are described by

$$\begin{Bmatrix} q^s_{i1} \\ q^s_{i2} \\ q^s_{i3} \end{Bmatrix} = -\left(K_i + D_i \frac{\partial}{\partial t}\right) \begin{Bmatrix} u^1 - \bar{u}^1 \\ u^2 - \bar{u}^2 \\ u^3 - \bar{u}^3 \end{Bmatrix}_{x=x_i}$$

where the matrices K_i and D_i contain the spring and damper coefficients, respectively, and the $\bar{u}^j$ count for the unstretched status of the springs. It can be shown that the matrix $L^{i,n}(s)$ in (16) is expressed in terms of the elements of $K_i + sD_i$. The response of the constrained shell can be determined based on (21) and (22).

Downloaded 04 May 2010 to 171.66.16.28. Redistribution subject to ASME license or copyright; see http://www.asme.org/terms/Terms_Use.cfm

In summary, the distributed transfer function analysis of the ring-stiffened shell follows three steps: (a) for given shell and ring parameters and boundary conditions, form the state-space matrices $F_n(s)$, $M_n(s)$, $N_n(s)$, and $L^{i,n}(s)$; (b) determine $\bar{A}_n(x, s)$ and $\bar{C}_n(x, s)$ by the recurrence procedure (21); and (c) evaluate the response of the shell by (22).

The result herein can be applied to stepped cylindrical shells stiffened by circumferential rings. A stepped shell is composed of a number of serially connected uniform shell segments. The analysis for such structures first obtains the distributed transfer functions and response of each stiffened shell segment based on (22), and then assembles all the shell segments by a synthesis given in our recent paper (Zhou and Yang, 1995).

4 Donnell-Mushtari Shell

As an application of the theory developed, free vibration of the Donnell-Mushtari shell is considered. Without loss of generality, assume that the shell is homogeneous, isotropic, and elastic. The dimensionless equations of motion are (Markus, 1988)

$$\frac{1}{\gamma_1^2}\frac{\partial^2 u}{\partial x^2} + \frac{1}{2}(1-\upsilon)\frac{\partial^2 u}{\partial \theta^2} + \frac{1+\upsilon}{2\gamma_1}\frac{\partial^2 v}{\partial x \partial \theta} - \frac{\upsilon}{\gamma_1}\frac{\partial w}{\partial x} = \bar{\rho}\frac{\partial^2 u}{\partial t^2} \quad (24a)$$

$$\frac{1+\upsilon}{2\gamma_1}\frac{\partial^2 u}{\partial x \partial \theta} + \frac{1-\upsilon}{2\gamma_1^2}\frac{\partial^2 v}{\partial x^2} + \frac{\partial^2 v}{\partial \theta^2} - \frac{\partial w}{\partial \theta} = \bar{\rho}\frac{\partial^2 v}{\partial t^2} \quad (24b)$$

$$\frac{\upsilon}{\gamma_1}\frac{\partial u}{\partial x} + \frac{\partial v}{\partial \theta} - w - k\left(\frac{1}{\gamma_1^4}\frac{\partial^4 w}{\partial x^4} + \frac{2}{\gamma_1^2}\frac{\partial^4 w}{\partial x^2 \partial \theta^2} + \frac{\partial^4 w}{\partial \theta^4}\right) + \frac{1}{J}\left(N_{x0}\frac{\partial^2 w}{\gamma_1^2 \partial x^2} + 2N_{x\theta 0}\frac{\partial^2 w}{\gamma_1 \partial x \partial \theta} + N_{\theta 0}\frac{\partial^2 w}{\partial \theta^2}\right) = \bar{\rho}\frac{\partial^2 w}{\partial t^2} \quad (24c)$$

with

$$(u, v, w) = \frac{1}{h}(u_0, v_0, w_0), \quad k = \frac{1}{12}\left(\frac{h}{R}\right)^2,$$

$$\bar{\rho} = \frac{\rho(1-\upsilon^2)R^2}{E}, \quad \gamma_1 = \frac{L}{R}, \quad J = \frac{Eh}{1-\upsilon^2}.$$

Here u_0, v_0, and w_0 are the displacements of the shell middle surface in the coordinate directions x, θ, and z, respectively; R, L, and h are the radius, length, and thickness of the shell, respectively; E and ν are Young's modulus and Poison's ratio; ρ is the density per unit volume; and N_{x0}, $N_{\theta 0}$ and $N_{x\theta 0}$ are the membrane stresses.

Four pairs of boundary conditions are as follows:

(i) $u(\bar{x}_i, \theta, t) = 0$ or

$$\frac{E}{1-\upsilon^2}\frac{h^2}{R}\left[\frac{1}{\gamma_1}u_{,x} + \upsilon(v_{,\theta} - w)\right]_{x=\bar{x}_i} = 0 \quad (25a)$$

(ii) $v(\bar{x}_i, \theta, t) = 0$ or

$$\frac{E}{2(1+\upsilon)}\frac{h^2}{R}\left[u_{,\theta} + \frac{1}{\gamma_1}v_{,x} + \frac{2k}{\gamma_1}w_{,x\theta}\right]_{x=\bar{x}_i} = 0 \quad (25b)$$

(iii) $w(\bar{x}_i, \theta, t) = 0$ or

$$-\frac{E}{12(1-\upsilon^2)}\frac{h^4}{R^3}\left[\frac{1}{\gamma_1^3}w_{,xxx} + \frac{2-\upsilon}{\gamma_1}w_{,x\theta\theta}\right]_{x=\bar{x}_i} = 0 \quad (25c)$$

(iv) $w_{,x}|_{x=\bar{x}_i} = 0$ or

$$-\frac{E}{12(1-\upsilon^2)}\frac{h^4}{R^2}\left[\frac{1}{\gamma_1^2}w_{,xx} + \upsilon w_{,\theta\theta}\right]_{x=\bar{x}_i} = 0 \quad (25d)$$

where $\bar{x}_i = 0$ and 1 for $i = 1$ and 2, and $u_{,x} = \partial u/\partial x$, etc.

The Fourier series of the shell displacements are written as

$$u = \sum_{n=0}^{\infty} u_n(x, t)\cos n\theta, \quad v = \sum_{n=0}^{\infty} v_n(x, t)\sin n\theta,$$

$$w = \sum_{n=0}^{\infty} w_n(x, t)\cos n\theta. \quad (26)$$

Following the procedure outlined in Section 2, η_n and F_n in (4) are found as

$$\eta_n(x, s) = \left\{\tilde{u}_n \frac{\partial \tilde{u}_n}{\partial x}\ \tilde{v}_n \frac{\partial \tilde{v}_n}{\partial x}\ \tilde{w}_n \frac{\partial \tilde{w}_n}{\partial x}\ \frac{\partial^2 \tilde{w}_n}{\partial x^2}\ \frac{\partial^3 \tilde{w}_n}{\partial x^3}\right\},$$

$$F_n(s) = \begin{bmatrix} F_{11} & F_{12} \\ F_{21} & F_{22} \end{bmatrix} \quad (27)$$

Downloaded 04 May 2010 to 171.66.16.28. Redistribution subject to ASME license or copyright; see http://www.asme.org/terms/Terms_Use.cfm

where

$$F_{11}(s) = \begin{bmatrix} 0 & 1 & 0 & 0 \\ \gamma_1^2\left(\frac{1-\nu}{2}n^2 + s^2\bar{\rho}\right) & 0 & 0 & -\frac{1+\upsilon}{2}n\gamma_1 \\ 0 & 0 & 0 & 1 \\ 0 & \gamma_1 n\frac{1+\upsilon}{1-\upsilon} & \frac{2n^2\gamma_1^2}{1-\upsilon} + \frac{2\bar{\rho}s^2\gamma_1^2}{1-\upsilon} & 0 \end{bmatrix}$$

$$F_{12}(s) = \begin{bmatrix} 0 & 0 & 0 & 0 \\ 0 & \upsilon\gamma_1 & 0 & 0 \\ 0 & 0 & 0 & 0 \\ -\frac{2n\gamma_1^2}{1-\upsilon} & 0 & 0 & 0 \end{bmatrix} \quad F_{21} = \begin{bmatrix} 0 & 0 & 0 & 0 \\ 0 & 0 & 0 & 0 \\ 0 & 0 & 0 & 0 \\ 0 & \gamma_1^3\frac{\upsilon}{k} & \frac{n\gamma_1^4}{k} & 0 \end{bmatrix}$$

$$F_{22} = \begin{bmatrix} 0 & 1 & 0 & 0 \\ 0 & 0 & 1 & 0 \\ 0 & 0 & 0 & 1 \\ -\gamma_1^4\left(\frac{1}{k} + n^4 + \frac{\bar{\rho}}{k}s^2\right) & -\frac{n^2\gamma_1^4 N_{\theta 0}}{kJ} & -\frac{2n\gamma_1^3 N_{x\theta 0}}{kJ} & 2n^2\gamma_1^2 + \frac{\gamma_1^2 N_{x0}}{kJ} & 0 \end{bmatrix}.$$

By (25), (26), and (27), η_n must satisfy the boundary conditions

$$B_i\Gamma_n\eta_n(\bar{x}_i, s) = 0, \quad i = 1, 2 \quad (28)$$

where

$$\Gamma_n = \begin{bmatrix} 1 & 0 & 0 & 0 & 0 & 0 & 0 & 0 \\ 0 & 1/\gamma_1 & n\upsilon & 0 & -\upsilon & 0 & 0 & 0 \\ 0 & 0 & 1 & 0 & 0 & 0 & 0 & 0 \\ -n & 0 & 0 & 1/\gamma_1 & 0 & -kn/(6\gamma_1) & 0 & 0 \\ 0 & 0 & 0 & 0 & 1 & 0 & 0 & 0 \\ 0 & 0 & 0 & 0 & 0 & -(2-\upsilon)n^2/\gamma_1 & 0 & 1/\gamma_1^3 \\ 0 & 0 & 0 & 0 & 0 & 1 & 0 & 0 \\ 0 & 0 & 0 & 0 & -\upsilon n^2 & 0 & 1/\gamma_1^2 & 0 \end{bmatrix} \quad (29)$$

and B_i is a 4×8 matrix containing 1 or 0. Write $B_i = [B_i(j, k)]$. Define the Kronecker delta by $\delta_m^k = 1$ for $k = m$ and 0 for $k \neq m$. If the kth boundary condition is of displacement type ($u = 0$, or $v = 0$, or $w = 0$, or $w_{,x} = 0$), the nonzero elements of the kth row of B_i are

$$B_i(j, 2j-1) = \delta_{2j-1}^k. \quad (30a)$$

If the kth boundary condition is of force type ($N_x = 0$, or $N_{x\theta} = 0$, $Q_x = 0$, or $M_x = 0$), then the nonzero element of the kth row of B_i is given by

$$B_i(j, k) = \delta_{2j}^k. \quad (30b)$$

The boundary matrices in (6) take the form

$$M_n(s) = \begin{bmatrix} B_1 L_n \\ 0_{4\times 8} \end{bmatrix} \quad N_n(s) = \begin{bmatrix} 0_{4\times 8} \\ B_2 L_n \end{bmatrix}. \quad (31)$$

The displacements u_i^r, v_i^r, and w_i^r of the ith stiffening ring are governed by

$$q_{ix}^r + q_{ix}^e = \rho_i A_i \frac{\partial^2 u_i^r}{\partial t^2} \quad (32a)$$

$$\frac{1}{R}\frac{\partial N_{i\theta}^r}{\partial \theta} + q_{i\theta}^r + q_{i\theta}^e = \rho_i A_i \frac{\partial^2 v_i^r}{\partial t^2} \quad (32b)$$

$$\frac{1}{R^2}\frac{\partial^2 M_{i\theta}^r}{\partial \theta^2} + \frac{N_{i\theta}^r}{R} + N_{\theta 0}\frac{\partial^2 w_i^r}{\partial \theta^2} + q_{iz}^r = \rho_i A_i \frac{\partial^2 w_i^r}{\partial t^2} \quad (32c)$$

where ρ_i and A_i are the density and the cross section area of the ith ring, respectively, and the superscript r indicates that the physical parameters are related to the ring. Here the middle surface of the shell has been chosen as the reference plane. The internal forces of the ring are related to the shell displacements by

$$N_{i\theta}^r = k_{11}^i\left(-\frac{w}{R} + \frac{1}{R}\frac{\partial v}{\partial \theta}\right) - k_{12}^i\frac{\partial^2 w}{R^2\partial\theta^2} \quad (33a)$$

$$M_{i\theta}^i = k_{12}^i\left(-\frac{w}{R} + \frac{1}{R}\frac{\partial v}{\partial \theta}\right) - k_{22}^i\frac{\partial^2 w}{R^2\partial\theta^2} \quad (33b)$$

where the coordinate z is measured from the middle surface of the shell,

$$k_{11}^i = E_i A_i, \quad k_{12}^i = E_i A_i e_i, \quad k_{22}^i = E_i I_{i\rho}, \quad (34)$$

and e_i is the eccentricity of the ring centroid shown (see Fig. 4(a)), and $I_{i\rho}$ is the second-order moment of the ring cross section with respect to the middle surface of the shell.

The key in estimating the response of the stiffened shell is to determine the matrix $L^{i,n}(s)$ in (16), whose nonzero elements $L_{j,l}^{i,n}$ are obtained as follows:

$$L_{2,1}^{i,n} = \bar{k}R^2\rho_i A_i\gamma_1^2 s^2, \quad L_{2,6}^{i,n} = -\bar{k}R^2\rho_i A_i\gamma_1^2 e_i s^2,$$

$$L_{4,3}^{i,n} = (n^2 k_{11}^i + \rho_i A_i R^2 s^2)\frac{2\bar{k}\gamma_1^2}{1-\upsilon}$$

Downloaded 04 May 2010 to 171.66.16.28. Redistribution subject to ASME license or copyright; see http://www.asme.org/terms/Terms_Use.cfm

$$L^{i,n}_{4,5} = -\left(nk^i_{11} - \frac{n^3k^i_{12}}{R} - n\rho_i A_i Rs^2 e_i\right)\frac{2\bar{k}\gamma_1^2}{1-\upsilon},$$

$$L^{i,n}_{8,3} = \left(nk^i_{11} - \frac{n^3k^i_{12}}{R}\right)\frac{\bar{k}\gamma_1^4}{k}$$

$$L^{i,n}_{8,5} = -\left(k^i_{11} - \frac{2}{R}k^i_{12}n^2 + \frac{n^4k^i_{22}}{R^2} + n^2N_{\theta 0} + R^2\rho_i A_i s^2\right)\frac{\bar{k}\gamma_1^4}{k}$$

with $\bar{k} = (1-\upsilon^2)/(Eh^2)$.

For the comparison purpose, the stiffened cylindrical shell is also approximated as an orthotropic shell by smearing the tension and bending stiffness of the rings on the shell. The internal force-strain relations in this case are given by

$$\begin{Bmatrix} N_x \\ N_\theta \\ N_{x\theta} \end{Bmatrix} = \frac{Eh}{1-\upsilon^2}\begin{bmatrix} 1 & \upsilon & 0 \\ \upsilon & 1+\Delta D_t & 0 \\ 0 & 0 & \dfrac{1-\upsilon}{2} \end{bmatrix}\begin{Bmatrix} \epsilon_{x0} \\ \epsilon_{\theta 0} \\ \epsilon_{x\theta 0} \end{Bmatrix} + \Delta B_{tb}\begin{Bmatrix} 0 \\ \kappa_\theta \\ 0 \end{Bmatrix} \quad (35a)$$

$$\begin{Bmatrix} M_x \\ M_\theta \\ M_{x\theta} \end{Bmatrix} = \frac{Eh^3}{12(1-\upsilon^2)}\begin{bmatrix} 1 & \upsilon & 0 \\ \upsilon & 1+\Delta D_b & 0 \\ 0 & 0 & 1-\upsilon \end{bmatrix}\begin{Bmatrix} \kappa_x \\ \kappa_\theta \\ \kappa_{x\theta} \end{Bmatrix} + \Delta B_{tb}\begin{Bmatrix} 0 \\ \epsilon_\theta \\ 0 \end{Bmatrix} \quad (35b)$$

where

$$\Delta D_t = \frac{1}{EhL}(1-\upsilon^2)\sum_{i=1}^{N^r} k^i_{11},$$

$$\Delta D_b = \frac{12}{Eh^3L}(1-\upsilon^2)\sum_{i=1}^{N^r} k^i_{22}, \quad \Delta B_{tb} = \frac{1}{L}\sum_{i=1}^{N^r} k^i_{12}.$$

For the shell simply supported ($N_x = \upsilon = w = M_x = 0$) at its both ends, the frequency equation is

$$\det(A + \omega^2 I) = 0 \quad (36)$$

where

$$A = \frac{E}{\bar{\rho}(1-\upsilon^2)R^2}\begin{bmatrix} -\left(\dfrac{m^2\pi^2}{\gamma_1^2} + \dfrac{1-\upsilon}{2}n^2\right) & \dfrac{1+\upsilon}{2\gamma_1}nm\pi & -\dfrac{\upsilon}{\gamma_1}m\pi \\ \dfrac{1+\upsilon}{2\gamma_1}nm\pi & -\left(\dfrac{1-\upsilon}{2\gamma_1^2}m^2\pi^2 + (1+\Delta D_t)n^2\right) & n(1+\Delta D_t) - \Delta\bar{B}_{tb}n^3 \\ -\dfrac{\upsilon}{\gamma_1}m\pi & n(1+\Delta D_t) - \Delta\bar{B}_{tb}n^3 & \bar{A}^{33}_{mn} \end{bmatrix}$$

with

$$\Delta\bar{B}_{tb} = \frac{\Delta B_{tb}(1-\upsilon^2)}{EhRL}, \quad \bar{\rho} = \rho + \frac{1}{Lh}\sum_{i=1}^{N^r}\rho_i b_i h_i$$

Table 1 The fundamental frequency of the cylindrical shell with inward stiffeners

N^r	Proposed Method	Orthotropic Approximation
1	0.2699(6)	0.2622(6)
2	0.2777(6)	0.2711(6)
3	0.2849(6)	0.2791(6)
4	0.2914(6)	0.2863(6)
5	0.2974(6)	0.2927(6)
6	0.3028(6)	0.2985(6)
7	0.3048(5)	0.3038(6)
8	0.3053(5)	0.3051(5)
9	0.3058(5)	0.3056(5)
10	0.3061(5)	0.3060(5)

$$\bar{A}^{33}_{mn} = -\left[1 + \Delta D_t - 2n^2\Delta\bar{B}_{tb} + k\left(\frac{m^4\pi^4}{\gamma_1^4} + \frac{2n^2m^2\pi^2}{\gamma_1^2} + n^4(1+\Delta D_b)\right)\right].$$

5 Numerical Results

Consider a Donnell-Mushtari shell stiffened by N^r identical rings that are equally spaced along the longitudinal direction x. The parameters of the shell and stiffening rings are chosen as

Shell: $R = L = 100$, $h = 1$, $E = 10^4$, $\upsilon = 0.3$

Rings: $E_i = 10^4$, $\upsilon_i = 0.3$, $b_i = 1$, $h_i = 2$

where b_i and h_i are the width and height of the rings, as shown in Fig. 4(*a*). The shell is simply supported at the both ends; i.e., $N_x = \upsilon = w = M_x = 0$ at $x = 1$ and 100.

The natural frequencies of the ring-stiffened shell are determined by four methods: (i) the proposed transfer function method (23); (ii) the orthotropic approximation (36); (iii) the stepped shell modeling given by Zhou and Yang (1995); and (iv) the finite element method. It should be noted that the last two methods are only valid for shells with symmetric stiffeners, i.e., the stiffener eccentricity e_i in Fig. 4(*a*) is zero. In this case, with each ring and the connecting shell segment taken as a short cylindrical shell, the whole stiffened shell becomes a stepped shell, which, accordingly, can be analyzed by the stepped shell synthesis and the finite element method. However, if inward or outward stiffeners are used (see Fig. 1), the shell can not be modeled as a stepped shell because the middle surfaces of those short shells do not coincide; the stepped shell assumption in Methods (iii) and (iv) may lead to inaccurate results.

Downloaded 04 May 2010 to 171.66.16.28. Redistribution subject to ASME license or copyright; see http://www.asme.org/terms/Terms_Use.cfm

Table 2 The fundamental frequency of the cylindrical shell with outward stiffeners

N^r	Proposed Method	Orthotropic Approximation
1	0.2670(6)	0.2617(6)
2	0.2742(6)	0.2702(6)
3	0.2814(6)	0.2777(6)
4	0.2881(6)	0.2844(6)
5	0.2940(6)	0.2905(6)
6	0.2993(6)	0.2960(6)
7	0.3040(6)	0.3009(6)
8	0.3083(6)	0.3054(6)
9	0.3102(5)	0.3094(6)
10	0.3108(5)	0.3106(5)

Shown in Tables 1 and 2 is the fundamental (lowest) natural frequency of the cylindrical shell with inward and outward stiffening rings, respectively, with the number N^r of the stiffeners varying from 1 to 10. The results obtained by the proposed method and the orthotropic approximation are in good agreement in all the cases. This is expected because the frequency is a global parameter and the orthotropic stiffness treatment is accurate enough for the frequency calculation if the stiffeners are densely spaced. However, it is impossible for the orthotropic approximation to predict the kinks and jumps in the distributions of the stresses or internal forces of the stiffened shell, as shall be seen in Figs. 5–8.

For the shell with symmetric stiffeners, its fundamental (lowest) natural frequency is calculated by the aforementioned four methods; see Table 3. It is seen that the frequency predicted by the first two methods is lower than that by the last two, especially for a larger N^r. This is mainly due to the fact that the stiffener width b_i, and therefore the tension and bending stiffness of the rings in the longitudinal direction are ignored in the proposed method and the orthotropic approximation. In all three tables, the digit in the brackets is the circumferential wave number n corresponding to the lowest natural frequency.

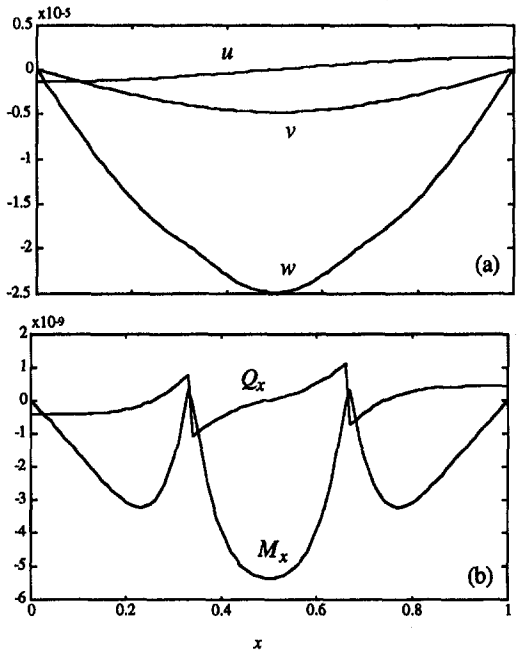


Fig. 6 Eigenfunctions of the shell with two symmetric stiffeners (N^r = 2, fundamental frequency = 0.2602): (*a*) mode shapes; (*b*) moment and shear force

The mode shapes (u, v, w), and the distributions of the bending moment (M_x) and shear force (Q_x) of the stiffened shell are plotted in Figs. 5 to 8 by the proposed transfer function method, corresponding to the fundamental frequency in Table 3 for N^r = 1, 2, 3, 4. The rings have most significant effect on the transverse displacement w and almost no effect on the longitudinal displacement u. The kinks in the M_x-plots and jumps in the Q_x are clearly seen, which can not be obtained by the orthotropic approximation. As N^r increases, more kinks and

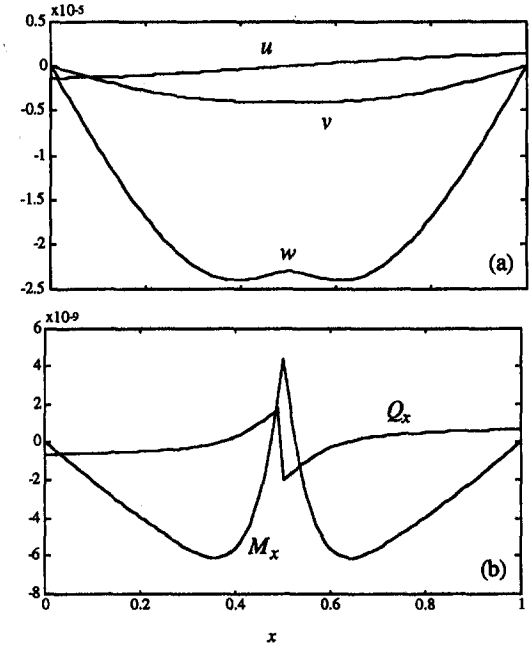


Fig. 5 Eigenfunctions of the shell with one symmetric stiffener (N^r = 1, fundamental frequency = 0.2567): (*a*) mode shapes; (*b*) moment and shear force

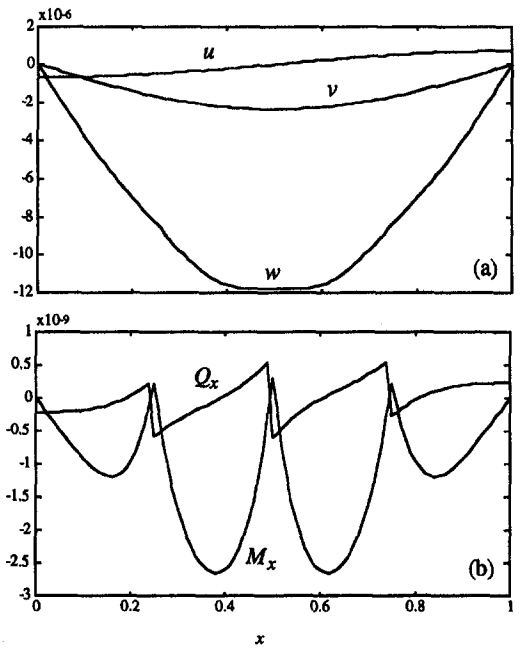


Fig. 7 Eigenfunctions of the shell with three symmetric stiffeners (N^r = 3, fundamental frequency = 0.2627): (*a*) mode shapes; (*b*) moment and shear force

Downloaded 04 May 2010 to 171.66.16.28. Redistribution subject to ASME license or copyright; see http://www.asme.org/terms/Terms_Use.cfm

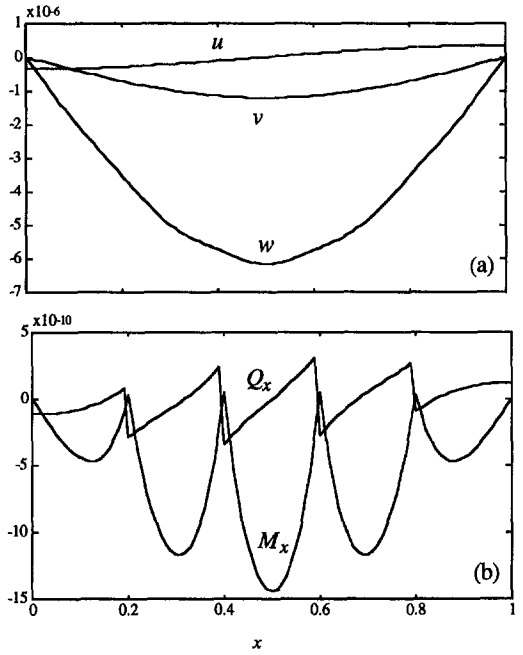


Fig. 8 Eigenfunctions of the shell with four symmetric stiffeners (N^r = 4, fundamental frequency = 0.2650): (*a*) mode shapes; (*b*) moment and shear force

jumps occur in the moment and shear force curves near the locations of the stiffeners.

6 Conclusions

We have analyzed cylindrical shells stiffened by circumferential rings. The shell and stiffening rings are modeled as individual structural components. By Fourier expansion, Laplace transform, and a spatial state-space formalism, the distributed transfer functions of the shell and rings are determined in exact and closed form. By imposing force balance and displacement compatibility among the structural components, the contact forces between the shell and stiffening rings are expressed in terms of the shell displacements by the transfer functions. In this way a general formulation for exact solution of various static and dynamic problems for constrained/combined, stiffened cylindrical shells is obtained.

The proposed transfer function method provides a systematic way to study ring-stiffened cylindrical shells; the solution procedure is the same for different shell models, stiffening conditions, initial and boundary conditions, and external loads. Consequently, the method is very convenient in computer coding and numerical simulation.

The numerical simulation on the free vibration of the stiffened Donnell-Mushtari shell reveals the following:

(i) If the number of the stiffeners is small, the stiffener positions have great influence on the shell response. If the number of stiffeners is large enough, smearing the stiffener stiffness on the shell is a good approximation for natural frequency calculation, but it is not accurate in estimating the stress/internal force distributions.

(ii) The stiffener eccentricity has significance influence on the natural frequencies and the dynamic behavior of the stiffened shell.

It should be noted that the current investigation takes into consideration the ring eccentricity and ring position with respect to the shell middle surface, which are difficult to depict in many modeling techniques. The transfer function method developed in this paper can easily handle inward, outward and symmetric ring stiffeners.

Table 3 The fundamental frequency of the cylindrical shell with symmetric stiffeners

N^r	Proposed Method	Orthotropic Approximation	Stepped Shell Synthesis	Finite Element Method
1	0.2567(7)	0.2497(7)	0.2571(7)	0.2542(7)
2	0.2602(6)	0.2570(7)	0.2631(6)	0.2606(6)
3	0.2627(7)	0.2603(6)	0.2676(6)	0.2650(6)
4	0.2650(6)	0.2627(6)	0.2720(6)	0.2692(6)
5	0.2672(6)	0.2650(6)	0.2762(6)	0.2733(6)
6	0.2693(6)	0.2672(6)	0.2804(6)	0.2772(6)
7	0.2714(6)	0.2693(6)	0.2843(6)	0.2810(6)
8	0.2733(6)	0.2714(6)	0.2881(6)	0.2847(6)
9	0.2752(6)	0.2733(6)	0.2918(6)	0.2882(6)
10	0.2770(6)	0.2752(6)	0.2953(6)	0.2915(6)

Acknowledgments

This work was partially supported by the U.S. Army Research Office under Grant No. DAAL03-93-G-0066 with Dr. Gary Anderson as the technical monitor.

References

Al-Najafi, A. M., and Warburton, G. B., 1970, "Free Vibration of Ring-Stiffened Cylindrical Shells," *Journal of Sound and Vibration,* Vol. 13, No. 1, pp. 9–25.

Deskos, D. E., and Oates, J. B., 1981, "Dynamic Analysis of Ring-Stiffened Circular Cylindrical Shells," *Journal of Sound and Vibration,* Vol. 75, No. 1, pp. 1–15.

Egle, D. M., and Sewall, J. L., 1968, "An Analysis of Free Vibration of Orthogonally Stiffened Cylindrical Shells with Stiffeners Treated as Discrete Elements," *AIAA Journal,* Vol. 6, No. 3, pp. 518–526.

Frosberg, K., 1969, "Exact Solution For Natural Frequencies of Ring-Stiffened Cylinders," *AIAA/ASME 10th Structures, Structural Dynamics and Materials Conference,* Volume on Structures and Materials, pp. 18–30.

Garnet, H., and Goldberg, M. A., 1962, "Free Vibrations of Ring-Stiffened Shells," RE-156, Grumman Aircraft Research.

Godzevich, V. G., and Ivanova, O. V., 1965, "Free Oscillations of Circular Conical and Cylindrical Shell Reinforced by Rigid Circular Ribs," TTF-291, NASA.

Huntington, D. E., and Lyrintzis, C. S., 1992, "Dynamics of Skin-Stringer Panels Using Modified Wave Methods," *AIAA Journal,* Vol. 30, No. 11, pp. 2765–2773.

Markus, S., 1989, *The Mechanics of Vibrations of Cylindrical Shells,* Elsevier, Amsterdam.

Mead, D. J., and Bardell, N. S., 1987, "Free Vibration of a Thin Cylindrical Shell with Periodic Circumferential Stiffeners," *Journal of Sound and Vibration,* Vol. 115, No. 3, pp. 499–520.

Reddy, B. D., 1980, "Buckling of Elastic-Plastic Discretely Stiffened Cylinders in Axial Compression," *International Journal of Solid and Structures,* Vol. 16, pp. 313–328.

Rigo, P., 1992, "Stiffened Sheathings of Orthotropic Cylindrical Shells," *Journal of Structural Engineering,* Vol. 118, No. 4, pp. 926–943.

Schnell, W., and Heinrichsbauer, F. J., 1964, "The Determination of Free Vibrations of Longitudinally Stiffened Thin-Walled Circular Shells," TTF-8856, NASA.

Soedel, W., 1981, *Vibrations of Shells and Plates,* Marcel Dekker, New York.

Sridharan, S., Zeggane, M., and Starnes, Jr., J. H., 1992, "Postbuckling Response of Stiffened Composite Cylindrical Shells," *AIAA Journal,* Vol. 30, No. 12, pp. 2897–2905.

Wang, J. T. S., 1970, "Orthogonally Stiffened Cylindrical Shells Subjected to Internal Pressure," *AIAA Journal,* Vol. 8, No. 3, pp. 455–461.

Wang, J. T. S., and Lin, Y. J., 1973, "Stability of Discretely Stringer-Stiffened Cylindrical Shells," *AIAA Journal,* Vol. 11, No. 6, pp. 810–813.

Wang, J. T. S., and Rinehart, S. A., 1974, "Free Vibrations of Longitudinally Stiffened Cylindrical Shells," ASME JOURNAL OF APPLIED MECHANICS, Vol. 41, No. 4, pp. 1087–1093.

Wang, J. T. S., and Hsu, T. M., 1985, "Discrete Analysis of Stiffened Composite Cylindrical Shells," *AIAA Journal,* Vol. 23, No. 11, pp. 1753–1761.

Wilken, I. D., and Soedel, W., 1976, "The Receptance Method Applied to Ring-Stiffened Cylindrical Shells: Analysis of Model Characteristics," *Journal of Sound and Vibration,* Vol. 44, No. 4, pp. 563–576.

Downloaded 04 May 2010 to 171.66.16.28. Redistribution subject to ASME license or copyright; see http://www.asme.org/terms/Terms_Use.cfm

Yang, B., 1992, "Transfer Functions of Constrained/Combined One-Dimensional Continuous Dynamic Systems," *Journal of Sound and Vibration,* Vol. 156, No. 3, pp. 425–443.

Yang, B., and Tan, C. A., 1992, "Transfer Functions of One Dimensional Distributed Parameter Systems," ASME JOURNAL OF APPLIED MECHANICS, Vol. 59, No. 4, pp. 1009–1014.

Yang, B., 1994, "Distributed Transfer Function Analysis of Complex Distributed Parameter Systems," ASME JOURNAL OF APPLIED MECHANICS, Vol. 61, No. 1, pp. 84–92.

Zhou, J., and Yang, B., 1995, "A Distributed Transfer Function Method for Analysis of Cylindrical Shells," *AIAA Journal,* Vol. 33, No. 9, pp. 1698–1708.

APPENDIX

Define

$$d_{mkij}(s) = \alpha_{mkij}s^2 + \beta_{mkij}s + \gamma_{mkij}$$

$$l_{1m} = \sum_{j=1}^{m} n_j, \quad l_{2m} = n_1 + n_2 + n_3 + \sum_{j=1}^{m} n_j.$$

Let δ_j^i be Kronecker delta. Let $[y]$ be the integer part of the number y. Denote the elements of $L^{i,n}(s)$ by $L_{j,k}^{i,n}$, $j, k = 1, \ldots, 2n_b$. The nonzero elements of $L^{i,n}(s)$ are as follows:

$$L_{l_{1m},l}^{i,n} = \delta_l^{l_{1k}} \sum_{j=0}^{[n_k/2]} d_{imk(2j)}s(-1)^j n^{2j} - \delta_l^{2n_1+2n_2+2n_3} \frac{ne_i}{R} \{ \sum_{j=0}^{[n_2/2]} d_{im2(2j)}(s)(-1)^j n^{2j} \}$$

$$L_{l_{1m},l}^{i,n} = \delta_l^{l_{2k}} \sum_{j=1}^{[(n_k+1)/2]} d_{imk(2j-1)}(s)(-1)^{j+1} n^{2j-1} - \delta_l^{n_1+n_2+n_3} \frac{ne_i}{R} \{ \sum_{j=1}^{[(n_2+1)/2]} d_{im2(2j-1)}(s)(-1)^j n^{2j-1} \}$$

$$L_{l_{2m},l}^{i,n} = \delta_l^{l_{1k}} \sum_{j=1}^{[(n_k+1)/2]} d_{imk(2j-1)}(s)(-1)^j n^{2j-1} - \delta_l^{2n_1+2n_2+2n_3} \frac{ne_i}{R} \{ \sum_{j=1}^{[(n_k+1)/2]} d_{im2(2j-1)}(s)(-1)^j n^{2j-1} \}$$

$$L_{l_{2m},l}^{i,n} = \delta_l^{l_{2k}} \sum_{j=0}^{[n_k/2]} d_{imk(2j)}(s)(-1)^j n^{2j} - \delta_l^{n_1+n_2+n_3} \frac{ne_i}{R} \{ \sum_{j=0}^{[n_2/2]} d_{im2(2j)}(-1)^{j+1} n^{2j} \}$$

$$L_{l_{2m},n_1+n_2+n_3}^{i,n} = -e_i \sum_{j=1}^{[(n_1+1)/2]} d_{im1(2j-1)}(s)(-1)^j n^{2j-1}$$

$$L_{l_{2m},2n_1+2n_2+2n_3}^{i,n} = -e_i \sum_{j=0}^{[n_1/2]} d_{im1(2j)}(s)(-1)^j n^{2j}$$

$$L_{l_{2m},n_1+n_2+n_3}^{i,n} = -e_i \sum_{j=1}^{[(n_1+1)/2]} d_{im1(2j-1)}(s)(-1)^j n^{2j-1}$$

$$L_{l_{2m},2n_1+2n_2+2n_3}^{i,n} = -e_i \sum_{j=0}^{[n_1/2]} d_{im1(2j)}(s)(-1)^j n^{2j}.$$

Downloaded 04 May 2010 to 171.66.16.28. Redistribution subject to ASME license or copyright; see http://www.asme.org/terms/Terms_Use.cfm

Combination Resonances of a Circular Plate With Three-Mode Interaction

Won Kyoung Lee
Associate Professor,
Mem. ASME,
Department of Mechanical Engineering,

Cheol Hong Kim
Researcher,
Institute of Industrial Technology,

Yeungnam University,
Gyongsan 712-749, Korea

A nonlinear analysis is presented for combination resonances in the symmetric responses of a clamped circular plate with the internal resonance, $\omega_3 \approx \omega_1 + 2\omega_2$. The combination resonances occur when the frequency of the excitation are near a combination of the natural frequencies, that is, when $\Omega \approx 2\omega_1 + \omega_2$. By means of the internal resonance condition, the frequency of the excitation is also near another combination of the natural frequencies, that is, $\Omega \approx \omega_1 - \omega_2 + \omega_3$. The effect of two near combination resonance frequencies on the response of the plate is examined. The method of multiple scales is used to solve the nonlinear nonautonomous system of equations governing the generalized coordinates in Galerkin's procedure. For steady-state responses, we determine the equilibrium points of the autonomous system transformed from the nonautonomous system and examine their stability. It has been found that in some cases resonance responses with nonzero-amplitude modes don't exist, and the amplitudes of the responses decrease with the excitation amplitude. We integrate numerically the nonautonomous system to find the long-term behaviors of the plate and to check the validity of the analytical solution. It is found that there exist multiple stable responses resulting in jumps. In this case the long-term response of the plate depends on the initial condition. In order to visualize total responses depending on the initial conditions, we draw the deflection curves of the plate.

1 Introduction

A clamped circular plate experiences midplane stretching when deflected. The influence of this stretching on the dynamic response increases with the amplitude of the response. This situation can be described with nonlinear strain-displacement equations and a linear stress-strain law which give us the nonlinear partial differential equation. Since the linear analysis for this problem gives us reasonable results for only small motions, we need the nonlinear analysis for large motions. Even though a circular plate is a continuous system, it can be approximated as a multi-degree-of-freedom system. When a nonlinear multi-degree-of-freedom system has two or more of its natural frequencies commensurable or nearly so, the system may possess internal resonances (which can lead to strong a modal interactions).

Many authors have examined responses of multi-degree-of-freedom systems with internal resonances to study nonlinear dynamic behaviors of structural elements (beam and plate) with fixed boundaries. Nayfeh et al. (1974) considered two-mode interactions to study the steady-state responses of a hinged-clamped beam under harmonic excitation. They found that the system can have multiple stable steady-state responses when certain resonance conditions are satisfied. In this case, Lee and Ghang (1994) obtained domains of attraction of the beam to recognize the set of initial states attracting eventually to each stable response. Lee and Soh (1994) included three-mode interaction for the hinged-clamped beam problem to compare two-mode and three-mode interactions. They found no significant difference between both modal interactions. It means that the more modes included in the analysis don't guarantee any different result for the problem. Nayfeh and his colleagues (Sridhar et al., 1975, 1978; Nayfeh and Mook, 1979; Hadian and Nayfeh, 1990) studied the primary resonance of a clamped circular plate with internal resonance and recently found the occurrence of Hopf bifurcations. Nayfeh and Mook (1979) studied a combination resonance of the hinged-clamped beam, and found the nonexistence of resonance responses and the decrease of resonance amplitudes with the excitation amplitude. It seems that they didn't pay much attention to these peculiar phenomena because they were interested in the resonance responses only.

In this paper, combination resonances in the symmetric responses of the clamped circular plate with a three-mode interaction is studied. We are interested in the resonance responses of the generalized coordinates as well as the actual responses of the plate. We numerically integrate the nonlinear nonautonomous ordinary differential equations governing the time-dependent coefficients in Galerkin's procedure to find the long-term behavior of the plate and to check the validity of the analytical solution. In order to visualize total responses depending on the initial conditions, we draw the deflection curves of the plate.

2 Equations of Motion and Steady-State Responses

For convenience, we refer to the existing works (Nayfeh et al., 1975; Nayfeh and Mook, 1979; Hadian and Nayfeh, 1990) for the equations of motion for the generalized coordinates as follows:

$$\frac{d^2\psi_n}{dt^2} + \omega_n^2\psi_n = \epsilon\left[-2c_n\frac{d\psi_n}{dt} + \sum_{m,}^{\infty}\sum_{p,}^{\infty}\sum_{q=1}^{\infty}\Gamma_{nmpq}\psi_m\psi_p\psi_q\right] + f_n(t) \quad (1)$$

where $\epsilon = [12(1-\nu^2)]h^2/R^2$ = dimensionless small parameter; ν = Poisson ratio; h = thickness of the plate; R = radius of the plate; c_n = damping ratio; Γ_{nmpq} = nonlinear coefficients; and $f_n(t) = 2K_n \cos \Omega t$ is the excitation (see the Appendix, Part

Contributed by the Applied Mechanics Division of THE AMERICAN SOCIETY OF MECHANICAL ENGINEERS for publication in the ASME JOURNAL OF APPLIED MECHANICS.

Discussion on this paper should be addressed to the Technical Editor, Professor Lewis T. Wheeler, Department of Mechanical Engineering, University of Houston, Houston, TX 77204-4792, and will be accepted until four months after final publication of the paper itself in the ASME JOURNAL OF APPLIED MECHANICS.

Manuscript received by the ASME Applied Mechanics Division, May 12, 1994; final revision, June 30, 1994. Associate Technical Editor: F. Y. M. Wan.

Copyright © 1995 by ASME

Downloaded 04 May 2010 to 171.66.16.28. Redistribution subject to ASME license or copyright; see http://www.asme.org/terms/Terms_Use.cfm

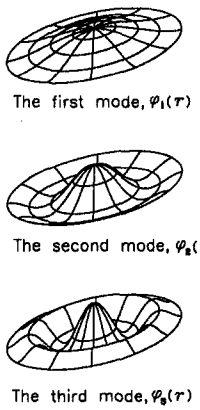


Fig. 1 Eigenfunctions of the symmetric vibration of a clamped circular plate

3). By the Galerkin's procedure, functions ψ_n represent the generalized coordinates of the deflection

$$w(r, t; \epsilon) = \sum_{m=1}^{\infty} \psi_m(t; \epsilon)\varphi_m(r). \tag{2}$$

The functions φ_m are the eigenfunctions to be obtained from the following eigenvalue problem:

$$\nabla^4\varphi_m - \omega_m^2\varphi_m = 0$$

$$\varphi_m(1) = 0, \quad \varphi_m'(1) = 0, \quad \varphi_m(0) < \infty \tag{3}$$

where the natural frequencies ω_m (Leissa, 1969) are as follows:

$$\omega_1 = 10.2, \quad \omega_2 = 39.8,$$

$$\omega_3 = 89.1, \quad \omega_4 = 158.2, \quad \omega_5 = 247.0. \tag{4}$$

The first three eigenfunctions are shown in Fig. 1 (see the Appendix, Part 2). Recognizing the internal resonance condition, including three modes, $\omega_1 + 2\omega_2 \approx \omega_3$, we can rewrite this condition by using the detuning parameter as follows:

$$\omega_1 + 2\omega_2 = \omega_3 + \epsilon\sigma_1 \tag{5}$$

where the parameter $\epsilon\sigma_1 = 0.6538$. For the combination resonance condition we use another detuning parameter $\epsilon\sigma_2$ as follows:

$$\Omega = 2\omega_1 + \omega_2 + \epsilon\sigma_2. \tag{6a}$$

Using Eqs. (5) and (6a), we have another expression

$$\Omega = \omega_1 - \omega_2 + \omega_3 + \epsilon(\sigma_1 + \sigma_2). \tag{6b}$$

We consider the contributions associated with both combinations of natural frequencies. For later use let $\hat{\sigma}_1 = \epsilon\sigma_1$ and $\hat{\sigma}_2 = \epsilon\sigma_2$.

The method of multiple scales can be used to construct a uniformly valid, asymptotic expansion (Nayfeh, 1973; Kevorkian, 1987). According to this method, we assume that each ψ_n is a function of different time scales which are defined by

$$T_n = \epsilon^n t \tag{7a}$$

and can be expanded in the form

$$\psi_n(t; \epsilon) = \sum_{j=0}^{\infty} \epsilon^j\psi_{nj}(T_0, T_1, \ldots), \quad n = 1, 2, \ldots. \tag{7b}$$

Derivatives with respect to time transform according to

$$d/dt = D_0 + \epsilon D_1 + \ldots, \tag{8a}$$

$$d^2/dt^2 = D_0^2 + \epsilon 2D_0D_1 + \ldots, \tag{8b}$$

where $D_j = \partial/\partial T_j$.

Substituting Eqs. (7) and (8) into Eq. (1) and equating the coefficients of equal powers of ϵ, we obtain

$$\epsilon^0; \ D_0^2\psi_{n0} + \omega_n^2\psi_{n0} = 2K_n \cos \Omega T_0, \quad n = 1, 2, \ldots \tag{9}$$

$$\epsilon^1; \ D_0^2\psi_{n1} + \omega_n^2\psi_{n1} = -2D_0D_1\psi_{n0} - 2c_nD_0\psi_{n0} + \sum_{m,p,q=1}^{\infty} \Gamma_{nmpq}\psi_{m0}\psi_{p0}\psi_{q0}, \quad n = 1, 2, \ldots \tag{10}$$

$$\epsilon^2; \ \vdots$$

where K_n is assumed to be $O(1)$. It is convenient to write the solution to (9) as follows:

$$\psi_{n0} = A_n(T_1, T_2, \ldots) \exp(i\omega_nT_0) + \Lambda_n \exp(i\Omega T_0) + cc \qquad n = 1, 2, \ldots \tag{11}$$

where $\Lambda_n = K_n/(\omega_n^2 - \Omega^2)$ and cc represents the complex conjugate of the terms to the left. The A_n are unknown at this point, but they are determined from the elimination of secular terms at the next level of approximation. Substituting (11) into (10) leads to

$$D_0^2\psi_{n1} + \omega_n^2\psi_{n1} = -2i\omega_n(D_1A_n + c_nA_n) \exp(i\omega_nT_0) - 2ic_n\Lambda_n\Omega \exp(i\Omega T_0) + \sum_{m,p,q=1}^{\infty} \Gamma_{nmpq}[\sum_{j=1}^{27} S_j \exp(i\lambda_jT_0)] + cc \qquad n = 1, 2, \ldots \tag{12}$$

where S_j and λ_j are given in the Appendix, Part 1.

In order to eliminate the secular terms from the ψ_{n1}, the A_n must be chosen so that the coefficient of $\exp(i\omega_nT_0)$ is zero. This coefficient will contain the nonlinear terms when the following conditions are satisfied:

$$\omega_n \approx \omega_m \pm \omega_p \pm \omega_q. \tag{13}$$

We can see that the condition (5) is one of the cases (13) with $n = 3$, $m = 1$, $p = q = 2$ and all signs of plus.

Substituting the resonance conditions (5) and (6) into Eqs. (12), and eliminating the secular terms, we have the following solvability conditions:

$n = 1$:

$$-2i\omega_1(A_1' + c_1A_1) + A_1\sum_{j=1}^{\infty} \alpha_{1j}A_j\overline{A_j} + Q_1\overline{A_2^2}A_3 \exp(-i\sigma_1T_1) + 2H_{11}A_1 + 2F\overline{A_1A_2} \exp(i\sigma_2T_1) + GA_2\overline{A_3} \exp(i(\sigma_1 + \sigma_2)T_1) = 0 \tag{14a}$$

$n = 2$:

$$-2i\omega_2(A_2' + c_2A_2) + A_2\sum_{j=1}^{\infty} \alpha_{2j}A_j\overline{A_j} + Q_2\overline{A_1A_2}A_3 \exp(-i\sigma_1T_1) + 2H_{22}A_2 + F\overline{A_1^2} \exp(i\sigma_2T_1) + GA_1A_3 \exp(-i(\sigma_1 + \sigma_2)T_1) = 0 \tag{14b}$$

$n = 3$:

$$-2i\omega_3(A_3' + c_3A_3) + A_3\sum_{j=1}^{\infty} \alpha_{3j}A_j\overline{A_j} + Q_3A_1A_2^2 \exp(i\sigma_1T_1) + 2H_{33}A_3 + G\overline{A_1}A_2 \exp(i(\sigma_1 + \sigma_2)T_1) = 0 \tag{14c}$$

$n \geq 4$:

$$-2i\omega_n(A_n' + c_nA_n) + A_n\sum_{j=1}^{\infty} \alpha_{nj}A_j\overline{A_j} + 2H_{nn}A_n = 0 \tag{14d}$$

Downloaded 04 May 2010 to 171.66.16.28. Redistribution subject to ASME license or copyright; see http://www.asme.org/terms/Terms_Use.cfm

where

$$\alpha_{nj} = \begin{cases} 4\Gamma_{njnj} + 2\Gamma_{nnjj} & (n \neq j) \\ 3\Gamma_{nnnn} & (n = j) \end{cases}$$

$$Q_1 = (2\Gamma_{1223} + \Gamma_{1322}) = Q_3$$

$$Q_2 = 2Q_1$$

$$H_{nk} = \sum_{m,j=1}^{\infty} (2\Gamma_{nmkj} + \Gamma_{nkmj})\Lambda_m\Lambda_j$$

$$F = \sum_{j=1}^{\infty} (2\Gamma_{121j} + \Gamma_{112j})\Lambda_j$$

$$G = 2\sum_{j=1}^{\infty} (\Gamma_{123j} + \Gamma_{132j} + \Gamma_{1j23})\Lambda_j$$

and the prime denotes the derivative with respect to $T_1 = \epsilon t$. The values of the coefficients are given in the Appendix, Parts 4 and 6. The coefficients Q_i and H_{nk} are due to the internal resonance and the secondary resonance (nonprimary resonance), respectively. The coefficients F and G are due to the combination resonances. The coefficients α_{nj} are not relevant to these resonances and appear even in the primary resonance and nonresonance cases.

To solve Eqs. (14), we write A_n in the polar form

$$A_n = \tfrac{1}{2}a_n \exp(i\beta_n), \quad n = 1, 2, \ldots$$

where a_n and β_n are real. Then we separate the result into real and imaginary parts and obtain

$n = 1, 2, 3$:

$$\omega_1(a_1' + c_1a_1) + Qa_2^2a_3 \sin \mu_1 + \tfrac{1}{2}Fa_1a_2 \sin \mu_2 + \tfrac{1}{4}Ga_2a_3 \sin (\mu_2 - \mu_1) = 0 \quad (15a)$$

$$\omega_1a_1\beta_1' + \tfrac{1}{8}a_1\sum_{j=1}^{\infty}\alpha_{1j}a_j^2 + Qa_2^2a_3 \cos \mu_1 + H_{11}a_1 + \tfrac{1}{2}Fa_1a_2 \cos \mu_2 + \tfrac{1}{4}Ga_2a_3 \cos (\mu_2 - \mu_1) = 0 \quad (15b)$$

$$\omega_2(a_2' + c_2a_2) + 2Qa_1a_2a_3 \sin \mu_1 + \tfrac{1}{4}Fa_1^2 \sin \mu_2 - \tfrac{1}{4}Ga_1a_3 \sin (\mu_2 - \mu_1) = 0 \quad (15c)$$

$$\omega_2a_2\beta_2' + \tfrac{1}{8}a_2\sum_{j=1}^{\infty}\alpha_{2j}a_j^2 + 2Qa_1a_2a_3 \cos \mu_1 + H_{22}a_2 + \tfrac{1}{4}Fa_1^2 \cos \mu_2 + \tfrac{1}{4}Ga_1a_3 \cos (\mu_2 - \mu_1) = 0 \quad (15d)$$

$$\omega_3(a_3' + c_3a_3) - Qa_1a_2^2 \sin \mu_1 + \tfrac{1}{4}Ga_1a_2 \sin (\mu_2 - \mu_1) = 0 \quad (15e)$$

$$\omega_3a_3\beta_3' + \tfrac{1}{8}a_3\sum_{j=1}^{\infty}\alpha_{3j}a_j^2 + Qa_1a_2^2 \cos \mu_1 + H_{33}a_3 + \tfrac{1}{4}Ga_1a_2 \cos (\mu_2 - \mu_1) = 0 \quad (15f)$$

$n \geq 4$:

$$\omega_n(a_n' + c_na_n) = 0 \quad (16a)$$

$$\omega_na_n\beta_n' + \tfrac{1}{8}a_n\sum_{j=1}^{\infty}\alpha_{nj}a_j^2 + H_{nn}a_n = 0 \quad (16b)$$

where

$$8Q = Q_1$$

$$\mu_1 = \beta_1 + 2\beta_2 - \beta_3 + \sigma_1T_1 \quad (17a)$$

$$\mu_2 = 2\beta_1 + \beta_2 - \sigma_2T_1. \quad (17b)$$

From Eq. (16a) we can see that the amplitudes a_n ($n \geq 4$) decay because

$$a_n \propto \exp(-c_nT_1), \quad n \geq 4.$$

Since we are interested in the steady-state response, we can disregard a_n ($n \geq 4$).

Then Eqs. (15) can be reduced to a set of autonomous ordinary differential equations in amplitudes a_n and phases μ_n for $n = 1, 2, 3$ as follows:

$$a_1' = -c_1a_1 - \frac{Qa_2^2a_3}{\omega_1}\sin \mu_1 - \frac{Fa_1a_2}{2\omega_1}\sin \mu_2 - \frac{Ga_2a_3}{4\omega_1}\sin (\mu_2 - \mu_1) \quad (18a)$$

$$a_2' = -c_2a_2 - \frac{2Qa_1a_2a_3}{\omega_2}\sin \mu_1 - \frac{Fa_1^2}{4\omega_2}\sin \mu_2 + \frac{Ga_1a_3}{4\omega_2}\sin (\mu_2 - \mu_1) \quad (18b)$$

$$a_3' = -c_3a_3 + \frac{Qa_1a_2^2}{\omega_3}\sin \mu_1 - \frac{Ga_1a_2}{4\omega_3}\sin (\mu_2 - \mu_1) \quad (18c)$$

$$a_1a_2a_3\mu_1' = a_1a_2a_3\sigma_1 + \frac{a_1a_2a_3}{8}\sum_{n=1}^{3}\left(\frac{\alpha_{3n}}{\omega_3} - \frac{2\alpha_{2n}}{\omega_2} - \frac{\alpha_{1n}}{\omega_1}\right)a_n^2 + Q\left(\frac{a_1^2a_2^3}{\omega_3} - \frac{4a_1^2a_2a_3^2}{\omega_2} - \frac{a_2^3a_3^2}{\omega_1}\right)\cos \mu_1 + a_1a_2a_3\left(\frac{H_{33}}{\omega_3} - \frac{2H_{22}}{\omega_2} - \frac{H_{11}}{\omega_1}\right) - \frac{Fa_1a_3}{2}\left(\frac{a_1^2}{\omega_2} + \frac{a_2^2}{\omega_1}\right)\cos \mu_2 + \frac{G}{2}\left(\frac{a_1^2a_2^2}{2\omega_3} - \frac{a_1^2a_3^2}{\omega_2} - \frac{a_2^2a_3^2}{2\omega_1}\right)\cos (\mu_2 - \mu_1) \quad (18d)$$

$$a_1a_2\mu_2' = -a_1a_2\sigma_2 - \frac{a_1a_2}{8}\sum_{n=1}^{3}\left(\frac{2\alpha_{1n}}{\omega_1} + \frac{\alpha_{2n}}{\omega_2}\right)a_n^2 - 2Qa_2a_3\left(\frac{a_2^2}{\omega_1} + \frac{a_1^2}{\omega_2}\right)\cos \mu_1 - a_1a_2\left(\frac{2H_{11}}{\omega_1} + \frac{H_{22}}{\omega_2}\right) - Fa_1\left(\frac{a_2^2}{\omega_1} + \frac{a_1^2}{4\omega_2}\right)\cos \mu_2 - \frac{Ga_3}{2}\left(\frac{a_2^2}{\omega_1} + \frac{a_1^2}{2\omega_2}\right)\cos (\mu_2 - \mu_1). \quad (18e)$$

By the observation of the above equations we can see that there are two types of steady-state responses ($a_1' = a_2' = a_3' = \mu_1' = \mu_2' = 0$) such as (I) $a_1 \neq 0$, $a_2 \neq 0$, $a_3 \neq 0$ and (II) $a_1 = a_2 = a_3 = 0$. Dividing (18d) and (18e) by $a_1a_2a_3$ and a_1a_2, respectively, we can obtain the following algebraic equations giving the steady-state response of $a_1 \neq 0$, $a_2 \neq 0$, $a_3 \neq 0$.

$$\omega_1c_1a_1 + Qa_2^2a_3 \sin \mu_1 + \frac{Fa_1a_2}{2}\sin \mu_2 + \frac{Ga_2a_3}{4}\sin (\mu_2 - \mu_1) = 0 \quad (19a)$$

$$\omega_2c_2a_2 + 2Qa_1a_2a_3 \sin \mu_1 + \frac{Fa_1^2}{4}\sin \mu_2 + \frac{Ga_1a_3}{4}\sin (\mu_2 - \mu_1) = 0 \quad (19b)$$

Downloaded 04 May 2010 to 171.66.16.28. Redistribution subject to ASME license or copyright; see http://www.asme.org/terms/Terms_Use.cfm

$$\omega_3 c_3 a_3 - Q a_1 a_2^2 \sin \mu_1 + \frac{G a_1 a_2}{4} \sin (\mu_2 - \mu_1) = 0 \quad (19c)$$

$$\sigma_1 + \frac{1}{8}\sum_{n=1}^{3}\left(\frac{\alpha_{3n}}{\omega_3} - \frac{2\alpha_{2n}}{\omega_2} - \frac{\alpha_{1n}}{\omega_1}\right)a_n^2 + Q\left(\frac{a_1 a_2^2}{\omega_3 a_3} - \frac{4 a_1 a_3}{\omega_2} - \frac{a_2^2 a_3}{\omega_1 a_1}\right)\cos \mu_1 + \left(\frac{H_{33}}{\omega_3} - \frac{2H_{22}}{\omega_2} - \frac{H_{11}}{\omega_1}\right) - \frac{F}{2}\left(\frac{a_1^2}{\omega_2 a_2} + \frac{a_2}{\omega_1}\right)\cos \mu_2 + \frac{G}{2}\left(\frac{a_1 a_2}{2\omega_3 a_3} - \frac{a_1 a_3}{\omega_2 a_2} - \frac{a_2 a_3}{2\omega_1 a_1}\right)\cos (\mu_2 - \mu_1) = 0 \quad (19d)$$

$$\sigma_2 + \frac{1}{8}\sum_{n=1}^{3}\left(\frac{2\alpha_{1n}}{\omega_1} + \frac{\alpha_{2n}}{\omega_2}\right)a_n^2 + 2Q\left(\frac{a_2^2}{\omega_1 a_1} + \frac{a_1}{\omega_2}\right)a_3 \cos \mu_1 + \left(\frac{2H_{11}}{\omega_1} + \frac{H_{22}}{\omega_2}\right) + F\left(\frac{a_2}{\omega_1} + \frac{a_1^2}{4\omega_2 a_2}\right)\cos \mu_2 + \frac{G}{2}\left(\frac{a_2}{\omega_1 a_1} + \frac{a_1}{2\omega_2 a_2}\right)a_3 \cos (\mu_2 - \mu_1) = 0. \quad (19e)$$

Using Eqs. (7*b*) and (11) we can express the generalized coordinates in the steady state as follows:

$$\psi_n = \begin{cases} a_n \cos (\omega_n t + \beta_n) + 2\Lambda_n \cos \Omega t + O(\epsilon), \\ \qquad\qquad n = 1, 2, 3 \\ 2\Lambda_n \cos \Omega t + O(\epsilon), \quad n \geq 4 \end{cases} \quad (20)$$

where

$$\beta_n = \epsilon\beta_n' t + \tau_n, \quad n = 1, 2, 3 \quad (21)$$

$$\Lambda_n = \frac{K_n}{\omega_n^2 - \Omega^2}, \quad n = 1, 2, 3, \ldots. \quad (22)$$

The τ_n in Eq. (21) are the integration constants depending on the initial conditions.

Substituting Eqs. (20)–(22) into Eq. (2), we have the deflection of the circular plate in the steady state as follows:

$$w(r, t) = w_{cr}(r, t) + w_{nr}(r, t) + O(\epsilon) \quad (23)$$

where

$$w_{cr}(r, t) = \sum_{n=1}^{3} a_n \cos [(\omega_n + \epsilon\beta_n')t + \tau_n]\varphi_n(r) \quad (24)$$

$$w_{nr}(r, t) = 2\sum_{n=1}^{\infty} \Lambda_n \varphi_n(r) \cos \Omega t. \quad (25)$$

Since the component of the deflection w_{cr} is due to the combination resonance a_n, β_n ($n = 1, 2, 3$), it is called the combination-resonance deflection. If the steady-state β_n' is constant, then $\omega_n + \epsilon\beta_n'$ is a constant frequency close to the natural frequency ω_n. Thus the combination-resonance deflection w_{cr} is almost the combination of three modes. On the other hand, the deflection w_{nr} has the same frequency as the excitation frequency Ω, which is not close to the natural frequency ω_n. The amplitude of w_{nr} is governed by Λ_n, which is not quite large because Ω is not close to ω_n. Now the deflection w_{nr} is called the nonresonance deflection because it is due to the nonresonance response Λ_n. For the steady-state response of $a_1 = a_2 = a_3 = 0$ this nonresonance deflection w_{nr} becomes the deflection $w(r, t)$. In other words, this nonresonance deflection is the only deflection we can obtain by linear analysis, because this deflection is due to the response of the forced vibration of the linear system which has the same frequency as the excitation frequency.

3 Asymptotic Stability Analysis

3.1 Steady-State Resonance Responses When $a_1 \neq 0$, $a_2 \neq 0$, $a_3 \neq 0$. Let one of the steady-state resonance responses of $a_1 \neq 0$, $a_2 \neq 0$, $a_3 \neq 0$ be a_{10}, a_{20}, a_{30}, μ_{10}, μ_{20}. To determine the stability of the various steady-state responses we examine the system behavior for small disturbance on the steady state. Let

$$a_1 = a_{10} + \delta a_1, \quad a_2 = a_{20} + \delta a_2, \quad a_3 = a_{30} + \delta a_3,$$
$$\mu_1 = \mu_{10} + \delta\mu_1, \quad \mu_2 = \mu_{20} + \delta\mu_2 \quad (26)$$

where $\delta(\ )$ represents a small disturbance of the steady state. Substituting Eq. (26) into Eq. (18), and retaining only linear terms leads to

$$\frac{d}{dT_1}\begin{Bmatrix}\delta a_1 \\ \delta a_2 \\ \delta a_3 \\ \delta\mu_1 \\ \delta\mu_2\end{Bmatrix} = \begin{bmatrix}\Phi_{11} & \Phi_{12} & \Phi_{13} & \Phi_{14} & \Phi_{15} \\ \Phi_{21} & \Phi_{22} & \Phi_{23} & \Phi_{24} & \Phi_{25} \\ \Phi_{31} & \Phi_{32} & \Phi_{33} & \Phi_{34} & \Phi_{35} \\ \Phi_{41} & \Phi_{42} & \Phi_{43} & \Phi_{44} & \Phi_{45} \\ \Phi_{51} & \Phi_{52} & \Phi_{53} & \Phi_{54} & \Phi_{55}\end{bmatrix}\begin{Bmatrix}\delta a_1 \\ \delta a_2 \\ \delta a_3 \\ \delta\mu_1 \\ \delta\mu_2\end{Bmatrix}. \quad (27)$$

The steady-state response is considered asymptotically stable if the real parts of all eigenvalues of the coefficient matrix $[\Phi_{ij}]$ are negative.

3.2 Steady-State Resonance Response When $a_1 = a_2 = a_3 = 0$. In this case $a_{10} = a_{20} = a_{30} = 0$ but μ_{10} and μ_{20} are indeterminate. In other words, this solution is a singular solution; thus, for the stability of the singular solution we cannot rely on the Eq. (27).

In order to use Eq. (14) instead of Eq. (27), we introduce a small disturbance as follows:

$$A_n = A_{n0} + \delta A_n, \quad n = 1, 2, 3 \quad (28)$$

where

$$A_{n0} = \tfrac{1}{2}a_{n0} \exp (i\beta_{n0}) = 0, \quad n = 1, 2, 3. \quad (29)$$

Thus

$$A_n = \delta A_n, \quad n = 1, 2, 3. \quad (30)$$

Substituting Eq. (30) into Eq. (14) we have

$$\delta A_n' = -\left(c_n + i\frac{H_{nn}}{\omega_n}\right)\delta A_n, \quad n = 1, 2, 3. \quad (31)$$

Let

$$\delta A_n = \delta A_{nr} + i\delta A_{ni}, \quad n = 1, 2, 3 \quad (32)$$

where δA_{nr} and δA_{ni} are real.

Substituting Eq. (32) into Eq. (31) we have

$$\frac{d}{dT_1}\begin{Bmatrix}\delta A_{nr} \\ \delta A_{ni}\end{Bmatrix} = \begin{bmatrix}-c_n & \dfrac{H_{nn}}{\omega_n} \\ -\dfrac{H_{nn}}{\omega_n} & -c_n\end{bmatrix}\begin{Bmatrix}\delta A_{nr} \\ \delta A_{ni}\end{Bmatrix}. \quad (33)$$

The eigenvalues of the coefficient matrix in Eq. (33) are

$$\lambda_{1,2} = -c_n \pm i\left|\frac{H_{nn}}{\omega_n}\right|, \quad n = 1, 2, 3.$$

Therefore the real parts of all eigenvalues are $-c_n < 0$ because the damping coefficients are positive. Conclusively the zero-amplitude response turns out to be stable as long as the damping coefficients are positive.

4 Numerical Results

Using Eq. (19) and stability criteria mentioned earlier, we have plotted the amplitude-parameter ($\epsilon\sigma_2 = \hat{\sigma}_2$ and B) response

Downloaded 04 May 2010 to 171.66.16.28. Redistribution subject to ASME license or copyright; see http://www.asme.org/terms/Terms_Use.cfm

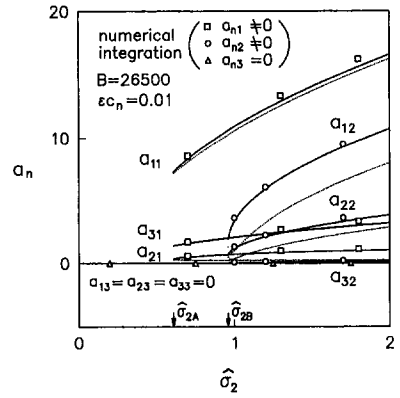


Fig. 2 Variation of steady-state combination resonance responses with the external detuning parameter

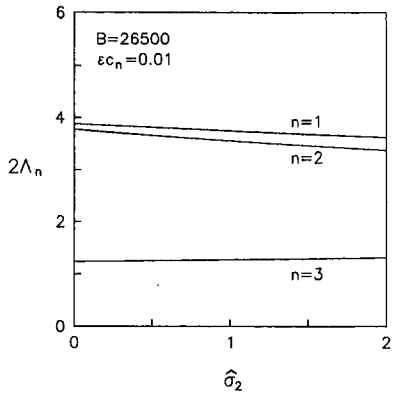


Fig. 4 Variation of nonresonance responses with the external detuning parameter

curves shown in Figs. 2 and 3, where solid and dotted lines denote, respectively, stable and unstable responses. There exist two pairs of nonzero-amplitude responses. Each pair has the stable and unstable branches. Since the zero-amplitude response is stable, the system has at most three stable responses. In this case, the long-term response of the system depends on the initial condition.

For convenience, let say, the first two stable responses are the nonzero-amplitude responses and the third stable response is the zero-amplitude response. Then the amplitude a_{nj} $(n, j = 1, 2, 3)$ denoted by solid lines implies the amplitude of the nth mode of the jth stable response. Thus we have $a_{11} \neq 0$, $a_{21} \neq 0$, $a_{31} \neq 0$, $a_{12} \neq 0$, $a_{22} \neq 0$, $a_{32} \neq 0$, and $a_{13} = 0$, $a_{23} = 0$, $a_{33} = 0$. According to this notation, we need to modify Eqs. (20), (23), and (24) as follows:

$$\psi_{nj} = \begin{cases} a_{nj} \cos(\omega_n t + \beta_{nj}) + 2\Lambda_n \cos \Omega t + O(\epsilon), \\ \qquad\qquad n, j = 1, 2, 3 \quad (20)' \\ 2\Lambda_n \cos \Omega t + O(\epsilon), \quad n \geq 4 \end{cases}$$

$$w_j(r, t) = w_{crj}(r, t) + w_{nr}(r, t) \qquad (23)'$$

where

$$w_{crj}(r, t) = \sum_{n=1}^{3} a_{nj} \cos[(\omega_n + \epsilon\beta'_{nj})t + \tau_{nj}]\varphi_n(r), \quad j = 1, 2, 3. \quad (24)'$$

In these expressions, the generalized coordinates ψ_{nj}, the total deflection w_j and the combination-resonance deflection w_{crj} are corresponding to the jth stable response. In order to check the validity of the analytical results, we have integrated numerically the system (1) and used the Eq. (20)′ to obtain the amplitudes of the stable steady-state responses. The symbols □, ○, and △ denotes the first, second, and third stable responses, respectively.

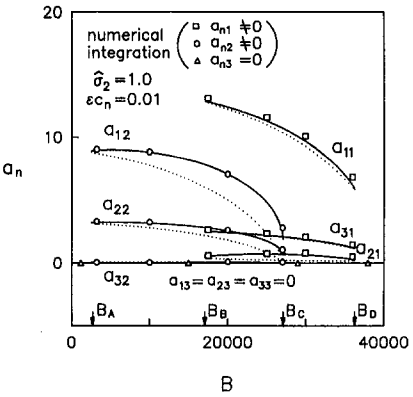


Fig. 3 Variation of steady-state combination resonance responses with the excitation amplitude

In Fig. 2, the amplitudes of three modes are shown as functions of $\hat{\sigma}_2$. We have bifurcations at $\hat{\sigma}_{2A}$ and $\hat{\sigma}_{2B}$. When $\hat{\sigma}_2 < \hat{\sigma}_{2A}$, the only stable response is the zero-amplitude response, a_{n3}. When $\hat{\sigma}_{2A} < \hat{\sigma}_2 < \hat{\sigma}_{2B}$, there exist two stable responses, a_{n2} and a_{n3}. When $\hat{\sigma}_2 > \hat{\sigma}_{2B}$, there exist three stable responses, a_{n1}, a_{n2} and a_{n3}. Since the amplitude a_{32} is almost zero, the amplitude and zero-amplitude the response a_{n3} almost overlap with each other in the figure. Because of the existence of multiple stable responses, we have two jumps at $\hat{\sigma}_{2A}$ and $\hat{\sigma}_{2B}$. By means of the numerical integration of the system (1), it has been found that both stable responses jump down to the zero-amplitude response as $\hat{\sigma}_2$ decreases.

In Fig. 3 the amplitudes are plotted as functions of B. The amplitudes of the both nonzero-amplitude responses, a_{n1} and a_{n2}, decrease with the excitation amplitude. This phenomenon is very peculiar even in nonlinear systems, though Nayfeh and Mook (1979) had also found this phenomenon in the combination resonance of a hinged-clamped beam. We have bifurcations at B_A, B_B, B_C, and B_D. When $B < B_A$ and $B > B_D$, the only stable response is the zero-amplitude response, a_{n3}. When $B_A < B < B_B$, there exist two stable responses, a_{n2} and a_{n3}. When $B_B < B < B_C$, there exist three stable responses, a_{n1}, a_{n2}, and a_{n3}. When $B_C < B < B_D$, there exist two stable responses, a_{n1}, and a_{n3}. By means of the numerical integration, jump phenomena are found at B_A, B_B, B_C, and B_D. All jumps but at B_B are downward to a_{n3}. At B_B the response a_{n1} jumps to a_{n2}. The jump at B_B cannot be recognized as a downward jump because the second mode jumps up, while the first and third modes jump down.

The variation of nonresonance response Λ_n with the detuning parameter $\epsilon\sigma_2$ obtained from Eq. (22) is shown in Fig. 4 where Λ_1 and Λ_2 decrease and Λ_3 increases with $\epsilon\sigma_2$. This results from the fact that the excitation frequency Ω is greater than ω_1 and ω_2, and is less than ω_3. In Fig. 5 the variation of nonresonance responses with the excitation amplitude B is shown. The proportionality of Λ_n to B tells us that those nonresonance responses are just the responses of the linearized system. This proportionality of linear responses to B is in contrast to the decrease of amplitudes of nonzero-amplitude responses (or nonlinear responses) with B.

Integrating the nonautonomous system (1) and using Eq. (20)′, we can draw Figs. 6–8 to show the time histories of three stable steady-state responses. We have used values for the system parameters as the following:

Downloaded 04 May 2010 to 171.66.16.28. Redistribution subject to ASME license or copyright; see http://www.asme.org/terms/Terms_Use.cfm

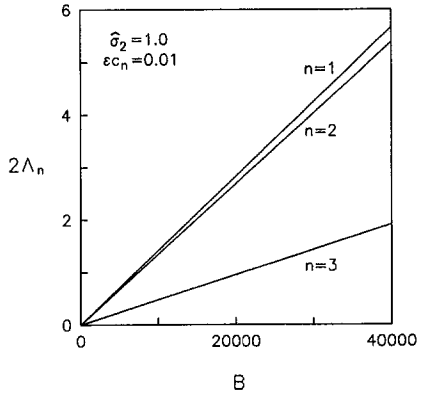


Fig. 5 Variation of nonresonance responses with the excitation amplitude

$$\{\hat{\sigma}_2, \epsilon c_n, B, \epsilon\} = \{1.0, 0.01, 26500, 1.063 \times 10^{-3}\}. \quad (34)$$

Since the system has three asymptotically stable steady-state responses, the long-term behavior of the plate depends on the initial condition. The initial conditions used for the figures are as follows:

$$\{\psi_1, \dot{\psi}_1, \psi_2, \dot{\psi}_2, \psi_3, \dot{\psi}_3\} = \{7.14, 0.0, 4.27, 0.0, 3.36, 0.0\} \quad \text{for Fig. 6}$$

$$\{\psi_1, \dot{\psi}_1, \psi_2, \dot{\psi}_2, \psi_3, \dot{\psi}_3\} = \{-0.40, 0.0, 4.76, 0.0, 1.29, 0.0\} \quad \text{for Fig. 7}$$

$$\{\psi_1, \dot{\psi}_1, \psi_2, \dot{\psi}_2, \psi_3, \dot{\psi}_3\} = \{-3.65, 0.0, 3.66, 0.0, 2.27, 0.0\} \quad \text{for Fig. 8}$$

For the numerical integration, in this study, we employ the Runge-Kutta fourth-order method with the time step size of integration, $\Delta t = 2\pi/(30\omega_3)$. The results in Figs. 6(b), 7(b), and 8(b) have been used to construct the numerical integration results in Figs. 2 and 3.

Using the analytical results and Eqs. (20)′, (23)′, and (24)′, we have plotted the nonresonance deflection $w_{nr}(r, t)$, the combination resonance deflections $w_{crj}(r, t)$ and the total deflections

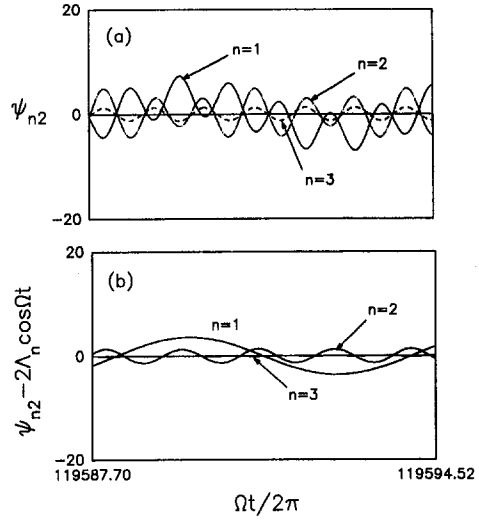


Fig. 7 Time histories of the second steady-state stable response with nonzero-amplitude modes (B = 26500, $\hat{\sigma}_2$ = 1.0, ϵc_n = 0.01, ϵ = 1.063 × 10^{-3}); (a) total response (b) three modes

$w_j(r, t)$ in the steady states, shown in Fig. 9. By means of Eqs. (17) and (21), the constant phases τ_{nj} are chosen as the follows:

$$\tau_{1j} = 0, \quad \tau_{2j} = \mu_{2j}, \quad \tau_{3j} = 2\mu_{2j} - \mu_{1j}$$

where μ_{1j} and μ_{2j} are the steady-state values of the jth stable responses obtained analytically. The values of system parameters used for this figure are the same as ones in Eq. (34). The results in the figure are for the duration $2T$, where T is the excitation period $2\pi/\Omega$. We need to note that the nonresonance deflection w_{nr} has the same period as the excitation period T, because it is a linear solution. The initial conditions determine which deflection of three deflections w_j represents the actual deflection.

In order to show how the parameter B and $\hat{\sigma}_2$ influence the system response, we plot stability regions in $B - \hat{\sigma}_2$ plane shown in Fig. 10. Bifurcations occur on two curves. In region I, there exist one stable response, a_{n3}. In region II, there exist two stable responses, a_{n2} and a_{n3}. In region III, there exist three stable responses, a_{n1}, a_{n2}, and a_{n3}. In region IV, there exist two stable responses, a_{n1} and a_{n3}.

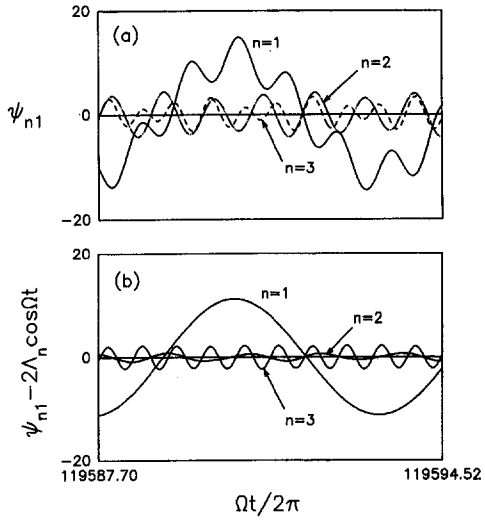


Fig. 6 Time histories of the first steady-state stable response with nonzero-amplitude modes (B = 26500, $\hat{\sigma}_2$ = 1.0, ϵc = 0.01, ϵ = 1.063 × 10^{-3}); (a) total response (b) three modes

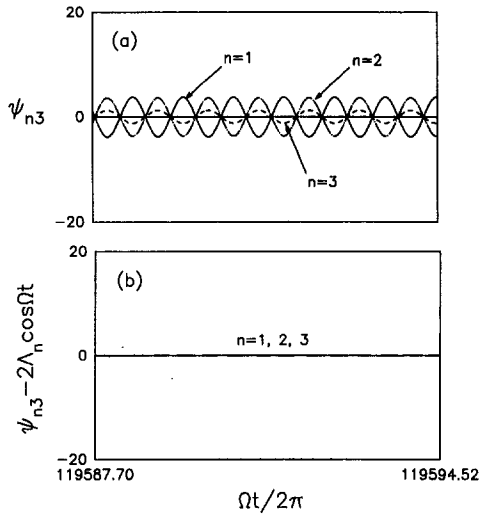


Fig. 8 Time histories of the steady-state stable response with zero-amplitude modes (B = 26500, $\hat{\sigma}_2$ = 1.0, ϵc_n = 0.01, ϵ = 1.063 × 10^{-3}); (a) total response (b) three modes

Downloaded 04 May 2010 to 171.66.16.28. Redistribution subject to ASME license or copyright; see http://www.asme.org/terms/Terms_Use.cfm

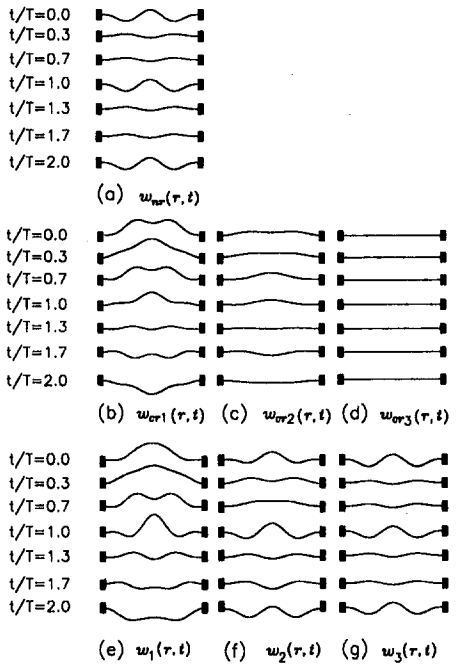


Fig. 9 Deflection curves of the circular plate for two periods of the excitation ($B = 26500$, $\hat{\sigma}_2 = 1.0$, $\epsilon c_n = 0.01$, $\epsilon = 1.063 \times 10^{-3}$); (*a*) nonresonance deflection curves, (*b*~*d*) combination resonance deflection curves, and (*e*~*g*) total deflection curves

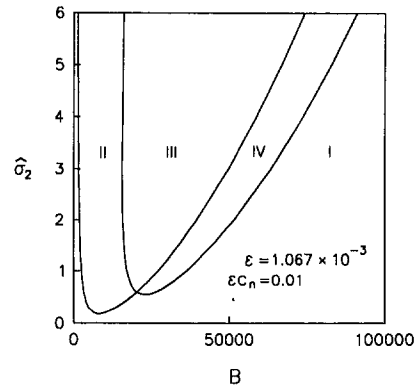


Fig. 10 The various regions in parameter space for the classifications of the steady-state combination resonance responses

5 Conclusions

An analysis of the combination resonances ($\Omega \approx 2\omega_1 + \omega_2 \approx \omega_1 - \omega_2 + \omega_3$) of a clamped circular plate with three mode interaction ($\omega_3 \approx \omega_1 + 2\omega_2$) has been presented. The effect of two near combination resonance frequencies on the long-term responses of the plate has also been examined. The results exhibit the following features.

(1) There exist at most three asymptotically stable resonance responses. Two responses with nonzero-amplitudes exist for limited values of parameters, while one response with zero-amplitude exists for all values of parameters. In the case of multiple stable responses, the long-term behavior of the plate depends on the initial condition.

(2) The amplitudes of the steady-state resonance response with nonzero-amplitude modes decrease with the excitation amplitude. On the other hand, the amplitudes of the nonresonance response increase linearly with the excitation amplitude.

Acknowledgment

This work was supported in part by the Korea Science and Engineering Foundation under Grant KOSEF 89-0202-03 and by the Korea Research Foundation under Grant Nondirected Research Fund 1993. The authors gratefully acknowledge one of the referees for his particularly helpful comments on this paper.

References

Hadian, J., and Nayfeh, A. H., 1990, "Modal Interaction in Circular Plates," *Journal of Sound and Vibration,* Vol. 142, pp. 279–292.

Kevorkian, J., 1987, "Perturbation Techniques for Oscillatory Systems with Slowly Varying Coefficients," *SIAM Review,* Vol. 29, No. 3, pp. 391–462.

Lee, W. K., and Soh, K. Y., 1994, "Nonlinear Analysis of the Forced Response of a Beam with Three Mode Interaction," *Nonlinear Dynamics,* Vol. 6, No. 1, pp. 49–68.

Lee, W. K., and Ghang, M. R., 1994, "Domains of Attraction of a Forced Beam by Interpolated Mapping," ASME JOURNAL OF APPLIED MECHANICS, Vol. 61, pp. 144–151.

Leissa, A. W., 1969, Vibration of Plates, NASA-SP-160, Government Printing Office, Washington, D.C.

Nayfeh, A. H., 1973, *Perturbation Methods,* John Wiley and Sons, New York.

Nayfeh, A. H., Mook, D. T., and Sridhar, S., 1974, "Nonlinear Analysis of the Forced Responses of Structural Elements," *Journal of the Acoustical Society of America,* Vol. 55, pp. 281–291.

Nayfeh, A. H., and Mook, D. T., 1979, *Nonlinear Oscillations,* John Wiley and Sons, New York.

Sridhar, S., Mook, D. T., and Nayfeh, A. H., 1975, "Nonlinear Resonances in the Forced Responses of Plates. Part I: Symmetric Responses of Circular Plates," *Journal of Sound and Vibration,* Vol. 41, pp. 359–373.

Sridhar, S., Mook, D. T., and Nayfeh, A. H., 1978, "Nonlinear Resonances in the Forced Responses of Plates. Part II: Asymmetric Responses of Circular Plates," *Journal of Sound and Vibration,* Vol. 59, pp. 159–170.

APPENDIX

1 Coefficients S_j and λ_j in Eq. (12):

$$\sum_{j=1}^{27} S_j \exp(i\lambda_j T_0).$$

j	S_j	λ_j	j	S_j	λ_j
1	$A_m A_p A_q$	$\omega_m + \omega_p + \omega_q$	15	$A_q \Lambda_m \Lambda_p$	$-2\Omega + \omega_q$
2	$A_m A_p \bar{A}_q$	$\omega_m + \omega_p - \omega_q$	16	$A_m A_p \Lambda_q$	$\Omega + \omega_m + \omega_p$
3	$A_m \bar{A}_p A_q$	$\omega_m - \omega_p + \omega_q$	17	$A_m A_p \Lambda_q$	$-\Omega + \omega_m + \omega_p$
4	$\bar{A}_m A_p A_q$	$-\omega_m + \omega_p + \omega_q$	18	$A_p A_q \Lambda_m$	$\Omega + \omega_p + \omega_q$
5	$2A_m \Lambda_p \Lambda_q$	ω_m	19	$A_p A_q \Lambda_m$	$-\Omega + \omega_p + \omega_q$
6	$2A_p \Lambda_q \Lambda_m$	ω_p	20	$A_q A_m \Lambda_p$	$\Omega + \omega_q + \omega_m$
7	$2A_q \Lambda_m \Lambda_p$	ω_q	21	$A_q A_m \Lambda_p$	$-\Omega + \omega_q + \omega_m$
8	$3\Lambda_m \Lambda_p \Lambda_q$	Ω	22	$A_m \bar{A}_p \Lambda_q$	$\Omega + \omega_m - \omega_p$
9	$\Lambda_m \Lambda_p \Lambda_q$	3Ω	23	$A_m \bar{A}_p \Lambda_q$	$-\Omega + \omega_m - \omega_p$
10	$A_m \Lambda_p \Lambda_q$	$2\Omega + \omega_m$	24	$A_p \bar{A}_q \Lambda_m$	$\Omega + \omega_p - \omega_q$
11	$A_m \Lambda_p \Lambda_q$	$-2\Omega + \omega_m$	25	$A_p \bar{A}_q \Lambda_m$	$-\Omega + \omega_p - \omega_q$
12	$A_p \Lambda_q \Lambda_m$	$2\Omega + \omega_p$	26	$A_q \bar{A}_m \Lambda_p$	$\Omega + \omega_q - \omega_m$
13	$A_p \Lambda_q \Lambda_m$	$-2\Omega + \omega_p$	27	$A_q \bar{A}_m \Lambda_p$	$-\Omega + \omega_q - \omega_m$
14	$A_q \Lambda_m \Lambda_q$	$2\Omega + \omega_q$			

2 Nonlinear coefficients Γ_{nmpq}:

$$\Gamma_{nmpq} = \sum_{k=1}^{3} \frac{\int_0^1 \varphi_p' \varphi_q' J_1(\zeta_k r)\, dr \int_0^1 \varphi_n' \varphi_m' J_1(\zeta_k r)\, dr}{(\zeta_k^2 - 1 + \nu^2) J_1^2(\zeta_k)},$$

$$n, m, p, q = 1, 2, 3$$

$$\varphi_m = C_m[J_0(k_m r) I_0(k_m) - J_0(k_m) I_0(k_m r)]$$

where

J_0; the Bessel function of the first kind of order 0
J_1; the Bessel function of the first kind of order 1
I_0; the modified Bessel function of the first kind of order 0
$k_m = \sqrt{\omega_m}$

Downloaded 04 May 2010 to 171.66.16.28. Redistribution subject to ASME license or copyright; see http://www.asme.org/terms/Terms_Use.cfm

ζ_k are roots of the equation

$$\zeta J_0(\zeta) - (1 + \nu)J_1(\zeta) = 0.$$

3 Coefficients c_n and f_n:

$$c_n = \int_0^1 cr\varphi_n dr$$

$$f_n(t) = \int_0^1 r\varphi_n f(r, t)dr.$$

4 Coefficients in Eq. (14):

$$\alpha_{11} = 3\Gamma_{1111}, \quad \alpha_{12} = 2(2\Gamma_{1212} + \Gamma_{1122}) = \alpha_{21},$$

$$\alpha_{13} = 2(2\Gamma_{1313} + \Gamma_{1133}) = \alpha_{31},$$

$$\alpha_{22} = 3\Gamma_{2222}, \quad \alpha_{23} = 2(2\Gamma_{2323} + \Gamma_{2233}) = \alpha_{32}, \quad \alpha_{33} = 3\Gamma_{3333},$$

$$Q_1 = (2\Gamma_{1223} + \Gamma_{1322}) = Q_3, \quad Q_2 = 2Q_1.$$

5 For uniformly distributed loads:

$$2K_n = B\int_0^1 r\varphi_n(r)dr.$$

6 Coefficients H_{nk}, F, and G:

$$H_{nk} = \sum_{m,j=1}^{3} (2\Gamma_{nmkj} + \Gamma_{nkmj})\Lambda_m\Lambda_j,$$

$$F = \sum_{j=1}^{3} (2\Gamma_{121j} + \Gamma_{112j})\Lambda_j,$$

$$G = 2\sum_{j=1}^{3} (\Gamma_{123j} + \Gamma_{132j} + \Gamma_{1j23})\Lambda_j.$$

Downloaded 04 May 2010 to 171.66.16.28. Redistribution subject to ASME license or copyright; see http://www.asme.org/terms/Terms_Use.cfm

Elastic Moduli of Composites Reinforced by Multiphase Particles

M. L. Dunn
Center for Acoustics, Mechanics, and Materials,
Department of Mechanical Engineering,
University of Colorado,
Boulder, CO 80309
Assoc. Mem. ASME

H. Ledbetter
Materials Science and Engineering Laboratory,
National Institute of Standards and Technology,
Boulder, CO 80303

A theoretical approach is proposed to estimate the elastic moduli of three-phase composites consisting of a matrix phase reinforced by two-phase particles. The theoretical predictions are based on a simple extension to nondilute concentrations of the mechanical concentration factors obtained from the recent analysis of the average elastic fields in a double inclusion by Hori and Nemat-Nasser (1993). The proposed micromechanics theory can account for the effects of shapes and concentrations of both the particles and the dispersed phase in the particles. Theoretical estimates of the concentration factors and the effective elastic moduli are obtained in closed form and are diagonally symmetric and fall within the Hashin-Shtrikman-Walpole bounds for all cases considered. The theoretical predictions are in excellent agreement with experimental results obtained from pulse-echo and rod-resonance measurements of the elastic moduli of a three-phase composite consisting of an aluminum matrix reinforced by mullite/alumina particles.

1 Introduction

Composite materials for engineering applications are being improved on many fronts including processing, microstructures, interfaces, and constituent properties. With regard to the constituents, the reinforcing phase sometimes consists of monocrystals, but usually of heterogeneous media. Common reinforcements are polycrystalline ceramics or metals, although other forms include lamina-based and matrix-based reinforcements. Composite materials reinforced by the latter are the subject of this study. The particular system of interest is a macroscopically isotropic metal-matrix composite consisting of an aluminum (Al) matrix reinforced by two-phase mullite/alumina (Al_2O_3) particles as shown in Fig. 1. The two-phase particles are roughly spherical while the Al_2O_3 particles are short rods embedded in the mullite.

To account more accurately for the fact that Al_2O_3 particles are embedded in the mullite, which is in turn embedded in an Al matrix, we developed a micromechanics theory based on a rigorous solution for the average elastic fields in a double inclusion (Fig. 2) as obtained recently by Hori and Nemat-Nasser (1993). The strain concentration factors obtained from this dilute solution are coupled with an approximation that is thought to better reflect a composite with finite particle concentrations. The new approximate strain concentration factors are then used with general expressions for the effective moduli resulting in closed-form expressions for the composite's effective elastic moduli.

The proposed micromechanics theory was assessed from both theoretical and experimental viewpoints. By theoretical we mean comparison with the Hashin-Shtrikman-Walpole bounds. By experimental, we mean that we measured a composite's complete elastic constants using pulse-echo (megahertz-frequency) and rod-resonance (kilohertz-frequency) methods. In particular, predictions are compared to the elastic moduli of Al/mullite/Al_2O_3 composites obtained from pulse-echo and rod-resonance measurements.

2 Effective Elastic Moduli of a Three-Phase Composite

Consider a general three-phase composite where the domains of the three phases are denoted by Ω_1, Ω_2, and Ω_3; Ω_2 and Ω_3 are assumed to be randomly distributed and randomly oriented in the matrix Ω_1. The constitutive equations relating the stress $\boldsymbol{\sigma}$ and strain $\boldsymbol{\epsilon}$ in each phase are

$$\boldsymbol{\sigma}_i = \mathbf{C}_i \boldsymbol{\epsilon}_i . \tag{1}$$

Here $\mathbf{C}_i$ denotes the tensor of elastic moduli (stiffnesses) and subscript i denotes the ith phase. In Eq. (1) and throughout, the well-known shorthand notation for tensors is adopted. For the perfectly bonded three-phase composite subjected to displacement boundary conditions compatible with a uniform overall strain $\boldsymbol{\epsilon}^0$, the overall response of a representative volume element of the composite can be defined by

$$\bar{\boldsymbol{\sigma}} = \mathbf{C}\bar{\boldsymbol{\epsilon}} = \mathbf{C}\boldsymbol{\epsilon}^0. \tag{2}$$

Here an overbar denotes the volume average of a quantity (in this case over the entire composite) and $\mathbf{C}$ is the tensor of effective elastic moduli of the composite. Following Hill (1963), general expressions for the effective elastic moduli can be derived by considering the volume average of the stress and strain over the composite:

$$\bar{\boldsymbol{\sigma}} = c_1\bar{\boldsymbol{\sigma}}_1 + c_2\{\bar{\boldsymbol{\sigma}}_2\} + c_3\{\bar{\boldsymbol{\sigma}}_3\}, \tag{3}$$

$$\bar{\boldsymbol{\epsilon}} = c_1\bar{\boldsymbol{\epsilon}}_1 + c_2\{\bar{\boldsymbol{\epsilon}}_2\} + c_3\{\bar{\boldsymbol{\epsilon}}_3\}, \tag{4}$$

Here subscript 1 denotes the matrix of the composite, 2 denotes the matrix of the particle, and 3 denotes the reinforcing phase in the particle, and c_i denotes the volume fraction of the ith phase. In Eqs. (3) and (4) $\{\cdot\}$ denotes the orientational average of an orientation-dependent quantity. Using Eqs. (2)–(4), the effective moduli of the composite can be expressed as

$$\begin{aligned}\mathbf{C} &= c_1\mathbf{C}_1\mathbf{A}_1 + c_2\mathbf{C}_2\mathbf{A}_2 + c_3\mathbf{C}_3\mathbf{A}_3, \\ &= \mathbf{C}_1 + c_2\{(\mathbf{C}_2 - \mathbf{C}_1)\mathbf{A}_2\} + c_3\{(\mathbf{C}_3 - \mathbf{C}_1)\mathbf{A}_3\}.\end{aligned} \tag{5}$$

Contributed by the Applied Mechanics Division of THE AMERICAN SOCIETY OF MECHANICAL ENGINEERS for publication in the ASME JOURNAL OF APPLIED MECHANICS.

Discussion on this paper should be addressed to the Technical Editor, Professor Lewis T. Wheeler, Department of Mechanical Engineering, University of Houston, Houston, TX 77204-4792, and will be accepted until four months after final publication of the paper itself in the ASME JOURNAL OF APPLIED MECHANICS.

Manuscript received by the ASME Applied Mechanics Division, Jan. 3, 1994; final revision, Aug. 24, 1994. Associate Technical Editor: G. J. Dvorak.

Copyright © 1995 by ASME

Downloaded 04 May 2010 to 171.66.16.28. Redistribution subject to ASME license or copyright; see http://www.asme.org/terms/Terms_Use.cfm

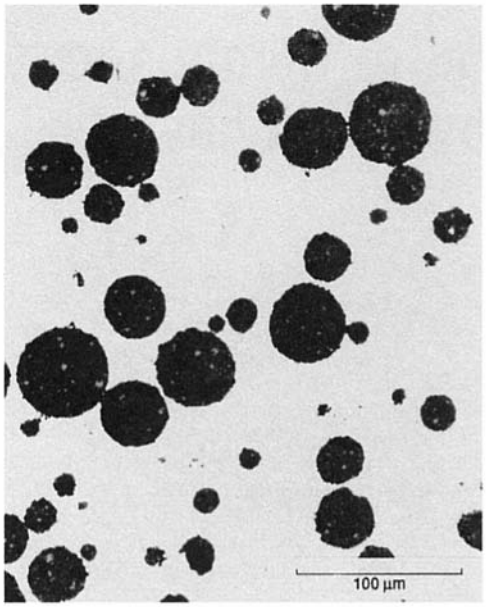


Fig. 1 Microstructure of the composite showing the Al matrix reinforced by spherical Al_2O_3/mullite particles. The composite particles consist of Al_2O_3 (light phases) dispersed in mullite (dark phases).

Here $\mathbf{A}_i$ are strain concentration factors (fourth-order tensors) that relate the average strain in the ith phase to that in the composite and are in general orientation dependent; that is,

$$\bar{\boldsymbol{\epsilon}}_i = \mathbf{A}_i \bar{\boldsymbol{\epsilon}} = \mathbf{A}_i \boldsymbol{\epsilon}^0. \tag{6}$$

The concentration factors obey the identity

$$c_1\mathbf{A}_1 + c_2\mathbf{A}_2 + c_3\mathbf{A}_3 = \mathbf{I}. \tag{7}$$

For the composite of interest here, which consists of a matrix reinforced by two-phase particles, it is convenient to consider the average fields in the particle. To this end we define

$$\bar{\boldsymbol{\epsilon}}_{23} = \mathbf{A}_{23} \bar{\boldsymbol{\epsilon}} = \mathbf{A}_{23} \boldsymbol{\epsilon}^0. \tag{8}$$

It follows from Eqs. (6)–(8) that

$$\mathbf{A}_{23} = \frac{c_2\mathbf{A}_2 + c_3\mathbf{A}_3}{c_2 + c_3}. \tag{9}$$

With Eqs. (7)–(9), the effective moduli can be expressed as

$$\mathbf{C} = \mathbf{C}_1 + (c_2 + c_3)\{(\mathbf{C}_2 - \mathbf{C}_1)\mathbf{A}_{23}\} + c_3\{(\mathbf{C}_3 - \mathbf{C}_2)\mathbf{A}_3\}. \tag{10}$$

Estimation of $\mathbf{A}_{23}$ and $\mathbf{A}_3$ is thus the key to predicting the effective elastic moduli $\mathbf{C}$. In general the concentration factors can not be obtained exactly and must be estimated by some approximate scheme as will be discussed in the following two sections. A dual development can be followed when considering uniform traction boundary conditions to express the effective compliance in terms of corresponding stress concentration factors.

3 Concentration Factors: Dilute and Nondilute Concentrations

The simplest approximation of $\mathbf{A}_i$ is $\mathbf{A}_3 = \mathbf{A}_{23} = \mathbf{I}$, which is the Voigt (1889) approximation. The next-simplest estimate is the dilute approximation where all interactions among the reinforcing phases are ignored. Here we desire to consider the fact that the particles themselves are composites consisting of a matrix with a dispersed phase. In general, this would involve the rigorous solution of a single particle embedded in a second phase, which itself is embedded in an infinite matrix. This solution would be the appropriate auxiliary problem from which the concentration factor $\mathbf{A}_i$ for dilute concentrations could be obtained. In general this problem requires recourse to numerical techniques, and its use as the building block for approximations at higher reinforcement concentrations would be limited. In terms of estimating the effective properties of a composite, however, only the *average* stress and strain fields in each phase are required. The recent results of Hori and Nemat-Nasser (1993) and Nemat-Nasser and Hori (1993) for the average fields in a *double inclusion* are thus useful for our purposes. In particular, Hori and Nemat-Nasser provided powerful results for the *average* stress and strain in a double inclusion (an inclusion embedded in a second inclusion, which is itself embedded in an infinite matrix) containing an eigenstrain distribution. Through a generalization of Eshelby's (1957) equivalence principle they obtained expressions for the average elastic fields in a double inhomogeneity. Here we adopt the terminology of Mura (1987), where an inclusion refers to a subdomain with elastic moduli the same as that of the matrix while an inhomogeneity is a subdomain with elastic moduli different than the matrix. For completeness, the solution of Hori and Nemat-Nasser for the average elastic fields in a double inclusion is briefly summarized in the Appendix. Here we use it to derive appropriate concentration factors for dilute and nondilute concentrations.

In the dilute limit the concentration factors $\mathbf{A}_i^{di}$ can be obtained by substituting Eqs. (A4)–(A6) into Eq. (A3) and solving for the total strain. After some manipulation they can be expressed as

$$\mathbf{A}_3^{di} = \mathbf{I} + \Delta\mathbf{S}\Phi_2 + \mathbf{S}_3\Phi_3,$$

$$\mathbf{A}_2^{di} = \mathbf{I} + \left[\mathbf{S}_2 - \frac{c_3}{c_2}\Delta\mathbf{S}\right]\Phi_2 + \frac{c_3}{c_2}\Delta\mathbf{S}\Phi_3,$$

$$\mathbf{A}_{23}^{di} = \mathbf{I} + \mathbf{S}_2\Phi_{23} = \frac{c_2}{c_2 + c_3}\mathbf{A}_2^{di} + \frac{c_3}{c_2 + c_3}\mathbf{A}_3^{di}. \tag{11}$$

Here $\mathbf{I}$ denotes the fourth-order identity tensor. In Eqs. (11), the superscript di denotes that the concentration factors are based on the solution for an isolated double inclusion in an infinite matrix. In other words, $\mathbf{A}_i^{di}$ are the concentration factors for the double inclusion in the dilute limit.

To consider, albeit, that both the particles and the matrix contain reinforcement at finite concentrations, we make the assumption that at finite concentrations, both the reinforcement in the particle (Ω_3) and the particle phase itself (Ω_{23}) feel the influence of the average stress and strain in the matrix phase in the same way that the isolated double inclusion feels the far-field applied stress and strain. This is a generalization of the assumption used by Mori and Tanaka (1973) to estimate the average stress in a matrix containing precipitates with eigenstrains and widely generalized and used in the analysis of composite materials. See Benveniste (1987) for a reformulation of the method for two-phase composites similar to the one proposed here. Mathematically this assumption can be phrased as follows:

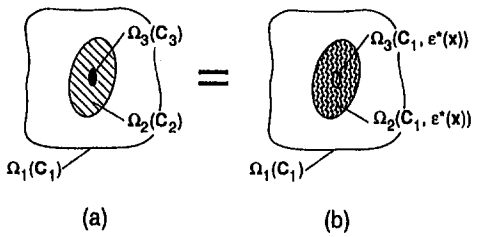


Fig. 2 Schematic showing (*a*) an isolated double inhomogeneity, and (*b*) an equivalent isolated double inclusion

Downloaded 04 May 2010 to 171.66.16.28. Redistribution subject to ASME license or copyright; see http://www.asme.org/terms/Terms_Use.cfm

$$\bar{\boldsymbol{\epsilon}}_3 = \mathbf{A}_3^{di}\bar{\boldsymbol{\epsilon}}_1 = \mathbf{A}_3\boldsymbol{\epsilon}^0 \quad \bar{\boldsymbol{\epsilon}}_{23} = \mathbf{A}_{23}^{di}\bar{\boldsymbol{\epsilon}}_1 = \mathbf{A}_{23}\boldsymbol{\epsilon}^0. \tag{12}$$

Here the $\mathbf{A}_i$ (without a superscript) denote the concentration factors better suited for finite concentrations. To solve for $\mathbf{A}_3$ and $\mathbf{A}_{23}$, recall that

$$c_1\bar{\boldsymbol{\epsilon}}_1 + (c_2 + c_3)\bar{\boldsymbol{\epsilon}}_{23} = c_1\bar{\boldsymbol{\epsilon}}_1 + c_2\bar{\boldsymbol{\epsilon}}_2 + c_3\bar{\boldsymbol{\epsilon}}_3 = \boldsymbol{\epsilon}^0. \tag{13}$$

Substitution of Eqs. (12) into Eqs. (13), followed by some manipulation, yields

$$\mathbf{A}_3 = \mathbf{A}_3^{di}[c_1\mathbf{I} + (c_2 + c_3)\{\mathbf{A}_{23}^{di}\}]^{-1},$$
$$\mathbf{A}_{23} = \mathbf{A}_{23}^{di}[c_1\mathbf{I} + (c_2 + c_3)\{\mathbf{A}_{23}^{di}\}]^{-1}. \tag{14}$$

Substitution of Eqs. (11) and (14) into Eq. (10) then yields the effective moduli of the three-phase composite consisting of a matrix reinforced by two-phase particles:

$$\mathbf{C} = \mathbf{C}_1 + [(c_2 + c_3)\{(\mathbf{C}_2 - \mathbf{C}_1)\mathbf{A}_{23}^{di}\} + c_3\{(\mathbf{C}_3 - \mathbf{C}_2)\mathbf{A}_3^{di}\}]\cdot[c_1\mathbf{I} + (c_2 + c_3)\{\mathbf{A}_{23}^{di}\}]^{-1}. \tag{15}$$

Equation (15) is an explicit, diagonally symmetric equation for $\mathbf{C}$ in terms of the volume fractions and elastic constants of each phase and the shapes of Ω_2 and Ω_3. This is clearly seen as all terms in curly brackets are isotropic, being averages over all orientations, and the only other tensorial terms, $\mathbf{I}$ and $\mathbf{C}_1$ are diagonally symmetric.

4 Measurements

4.1 Materials. Seven Al_2O_3/mullite/Al composites were obtained from a commercial source. The particles were approximately spherical and consisted of Al_2O_3 reinforced mullite as shown in Fig. 1. The dispersed Al_2O_3 phase was roughly in the form of short rods with an average aspect ratio of four. The volume fraction of Al_2O_3 in the mullite, $c_3/(c_2 + c_3)$, was 20 percent. Specimens contained three average Al_2O_3/mullite particle diameters: 30, 45, and 100 μm. Table 1 shows the elastic moduli and density of the three constituents. The elastic properties of the 6061 aluminum alloy and the mullite were measured while those of the Al_2O_3 were obtained from polycrystalline estimates using Hill's (1952) arithmetic-averaging method and the monocrystal elastic constants of Tefft (1966). The Al_2O_3/mullite particle volume fractions were obtained by quantitative metallography and ranged from 14.5 percent to 24.0 percent.

4.2 Elastic Constants. Elastic constants were determined using two measurement methods; (i) pulse-echo and (ii) rod-resonance. With the pulse-echo method, the velocities of longitudinal and shear waves were measured and then the elastic constants were computed from the general relationship

$$C = \rho v^2. \tag{23}$$

Here C denotes an elastic stiffness constant (C_{11} or C_{44} since the composite is macroscopically isotropic) and ρ its mass density which was measured by Archimedes' method using distilled water and is well described by a rule of mixtures. Details of the pulse-echo method were given previously by Ledbetter et al. (1980). Briefly, velocities were measured along the rod axis of 1 cm long, 1.5-cm dia. cylinders by launching an ultrasonic pulse in the low-megahertz frequency range and measuring the transit time between subsequent sound echoes with an oscilloscope. Macroscopic isotropy was verified by machining some of the cylinders into parallelepipeds and measuring the nine principal sound velocities. These results indicated that texture effects were insignificant. The rod-resonance method entails measuring the kilohertz-range resonance of rod specimens (4-mm dia., 5 cm long). Details of this composite-oscillator method are given by Marx (1951) and Ledbetter (1980). The measurements directly yield the specimen compliance S_{ii} from which Young's modulus is obtained by inversion

$$E_{ii} = 1/S_{ii} \quad \text{(no sum on } i\text{)}. \tag{23}$$

For these materials, by these methods, the measurement uncertainties are typically about 2:1000. In both cases the transducer-specimen bond was phenyl salicylate. All resonance measurements were made at 50 kHz. Pulse-echo measurements were made at 3-9 MHz. No dispersion appeared in either case.

Table 1 Constituent properties

	B (GPa)	G (GPa)	E (GPa)	ν	ρ (g/cm³)
6061 Al	74.1	27.1	72.4	0.337	2.704
Mullite	173.9	89.5	229.1	0.280	3.168
Al_2O_3	252.0	163.0	403.0	0.234	3.986

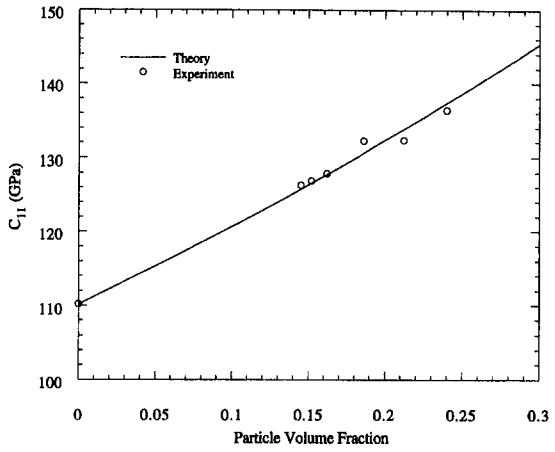


Fig. 3 Elastic constant C_{11} of the composite as a function of the Al_2O_3/mullite particle volume fraction where the volume fraction of Al_2O_3 in mullite is 20 percent. Circles denote values obtained from pulse-echo measurements.

5 Results

Figures 3 and 4 show the elastic constants C_{11} and $G = C_{44}$ of the seven Al_2O_3/mullite/Al composites as determined by the pulse-echo method. The corresponding analytical predictions obtained from the analysis presented in Section 2 and Section 3 and using an aspect ratio of four for the Al_2O_3 particles are also

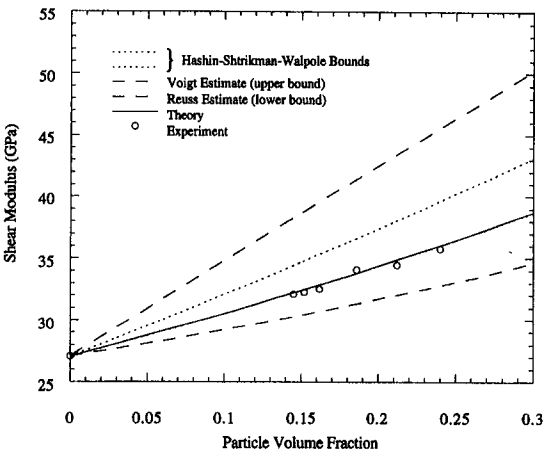


Fig. 4 Shear modulus $G = C_{44}$ of the composite as a function of the Al_2O_3/mullite particle volume fraction where the volume fraction of Al_2O_3 in mullite is 20 percent. Circles denote values obtained from pulse-echo measurements.

Downloaded 04 May 2010 to 171.66.16.28. Redistribution subject to ASME license or copyright; see http://www.asme.org/terms/Terms_Use.cfm

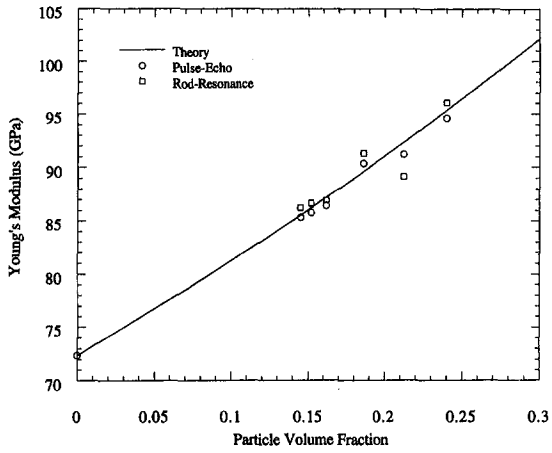


Fig. 5 Young's modulus E of the composite as a function of the Al_2O_3/mullite particle volume fraction where the volume fraction of Al_2O_3 in mullite is 20 percent. Circles and squares denote values obtained from pulse-echo and rod-resonance measurements, respectively.

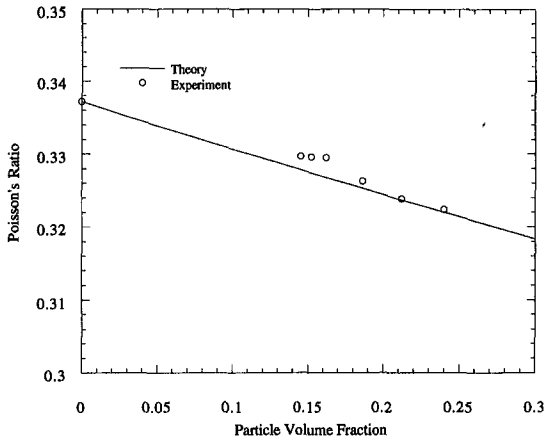


Fig. 7 Poisson's ratio ν of the composite as a function of the Al_2O_3/mullite particle volume fraction where the volume fraction of Al_2O_3 in mullite is 20 percent. Circles denote values obtained from pulse-echo measurements.

shown by solid lines. Theoretical predictions are in excellent agreement with the measured elastic constants; the relative difference between the two is less than two percent for all cases. Figure 5 shows Young's modulus of the composites with both the measurements made directly from the rod-resonance method and those computed in the standard manner from C_{11} and $G = C_{44}$ as obtained from the pulse-echo method. Figures 6 and 7 show the bulk modulus and Poisson's ratio of the composite computed from both the measured and predicted C_{11} and $G = C_{44}$ by using the standard relationships between the elastic constants for an isotropic material. In Figs. 4 and 6, predictions corresponding to both the Voigt (1889) and Reuss (1929) estimates of the effective bulk and shear moduli of the composite are shown. In addition, for both the bulk and shear moduli, the Hashin-Shtrikman (1963)–Walpole (1969) lower and upper bounds are shown. These were computed from equations given by Walpole (1969) using the phase properties given in Table 1 and the constant value of $c_3/(c_2 + c_3) = 0.2$. In Fig. 6 we have also shown Qiu and Weng's (1991) exact solution for the effective bulk modulus a composite with a microgeometry consisting of a progressively filled assemblage of thickly coated spherical particles.

6 Discussion

Agreement between analytical predictions and measurements is excellent; the maximum discrepancy in C_{11} is less than two percent and that in $G = C_{44}$ is less than one percent. The scatter in Young's modulus as measured by rod resonance is slightly larger than that obtained from pulse-echo measurements. Nevertheless, the agreement with the theoretical predictions is excellent. Within the range of measurement uncertainty, there is no dependence of the elastic constants on the average particle size which was 30, 45, or 100 μm in the various specimens. This is expected as the experimental ultrasonic wavelengths are long compared to the particle sizes.

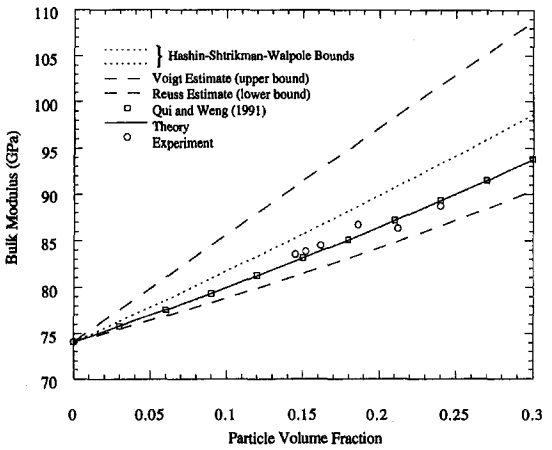


Fig. 6 Bulk modulus B of the composite as a function of the Al_2O_3/mullite particle volume fraction where the volume fraction of Al_2O_3 in mullite is 20 percent. Circles denote values obtained from pulse-echo measurements.

To further study the soundness of the theoretical approach, we focus on Figs. 4 and 6, the shear and bulk moduli, respectively. The analytical predictions are well within the Voigt and Reuss estimates, which are quite wide, approximately 40 percent of the actual value at a particle volume fraction of 25 percent. Both the analytical predictions and experimental results are poorly described by these estimates. The Hashin-Shtrikman-Walpole bounds are significantly tighter than the Voigt-Reuss estimates. In fact, for both the bulk and shear moduli, the analytical predictions are indistinguishable from the lower bound at the resolution of the plot. The predictions, however, are slightly above the lower bound in all cases. Qiu and Weng's (1991) exact solution for the effective bulk modulus of the thickly coated sphere assemblage is also slightly above the Hashin-Shtrikman-Walpole bounds, but also is indistinguishable from the lower bound at the resolution of the plot. The microstructure of the composite, which consists of short Al_2O_3 rods embedded in mullite which is in turn embedded in Al, is quite complicated. Nevertheless, it is macroscopically isotropic. As such we think that the Hashin-Shtrikman-Walpole bounds are the most appropriate bounds with which to compare the analytical predictions as they consider only the phase properties and concentrations. Tighter bounds (in some cases) have been obtained by Qiu and Weng (1991) for the shear modulus of the thickly coated sphere assemblage, and they have suggested that the narrower of the Qiu-Weng and the Hashin-Shtrikman-Walpole bounds be used in practice. The Qiu-Weng bounds, however, are obtained for a specific microstructure, namely an assemblage of spherical particles concentrically embedded in a second spherical shell which progressively fills the matrix material. As such they contain more detailed information regarding the microstructure than the Hashin-Shtrikman-Walpole bounds and should be expected to be tighter. These bounds are not applicable to the present theory which considers that the particles contain randomly oriented spheroidal inclusions which are not necessarily surrounded by a concentric shell. Nevertheless, it is of interest to compare the results of the present theory with Qiu and Weng's (1991) bounds when the aspect ratio of both inclusions in the

Downloaded 04 May 2010 to 171.66.16.28. Redistribution subject to ASME license or copyright; see http://www.asme.org/terms/Terms_Use.cfm

present case are taken to be unity. We have carried out such a comparison for the six cases studied by Qiu and Weng which consist of six different particle/coating/matrix Young's modulus ratios with a fixed value of Poisson's ratio of 0.3 for all phases and a constant coating-to-particle concentration ratio of 0.2. These composite systems allow for all possible combinations of soft and stiff particles, coatings, and matrices. Our results show that when the matrix is the hardest (softest) phase, our predictions virtually coincide (to within four digits of our numerical calculations) with the corresponding Hashin-Shtrikman-Walpole upper (lower) bounds. In these cases, the Qiu-Weng bounds lie inside the Hashin-Shtrikman-Walpole bounds for nearly the entire range of concentrations, i.e., the Hashin-Shtrikman-Walpole upper (lower) bounds are lower (higher) than the Qiu-Weng bounds. When the coating phase is the hardest or softest (Figs. 1*b*, *d*), our analytical predictions lie well within the Hashin-Shtrikman-Walpole bounds, almost right in the middle, but are outside the corresponding Qiu-Weng bounds. It is in this case that the Qiu-Weng bounds are extremely close and exhibit the interesting behavior of diverging then converging to the point of actually coinciding, and then diverging again. We contribute the difference between our predictions and the Qiu-Weng bounds to the difference in microstructure upon which the Qiu-Weng bounds are based. Finally, we note that our numerical studies have shown that our predictions lie safely inside the Hashin-Shtrikman-Walpole bounds when the aspect ratio of the particle is not spherical.

Because of the nature of the material considered here, which is essentially two composites, one within another, it is of interest to compute the effective elastic moduli of the composite by analyzing the particles as a two-phase composite and subsequently using the effective properties so obtained as those of the particles in a second two-phase composite. We performed these calculations for two methods appropriate to two-phase composites: (i) the Mori-Tanaka (1973) mean-field approach (see also Benveniste (1987) and Chen et al. (1992) for details and explicit equations) based on estimating the average stress in the matrix of the composite at finite concentrations; and (ii) the Ledbetter-Datta (1986) model obtained in the low-frequency limit of an ensemble-averaged multiple-scattering theory. For both approaches, the predicted properties of the composite were also in good agreement with the measured results. This is not too surprising, because both the composite particle and the actual composite itself are matrix-based composites containing modest concentrations of reinforcement, 15-25 percent.

The approach of using a two-phase composite model twice would not be expected to be as successful in analyzing such problems as thermal expansion or internal stresses in these composites. As an extreme example, if a composite were reinforced with particles that contained voids, as predicted by two applications of a two-phase model, the voids in the particle domain would not affect the thermal-expansion coefficient of the particle and thus would not affect the thermal-expansion coefficient of the composite. They would, however, have an effect when the concentration factors based on the double-inclusion model were used. Similar shortcomings would also exist when using a two-phase model twice with regard to the self equilibrium of internal stresses. We think that the mechanical concentration factors presented in this work more accurately consider the fact that the reinforcement in the particles (the Al_2O_3) is actually embedded in the particle matrix (mullite) and is not in contact with the matrix (Al) and thus are better suited for the analysis of composites reinforced by composite particles. Finally, although the proposed micromechanics theory can account for the shape and volume fraction of both the particles and the dispersed phase in the particles, space limitations preclude a comprehensive parametric study.

7 Conclusions

A theoretical approach was developed to predict the effective elastic moduli of composite materials consisting of a matrix reinforced by two-phase particles. Explicit expressions were obtained for the effective moduli in terms of phase concentration factors, which account for the shape and volume fraction of both the particles and the dispersed phase in the particle, and are estimated by a micromechanics theory. In an attempt to more accurately describe the physical situation where the particles themselves are two-phase matrix-based composites, the proposed micromechanics model is based on the recent results of Hori and Nemat-Nasser (1993) for the average elastic fields in a double inclusion. In particular, the strain concentration factors at finite concentrations are estimated by assuming they are given by the average strain in an isolated double inclusion subjected to a far-field load equivalent to the average strain in the matrix. The theoretical estimates are diagonally symmetric and lie within the Hashin-Shtrikman-Walpole bounds for all cases considered. Theoretical predictions are in excellent agreement with measured elastic constants of a macroscopically isotropic composite consisting of an Al matrix reinforced by spherical mullite/Al_2O_3 particles, where the Al_2O_3 phase was in the form of short rods and randomly oriented in the mullite. Elastic constant measurements made by pulse-echo and rod-resonance methods were internally consistent and showed no dependence on particle size.

Acknowledgments

S. Kim (NIST) helped with measurements. Materials were supplied by Comalco Research Centre (Thomastown, Australia), where the assistance of Dr. M. Couper is gratefully acknowledged.

References

Benveniste, Y., 1987, "A New Approach to the Application of Mori-Tanaka's Theory in Composite Materials," *Mechanics of Materials,* Vol. 6, pp. 147–157.

Benveniste, Y., Dvorak, G. J., and Chen, T., 1991, "On Diagonal Symmetry of the Approximate Effective Stiffness Tensor of Heterogeneous Media," *Journal of the Mechanics and Physics of Solids,* Vol. 39, pp. 927–946.

Chen, T., Dvorak, G. J., and Benveniste, Y., 1992, "Mori-Tanaka Estimates of the Overall Elastic Moduli of Certain Composite Materials," ASME JOURNAL OF APPLIED MECHANICS, Vol. 59, pp. 539–546.

Eshelby, J. D., 1957, "The Determination of the Elastic Field of an Ellipsoidal Inclusion, and Related Problems," *Proceedings of the Royal Society of London,* Vol. A241, pp. 376–396.

Hashin, Z., and Shtrikman, T., 1963, "A Variational Approach to the Elastic Behavior of Multiphase Materials," *Journal of the Mechanics and Physics of Solids,* Vol. 11, pp. 127–140.

Hill, R., 1952, "The Elastic Behavior of a Crystalline Aggregate," *Proceedings of the Physical Society,* Vol. A65, pp. 349–354.

Hill, R., 1963, "Elastic Properties of Reinforced Solids: Some Theoretical Principles," *Journal of the Mechanics and Physics of Solids,* Vol. 11, pp. 357–372.

Hori, M., and Nemat-Nasser, S., 1993, "Double-Inclusion Model and Overall Moduli of Multi-Phase Composites," *Mechanics of Materials,* Vol. 14, pp. 189–206.

Ledbetter, H. M., 1980, "Dynamic Elastic Modulus and Internal Friction in G10-CR and G-11CR Fiberglass-Cloth-Epoxy Composites," *Cryogenics,* Vol. 20, pp. 637–640.

Ledbetter, H. M., and Datta, S. K., 1986, "Effective Wave Speeds in a SiC-Particle-Reinforced Al Composite," *Journal of the Acoustical Society of America,* Vol. 79, pp. 239–248.

Ledbetter, H. M., Frederick, N. V., and Austin, M. W., 1980, *Journal of Applied Physics,* Vol. 51, p. 305.

Luo, H. A., and Weng, G. J., 1987, "On Eshelby's Inclusion Problem in a Three-Phase Spherically Concentric Solid and a Modification of Mori-Tanaka's Method," *Mechanics of Materials,* Vol. 6, pp. 347–361.

Marx, J., 1951, "Use of the Piezoelectric Gauge for Internal Friction Measurements," *Review of Scientific Instruments,* Vol. 22, p. 503.

Mori, T., and Tanaka, K., 1973, "Average Stress in Matrix and Average Elastic Energy of Materials With Misfitting Inclusions," *Acta Metallurgica,* Vol. 21, pp. 571–574.

Mura, T., 1987, *Micromechanics of Defects in Solids,* 2nd ed., Martinus Nijhoff, The Hague.

Nemat-Nasser, S., and Hori, M., 1993, *Micromechanics: Overall Properties of Heterogeneous Materials,* Elsevier, New York.

Downloaded 04 May 2010 to 171.66.16.28. Redistribution subject to ASME license or copyright; see http://www.asme.org/terms/Terms_Use.cfm

Qiu, Y. P., and Weng, G. J., 1991, "Elastic Moduli of Thickly Coated Particle and Fiber-Reinforced Composites," ASME JOURNAL OF APPLIED MECHANICS, Vol. 58, pp. 388–398.

Reuss, A., 1929, "Berechnung der Fliessgrenze von Mischkristallen auf Grund der Plastizitätsbedingung für Einkristalle," *Zeitschrift für angewandte Mathematik und Mechanik,* Vol. 9, pp. 49–58.

Tanaka, K., and Mori, T., 1972, "Note on Volume Integrals of the Elastic Field Around an Ellipsoidal Inclusion," *Journal of Elasticity,* Vol. 2, pp. 199–200.

Tefft, W. E., 1966, "Elastic Constants of Single Crystal Corundum," *Journal of Research of the National Bureau of Standards,* Vol. 70A, pp. 277–280.

Voigt, W., 1889, "Ueber die Beziehung zwischen den beiden Elastizitätskonstanten isotroper Körper," *Annalen der Physik,* Vol. 38, pp. 573–587.

Walpole, L. J., 1969, "On the Overall Elastic Moduli of Composite Materials," *Journal of the Mechanics and Physics of Solids,* Vol. 17, pp. 235–251.

APPENDIX

A Dilute Approximation: Double Inclusion Model

Hori and Nemat-Nasser (1993) used the equivalent-inclusion idea of Eshelby (1957) to simulate the double inhomogeneity in Fig. 2(*a*) by the equivalent double inclusion containing an appropriate distribution of eigenstrains as shown in Fig. 2(*b*). In particular, when the composite is subjected to an applied uniform stress $\boldsymbol{\epsilon}^0$, the equivalency criterion can be expressed as

$$\begin{aligned}&\boldsymbol{\sigma}^0 + \boldsymbol{\sigma}^p(\mathbf{x})\\ &\quad = \mathbf{C}_3[\boldsymbol{\epsilon}^0 + \boldsymbol{\epsilon}^p(\mathbf{x})] = \mathbf{C}_1[\boldsymbol{\epsilon}^0 + \boldsymbol{\epsilon}^p(\mathbf{x}) + \boldsymbol{\epsilon}^*(\mathbf{x})] \quad \text{for } \mathbf{x} \in \Omega_3,\\ &\quad = \mathbf{C}_2[\boldsymbol{\epsilon}^0 + \boldsymbol{\epsilon}^p(\mathbf{x})] = \mathbf{C}_1[\boldsymbol{\epsilon}^0 + \boldsymbol{\epsilon}^p(\mathbf{x}) + \boldsymbol{\epsilon}^*(\mathbf{x})] \quad \text{for } \mathbf{x} \in \Omega_2,\\ &\quad = \mathbf{C}_1[\boldsymbol{\epsilon}^0 + \boldsymbol{\epsilon}^p(\mathbf{x})] \quad \text{for } \mathbf{x} \in \Omega_1.\end{aligned} \tag{A1}$$

Here $\boldsymbol{\sigma}^p(\mathbf{x})$ and $\boldsymbol{\epsilon}^p(\mathbf{x})$ are the position-dependent perturbations (denoted by the explicit dependence on position $\mathbf{x}$) of the otherwise uniform fields $\boldsymbol{\sigma}^0 = \mathbf{C}_1\boldsymbol{\epsilon}^0$, and $\boldsymbol{\epsilon}^*(\mathbf{x})$ is the eigenstrain field required to simulate the double inhomogeneity (the first right-hand side) by the equivalent double inclusion (the second right-hand side) and is identically zero outside $\Omega_{23} = \Omega_2 + \Omega_3$. The perturbation strain caused by an eigenstrain distribution in Ω_{23} is obtained using a Green's function approach (see Mura (1987) for details of the general approach)

$$\boldsymbol{\epsilon}^p_{ij}(\mathbf{x}) = -\tfrac{1}{2}\int_{\Omega_{23}} C_{1_{klmn}}\boldsymbol{\epsilon}^*_{mn}(\mathbf{x})[G_{ik,lj}(\mathbf{x} - \mathbf{x}') + G_{jk,li}(\mathbf{x} - \mathbf{x}')]d\mathbf{x}'. \tag{A2}$$

Here $G_{ij}(\mathbf{x} - \mathbf{x}')$ denotes the well-known infinite-body Green's function for an elastic solid and a comma denotes partial differentiation. Substitution of Eq. (A2) into Eqs. (A1) results in integral equations for the unknown $\boldsymbol{\epsilon}^*(\mathbf{x})$, which in general must be solved numerically after specifying the relative positions and orientations of Ω_2 and Ω_3.

Rather than solve these equations directly, Hori and Nemat-Nasser (1993) used the Tanaka-Mori (1972) theorem for volume integrals of the elastic field around an ellipsoid to obtain closed-form expressions for the *average* elastic fields in terms of the average eigenstrains in each phase (see Mura (1987) for additional discussion of the Tanaka-Mori theorem). The essence of the Tanaka-Mori theorem is that certain volume integrals (and thus averages) around an inclusion of the strain caused by eigenstrains in the inclusion can be simply expressed without knowing the explicit spatial dependence of the strain. Using the Tanaka-Mori theorem, Hori and Nemat-Nasser showed that the average of the perturbation strain in each phase is

$$\begin{aligned}\bar{\boldsymbol{\epsilon}}^p_3 &= \mathbf{S}_3\bar{\boldsymbol{\epsilon}}^*_3 + [\mathbf{S}_2 - \mathbf{S}_3]\bar{\boldsymbol{\epsilon}}^*_2,\\ \bar{\boldsymbol{\epsilon}}^p_2 &= \mathbf{S}_2\bar{\boldsymbol{\epsilon}}^*_2 + \frac{c_3}{c_2}[\mathbf{S}_2 - \mathbf{S}_3][\bar{\boldsymbol{\epsilon}}^*_3 - \bar{\boldsymbol{\epsilon}}^*_2],\\ \bar{\boldsymbol{\epsilon}}^p_{23} &= \mathbf{S}_2\bar{\boldsymbol{\epsilon}}^*_{23}.\end{aligned} \tag{A3}$$

Here $\mathbf{S}_3$ and $\mathbf{S}_2$ are Eshelby's (1957) tensor (explicit expressions are given by Mura (1987)) calculated using the domains Ω_3 and $\Omega_{23} = \Omega_2 + \Omega_3$, respectively, and both computations are based on the elastic moduli of the matrix, that is, $\mathbf{S}_3 = \mathbf{S}_3(\Omega_3, \mathbf{C}_1)$ and $\mathbf{S}_2 = \mathbf{S}_2(\Omega_{23}, \mathbf{C}_1)$. Taking the volume average of Eqs. $(A1)_{1,2}$ yields the two equivalency equations that can be solved simultaneously for $\bar{\boldsymbol{\epsilon}}^*_2$ and $\bar{\boldsymbol{\epsilon}}^*_3$ to yield

$$\bar{\boldsymbol{\epsilon}}^*_3 = \Phi_3\boldsymbol{\epsilon}^0 \quad \bar{\boldsymbol{\epsilon}}^*_2 = \Phi_2\boldsymbol{\epsilon}^0 \quad \bar{\boldsymbol{\epsilon}}^*_{23} = \Phi_{23}\boldsymbol{\epsilon}^0. \tag{A4}$$

The fourth-order tensors Φ_i are given by

$$\begin{aligned}\Phi_3 = -\Bigg[&(\mathbf{S}_2 + \mathbf{E}_3) + \Delta\mathbf{S}\left(\mathbf{S}_3 - \frac{c_3}{c_2}\Delta\mathbf{S} + \mathbf{E}_2\right)^{-1}\\ &\times\left(\mathbf{S}_3 - \frac{c_3}{c_2}\Delta\mathbf{S} + \mathbf{E}_3\right)\Bigg]^{-1},\\ \Phi_2 = -\Bigg[&\Delta\mathbf{S} + (\mathbf{S}_3 + \mathbf{E}_3)\left(\mathbf{S}_3 - \frac{c_3}{c_2}\Delta\mathbf{S} + \mathbf{E}_3\right)^{-1}\\ &\times\left(\mathbf{S}_3 - \frac{c_3}{c_2}\Delta\mathbf{S} + \mathbf{E}_2\right)\Bigg]^{-1},\\ \Phi_{23} = &\frac{c_3}{c_2 + c_3}\Phi_3 + \frac{c_2}{c_2 + c_3}\Phi_2.\end{aligned} \tag{A5}$$

In Eq. (A5)

$$\begin{aligned}&\mathbf{E}_3 = (\mathbf{C}_3 - \mathbf{C}_1)^{-1}\mathbf{C}_1 \quad \mathbf{E}_2 = (\mathbf{C}_2 - \mathbf{C}_1)^{-1}\mathbf{C}_1\\ &\Delta\mathbf{S} = \mathbf{S}_3 - \mathbf{S}_2.\end{aligned} \tag{A6}$$

As noted by Hori and Nemat-Nasser (1993), $\bar{\boldsymbol{\epsilon}}^*_3$ is the exact volume average of the eigenstrain $\boldsymbol{\epsilon}^*_3$ while $\bar{\boldsymbol{\epsilon}}^*_2$ is an approximation to the eigenstrain $\boldsymbol{\epsilon}^*_2$. Justification for the approximation involves the assumption that the term in $\bar{\boldsymbol{\epsilon}}^*_2$ involving the integration over Ω_2 of the inner product of $(\bar{\boldsymbol{\epsilon}}^*_2 - \boldsymbol{\epsilon}^*_2)$ and the second spatial derivatives of the infinite-body Green's functions can be neglected ($\bar{\boldsymbol{\epsilon}}^*_2 - \boldsymbol{\epsilon}^*_2$ itself vanishes identically). This term corresponds, in part, to the geometry of Ω_2 and the position and orientation of Ω_3 in Ω_2 and thus affects the actual boundary conditions on the surface of Ω_3. As argued by Hori and Nemat-Nasser, this term would vanish when an ensemble of boundary conditions on the surface of Ω_3 was considered. This corresponds to the average fields obtained when random distributions of orientations and positions of Ω_3 in Ω_2 were considered and thus is most appropriate in the present context where these assumptions are reasonable.

Downloaded 04 May 2010 to 171.66.16.28. Redistribution subject to ASME license or copyright; see http://www.asme.org/terms/Terms_Use.cfm

Transient Analysis of Dynamic Crack Propagation With Boundary Effect

Chien-Ching Ma
Professor.

Yi-Shyong Ing
Graduate Student.

Department of Mechanical Engineering,
National Taiwan University,
Taipei, Taiwan 10617
R.O.C.

In this study, a dynamic antiplane crack propagation with constant velocity in a configuration with boundary is investigated in detail. The reflected cylindrical waves which are generated from the free boundary will interact with the propagating crack and make the problem extremely difficult to analyze. A useful fundamental solution is proposed in this study and the solution is determined by superposition of the fundamental solution in the Laplace transform domain. The proposed fundamental problem is the problem of applying exponentially distributed traction (in the Laplace transform domain) on the propagating crack faces. The Cagniard's method for Laplace inversion is used to obtain the transient solution in time domain. Numerical results of dynamic stress intensity factors for the propagation crack are evaluated in detail.

1 Introduction

Most of the analyses done regarding cracked bodies are quasi-static. There are numerous situations that the material inertia becomes significant and must be taken into account in the analyses. The question of whether or not inertial effects are significant depends on the loading conditions and the geometrical configuration of the body. Inertial effects can arise either from applying dynamic loading on a cracked solid or from rapid crack propagation. The inherent time dependence of a dynamic fracture process results in mathematical models that are more complex than equivalent quasi-static models. However, there is substantial interest in the dynamic fracture problem due to its importance in many engineering applications. The problem is encountered in impact damage to fan blades, automotive and aircraft windshields. There is also considerable interest in the problem of arrest of a fast running crack, especially in large structures like pipelines, ships, and nuclear reactors.

The main purpose in solving problems concerned with dynamic crack propagation is to determine the dependence of the crack-tip field characterizing parameters on the applied loading and on the configuration of the body. The investigation of a propagation crack in a brittle solid began with the pioneering analysis of Yoffe (1951). She considered a steady-state crack growth problem of a crack of fixed length propagating in an infinite elastic body subjected to a uniform remote tensile loading normal to the crack line. Although this is a physically unrealistic problem, it did at least provide an indication of the influence of crack speed on the stress state of a rapidly propagating crack. Craggs (1960) considered a semi-infinite crack extending at constant speed, with the crack face loading moving with the same speed as the crack tip in such a way that the entire deformation field is constant as seen by an observer moving with the crack tip. The self-similar dynamic crack propagation problem was contributed by Broberg (1960) who was among the first to present detailed analyses of crack propagation as a transient process. He solved the dynamic problem of a crack that suddenly grows from zero length at a constant speed. Baker (1962) subsequently generalized Broberg's solution to include a finite initial crack. Although the aforementioned artificial solutions have no direct application, they also have provided useful insights and continue to be used today for the assessment of dynamic numerical analyses.

In a series of papers, Freund (1972a, 1972b, 1973, 1974) developed important analytical methods for evaluation of the transient stress field of a propagating crack in a two-dimensional geometric configuration under quite general dynamic loading situation. These particular cases analyzed by Freund are also self-similar, but they are solved by means of integral transform methods rather than by direct application to similarity arguments. An indirect analytical approach proposed by Freund based on superposition over a fundamental solution, which opens a way for analysis of certain problems of crack propagation at nonuniform speed. Based on the superposition method proposed by Freund, a series of problems for nonplanar crack propagation in an infinite domain was solved by Ma and Burgers (1986, 1987, 1988) and Ma (1988, 1990). The structure of the near-tip field of crack propagation at nonuniform speeds was discussed in detail by Freund and Rosakis (1992). A representation of the crack-tip field was obtained in the form of an expansion about the crack tip in powers of radial coordinate, with the coefficients depending on the time rates of change of crack-tip speed and stress intensity factor. This representation was used to interpret some experimental observations and some estimates were made of the practical limits of using a stress intensity factor field alone to characterize the local fields.

Most of the solved dynamic fracture problems are regarded as a crack subjected to applying a uniformly distributed dynamic loading on the crack faces or subjected to incident plane waves. For the aforementioned problems, either the direct application of the well-known Wiener-Hopf technique is used or the superposition method proposed by Freund is performed to solve the problems. However, if a crack is subjected to incident nonplanar waves, none of the known methods can be used to obtain the transient solutions. Recently Tsai and Ma (1992) proposed a new fundamental solution to overcome these difficulties. The fundamental problem they considered is an exponentially distributed traction applied on crack faces and the solution is constructed by superposition of the fundamental solution in the Laplace transform domain. Tsai and Ma (1992) used this new fundamental solution to obtain the transient solution for a stationary semi-infinite crack subjected to a suddenly applied dy-

Contributed by the Applied Mechanics Division of THE AMERICAN SOCIETY OF MECHANICAL ENGINEERS for publication in the ASME JOURNAL OF APPLIED MECHANICS.

Discussion on this paper should be addressed to the Technical Editor, Professor Lewis T. Wheeler, Department of Mechanical Engineering, University of Houston, Houston, TX 77204-4792, and will be accepted until four months after final publication of the paper itself in the ASME JOURNAL OF APPLIED MECHANICS.

Manuscript received and accepted by the ASME Applied Mechanics Division, Jan. 4, 1994. Associate Technical Editor: X. Markenscoff.

Copyright © 1995 by ASME

Downloaded 04 May 2010 to 171.66.16.28. Redistribution subject to ASME license or copyright; see http://www.asme.org/terms/Terms_Use.cfm

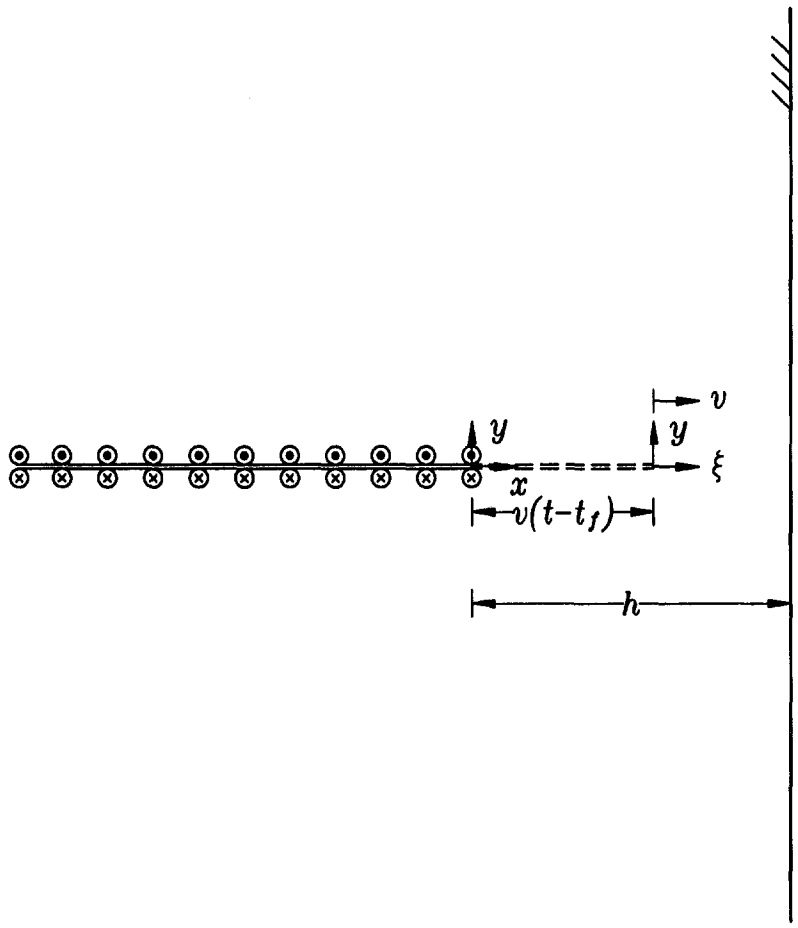


Fig. 1 Coordinate systems of a propagating crack in the configuration with vertical boundary

namic inplane body force in an unbounded medium. This alternative fundamental solution is also successfully applied towards solving more complicated transient problems (Tsai and Ma, 1993a, 1993b; Ma and Chen, 1994) for a subsurface stationary inclined crack subjected to dynamic loadings.

Determination of the dependence of the dynamic stress intensity factor on body configuration and applied loading during rapid crack propagation is a principal objective in dynamic fracture. Analytical results for configurations with boundaries other than the crack faces are rare. It was noted that after the stress waves reflected from the boundaries arrived at the crack tip, the nature of crack propagation changed. The interaction of stress waves with propagating cracks provides a way of altering the crack-tip stress field, and thus provide the basis for the crack branching phenomenon. Dynamic analysis of a mode III crack in a strip was discussed in a paper by Nilsson (1973). He considered the problem of a semi-infinite crack in a strip of finite width subjected to a uniformly distributed static load and propagating with a constant velocity, only the stress intensity factor and its time dependence was determined.

Since the interaction of stress waves with a propagating crack is an important event, we shall investigate it in greater detail in the following. In this study, we will extend the methodology that was used successfully in solving dynamic stationary crack problem to construct the transient solution for crack propagation in the configuration with boundary. Two different cases will be considered in this study in some detail. The first problem considered in this study is a horizontal semi-infinite crack propagating with constant velocity towards a vertical free boundary as shown in Fig. 1. The second problem is a horizontal semi-infinite crack propagates in a strip with finite width as shown in Fig. 2. In analyzing the aforementioned problems, free boundary and propagating crack are involved into the analysis. The interaction of the reflected waves generated from the free boundary and the propagating crack must be taken into account which will make the analysis extremely difficult. A useful fundamental solution is proposed to overcome these difficulties. This proposed fundamental solution is successfully applied towards solving the problem and is demonstrated as an efficient methodology to solve similar problems. Since the stress intensity factor is the key parameter in characterizing dynamic crack grows, we will focus our attention mainly on the determination of the dynamic stress intensity factor.

2 Required Fundamental Solutions

As usual in problems of the type considered here, superposition of solutions plays a significant role. The solutions of the problem considered in this study can be determined by superposition of the following problems. Problem A treats a dynamic uniformly distributed traction acting on semi-infinite crack faces in an unbounded medium at time $t = 0$, at $t = t_f$, a new crack propagates out of the original semi-infinite crack with constant velocity, which induces a traction on the plane that will eventually define the vertical or horizontal half-plane boundary. In problem B, a semi-infinite half-plane is considered in which the boundary is subjected to tractions which are equal and opposite to those on the corresponding planes in problem A. Problem C considers an infinite body containing a propagating semi-infinite crack in which the crack face is subjected to the reflected waves which are generated by the half-plane boundary in problem B. The three fundamental problems A, B, and C, which are

Downloaded 04 May 2010 to 171.66.16.28. Redistribution subject to ASME license or copyright; see http://www.asme.org/terms/Terms_Use.cfm

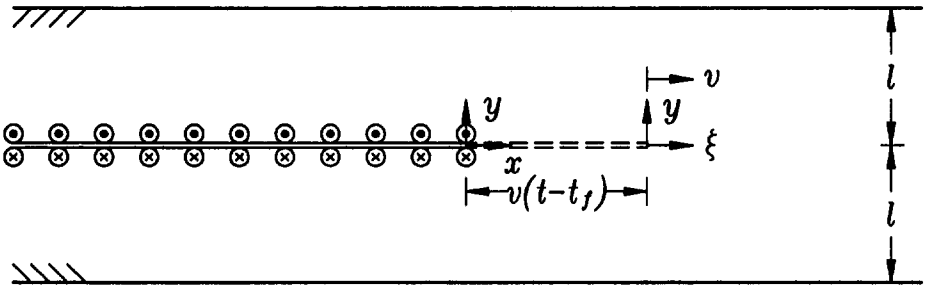


Fig. 2 Configuration and coordinate systems of a propagating crack in a finite strip

superimposed to obtain the solution for propagating crack interaction with stress wave, are shown in Fig. 3. The reflected waves induced from the half-plane boundary as indicated in problem B, can be easily obtained by employing the method of images. While problem A is a well-known problem for a semi-infinite crack propagating in an unbounded medium and many efforts have been devoted to analyze this problem.

Problem C in the above mentioned three fundamental problems is the only one which needs careful analysis. The problem we will deal with is the interaction of the propagating crack with cylindrical reflected waves, which causes the only difficulty in this investigation. For most of the dynamic problems, the propagating waves can be represented in an exponential functional form in the Laplace transform domain of time. The reflected and diffracted waves generated by the half-plane boundary and by the crack can thus be constructed by the superposition method; that is, if the responses toward an applied exponentially distributed traction on boundaries in the Laplace transform domain can be obtained preliminarily. The superposition scheme proposed in this study, unlike usual superposition methods which are performed in the time domain, is performed in the Laplace transform domain.

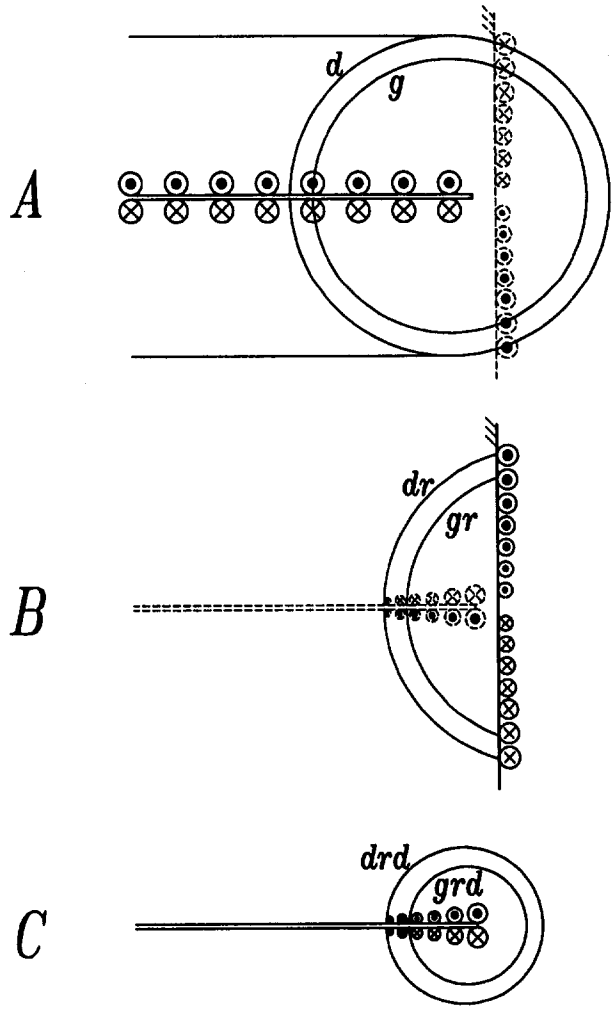


Fig. 3 Three fundamental problems which are superimposed to obtain the solution for constant velocity crack extension and interaction with the stress wave reflected from boundary

Consider the fundamental problem of antiplane deformation for a propagating semi-infinite crack with constant velocity in an unbounded medium. The solution for an exponentially distributed loading applied at the crack faces in the Laplace transform domain will be referred to as the fundamental solution. The problem can be viewed as a half-plane problem with the material occupying the region $y \geq 0$, subjected to the following mixed boundary conditions in the Laplace transform domain

$$\bar{\tau}_{yz}(\xi, 0, s) = e^{s\eta\xi} \quad -\infty < \xi < 0, \tag{2.1}$$

$$\bar{w}(\xi, 0, s) = 0 \quad 0 < \xi < \infty, \tag{2.2}$$

where s is the Laplace transform parameter and η is a constant. The coordinate ξ defined by $\xi = x - vt$ is fixed with respect to the moving crack tip. The overbar symbol is used for denoting the transform on time t. The one-sided Laplace transform with respect to time and the two-sided Laplace transform with respect to ξ are defined by

$$\bar{w}(\xi, y, s) = \int_0^\infty w(\xi, y, t)e^{-st}dt,$$

$$\tilde{w}(\lambda, y, s) = \int_{-\infty}^\infty \bar{w}(\xi, y, s)e^{-s\lambda\xi}d\xi.$$

This fundamental problem can be solved by using the standard transform method and the Wiener-Hopf technique. The governing equation can be represented by the two-dimensional wave equation

$$\frac{\partial^2 w}{\partial x^2} + \frac{\partial^2 w}{\partial y^2} = b^2 \frac{\partial^2 w}{\partial t^2}, \tag{2.3}$$

where b is the slowness of the shear wave given by

$$b = 1/v_s = \sqrt{\rho/\mu},$$

in which $w(x, y, t)$ is the displacement normal to the xy-plane; v_s is the shear wave speed, and μ and ρ are the respective shear modulus and the mass density of the material. The nonvanishing shear stresses are

$$\tau_{yz} = \mu \frac{\partial w}{\partial y}, \quad \tau_{xz} = \mu \frac{\partial w}{\partial x}. \tag{2.4}$$

In analyzing this problem, it is convenient to express the governing equation in the moving coordinates $\xi - y$ as follows:

$$(1 - b^2v^2)\frac{\partial^2 w}{\partial \xi^2} + \frac{\partial^2 w}{\partial y^2} + 2(b^2v)\frac{\partial^2 w}{\partial \xi \partial t} - b^2 \frac{\partial^2 w}{\partial t^2} = 0.$$

Downloaded 04 May 2010 to 171.66.16.28. Redistribution subject to ASME license or copyright; see http://www.asme.org/terms/Terms_Use.cfm

This fundamental problem can be solved by the application of integral transforms. Applying the one-sided Laplace transform over time, the two-sided Laplace transform over ξ under the restriction of $\mathrm{Re}(\eta) > \mathrm{Re}(\lambda)$, finally the Wiener-Hopf technique is implemented. The solutions of stresses and displacement for the boundary conditions (2.1) and (2.2) expressed in the transform domain are

$$\bar{\tau}_{yz}(\xi, y, s) = \frac{1}{2\pi i}\int_{\Gamma_\lambda} \frac{\alpha^{\ddagger}(\lambda)e^{-s(\alpha^* y - \lambda\xi)}}{\alpha^{\ddagger}(\eta)(\eta - \lambda)}\, d\lambda, \quad (2.5)$$

$$\bar{\tau}_{xz}(\xi, y, s) = -\frac{1}{2\pi i}\int_{\Gamma_\lambda} \frac{\lambda e^{-s(\alpha^* y - \lambda\xi)}}{\alpha^{\ddagger}(\eta)(\eta - \lambda)\alpha^{\pm}(\lambda)}\, d\lambda, \quad (2.6)$$

$$\bar{w}(\xi, y, s) = -\frac{1}{2\pi i}\int_{\Gamma_\lambda} \frac{e^{-s(\alpha^* y - \lambda\xi)}}{\mu s\alpha^{\ddagger}(\eta)(\eta - \lambda)\alpha^{\pm}(\lambda)}\, d\lambda, \quad (2.7)$$

where

$$\alpha^*(\lambda) = \sqrt{b + \lambda(1 - bv)}\sqrt{b - \lambda(1 + bv)} = \alpha^{\ddagger}(\lambda)\alpha^{\pm}(\lambda).$$

The corresponding result of the dynamic stress intensity factor in the Laplace transform domain is

$$\bar{K}(s) = \lim_{\xi \to 0} \sqrt{2\pi\xi}\,\bar{\tau}_{yz}(\xi, 0, s) = -\frac{\sqrt{2}\sqrt{1 - bv}}{\sqrt{s}\alpha^{\ddagger}(\eta)}. \quad (2.8)$$

3 Transient Analysis for Propagating Crack Interaction With Vertical Boundary

Consider a half-plane with a vertical boundary containing a horizontal semi-infinite crack which is stress free and at rest. At time $t = 0$, an antiplane uniformly distributed dynamic loading with magnitude τ_0 is applied at the crack faces of the semi-infinite crack. The time dependence of the loading is represented by the Heaviside step function $H(t)$. At time $t = t_f$, the semi-infinite crack suddenly propagates along the crack-tip line with constant velocity v toward the vertical half-plane boundary as shown in Fig. 1. The transient elastodynamic problem is solved by superposition of the fundamental solutions obtained in the previous section in the Laplace transform domain. The transient solutions are composed of an incident field, reflected field, and diffracted field, which are denoted by superscripts of i, r, and d, respectively. The incident wave is the propagating plane wave in an unbounded medium which is induced by applying a uniformly distributed loading on crack faces. The diffracted wave includes two parts, the first one is induced from the stationary crack tip by the application of a uniformly distributed traction on crack faces and the second one is generated from the propagating crack tip when the crack starts to move. We now focus the analysis on the diffracted field generated by the stationary crack due to the incident plane wave. This problem can also be solved by other methods, but the following analysis will be performed by the proposed superposition method in this study to indicate how the transient solution to be constructed. The incident field of the plane wave expressed in the Laplace transform domain can be obtained as follows:

$$\bar{\tau}^i_{yz}(x, 0, s) = \frac{1}{2\pi i}\int_{\Gamma_\lambda} \frac{\tau_0}{s\lambda} e^{s\lambda x} d\lambda. \quad (3.1)$$

The applied traction on the crack face as indicated in (3.1), has the functional form $e^{s\lambda x}$. Since the solutions of applying traction $e^{s\eta x}$ on crack faces have been solved in Section 2 by setting $v = 0$, the diffracted field generated from the stationary semi-infinite crack can be constructed by superimposing the incident wave traction that is equal to (3.1). When we combine (2.5) (by setting $v = 0$) and (3.1), the solution of diffracted wave for $\bar{\tau}^d_{yz}$ and $\bar{\tau}^d_{xz}$ in the Laplace transform domain can be expressed as follows:

$$\bar{\tau}^d_{yz}(x, y, s) = \frac{1}{2\pi i}\int_{\Gamma_\lambda} \frac{\tau_0}{s\lambda} \times \left\{\frac{1}{2\pi i}\int_{\Gamma_{\eta_2}} \frac{(b + \eta_2)^{1/2}}{(\lambda - \eta_2)(b + \lambda)^{1/2}} e^{-s(\alpha y - \eta_2 x)} d\eta_2\right\} d\lambda = \frac{1}{2\pi i}\int_{\Gamma_\lambda} \frac{\tau_0\sqrt{b + \lambda}}{s\lambda\sqrt{b}} e^{-s(\alpha y - \lambda x)} d\lambda, \quad (3.2)$$

$$\bar{\tau}^d_{xz}(x, y, s) = \frac{1}{2\pi i}\int_{\Gamma_\lambda} \frac{-\tau_0}{s\sqrt{b - \lambda}\sqrt{b}} e^{-s(\alpha y - \lambda z)} d\lambda. \quad (3.3)$$

By using the Cagniard-de Hoop method of Laplace inversion, the diffracted stress field in time domain is obtained as follows:

$$\tau^d_{yz}(x, y, t) = \frac{\tau_0}{\pi\sqrt{b}}\int_{br}^{t} \mathrm{Im}\left[\frac{\sqrt{b + \lambda^+}}{\lambda^+}\frac{\partial\lambda^+}{\partial t}\right] dt, \quad (3.4)$$

$$\tau^d_{xz}(x, y, t) = \frac{-\tau_0}{\pi\sqrt{b}}\int_{br}^{t} \mathrm{Im}\left[\frac{1}{\sqrt{b - \lambda^+}}\frac{\partial\lambda^+}{\partial t}\right] dt, \quad (3.5)$$

where

$$\lambda^+ = -\frac{t}{r}\cos\theta + i\left(\frac{t^2}{r^2} - b^2\right)^{1/2}\sin\theta,$$

$$r = (x^2 + y^2)^{1/2}, \quad \theta = \cos^{-1}(x/r).$$

Equations (3.4) and (3.5) can be integrated and further simplified as ($\theta < \pi/2$)

$$\tau^d_{yz}(x, y, t) = \frac{\tau_0}{\pi}\left\{2\cos(\theta/2)\sqrt{\frac{t}{br} - 1} - \tan^{-1}\sqrt{\frac{t/br - 1}{1 - \sin\theta}} - \tan^{-1}\sqrt{\frac{t/br - 1}{1 + \sin\theta}}\right\}, \quad (3.6)$$

$$\tau^d_{xz}(x, y, t) = -\frac{2\tau_0}{\pi}\sin(\theta/2)\sqrt{\frac{t}{br} - 1}. \quad (3.7)$$

The corresponding stress intensity factor in the Laplace transform domain is

$$\bar{K}^d(s) = \frac{1}{2\pi i}\int_{\Gamma_\lambda} \frac{\tau_0}{s\lambda}\left[\frac{-\sqrt{2}}{\sqrt{s}(b + \lambda)^{1/2}}\right] d\lambda = \frac{\tau_0\sqrt{2}}{s^{3/2}\sqrt{b}}. \quad (3.8)$$

The dynamic stress intensity factor induced by diffracted d wave expressed in time domain will be

$$K^d(t) = 2\tau_0\sqrt{\frac{2t}{\pi b}}. \quad (3.9)$$

The results expressed in (3.6), (3.7), and (3.9) are the well-known solutions for a semi-infinite crack in an unbounded medium subjected to a uniformly distributed loading on crack faces. The dynamic stress intensity factor shown in (3.9) increases from zero as the square root of the time measured from the instant the uniformly distributed loading applied on crack faces. At time $t = t_f$, the dynamic stress intensity factor reaches its critical value and the crack starts to propagate with constant velocity v. The transient full-field analysis for a propagating crack just mentioned above has also been solved by Ma and

Downloaded 04 May 2010 to 171.66.16.28. Redistribution subject to ASME license or copyright; see http://www.asme.org/terms/Terms_Use.cfm

Burgers (1988) by using the method proposed by Freund (1972b). In their investigations, the transient solution for constant speed crack propagation is obtained by determining a fundamental solution for a concentrated force appearing through the moving crack tip, and then building up the general solution by superposition. In this study, a more direct and simple methodology will be used to solve this problem. We consider the transient problem of a semi-infinite crack propagates at $t = t_f$ with uniformly distributed loading applied only on the original crack face $-\infty < x < 0$. The applied uniform stress τ_0 on the original crack face written in the Laplace transform domain for the moving coordinate system will have the following form:

$$\bar{\tau}_{yz}(\xi, 0, s) = \frac{1}{2\pi i}\int_{\Gamma_\lambda} \frac{-\tau_0 d}{s\lambda(\lambda - d)} e^{s\lambda(\xi - vt_f)} d\lambda, \quad (3.10)$$

in which $d = 1/v$ is the slowness of the crack velocity and $\xi = x - v(t - t_f)$. The applied traction on crack faces as expressed in (3.10), has the functional form $e^{s\lambda\xi}$. Since the Laplace transform solutions of applying traction $e^{s\eta\xi}$ on crack faces have been solved in the previous section, the diffracted field generated from the propagating crack tip can be constructed by superimposing the fundamental solution and the stress distribution in (3.10). The results of shear stresses expressed in the Laplace transform domain will be

$$\bar{\tau}^g_{yz}(\xi, y, s) = \frac{1}{2\pi i}\int_{\Gamma_{\eta_1}} \frac{-\tau_0 d}{s\eta_1(\eta_1 - d)} e^{-s\eta_1 vt_f}$$

$$\times \left\{\frac{1}{2\pi i}\int_{\Gamma_{\eta_2}} \frac{\alpha^*_+(\eta_2)}{(\eta_1 - \eta_2)\alpha^*_+(\eta_1)} e^{-s[\alpha^* y - \eta_2\xi]} d\eta_2\right\} d\eta_1, \quad (3.11)$$

$$\bar{\tau}^g_{xz}(\xi, y, s) = \frac{1}{2\pi i}\int_{\Gamma_{\eta_1}} \frac{-\tau_0 d}{s\eta_1(\eta_1 - d)} e^{-s\eta_1 vt_f}\left\{\frac{1}{2\pi i}\right.$$

$$\left.\times \int_{\Gamma_{\eta_2}} \frac{-\eta_2}{\alpha^-_*(\eta_2)(\eta_1 - \eta_2)\alpha^*_+(\eta_1)} e^{-s[\alpha^* y - \eta_2\xi]} d\eta_2\right\} d\eta_1. \quad (3.12)$$

The exact transient solutions for a propagating crack at unbounded medium in time domain can be obtained by inverting the Laplace transform domain of (3.11) and (3.12). The results are

$$\tau^g_{yz}(\xi, y, t) = \frac{\tau_0}{\pi\sqrt{b}}\int_{t_m}^{t} \mathrm{Im}\left\{\frac{\alpha^*_+(\lambda^+)}{\lambda^+}\frac{\partial\lambda^+}{\partial\tau}\right\}_{t=\tau} d\tau - \frac{\tau_0}{\pi\sqrt{d}}\int_{t_m}^{t-t_f}$$

$$\mathrm{Im}\left\{\frac{\alpha^*_+(\lambda^+)}{\lambda^+ - d}\frac{\partial\lambda^+}{\partial\tau}\right\}_{t=\tau} d\tau, \quad (3.13)$$

$$\tau^g_{xz}(\xi, y, t) = \frac{-\tau_0}{\pi\sqrt{b}}\int_{t_m}^{t} \mathrm{Im}\left\{\frac{1}{\alpha^*_-(\lambda^+)}\frac{\partial\lambda^+}{\partial\tau}\right\}_{t=\tau} d\tau + \frac{\tau_0}{\pi\sqrt{d}}\int_{t_m}^{t-t_f}$$

$$\mathrm{Im}\left\{\frac{\lambda^+}{(\lambda^+ - d)\alpha^*_-(\lambda^+)}\frac{\partial\lambda^+}{\partial\tau}\right\}_{t=\tau} d\tau, \quad (3.14)$$

where

$$\lambda^+ = \frac{-(\xi t + b^2 v y^2) + iy\sqrt{t^2 - b^2[y^2 + (\xi + vt)^2]}}{\xi^2 + (1 - b^2v^2)y^2},$$

$$\frac{\partial\lambda^+}{\partial t} = \frac{-\xi + iy\{t^2 - b^2[y^2 + (\xi + vt)^2]\}^{-1/2} \times [t(1 - b^2v^2) - b^2v\xi]}{\xi^2 + (1 - b^2v^2)y^2},$$

$$t_m = \frac{b\{bv\xi + [\xi^2 + (1 - b^2v^2)y^2]^{1/2}\}}{1 - b^2v^2}.$$

It is very interesting to see that the full-field solution of a crack propagating with constant speed subjected to loads applied on the original crack faces as shown in (3.13) and (3.14) can be expressed by two terms, each term having its own physical meaning. The first term represents the solution due to applying the uniform loading on the original and new crack faces for a crack which begins to grow at constant speed at time t_f after the loading is applied. The functional form of the first term is the same as the solution to the problem with a uniform loading applied on the original and new crack faces with no delay time. The only dependence on delay time is through the definition of ξ. This problem corresponds to Baker's problem (Baker, 1962) in mode III. The second term represents the solution for a crack which starts to propagate at time t_f for constant speed with loading applied uniformly on the new crack faces only. The results shown in (3.13) and (3.14) are also found to be the same as that obtained by Ma and Burgers (1988) from different methodology.

The dynamic stress intensity factor for a propagating crack at infinite medium can also be constructed by a similar manner. The result in the Laplace transform domain can be obtained from (2.8) and (3.10) and is expressed as follows:

$$K^g(s) = \frac{1}{2\pi i}\int_{\Gamma_\lambda} \frac{-\tau_0 d}{s\lambda(\lambda - d)} e^{-s\lambda vt_f}\left\{\frac{-\sqrt{2}\sqrt{1 - bv}}{\sqrt{s}\alpha^*_+(\lambda)}\right\} d\lambda. \quad (3.15)$$

The inversion Laplace transform of (3.15) will have the following form:

$$K^g(t) = 2\sqrt{\frac{2}{\pi}}\tau_0\sqrt{1 - bv}\left[\sqrt{\frac{t}{b}} - \sqrt{\frac{t - t_f}{d}}\right]. \quad (3.16)$$

After some later time, the diffracted wave (d wave) generated from the stationary crack and the shear wave (g wave) radiated out from the propagating crack will be reflected from the free vertical half-plane which will be indicated as the dr and gr wave, respectively. The solutions for reflected waves generated from the free boundary can be constructed by employing the method of images, which can be easily obtained from the solution of d wave and g wave just constructed previously, the result for dr wave in the fixed coordinate x–y system will be

$$\bar{\tau}^{dr}_{yz}(x, y, s) = \frac{-1}{2\pi i}\int_{\Gamma_\lambda} \frac{\tau_0\sqrt{b - \lambda}}{s\sqrt{b}\lambda} e^{-s[\alpha y - \lambda(x - 2h)]} d\lambda. \quad (3.17)$$

The solution expressed in the moving coordinate ξ–y system will become

$$\bar{\tau}^{dr}_{yz}(\xi, y, s) = \frac{-1}{2\pi i}\int_{\Gamma_\lambda} \frac{\tau_0\sqrt{b - \bar{\lambda}}}{s\bar{\lambda}\sqrt{b}(1 - \lambda v)} e^{-s[\alpha^* y - \lambda(\xi - vt_f - 2h)]} d\lambda, \quad (3.18)$$

where

$$\bar{\lambda} = \frac{\lambda}{1 - \lambda v}.$$

The reflected dr wave will arrive at the propagating crack tip at later time and will induce additional contribution on dynamic stress intensity factor. The induced stress intensity factor by dr wave can be obtained by setting $y = 0$ in (3.18) and the fundamental solution expressed in (2.8). The result written in the Laplace transform domain will have the following form:

Downloaded 04 May 2010 to 171.66.16.28. Redistribution subject to ASME license or copyright; see http://www.asme.org/terms/Terms_Use.cfm

$$\bar{K}^{dr}(s) = \frac{1}{2\pi i}\int_{\Gamma_\lambda} \frac{\tau_0\sqrt{b-\bar{\lambda}}}{s\bar{\lambda}\sqrt{b}(1-\lambda v)} e^{-s\lambda(2h+vt_f)}\left\{-\frac{\sqrt{2}\sqrt{1-bv}}{\sqrt{s}\alpha^{\ddagger}(\lambda)}\right\}d\lambda$$

$$= -\frac{\sqrt{2}\tau_0\sqrt{1-bv}}{\sqrt{b}s^{3/2}}\frac{1}{2\pi i}\int_{\Gamma_\lambda}\frac{\alpha^{*}(\lambda)}{\sqrt{1-\lambda v}\alpha^{\ddagger}(\lambda)\lambda} e^{-s\lambda(2h+vt_f)}d\lambda. \quad (3.19)$$

The inversion Laplace transform of (3.19) will become

$$K^{dr}(t) = \frac{-2\sqrt{2}\tau_0\sqrt{1-bv}}{\sqrt{b}\pi^{3/2}}\int_{t_d}^{t}\sqrt{t-\tau}\,\mathrm{Im}\left\{\frac{\alpha^{*}(\lambda^{+})}{\sqrt{1-\lambda^{+}v}\alpha^{\ddagger}(\lambda^{+})\lambda^{+}}\frac{\partial\lambda^{+}}{\partial\tau}\right\}_{t=\tau}d\tau$$

$$= \frac{2\sqrt{2}\tau_0\sqrt{1-bv}}{\sqrt{b}\pi^{3/2}}\int_{t_d}^{t}\frac{\sqrt{(t-\tau)[(1+bv)\tau - b(2h+vt_f)](2h+vt_f)}}{\tau\sqrt{(2h+vt_f-\tau v)[b(2h+vt_f)+\tau(1-bv)]}}d\tau, \quad (3.20)$$

where

$$\lambda^{+} = \frac{t}{2h+vt_f},$$

$$t_d = \frac{b(2h+vt_f)}{1+bv}.$$

The value of t_d denotes the time for a wave (d wave) generated from the stationary crack, reflected from the vertical boundary and arrives at the moving crack tip. In a similar way, the wave (g wave) generated from the propagating crack at time t_f as shown in (3.13) and (3.14) will also be reflected from the vertical free boundary. The reflected gr wave expressed in the Laplace transform domain for the moving coordinate system will have the following form:

$$\bar{\tau}^{gr}_{yz}(\xi, y, s) = \frac{-1}{2\pi i}\int_{\Gamma_\lambda}\frac{\tau_0\alpha^{*}(\lambda)}{s\sqrt{1-2\lambda v}} \times\left[\frac{1}{\lambda\sqrt{b}}+\frac{e^{-st_f}}{(\lambda-d)\sqrt{d}}\right]e^{-s[\alpha^{*}y-\lambda(\xi-2h)]}d\lambda, \quad (3.21)$$

$$\bar{\tau}^{gr}_{xz}(\xi, y, s) = \frac{1}{2\pi i}\int_{\Gamma_\lambda}\frac{\tau_0\lambda}{s\alpha^{\ddagger}(\lambda)\sqrt{1-2\lambda v}} \times\left[\frac{1}{\lambda\sqrt{b}}+\frac{e^{-st_f}}{(\lambda-d)\sqrt{d}}\right]e^{-s[\alpha^{*}y-\lambda(\xi-2h)]}d\lambda. \quad (3.22)$$

The reflected gr wave will also arrive at the propagating crack tip at some later time. The induced stress intensity factor by gr wave in the Laplace transform domain is

$$\bar{K}^{gr}(s) = \frac{1}{2\pi i}\int_{\Gamma_\lambda}\frac{\tau_0\alpha^{*}(\lambda)}{s\sqrt{1-2\lambda v}} \times\left[\frac{1}{\lambda\sqrt{b}}+\frac{e^{-st_f}}{(\lambda-d)\sqrt{d}}\right]e^{-2s\lambda h}\left\{-\frac{\sqrt{2}\sqrt{1-bv}}{\sqrt{s}\alpha^{\ddagger}(\lambda)}\right\}d\lambda. \quad (3.23)$$

The Laplace inverse transform of (3.23) in time domain can be expressed as follows:

where

$$t_p = \frac{2bh}{1+bv}.$$

For the numerical investigation, we consider a semi-infinite crack subjected to a uniformly distributed loading τ_0 at time $t = 0$. At some delay time $t_f/bh = 0.5$, the crack start to propagate out of the original semi-infinite crack with constant velocity toward the vertical free boundary and the loading is applied only on the original crack faces. The pattern of wave fronts and the position of the crack tip for $t > t_f$ is shown in Fig. 4. The dimensionless dynamic stress intensity factors (solid lines) for various value of crack propagation velocity are shown in Fig. 5, which account the contribution of reflected dr and gr waves on the calculation of stress intensity factor. The dot lines in Fig. 5 represent the solution for a semi-infinite crack propagating in an infinite medium and the difference of solid and dot lines is the influence due to the vertical free boundary. Where K_0 represents the dynamic stress intensity factor for the crack starts to propagate at time t_f. It shows clearly from this figure that the vertical free-boundary effect will increase the dynamic stress intensity factor due to the reflected waves (dr and gr waves) generated from the free boundary. However, the influence of the first few reflected waves on the dynamic stress intensity factor is very small.

4 Transient Analysis for Propagating Crack in a Strip

Consider an elastic strip in the region of the x, y-plane with $-\infty < x < \infty$, $-l < y < l$, contains a semi-infinite crack as shown in Fig. 2. At time $t = 0$, a uniformly distributed antiplane dynamic loading with magnitude τ_0 is applied at the crack faces, the crack starts to propagate with constant velocity v at time t_f in the x-direction along the symmetry line $y = 0$ of the strip. This transient problem will be solved in a similar way as we have proposed in the last section for analyzing the problem of the interaction of a propagating crack with a vertical boundary. In this problem, the plane wave induced from the uniformly

$$K^{gr}(t) = \frac{2\sqrt{2}\tau_0\sqrt{1-bv}}{\pi^{3/2}}\left\{\sqrt{\frac{h}{b}}\int_{t_p}^{t}\frac{\sqrt{(t-\tau)[(1+bv)\tau-2bh]}}{\tau\sqrt{v(bv-1)\tau^2+(1-3bv)h\tau+2bh^2}}d\tau\right.$$

$$\left.+\sqrt{\frac{h}{d}}\int_{t_f+t_p}^{t}\frac{\sqrt{(t-\tau)[(1+bv)(\tau-t_f)-2bh]}}{(\tau-2hd-t_f)\sqrt{v(bv-1)(\tau-t_f)^2+h(1-3bv)(\tau-t_f)+2bh^2}}d\tau\right\}, \quad (3.24)$$

Downloaded 04 May 2010 to 171.66.16.28. Redistribution subject to ASME license or copyright; see http://www.asme.org/terms/Terms_Use.cfm

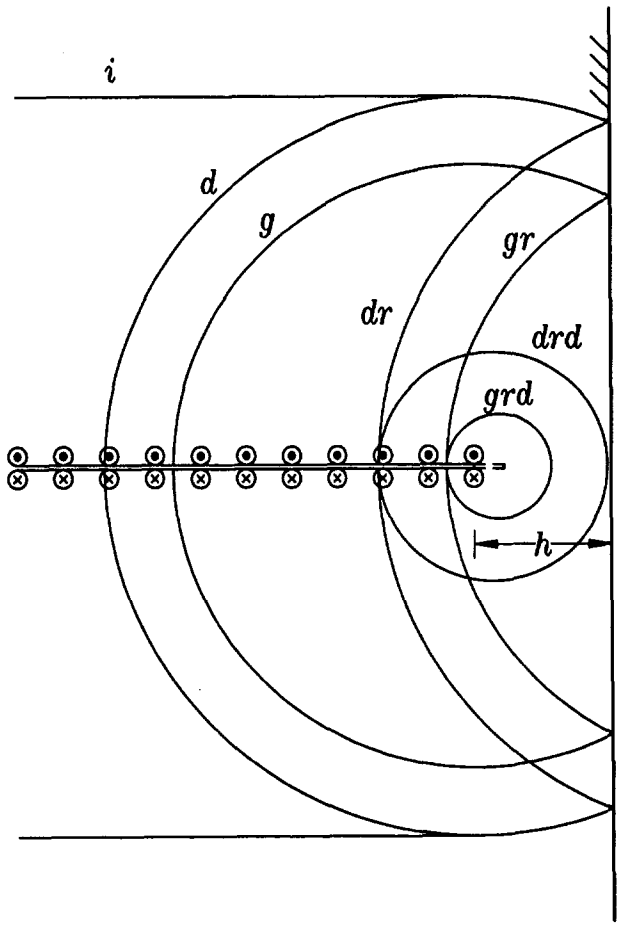


Fig. 4 Wave fronts of the incident, reflected and diffracted waves in the configuration with vertical boundary

distributed loading and the diffracted waves generated from the stationary crack tip and from the propagating crack tip will be reflected from horizontal boundaries, these waves will interact with the propagating crack at some later time. The pattern of wave fronts for $t > t_f$ is indicated in Fig. 5. The major difficulty in analyzing this problem will be the one that deals with the interaction of reflected waves with the propagating crack and the superposition technique of the fundamental solutions in the Laplace transform domain will be used. Before the time that the i, d, and g waves reflected from the horizontal boundary of the strip, the problem can be considered as a semi-infinite crack propagating in an unbounded medium and the solutions have been analyzed and presented in the previous section. In the following analysis, the solution is valid for the case that crack starts to propagating before the waves (i.e., i wave and d wave) generated from the stationary crack returns to the stationary crack (i.e., $t_f < 2bl$).

The diffracted d wave generated from the stationary crack tip will be reflected from the horizontal traction-free boundary to interact with the moving crack tip at later time. The solution of diffracted d wave in the Laplace transform domain is expressed in (3.2) and the reflected dr wave from the horizontal boundary can be constructed by applying the method of images, the result will be

$$\bar{\tau}_{yz}^{dr}(x, y, s) = \frac{-1}{2\pi i}\int_{\Gamma_\lambda} \frac{\tau_0 \alpha_+(\lambda)}{s\lambda\sqrt{b}}\, e^{s[\alpha(y-2l)+\lambda x]}d\lambda. \quad (4.1)$$

If we express the solution in (4.1) in the moving coordinate $\xi - y$ system, where $\xi = x + vt_f - vt$, the result will become

$$\bar{\tau}_{yz}^{dr}(\xi, y, s) = -\frac{1}{2\pi i}\int_{\Gamma_\lambda} \frac{\tau_0 \alpha_+(\bar{\lambda})}{s\bar{\lambda}\sqrt{b}(1-\lambda v)}\, e^{s[\alpha^*(y-2l)+\lambda(\xi - vt_f)]}d\lambda, \quad (4.2)$$

where

$$\bar{\lambda} = \frac{\lambda}{1-\lambda v}.$$

The induced dynamic stress intensity factor by dr wave can be obtained by setting $y = 0$ in (4.2) and the fundamental solution expressed in (2.8). The result for the stress intensity factor expressed in the Laplace transform domain will have the following form:

$$\bar{K}^{dr}(s) = -\frac{2\sqrt{2}\tau_0\sqrt{1-bv}}{\sqrt{b}s^{3/2}}\frac{1}{2\pi i}\int_{\Gamma_\lambda}\frac{1}{\lambda\sqrt{1-\lambda v}}\, e^{-s(2\alpha^* l+\lambda v t_f)}d\lambda$$

$$= -\frac{2\sqrt{2}\tau_0\sqrt{1-bv}}{\sqrt{b}s^{3/2}\pi} \times \int_{t_d}^{\infty} \mathrm{Im}\left\{\frac{1}{\lambda_d^+\sqrt{1-\lambda_d^+ v}}\frac{\partial\lambda_d^+}{\partial t}\right\}e^{-st}dt, \quad (4.3)$$

where

$$\lambda_d^+ = \frac{vt_f t - 4b^2vl^2 + i2l\sqrt{t^2 - b^2[(vt - vt_f)^2 + 4l^2]}}{v^2t_f^2 + 4l^2(1-b^2v^2)},$$

$$t_d = \frac{-b^2v^2t_f + \sqrt{b^2v^2t_f^2 + 4l^2b^2(1-b^2v^2)}}{1-b^2v^2}.$$

The dynamic stress intensity factor expressed in time domain will be

$$K^{dr}(t) = -\frac{4\sqrt{2}\tau_0\sqrt{1-bv}}{\pi^{3/2}\sqrt{b}} \times \int_{t_d}^{t}\sqrt{t-\tau}\,\mathrm{Im}\left\{\frac{1}{\lambda_d^+\sqrt{1-\lambda_d^+ v}}\frac{\partial\lambda_d^+}{\partial\tau}\right\}_{t=\tau}d\tau. \quad (4.4)$$

The value of t_d denotes the time required for diffracted d wave generated from the stationary crack, reflected from the horizontal boundary and arrives at the moving crack tip.

Finally, we consider the contribution from the reflected gr wave which is originally generated from the propagating crack tip. The full-field analysis for this diffracted g wave has already been solved and discussed in the previous section. The solution expressed in the Laplace transform domain will be

$$\bar{\tau}_{yz}^{g}(\xi, y, s) = \frac{1}{2\pi i}\int_{\Gamma_\lambda}\frac{\tau_0\alpha_+^*(\lambda)}{s} \times \left[\frac{1}{\lambda\sqrt{b}} - \frac{e^{-st_f}}{(\lambda - d)\sqrt{d}}\right]e^{-s(\alpha^* y - \lambda\xi)}d\lambda. \quad (4.5)$$

The reflected gr wave generated from the horizontal boundary can be easily constructed from (4.5) by the image method and the result is

$$\bar{\tau}_{yz}^{gr}(\xi, y, s) = \frac{-1}{2\pi i}\int_{\Gamma_\lambda}\frac{\tau_0\alpha_+^*(\lambda)}{s} \times \left[\frac{1}{\lambda\sqrt{b}} - \frac{e^{-st_f}}{(\lambda - d)\sqrt{d}}\right]e^{s[\alpha^*(y-2l)+\lambda\xi]}d\lambda. \quad (4.6)$$

This reflected gr wave will interact with the propagating crack which will induce additional contribution on the dynamic stress intensity factor. The induced stress intensity factor by gr wave can be constructed by superimposing the fundamental solution in (2.8) and the stress distribution induced by gr wave

Downloaded 04 May 2010 to 171.66.16.28. Redistribution subject to ASME license or copyright; see http://www.asme.org/terms/Terms_Use.cfm

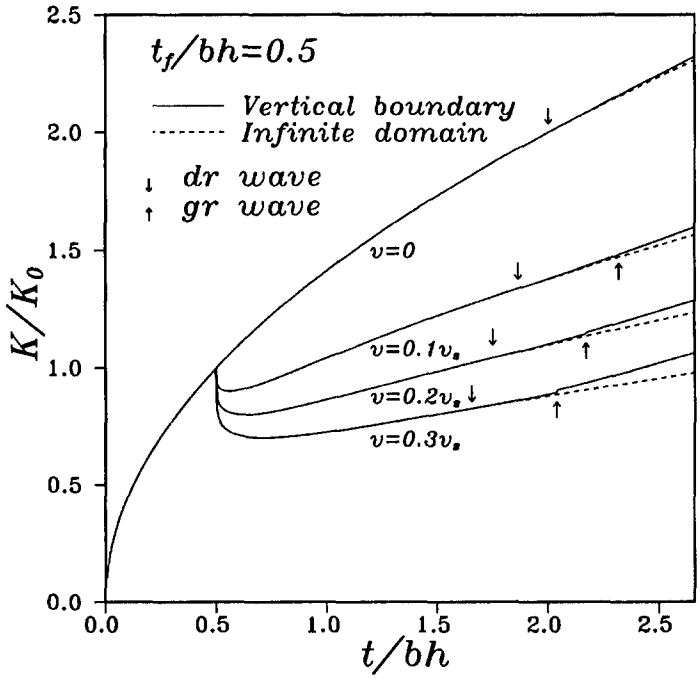


Fig. 5 Transient response of the dynamic stress intensity factor for a propagating crack in the configuration with vertical boundary

on the propagating crack face. The result is obtained in the Laplace transform domain as follows:

$$\bar{K}^{gr}(s) = -\frac{2\sqrt{2}\tau_0\sqrt{1-bv}}{s^{3/2}}\frac{1}{2\pi i} \times \int_{\Gamma_\lambda}\left[\frac{1}{\lambda\sqrt{b}} - \frac{e^{-st_f}}{(\lambda-d)\sqrt{d}}\right]e^{-2s\alpha^* l}d\lambda. \quad (4.7)$$

$$\bar{K}^{gr}(s) = -\frac{2\sqrt{2}\tau_0\sqrt{1-bv}}{\pi}\left\{\frac{1}{s^{3/2}}\int_{t_p}^{\infty}\mathrm{Im}\left[\frac{1}{\lambda_p^+\sqrt{b}}\frac{\partial\lambda_p^+}{\partial t}\right]e^{-st}dt - \frac{e^{-st_f}}{s^{3/2}}\int_{t_p}^{\infty}\mathrm{Im}\left[\frac{1}{(\lambda_p^+-d)\sqrt{d}}\frac{\partial\lambda_p^+}{\partial t}\right]e^{-st}dt\right\}, \quad (4.9)$$

where

$$t_p = \frac{2lb}{\sqrt{1-b^2v^2}}.$$

The inverse Laplace transform of (4.9) to time domain can be expressed as

$$K^{gr}(t) = -\frac{4\sqrt{2}\tau_0\sqrt{1-bv}}{\pi^{3/2}}\left\{\int_{t_p}^{t}\sqrt{t-\tau}\,\mathrm{Im}\left[\frac{1}{\lambda_p^+\sqrt{b}}\frac{\partial\lambda_p^+}{\partial\tau}\right]_{t=\tau}d\tau - \int_{t_p}^{t-t_f}\sqrt{t-t_f-\tau}\,\mathrm{Im}\left[\frac{1}{(\lambda_p^+-d)\sqrt{d}}\frac{\partial\lambda_p^+}{\partial\tau}\right]_{t=\tau}d\tau\right\}$$
$$= \frac{8\sqrt{2}\tau_0\sqrt{1-bv}lv}{\pi^{3/2}}\left\{\sqrt{b^3}\int_{t_p}^{t}\frac{\tau\sqrt{(t-\tau)[(1-b^2v^2)\tau^2-4l^2b^2]}}{[(1-b^2v^2)\tau^2-4l^2b^2](\tau^2-4b^2l^2)}d\tau - \frac{1}{\sqrt{d}}\int_{t_p}^{t-t_f}\frac{\tau\sqrt{(t-t_f-\tau)[(1-b^2v^2)\tau^2-4l^2b^2]}}{[(1-b^2v^2)\tau^2-4l^2b^2](v^2\tau^2+4l^2)}d\tau\right\}. \quad (4.10)$$

We deform the path of integration to a path along which the integral can be recognized as a one-sided Laplace transform. The desired path of integration in the λ-plane is obviously defined by the equation

$$2l\alpha^* = 2l(b^2 - \lambda^2 + b^2v^2\lambda^2 - 2b^2v\lambda)^{1/2} = t. \quad (4.8)$$

The foregoing equation can be solved for λ to yield

$$\lambda_p^+ = \frac{-2b^2vl + i\sqrt{(1-b^2v^2)t^2 - 4l^2b^2}}{2l(1-b^2v^2)}.$$

Along this new contour, the variable t is set as the new variable, which leads to

The value of t_p denotes the time needed for the diffracted g wave generated from the propagating crack at time t_f, reflected from the horizontal boundary and reach the propagating crack tip.

For the numerical calculation of the transient stress intensity factor, we consider a semi-infinite crack subjected to a uniformly distributed loading τ_0 on the stationary crack faces at time $t = 0$. At nondimensional delay time $t_f/bl = 0.5$, the crack start to propagate with a constant speed from the semi-infinite crack and the dynamic loading is applied only on the original crack faces. The pattern for the incident, reflected and diffracted wave fronts for $t > t_f$ is shown in Fig. 6. The dynamic stress intensity factors for stationary crack and for various value of crack propagation velocity

Downloaded 04 May 2010 to 171.66.16.28. Redistribution subject to ASME license or copyright; see http://www.asme.org/terms/Terms_Use.cfm

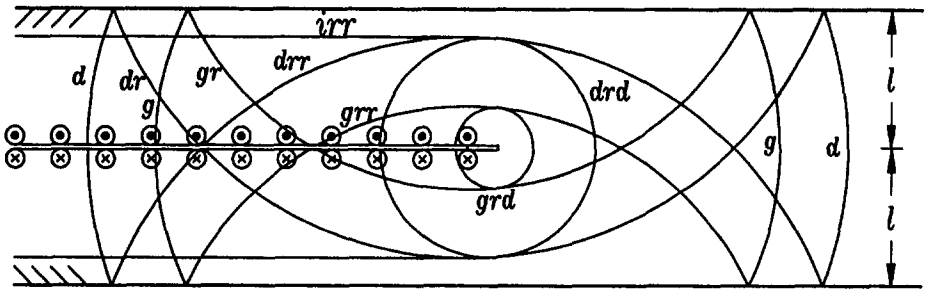


Fig. 6 Wave fronts of the incident, reflected and diffracted waves for a propagating crack in a finite strip

are shown in Fig. 7, which account the contribution from the reflected *dr* and *gr* waves after the crack grows. The stress intensity factor is normalized by K_0 which is the stress intensity factor at $t/bl = 0.5$. The dot lines in Fig. 7 represent the solution for a semi-infinite crack propagating in an infinite medium, and the influence of the horizontal boundary on the stress intensity factor can be evaluated from the difference of solid and dot lines. It also indicates that the reflected waves will increase the value of the dynamic stress intensity factor and the influence is much larger than the case of the vertical boundary discussed in the previous section.

5 Conclusions

The phenomena of crack propagation, arrest, and branching are important subjects in the areas of dynamic fracture analysis. The interaction of reflected waves with the moving crack subjected to dynamic loading had only been discussed in experimental works. Experimental results indicated that the reflected waves dominate the stability of crack propagation. It is very important to have the analytical results to investigate this important event. But it seems difficult to obtain the analytical solutions by using the well-known conventional method.

We have proposed a powerful superposition methodology and a useful fundamental solution is constructed in this study. The fundamental solution is the problem of applying an exponentially distributed traction on the propagating crack face and the solution is determined by superposition of the fundamental solution in the Laplace transform domain. The dynamic crack propagation with constant velocity in a configuration with boundary is investigated. The orientations of crack face respected to the boundary of half-plane are horizontal and vertical types. We only focus our attention on the interaction of first two reflected waves from the boundary with the moving crack. An explicit result of the dynamic stress intensity factor is obtained in closed form and numerical results are evaluated in detail. The numerical results show that the stress intensity factors induced by reflected waves from horizontal boundary are more significant than that of vertical boundary. When reflected waves generated from horizontal boundary return to the moving crack tip, the stress intensity factor will generally increase rapidly.

There still have many unanswered questions in dynamic fracture and this work may provide a useful technique for further investigation in more complicated dynamic fracture problems especially on the crack propagation event. The proposed method in this study has already been extended to solve more difficult

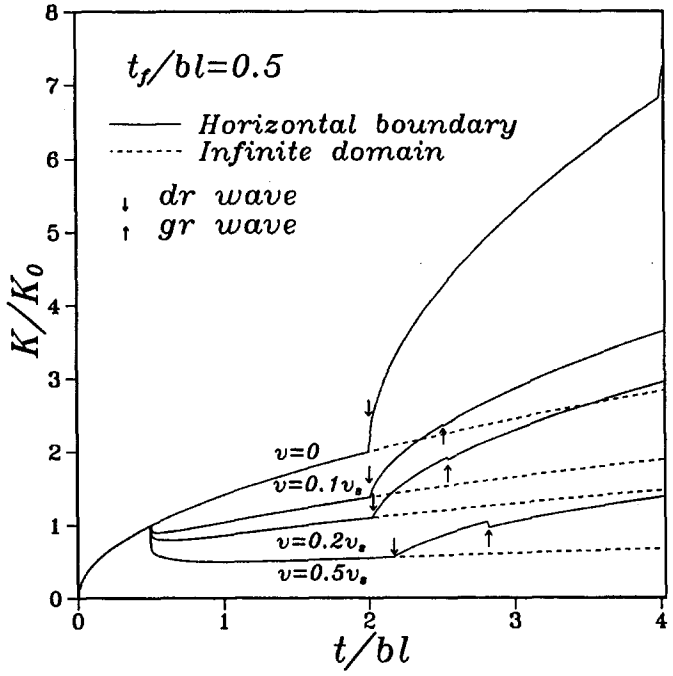


Fig. 7 Transient response of the dynamic stress intensity factor for a propagating crack in a finite strip

Downloaded 04 May 2010 to 171.66.16.28. Redistribution subject to ASME license or copyright; see http://www.asme.org/terms/Terms_Use.cfm

inplane problem of crack propagation with boundary effect, the results will be shown in a future paper.

Acknowledgments

The authors gratefully acknowledge the financial support of this research by the National Science Council (Republic of China) under Grant NSC 83-0401-E-002-115.

References

Baker, B. R., 1962, "Dynamic Stresses Created by a Moving Crack," ASME JOURNAL OF APPLIED MECHANICS, Vol. 29, pp. 449–458.

Broberg, K. B., 1960, "The Propagation of a Brittle Crack," *Arkiv for Fysik,* Vol. 18, pp. 159–192.

Craggs, J. W., 1960, "On the Propagation of a Crack in an Elastic-Brittle Solid," *Journal of the Mechanics and Physics of Solids,* Vol. 8, pp. 66–75.

Freund, L. B., 1972a, "Crack Propagation in an Elastic Solid Subjected to General Loading-I. Constant Rate of Extension," *Journal of the Mechanics and Physics of Solids,* Vol. 20, pp. 129–140.

Freund, L. B., 1972b, "Crack Propagation in an Elastic Solid Subjected to General Loading-II. Non-uniform Rate of Extension," *Journal of the Mechanics and Physics of Solids,* Vol. 20, pp. 141–152.

Freund, L. B., 1973, "Crack Propagation in an Elastic Solid Subjected to General Loading-III. Stress Wave Loading," *Journal of the Mechanics and Physics of Solids,* Vol. 21, pp. 47–61.

Freund, L. B., 1974, "Crack Propagation in an Elastic Solid Subjected to General Loading-IV. Obliquely Incident Stress Pulse," *Journal of the Mechanics and Physics of Solids,* Vol. 22, pp. 137–146.

Freund, L. B., and Rosakis, A. J., 1992, "The Structure of the Near-tip Field during Transient Elastodynamic Crack Growth," *Journal of the Mechanics and Physics of Solids,* Vol. 40, pp. 699–719.

Ma, C. C., and Burgers, P., 1986, "Mode III Crack Kinking with Delay Time: An Analytical Approximation," *International Journal of Solids and Structures,* Vol. 22, pp. 883–899.

Ma, C. C., and Burgers, P., 1987, "Dynamic Mode I and Mode II Crack Kinking Including Delay Time Effects," *International Journal of Solids and Structures,* Vol. 23, pp. 897–918.

Ma, C. C., and Burgers, P., 1988, "Initiation, Propagation, and Kinking of an Antiplane Crack," ASME JOURNAL OF APPLIED MECHANICS, Vol. 55, pp. 111–119.

Ma, C. C., 1988, "Initiation, Propagation, and Kinking of an In-plane Crack," ASME JOURNAL OF APPLIED MECHANICS, Vol. 55, pp. 587–595.

Ma, C. C., 1990, "Dynamic Mixed Mode I–II Crack Kinking under Oblique Stress Wave Loading in Brittle Solids," ASME JOURNAL OF APPLIED MECHANICS, Vol. 57, pp. 117–127.

Ma, C. C., and Chen, S. K., 1994, "Exact Transient Full Field Analysis of an Antiplane Subsurface Crack Subjected to Dynamic Impact Loading," ASME JOURNAL OF APPLIED MECHANICS, Vol. 61, pp. 649–655.

Nilsson, F., 1973, "A Transient Crack Problem for an Infinite Strip under Antiplane Shear," *Dynamic Crack Propagation,* G. C. Sih, ed., The Netherlands, pp. 543–551. Nordhoff,

Tsai, C. H., and Ma, C. C., 1992, "Transient Analysis of a Semi-infinite Crack Subjected to Dynamic Concentrated Forces," ASME JOURNAL OF APPLIED MECHANICS, Vol. 59, pp. 804–811.

Tsai, C. H., and Ma, C. C., 1993a, "The Transient Analysis of a Subsurface Inclined Crack Subjected to a Buried Dynamic Dilatational Source," *International Journal of Solids and Structures,* Vol. 30, pp. 399–412.

Tsai, C. H., and Ma, C. C., 1993b, "The Stress Intensity Factor of a Subsurface Inclined Crack Subjected to a Dynamic Impact Loading," *International Journal of Solids and Structures,* Vol. 30, pp. 2163–2175.

Yoffe, E. H., 1951, "The Moving Griffith Crack," *Philosophical Magazine,* Vol. 42, pp. 739–750.

Downloaded 04 May 2010 to 171.66.16.28. Redistribution subject to ASME license or copyright; see http://www.asme.org/terms/Terms_Use.cfm

An Energy Approach to the Plasticity of a Two-Phase Composite Containing Aligned Inclusions

Y. P. Qiu
Senior Research Associate,
Sonoco Products Co.,
555 Science Drive, Suite B,
University of Wisconsin Research Park,
Madison, WI 53711
Assoc. Mem. ASME

G. J. Weng
Professor,
Department of Mechanical and
Aerospace Engineering,
Rutgers University,
New Brunswick, NJ 08903
Fellow ASME

Based on a linear comparison composite (Tandon and Weng, 1988) and an energy criterion for the effective stress of the ductile matrix (Qiu and Weng, 1992), a nonlinear theory is developed to estimate the strain potential and the overall stress-strain relations of a two-phase composite containing aligned spheroidal inclusions. The plastic state of the ductile matrix under a given external load is determined by solving two simultaneous equations, one being its constitutive equation and the other the expression of its effective stress as a function of its secant shear modulus. Then by means of the effective properties of the linear comparison composite, the overall strain and strain potential of the nonlinear system are evaluated. It is demonstrated that, for an elastically incompressible matrix containing either aligned voids or rigid inclusions, the derived strain potential is exactly equal to Ponte Castaneda's (1991) bound or estimate, respectively, of Willis' (1977) type. Comparison with an exact solution of a fiber-reinforced composite under the plane-strain biaxial loading also shows an excellent agreement. The theory is generally intended for the condition when the concentration is not high, and is finally applied to examine the aspect-ratio dependence of the overall response for a silicon carbide/aluminum system. It is found that, more so than the elastic behavior, the nonlinear plastic response of the two-phase composite is very sensitive to the inclusion shape under most types of loading.

1 Introduction

It is generally recognized that the lack of a simple, analytical solution to the single-inclusion problem in a nonlinear matrix has resulted in a much slower progress in the micromechanical study of composite plasticity. Recently, a new avenue has been opened to estimate or bound the properties of the nonlinear composite by making use of the known elastic properties of a system with an identical microgeometry. Most notably, Talbot and Willis (1985), Ponte Castaneda (1991), and Willis (1991) have developed some elegant variational principles for this purpose. Willis' formulation is an extension of the classical Hashin-Shtrikman (1963) bounds to the nonlinear solid. The starting point of Ponte Castaneda's approach is a linear heterogenous comparison material, and therefore, his bounds or estimates are not restricted to the Hashin and Shtrikman type, and can also be of any higher-order bounds. Willis (1991) has proved that, when the properties of the homogeneous comparison material are chosen properly, his results can be as good as those derived from Ponte Castaneda's method.

In a separate development, Weng and his co-workers (Tandon and Weng, 1988; Qiu and Weng, 1992) have also recognized the advantage of using the linear effective properties of a comparison composite to estimate its nonlinear ones. Their idea evolved out of the earlier work on polycrystal plasticity (Berveiller and Zaoui, 1979; Weng, 1982), and at the outset, they have chosen the properties of the linear comparison matrix to be equal to the secant moduli of the nonlinear matrix at a given stage of deformation. The rationale is that, under a proportional loading, the secant moduli continue to decrease during plastic deformation, and therefore the weakening constraint power of the matrix as uncovered by Hill (1965) can be accounted for with such a choice. While the points of departure are somewhat different, it turns out that, by applying the minimization principles of Willis and Ponte Castaneda, the elastic properties of their comparison matrix are always equal to the secant moduli of the nonlinear matrix.

This is not to say that these two approaches always lead to identical results, as the outcome of the predicted nonlinear behavior still depends on, among others, how one proceeds to determine the effective stress of the nonlinear matrix. Ponte Castaneda's approach is to apply another round of minimization procedure to minimize the strain potential of the nonlinear composite. On the other hand, Qiu and Weng (1992) observed that, in the composite system, the deformation of the matrix is generally heterogeneous, and so they proposed to define the effective stress of the heterogeneously deformed matrix in terms of its distortional energy. The novel feature of this definition is that, unlike the traditional mean-field theory where the effective stress is usually defined in terms of the averaged deviatoric stress of the matrix alone, this approach can account for the contribution of the locally perturbed stress to yielding to a certain extent, and the results of the prediction can be quite encouraging. This energy approach can be easily appreciated if one considers the deformation of an isotropic, porous material under a pure hydrostatic tension (or pressure), under which the effective stress based on the traditional mean deviatoric stress alone would vanish (and thus no yielding), but with this distortional energy the theory would lead to a nonlinear response for the porous system. This new definition automatically reduces to the traditional one if the deformation field is uniform, and, as demonstrated by Qiu and Weng (1992), the predicted stress-

Contributed by the Applied Mechanics Division of THE AMERICAN SOCIETY OF MECHANICAL ENGINEERS for publication in the ASME JOURNAL OF APPLIED MECHANICS.

Discussion on this paper should be addressed to the Technical Editor, Professor Lewis T. Wheeler, Department of Mechanical Engineering, University of Houston, Houston, TX 77204-4792, and will be accepted until four months after final publication of the paper itself in the ASME JOURNAL OF APPLIED MECHANICS.

Manuscript received by the ASME Applied Mechanics Division, Feb. 7, 1994; final revision, Aug. 8, 1994. Associate Technical Editor: G. J. Dvorak.

Copyright © 1995 by ASME

Downloaded 04 May 2010 to 171.66.16.28. Redistribution subject to ASME license or copyright; see http://www.asme.org/terms/Terms_Use.cfm

strain curves of the porous material and an isotropic composite containing elastic spherical particles are closely in line with available exact solution and finite element calculations.

The objective of this paper is to examine the influence of inclusion shape on the plastic anisotropy of a two-phase composite containing aligned elastic inclusions. This will be done by developing the energy approach further, so that the overall elastoplastic behavior of the system can be estimated as a function of the properties of its constituents, and the shape and volume fraction of inclusions. The reinforcing inclusions are taken to be homogeneously dispersed in the ductile matrix, and perfectly bounded together without any void nucleation or growth. While varying in size, the inclusions are assumed to be all spheroidal, with a common aspect ratio α (the length-to-diameter ratio). The overall system is then transversely isotropic, and its properties will be examined under five independent loadings. The theory is generally intended for the low concentration range, even though for a fiber-reinforced composite under a plane-strain biaxial loading and for a particle-reinforced one under a pure hydrostatic tension its accuracy can still be quite satisfactory at a higher concentration.

2 Constitutive Equations of the Ductile Matrix

The elastic inclusions in the two-phase system will be referred to as phase 1, and the ductile matrix as phase 0. The elastic bulk and shear moduli of the rth phase will be denoted by κ_r and μ_r, respectively, and its volume concentration by c_r ($c_1 + c_0 = 1$). The nonlinear plastic behavior of the ductile matrix may be described by the distortional part of the strain potential $f(\sigma_e)$, such that the effective total strain ϵ_e is given by

$$\epsilon_e = \frac{\partial f(\sigma_e)}{\partial \sigma_e} = f'(\sigma_e), \tag{2.1}$$

in terms of the effective stress σ_e. The dilatational behavior is taken to be purely elastic, with a strain potential $(1/2\kappa_0)\sigma_m^2$ in terms of the mean tension σ_m ($\sigma_m = \sigma_{kk}/3$). Together, they provide the total potential

$$U_0(\sigma_e, \sigma_m) = f(\sigma_e) + \frac{1}{2\kappa_0}\sigma_m^2. \tag{2.2}$$

In particular, when the stress-strain relation takes the Ludwick form

$$\sigma_e = \sigma_y + h\cdot(\epsilon_e^p)^n, \tag{2.3}$$

in terms of the effective plastic strain ϵ_e^p, one has

$$f(\sigma_e) = \frac{1}{6\mu_0}\sigma_e^2 + \frac{n}{n+1}\frac{1}{h^{1/n}}(\sigma_e - \sigma_y)^{(n+1)/n} \tag{2.4}$$

beyond the yield point, with σ_y, h and n representing the initial yield stress, strength coefficient, and work-hardening exponent, in turn.

For simplicity we shall restrict our consideration to the proportionally increasing loading. While it is appreciated that even under such a loading the stress state of the ductile matrix does not remain strictly proportional, its deviation usually lies within Budiansky's (1959) limit, and therefore the deformation theory of plasticity will be used. This would allow the theory to stay in an analytical form. It then follows that the secant shear modulus of the ductile matrix is given by

$$\mu_0^s = \frac{\sigma_e}{3\epsilon_e} = \frac{\sigma_e}{3f'(\sigma_e)}, \tag{2.5}$$

at a given σ_e, and the secant Young's modulus, secant Poisson's ratio, and the secant plane-strain bulk modulus follow as

$$E_0^s = \frac{9\kappa_0\mu_0^s}{3\kappa_0 + \mu_0^s}, \quad \nu_0^s = \frac{E_0^s}{2\mu_0^s} - 1, \quad k_0^s = \kappa_0 + \frac{1}{3}\mu_0^s. \tag{2.6}$$

Thus if σ_e is known, or conversely if μ_0^s is known, the plastic state of the ductile matrix can be determined.

Since the elastic moduli of the linear comparison matrix are set to be equal to the secant moduli of the nonlinear matrix at a given stage of deformation, its strain potential is simply

$$U_0^s = \frac{1}{6\mu_0^s}\sigma_e^2 + \frac{1}{2\kappa_0}\sigma_m^2. \tag{2.7}$$

For a convex $f(\sigma_e)$ which is stronger than quadratic as the norm of σ_e becomes large, this value is always greater than U_0, with the difference

$$\Delta U_0 = U_0^s - U_0 = \frac{1}{6\mu_0^s}\sigma_e^2 - f(\sigma_e). \tag{2.8}$$

Such a difference is depicted as the shaded area in Fig. 1(a) of the σ_e versus ϵ_e curve. Since the plastic behavior of the ductile matrix is taken to be pressure independent and incompressible, this difference is contributed solely by the distortional part. In retrospect, if the strain potential of the linear matrix U_0^s is known, the potential of the nonlinear matrix U_0 can be readily determined by subtracting from it the ΔU_0 value. This point will prove useful later when we wish to determine the strain potential of the nonlinear composite from that of the linear one.

3 The Linear Comparison Composite

The nonlinear composite with aligned inclusions is schematically depicted in Fig. 1(b), and the linear comparison composite, which possesses an identical microgeometry to the real one but whose matrix has the elastic moduli $L_0^s = (3\kappa_0, 2\mu_0^s)$, is depicted alongside in Fig. 1(c). Both systems are subjected to the same boundary traction which gives rise to a uniform stress $\bar{\sigma}_{ij}$ (an overbar signifies the averaged value). Since the two-phase material is transversely isotropic, the five effective elastic moduli of the linear system may be denoted as

$$E_{11}^s,\ \nu_{12}^s,\ \kappa_{23}^s,\ \mu_{12}^s, \text{ and } \mu_{23}^s, \tag{3.1}$$

for the longitudinal Young's modulus, major Poisson's ratio, plane-strain bulk modulus, axial and transverse shear moduli, respectively. Then, the strain potential of the linear comparison composite U_s can be written as

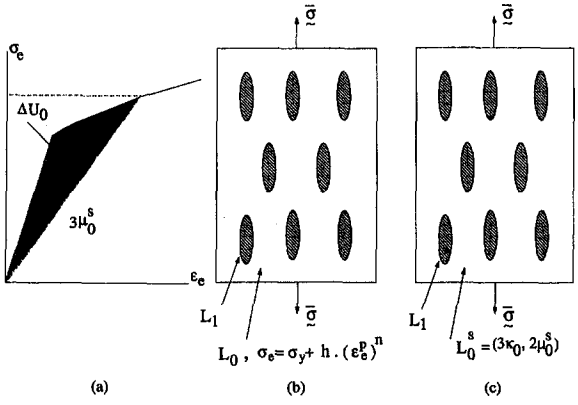


Fig. 1 (a) The difference of strain potential ΔU_0 between the linear comparison matrix and the nonlinear matrix, (b) the original nonlinear composite, and (c) the linear comparison composite

Downloaded 04 May 2010 to 171.66.16.28. Redistribution subject to ASME license or copyright; see http://www.asme.org/terms/Terms_Use.cfm

$$U_s(\bar{\sigma}_{ij}) = \frac{1}{2}\left[\frac{1}{E^s_{11}}\bar{\sigma}^2_{11} - \frac{2\nu^s_{12}}{E^s_{22}}\bar{\sigma}_{11}(\bar{\sigma}_{22}+\bar{\sigma}_{33}) + \frac{1}{E^s_{22}}(\bar{\sigma}_{22}+\bar{\sigma}_{33})^2 + \frac{1}{\mu^s_{12}}(\bar{\sigma}^2_{12}+\bar{\sigma}^2_{13}) + \frac{1}{\mu^s_{23}}(\bar{\sigma}^2_{23} - \bar{\sigma}_{22}\bar{\sigma}_{33})\right]. \quad (3.2)$$

Since the effective moduli depend on the yet unknown μ^s_0 under a given $\bar{\sigma}_{ij}$, the current plastic state of the ductile matrix must be determined first.

To this end we note from (2.5) that the secant modulus μ^s_0 depends on the effective stress σ_e. Following Qiu and Weng (1992), we define it from the distortional energy of the heterogeneously deformed matrix as

$$U^s_{0(\text{distortional})} = \frac{\sigma^2_e}{6\mu^s_0}. \quad (3.3)$$

The total energy in (3.2) is contributed by both phases. If we decompose the generally nonuniform stress field in the rth phase $\sigma^{(r)}_{ij}(x)$, into its average and the locally perturbed (with respect to its own mean) parts

$$\sigma^{(r)}_{ij}(x) = \bar{\sigma}^{(r)}_{ij} + \sigma^{pt(r)}_{ij}(x), \quad (3.4)$$

the strain energy U_s can be recast as

$$U_s = c_0\left[\frac{1}{6\mu^s_0}\sigma^2_e + \frac{1}{2\kappa_0}(\bar{\sigma}^{(0)2}_m + \langle\sigma^{pt(0)2}_m\rangle)\right] + c_1\left[\frac{1}{6\mu_1}\left(\bar{\sigma}^{(1)2}_e + \frac{3}{2}\langle\sigma'^{pt(1)}_{ij}(x)\sigma'^{pt(1)}_{ij}(x)\rangle\right) + \frac{1}{2\kappa_1}(\bar{\sigma}^{(1)2}_m + \langle\sigma^{pt(1)2}_m(x)\rangle)\right], \quad (3.5)$$

where the angle brackets $\langle\cdot\rangle$ represent the volume average of the said quantity over its own phase and $\bar{\sigma}^{(1)2}_e = \frac{3}{2}\bar{\sigma}'^{(1)}_{ij}\bar{\sigma}'^{(1)}_{ij}$. The average stress $\bar{\sigma}^{(r)}_{ij}$ is associated with a stress concentration tensor B_r as $\bar{\boldsymbol{\sigma}}^{(r)} = B_r\bar{\boldsymbol{\sigma}}_r$, such that the effective moduli given in (3.1) must satisfy Hill's (1963) relation for the overall compliances tensor $M = \Sigma c_r M_r B_r$, in terms of the compliances tensor M_r of the rth phase.

By equating (3.2) to (3.5), we arrive at an expression for σ^2_e after bring other terms on the right side of (3.5) to join those in (3.2).

4 Determination of the Effective Stress σ_e

The principle developed in Section 3 is not restricted to a particular micromechanical model, and indeed as in Ponte Castaneda's (1991) approach, it could be applied to any linear theories. For the present calculation, we shall adopt the results of Mori and Tanaka (1973) and Willis (1977), for the inclusion shape dependence. As recently proved by Weng (1992), Mori-Tanaka's moduli coincide with Willis' lower (upper) bounds if the matrix is the softer (harder) phase, and if it is neither of the two, the M-T moduli always lie within Willis' bounds. This approach could also provide the needed values for the average stress $\bar{\sigma}^{(r)}_{ij}$, but it still cannot offer information on the locally perturbed field $\sigma^{pt(r)}_{ij}(x)$. The evaluation of such a term, however, would require consideration of more specific microgeometry.

In light of Eshelby's (1957) result for an ellipsoidal inclusion, the stress field in the inclusions must be reasonably uniform if the concentration is not high. We shall therefore retain only the contribution from the mean stress $\bar{\sigma}^{(1)}_{ij}$ for phase 1. This of course is known to be valid for the composite sphere model (Hashin, 1962) and the composite cylinder model (Hashin and Rosen, 1964) in the derivations of the effective bulk modulus κ, and of the E_{11}, ν_{12}, κ_{23}, and μ_{12}, respectively, even when the concentration is high. The stress fields in the matrix associated with these derivations further indicate that the mean hydrostatic stress $\sigma^{(0)}_m(x)$ is truly uniform; thus $\sigma^{(0)}_m(x) = \bar{\sigma}^{(0)}_m$ and $\sigma^{pt(0)}_m(x) = 0$, exactly. These desirable features no longer hold under a pure shear and a transverse shear for these two types of composite, but, limiting our consideration to the condition that the inclusion concentration is not high, we shall assume that the contribution of the dilatational perturbed field $\sigma^{pt(0)}_m(x)$, to be negligible. The contribution of the deviatoric perturbed field $\sigma'^{pt(0)}_{ij}(x)$, together with $\bar{\sigma}'^{(0)}_{ij}$, is absorbed into the σ_e-term, and is fully accounted for.

It follows that the effective stress of the ductile matrix is given by

$$\sigma^2_e = \frac{6\mu^s_0}{c_0}\left[U_s - c_1\left(\frac{1}{6\mu_1}\bar{\sigma}^{(1)2}_e + \frac{1}{2\kappa_1}\bar{\sigma}^{(1)2}_m\right)\right] - \frac{3\mu^s_0}{\kappa_0}\bar{\sigma}^{(0)2}_m, \quad (4.1)$$

where U_s is in turn available from (3.2).

The explicit results of the effective moduli have been previously derived by Tandon and Weng (1984), in line with the Mori-Tanaka-Willis formulation. Keeping their original notations, one has

$$\frac{E^s_{11}}{E^s_0} = \frac{1}{1 + c_1(A_1 + 2\nu^s_0 A_2)/A},$$

$$\nu^s_{12} = \nu^s_0 - c_1\frac{\nu^s_0(A_1 + 2\nu^s_0 A_2) + (A_3 - \nu^s_0 A_4)}{A + c_1(A_1 + 2\nu^s_0 A_2)},$$

$$\frac{\kappa^s_{23}}{k^s_0} = \frac{(1+\nu^s_0)(1-2\nu^s_0)}{1 - \nu^s_0(1+2\nu^s_{12}) + c_1\{2(\nu^s_{12} - \nu^s_0)A_3 + [1 - \nu^s_0(1+2\nu^s_{12})]A_4\}/A},$$

$$\frac{\mu^s_{12}}{\mu^s_0} = 1 + \frac{c_1}{\mu^s_0/(\mu_1 - \mu^s_0) + 2c_0 S_{1212}},$$

$$\frac{\mu^s_{23}}{\mu^s_0} = 1 + \frac{c_1}{\mu^s_0/(\mu_1 - \mu^s_0) + 2c_0 S_{2323}},$$

and

$$\frac{1}{E^s_{22}} = \frac{\nu^{s2}_{12}}{E^s_{11}} + \frac{1}{4}\left(\frac{1}{\kappa^s_{23}} + \frac{1}{\mu^s_{23}}\right), \quad (4.2)$$

where the constants $A_1, A_2, \ldots, A$ are listed in the Appendix, and S_{ijkl} are the components of Eshelby's S-tensor, with ν_0 replaced by ν^s_0. As pointed out by Weng (1992), this set of moduli with spherical inclusions and circular cylinders also coincide with the lower (upper) bounds of Hashin and Shtrikman (1963), and of Hill (1964) and Hashin (1965), when the matrix is the softer (harder) phase. When the aspect ratio of inclusions approaches 0 (thin disks), they also coincide with Walpole's (1969) exact solution.

Associated with this set of moduli and consistent with Hill's relation $M = \Sigma c_r M_r B_r$, are the following average stress components for the matrix:

$$\bar{\sigma}'^{(0)}_{11} = \frac{1}{c_0}\bar{\sigma}'_{11} - \frac{c_1}{c^2_0 p}\frac{1}{1 - \mu^s_0/\mu_1}\left[\left(\frac{1}{c_0}\frac{1}{1 - \kappa_0/\kappa_1} - \frac{2}{3}\frac{1-2\nu^s_0}{1-\nu^s_0}\right)\bar{\sigma}'_{11} - \frac{1}{9}\frac{1-2\nu^s_0}{1-\nu^s_0}(2-3g)\bar{\sigma}_{kk}\right],$$

Downloaded 04 May 2010 to 171.66.16.28. Redistribution subject to ASME license or copyright; see http://www.asme.org/terms/Terms_Use.cfm

$$\bar{\sigma}'^{(0)}_{22} = \frac{1}{c_0}\bar{\sigma}'_{22} - \frac{c_1}{c_0^2 p}\left\{\frac{1}{1-\mu_0^s/\mu_1}\left[\left(\frac{1}{c_0}\frac{1}{1-\kappa_0/\kappa_1} - \frac{2}{3}\frac{1-2\nu_0^s}{1-\nu_0^s}\right)\frac{\bar{\sigma}'_{22}+\bar{\sigma}'_{33}}{2} + \frac{1}{18}\frac{1-2\nu_0^s}{1-\nu_0^s}(2-3g)\bar{\sigma}_{kk}\right] + \frac{c_0 p}{1+c_0(1-\mu_0^s/\mu_1)(S_{2222}-S_{2233}-1)}\frac{\bar{\sigma}'_{22}-\bar{\sigma}'_{33}}{2}\right\},$$

$$\bar{\sigma}'^{(0)}_{33} = \frac{1}{c_0}\bar{\sigma}'_{33} - \frac{c_1}{c_0^2 p}\left\{\frac{1}{1-\mu_0^s/\mu_1}\left[\left(\frac{1}{c_0}\frac{1}{1-\kappa_0/\kappa_1} - \frac{2}{3}\frac{1-2\nu_0^s}{1-\nu_0^s}\right)\frac{\bar{\sigma}'_{22}+\bar{\sigma}'_{33}}{2} + \frac{1}{18}\frac{1-2\nu_0^s}{1-\nu_0^s}(2-3g)\bar{\sigma}_{kk}\right] + \frac{c_0 p}{1+c_0(1-\mu_0^s/\mu_1)(S_{2222}-S_{2233}-1)}\frac{\bar{\sigma}'_{33}-\bar{\sigma}'_{22}}{2}\right\},$$

$$\bar{\sigma}^{(0)}_{kk} = \frac{1}{c_0}\bar{\sigma}_{kk} - \frac{c_1}{c_0^2 p}\frac{1}{1-\kappa_0/\kappa_1}\left[-\frac{1+\nu_0^s}{2(1-\nu_0^s)}(2-3g)\bar{\sigma}'_{11} + h\bar{\sigma}_{kk}\right], \quad (4.3)$$

and for the shear components with $i \neq j$,

$$\bar{\sigma}^{(0)}_{ij} = \frac{2(\mu_1-\mu_0^s)S_{ijij}+\mu_0^s}{(c_1+2c_0 S_{ijij})(\mu_1-\mu_0^s)+\mu_0^s}\bar{\sigma}_{ij}, \quad (i\neq j;\ i,j \text{ no sum}). \quad (4.4)$$

The three constants p, g, and h are functions of the aspect ratio α, with

$$p = (S_{1111}+a+b)(S_{2222}+S_{2233}+a+2b) - 2(S_{1122}+b)(S_{2211}+b),$$

$$h = \begin{cases} \dfrac{1}{c_0(1-\mu_0^s/\mu_1)} + \dfrac{1}{12(1-\nu_0^s)}\left\{2(7-2\nu_0^s) + \dfrac{18}{\alpha^2-1} - \left[12(2-\nu_0^s) + \dfrac{27}{\alpha^2-1}\right]g\right\}, & \text{when } \alpha \neq 1, \\ \dfrac{2}{15}\dfrac{4-5\nu_0^s}{1-\nu_0^s} + a, & \text{when } \alpha = 1, \end{cases}$$

$$a = \frac{1}{c_0(1-\mu_0^s/\mu_1)} - 1,$$

$$b = \frac{1}{3c_0}\left(\frac{1}{1-\kappa_0/\kappa_1} - \frac{1}{1-\mu_0^s/\mu_1}\right),$$

$$g = \begin{cases} 1 & \alpha \to \infty \\ \dfrac{\alpha}{(\alpha^2-1)^{3/2}}[\alpha(\alpha^2-1)^{1/2} - \cosh^{-1}\alpha] & \alpha > 1 \\ \dfrac{2}{3} & \alpha = 1 \\ \dfrac{\alpha}{(1-\alpha^2)^{3/2}}[\cos^{-1}\alpha - \alpha(1-\alpha^2)^{1/2}] & \alpha < 1 \\ 0 & \alpha \to 0. \end{cases} \quad (4.5)$$

The average stress of the inclusions then follows from

$$\bar{\sigma}^{(1)}_{ij} = \frac{1}{c_1}(\bar{\sigma}_{ij} - c_0\bar{\sigma}^{(0)}_{ij}). \quad (4.6)$$

Returning to (4.1) with this set of information, the effective stress σ_e is then given as a function of the secant shear modulus μ_0^s. Their relation must also satisfy the constitutive Eq. (2.5) and, together, these two connections provide a solution for both μ_0^s and σ_e at a given applied $\bar{\sigma}_{ij}$. The secant moduli E^s_{11}, E^s_{22}, ... , etc., are then known, and so is the strain potential $U_s(\bar{\sigma}_{ij})$ of the linear comparison composite. The strain potential $U(\bar{\sigma}_{ij})$ of the original, nonlinear composite differs from U_s by $c_0\Delta U_0$ from the matrix phase; in light of (2.8), it is given by

$$U(\bar{\sigma}_{ij}) = U_s(\bar{\sigma}_{ij}) - c_0\left[\frac{1}{6\mu_0^s}\sigma_e^2 - f(\sigma_e)\right]. \quad (4.7)$$

5 Connection With Ponte Castaneda's Bounds or Estimates of Willis' Type for an Elastically Incompressible Matrix Containing Voids or Rigid Inclusions

We now consider the special cases of voids or rigid inclusions embedded in an elastically incompressible matrix ($\nu_0 = \frac{1}{2}$). Constants $A_1, A_2, \ldots A$ in (4.2) then depend only on α and c_1 and the S-tensor depends only on α. With

$$E_0^s = 3\mu_0^s, \quad \nu_0^s = \tfrac{1}{2}, \quad k_0^s(1-2\nu_0^s) = \mu_0^s, \quad (5.1)$$

Eq. (4.2) can be cast into the form

$$\frac{E^s_{11}}{3\mu_0^s} = \frac{1}{m_1(\alpha, c_1)}, \quad \nu^s_{12} = \nu^s_{12}(\alpha, c_1), \quad \frac{E^s_{22}}{3\mu_0^s} = \frac{1}{m_2(\alpha, c_1)},$$

$$\frac{\mu^s_{23}}{\mu_0^s} = \frac{1}{m_4(\alpha, c_1)}, \quad \frac{\mu^s_{12}}{\mu_0^s} = \frac{1}{m_5(\alpha, c_1)}, \quad (5.2)$$

where functions m_1, m_2, m_4, and m_5 are independent of μ_0^s.

Ponte Castaneda's lower bound or estimate of Willis' type under this condition becomes

$$\check{U}_-(\bar{\boldsymbol{\sigma}}) = \sup_{\hat{\mu}_0}\{\check{\tilde{U}}(\bar{\boldsymbol{\sigma}}) - V(\hat{\mu}_0)\}, \quad \text{in his notations}$$

$$= \sup_{\mu_0^s}\left\{U_s(\bar{\boldsymbol{\sigma}}) - c_0\left[\frac{1}{2}\sigma_e f'(\sigma_e) - f(\sigma_e)\right]\right\}, \quad \text{in the present notations}$$

$$= c_0 \sup_{\mu_0^s}\left\{\frac{1}{6\mu_0^s}s^2 - \left[\frac{1}{2}sf'(s) - f(s)\right]\right\}$$

$$= c_0 f(s), \quad (5.3)$$

where from (3.2), the quadratic strain potential $U_s(\bar{\boldsymbol{\sigma}})$ has been written as $U_s(\bar{\boldsymbol{\sigma}}) = c_0(1/6\mu_0^s)s^2$, with

$$s^2 = \frac{1}{c_0}\{m_1\bar{\sigma}^2_{11} - 2\nu^s_{12}m_2(\bar{\sigma}_{22}+\bar{\sigma}_{33}) + m_2(\bar{\sigma}_{22}+\bar{\sigma}_{33})^2 + 3[m_4(\bar{\sigma}^2_{23} - \bar{\sigma}_{22}\bar{\sigma}_{33}) + m_5(\bar{\sigma}^2_{12}+\bar{\sigma}^2_{13})]\}. \quad (5.4)$$

On the other hand from the present theory in (4.1), since the inclusion phase now contributes no energy and $\kappa_0 \to \infty$, it is evident that this s is exactly equal to our effective stress σ_e. The nonlinear strain potential of the composite, given by (4.7), then becomes

$$U(\bar{\sigma}_{ij}) = c_0 f(s), \quad (5.5)$$

which is exactly the value in (5.3) obtained by Ponte Castaneda's optimization process. The present theory therefore coincides with Ponte Castaneda's lower bound of strain potential of Willis' type for aligned spheroidal voids, and with his estimate for aligned rigid inclusions.

The close connection between Qiu and Weng's energy approach and Ponte Castaneda's bounds or estimates with an incompressible matrix is likely to go beyond the two special cases of voids and rigid inclusions as demonstrated here. More

Downloaded 04 May 2010 to 171.66.16.28. Redistribution subject to ASME license or copyright; see http://www.asme.org/terms/Terms_Use.cfm

recently, Li et al. (1993) used Ponte Castaneda's method to study the problem of aligned and three-dimensional randomly oriented rigid inclusions in an incompressible matrix, and Bhattacharyya and Weng (1994) also used the energy approach to address the same problem in both compressible and incompressible matrix. As the expositions are somewhat different, it is not easy to see the immediate connection between the two. Ponte Castaneda's variational principle has also been applied by deBotton and Ponte Castaneda (1993) to a fiber-reinforced composite ($\alpha \to \infty$) and by Li and Ponte Castaneda (1993) to a similar problem addressed here, but with incompressible matrix and incompressible inclusions. Since with the general spheroidal shape and elastic inclusions the analytical results are difficult to put in a simple form, it is also not easy to prove their correspondence in these two cases. But the similarity between ΔU_0 here and PC's V, and the same choice of the Hashin-Shtrikman-Walpole bounds or the Willis bounds to represent the effective elastic properties of the linear comparison composite, lead one to believe that these two approaches are likely to coincide when the matrix is incompressible. The second writer is in the process of exploring their theoretical connection when the matrix is incompressible, both methods lead to the same results for several cases, but that when the matrix is compressible, PC's procedure and the energy approach do not seem to give the same results. Since the energy approach requires no optimization procedure it is much easier to use (especially with multiphase or randomly oriented ductile inclusions; see Bhattacharyya and Weng, 1996), and yet Ponte Castaneda's bounds or estimates are firmly based on the variational principle it is more rigorous. Such a connection will prove useful in estimating the overall nonlinear behavior of a heterogeneous system where both approaches provide the same results.

6 Comparison With an Exact Solution for a Fiber-Reinforced Composite

Before we proceed to apply this theory, it is desirable to evaluate its numerical accuracy first. To this end we note that, when the aligned spheroids take the shape of a long circular cylinder, exact local analytical solution can be derived under the plane-strain biaxial loading. For simplicity we shall assume the matrix to be elastically incompressible and its nonlinear stress-strain curve obey the simple bilinear form, with $n = 1$ in (2.3). Using the composite cylinder model, the analysis can be carried out following Hill's (1950) framework for an ideally plastic hollow cylinder. Though elementary, the derivation process is not short and therefore only the principal results are recalled here.

Under the plane-strain biaxial loading ($\bar{\epsilon}_{11} = 0$, $\bar{\sigma}_{22} = \bar{\sigma}_{33} = \bar{\sigma}$), the biaxial stress-strain curve of the composite exhibits the typical three stages of deformation: elastic, partially plastic, and fully plastic. Onset of yielding, which occurs at the fiber-matrix interface, takes place when the biaxial stress reaches

$$\bar{\sigma} = (\bar{\sigma}_{22} = \bar{\sigma}_{33}) = \frac{\sigma_y}{\sqrt{3}}\left(c_0 + \frac{k_1}{\mu_0}\right), \tag{6.1}$$

and this corresponds to a biaxial composite strain

$$\bar{\epsilon} = (\bar{\epsilon}_{22} = \bar{\epsilon}_{33}) = \frac{\sqrt{3}c_1}{2E_0}\sigma_y. \tag{6.2}$$

During partial yielding, with $r = R$ denoting the elastic/plastic boundary, the corresponding $\bar{\sigma}$ and $\bar{\epsilon}$ are

$$\bar{\sigma} = \frac{\sigma_y}{\sqrt{3}}\left(1 - \frac{R^2}{a_2^2}\right) + \frac{2}{\sqrt{3}}\frac{\sigma_y}{(E_0 + h)} \times \left[E_0 \ln\frac{R}{a_1} + \frac{h}{2}\left(\frac{R^2}{a_1^2} - 1\right)\right] + \frac{\sqrt{3}k_1}{E_0}\sigma_y\frac{R_1^2}{a_1^2},$$

$$\bar{\epsilon} = \frac{\sqrt{3}\sigma_y}{2E_0}\frac{R^2}{a_2^2}, \tag{6.3}$$

where a_1 and a_2 are the inner and the outer radii, respectively, of the matrix phase. By increasing the value of R from a_1 to a_2, the biaxial $\bar{\sigma}$ versus $\bar{\epsilon}$ curve can be obtained. In the fully plastic state, the biaxial strain $\bar{\epsilon}$ will continue to increase from the initial value $(\sqrt{3}/2E_0)\sigma_y$. The subsequent biaxial stress is governed by

$$\bar{\sigma} = \frac{2E_0}{\sqrt{3}(E_0 + h)}\left[\frac{1}{2}\sigma_y \ln\frac{1}{c_1} + \frac{h}{\sqrt{3}}\frac{c_0}{c_1}\bar{\epsilon}\right] + \frac{2k_1}{c_1}\bar{\epsilon}. \tag{6.4}$$

On the other hand with the present energy method, we first note that, as $\alpha \to \infty$, κ_{23}^s in (4.2) can be first simplified to

$$\frac{\kappa_{23}^s}{k_0^s} = 1 + \frac{c_1}{k_0^s/(k_1 - k_0^s) + c_0 k_0^s/(k_0^s + \mu_0^s)}, \tag{6.5}$$

for the fiber-reinforced composite. This is also the familiar result of Hashin and Rosen's (1964) composite cylinder model, and the expression of the Hill (1964)–Hashin (1965) bounds for

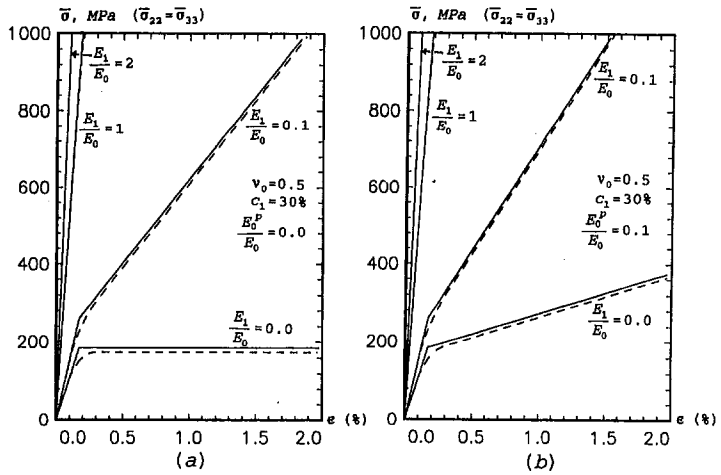


Fig. 2 Comparison between the energy approach and the exact, local analysis for a fiber-reinforced composite under plane-strain, biaxial loading with (*a*) ideally plastic matrix and (*b*) a work-hardening matrix

Downloaded 04 May 2010 to 171.66.16.28. Redistribution subject to ASME license or copyright; see http://www.asme.org/terms/Terms_Use.cfm

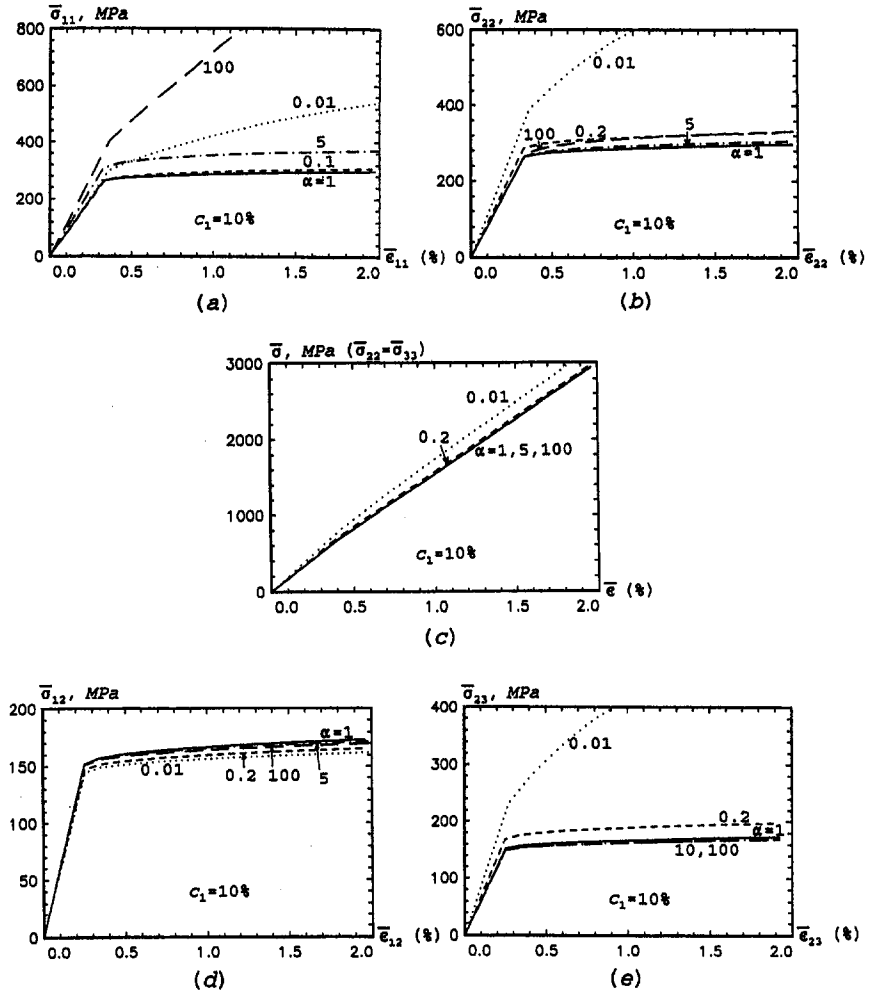


Fig. 3 The aspect ratio dependence of the overall elastoplastic behavior under five respective loadings

the plane-strain bulk modulus of a fiber-reinforced composite. Now, with an elastically incompressible matrix, it further reduces to

$$\kappa_{23}^s = \frac{1}{c_1}(c_0\mu_0^s + k_1), \tag{6.6}$$

which provides the biaxial strain $\bar{\varepsilon} = \bar{\sigma}/(2\kappa_{23}^s)$, at the applied biaxial stress $\bar{\sigma}$. The effective stress σ_e, given by (4.1), takes the form

$$\sigma_e^2 = \frac{3\mu_0^s}{c_0}\left(\frac{1}{\kappa_{23}^s}\bar{\sigma}^2 - \frac{c_1}{k_1}\bar{\sigma}^{(1)^2}\right), \tag{6.7}$$

where $\bar{\sigma}^{(1)} = (1/c_1)(\bar{\sigma} - c_0\bar{\sigma}^{(0)})$, and from (4.3), the average plane-strain biaxial stress of the matrix is given by

$$\bar{\sigma}^{(0)} = \frac{2(\nu_{12}^s - 1)}{c_0(1 - 2\nu_1)}\bar{\sigma}. \tag{6.8}$$

The major Poisson's ratio ν_{12}^s appears in this equation due to the plane-strain condition; it is given by (4.2) as

$$\nu_{12}^s = c_1\nu_1 + \frac{1}{2}c_0 + \frac{c_1c_0(\frac{1}{2} - \nu_1)\mu_0^s}{c_0\mu_0^s + k_1} \tag{6.9}$$

under the condition $\alpha \to \infty$.

At the applied $\bar{\sigma}$, the effective stress σ_e is seen to depend on μ_0^s from (6.6) to (6.9), and they are also connected to each other through the constitutive Eq. (2.5) and (2.4), with $n = 1$ here. A simple iterative scheme is required to determine the precise value of σ_e and μ_0^s from these two equations under a given $\bar{\sigma}$. Once μ_0^s is found, the biaxial plane-strain $\bar{\varepsilon}$ can be determined from the corresponding κ_{23}^s value in (6.6).

The comparison between the predictions of the energy approach and of the exact, local analysis is shown in Fig. 2, depicted as the solid and dashed lines, respectively. These curves have been calculated by taking the Young's modulus and yield stress of the matrix as those of a 6061-T6 aluminum, with $E_0 = 68.3$ GPa and $\sigma_y = 250$ MPa. In Fig. 2(a), the plastic behavior of the matrix was taken to be ideally plastic, but in Fig. 2(b), it is with the work-hardening modulus ratio $E_0^p/E_0 = 0.1$ (Note: $E_0^p = d\bar{\sigma}/d\bar{\varepsilon}$; it is related to h through $1/E_0^p = 1/E_0 + 1/h$). By varying the elastic modular ratio E_1/E_0 (with the Poisson ratio set at $\nu_1 = 0.17$ as that of a silicon carbide), the calculated overall nonlinear behaviors of the composite at the fiber concentration $c_1 = 0.30$ are seen to compare well with those of the exact, local analysis. In particular, both approaches yield almost linear behavior when the fibers are stiffer than the matrix, and the nonlinearity increases progressively with increasing compliances in the fibers, with the channel pores ($E_1/E_0 = 0$) exhibiting the softest nonlinear response.

Of some theoretical interest is the asymptotic state in the fully plastic range. According to the exact solution (6.4), the tangent modulus of the composite is given by

Downloaded 04 May 2010 to 171.66.16.28. Redistribution subject to ASME license or copyright; see http://www.asme.org/terms/Terms_Use.cfm

$$\frac{d\bar{\sigma}}{d\bar{\epsilon}} = \frac{2}{c_1}\left(\frac{c_0 E_0^p}{3} + k_1\right) \approx \frac{2}{c_1}(c_0\mu_0^s + k_1), \qquad (6.10)$$

and according to the energy approach, it is

$$\frac{d\bar{\sigma}}{d\bar{\epsilon}} \approx 2\kappa_{23}^s = \frac{2}{c_1}(c_0\mu_0^s + k_1), \qquad (6.11)$$

according to (6.6). Thus in the deeply plastic range, these two curves display the same work-hardening rate and become parallel to each other.

The difference between the flow stresses predicted by the energy method and by the exact, local analysis in the fully plastic range is

$$\bar{\sigma}_{\text{energy}} - \bar{\sigma}_{\text{exact}} = \frac{2c_0}{c_1}\left(\mu_0^s - \frac{E_0^p}{3}\right)\bar{\epsilon} - \frac{1}{\sqrt{3}}\frac{E_0}{E_0 + h}\sigma_y \ln\frac{1}{c_1}, \qquad (6.12)$$

which reduces to $(2c_0/c_1)\mu_0^s\bar{\epsilon} - (1/\sqrt{3})\sigma_y \ln 1/c_1$, for an ideally plastic matrix.

7 The Aspect-Ratio Dependence of the Silicon-Carbide/Aluminum System

We now apply the developed theory to a practical system, and for this we choose the silicon-carbide/6061-T6 aluminum composite with (Arsenault, 1984; Chellman and Nieh, 1984)

$$E_1 = 490 \text{ GPa}, \quad \nu_1 = 0.17$$
$$E_0 = 68.3 \text{ GPa}, \quad \nu_0 = 0.33, \quad \sigma_y = 250 \text{ MPa}, \qquad (7.1)$$
$$h = 173 \text{ MPa}, \quad n = 0.455.$$

At $c_1 = 10$ percent, the aspect-ratio (α) dependence of the stress-strain curves under five respective loadings is displayed in Fig. 3. In these figures the values of α selected for consideration are $\alpha = 100$, 5, 1, 0.2, and 0.01, representing the long and short fibers, spheres, oblate inclusions, and disks, in turn. A quick glance over these figures indicates that, more so than the elastic behavior, the overall plastic behavior of the composite is strongly dependent upon the inclusion shape. Along the axial direction, fiber reinforcement is seen to be most effective and spheres the least effective. The stronger response provided by disks ($\alpha = 0.01$) over spheres here is perhaps somewhat unexpected, but Tandon and Weng's (1984) calculation for the elastic moduli also reflect such a property at low concentration. At a higher concentration, however, spherical inclusions can become more effective than the aligned disks. Similar trend has also been reported by Lee and Mear (1991), using a self-consistent scheme. On the other hand, if the matrix is elastically also incompressible, disks always provide more stiffening effect than spheres.

The in-plane elastoplastic responses, such as those under the transverse tension $\bar{\sigma}_{22}$, plane-strain biaxial tension ($\bar{\sigma}_{22} = \bar{\sigma}_{33}$), and the transverse shear $\bar{\sigma}_{23}$, all point to the superior reinforcement by the disks; this is especially pronounced under $\bar{\sigma}_{22}$ and $\bar{\sigma}_{23}$. Under these two types of loading, all other inclusion shapes lead to a similar level of flow stress. The axial shear behavior under $\bar{\sigma}_{12}$ appears to exhibit the lowest inclusion-shape sensitivity at this concentration level.

Finally, it is useful to examine the influence of Poisson ratio ν_0, of the matrix on the stress-strain curves of the composite. As the present method permits one to calculate the stress-strain behavior of the system alike regardless of the state of Poisson contraction, whereas many other nonlinear analyses, such as those by Budiansky et al. (1982) and Lee and Mear (1991), could only address the problem involving an incompressible matrix ($\nu_0 = \nu_0^s = \frac{1}{2}$), comparison between the overall responses

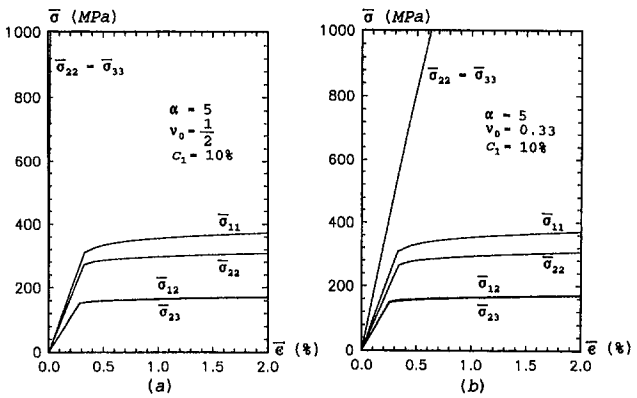


Fig. 4 The influence of Poisson's ratio of the ductile matrix on the overall elastoplastic behavior of a short-fiber reinforced composite: (*a*) $\nu_0 = \frac{1}{2}$ and (*b*) $\nu_0 = 0.33$

of the composite—one with $\nu_0 = \frac{1}{2}$ and the other with $\nu_0 \neq \frac{1}{2}$—would allow one to make a useful interpretation of their calculations for a system with an elastically compressible matrix. To this end we plot in Fig. 4 the five respective responses of an aligned composite with $\alpha = 5$. The results with an elastically incompressible matrix ($\nu_0 = \frac{1}{2}$) are depicted on the left, whereas those with $\nu_0 = 0.33$ are plotted on the right. These curves have been calculated using the properties of the silicon-carbide/aluminum, except for ν_0. This comparison suggests that the Poisson ratio only has an appreciable level of influence on the plane-strain, biaxial loading, and that for the other four types of loading, it has no significant effect. We have also carried out the computations with the aspect ratios of $\alpha \to \infty$, 1, and 0.2, and found the nature of difference to be exactly the same. One is led to conclude that, for the class of composites containing aligned spheroidal inclusions, computations based on an incompressible matrix are likely to provide accurate approximations for a composite with a compressible matrix, except for the plane-strain biaxial behavior.

Acknowledgment

This work has been supported by the National Science Foundation, Mechanics and Materials Program, under Grant MSS-9114745, and by the Office of Naval Research, under Grant N-00014-91-J-1937. G.J.W. is grateful to Dr. Yapa Rajapakse, the Program Manager at ONR, for his interest in this work. Y.P.Q. thanks Dr. T. D. Gerhardt, Senior Research Fellow of Sonoco Products Company, for his support and understanding.

References

Arsenault, R. J., 1984, "The Strengthening of Aluminum Alloy 6061 by Fiber and Platelet Silicon Carbide," *Material Science and Engineering,* Vol. 64, pp. 171–181.

Berveiller, M., and Zaoui, A., 1979, "An Extension of the Self-consistent Scheme to Plastically-Flowing Polycrystals," *Journal of the Mechanics and Physics of Solids,* Vol. 26, pp. 325–344.

Bhattacharyya, A., and Weng, G. J., 1994, "The Elastoplastic Behavior of a Class of Two-Phase Composites Containing Rigid Inclusions," ASME *Applied Mechanics Reviews,* Vol. 47, pp. S45–S65.

Bhattacharyya, A., and Weng, G. J., 1996, "Theoretical Calculation of Stress-Strain Behavior of Dual-Phase Metals with Randomly Oriented Spheroidal Inclusions," *Metallurgical and Materials Transactions,* in press.

Budiansky, B., 1959, "A Reassessment of Deformation Theories of Plasticsity," ASME JOURNAL OF APPLIED MECHANICS, Vol. 26, pp. 259–264.

Budiansky, B., Hutchinson, J. W., and Slutsky, S., 1982, "Void Growth and Collapse in Viscous Solids," *Mechanics of Solids,* The Rodney Hill 60th Anniversary Volume, H. G. Hopkins and M. J. Sewell, eds., Pergamon, Oxford, pp. 13–45.

deBotton, G., and Ponte Castaneda, P., 1993, "Elastoplastic Constitutive Relations for Fiber-Reinforced Solids," *International Journal of Solids and Structures,* Vol. 30, pp. 1865–1890.

Eshelby, J. D., 1957, "The Determination of the Elastic Field of an Ellipsoidal Inclusion, and Related Problems," *Proceedings of the Royal Society, London,* Vol. A241, pp. 376–396.

Downloaded 04 May 2010 to 171.66.16.28. Redistribution subject to ASME license or copyright; see http://www.asme.org/terms/Terms_Use.cfm

Hashin, Z., 1962, "The Elastic Moduli of Heterogeneous Materials," ASME JOURNAL OF APPLIED MECHANICS, Vol. 29, pp. 143–150.

Hashin, Z., and Shtrikman, S., 1963, "A Variational Approach to the Theory of the Elastic Behavior of Multiphase Materials," *Journal of the Mechanics and Physics of Solids,* Vol. 11, pp. 127–140.

Hashin, Z., and Rosen, B. W., 1964, "The Elastic Moduli of Fiber-Reinforced Materials," ASME JOURNAL OF APPLIED MECHANICS, Vol. 31, pp. 223–232.

Hill, R., 1950, *The Mathematical Theory of Plasticity,* Clarendon Press, Oxford, pp. 97–106.

Hill, R., 1963, "Elastic Properties of Reinforced Solids: Some Theoretical Principles," *Journal of the Mechanics and Physics of Solids,* Vol. 11, pp. 357–372.

Hill, R., 1965, "Continuum Micro-Mechanics of Elastoplastic Polycrystals," *Journal of the Mechanics and Physics of Solids,* Vol. 13, pp. 89–101.

Lee, B. J., and Mear, M. E., 1991, "Effect of Inclusion Shape on the Stiffness of Non-Linear Two Phase Composites," *Journal of the Mechanics and Physics of Solids,* Vol. 39, pp. 627–649.

Li, G., Ponte Castaneda, P., and Douglas, A. S., 1993, "Constitutive Models for Ductile Solids Reinforced by Rigid Spheroidal Inclusions," *Mechanics of Materials,* Vol. 15, pp. 279–300.

Li, G., and Ponte Castaneda, P., 1993, "The Effect of Particle Shape and Stiffness on the Constitutive Behavior of Metal-Matrix Composites," *International Journal of Solids and Structures,* Vol. 30, pp. 3189–3209.

Mori, T., and Tanaka, K., 1973, "Average Stress in the Matrix and Average Elastic Energy of Materials with Misfitting Inclusions," *Acta Metallurgica,* Vol. 21, pp. 571–574.

Nieh, T. G., and Chellman, D. J., 1984, "Modulus Measurements in Discontinuous Reinforced Aluminum Composites," *Scripta Metallurgica,* Vol. 8, pp. 925–928.

Ponte Castaneda, P., 1991, "The Effective Mechanical Properties of Nonlinear Isotropic Composites," *Journal of the Mechanics and Physics of Solids,* Vol. 39, pp. 45–71.

Qiu, Y. P., and Weng, G. J., 1992, "A Theory of Plasticity for Porous Materials and Particle-Reinforced Composites," ASME JOURNAL OF APPLIED MECHANICS, Vol. 59, pp. 261–268.

Talbot, D. R. S., and Willis, J. R., 1985, "Variational Principle for Inhomogeneous Nonlinear Media," *IMA Journal of Applied Mathematics,* Vol. 35, pp. 39–54.

Tandon, G. P., and Weng, G. J., 1984, "The Effect of Aspect Ratio of Inclusions on the Elastic Properties of Unidirectionally Aligned Composites," *Polymer Composites,* Vol. 5, pp. 327–333.

Tandon, G. P., and Weng, G. J., 1988, "A Theory of Particle-Reinforced Plasticity," ASME JOURNAL OF APPLIED MECHANICS, Vol. 55, pp. 126–135.

Weng, G. J., 1982, "A Unified, Self-Consistent Theory for the Plastic-Creep Deformation of Metals," ASME JOURNAL OF APPLIED MECHANICS, Vol. 49, pp. 728–734.

Weng, G. J., 1992, "Explicit Evaluation of Willis' Bounds with Ellipsoidal Inclusions," *International Journal of Engineering Science,* Vol. 30, pp. 83–92.

Willis, J. R., 1977, "Bounds and Self-Consistent Estimates for Overall Properties of Anisotropic Composites," *Journal of the Mechanics and Physics of Solids,* Vol. 25, pp. 185–202.

Willis, J. R., 1991, "On Methods for Bounding the Overall Properties of Nonlinear Composites," *Journal of the Mechanics and Physics of Solids,* Vol. 39, pp. 73–86.

APPENDIX

Appendix Constants A_1, A_2, A_3, A_4, A_5 and A

Keeping Tandon and Weng's (1984) original notations, these constants are given by

$$A_1 = D_1(B_4 + B_5) - 2B_2,$$

$$A_2 = (1 + D_1)B_2 - (B_4 + B_5),$$

$$A_3 = B_1 - D_1B_3,$$

$$A_4 = (1 + D_1)B_1 - 2B_3,$$

$$A_5 = (1 - D_1)/(B_4 - B_5),$$

and

$$A = 2B_2B_3 - B_1(B_4 + B_5), \tag{A1}$$

where in terms of the (secant) Lamé constants μ_r^s and λ_r^s of the rth phase,

$$D_1 = 1 + 2(\mu_1 - \mu_0^s)/(\lambda_1 - \lambda_0^s),$$

$$D_2 = (\lambda_0^s + 2\mu_0^s)/(\lambda_1 - \lambda_0^s),$$

$$D_3 = \lambda_0^s/(\lambda_1 - \lambda_0^s), \tag{A2}$$

and

$$B_1 = c_1D_1 + D_2 + c_0(D_1S_{1111} + 2S_{2211}),$$

$$B_2 = c_1 + D_3 + c_0(D_1S_{1122} + S_{2222} + S_{2233}),$$

$$B_3 = c_1 + D_3 + c_0[S_{1111} + (1 + D_1)S_{2211}],$$

$$B_4 = c_1D_1 + D_2 + c_0(S_{1122} + D_1S_{2222} + S_{2233}),$$

$$B_5 = c_1 + D_3 + c_0(S_{1122} + S_{2222} + D_1S_{2233}). \tag{A3}$$

Downloaded 04 May 2010 to 171.66.16.28. Redistribution subject to ASME license or copyright; see http://www.asme.org/terms/Terms_Use.cfm

Symmetrical Propagation of a Central Crack in Orthotropic Material

Y. M. Tsai
Department of Aerospace Engineering and Engineering Mechanics, Iowa State University, Ames, IA 50011

A central crack which propagates symmetrically in an orthotropic composite plate is investigated using the techniques of Fourier and Laplace transforms. The crack is located along one of the principal axes of the material. Complete contour integrations are carried out in the evaluation of the Laplace inversion integrals. For the crack tips running at a constant speed, exact expressions for the dynamic crack shape and the dynamic stress distribution with singularities in the crack plane are obtained in terms of anisotropic material constants and crack speed. The dynamic expressions are evaluated numerically by using graphite/epoxy and glass/epoxy composites and an isotropic material as sample materials. The dynamic solution reduces to the static solution at zero crack speed. During crack propagation, the deviation between dynamic and static solutions is governed by dynamic correction factors which are nondimensional functions of the ratios among anisotropic material constants and the ratio of crack speed to shear-wave speed. Values of these dynamic factors are obtained for the sample composites at a large range of crack speed. The dynamic stress intensity factor vanishes at the corresponding Rayleigh wave speed.

Introduction

The dynamic problem of a propagating crack has been investigated for an infinite isotropic material by Broberg (1960) and Tsai (1973). A central crack was growing symmetrically in its crack plane. The dynamic stress intensity factor was shown to be a function of crack speed, wave speeds, and Poisson's ratio (Broberg, 1960; Tsai, 1973). Freund and Rosakis (1992) studied the asymptotic field ahead of a crack during nonsteady growth in an isotropic material. The technique of caustics was used to measure the dynamic toughness of a propagating crack for various crack speeds (Kalthoff, Beinart, Winkler, and Klemm, 1980). Study of rapid crack propagation is important in the understanding of dynamic fracture and crack arrest.

Various stress-strain relations in terms of elastic material constants were defined to describe the stiffness of composite materials (Tsai and Hahn, 1980). Plane waves were shown to be able to propagate in a transversely isotropic, infinite elastic solid (Stoneley, 1949). The wave speeds for plane waves in an anisotropic plate were described in terms of the anisotropic material constants (Moon, 1975). The propagations of various wave modes were involved in characterizing the elastic properties of composite materials (Papadakis, etc., 1990). The mode III problems of cracked orthotropic strips were analyzed under the assumption of a steady-state crack motion (Georgiadis, 1986). Solutions of the stress intensity factor were presented by Willis (1992) for a propagating semi-infinite crack in an orthotropic material.

The propagation of a central crack in an orthotropic composite plate is investigated in the present work. The crack is growing symmetrically in the crack plane. Stress waves are emitted during the crack propagation. The problem is solved using the techniques of Fourier and Laplace transforms. A complete contour integration is carried out in the process of the Laplace inversion. When the crack is propagating at a constant speed, the crack shape function and the stress intensity factor are obtained in exact expressions in terms of orthotropic material constants and crack speed. The effects that the material orthotropy and the crack speed have on the dynamic fracture behavior are investigated for graphite/epoxy and glass/epoxy composites.

Formal Solution

The stress-strain relationship for an orthotropic composite material in a two-dimensional state of stress has the following form (Tsai and Hahn, 1980):

$$\sigma_{xx} = Q_{11}\epsilon_{xx} + Q_{12}\epsilon_{yy}$$

$$\sigma_{yy} = Q_{12}\epsilon_{xx} + Q_{22}\epsilon_{yy}$$

$$\sigma_{xy} = Q_{66}\epsilon_{xy}. \tag{1}$$

The x and y-axes are the principal axes of the material and the stiffness moduli Q_{ij} are related to the engineering constants E_i and ν_{ij}. An infinite orthotropic plate is assumed to carry a uniform tension p_o in the y-direction at infinite. A central crack starts to propagate at time t equal to zero. The crack is growing symmetrically with current half-crack length $a(t)$ in a plane normal to the direction of tension. Solution of the problem can be obtained by superposing a uniform tension p_o on the stress fields set up by a uniform pressure, $-p_o$, which acts on the crack surfaces.

The wave field generated by the propagating crack is symmetrical with respect to the x and y-axes. The displacement components in the x and y directions are, respectively, described as u and v. The boundary conditions on the crack plane $y = 0$ for $t > o$ are

$$\sigma_{xy} = o \tag{2}$$

$$v = \begin{cases} w(x), & |x| < a \\ 0, & |x| > a. \end{cases} \tag{3}$$

Contributed by the Applied Mechanics Division of THE AMERICAN SOCIETY OF MECHANICAL ENGINEERS for publication in the ASME JOURNAL OF APPLIED MECHANICS.

Discussion on this paper should be addressed to the Technical Editor, Professor Lewis T. Wheeler, Department of Mechanical Engineering, University of Houston, Houston, TX 77204-4792, and will be accepted until four months after final publication of the paper itself in the ASME JOURNAL OF APPLIED MECHANICS.

Manuscript received by the ASME Applied Mechanics Division, Feb. 17, 1994; final revision, Aug. 3, 1994. Associate Technical Editor: D. M. Barnett.

Copyright © 1995 by ASME

Downloaded 04 May 2010 to 171.66.16.28. Redistribution subject to ASME license or copyright; see http://www.asme.org/terms/Terms_Use.cfm

The unknown function w describes the crack surface opening and will be determined later in terms of the prescribed uniform pressure, $-p_o$. If the strain-displacement relations are used, the equations of motion can be written in terms of the displacement components as follows:

$$\beta \frac{\partial^2 u}{\partial x^2} + (1 + \delta) \frac{\partial^2 v}{\partial x \partial y} + \frac{\partial^2 u}{\partial y^2} = \frac{1}{c_2^2} \frac{\partial^2 u}{\partial t^2} \tag{4}$$

$$(1 + \delta) \frac{\partial^2 u}{\partial x \partial y} + \frac{\partial^2 v}{\partial x^2} + \alpha \frac{\partial^2 v}{\partial y^2} = \frac{1}{c_2^2} \frac{\partial^2 v}{\partial t^2}. \tag{5}$$

The normalized material constants and the shear wave speed c_2 are

$$\alpha = Q_{22}/Q_{66}, \quad \beta = Q_{11}/Q_{66}, \quad \delta = Q_{12}/Q_{66}$$
$$c_2^2 = Q_{66}/\rho \tag{6}$$

where the quantity ρ is the density of the medium.

The Laplace transform is operated over the time variable t in Eqs. (4) and (5), and the transformed function of $f(t)$ is designated as $f^*(p)$, p being the Laplace transform parameter. In order to satisfy the symmetry features of the problem described above, the sine transform is applied over x variable in Eq. (4) while the cosine transform is applied over Eq. (5) in terms of the transform parameter s. The transformed equations have the following forms of telegraph equations:

$$\frac{\partial^2 \bar{u}_s^*}{\partial y^2} - (s^2\beta + p^2/c_2^2)\bar{u}_s^* - (1 + \delta)s \frac{\partial \bar{v}_c^*}{\partial y} = 0 \tag{7}$$

$$\alpha \frac{\partial^2 \bar{v}_c^*}{\partial y^2} - (s^2 + p^2/c_2^2)\bar{v}_c^* + (1 + \delta)s \frac{\partial \bar{u}_s^*}{\partial y} = 0. \tag{8}$$

The function $\bar{u}_s$ is the sine transform of u while $\bar{v}_c$ is the cosine transform of v. Solution of the above telegraph equations yields the Laplace and Fourier transforms of u and v. The transform functions are to be evaluated later to obtain their expressions in the physical space. To solve the problem, the transformed displacements are chosen as follows:

$$\bar{u}_s^* = \sum_{i=1}^{2} A_i e^{-k_i y}, \quad \bar{v}_c^* = \sum_{i=1}^{2} B_i e^{-k_i y}. \tag{9}$$

Equations (7) and (8) require the parameter k_i to satisfy the following characteristic equation:

$$[k_i^2 - (\beta s^2 + p^2/c_2^2)][\alpha k_i^2 - (s^2 + p^2/c_2^2)] + (1 + \delta)^2 s^2 k_i^2 = 0. \tag{10}$$

The equation can be seen as a quadratic equation and k_i^2 are the roots of the equation. Furthermore, the positive square roots of k_i^2 are used in Eq. (9) in order to satisfy the radiation conditions. The properties of the roots will be described later in more detail in connection with the Laplace inversion. The unknown quantities A_i and B_i in Eq. (9) are related through Eq. (8) in the following forms:

$$k_i s(1 + \delta)A_i = [\alpha k_i^2 - (s^2 + p^2/c_2^2)]B_i. \tag{11}$$

The above relationship holds for i equal to 1 and 2.

The shearing stress σ_{xy} is calculated in terms of Eqs. (1), (9), and (11). Satisfying the shearing stress boundary condition in Eq. (2) yields

$$B_1 = -(\alpha k_2^2 + \delta s^2 - p^2/c_2^2)B_2/(\alpha k_1^2 + \delta s^2 - p^2/c_2^2). \tag{12}$$

In addition, the displacement component v is calculated in terms of Eqs. (9) and (12). The displacement boundary conditions in Eq. (3) gives

$$B_2 = [\alpha k_1^2 + \delta s^2 - p^2/c_2^2]\bar{w}_c^*/(k_1^2 - k_2^2)\alpha \tag{13}$$

$$\bar{w}_c = \sqrt{\frac{2}{\pi}} \int_o^a w(x) \cos(sx)dx. \tag{14}$$

In order to satisfy the boundary condition for the normal stress σ_{yy}, the cosine transform of the normal stress is calculated in terms of Eqs. (1), (9), and (11)–(14). For convenience in later calculations, the result is written as the sum of the following two terms:

$${}_c\bar{\sigma}_{yy}^* = -\bar{w}_c^*[\rho p^2 H_1 + Q_{66} p H_2] \tag{15}$$

$$H_1 = [1 + p^2/k_1 k_2 c_2^2]/(k_1 + k_2) \tag{16}$$

$$H_2 = [a_1 s^4 + b_1 p^2 s^2/c_2^2]/pk_1 k_2 (k_1 + k_2) \tag{17}$$

$$a_1 = \beta - \delta^2/\alpha, \quad b_1 = 1 + a_1. \tag{18}$$

The Laplace inversion of Eq. (15) is carried out in the next section in order to establish an integral equation to solve for the unknown crack shape function $w(x)$.

Dynamic Crack Surface Opening

Each term on the right-hand side of Eq. (15) is treated as a separate transform function in the process of carrying out the inverse transform of the entire function. The transformation $p = sc_2\zeta$ is used in the evaluation of the Laplace inversion integrals. If the transformation is applied to Eq. (10), the characteristic roots can be written as

$$q_1 = k_1/s = \{[(1 + \alpha)\zeta^2 + \gamma + \varphi]/2\alpha\}^{1/2} \tag{19}$$

$$q_2 = k_2/s = \{[(1 + \alpha)\zeta^2 + \gamma - \varphi]/2\alpha\}^{1/2} \tag{20}$$

$$\varphi^2 = [(1 + \alpha)\zeta^2 + \gamma]^2 - 4\alpha[\zeta^4 + (1 + \beta)\zeta^2 + \beta] \tag{21}$$

$$\gamma = 1 + \alpha\beta - (1 + \delta)^2. \tag{22}$$

In the complex ζ-plane of inversion, the roots of φ in Eq. (21) are complex for the composite materials to be considered. The roots are the branch points of q_1 and q_2 (Payton, 1983; Tsai and Kolsky, 1967; Tsai, 1989). Furthermore, q_1 has the branch points at $\zeta = \pm i\beta^{1/2}$ and q_3 has the branch points at $\zeta = \pm i$. The evaluations of the Laplace inversion integrals are carried out by using the contour integration techniques similar to those in the earlier work (Tsai, 1973, 1989). The result from the inversion of H_1 in Eq. (16) can be written in the following form:

$$h_1 = L^{-1}[H_1] = c_3 J_o(sc_1 t) + c_2 L_1 \sin(sc_2\eta t). \tag{23}$$

The longitudinal wave speeds are $c_3 = c_2\alpha^{1/2}$ and $c_1 = c_2\beta^{1/2}$. The operator L_1 operates over η and has the following form:

$$L_1 f(g\eta) = \frac{2}{\pi} \int_1^{\sqrt{\beta}} [|q_2| - q_1\eta^2\alpha^{1/2}(\beta - \eta^2)^{-1/2}(\eta^2 - 1)^{-1/2}] \times \alpha f(g\eta)d\eta/\varphi + \frac{2}{\pi} \int_{\sqrt{\beta}}^{\infty} \{[1 + \eta^2\alpha^{1/2}(\eta^2 - 1)^{-1/2} \times (\eta^2 - \beta)^{-1/2}]/(|q_1| + |q_2|) - [\alpha/(\eta^2 - \beta)]^{1/2}\} f(g\eta)d\eta. \tag{24}$$

The other Laplace transform function H_2 in Eq. (17) has a pole at $p = 0$. The contributions of the pole and the branch cuts result in the following form:

$$h_2 = L^{-1}[H_2] = s[h_o + L_2 \cos(sc_2\eta t)] \tag{25}$$

$$h_o = \alpha a_1/[2 + \gamma(\alpha\beta)^{-1/2}]\beta \tag{26}$$

Downloaded 04 May 2010 to 171.66.16.28. Redistribution subject to ASME license or copyright; see http://www.asme.org/terms/Terms_Use.cfm

$$L_2 f(g\eta) = \frac{2}{\pi}\int_1^{\sqrt{\beta}} q_1(b_1\eta^2 - a_1) \times [\alpha^3/(\beta - \eta^2)(\eta^2 - 1)]^{1/2} f(g\eta)d\eta/\eta\varphi + \frac{2}{\pi}\int_{\sqrt{\beta}}^{\infty}(a_1 - b_1\eta^2)[\alpha/(\eta^2 - \beta)(\eta^2 - 1)]^{1/2} \times f(g\eta)d\eta/(|q_1| + |q_2|)\eta. \quad (27)$$

The material constants ratio h_o is the contribution of the pole.

Laplace and Fourier inversions of Eq. (15) give the normal stress at $y = 0$ as

$$\sigma_{yy}(x, t) = \sigma_{yy}^o - \rho c_3 Q - \rho c_2 L_1 Q_1 - Q_{66} L_2 Q_2 \quad (28)$$

$$\sigma_{yy}^o = -Q_{66} h_o \sqrt{\frac{2}{\pi}}\int_o^{\infty} s\cos(sx)\bar{w}_c ds \quad (29)$$

$$Q = \sqrt{\frac{2}{\pi}}\int_o^{\infty}\cos(sx)\frac{\partial}{\partial t}\int_o^t J_o[sc_1(t-\tau)]\frac{\partial}{\partial \tau}\bar{w}_c d\tau ds \quad (30)$$

$$Q_1 = \sqrt{\frac{2}{\pi}}\int_o^{\infty}\cos(sx)\frac{\partial}{\partial t}\int_o^t \sin[sc_2\eta(t-\tau)] \times \frac{\partial}{\partial \tau}\bar{w}_c d\tau ds \quad (31)$$

$$Q_2 = \sqrt{\frac{2}{\pi}}\int_o^{\infty} s\cos(sx)\int_o^t \cos[sc_2\eta(t-\tau)] \times \frac{\partial}{\partial \tau}\bar{w}_c d\tau ds. \quad (32)$$

The function $J_o(x)$ is the zeroth-order Bessel function. Equation (28) is used to satisfy the crack surface pressure condition and converted into an integral equation to solve for the unknown crack surface function w. The integral equation is solved using the successive approximation techniques similar to those used in an earlier work (Tsai, 1973). The last three terms on the right-hand side of Eq. (28) are the wave-effects terms. In the process of determining a solution, these three terms are first dropped to form a reduced integral equation. The double integration techniques (Tsai, 1973) are then applied to the reduced equation to obtain the following first approximation:

$$w_1(x, t) = -\frac{2}{\pi}\frac{1}{h_o Q_{66}}\int_x^a \frac{ndn}{\sqrt{n^2 - x^2}}\int_o^n \frac{\sigma_{yy}d\lambda}{\sqrt{n^2 - \lambda^2}}. \quad (33)$$

The normal stress σ_{yy} is equal to the pressure $-p_o$ over the crack surface. Under this condition, integrations of Eq. (33) give the associated static crack shape function w_1 as follows:

$$w_1 = \frac{p_o}{h_o Q_{66}}(a^2 - x^2)^{1/2}. \quad (34)$$

The wave-effects integrals in Eqs. (30)–(32) need to be evaluated in order to obtain the second approximation of w. For this purpose, the time derivative of the transform of w_1 in Eq. (34) is calculated and has the following form:

$$\frac{\partial}{\partial t}{}_1\bar{w}_c = \frac{\partial}{\partial t}\sqrt{\frac{2}{\pi}}\int_o^a w_1\cos(sx)dx = \sqrt{\frac{\pi}{2}}\frac{p_o}{h_o Q_{66}}J_o(sa)a\dot{a}. \quad (35)$$

If Eq. (35) is substituted into Eq. (31), the first approximation of Q_1 can be written as

$$2Q_1^1 Q_{66} h_o/p_o = \frac{\partial}{\partial t}\int_o^t a\dot{a}\int_o^{\infty}[\sin(sd_1) + \sin(sd_2)]J_o(sa)dsd\tau = \frac{\partial}{\partial t}\int_o^t a\dot{a}[H(d_1 - a)(d_1^2 - a^2)^{-1/2} + H(d_2 - a)(d_2^2 - a^2)^{-1/2}]d\tau \quad (36)$$

$$d_1 = c_2\eta(t - \tau) + x,\ d_2 = c_2\eta(t - \tau) - x \quad (37)$$

where H is the Heaviside function. For a crack propagating at a constant speed V, the quantities a and $\dot{a}$ are, respectively, equal to $V\tau$ and V. For $x < a$, the integrations over τ in Eq. (36) are carried out. The result can be written as

$$Q_1^1 = p_o c_2\eta D_2/Q_{66}h_o \quad (38)$$

$$D_2 = \frac{\upsilon_2^2}{(\eta^2 - \upsilon_2^2)^{3/2}} \times \left[2\eta\ln\frac{\sqrt{\eta - \upsilon_2} + \sqrt{\eta + \upsilon_2}}{\sqrt{2\upsilon_2}} - \sqrt{\eta^2 - \upsilon_2^2}\right] \quad (39)$$

where υ_2 is equal to V/c_2.

The integral Q_2 in Eq. (32) can be written in terms of w_1 as follows:

$$2Q_2^1 Q_{66}h_o/p_o = \frac{\partial}{\partial x}\int_o^t a\dot{a}\int_o^{\infty}[\sin(d_1 s) - \sin(d_2 s)]J_o(sa)dsd\tau. \quad (40)$$

The integral is evaluated using the techniques similar to those for Q_1^1. The result has the following form:

$$Q_2^1 = p_o D_2/Q_{66}h_o. \quad (41)$$

The zeroth-order Bessel function in Eq. (30) for Q is replaced by an integral representation in terms of a sine function (Abromowitz and Stegun, 1965). As a result, the Q integral can now be written as

$$Q = \frac{2}{\pi}\int_{\sqrt{\beta}}^{\infty}(\eta^2 - \beta)^{-1/2}Q_1 d\eta = LQ_1. \quad (42)$$

The new operator L is operated over the variable η of Q_1. The first approximation of Q^1 is obtained if the value of Q_1^1 in Eq. (38) is substituted into Eq. (42).

The double integrations on the right-hand side of Eq. (33) are applied over Eq. (28) to obtain an integral equation for w as follows:

$$w = w_1 - \frac{2}{\pi}\frac{1}{h_o Q_{66}}\int_x^a \frac{ndn}{\sqrt{n^2 - x^2}}\int_o^n \frac{\sigma_w d\lambda}{\sqrt{n^2 - \lambda^2}} \quad (43)$$

$$\sigma_w = \rho c_3 Q + \rho c_2 L_1 Q_1 + Q_{66} L_2 Q_2. \quad (44)$$

If the first approximations of Q, Q_1, and Q_2 are substituted into Eq. (43), the second approximation of w is found to have the following form:

$$w_2 = w_1[1 - \epsilon] \quad (45)$$

$$\epsilon = \frac{1}{h_o}[L\eta D_2 + L_1\eta D_2 + L_2 D_2]. \quad (46)$$

All the higher order approximations are carried out in the way similar to that for w_2. The solution for $w(x, t)$ results in an infinite series which can be summed into a closed form as follows:

Downloaded 04 May 2010 to 171.66.16.28. Redistribution subject to ASME license or copyright; see http://www.asme.org/terms/Terms_Use.cfm

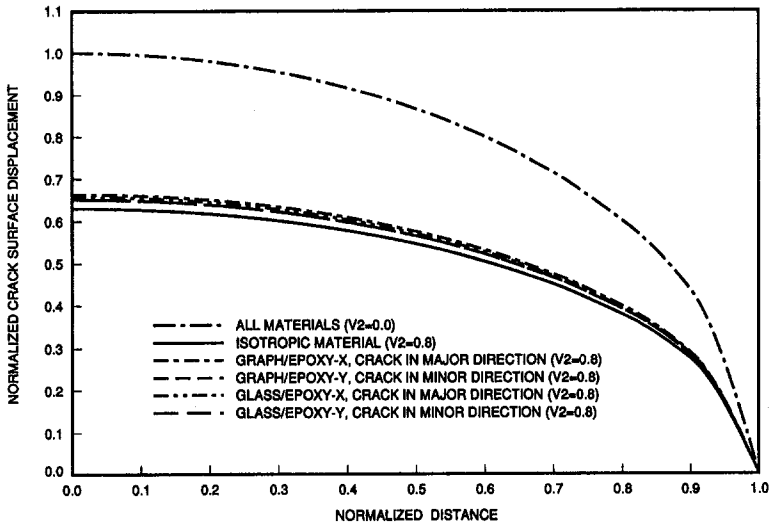


Fig. 1 Normalized crack surface opening $w/(ap_o/h_oQ_{66})$ as a function of normalized distance x/a

$$w = w_1(1 - \epsilon + \epsilon^2 - \epsilon^3 + \ldots\ldots) = \frac{p_o}{K_D}(a^2 - x^2)^{1/2} \quad (47)$$

$$K_D = h_oQ_{66}(1 + \epsilon). \quad (48)$$

The dynamic correction term ϵ can be seen in Eqs. (39) and (48) to be vanishing when the crack speed V tends to zero. In this limiting case, the dynamic crack surface function in Eq. (47) reduces to the corresponding static function in Eq. (34).

Dynamic Stress Intensity Factor

The solution for the crack shape function w in Eq. (47) is used to calculate the normal stress σ_{yy} in Eq. (28). The stress is found to be singular at the crack tip. For $x > a$, the associated static stress in Eq. (29) is calculated by using the techniques similar to those used in an earlier work (Tsai, 1973) to have the following form:

$$\sigma^o_{yy} = \frac{p_o}{1 + \epsilon}\left[\frac{x}{\sqrt{x^2 - a^2}} - 1\right]. \quad (49)$$

The wave-effect integral Q_1 in Eq. (31) is first integrated over the variable s as was done for Eq. (36). For $a < x < c_2\eta t$, the integral can be written as

$$Q_1 = \frac{p_oV^2}{2K_D}\frac{\partial}{\partial t} \times \left[\int_o^t \frac{\tau d\tau}{\sqrt{d_1^2 - a^2}} + \int_o^{t_2} \frac{\tau d\tau}{\sqrt{d_2^2 - a^2}} - \int_{t_6}^t \frac{\tau d\tau}{\sqrt{d_3^2 - a^2}}\right] \quad (50)$$

$$d_3 = x - c_2\eta(t - \tau), \quad t_2 = (c_2\eta t - x)/(c_2\eta + V)$$

$$t_6 = (c_2\eta t - x)/(c_2\eta - V). \quad (51)$$

After integrations over τ, the integral has the following form:

$$Q_1 = \frac{p_oc_2\eta}{K_D}\left[D_3\left(\frac{x}{\sqrt{x^2 - a^2}} - 1\right) + D_4\right] \quad (52)$$

$$D_3 = v_2^2/(\eta^2 - v_2^2)$$

$$D_4 = \frac{v_2^2\eta}{(\eta^2 - v_2^2)^{3/2}} \times \ln\frac{\sqrt{c_2^2\eta^2t^2 - x^2}[1 + \eta(\eta^2 - v_2^2)^{-1/2}]}{x + \eta[(x^2 - a^2)/(\eta^2 - v_2^2)]^{1/2}}. \quad (53)$$

If the integration techniques similar to those for Q_1 are applied to Q_2 in Eq. (32), the results take the form $Q_2 = Q_1/c_2\eta$. The integral Q in Eq. (42) is calculated in terms of Q_1 in Eq. (52). The integrated forms of Q_1, Q_2, and Q, together with Eq. (49), are substituted into Eq. (28) to obtain the following dynamic normal stress:

$$\sigma_{yy} = p_o\left\{K_v\left[\frac{x}{\sqrt{x^2 - a^2}} - 1\right] - G_2\right\} \quad (54)$$

$$K_v(1 + \epsilon) = 1 - [(\alpha\beta)^{1/2}v_1^2(1 - v_1^2)^{-1/2} + L_1\eta D_3 + L_2D_3]/h_o \quad (55)$$

$$G_2(1 + \epsilon) = [L\eta D_4 + L_1\eta D_4 + L_2D_4]/h_o \quad (56)$$

where the speed ratio is $v_1 = V/c_1$. The first term on the right-hand side of Eq. (54) is a singular term. The dynamic stress intensity factor is calculated from this singular term as

$$K_{ID} = K_vK_I; \quad K_I = p_o(\pi a)^{1/2}. \quad (57)$$

The quantity K_I is the static stress intensity factor and K_v is the dynamic correction factor for the dynamic stress intensity factor K_{ID}. From Eqs. (55) and (57), the dynamic stress intensity factor can readily be seen as a function of the crack speed and crack size. This is in agreement with the results obtained by Willis (1992) that the dominant square-root singular terms near an accelerating crack tip depend on the crack speed and crack position.

For an isotropic plane-strain problem, the planar moduli are $Q_{66} = E/2(1 + \nu)$, $Q_{11} = Q_{22} = E(1 - \nu)/(1 + \nu)(1 - 2\nu)$ and $Q_{12} = \nu E/(1 + \nu)(1 - 2\nu)$, where E and ν are, respectively, Young's modulus and Poisson's ratio. For these constants, the quantity h_o in Eq. (26) becomes $1/(1 - \nu)$. The current results reduce to the corresponding results for an isotropic problem (Tsai, 1973).

The dependency of the stress intensity factor and the crack surface displacement on the crack speed and the material constants is studied by numerical evaluations of the corresponding expressions. Graphite/epoxy (AS/3501) and glass/epoxy (Scotchply 1002) composite materials (Tsai and Hahn, 1980) are used as the sample materials in the numerical calculations. For the graphite/epoxy composite, the orthotropic Young's and shear moduli and Poisson's ratio are $E_x = 138$, $E_y = 8.96$, $E_s = 7.1$, and $\nu_x = 0.3$. The corresponding constants for the glass/epoxy are $E_x = 38.6$, $E_y = 8.27$, $E_s = 4.14$, and $\nu_x = 0.26$. All

Downloaded 04 May 2010 to 171.66.16.28. Redistribution subject to ASME license or copyright; see http://www.asme.org/terms/Terms_Use.cfm

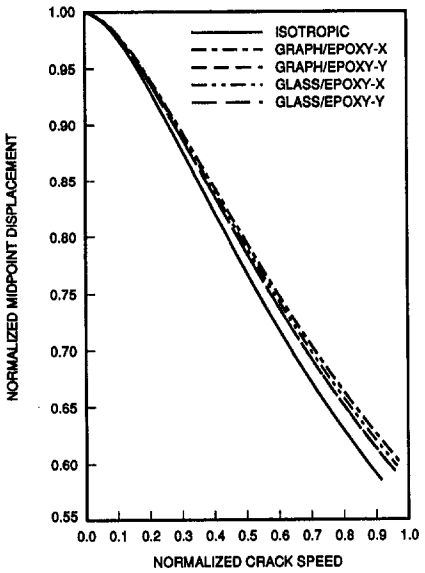


Fig. 2 Variation of the normalized crack center displacement $w(o)/(ap_o/h_oQ_{66})$ with respect to the normalized crack speed $v_2 = V/c_2$

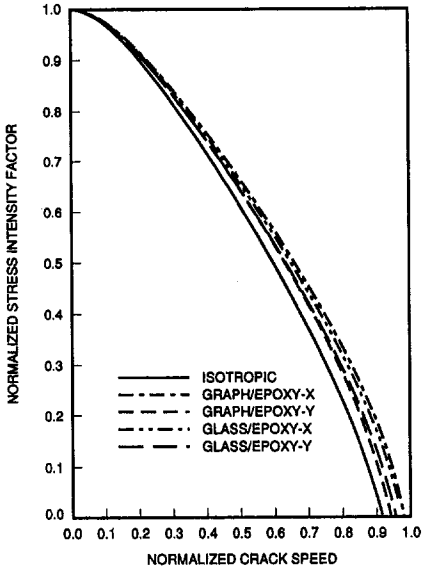


Fig. 3 Variation of the normalized dynamic stress intensity factor K_{ID}/K_I with respect to the normalized crack speed $v_2 = V/c_2$

the moduli are in units of GPa. Two cases of calculations are carried out. In the first case, the coordinates of the above material constants coincide with the coordinates of the above derivations. In other words, the crack is located along the major material axis. In the second case of calculations, the crack is rotated 90 deg and then lies along the minor material axis. In this case, the material constants are properly adjusted. For comparison, polycrystalline magnesium with Young's modulus $E = 41$ GPa and Poisson's ratio $\nu = 0.3$ is also used as an example of isotropic material.

The dynamic crack surface displacement w in Eq. (47) is calculated for the sample materials for various values of crack speed. In the calculations, the values of ϵ satisfy the convergent conditions of the infinite series in Eq. (47), and thus the closed-form expression in the equation is valid. The results are normalized by the associated maximum static crack opening $p_o a/h_o Q_{66}$. Typical normalized crack openings for cracks located along the major or minor material axis are shown in Fig. 1 for $v_2 = 0$ and $v_2 = 0.8$. The normalized crack surface displacement at the center of the crack is shown in Fig. 2 as a function of the normalized crack speed for the sample materials. The dynamic stress intensity factor is also calculated from Eq. (57). The values are normalized by the associated static stress intensity factor and shown in Fig. 3 for the crack speed which ranges from zero to the Rayleigh surface wave speed (Stoneley, 1949; Tsai, 1973). For the sample isotropic material, the Rayleigh wave speed is equal to $0.92c_2$. For the graphite/epoxy composite, the Rayleigh wave which propagates in the free surface along the major material axis is found to have a speed of $0.98c_2$. If the Rayleigh wave propagates along the minor material axis, its speed becomes $0.94c_2$. The surface wave speed is $0.97c_2$ when the wave propagates along the major axis of the glass/epoxy composite. The wave has a speed of $0.96c_2$ when propagating along the minor material axis.

Discussion and Conclusion

A central crack which grows symmetrically with inertia effects in an orthotropic composite plate is investigated using the techniques of Fourier and Laplace transforms. Complete contour integrations have been carried out in the evaluations of the Laplace inversion integrals. For the crack running at a constant speed, exact expressions for the dynamic crack shape and the dynamic normal stress distribution with singularities in the crack plane are obtained in terms of orthotropic material constants and crack speed. The anisotropic solutions reduce to the corresponding solution of an earlier work (Tsai, 1973) for an isotropic material. In the limiting case of zero crack speed, the dynamic solution reduces to the associated static solution. When the crack grows, the deviation of the dynamic result from the static result is governed by dynamic correction factors which are nondimensional functions of the ratio of the crack speed to the shear-wave speed and the ratios among orthotropic material constants.

The expressions for the dynamic stress intensity factor and the crack surface opening are evaluated numerically for graphite/epoxy and glass/epoxy composites and an isotropic material. The crack speed used in the numerical calculations ranges from zero to the Rayleigh surface wave speed. The crack surface openings for the propagating cracks are seen in Fig. 1 to be less than the corresponding static opening for both composite and isotropic materials. The crack surface displacement at the center of the crack in the composites are shown in Fig. 2 to be larger than the corresponding isotropic crack surface displacement at various crack speeds. Because of different degrees of anisotropy, the dynamic crack surface openings for the graphite/epoxy composite are shown in Figs. 1 and 2 to be higher than the corresponding values for the glass/epoxy composite when the crack is located along the major material axis. However, the crack openings for these two materials become very close to one another when the crack is located in the direction of the minor material axis.

The dynamic stress intensity factors for the composites are also seen to be higher than the dynamic isotropic values in Fig. 3. The values of the dynamic stress intensity factors decrease with increasing crack speed and become zero at the corresponding Rayleigh wave speeds. Therefore, the surface wave speed may be suggested as the maximum possible value of the crack speed for an orthotropic composite.

References

Abramowitz, M., and Stegun, I. A., 1965, *Handbook of Mathematical Functions,* Dover, New York, N.Y., p. 360.

Broberg, K. B., 1960, "The Propagation of a Brittle Crack," *Arkiv for Fysik,* Vol. 18, pp. 159–192.

Freund, L. B., and Rosakis, A. J., 1992, "The Structure of the Near-tip Field during Transient Elastodynamic Crack Growth," *J. Mech. Phys. Solids,* Vol. 40, No. 3, pp. 699–719.

Downloaded 04 May 2010 to 171.66.16.28. Redistribution subject to ASME license or copyright; see http://www.asme.org/terms/Terms_Use.cfm

Georgiadis, H. G., 1986, "Complex-Variable and Integral-Transform Methods for Elastodynamic Solutions of Cracked Orthotropic Strips," *Engr Frac Mech,* Vol. 24, pp. 727–735.

Kalthoff, J. F., Beinart, J., Winkler, S., and Klemm, W., 1980, "Experimental Analysis of Dynamic Effects in Different Crack Arrest Test Specimens," *ASTM STP,* Vol. 711, ASTM, Philadelphia, PA, pp. 109–127.

Moon, F. C., 1975, "Wave Propagation and Impact in Composite Materials," *Composite Materials,* L. J. Broutman and R. H. Krock, eds., Vol. 7, pp. 259–332.

Papadakis, E. P., Patton, T., Tsai, Y. M., Thompson, D. O., and Thompson, R. B., 1990, "The Elastic Moduli of a Thick Composite as Measured by Ultrasonic Bulk Wave Pulse Velocity," *J. Acoust. Soc. Am.,* Vol. 89, No. 6, pp. 2753–2757.

Payton, R. G., 1983, "*Elastic Wave Propagation in Transversely Isotropic Media,*" Martinus Nijhoff, The Hague, The Netherlands, p. 134.

Stoneley, R., 1949, "The Seismological Implications of Aeolotropy in Continental Structure," *Geophysical Supplements,* Royal Astronomical Society, London, Vol. 5, pp. 343–353.

Tsai, S. W., and Hahn, H. T., 1980, *Introduction to Composite Materials,* Technomic, p. 14.

Tsai, Y. M., 1973, "Propagation of a Brittle Crack at Constant and Accelerating Speeds," *Int. J. Solids Structures,* Vol. 9, pp. 625–642.

Tsai, Y. M., 1989, "Dynamic Behavior of an Orthotropic Material Containing a Central Crack," ASME *Journal of Pressure Vessel Technology,* Vol. 111, pp. 172–176.

Tsai, Y. M., and Kolsky, H., 1967, "A Study of the Fractures Produced in Glass Blocks by Impact," *J. Mech. Phys. Solids,* Vol. 15, pp. 263–278.

Willis, J. R., 1992, "The Stress Field Near the Tip of an Accelerating Crack," *J. Mech. Phys. Solids,* Vol. 40, No. 7, pp. 1671–1681.

Downloaded 04 May 2010 to 171.66.16.28. Redistribution subject to ASME license or copyright; see http://www.asme.org/terms/Terms_Use.cfm

Realizability of Negative Pore Compressibility in Poroelastic Composites

P. A. Berge

J. G. Berryman

Lawrence Livermore National Laboratory, Livermore, CA 94551-9900

For elastic materials containing fluid-saturated porosity, the pore compressibility is a measure of the deformation of a unit pore volume in response to a change in fluid pressure. Rather than being measured, this quantity has been routinely set equal to an effective solid compressibility, since this equality is exact whenever a single solid component is present. However, we show that the pore compressibility and solid compressibility may be uncorrelated in general. In certain special circumstances they do not even share the same sign. Although thermodynamic and mechanical stability constraints cause solid and drained-frame bulk moduli of a porous composite to be positive and bounded by component properties, the pore compressibility is unconstrained and, therefore, can have negative values. For special realizable model materials, the value of the pore compressibility can be found using an exact expression valid for a composite made up of one fluid and two solid components, i.e., two porous components. In order to quantify how various factors affect the sign and magnitude of the pore compressibility, pore compressibilities were calculated for models that used two porous components having the microgeometry of an assemblage of concentric spheres. This model implicitly assumes the pores are on a much smaller length scale than the concentric spheres. Modeling results show that with the stiffer porous material forming the outer shells of the concentric spheres, the pore compressibility of such materials is negative when solid component bulk moduli differ by at least a factor of 5, if, in addition, the porosities and drained frame moduli of the two porous components are relatively low. Negative pore compressibilities were found for realizable models whose two porous constituents had the properties of silicon nitride and either sandstone or clay. For models using combinations of alumina and glass foam properties, pore compressibilities were non-negative but smaller than the compressibilities of the solid components.

1 Introduction

Biot (1956, 1962) showed that four elastic coefficients are required in the equations describing the deformation of a porous elastic solid containing a compressible fluid. The physical interpretation of all four coefficients was first discussed by Biot and Willis (1957). For an isotropic fluid-saturated porous material, the coefficients in Biot's constitutive relations can be expressed in terms of the bulk modulus of the saturated material, the shear modulus of the material, the bulk modulus of the solid portion (sometimes called the unjacketed bulk modulus), and a fourth term related to the amount of fluid entering a unit volume of the porous material for a given change in fluid pressure.

In the quasi-static limit, the saturated bulk modulus can be related to the drained-frame bulk modulus of the material (Gassmann, 1951; Biot and Willis, 1957). The unjacketed bulk modulus K_s, the unjacketed pore modulus K_ϕ describing the response due to fluid moving into a unit volume as fluid pressure changes, and the drained-frame modulus K_d are defined by

$$\frac{1}{K_s} = -\frac{1}{V}\left(\frac{\partial V}{\partial p_f}\right)_{p_d=\text{const.}}, \tag{1}$$

$$\frac{1}{K_\phi} = -\frac{1}{\phi V}\left(\frac{\partial(\phi V)}{\partial p_f}\right)_{p_d=\text{const.}}, \tag{2}$$

and

$$\frac{1}{K_d} = -\frac{1}{V}\left(\frac{\partial V}{\partial p_d}\right)_{p_f=\text{const.}}, \tag{3}$$

where V is the sample volume, ϕ is the porosity, p_d is the difference between external (confining) and pore pressures, and p_f is pore pressure (Brown and Korringa, 1975; Rice and Cleary, 1976). It is important to note that, because of reciprocity, an additional constant defined by

$$\frac{1}{K_p} = -\frac{1}{\phi V}\left(\frac{\partial(\phi V)}{\partial p_d}\right)_{p_f=\text{const.}} \tag{4}$$

is not independent:

$$\frac{1}{K_p} = \frac{1}{\phi}\left(\frac{1}{K_d} - \frac{1}{K_s}\right) \tag{5}$$

(Brown and Korringa, 1975; Rice and Cleary, 1976; Berryman and Milton, 1991). Although the term "pore compressibility" is also used to describe $1/K_p$ (e.g., Hughes and Cook, 1953; Van der Knaap, 1959; Newman, 1973; Sampath, 1982; Zimmerman et al., 1986) and $(1/K_\phi - 1/K_p)$ (the result of measurements made holding the external pressure constant) (e.g., Hall,

Contributed by the Applied Mechanics Division of THE AMERICAN SOCIETY OF MECHANICAL ENGINEERS for publication in the ASME JOURNAL OF APPLIED MECHANICS.

Discussion on this paper should be addressed to the Technical Editor, Professor Lewis T. Wheeler, Department of Mechanical Engineering, University of Houston, Houston, TX 77204-4792, and will be accepted until four months after final publication of the paper itself in the ASME JOURNAL OF APPLIED MECHANICS.

Manuscript received by the ASME Applied Mechanics Division, Jan. 27, 1994; final revision, July 27, 1994. Associate Technical Editor: J. T. Jenkins.

Copyright © 1995 by ASME

Downloaded 04 May 2010 to 171.66.16.28. Redistribution subject to ASME license or copyright; see http://www.asme.org/terms/Terms_Use.cfm

1953; Fatt, 1958; Newman, 1973; Greenwald, 1980), in this paper "pore compressibility" refers only to the independent parameter $1/K_\phi$ defined in (2).

Thermodynamic and mechanical stability considerations provide the constraint

$$\frac{1}{K_s}\left(1-\frac{K_d}{K_s}\right)+\phi\left(\frac{1}{K_f}-\frac{1}{K_\phi}\right)\geq 0 \qquad (6)$$

for any porous elastic solid saturated with a fluid having bulk modulus K_f (Berryman and Milton, 1991). Since the parameters defined in Eqs. (1)–(3) are assumed not to depend on the fluid, we can allow K_f to approach infinity so that the constraint in (6) becomes

$$\frac{1}{K_s}\left(1-\frac{K_d}{K_s}\right)-\frac{\phi}{K_\phi}\geq 0 \qquad (7)$$

(Berryman and Milton, 1991), providing one general relation among these moduli. In the special case where the porous material contains only one solid component having bulk modulus K_m, $K_s = K_\phi = K_m$ (Brown and Korringa, 1975). Such a simple expression relating K_s and K_ϕ does not exist in general, but exact results for these moduli can be found when the porous material is made up of a fluid and two solid components arranged as two porous components in welded contact (Berryman and Milton, 1991, 1992).

The parameters K_d and K_s have been routinely measured for decades, for various rock samples (e.g., Adams and Williamson, 1923; Zisman, 1933; Birch and Law, 1935; Fatt, 1958, 1959; Van der Knaap, 1959; Birch, 1960, 1961; Brace, 1965; Nur and Byerlee, 1971; Coyner, 1984; Zimmerman et al., 1986). Attempts to measure K_ϕ directly have been less successful. The difference $(1/K_\phi - 1/K_p)$ has been measured by Hall (1953), Fatt (1958), Newman (1973), and Greenwald (1980), for various sandstones and limestones. Since neither Fatt (1958) nor Greenwald (1980) measured $1/K_p$ and since compounded measurement uncertainty and nonlinear behavior of K_d preclude using reciprocity to estimate K_p, their data do not yield estimates of K_ϕ. Newman (1973) did measure $1/K_p$ for his 256 sandstone and limestone samples, but did not distinguish between the $1/K_p$ and the $(1/K_\phi - 1/K_p)$ values in the plots presenting his data. Although Hall (1953) measured both $1/K_p$ and $(1/K_\phi - 1/K_p)$ for ten sandstone and limestone samples, he did not add the results to obtain estimates of K_ϕ, and his measurements suffered from excessive uncertainty because of corrections made to account for expansion in the fluid lines leading from the sample to the pore-pressure transducer. The compressibility apparatus of Zimmerman et al. (1986) could be used to find accurate estimates of K_ϕ since it has the pore-pressure transducer in direct contact with the sample, but they chose to measure only $1/K_p$ and $(1/K_s - 1/K_d)$.

K_ϕ can also be estimated from measured values of K_d, K_s, and the change in pore pressure with change in confining pressure (e.g., Green and Wang, 1986), but the measurements must all be made on the same sample in order to be reliable. Green and Wang (1986) measured the change in pore pressure with change in confining pressure for a Berea sandstone sample, using an apparatus that had the pore-pressure transducer in direct contact with the sample. They then used literature values of K_d and K_s for Berea sandstone to estimate K_ϕ. Their results may be shown to violate the constraint in (7), possibly because of inconsistent samples or because the moduli are not in fact independent of the fluid properties as assumed in the theory.

Measured values of K_ϕ are unavailable because of the problems described above. The assumption that $K_\phi = K_m$ is commonly made, even though this is strictly true only for systems having a single solid component. The values of K_ϕ and solid bulk moduli in multi-component systems are uncorrelated in general, and K_ϕ may even have a different sign. For example, if a porous composite contains a very stiff solid component and a very compliant solid component, raising the external and fluid pressures may lead to an increase in the pore volume at the expense of the volume of the very compliant component. In such a case, K_ϕ would be negative. In poroelastic materials, the stresses and strains in the solid frame are coupled to the fluid pressure and dilatation (Biot, 1956; 1962). Other coupled field problems such as thermal expansion and piezoelectricity have cross-coupling coefficients that can be positive or negative, such as the thermal expansion coefficient and piezoelectric modulus elements (e.g., Nye, 1957). The cross-coupling coefficient K_ϕ relates changes in the stress fields to pore volume strain. Therefore, some theoretical work to provide insight into the behavior of this parameter seems in order.

This paper will focus on the parameter K_ϕ for certain isotropic porous materials made up of one fluid and two solid components arranged as two porous components in welded contact. We assume the quasi-static case, and all pores are assumed to be connected so that the fluid is in equilibrium. In this case the material properties do not depend on frequency or time. (The properties of a composite will be indicated using a * superscript, and the properties of porous components will be indicated using subscripts 1 and 2.) Let a porous composite be made of two

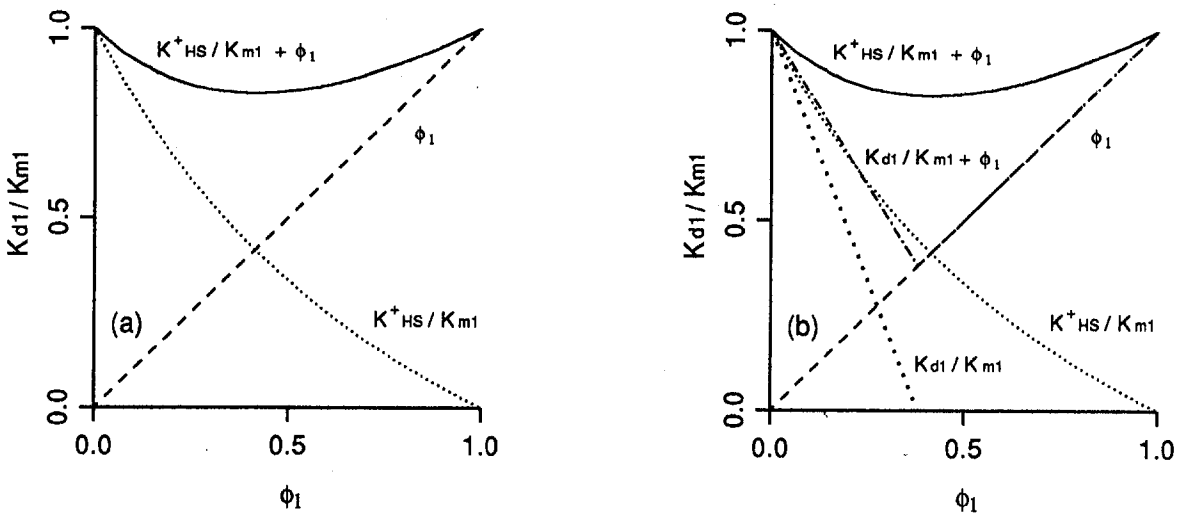


Fig. 1 Range of variation of $K_{d1}/K_{m1} + \phi_1$ with porosity for (*a*) all materials and (*b*) most real materials, illustrated using $3K_{m1}/4\mu_{m1} = 1$

Downloaded 04 May 2010 to 171.66.16.28. Redistribution subject to ASME license or copyright; see http://www.asme.org/terms/Terms_Use.cfm

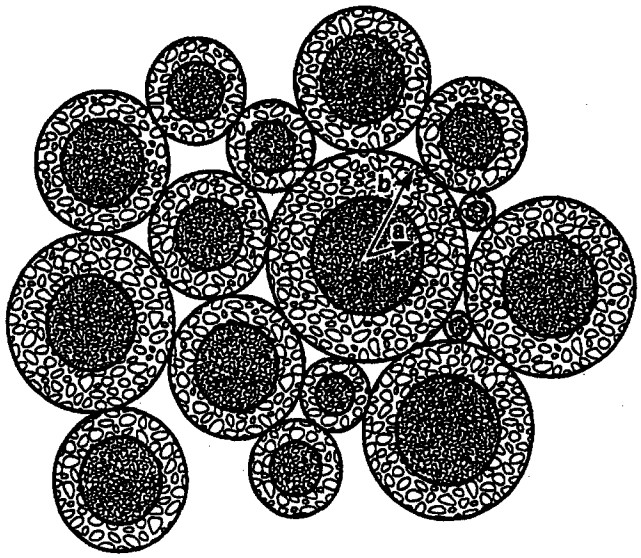


Fig. 2 Schematic illustration of the composite spheres assemblage model of Hashin (1962), generalized for porous components having relative volumes $(a/b)^3$ and $1 - (a/b)^3$

porous materials having porosities ϕ_1 and ϕ_2. Each of these two porous components is made up of voids in an otherwise homogeneous solid, where the solid bulk moduli of the homogeneous constituents are K_{m1} and K_{m2}. The drained-frame moduli of the two porous components are K_{d1} and K_{d2}. Berryman and Milton (1991) showed that for such a composite material having porosity ϕ^*, drained-frame bulk modulus K_d^*, and unjacketed modulus K_s^*, if the porosities satisfy $\phi_1 = \phi_2 = \phi^*$ and if

$$\frac{K_{d1}}{K_{m1}} = \frac{K_{d2}}{K_{m2}} = \frac{K_d^*}{K_s^*}, \tag{8}$$

then

$$\frac{1}{K_\phi^*} = \frac{1}{K_s^*}\left\{1 - \left[\frac{1}{\phi^*}\left(1 - \frac{K_{d1}}{K_{m1}} - \phi^*\right) \times \left(K_d^*\left\langle\frac{1}{K_d(x)}\right\rangle - 1\right)\right]\right\}. \tag{9}$$

Here the brackets $\langle\ \rangle$ denote a volume average over the spatial coordinate x, and $K_d(x) = K_{d1}$ when x lies within the type-1 constituent while $K_d(x) = K_{d2}$ when x lies within the type-2 constituent. All the moduli in (8) are non-negative. The term inside the square brackets in (9) is non-negative, and vanishes when only one solid is present (Berryman and Milton, 1991). When the square-bracket term does not vanish, then either $K_s^* \le K_\phi^*$, or $K_\phi^* \le 0$. The first case is expected to be the more common situation, and has been found in numerical examples using various equivalent medium approximations for K_d^* in Eq. (9) (Berryman, 1986, 1992a). This paper explores the second case, where K_ϕ^* may become negative.

In contrast to bulk modulus, shear modulus, and Young's modulus, Poisson's ratio of a material is not always non-negative (e.g., Lakes, 1987; Milton, 1992; Yeganeh-Haeri et al., 1992; Keskar and Chelikowsky, 1993). Although positive values are most often seen in nature, the physics describing composite materials does not prevent negative values, either in the case of Poisson's ratio or in the case of pore compressibility. Since (9) is an exact result for K_ϕ^*, it is expected to provide useful estimates of K_ϕ^* for materials having the appropriate

Table 1 Model material properties

Material	K_m	K_d	μ_m	μ_d
1*	4.00	1.00	3.00	0.75
2	1.33	0.33	0.99	0.25
3	1.00	0.25	0.75	0.19
4*	0.80	0.20	0.60	0.15
5	0.64	0.16	0.48	0.12
6	0.50	0.125	0.375	0.094
7*	0.40	0.10	0.30	0.075
8	0.080	0.020	0.060	0.015
9*	0.040	0.010	0.030	0.0075

Units are arbitrary.

***From Berryman (1992a).**

Table 2 Composite properties for some stiff concentric spheres assemblages

Materials 1 and 4			
v_1	K_d^*	K_s^*	K_ϕ^*
0.00	0.20	0.80	0.80
0.10	0.25	1.00	1.21
0.20	0.30	1.22	1.79
0.30	0.36	1.45	2.58
0.40	0.43	1.71	3.59
0.50	0.50	2.00	4.67
0.60	0.58	2.32	5.48
0.70	0.67	2.67	5.71
0.80	0.76	3.06	5.37
0.90	0.88	3.50	4.71
1.00	1.00	4.00	4.00
Materials 1 and 7			
v_1	K_d^*	K_s^*	K_ϕ^*
0.00	0.10	0.40	0.40
0.10	0.15	0.61	1.08
0.20	0.21	0.84	4.49
0.30	0.27	1.09	-8.79
0.40	0.34	1.37	-3.85
0.50	0.42	1.68	-3.40
0.60	0.51	2.03	-3.89
0.70	0.61	2.42	-5.78
0.80	0.72	2.88	-18.30
0.90	0.85	3.39	11.32
1.00	1.00	4.00	4.00
Materials 1 and 9			
v_1	K_d^*	K_s^*	K_ϕ^*
0.00	0.01	0.04	0.04
0.10	0.06	0.25	-0.06
0.20	0.12	0.48	-0.05
0.30	0.19	0.74	-0.06
0.40	0.26	1.04	-0.07
0.50	0.34	1.37	-0.08
0.60	0.44	1.75	-0.10
0.70	0.55	2.18	-0.13
0.80	0.67	2.69	-0.19
0.90	0.82	3.29	-0.41
1.00	1.00	4.00	4.00

Units are arbitrary.

$\phi = 0.35$, $K_d/K_m + \phi = 0.60$

Downloaded 04 May 2010 to 171.66.16.28. Redistribution subject to ASME license or copyright; see http://www.asme.org/terms/Terms_Use.cfm

Table 3 Composite properties for some weak concentric spheres assemblages

Materials 1 and 4			
v_1	K_d^*	K_s^*	K_ϕ^*
0.00	0.20	0.80	0.80
0.10	0.23	0.91	0.97
0.20	0.26	1.05	1.18
0.30	0.30	1.20	1.43
0.40	0.35	1.38	1.73
0.50	0.40	1.60	2.07
0.60	0.47	1.87	2.47
0.70	0.55	2.20	2.89
0.80	0.66	2.63	3.32
0.90	0.80	3.20	3.71
1.00	1.00	4.00	4.00
Materials 1 and 7			
v_1	K_d^*	K_s^*	K_ϕ^*
0.00	0.10	0.40	0.40
0.10	0.12	0.47	0.51
0.20	0.14	0.56	0.66
0.30	0.17	0.66	0.86
0.40	0.20	0.79	1.13
0.50	0.24	0.95	1.48
0.60	0.29	1.17	1.94
0.70	0.37	1.47	2.51
0.80	0.48	1.92	3.14
0.90	0.66	2.63	3.70
1.00	1.00	4.00	4.00
Materials 1 and 9			
v_1	K_d^*	K_s^*	K_ϕ^*
0.00	0.010	0.040	0.040
0.10	0.010	0.050	0.050
0.20	0.010	0.060	0.080
0.30	0.020	0.070	0.11
0.40	0.020	0.090	0.16
0.50	0.030	0.12	0.26
0.60	0.040	0.15	0.44
0.70	0.050	0.21	0.83
0.80	0.080	0.33	1.86
0.90	0.16	0.64	4.18
1.00	1.00	4.00	4.00

Units are arbitrary.

$\phi = 0.35$, $K_d/K_m + \phi = 0.60$

microgeometry, and also allows detailed analysis of how different factors such as porosity and component properties affect the sign and magnitude of K_ϕ^*.

2 Negative K_ϕ^*

2.1 Necessary Conditions. In numerical simulations, Berryman (1992a) found some models having negative K_ϕ^* values for composites made up of two porous components, but these models all used approximations for K_d^* in the exact expression for K_ϕ^*. The theories used were ones that are known to correspond to realizable microstructures. But these microstructures are special, and the results do not show what conditions might produce negative K_ϕ^* values in real materials; nor do they take full advantage of the exact expression for K_ϕ^*. This paper will first consider what conditions produce negative K_ϕ^* in Eq. (9), before using some exact results for K_d^* to model materials having negative K_ϕ^* values.

Recalling the well-known fact that

$$K_d^* \geq \left\langle \frac{1}{K_d(x)} \right\rangle^{-1} \tag{10}$$

(Reuss, 1929), i.e., the overall frame modulus is greater than or equal to the harmonic mean of the constituents, clearly $K_\phi^* < 0$ in Eq. (9) whenever

$$\frac{1}{\phi^*}\left(1 - \frac{K_{d1}}{K_{m1}} - \phi^*\right) \gg 1 \tag{11}$$

for non-vanishing $(K_d^*\langle 1/K_d(x)\rangle - 1)$. Similarly, recalling that

$$K_d \leq (1 - \phi)K_m \tag{12}$$

(Voigt, 1928), then $K_\phi^* < 0$ in Eq. (9) whenever

$$\left(K_d^*\left\langle \frac{1}{K_d(x)} \right\rangle - 1\right) \gg 1 \tag{13}$$

for non-vanishing $1/\phi^*\ (1 - K_{d1}/K_{m1} - \phi^*)$.

Consider the behavior of $1/\phi^*\ (1 - K_{d1}/K_{m1} - \phi^*)$. The value of K_{d1} is bounded by the Voigt and Reuss bounds (Voigt, 1928; Reuss, 1929; Hill, 1952):

$$K_{\text{Reuss}} = 0 \leq K_{d1} \leq (1 - \phi_1)K_{m1} = K_{\text{Voigt}}. \tag{14}$$

$K_{d1} \to 0$ as $\phi_1 \to 1$, and $K_{d1} \to K_{m1}$ as $\phi_1 \to 0$. Then since $\phi^* = \phi_1$, $(1 - K_{d1}/K_{m1} - \phi^*) \to 0$ as $\phi^* \to 0$. Allowing $1/\phi^*$ to grow large will not guarantee that the left side of (11) will grow large. The Voigt bound and the thermodynamic requirement that $K_{d1} \geq 0$ (Berryman and Milton, 1991) give

$$1 - \phi_1 \geq \left(1 - \frac{K_{d1}}{K_{m1}} - \phi_1\right) \geq 0. \tag{15}$$

The left side of (11) will not grow large unless $1/\phi^* \gg 1$, but $K_{d1}/K_{m1} + \phi_1$ must remain small to keep $(1 - K_{d1}/K_{m1} - \phi_1)$ from vanishing. The dependence of K_{d1} on $\phi^* = \phi_1$ is critical in (11).

In general, we do not know how K_{d1} depends on ϕ_1, but we can gain some insight by making use of better known bounds on K_{d1}. The Hashin-Shtrikman bounds provide rigorous upper and lower bounds on the bulk and shear moduli of isotropic composite materials (Hashin, 1962; Hashin and Shtrikman, 1963). For a dry porous material having porosity ϕ_1 and solid bulk and shear moduli K_{m1} and μ_{m1}, the Hashin-Shtrikman lower bounds vanish, while the upper bound K_{HS}^+ in $K_{HS}^+ \geq K_{d1} \geq 0$ is given by

$$K_{HS}^+ = \frac{(1 - \phi_1)K_{m1}}{1 + \phi_1\left(\dfrac{3K_{m1}}{4\mu_{m1}}\right)} \tag{16}$$

(Hashin and Shtrikman, 1963).

Although the exact behavior of K_{d1} and $K_{d1}/K_{m1} + \phi_1$ as functions of ϕ_1 will vary for different materials, two typical end-members are represented by relatively stiff materials having $K_{d1} = K_{HS}^+$, and by relatively compliant granular materials that become disaggregated at some finite porosity so that K_{d1} vanishes. K_{HS}^+ is a monotonic decreasing function of ϕ_1 and

$$\frac{K_{HS}^+}{K_{m1}} + \phi_1 \geq \frac{K_{d1}}{K_{m1}} + \phi_1 \geq \phi_1 \tag{17}$$

Downloaded 04 May 2010 to 171.66.16.28. Redistribution subject to ASME license or copyright; see http://www.asme.org/terms/Terms_Use.cfm

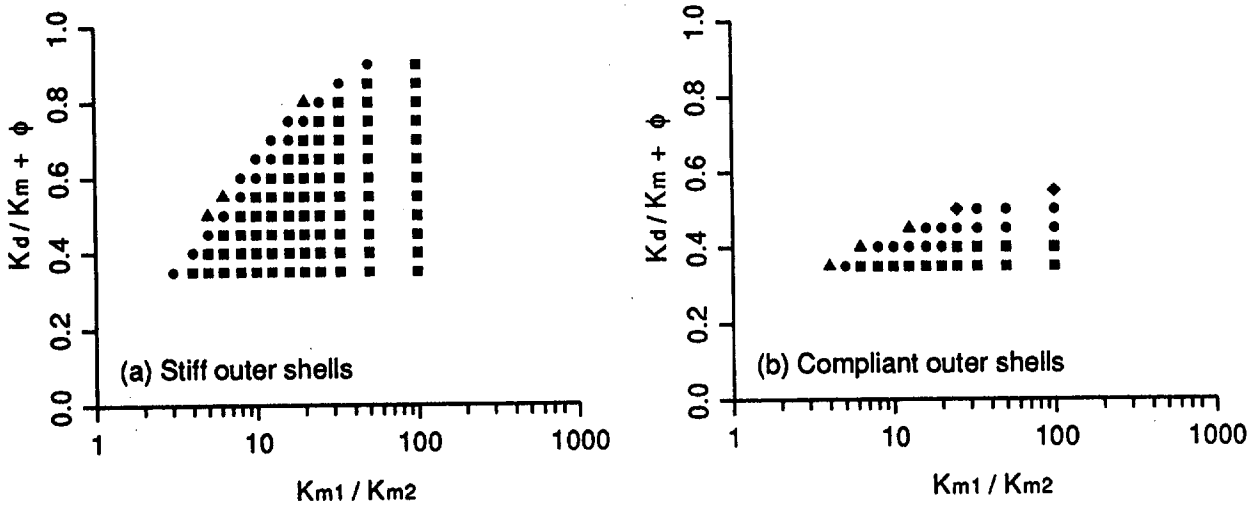


Fig. 3 Component moduli, porosity, concentration values leading to negative K_ϕ^* in concentric spheres assemblages with (*a*) stiff and (*b*) compliant outer shells. Axes show ranges of porosities and ratios of components' solid bulk moduli used in modeling. Different symbols indicate combining different volumes of pairs of materials in the models.

(see Fig. 1(*a*)). Note that $K_{HS}^+/K_{m1} + \phi_1$ has a minimum at

$$\phi_1 = \frac{\sqrt{1 + \left(\frac{3K_{m1}}{4\mu_{m1}}\right)} - 1}{\left(\frac{3K_{m1}}{4\mu_{m1}}\right)}, \qquad (18)$$

which will be near $\phi_1 = 0.41$ if $3K_{m1}/4\mu_{m1} = 1$. In the case of uniform spherical grains, the random-packing point at which a compliant granular material's K_{d1} vanishes is near $\phi_1 = 0.38$ (Bernal and Mason, 1960). For most real materials, the value of $K_{d1}/K_{m1} + \phi_1$ will lie between ~0.4 and 1.0 for all values of ϕ_1 and will have a minimum near $\phi_1 = 0.4$ (Fig. 1(*b*)). Porosities near 0.4 in (11) are expected to bring about negative K_ϕ^* in (9).

Now consider the behavior of the left side of (13). The expression $(K_d^*\langle 1/K_d(x)\rangle - 1)$ vanishes if $K_{d1} = K_{d2}$. Otherwise, this expression is positive and has no finite upper bound. Negative K_ϕ^* values are expected in (9) for materials having greatly dissimilar values of K_{d1} and K_{d2} in (13). From (8), we see that this condition requires greatly dissimilar values of K_{m1} and K_{m2}. In addition, the porosity must not approach 1 or 0, to prevent ($[1 - K_{d1}/K_{m1} - \phi^*$) from vanishing in (9).

It is apparent from (11) and (13) that for composite materials made up of two porous components, negative K_ϕ^* values in (9) are most likely for composite materials having intermediate porosities and either $K_{m1} \gg K_{m2}$ or $K_{m2} \gg K_{m1}$. Further analysis of the sign of K_ϕ^* requires more specific information about the value of K_d^*.

2.2 Using Exact Results for K_d^*. In general there is no exact expression giving K_d^* in terms of component properties, although it can be estimated using various effective medium theories (e.g., Berryman, 1992a). The exact value of K_d^* is available in the specific case of a material having the microgeometry of an assemblage of concentric spheres, where the sphere sizes may vary but the relative volumes and radii of the inner and outer spheres maintain a constant ratio. This realizable microgeometry is known as the composite spheres assemblage (see Fig. 2). The Hashin-Shtrikman bounds give exact results for such materials (Hashin, 1962):

$$K_d^* = K_{HS}^* = \left\langle \frac{1}{K_d(x) + 4\mu_d^*/3} \right\rangle^{-1} - 4\mu_d^*/3, \qquad (19)$$

where $K_d(x)$ and the $\langle\ \rangle$ bracket notation have the same significance as in (9). (To make use of Hashin's result for our porous materials, we are implicitly assuming a separation of length scales: the pores are on a much smaller length scale than the size of the concentric spheres in the sphere assemblage model.) If the stiffer porous material (having the larger K_d) forms the outer shells of the concentric spheres, then (19) is the Hashin-Shtrikman upper-bound expression and uses the larger of the component drained-frame shear moduli (μ_{d1} and μ_{d2}) for μ_d^*. If instead the more compliant of the two porous components forms the outer shells, then (19) is the Hashin-Shtrikman lower-bound expression and uses the smaller drained-frame shear modulus for μ_d^*. (Note that (19) gives K_d^* for the composite, whereas (16) provided an upper bound on K_d for one porous component.)

For a composite material having the microgeometry shown in Fig. 2, we can use (19) for K_d^*, and then use Eq. (9) to find K_ϕ^*. Again (11) and (13) are the conditions that result in $K_\phi^* < 0$, and now the left side of (13) can be written

$$\left(K_d^*\left\langle\frac{1}{K_d(x)}\right\rangle - 1\right) = \left(K_{HS}^*\left\langle\frac{1}{K_d(x)}\right\rangle - 1\right)$$
$$= \frac{1 + \frac{4}{3}\mu_d^*[v_1/(K_{d2}) + v_2/(K_{d1})]}{1 + \frac{4}{3}\mu_d^*[v_1(K_{d2}) + v_2(K_{d1})]^{-1}} - 1, \qquad (20)$$

where v_1 and $v_2 = (1 - v_1)$ are the relative volumes of the type-1 and type-2 constituents. This expression vanishes if $\mu_d^* \to 0$ (i.e., one component is a liquid), if v_1 or v_2 vanishes (only one solid is present), or if $K_{d1} = K_{d2}$. On the other hand, this expression grows large if $K_{d1} \gg K_{d2}$ or if $K_{d2} \gg K_{d1}$, i.e., if $K_{m1} \gg K_{m2}$ or if $K_{m2} \gg K_{m1}$.

A difference of a factor of ten in the values of K_{m1} and K_{m2} in (20) should suffice to produce $K_\phi^* < 0$ in (9), particularly if $K_{d1}/K_{m1} + \phi_1$ is small. If the outer shells of the concentric spheres are formed by the more compliant material and μ_d^* is therefore the smaller of the two drained-frame shear moduli, a negative K_ϕ^* value is only possible if μ_d^* is not small compared to K_{d1} and K_{d2}. For solids, the bulk and shear moduli are often of similar magnitudes, and therefore when K_{m1} and K_{m2} are

Downloaded 04 May 2010 to 171.66.16.28. Redistribution subject to ASME license or copyright; see http://www.asme.org/terms/Terms_Use.cfm

Table 4 Measured properties of some natural materials

Material	ϕ	K_m (GPa)	K_d (GPa)	$\frac{K_d}{K_m}$	μ_m (GPa)	μ_d (GPa)
Berea ss[1]	0.16	33.0	12.6	0.38	26.0	9.0
Si_3N_4 [2]	0.21	173.6	72.0	0.41	118.2	61.1
	0.26	173.6	64.7	0.37	118.2	54.8
Boise ss[1]	0.25	30.0	8.7	0.29	18.0	8.1
Clean ss[3]	0.20	35.0	17.0	0.49	40.0	16.0
Clay[4]	0.20	21.4	11.6 [7]	0.54	6.7	4.6 [7]
	0.25	21.4	10.0 [7]	0.47	6.7	4.2 [7]
Glass foam[5]	0.25	46.1	23.8	0.52	30.4	15.7 [8]
Al_2O_3 [6]	0.25	281.9	159.8 [7]	0.57	163.5	99.1 [7]

[1]Measured properties from Cheng (1978).

[2]Measured properties from Fate (1975), Berryman (1993a).

[3]Measured properties from Blangy et al. (1993).

[4]Measured properties from Castagna et al. (1985).

[5]Measured properties from Walsh et al. (1965).

[6]Measured properties from Hasselman & Fulrath (1965), Berryman (1993b).

[7]Estimated assuming spherical pores.

[8]Estimated assuming Poisson's ratio is independent of porosity.

greatly dissimilar, $K_\phi^* < 0$ is much more likely if the stiffer material forms the outer shells of the concentric spheres.

From (8), (11), (13), and (20), we see that the sign of K_ϕ^* for the concentric spheres assemblage depends only on K_{m1}/K_{m2}, K_{d1}/K_{m1}, μ_d^*/K_{d1}, ϕ^*, and υ_1. Numerical examples can be used to illustrate the relative importance of these factors. Such modeling is particularly useful since (9) is an exact expression, rather than an estimate, for the value of K_ϕ^*.

3 Numerical Results

3.1 Synthetic Examples. Physical properties of nine sample materials are summarized in Table 1. These examples all have $K_d/K_m = 0.25$ and Poisson's ratio values of 0.20, but the value of K_m varies by two orders of magnitude among these materials. In real materials, K_d changes with porosity. It has been kept independent of porosity here to reduce the number of free parameters in the modeling. Varying the value of ϕ causes the value of $K_d/K_m + \phi$ to vary. Equations (8), (9), and (19) were used to find K_ϕ^* for composites constructed from porous concentric spheres made from pairs of these sample materials. The materials were combined in different proportions υ_1 and υ_2, and different pairs were used to vary K_{m1}/K_{m2}. The μ_d/K_d values have been kept constant, but the effects of varying μ_d can be seen by using concentric sphere models with the stiffer material forming the outer shells and then comparing results for models made from the same materials but having the more compliant material forming the outer shells.

Calculated K_d^* and K_ϕ^* are given in Tables 2 and 3 for some pairs of materials described in Table 1, for models using $\phi^* = 0.35$. Table 2 presents results for models having the stiffer material forming the outer shells of concentric spheres, whereas Table 3 gives results for models having the more compliant material forming the outer shells. Using the convention that the stiffer material is component 1 and the more compliant material is component 2, the composites in Tables 2 and 3 have K_{m1}/K_{m2} ratios of 5, 10, and 100. None of the models in Table 3 produces $K_\phi^* < 0$, but in Table 2 K_ϕ^* is negative for composites having large K_{m1}/K_{m2} ratios. For models having $\upsilon_1 = 0$, $K_\phi^* = K_s^* = K_{m2}$, and for models having $\upsilon_1 = 1$, $K_\phi^* = K_s^* = K_{m1}$, as expected. Although, as required, $K_{m1} \geq K_s^* \geq K_{m2}$ and $K_{d1} \geq K_d^* \geq K_{d2}$ for all the composites in Tables 2 and 3, K_ϕ^* does not necessarily lie between K_{m1} and K_{m2}.

The K_ϕ^* values presented in Tables 2 and 3 can be compared to results that Berryman (1992a) obtained using these same composites and effective medium theory estimates for K_d^*. One effective medium theory modeled the composites by assuming a microgeometry in which one porous component was present as isolated spherical inclusions embedded in a homogeneous background consisting of the other porous composite (Berryman, 1992a). Such a microgeometry is similar to the Hashin-Shtrikman composite spheres assemblage, and the corresponding K_ϕ^* values lie between the Hashin-Shtrikman bounds. If the stiffer material forms the background, the effective medium theory estimate of K_d^* is smaller than the value shown in Table 2. On the other hand, if the effective medium theory assumes that the more compliant material forms the background, the K_d^* estimate is larger than the value shown in Table 3. Berryman's (1992a) estimates of K_d^* are similar to the exact results for concentric spheres assemblages given in Tables 2 and 3 for models having $K_{m1}/K_{m2} = 5$, and for all models in the Tables when the inclusion concentration is small, ≤ 0.2. For models having $K_{m1}/K_{m2} = 10$ and inclusion concentrations ≥ 0.5, Berryman's estimated K_d^* values differ from the values in Tables 2 and 3 by factors of about 10-15 percent. The differences are

Downloaded 04 May 2010 to 171.66.16.28. Redistribution subject to ASME license or copyright; see http://www.asme.org/terms/Terms_Use.cfm

Table 5 Stiff concentric spheres assemblages made from natural materials

Clean ss and clay $K_{m1}/K_{m2} = 1.6$, $K_d/K_m = 0.52$				
ϕ^*	v_1	K_d^*	K_s^*	K_ϕ^*
0.20	0.00	11.13	21.40	21.40
0.20	0.10	11.72	22.54	22.93
0.20	0.20	12.33	23.72	24.47
0.20	0.30	12.97	24.94	26.02
0.20	0.40	13.63	26.21	27.54
0.20	0.50	14.32	27.53	29.02
0.20	0.60	15.03	28.91	30.43
0.20	0.70	15.77	30.34	31.76
0.20	0.80	16.55	31.83	32.97
0.20	0.90	17.36	33.38	34.06
0.20	1.00	18.20	35.00	35.00
Glass foam and clay $K_{m1}/K_{m2} = 2.2$, $K_d/K_m = 0.50$				
ϕ^*	v_1	K_d^*	K_s^*	K_ϕ^*
0.25	0.00	10.70	21.40	21.40
0.25	0.10	11.61	23.23	23.88
0.25	0.20	12.58	25.16	26.49
0.25	0.30	13.61	27.22	29.19
0.25	0.40	14.70	29.40	31.95
0.25	0.50	15.87	31.73	34.70
0.25	0.60	17.11	34.22	37.39
0.25	0.70	18.44	36.88	39.95
0.25	0.80	19.86	39.73	42.30
0.25	0.90	21.40	42.79	44.37
0.25	1.00	23.05	46.10	46.10
Si_3N_4 and Berea ss $K_{m1}/K_{m2} = 5.3$, $K_d/K_m = 0.40$				
ϕ^*	v_1	K_d^*	K_s^*	K_ϕ^*
0.19	0.00	13.20	33.00	33.00
0.19	0.10	16.86	42.16	67.54
0.19	0.20	20.82	52.06	170.68
0.19	0.30	25.12	62.79	1266.64
0.19	0.40	29.78	74.46	-556.61
0.19	0.50	34.88	87.20	-370.89
0.19	0.60	40.46	101.16	-416.95
0.19	0.70	46.61	116.53	-819.97
0.19	0.80	53.41	133.53	1597.14
0.19	0.90	60.98	152.44	334.58
0.19	1.00	69.44	173.60	173.60

Table 5 (continued)

Si_3N_4 and Boise ss $K_{m1}/K_{m2} = 5.8$, $K_d/K_m = 0.33$				
ϕ^*	v_1	K_d^*	K_s^*	K_ϕ^*
0.26	0.00	9.90	30.00	30.00
0.26	0.10	13.03	39.48	58.66
0.26	0.20	16.41	49.71	125.50
0.26	0.30	20.06	60.78	347.13
0.26	0.40	24.02	72.78	4248.52
0.26	0.50	28.33	85.85	-1238.65
0.26	0.60	33.04	100.14	-1348.36
0.26	0.70	38.22	115.82	8166.13
0.26	0.80	43.92	133.10	632.62
0.26	0.90	50.24	152.26	286.28
0.26	1.00	57.29	173.60	173.60
Al_2O_3 and glass foam $K_{m1}/K_{m2} = 6.1$, $K_d/K_m = 0.55$				
ϕ^*	v_1	K_d^*	K_s^*	K_ϕ^*
0.25	0.00	25.36	46.10	46.10
0.25	0.10	32.80	59.64	70.04
0.25	0.20	40.99	74.53	103.08
0.25	0.30	50.04	90.97	147.34
0.25	0.40	60.08	109.23	202.76
0.25	0.50	71.29	129.61	263.73
0.25	0.60	83.89	152.52	316.73
0.25	0.70	98.15	178.46	345.58
0.25	0.80	114.44	208.06	343.63
0.25	0.90	133.20	242.17	318.14
0.25	1.00	155.04	281.90	281.90
Si_3N_4 and clay $K_{m1}/K_{m2} = 8.1$, $K_d/K_m = 0.42$				
ϕ^*	v_1	K_d^*	K_s^*	K_ϕ^*
0.26	0.00	8.99	21.40	21.40
0.26	0.10	12.75	30.35	47.53
0.26	0.20	16.86	40.15	123.01
0.26	0.30	21.40	50.95	714.15
0.26	0.40	26.41	62.89	-534.43
0.26	0.50	31.99	76.17	-331.86
0.26	0.60	38.23	91.02	-363.46
0.26	0.70	45.26	107.76	-660.17
0.26	0.80	53.23	126.75	2347.32
0.26	0.90	62.36	148.48	345.77
0.26	1.00	72.91	173.60	173.60

up to 50 percent for models having $K_{m1}/K_{m2} = 100$. Small differences in K_d^* lead to larger differences in calculated K_ϕ^* values. For models in which the effective medium theory estimates of K_d^* differed by a few percent from those listed in Tables 2 and 3, K_ϕ^* values in Tables 2 and 3 differ from Berryman's calculated values by about 15 percent. For models having $K_{m1}/K_{m2} = 100$, Berryman's estimated K_ϕ^* values were negative for some of the composites in Table 3. Because K_ϕ^* is so sensitive to the value of K_d^* while K_d^* depends on microgeometry, theoretical estimates of K_d^* may not always be accurate enough to determine K_ϕ^* reliably for models having arbitrary microgeometry.

In addition to the results presented in Tables 2 and 3, K_d^* and K_ϕ^* values were computed using 11 other combinations of materials from Table 1, with K_{m1}/K_{m2} varying between 2 and 100 and with $K_d/K_m + \phi$ varying from 0.35 to 0.90. Figure 3 summarizes the relative importance of factors contributing to $K_\phi^* < 0$ for these models. Plot axes show the range of $K_d/K_m + \phi$ and K_{m1}/K_{m2} values used in the modeling. The physical meanings of these axes are the porosity contribution and the effects of different bulk moduli ratios for the two solid components. Different symbols were used in Fig. 3 to indicate effects of different volume concentrations of the two porous components. Combinations of K_{m1}/K_{m2} and $K_d/K_m + \phi$ that lead to negative values for K_ϕ^* are indicated for concentric spheres assemblages having the stiffer porous component forming the outer shells (Fig. 3(a)), and for the more compliant porous component forming the outer shells (Fig. 3(b)). In Fig. 3(a), models having negative K_ϕ^* for all $v_1 = 1 - v_2$ relative concentrations between about 0.2 and 0.8 are indicated by the squares. Models having $K_\phi^* < 0$ for all v_1 between about 0.3 and 0.7 are indicated by the dots in Fig. 3(a), while models having $K_\phi^* < 0$ only for $v_1 \approx v_2$ are indicated by triangles. The models in Fig. 3(b) are less symmetric with respect to v_1 and v_2, since

Downloaded 04 May 2010 to 171.66.16.28. Redistribution subject to ASME license or copyright; see http://www.asme.org/terms/Terms_Use.cfm

Table 6 Weak concentric spheres assemblages made from natural materials

Clean ss and clay $K_{m1}/K_{m2} = 1.6$, $K_d/K_m = 0.52$				
ϕ^*	ν_1	K_d^*	K_s^*	K_ϕ^*
0.20	0.00	11.13	21.40	21.40
0.20	0.10	11.64	22.39	22.58
0.20	0.20	12.19	23.45	23.80
0.20	0.30	12.78	24.57	25.07
0.20	0.40	13.40	25.77	26.39
0.20	0.50	14.06	27.04	27.75
0.20	0.60	14.77	28.41	29.15
0.20	0.70	15.54	29.88	30.58
0.20	0.80	16.36	31.46	32.04
0.20	0.90	17.24	33.16	33.51
0.20	1.00	18.20	35.00	35.00
Glass foam and clay $K_{m1}/K_{m2} = 2.2$, $K_d/K_m = 0.50$				
ϕ^*	ν_1	K_d^*	K_s^*	K_ϕ^*
0.25	0.00	10.70	21.40	21.40
0.25	0.10	11.43	22.87	23.13
0.25	0.20	12.24	24.48	25.00
0.25	0.30	13.12	26.24	27.03
0.25	0.40	14.10	28.19	29.22
0.25	0.50	15.18	30.36	31.57
0.25	0.60	16.39	32.77	34.11
0.25	0.70	17.74	35.49	36.83
0.25	0.80	19.28	38.56	39.73
0.25	0.90	21.03	42.06	42.83
0.25	1.00	23.05	46.10	46.10
Si_3N_4 and Berea ss $K_{m1}/K_{m2} = 5.3$, $K_d/K_m = 0.40$				
ϕ^*	ν_1	K_d^*	K_s^*	K_ϕ^*
0.19	0.00	13.20	33.00	33.00
0.19	0.10	15.07	37.67	42.14
0.19	0.20	17.24	43.10	54.12
0.19	0.30	19.78	49.46	69.73
0.19	0.40	22.82	57.04	89.67
0.19	0.50	26.49	66.23	113.98
0.19	0.60	31.03	77.57	140.94
0.19	0.70	36.78	91.95	165.98
0.19	0.80	44.31	110.77	182.26
0.19	0.90	54.58	136.45	184.62
0.19	1.00	69.44	173.60	173.60

Table 6 (continued)

Si_3N_4 and Boise ss $K_{m1}/K_{m2} = 5.8$, $K_d/K_m = 0.33$				
ϕ^*	ν_1	K_d^*	K_s^*	K_ϕ^*
0.26	0.00	9.90	30.00	30.00
0.26	0.10	11.45	34.69	38.37
0.26	0.20	13.25	40.14	49.20
0.26	0.30	15.36	46.55	63.15
0.26	0.40	17.89	54.20	80.82
0.26	0.50	20.95	63.48	102.34
0.26	0.60	24.74	74.98	126.67
0.26	0.70	29.57	89.59	150.72
0.26	0.80	35.90	108.80	169.35
0.26	0.90	44.60	135.16	177.51
0.26	1.00	57.29	173.60	173.60
Al_2O_3 and glass foam $K_{m1}/K_{m2} = 6.1$, $K_d/K_m = 0.55$				
ϕ^*	ν_1	K_d^*	K_s^*	K_ϕ^*
0.25	0.00	25.36	46.10	46.10
0.25	0.10	29.04	52.80	54.97
0.25	0.20	33.36	60.65	65.67
0.25	0.30	38.49	69.99	78.62
0.25	0.40	44.70	81.28	94.35
0.25	0.50	52.36	95.21	113.50
0.25	0.60	62.05	112.81	136.77
0.25	0.70	74.68	135.78	164.90
0.25	0.80	91.85	167.00	198.50
0.25	0.90	116.53	211.87	237.75
0.25	1.00	155.04	281.90	281.90
Si_3N_4 and clay $K_{m1}/K_{m2} = 8.1$, $K_d/K_m = 0.42$				
ϕ^*	ν_1	K_d^*	K_s^*	K_ϕ^*
0.26	0.00	8.99	21.40	21.40
0.26	0.10	10.28	24.48	25.87
0.26	0.20	11.83	28.16	31.45
0.26	0.30	13.70	32.63	38.48
0.26	0.40	16.03	38.18	47.41
0.26	0.50	19.00	45.25	58.83
0.26	0.60	22.92	54.57	73.44
0.26	0.70	28.32	67.43	92.03
0.26	0.80	36.24	86.29	115.24
0.26	0.90	48.99	116.64	143.01
0.26	1.00	72.91	173.60	173.60

more of the stiff material must be present to attain a given composite stiffness when the more compliant material forms the outer shells. Squares in Fig. 3(b) indicate models having negative K_ϕ^* values for all ν_1 between about 0.3 and 0.9. Dots indicate ν_1 between about 0.5 and 0.8, triangles show models with ν_1 between about 0.6 and 0.7, and diamonds are for models with negative K_ϕ^* only for $\nu_1 \approx 0.8$, in Fig. 3(b).

For models having the more compliant of two porous components forming the outer shells of concentric spheres, $K_\phi^* < 0$ only if $K_d/K_m + \phi \leq 0.55$. If the stiffer material forms the outer shells, $K_\phi^* < 0$ even for fairly large values of $K_d/K_m + \phi$, as long as the ratio K_{m1}/K_{m2} is large. Some models in Fig. 3(a) having $K_{m1}/K_{m2} < 10$ had $K_\phi^* < 0$, when $K_d/K_m + \phi \leq 0.6$. Since most real materials are expected to have $K_d/K_m + \phi \geq 0.4$ and $K_{m1}/K_{m2} < 10$, results in Fig. 3(b) imply that $K_\phi^* < 0$ is unlikely in a porous composite having the Hashin-Shtrikman composite spheres assemblage microgeometry if the more compliant component forms the outer shells of concentric spheres.

3.2 Computations Using Properties of Real Materials. The models described in Tables 1-3 and in Fig. 3 show that $K_\phi^* < 0$ is possible in composite materials containing two solid components if the component properties have large enough K_{m1}/K_{m2} and small enough $K_d/K_m + \phi$ values. But since the material properties listed in Table 1 are *synthetic*, this modeling does not demonstrate the possibility of observing $K_\phi^* < 0$ in *real* materials. Calculation of K_d^* and K_ϕ^* using Eq. (19) and (9) requires measured values of ϕ, K_m, K_d, and μ_d for pairs of porous materials having equal porosities and satisfying the constraint in (8). Although measured values of the relevant properties are available for many natural materials, it is more difficult to find materials of equal porosity that have the same K_d/K_m.

Table 4 presents measured properties of seven natural materials that can be combined in pairs having similar porosities and

Downloaded 04 May 2010 to 171.66.16.28. Redistribution subject to ASME license or copyright; see http://www.asme.org/terms/Terms_Use.cfm

approximately the same K_d/K_m values. Equations (9) and (19) were used to find K_ϕ^* and K_d^* for models of composites formed using the properties of these natural materials, assuming the composite microgeometry illustrated in Fig. 2. Results in Table 5 assume that the outer shells of concentric spheres were made up of the stiffer of two porous components (component 1). Table 6 gives results for the more compliant material forming the outer shells. These models have values of $K_d/K_m + \phi$ between 0.59 and 0.80, and K_{m1}/K_{m2} ratios of 1.6 to 8.1.

In Tables 5 and 6, K_d^* is bounded by the K_d values of the porous components, and K_s^* is bounded by the K_m values of the solid components. Although $K_\phi^* = K_s^* = K_m$ for models having $v_1 = 0.0$ or $v_1 = 1.0$, the value of K_ϕ^* is not bounded by the K_m values for all models. Fortunately, the exact expression (9) for K_ϕ^* allows us to examine the behavior of this unbounded parameter. We see that K_ϕ^* does not always lie between K_{m1} and K_{m2} for models in Table 5 having large values of K_{m1}/K_{m2} or for models in Table 6 having small values of $K_d/K_m + \phi$.

In both Tables the non-negative K_ϕ^* values are slightly larger than respective K_s^* values when K_{m1}/K_{m2} is small. In Table 5, $K_\phi^* < 0$ for models having $K_{m1}/K_{m2} > 5$ and $K_d/K_m + \phi < 0.7$, with approximately equal amounts of the two porous components ($v_1 \approx v_2$). None of the models in Table 6 has $K_\phi^* < 0$.

4 Conclusion

The physical meaning of negative K_ϕ^* is this: if the external and internal (fluid) pressures are increased, the relative pore volume of a porous composite also increases. The presence of a highly compressible solid component ($1/K_{m2} \gg 1/K_{m1}$) enables the pore volume to increase at the expense of the solid volume. The parameter K_ϕ^* appears in expressions for effective stress laws describing the response of poroelastic materials (Berryman, 1992b).

Most solids have values of K_m between a few and a few hundred GPa, implying that $0.01 < K_{m1}/K_{m2} < 100$ for most combinations of natural materials. The more common case is $0.1 < K_{m1}/K_{m2} < 10$. The modeling in the previous section, using the exact expression for K_ϕ^*, demonstrates that it should be possible to find $K_\phi^* < 0$ for natural materials, assuming the composites have a microstructure analogous to that shown in Fig. 2. If the more compliant material forms the outside shells of the concentric spheres, $K_\phi^* < 0$ can be expected if $K_d/K_m + \phi < 0.6$ and $K_{m1}/K_{m2} > 10$. On the other hand, if the stiffer material forms the outer shells, $K_\phi^* < 0$ can be expected if $K_d/K_m + \phi < 0.7$ and $K_{m1}/K_{m2} > 5$. If the two porous components making up the composite are combined in very unequal proportions, the ratio K_{m1}/K_{m2} must be extremely large in order for K_ϕ^* to be negative.

These results show clearly that in some circumstances it is inadequate to use the common assumption that the pore compressibility is equal to the solid compressibility. The challenge to measure K_ϕ^* accurately is one of the next steps in the task of refining our understanding of poroelastic materials. Construction of materials whose microstructures are analogs of realizable theoretical models will also help to resolve some of the remaining questions about the behavior of poroelastic materials.

Acknowledgment

This work was performed under the auspices of the U.S. Department of Energy by the Lawrence Livermore National Laboratory under contract No. W-7405-ENG-48 and supported specifically by the Geosciences Research Program of the DOE Office of Energy Research within the Office of Basic Energy Sciences, Division of Engineering and Geosciences.

References

Adams, L. H., and Williamson, E. D., 1923, "The Compressibility of Minerals and Rocks at High Pressure," *Journal of the Franklin Institute,* Vol. 195, pp. 475–529.

Bernal, J. D., and Mason, J., 1960, "Co-ordination of Randomly Packed Spheres," *Nature,* Vol. 188, No. 4754, pp. 910–911.

Berryman, J. G., 1986, "Effective Medium Approximation for Elastic Constants of Porous Solids with Microscopic Heterogeneity," *Journal of Applied Physics,* Vol. 59, pp. 1136–1140.

Berryman, J. G., 1992a, "Single-Scattering Approximations for Coefficients in Biot's Equations of Poroelasticity," *Journal of the Acoustical Society of America,* Vol. 91, No. 2, pp. 551–571.

Berryman, J. G., 1992b, "Effective Stress for Transport Properties of Inhomogeneous Porous Rock," *Journal of Geophysical Research,* Vol. 97, No. B12, pp. 17,409–17,424.

Berryman, J. G., 1993a, "Mixture Theories for Rock Properties," *Handbook of Physical Constants,* T. J. Ahrens, ed., American Geophysical Union, Washington, D.C., in press.

Berryman, J. G., 1993b, "Role of Porosity in Estimates of Composite Elastic Constants," *Composite Material Technology,* PD-Vol. 53, D. Hui, T. J. Kozik, and O. O. Ochoa, eds., ASME, New York, pp. 223–235.

Berryman, J. G., and Milton, G. W., 1991, "Exact Results for Generalized Gassmann's Equations in Composite Porous Media with Two Constituents," *Geophysics,* Vol. 56, No. 12, pp. 1950–1960.

Berryman, J. G., and Milton, G. W., 1992, "Exact Results in Linear Thermomechanics of Fluid-Saturated Porous Media," *Applied Physics Letters,* Vol. 61, No. 17, pp. 2030–2032.

Biot, M. A., 1956, "Theory of Propagation of Elastic Waves in a Fluid-Saturated Porous Solid. I. Low-Frequency Range," *Journal of the Acoustical Society of America,* Vol. 28, No. 2, pp. 168–178.

Biot, M. A., 1962, "Mechanics of Deformation and Acoustic Propagation in Porous Media," *Journal of Applied Physics,* Vol. 33, No. 4, pp. 1482–1498.

Biot, M. A., and Willis, D. G., 1957, "The Elastic Coefficients of the Theory of Consolidation," ASME JOURNAL OF APPLIED MECHANICS, Vol. 24, pp. 594–601.

Birch, F., 1960, "The Velocity of Compressional Waves in Rocks to 10 Kilobars, Part 1," *Journal of Geophysical Research,* Vol. 65, pp. 1083–1102.

Birch, F., 1961, "The Velocity of Compressional Waves in Rocks to 10 Kilobars, Part 2," *Journal of Geophysical Research,* Vol. 66, pp. 2199–2224.

Birch, F., and Law, R. R., 1935, "Measurement of Compressibility at High Pressures and High Temperatures," *Bulletin of the Geological Society of America,* Vol. 46, pp. 1219–1250.

Blangy, J. P., Strandenes, S., Moos, D., and Nur, A., 1993, "Ultrasonic Velocities in Sands–Revisited," *Geophysics,* Vol. 58, No. 3, pp. 344–356.

Brace, W. F., 1965, "Some New Measurements of Linear Compressibility of Rocks," *Journal of Geophysical Research,* Vol. 70, No. 2, pp. 391–398.

Brown, R. J. S., and Korringa, J., 1975, "On the Dependence of the Elastic Properties of a Porous Rock on the Compressibility of the Pore Fluid," *Geophysics,* Vol. 40, No. 4, pp. 608–616.

Castagna, J. P., Batzle, M. L., and Eastwood, R. L., 1985, "Relationships between Compressional-Wave and Shear-Wave Velocities in Clastic Silicate Rocks," *Geophysics,* Vol. 50, No. 4, pp. 571–581.

Cheng, C. H. A., 1978, "Seismic Velocities in Porous Rocks: Direct and Inverse Problems," Ph.D. Thesis, Massachusetts Institute of Technology, Cambridge, MA.

Coyner, K. B., 1984, "Effects of Stress, Pore Pressure, and Pore Fluids on Bulk Strain, Velocity, and Permeability of Rocks," Ph.D. Thesis, Massachusetts Institute of Technology, Cambridge, MA.

Fate, W. A., 1975, "High Temperature Elastic Moduli of Polycrystalline Silicon Nitride," *Journal of Applied Physics,* Vol. 46, pp. 2375–2377.

Fatt, I., 1958, "Pore Volume Compressibilities of Sandstone Reservoir Rocks," *Society of Petroleum Engineers Transactions, AIME,* Vol. 213, pp. 362–364.

Fatt, I., 1959, "The Biot-Willis Elastic Coefficients for a Sandstone," ASME JOURNAL OF APPLIED MECHANICS, Vol. 26, pp. 296–297.

Gassmann, F., 1951, "Über die elastizität poröser medien," *Veirteljahrsschrift der Naturforschenden Gesellschaft in Zürich,* Vol. 96, pp. 1–23.

Green, D. H., and Wang, H. F., 1986, "Fluid Pressure Response to Undrained Compression in Saturated Sedimentary Rock," *Geophysics,* Vol. 51, No. 4, pp. 948–956.

Greenwald, R. F., 1980, "Volumetric Response of Porous Media to Pressure Variations," Ph.D. Thesis, University of California, Berkeley, CA.

Hall, H. H., 1953, "Compressibility of Reservoir Rocks," *Society of Petroleum Engineers Transactions, AIME,* Vol. 198, pp. 309–311.

Hashin, Z., 1962, "The Elastic Moduli of Heterogeneous Materials," ASME JOURNAL OF APPLIED MECHANICS, Vol. 29, pp. 143–150.

Hashin, Z., and Shtrikman, S., 1963, "A Variational Approach to the Theory of the Elastic Behaviour of Multiphase Materials," *Journal of the Mechanics and Physics of Solids,* Vol. 11, pp. 127–140.

Hasselman, D. P. H., and Fulrath, R. M., 1965, "Effect of Alumina Dispersions on Young's Modulus of a Glass," *Journal of the American Ceramic Society,* Vol. 48, pp. 218–219.

Hill, R., 1952, "The Elastic Behaviour of a Crystalline Aggregate," *Proceedings of the Physical Society of London,* Vol. A65, pp. 349–354.

Hughes, D. S., and Cook, C. E., Jr., 1953, "The Effect of Pressure on the Reduction of Pore Volume of Consolidated Sanstones," *Geophysics,* Vol. 18, pp. 298–309.

Keskar, N. R., and Chelikowsky, J. R., 1993, "Anomalous elastic behavior in crystalline silica," *Phys. Rev. B,* Vol. 48, No. 22, pp. 16,227–16,233.

Lakes, R., 1987, "Foam Structures with a Negative Poisson's Ratio," *Science,* Vol. 235, pp. 1038–1040.

Downloaded 04 May 2010 to 171.66.16.28. Redistribution subject to ASME license or copyright; see http://www.asme.org/terms/Terms_Use.cfm

Milton, G. W., 1992, "Composite Materials with Poisson's Ratios Close to −1," *Journal of the Mechanics and Physics of Solids,* Vol. 40, No. 5, pp. 1105–1137.

Newman, G. H., 1973, "Pore-Volume Compressibility of Consolidated, Friable, and Unconsolidated Reservoir Rocks under Hydrostatic Loading," *Journal of Petroleum Technology,* Vol. 25, pp. 129–134.

Nur, A., and Byerlee, J. D., 1971, "An Exact Effective Stress Law for Elastic Deformation of Rock with Fluids," *Journal of Geophysical Research,* Vol. 76, No. 26, pp. 6414–6419.

Nye, J. F., 1957, *Physical Properties of Crystals-Their Representation by Tensors and Matrices,* Oxford University Press, Oxford, U.K.

Reuss, A., 1929, "Berechnung der Fliessgrense von Mischkristallen auf Grund der Plastizitatsbedingung fur Einkristalle," *Zeitschrift fur Angewandte Mathematik and Mechanik,* Vol. 9, pp. 49–58.

Rice, J. R., and Cleary, M. P., 1976, "Some Basic Stress Diffusion Solutions for Fluid-Saturated Elastic Porous Media with Compressible Constituents," *Reviews of Geophysics and Space Physics,* Vol. 14, No. 2, pp. 227–241.

Sampath, K., 1982, "A New Method to Measure Pore Volume Compressibility of Sandstones," *Journal of Petroleum Technology,* Vol. 34, No. 6, pp. 1360–1362.

Van der Knaap, W., 1959, "Nonlinear Behavior of Elastic Porous Media," *Society of Petroleum Engineers Transactions, AIME,* Vol. 216, pp. 179–186.

Voigt, W., 1928, *Lehrbuch der Kristallphysik,* Teubner, Leipzig.

Walsh, J. B., Brace, W. F., and England, A. W., 1965, "Effect of Porosity on Compressibility of Glass," *Journal of the American Ceramic Society,* Vol. 48, No. 12, pp. 605–608.

Yeganeh-Haeri, A., Weidner, D. J., and Parise, J. B., 1992, "Elasticity of α-Cristobalite: A Silicon Dioxide with a Negative Poisson's Ratio," *Science,* Vol. 257, pp. 650–652.

Zimmerman, R. W., Somerton, M. H., and King, M. S., 1986, "Compressibility of Porous Rocks," *Journal of Geophysical Research,* Vol. 91, No. B12, pp. 12,765–12,777.

Zisman, W. A., 1933, "Compressibility and Anisotropy of Rocks at or Near the Earth's Surface," *Proceedings of the National Academy of Sciences,* Vol. 19, pp. 666–680.

Downloaded 04 May 2010 to 171.66.16.28. Redistribution subject to ASME license or copyright; see http://www.asme.org/terms/Terms_Use.cfm

Journal of Applied Mechanics

Brief Notes

A Brief Note is a short paper that presents a specific solution of technical interest in mechanics but which does not necessarily contain new general methods or results. A Brief Note should not exceed 1500 words *or equivalent* (a typical one-column figure or table is equivalent to 250 words; a one line equation to 30 words). Brief Notes will be subject to the usual review procedures prior to publication. After approval such Notes will be published as soon as possible. The Notes should be submitted to the Technical Editor of the JOURNAL OF APPLIED MECHANICS. Discussions on the Brief Notes should be addressed to the Editorial Department, ASME, United Engineering Center, 345 East 47th Street, New York, N. Y. 10017, or to the Technical Editor of the JOURNAL OF APPLIED MECHANICS. Discussions on Brief Notes appearing in this issue will be accepted until two months after publication. Readers who need more time to prepare a Discussion should request an extension of the deadline from the Editorial Department.

Anisotrophy of the Vigdergauz Microstructure

Y. Grabovsky[1] and R. V. Kohn[2]

A recent article by Vigdergauz considered two-component, linearly elastic plates. It showed the existence of spatially periodic microstructures producing plates of extremal rigidity. For the microstructures which maximize or minimize the effective bulk modulus, Vigdergauz asserted that the effective behavior was isotropic. We show this is wrong: the effective tensor is in fact anisotropic.

This note is motivated by a recent article of Vigdergauz (1994) concerning composite, linearly elastic plates. The effective behavior of such a plate can be represented by a quadratic form $\langle C_* M, M\rangle$, the energy associated with macroscopic bending moment M. For given ξ, it is natural to seek a microstructure which is elastically extremal in the sense that it minimizes or maximizes $\langle C_*\xi, \xi\rangle$ or $\langle C_*^{-1}\xi, \xi\rangle$. Sections 1-3 of Vigdergauz (1994) address this problem in the setting of plates made from two isotropic materials in fixed proportions. They show that under certain conditions on ξ, there exists an extremal microstructure consisting of a periodic array of properly shaped inclusions of one phase embedded in a matrix of the other. An alternative development of this microstructure and its properties is given in Grabovsky and Kohn (1995).

Vigdergauz also attempts, in Section 4, to evaluate the full effective tensor C_* associated with this extremal periodic microstructure. That calculation is wrong, as one of us has shown elsewhere (Grabovsky, 1995). Here we shall show, by a different method, that the conclusion of Section 4 is also wrong.

The specific issue we address is Vigdergauz's assertion that the effective tensor C_* is isotropic when $\xi = I$; see the displayed formulas between Eqs. (22) and (23) of (Vigdergauz, 1994). We shall show this is not the case. Our strategy is as follows: first we consider the limiting behavior when the inclusions are perfectly rigid and their volume fraction is large; then we consider the more general case of elastic rather than rigid inclusions.

Vigdergauz's presentation concentrates mainly on inclusions which are less rigid than the matrix, but he notes at the end of Section 3 that the opposite case is similar. Our presentation in Grabovsky and Kohn (1995) gives a detailed treatment of both situations. These papers show that when the inclusion phase is more rigid, the "symmetric" Vigdergauz microstructure minimizes $\langle C_*^{-1} I, I\rangle$. Similarly, when the inclusion phase is less rigid, the "symmetric" Vigdergauz microstructure minimizes $\langle C_* I, I\rangle$.

Plates With Rigid Inclusions

When the inclusions are perfectly rigid, $C_* \to 0$ as the volume fraction of inclusions tends to 1. We shall demonstrate the anisotropy of C_* in this case by showing that the two effective shear moduli have different asymptotic behaviors as the matrix volume fraction θ tends to 0:

$$\langle C_* M_1, M_1\rangle \sim \theta^3 \quad \text{for} \quad M_1 = \begin{pmatrix} 0 & 1 \\ 1 & 0 \end{pmatrix} \quad , \qquad (1)$$

whereas

$$\langle C_* M_2, M_2\rangle \sim \theta \quad \text{for} \quad M_2 = \begin{pmatrix} 1 & 0 \\ 0 & -1 \end{pmatrix} . \qquad (2)$$

The essence of the matter is the following observation: As the volume fraction of the matrix phase tends to zero, the symmetric Vigdergauz inclusion consists of an array of nearly square inclusions (see Fig. 1). The matrix phase thus has nearly the geometry of a "square honeycomb."

Estimating the effective behavior of such a microstructure is a fairly standard matter; see, e.g., Gibson et al. (1982). It is convenient to use the variational characterization of C_*:

$$\langle C_* M, M\rangle = \min \int_{\text{matrix}} \langle C_{\text{matrix}} m, m\rangle dx, \qquad (3)$$

in which $m(x)$ ranges over spatially periodic, "statically admissible" bending moments (div div $m = 0$) with average value M. The domain of integration is just the part of the unit cell

[1] Department of Mathematics, Carnegie Mellon University, Pittsburgh, PA 15213.

[2] Courant Institute, New York University, New York, NY 10012.

Contributed by the Applied Mechanics Division of THE AMERICAN SOCIETY OF MECHANICAL ENGINEERS for publication in the ASME JOURNAL OF APPLIED MECHANICS. Manuscript received and accepted by the ASME Applied Mechanics Division, Nov. 30, 1994. Associate Technical Editor: X. Markenscoff.

Copyright © 1995 by ASME

Downloaded 04 May 2010 to 171.66.16.28. Redistribution subject to ASME license or copyright; see http://www.asme.org/terms/Terms_Use.cfm

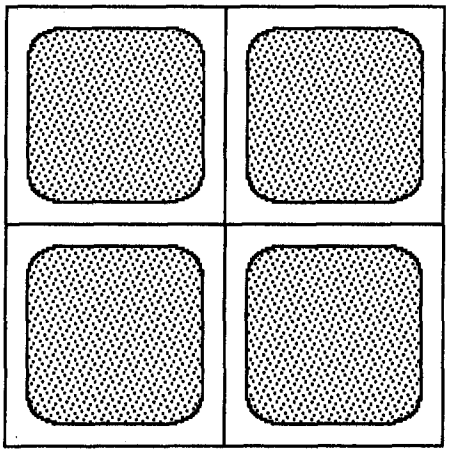


Fig. 1 Four unit cells of the Vigdergauz microstructure, when the volume fraction of the matrix is small. The sides are not actually flat, just nearly so.

occupied by the matrix, because the inclusions, being rigid, can sustain any bending moment without contributing to the energy.

There is a well-known correspondence between plate theory and two-dimensional elasticity, and we find the elastic version of this problem easier to visualize. The correspon dence identifies statically admissible bending moments (div div $m = 0$) with kinematically admissible strain fields ($e_{11,22} + e_{22,11} - 2e_{12,12} = 0$) through the relation

$$e_{11} = m_{22}, \quad e_{22} = m_{11}, \quad e_{12} = -m_{12}.$$

Thus (3) has an alternative interpretation as the effective energy of an elastic membrane perforated by a periodic array of holes. In this setting, the symmetric Vigdergauz microstructure gives a perforated composite which is maximally rigid under hydrostatic loading. Notice that as defined above for plate theory, C_* represents the effective compliance; however in the two-dimensional elastic analogue C_* is instead (equivalent to) the effective rigidity.

In the context of perforated elastic membranes, the justification of (1)-(2) is as follows. As the matrix volume fraction θ tends to zero, the structure resembles the square honeycomb whose period cell is shown in Fig. 2. Such a honeycomb can accommodate macroscopic shear of the type $\left(\begin{smallmatrix} 0 & 1 \\ 1 & 0 \end{smallmatrix}\right)$ by bending its members, so the associated elastic energy is of order θ^3. But the other macroscopic shear $\left(\begin{smallmatrix} 1 & 0 \\ 0 & -1 \end{smallmatrix}\right)$ cannot be accommodated by bending; rather, it induces tensile extension in the horizontal

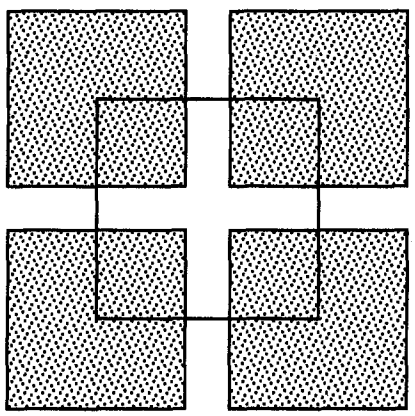


Fig. 2 If we replace the Vigdergauz inclusions by squares then the matrix forms a "square honeycomb." The central box in the figure is its unit cell.

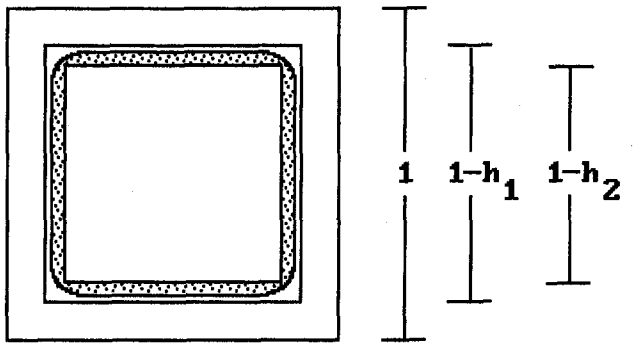


Fig. 3 The inscribed and circumscribed squares determine comparison honeycombs. One has members of thickness h_1 and volume fraction $\theta = 2h_1 - h_1^2$; the other has members of thickness h_2 and volume fraction $\theta = 2h_2 - h_2^2$.

members and tensile compression in the vertical ones. Therefore its elastic energy is of order θ.

For a true square honeycomb the unit cell has members of constant thickness h, and matrix has volume fraction $\theta = 2h - h^2$. For this structure our assertions can easily be proved with full mathematical rigor by constructing suitable test functions for (3) and its dual.

Now, the Vigdergauz microstructure is not exactly a square honeycomb. But it contains one honeycomb (with members of thickness h_1) and is contained in another (with members of thickness h_2). Equivalently, the symmetric Vigdergauz inclusion is contained in a square of side $1 - h_1$, and it contains a square of side $1 - h_2$ (see Fig. 3). *We shall show that h_1 and h_2 are both of order θ.* This implies our assertions (1)-(2), since the effective tensor C_* is monotone with respect to inclusion.

In demonstrating our assertion about h_1 and h_2 we shall actually show somewhat more, namely that

$$h_1 = \tfrac{1}{2}\theta + o(\theta) \tag{4}$$

and

$$h_2 \leq \left(\frac{1}{2} + \frac{1}{\pi}\right)\theta + o(\theta) \tag{5}$$

as $\theta \to 0$. To be sure there is no confusion: (4) means that $\lim_{\theta\to 0} h_1/\theta = \frac{1}{2}$, and (5) means that $\lim_{\theta\to 0} h_2/\theta \leq \frac{1}{2} + 1/\pi$.

Our starting point is formula (6.4) of Grabovsky and Kohn (1995) which gives an explicit expression for the shape of the Vigdergauz inclusion. Specializing that formula to the present context (a perforated elastic membrane with maximal rigidity under hydrostatic loading) gives the following characterization for h_1 and h_2. Let

$$F(x|\mu) = \int_0^x \frac{dt}{\sqrt{(1-t^2)(1-\mu t^2)}}$$

and set

$$K(\mu) = F(1|\mu);$$

given θ, define $m = m(\theta)$ by

$$\frac{K(1-m)}{K(m)} = \frac{\theta}{2-\theta} \tag{6}$$

(so $m \to 1$ as $\theta \to 0$), and set

$$M = \left(\frac{1-m}{m}\right)^2;$$

Downloaded 04 May 2010 to 171.66.16.28. Redistribution subject to ASME license or copyright; see http://www.asme.org/terms/Terms_Use.cfm

then h_1 and h_2 are given explicitly as

$$\frac{1}{2}h_1 = \frac{1}{2} - \frac{2-\theta}{4K(m)}F(\sqrt{1-M}|m) \tag{7}$$

$$\frac{1}{2}h_2 = \frac{1}{2} - \frac{2-\theta}{4K(m)}F(\sqrt{1-M^{1/2}}|m). \tag{8}$$

Remarkably, these formulas do not depend on the Hooke's law of the matrix; this is a special feature of the *symmetric* Vigdergauz inclusion.

We may rewrite (7)-(8), after some elementary manipulation, as

$$h_1 = \frac{\theta}{2} + \frac{2-\theta}{2K(m)}\int_{\sqrt{1-M}}^{1}\frac{dt}{\sqrt{(1-t^2)(1-mt^2)}} \tag{9}$$

$$h_2 = \frac{\theta}{2} + \frac{2-\theta}{2K(m)}\int_{\sqrt{1-M^{1/2}}}^{1}\frac{dt}{\sqrt{(1-t^2)(1-mt^2)}}. \tag{10}$$

We shall estimate separately the factor $1/K(m)$ and the two integrals on the right-hand side of (9)-(10). The function $K(\mu)$ is continuous at $\mu = 0$, and $K(0) = \pi/2$, so it follows from (6) that

$$\frac{1}{K(m)} = \frac{\theta}{\pi} + o(\theta).$$

To estimate the first integral, we observe that $1 - mt^2 \geq 1 - m$ for $0 \leq t \leq 1$, so

$$\int_{\sqrt{1-M}}^{1}\frac{dt}{\sqrt{(1-t^2)(1-mt^2)}} \leq \frac{1}{\sqrt{1-m}}\int_{\sqrt{1-M}}^{1}\frac{dt}{\sqrt{1-t^2}} = \frac{\arccos(\sqrt{1-M})}{\sqrt{1-m}}.$$

The same argument applied to the other integral gives

$$\int_{\sqrt{1-M^{1/2}}}^{1}\frac{dt}{\sqrt{(1-t^2)(1-mt^2)}} \leq \frac{\arccos(\sqrt{1-M^{1/2}})}{\sqrt{1-m}}.$$

It is now an easy matter to deduce (4) and (5). For the former, we use the knowledge that $m \to 1$ and $M \to 0$ as $\theta \to 0$ and the relation $\arccos(\sqrt{1-M}) \approx \sqrt{M}$ to get

$$\left|h_1 - \frac{\theta}{2}\right| \leq C\frac{1}{K(m)}\frac{\sqrt{1-m}}{m} = o(\theta)$$

as $\theta \to 0$. For (5) we argue similarly, using $\arccos(\sqrt{1-M^{1/2}}) \approx M^{1/4}$ to get

$$h_2 - \frac{\theta}{2} \leq \frac{1}{K(m)}\frac{\arccos(\sqrt{1-M^{1/2}})}{\sqrt{1-m}} = \frac{\theta}{\pi} + o(\theta)$$

as $\theta \to 0$. This completes our treatment of plates with rigid inclusions.

Plates With Elastic Inclusions

We turn now to the more general case when the inclusions are elastic rather than rigid. It is clear by continuity that the symmetric Vigdergauz inclusion determines an anisotropic composite when the inclusion phase is nearly rigid. But actually we can say more. The analysis of (Grabovsky and Kohn, 1995) shows that *the shape of the symmetric Vigdergauz inclusion depends only on its volume fraction,* not on the elastic moduli of the component materials, nor even on whether the inclusion phase is more rigid or less rigid. The effective tensor C_* is therefore a (complex) analytic function of the component moduli. It follows that there are only two alternatives: Either C_* is isotropic for *every* choice of the component moduli, or else it is isotropic at most for *exceptional* choices of component moduli. The first alternative is ruled out by our results about rigid inclusions. Thus the Hooke's law of the symmetric Vigdergauz microstructure is generally anisotropic.

In conclusion: contrary to Vigdergauz's assertion in Section 4 of his 1994 paper, the effective tensor of his microstructure is anisotropic even in the symmetric case $\xi = I$.

Acknowledgment

The work of YG was supported by ARO and NSF through grants to the Center for Nonlinear Analysis at CMU; that of RVK was supported by ARO contract DAAL03-92-G-0011 and NSF grants DMS-9402763 and DMS-9404376.

References

Gibson, L. J., Ashby, M. F., Schajer, G. S., and Robertson, C. I., 1982, "The mechanics of two-dimensional cellular materials," *Proceedings of the Royal Society of London, A,* Vol. 382, pp. 25–42.

Grabovsky, Y., 1995, discussion, ASME JOURNAL OF APPLIED MECHANICS, Vol. 62, p. 550.

Grabovsky, Y., and Kohn, R. V., 1995, "Microstructures minimizing the energy of a two phase elastic composite in two space dimensions. II: the Vigdergauz microstructure," *Journal of the Mechanics and Physics of Solids,* Vol. 43, pp. 949–972.

Vigdergauz, S., 1994, "Two-Dimensional Grained Composites of Extreme Rigidity," ASME JOURNAL OF APPLIED MECHANICS, Vol. 61, pp. 390–394.

Radially Inhomogeneous Sheets Under Stress

H. O. K. Kirchner[3]

Consider a thin sheet, where Young's modulus $E(r)$, Poisson's ratio $\nu(r)$ and the thickness $h(r)$ are functions of the radius r. In particular we will consider a hole of radius $r = \rho$, or rigid inclusion of radius $r = \rho$ inserted at the center. Modern manufacturing techniques allow tailoring of the quantity that matters, the product of stiffness and thickness, $h(r)E(r)$: Both can be continuous functions of r, rather than discontinuous ones as for inserted rings or reinforcing beads. The situation most easily visualized is a hole (or inserted pin) in a sail, or the textile of an inflatable structure, which is reinforced by additional material or glued together from different layers. The biaxial situation of tailored nonuniform sheets (Budiansky et al., 1993) belongs to this class of problems.

Our approach exploits the duality between displacement $\mathbf{u}$ and first-order stress function vector $\mathbf{\Phi}$ familar from anisotropic elasticity (Stroh, 1958; Malen, 1971; Kirchner, 1987, 1989). It does not cast the problem in terms of second-order differential equations for the displacement (equilibrium) or strains (compatibility). Instead it derives a first-order differential equation of twice the dimension of the second-order systems.

In a polar coordinate system r, θ Hooke's law between the strains e_r, e_θ, $e_{r\theta}$ and the stresses s_r, s_θ, $s_{r\theta}$ reads

$$e_r = (s_r - \nu s_\theta)/Eh \tag{1a}$$

[3] Professor of Multimaterials, Institut de Sciences des Materiaux, Université Paris-Sud, F-91405 Orsay, France.

Contributed by the Applied Mechanics Division of THE AMERICAN SOCIETY OF MECHANICAL ENGINEERS for publication in the ASME JOURNAL OF APPLIED MECHANICS. Manuscript received and accepted by the ASME Applied Mechanics Division, Aug. 15, 1994. Associate Technical Editor: X. Markenscoff.

Downloaded 04 May 2010 to 171.66.16.28. Redistribution subject to ASME license or copyright; see http://www.asme.org/terms/Terms_Use.cfm

then h_1 and h_2 are given explicitly as

$$\frac{1}{2}h_1 = \frac{1}{2} - \frac{2-\theta}{4K(m)}F(\sqrt{1-M}|m) \tag{7}$$

$$\frac{1}{2}h_2 = \frac{1}{2} - \frac{2-\theta}{4K(m)}F(\sqrt{1-M^{1/2}}|m). \tag{8}$$

Remarkably, these formulas do not depend on the Hooke's law of the matrix; this is a special feature of the *symmetric* Vigdergauz inclusion.

We may rewrite (7)-(8), after some elementary manipulation, as

$$h_1 = \frac{\theta}{2} + \frac{2-\theta}{2K(m)}\int_{\sqrt{1-M}}^{1}\frac{dt}{\sqrt{(1-t^2)(1-mt^2)}} \tag{9}$$

$$h_2 = \frac{\theta}{2} + \frac{2-\theta}{2K(m)}\int_{\sqrt{1-M^{1/2}}}^{1}\frac{dt}{\sqrt{(1-t^2)(1-mt^2)}}. \tag{10}$$

We shall estimate separately the factor $1/K(m)$ and the two integrals on the right-hand side of (9)-(10). The function $K(\mu)$ is continuous at $\mu = 0$, and $K(0) = \pi/2$, so it follows from (6) that

$$\frac{1}{K(m)} = \frac{\theta}{\pi} + o(\theta).$$

To estimate the first integral, we observe that $1 - mt^2 \geq 1 - m$ for $0 \leq t \leq 1$, so

$$\int_{\sqrt{1-M}}^{1}\frac{dt}{\sqrt{(1-t^2)(1-mt^2)}} \leq \frac{1}{\sqrt{1-m}}\int_{\sqrt{1-M}}^{1}\frac{dt}{\sqrt{1-t^2}} = \frac{\arccos(\sqrt{1-M})}{\sqrt{1-m}}.$$

The same argument applied to the other integral gives

$$\int_{\sqrt{1-M^{1/2}}}^{1}\frac{dt}{\sqrt{(1-t^2)(1-mt^2)}} \leq \frac{\arccos(\sqrt{1-M^{1/2}})}{\sqrt{1-m}}.$$

It is now an easy matter to deduce (4) and (5). For the former, we use the knowledge that $m \to 1$ and $M \to 0$ as $\theta \to 0$ and the relation $\arccos(\sqrt{1-M}) \approx \sqrt{M}$ to get

$$\left|h_1 - \frac{\theta}{2}\right| \leq C\frac{1}{K(m)}\frac{\sqrt{1-m}}{m} = o(\theta)$$

as $\theta \to 0$. For (5) we argue similarly, using $\arccos(\sqrt{1-M^{1/2}}) \approx M^{1/4}$ to get

$$h_2 - \frac{\theta}{2} \leq \frac{1}{K(m)}\frac{\arccos(\sqrt{1-M^{1/2}})}{\sqrt{1-m}} = \frac{\theta}{\pi} + o(\theta)$$

as $\theta \to 0$. This completes our treatment of plates with rigid inclusions.

Plates With Elastic Inclusions

We turn now to the more general case when the inclusions are elastic rather than rigid. It is clear by continuity that the symmetric Vigdergauz inclusion determines an anisotropic composite when the inclusion phase is nearly rigid. But actually we can say more. The analysis of (Grabovsky and Kohn, 1995) shows that *the shape of the symmetric Vigdergauz inclusion depends only on its volume fraction,* not on the elastic moduli of the component materials, nor even on whether the inclusion phase is more rigid or less rigid. The effective tensor C_* is therefore a (complex) analytic function of the component moduli. It follows that there are only two alternatives: Either C_* is isotropic for *every* choice of the component moduli, or else it is isotropic at most for *exceptional* choices of component moduli. The first alternative is ruled out by our results about rigid inclusions. Thus the Hooke's law of the symmetric Vigdergauz microstructure is generally anisotropic.

In conclusion: contrary to Vigdergauz's assertion in Section 4 of his 1994 paper, the effective tensor of his microstructure is anisotropic even in the symmetric case $\xi = I$.

Acknowledgment

The work of YG was supported by ARO and NSF through grants to the Center for Nonlinear Analysis at CMU; that of RVK was supported by ARO contract DAAL03-92-G-0011 and NSF grants DMS-9402763 and DMS-9404376.

References

Gibson, L. J., Ashby, M. F., Schajer, G. S., and Robertson, C. I., 1982, "The mechanics of two-dimensional cellular materials," *Proceedings of the Royal Society of London, A,* Vol. 382, pp. 25–42.

Grabovsky, Y., 1995, discussion, ASME JOURNAL OF APPLIED MECHANICS, Vol. 62, p. 550.

Grabovsky, Y., and Kohn, R. V., 1995, "Microstructures minimizing the energy of a two phase elastic composite in two space dimensions. II: the Vigdergauz microstructure," *Journal of the Mechanics and Physics of Solids,* Vol. 43, pp. 949–972.

Vigdergauz, S., 1994, "Two-Dimensional Grained Composites of Extreme Rigidity," ASME JOURNAL OF APPLIED MECHANICS, Vol. 61, pp. 390–394.

Radially Inhomogeneous Sheets Under Stress

H. O. K. Kirchner[3]

Consider a thin sheet, where Young's modulus $E(r)$, Poisson's ratio $\nu(r)$ and the thickness $h(r)$ are functions of the radius r. In particular we will consider a hole of radius $r = \rho$, or rigid inclusion of radius $r = \rho$ inserted at the center. Modern manufacturing techniques allow tailoring of the quantity that matters, the product of stiffness and thickness, $h(r)E(r)$: Both can be continuous functions of r, rather than discontinuous ones as for inserted rings or reinforcing beads. The situation most easily visualized is a hole (or inserted pin) in a sail, or the textile of an inflatable structure, which is reinforced by additional material or glued together from different layers. The biaxial situation of tailored nonuniform sheets (Budiansky et al., 1993) belongs to this class of problems.

Our approach exploits the duality between displacement $\mathbf{u}$ and first-order stress function vector Φ familar from anisotropic elasticity (Stroh, 1958; Malen, 1971; Kirchner, 1987, 1989). It does not cast the problem in terms of second-order differential equations for the displacement (equilibrium) or strains (compatibility). Instead it derives a first-order differential equation of twice the dimension of the second-order systems.

In a polar coordinate system r, θ Hooke's law between the strains e_r, e_θ, $e_{r\theta}$ and the stresses s_r, s_θ, $s_{r\theta}$ reads

$$e_r = (s_r - \nu s_\theta)/Eh \tag{1a}$$

[3] Professor of Multimaterials, Institut de Sciences des Materiaux, Université Paris-Sud, F-91405 Orsay, France.

Contributed by the Applied Mechanics Division of THE AMERICAN SOCIETY OF MECHANICAL ENGINEERS for publication in the ASME JOURNAL OF APPLIED MECHANICS. Manuscript received and accepted by the ASME Applied Mechanics Division, Aug. 15, 1994. Associate Technical Editor: X. Markenscoff.

 Copyright © 1995 by ASME

Downloaded 04 May 2010 to 171.66.16.28. Redistribution subject to ASME license or copyright; see http://www.asme.org/terms/Terms_Use.cfm

$$e_\theta = (s_\theta - \nu s_r)/Eh \tag{1b}$$

$$e_{r\theta} = 2(1 + \nu)s_{r\theta}/Eh. \tag{1c}$$

The compatibility condition (Malvern, 1969)

$$2(\partial^2 e_{r\theta}/\partial r\partial\theta)/r - (\partial^2 e_{\theta\theta}/\partial r^2) - (\partial^2 e_{rr}/\partial\theta^2)/r^2 + (\partial e_{rr}/\partial r)/r + 2(\partial e_{r\theta}/\partial\theta)/r^2 - 2(\partial e_{\theta\theta}/\partial r)/r = 0 \tag{2}$$

is satisfied by deriving the strain components from a displacement vector with the radial component $\mathbf{u}_r$ and the tangential component $\mathbf{u}_\theta$

$$e_r = \partial \mathbf{u}_r/\partial r \tag{3a}$$

$$e_\theta = \mathbf{u}_r/r + (\partial \mathbf{u}_\theta/\partial\theta)/r \tag{3b}$$

$$e_{r\theta} = (\partial \mathbf{u}_r/\partial\theta)/r + (\partial \mathbf{u}_\theta/\partial r) - \mathbf{u}_\theta/r. \tag{3c}$$

In an analogous manner the equilibrium equations

$$[\partial(hs_r)/\partial r] + [\partial(hs_{r\theta})/\partial\theta]/r + (hs_r - hs_\theta)/r = 0 \tag{4a}$$

$$[\partial(hs_{r\theta})/\partial r] + [\partial(hs_\theta)/\partial\theta]/r + 2hs_{r\theta}/r = 0 \tag{4b}$$

are satisfied by deriving the stress components from a first-order stress function vector $\mathbf{\Phi}$ with radial component Φ_r and tangential component Φ_θ according to

$$hs_r = -\Phi_r/r + (\partial\Phi_r/\partial\theta)/r \tag{5a}$$

$$hs_\theta = -(\partial\Phi_\theta/\partial_r) \tag{5b}$$

$$hs_{r\theta} = \Phi_r/r - [\partial(r\Phi_r)/\partial r]/r = -\partial\Phi_r/\partial r. \tag{5c}$$

The stress tensor is symmetric, provided that the vector $\mathbf{\Phi}$ is divergence-free

$$-(\partial\Phi_r/\partial r) = -\Phi_r/r + (\partial\Phi_\theta/\partial\theta)/r. \tag{6}$$

If the stresses and strains, expressed in terms of $\mathbf{\Phi}$ and $\mathbf{u}$ and their gradients according to Eqs. (5) and (3) are inserted into Hooke's law (1), and the divergence condition (6) is used, one obtains the following matrix equation for the four-dimensional aggregate $(\mathbf{u}_r, \mathbf{u}_\theta, \mathbf{\Phi}_r, \mathbf{\Phi}_\theta)^t$:

$$\left[rM(r)\frac{\partial}{\partial r} + N(r)\frac{\partial}{\partial\theta} - I\right]\begin{pmatrix}\mathbf{u}_r(r,\theta)\\ \mathbf{u}_\theta(r,\theta)\\ \mathbf{\Phi}_r(r,\theta)\\ \mathbf{\Phi}_\theta(r,\theta)\end{pmatrix} = 0 \tag{7a}$$

with

$$M(r) = \begin{pmatrix}-\nu & 0 & 0 & (\nu^2-1)/Eh\\ 0 & 1 & 2(1+\nu)/Eh & 0\\ 0 & 0 & -1 & 0\\ -Eh & 0 & 0 & \nu\end{pmatrix} \tag{7b}$$

$$N = \begin{pmatrix}0 & -1 & 0 & 0\\ 1 & 0 & 0 & 0\\ 0 & 0 & 0 & -1\\ 0 & 0 & 1 & 0\end{pmatrix}. \tag{7c}$$

Notice that N is r-independent with eigenvalues $+i, +i, -i, -i$. The elastic constants enter (7) through the matrix $M(r)$, but its eigenvalues are simply $+1, +1, -1, -1$. For radial inhomogeneity, the $M(r)$ matrices for two different radii r_1 and r_2 do not commute,

$$M(r_1)M(r_2) \neq M(r_2)M(r_1). \tag{8}$$

Equation (8) can be solved by a series over separation of variables

$$\begin{pmatrix}\mathbf{u}_r(r,\theta)\\ \mathbf{u}_\theta(r,\theta)\\ \mathbf{\Phi}_r(r,\theta)\\ \mathbf{\Phi}_\theta(r,\theta)\end{pmatrix} = \sum_s V^{(s)}(r)f^{(s)}(\theta)\begin{pmatrix}a^{(s)}\\ b^{(s)}\\ c^{(s)}\\ d^{(s)}\end{pmatrix} \tag{9}$$

where $V^{(s)}(r)$ is a matrix and $f^{(s)}(\theta)$ a scalar. The field is excited by source vectors $(a^{(s)}b^{(s)}c^{(s)}d^{(s)})^t$, chosen to satisfy boundary conditions. The sum runs over all values of s that satisfy the closure requirement

$$f^{(s)}(0) = f^{(s)}(2\pi) \tag{10a}$$

or

$$s = in \tag{10b}$$

with n being any integer. Separation of variables gives

$$\frac{df^{(s)}(\theta)}{d\theta}[f^{(s)}(\theta)]^{-1} = -s \tag{11a}$$

and

$$rM(r)\frac{dV^{(s)}(r)}{dr} = V^{(s)}(r)[1 + sN] \tag{11b}$$

with the solutions

$$f^{(s)}(\theta) = e^{-s\theta} \tag{12a}$$

and

$$V^{(s)}(r) = \text{Ordexp}\int_\rho^r [xM(x)]^{-1}[I + sN]dx. \tag{12b}$$

The ordered matrix exponential, already familiar in an elasticity context (Belov, 1993; Belov and Kirchner, 1994; Kirchner, 1987, 1989) is defined by

$$\text{Ordexp}[G(x_1) + G(x_2)] = \exp[G(x_1)]\cdot\exp[G(x_2)] \quad \text{if} \quad x_1 < x_2 \tag{13}$$

if $G(x)$ is a matrix that depends on the scalar x. Because of the noncommutability (8) ordering of the exponential is necessary, the product on the right-hand side of (13) must not be taken in the reverse order. For a hole of radius $r = \rho$ with a free edge one requires $\mathbf{\Phi}(\rho) = 0$. Since according to (12b), $V^{(s)}(\rho) = e^0 = I$, this is satisfied by choosing $c^{(s)} = d^{(s)} = 0$. For a rigid insert of radius $r = \rho$, one requires $\mathbf{u}(\rho) = 0$, which is satisfied by choosing $a^{(s)} = b^{(s)} = 0$.

For the special case of biaxial stress the displacement is purely radial, $\mathbf{u}_\theta = 0$, and the shear stress vanishes, making the stress function vector purely tangential, $\mathbf{\Phi}_r = 0$. There is no θ-dependence. The four-dimensional system (7) reduces to a two-dimensional one,

$$\left[\frac{d}{dr} - \frac{m(r)}{r}\right]\begin{pmatrix}\mathbf{u}_r(r)\\ \mathbf{\Phi}_\theta(r)\end{pmatrix} = 0 \tag{14a}$$

with

$$m(r) = \begin{pmatrix}-\nu & (\nu^2-1)/Eh\\ -Eh & \nu\end{pmatrix} \tag{14b}$$

having the eigenvalues $+1, -1$ and the property

$$m^2 = I. \tag{14c}$$

The solution of the governing differential Eq. (14) is

$$\begin{pmatrix}u_r(r)\\ \Phi_\theta(r)\end{pmatrix} = \text{Ordexp}\int_\rho^r [m(x)/x]dx\begin{pmatrix}a\\ b\end{pmatrix} \tag{15a}$$

Downloaded 04 May 2010 to 171.66.16.28. Redistribution subject to ASME license or copyright; see http://www.asme.org/terms/Terms_Use.cfm

so that

$$\begin{pmatrix} u_r(\rho) \\ \Phi_\theta(\rho) \end{pmatrix} = \begin{pmatrix} a \\ b \end{pmatrix}. \tag{15b}$$

For a hole one chooses $b = 0$, for a rigid insert $a = 0$. The quantity of greatest interest is the ratio of the stresses at the hole and at infinity, $s_\theta(\rho)/s_\theta(\infty)$. Because of (3$a$, b), (5a, b), and (14a), the stress and strain components are directly expressible in terms of displacement and stress function,

$$\begin{pmatrix} \mathbf{u}_r \\ \mathbf{\Phi}_\theta \end{pmatrix} = r\begin{pmatrix} e_\theta \\ -hs_r \end{pmatrix} = mr\begin{pmatrix} e_r \\ -hs_\theta \end{pmatrix}. \tag{16}$$

The values at infinity are controlled by the integral in the ordered exponent. Roughly speaking, because of the x in the denominator of the exponential function in (15), the behavior of $m(r)$ near $r = \rho$ is dominating the behavior of $\mathbf{u}$ and $\mathbf{\Phi}$ at infinity. The stress concentration factor can, therefore, be reduced by increasing Eh near the edge of the hole $r = \rho$. It can even be made one, the so-called neutral hole (Budiansky et al., 1993), or smaller than one, so that the stresses at the hole are smaller than at infinity.

Writing both the identity I as sum and m as linear combinations of the eigenvalues $+1$, -1 of m, we find, because of (14c),

$$I = m^2 = m^4 = \ldots = A + B \tag{17a}$$

$$m = m^3 = m^5 = \ldots = (+1)A + (-1)B \tag{17b}$$

with

$$A = \tfrac{1}{2}\begin{pmatrix} 1 - \nu & (\nu^2 - 1)/Eh \\ -Eh & 1 + \nu \end{pmatrix} \tag{17c}$$

$$B = \tfrac{1}{2}\begin{pmatrix} 1 + \nu & (1 - \nu^2)/Eh \\ Eh & 1 - \nu \end{pmatrix}. \tag{17d}$$

It follows that

$$m^n = (+1)^n A + (-1)^n B \tag{18a}$$

and

$$\mathbf{f(m) = f(+1)A + f(-1)B} \tag{18b}$$

for any matrix function $f(m)$ that can be expanded into a power series. Thus also the matrix exponential e^{m} and with $e^{t} = (r/\rho)$ the scalar (r/ρ) taken to the matrix power m can be expressed that way

$$e^{\mathbf{tm}} = e^{t}A + e^{-t}\mathbf{B} \tag{18c}$$

$$(r/\rho)^{\mathbf{m}} = (r/\rho)^{+1}A + (\mathbf{r/\rho})^{-1}\mathbf{B}. \tag{18d}$$

The solution of the problem of a homogeneous sheet in biaxial tension is well known, here we show how the solution (14) for arbitrary radial inhomogeneity $E(r)$, $\nu(r)$ and radially varying thickness $h(r)$ degenerates to the classical one when E, ν, and h are constant. Now $m(r) = m$ is independent of r, and the ordered matrix exponential becomes an ordinary matrix exponential,

$$\begin{pmatrix} \mathbf{u_r(r)} \\ \mathbf{\Phi_\theta(r)} \end{pmatrix} = \exp\left\{m\int_\zeta^r \frac{dx}{x}\right\}\begin{pmatrix} a \\ b \end{pmatrix} = \exp\{m\ln(r/\rho)\}\begin{pmatrix} a \\ b \end{pmatrix}$$

$$= (r/\rho)^m\begin{pmatrix} a \\ b \end{pmatrix} = [A/2(r/\rho) + B/2(\rho/r)]\begin{pmatrix} a \\ b \end{pmatrix}. \tag{19}$$

For a hole with a free edge at $r = \rho$, $\Phi_\theta(\rho) = 0$ which makes $b = 0$ and there remains only

$$\begin{pmatrix} \mathbf{u_r} \\ \mathbf{\Phi_\theta} \end{pmatrix} = \left\{\begin{pmatrix} 1 - \nu \\ -Eh \end{pmatrix}(r/\rho) + \begin{pmatrix} 1 + \nu \\ Eh \end{pmatrix}(\rho/r)\right\}a \tag{20a}$$

The stress $s_r = P$ at infinity is obtained by choosing the source strength as

$$a = 2\rho P/Eh \tag{20b}$$

Equations (30a) and (30b) together give, according to (5a) the stresses

$$s_r = P[1 - (\rho/r)^2], \quad s_\theta = P[1 + (\rho/r)^2], \tag{20c}$$

which is the classical solution (Sokolnikoff, 1956).

References

Belov, A., 1993, "Scaling regimes and anomalies of wedge disclination stresses in anisotropic rotationally inhomogeneous media," *Phil. Mag.*, Vol. A68, pp. 1215–1231.

Belov, and Kirchner, H. O. K., 1994, "Critical Angles in Bending of Rotationally Inhomogeneous Elastic Wedges," ASME JOURNAL OF APPLIED MECHANICS, in press.

Budiansky, B., Hutchinson, J. W., and Evans, A. G., 1993, "On Neutral Holes in Tailored, Layered Sheets," ASME JOURNAL OF APPLIED MECHANICS, Vol. 60, pp. 1056–1058.

Kirchner, H. O. K., 1987, "Line Defects along the Axis of Rotationally Inhomogeneous Media," *Phil. Mag.*, Vol. A55, pp. 537–542.

Kirchner, H. O. K., 1989, "Elastically Anisotropic Inhomogeneous Media, Part I: A new formalism," *Phil. Mag.*, Vol. B60, pp. 423–432.

Malen, K., 1971, "A Unified Six-Dimensional Treatment of Elastic Green's Functions and Dislocations," *phys. stat. sol. (b)*, Vol. 44, pp. 661–672.

Malvern, L., 1969, *Introduction to the Mechanics of a Continuous Medium*, Prentice-Hall, Englewood Cliffs, NJ, p. 669.

Stroh, A. N., 1958, "Dislocations and Cracks in Anisotropic Elasticity," *Phil. Mag.*, Vol. 7, pp. 625–646.

Sokolnikoff, I. S., 1956, *Mathematical Theory of Elasticity*, McGraw-Hill, New York.

Transient Thermal Stresses in a Multilayered Anisotropic Medium

Tei-Chen Chen,[4,6] Horng-I Jang,[5,6] Ampere A. Tseng[7]

A transient thermoelasticity problem of a multilayered anisotropic medium under the state of generalized plane deformation is considered in this note. The flexibility/stiffness matrix method is adopted here to obtain the complete solution of the entire layered medium by introducing the thermal and mechanical boundary and layer interface conditions in the Fourier and Laplace transform domains. As a numerical illustration, the distributions of transient temperatures and thermal stresses in a laminated anisotropic slab subjected to a uniform surface temperature rise are presented for some stacking sequences of fiber-reinforced layers.

Introduction

The use of fiber-reinforced composite materials has been rapidly increasing in structures for commercial, military, and space

[4] Associate Professor.

[5] Graduate Student.

[6] Department of Mechanical Engineering, National Cheng Kung University, Tainan, Taiwan, R.O.C.

[7] Professor, Department of Mechanical Engineering and Mechanics, Drexel University, Philadelphia, PA, 19104.

Contributed by the Applied Mechanics Division of THE AMERICAN SOCIETY OF MECHANICAL ENGINEERS for publication in the ASME JOURNAL OF APPLIED MECHANICS. Manuscript received and accepted by the ASME Applied Mechanics Division, Feb. 10, 1995. Associate Technical Editor: M. Taya.

Downloaded 04 May 2010 to 171.66.16.28. Redistribution subject to ASME license or copyright; see http://www.asme.org/terms/Terms_Use.cfm

so that

$$\begin{pmatrix} u_r(\rho) \\ \Phi_\theta(\rho) \end{pmatrix} = \begin{pmatrix} a \\ b \end{pmatrix}. \tag{15b}$$

For a hole one chooses $b = 0$, for a rigid insert $a = 0$. The quantity of greatest interest is the ratio of the stresses at the hole and at infinity, $s_\theta(\rho)/s_\theta(\infty)$. Because of (3*a*, *b*), (5*a*, *b*), and (14*a*), the stress and strain components are directly expressible in terms of displacement and stress function,

$$\begin{pmatrix} \mathbf{u}_r \\ \mathbf{\Phi}_\theta \end{pmatrix} = r\begin{pmatrix} e_\theta \\ -hs_r \end{pmatrix} = mr\begin{pmatrix} e_r \\ -hs_\theta \end{pmatrix}. \tag{16}$$

The values at infinity are controlled by the integral in the ordered exponent. Roughly speaking, because of the x in the denominator of the exponential function in (15), the behavior of $m(r)$ near $r = \rho$ is dominating the behavior of $\mathbf{u}$ and $\mathbf{\Phi}$ at infinity. The stress concentration factor can, therefore, be reduced by increasing Eh near the edge of the hole $r = \rho$. It can even be made one, the so-called neutral hole (Budiansky et al., 1993), or smaller than one, so that the stresses at the hole are smaller than at infinity.

Writing both the identity I as sum and m as linear combinations of the eigenvalues $+1$, -1 of m, we find, because of (14*c*),

$$I = m^2 = m^4 = \ldots = A + B \tag{17a}$$

$$m = m^3 = m^5 = \ldots = (+1)A + (-1)B \tag{17b}$$

with

$$A = \tfrac{1}{2}\begin{pmatrix} 1-\nu & (\nu^2-1)/Eh \\ -Eh & 1+\nu \end{pmatrix} \tag{17c}$$

$$B = \tfrac{1}{2}\begin{pmatrix} 1+\nu & (1-\nu^2)/Eh \\ Eh & 1-\nu \end{pmatrix}. \tag{17d}$$

It follows that

$$m^n = (+1)^n A + (-1)^n B \tag{18a}$$

and

$$\mathbf{f(m) = f(+1)A + f(-1)B} \tag{18b}$$

for any matrix function $f(m)$ that can be expanded into a power series. Thus also the matrix exponential e^{tm} and with $e^t = (r/\rho)$ the scalar (r/ρ) taken to the matrix power m can be expressed that way

$$e^{\mathbf{tm}} = e^t A + e^{-t}\mathbf{B} \tag{18c}$$

$$(r/\rho)^{\mathbf{m}} = (r/\rho)^{+1}A + (\mathbf{r/\rho})^{-1}\mathbf{B}. \tag{18d}$$

The solution of the problem of a homogeneous sheet in biaxial tension is well known, here we show how the solution (14) for arbitrary radial inhomogeneity $E(r)$, $\nu(r)$ and radially varying thickness $h(r)$ degenerates to the classical one when E, ν, and h are constant. Now $m(r) = m$ is independent of r, and the ordered matrix exponential becomes an ordinary matrix exponential,

$$\begin{pmatrix} \mathbf{u_r(r)} \\ \mathbf{\Phi_\theta(r)} \end{pmatrix} = \exp\left\{m\int_\zeta^r \frac{dx}{x}\right\}\begin{pmatrix} a \\ b \end{pmatrix} = \exp\{m\ln(r/\rho)\}\begin{pmatrix} a \\ b \end{pmatrix}$$

$$= (r/\rho)^m\begin{pmatrix} a \\ b \end{pmatrix} = [A/2(r/\rho) + B/2(\rho/r)]\begin{pmatrix} a \\ b \end{pmatrix}. \tag{19}$$

For a hole with a free edge at $r = \rho$, $\Phi_\theta(\rho) = 0$ which makes $b = 0$ and there remains only

$$\begin{pmatrix} \mathbf{u_r} \\ \mathbf{\Phi_\theta} \end{pmatrix} = \left\{\begin{pmatrix} 1-\nu \\ -Eh \end{pmatrix}(r/\rho) + \begin{pmatrix} 1+\nu \\ Eh \end{pmatrix}(\rho/r)\right\}a \tag{20a}$$

The stress $s_r = P$ at infinity is obtained by choosing the source strength as

$$a = 2\rho P/Eh \tag{20b}$$

Equations (30*a*) and (30*b*) together give, according to (5*a*) the stresses

$$s_r = P[1 - (\rho/r)^2], \quad s_\theta = P[1 + (\rho/r)^2], \tag{20c}$$

which is the classical solution (Sokolnikoff, 1956).

References

Belov, A., 1993, "Scaling regimes and anomalies of wedge disclination stresses in anisotropic rotationally inhomogeneous media," *Phil. Mag.*, Vol. A68, pp. 1215–1231.

Belov, and Kirchner, H. O. K., 1994, "Critical Angles in Bending of Rotationally Inhomogeneous Elastic Wedges," ASME JOURNAL OF APPLIED MECHANICS, in press.

Budiansky, B., Hutchinson, J. W., and Evans, A. G., 1993, "On Neutral Holes in Tailored, Layered Sheets," ASME JOURNAL OF APPLIED MECHANICS, Vol. 60, pp. 1056–1058.

Kirchner, H. O. K., 1987, "Line Defects along the Axis of Rotationally Inhomogeneous Media," *Phil. Mag.*, Vol. A55, pp. 537–542.

Kirchner, H. O. K., 1989, "Elastically Anisotropic Inhomogeneous Media, Part I: A new formalism," *Phil. Mag.*, Vol. B60, pp. 423–432.

Malen, K., 1971, "A Unified Six-Dimensional Treatment of Elastic Green's Functions and Dislocations," *phys. stat. sol. (b)*, Vol. 44, pp. 661–672.

Malvern, L., 1969, *Introduction to the Mechanics of a Continuous Medium*, Prentice-Hall, Englewood Cliffs, NJ, p. 669.

Stroh, A. N., 1958, "Dislocations and Cracks in Anisotropic Elasticity," *Phil. Mag.*, Vol. 7, pp. 625–646.

Sokolnikoff, I. S., 1956, *Mathematical Theory of Elasticity*, McGraw-Hill, New York.

Transient Thermal Stresses in a Multilayered Anisotropic Medium

Tei-Chen Chen,[4,6] Horng-I Jang,[5,6] Ampere A. Tseng[7]

A transient thermoelasticity problem of a multilayered anisotropic medium under the state of generalized plane deformation is considered in this note. The flexibility/stiffness matrix method is adopted here to obtain the complete solution of the entire layered medium by introducing the thermal and mechanical boundary and layer interface conditions in the Fourier and Laplace transform domains. As a numerical illustration, the distributions of transient temperatures and thermal stresses in a laminated anisotropic slab subjected to a uniform surface temperature rise are presented for some stacking sequences of fiber-reinforced layers.

Introduction

The use of fiber-reinforced composite materials has been rapidly increasing in structures for commercial, military, and space

[4] Associate Professor.

[5] Graduate Student.

[6] Department of Mechanical Engineering, National Cheng Kung University, Tainan, Taiwan, R.O.C.

[7] Professor, Department of Mechanical Engineering and Mechanics, Drexel University, Philadelphia, PA, 19104.

Contributed by the Applied Mechanics Division of THE AMERICAN SOCIETY OF MECHANICAL ENGINEERS for publication in the ASME JOURNAL OF APPLIED MECHANICS. Manuscript received and accepted by the ASME Applied Mechanics Division, Feb. 10, 1995. Associate Technical Editor: M. Taya.

Copyright © 1995 by ASME

Downloaded 04 May 2010 to 171.66.16.28. Redistribution subject to ASME license or copyright; see http://www.asme.org/terms/Terms_Use.cfm

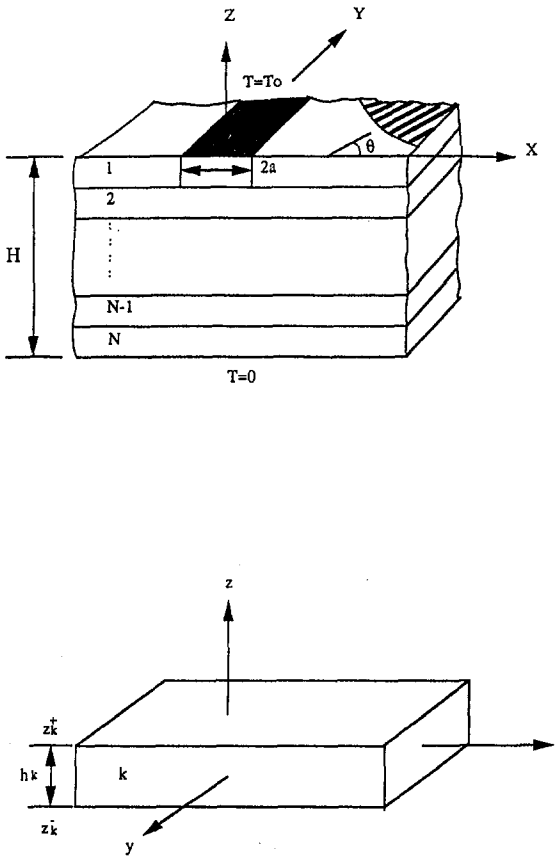


Fig. 1 Configuration and local coordinate for *k*th layer of *N*-layer anisotropic medium

applications over the past few decades. The transient thermal response of composites is an important consideration not only in their fabrication processing but also for their long-term performance. Compared with steady-state thermoelastic problems of multilayer anisotropic medium, a corresponding transient case generally has steep temperature gradient or stress distributions. Therefore, finer mesh arrangement shall be provided to accurately predict the transient behaviors. Consequently, an excessive amount of memory storage and computation time may be required to treat the transient problem either by finite element or finite difference method. Therefore, some existing analytical approaches may be more appropriate to treat this kind of transient problem with simple and regular geometry from viewpoints of both physical interpretation and saving computer time. The flexibility/stiffness matrix method is one of the efficient approaches. Choi and Thangjitham (1991, 1992) studied the steady-state thermoelasticity problem and obtained the distributions of temperature and thermal stresses in a laminated anisotropic slab subjected to a uniform surface temperature rise by this method. The objective of this study is to further extend the flexibility/stiffness method to the transient thermoelasticity problem of a multilayered anisotropic medium. As an illustrated example, the transient thermoelastic response of a multilayered fiber-reinforced slab subjected to a uniform surface temperature rise is examined for some stacking sequences.

Analysis

A layered slab (Fig. 1) composed of N fiber-reinforced layers is considered in this study. For the off-axis monoclinic layers with planes of material symmetry normal to the z-axis, the temperature field satisfies the transient-state heat conduction equation

$$\tilde{k}_{11}\frac{\partial^2 T}{\partial x^2} + \tilde{k}_{33}\frac{\partial^2 T}{\partial z^2} = \rho c\frac{\partial T}{\partial t} \tag{1}$$

where $\tilde{k}_{ij}$, $i,j = 1, 2, 3$, are the coefficients of thermal conductivity in the structural coordinates of the medium; ρ is the density; and c is the specific heat (Fig. 1).

To solve the heat conduction equation (1) and thermoelasticity equations, the Fourier and Laplace transforms are applied over the variables x and t. The transform pairs for an arbitrary function $g(x, t)$ are defined as

$$\bar{g}(s, t) = \int_{-\infty}^{\infty} g(x, t)e^{isx}dx,$$

$$g(x, t) = \frac{1}{2\pi}\int_{-\infty}^{\infty} \bar{g}(s, t)e^{-isx}ds \tag{2a}$$

$$\bar{g}^*(s, p) = \int_0^{\infty} \bar{g}(s, t)e^{-pt}dt,$$

$$\bar{g}(s, t) = \frac{1}{2\pi i}\int_{v-i\infty}^{v+i\infty} \bar{g}^*(s, p)e^{pt}dp \tag{2b}$$

where an overbar denotes the Fourier transformed quantity, a superscript * denotes the Laplace transformed quantity; and s and p are the Fourier and Laplace transform parameters, respectively.

Under the conditions that the field variables and their first derivatives with respect to x vanish as $x \to \pm\infty$ as well as that the initial value is zero, the heat conduction Eq. (1) is readily solved to give the temperature field, $\bar{T}^*(s, z, p)$, in the transform domain as

$$\bar{T}^*(s, z, p) = H_1 \cosh(\kappa z) + H_2 \sinh(\kappa z) \tag{3}$$

where $H_j(s, p)$, $j = 1, 2$, are the unknown constants to be evaluated from the proper boundary conditions and $\kappa = s\sqrt{(\rho cp/s^2 + \tilde{k}_{11})/\tilde{k}_{33}}$. It is noted that the variables s and p in the above equation are regarded as parameters. When the Laplace tranform parameter $p = 0$, then $\kappa = s\sqrt{\tilde{k}_{11}/\tilde{k}_{33}}$, and this case represents the steady-state condition.

The detailed formulation of matrix equations and solution procedures in the transform domain as well as the formulations of flexibility/stiffness matrix equations for heat conduction/thermal stress analysis are similar to the steady-state problem and can be found in the literature (Thangjitham and Choi, 1991). Finally, the inter and intralaminar temperature, displacements, and stresses within the medium shall be calculated by taking the inverse Fourier and Laplace transforms. In this note, the inversion integral of Laplace transform Eq. (2b) is numerically carried out by Fourier series expansion developed by Durbin (1973).

Numerical Examples and Discussions

In order to demonstrate the accuracy of this method and make comparison between the steady-state and the transient solutions, the same numerical example analyzed in previous literature (Thangjithamis and Choi, 1991) is enumerated again in this article. The same thermal and elastic properties, as given in literature (Thangjithamis and Choi, 1991), are adopted for our numerical calculation in order to demonstrate the transient effects. The values of density and the specific heat are

$$\rho = 1.44 \times 10^3 \text{ kg/m}^3, \quad c = 1.76 \times 10^3 \text{ J/kg}\cdot\text{K}.$$

The gross properties in the real structural coordinates for a given fiber orientation θ of the layer can be determined by tensor transformation equations.

Downloaded 04 May 2010 to 171.66.16.28. Redistribution subject to ASME license or copyright; see http://www.asme.org/terms/Terms_Use.cfm

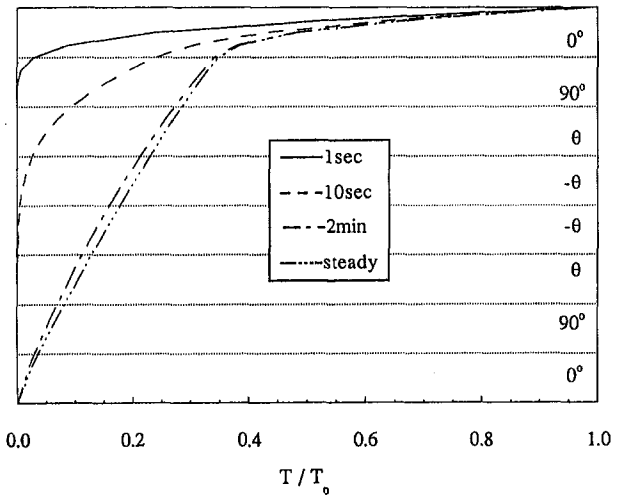


Fig. 2 Transient temperature distribution for $\theta = 90$ deg

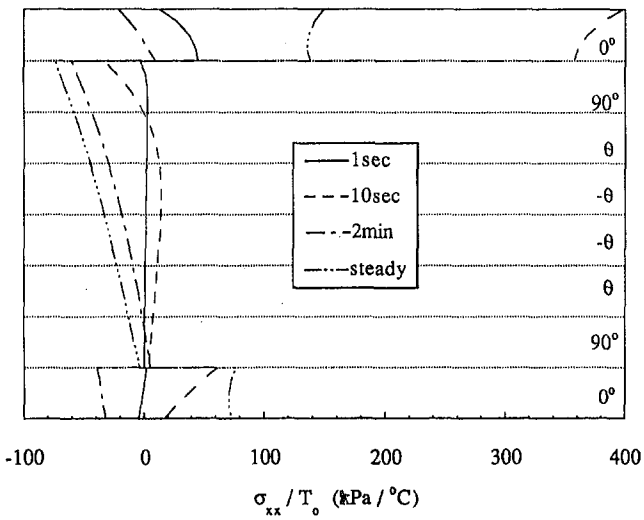


Fig. 3 Transient thermal stress σ_{xx} distribution for $\theta = 90$ deg

Eight layered composite slab with same layer thickness $h_i = 1.25$ mm, $i = 1, 2, \ldots, 8$, is considered in this study. Figures 2–3 show the transient distributions of temperature, T, and the stress, σ_{xx}, through the thickness at $x = 0$ with fiber angle $\theta = 90$ deg, respectively. It can be seen the maximum temperature gradient of transient case is always higher than that of the corresponding steady-state case. Moreover, all the steady-state solutions shown here, which are the special case of the present study, agree completely with the results shown in literature (Thangjithamis and Choi, 1991). By the way, the computation time was around one minute for each case of steady-state and 20 minutes for each case of transient state by using a personal computer with a 486-33 processor.

Acknowledgments

This work was supported by the National Science Council of Taiwan, R.O.C. (Grant No. NSC 84-2212-E006-029).

References

Choi, H. J., and Thangjitham, S., 1992, "Thermal Induced Local Effects in Laminated Composite," *Journal of Thermal Stresses,* Vol. 15, pp. 311–327.

Dubin, F., 1974, "Numerical Inversion of Laplace Transform: An Efficient Improvement to Dubner and Abate's method," *Comput. J.* Vol. 17, pp. 371–376.

Thangjitham, S., and Choi, H. J., 1991, "Thermal Stresses in a Multilayered Anisotropic Medium," ASME JOURNAL OF APPLIED MECHANICS, Vol. 58, pp. 1021–1027.

Downloaded 04 May 2010 to 171.66.16.28. Redistribution subject to ASME license or copyright; see http://www.asme.org/terms/Terms_Use.cfm